Lehrstuhl für Experimentalphysik V
Universität Augsburg

Relationship between composition, crystal structure, and physical properties in perovskite-related ruthenates

Dipl.-Phys. Stefan Riegg

aus Landsberg am Lech (Bayern)

Augsburg 2013

Erstgutachter: Prof. Dr. Alois Loidl

Zweitgutachter: Prof. Dr. Armin Reller

Tag der Einreichung: 29. November 2013

Tag der mündlichen Prüfung: 30. Januar 2014

*" **Everything starts somewhere, although many physicists disagree.** "*

taken from Terry Pratchett's "*Hogfather*"

Contents

1. Introduction

As an example of transition-metal oxides, perovskites and perovskite-related oxides show a versatile variety of physical properties. These are, for example, ferroelectricity [Bha00, Auc97], piezoelectricity [Dam05], magnetic ordering [Dag01], heavy-fermion behavior [Bue10], and superconductivity [Fi97, Ima98]. In addition, they commonly yield complex phase diagrams emerging from electronic correlations [Dag05]. Perovskites and perovskite-related oxides are therefore highly interesting for scientific studies with the goal of discovery of new compounds yielding interesting properties for application with prospects of, for example, improved performance as well as reduced size of the electronic component or increased energy efficiency. This could, on the one hand, improve the quality for application and, on the other hand, it provides the possibility to substitute already used materials containing rare or environmentally problematic elements by alternative ones to comply with the law or due to resource-strategy issues.

To explore new and exotic electornic properties and to be able to describe their physics in detail, usually new compounds are required. The substitution of one or more elements of the perovskites with the general sum formula ABX_3 is one way to influence the physical properties. Another way is to transform the three-dimensional (3D) perovskite structure to related 2D or even 1D structures composed of layers or chains, respectively. By this the interatomic exchange interactions are strongly affected and the lower dimensionality is known to be responsible for unusual magnetic-ordering phenomena. Hence, a close relationship between crystal structure and physical properties can be observed by slight changes of bond lengths and angles, resulting in a variation of exchange interactions between the ions, which then triggers the occurrence of a plethora of magnetic-ordering phenomena.

The cubic perovskite crystal structure can be described as cubic close packing of A and X ions with B ions occupying one quarter of the octahedral sites. This increases stability of the close packing against displacement. In Fig. 1.1 the ideal cubic perovskite structure is depicted. The unit cell is marked by solid lines in the lower left corner. In the general sum formula of perovskites the A-site cations are typically large alkali metals, alkaline earths, and lanthanides. On the B-site usually the smaller $3d$ or $4d$ (or even $5d$) transition-metals are found, which are known to provide flexibility of their oxidation state. This is also a utile property, since the size of the ions depends on their valence. On the other hand, different configurations of the electrons in the d orbitals, which are split into typically two e_g and three t_{2g} states in the octahedral crystal field, can lead to deformations of the local coordination. This is a result of Hund's rules and the Pauli-repulsion and is described as Jahn-Teller activity [Jah37]. The X-site is occupied by large anions, which are typically fluorine, nitrogen, or for this work oxygen with formal oxidation states of minus one, three, or two, respectively. Also chlorine is a candidate for the X-site, but due to its size it usually
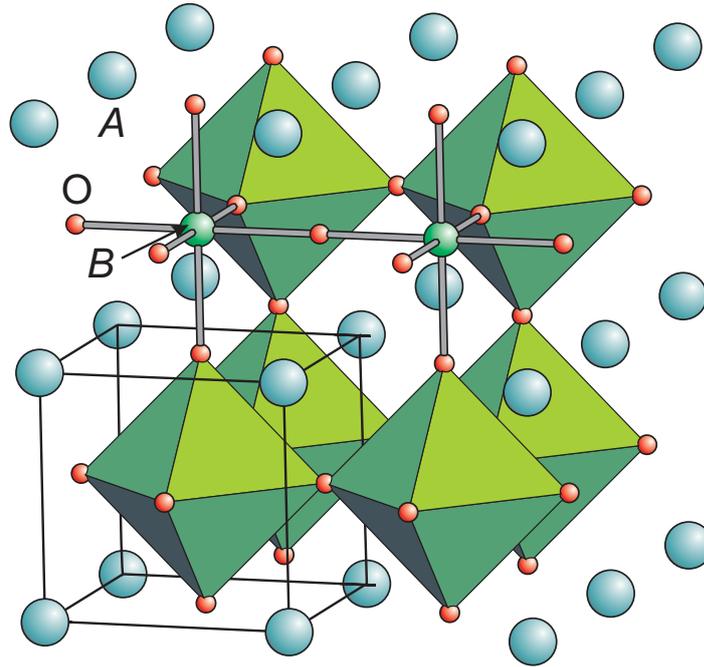
Figure 1.1.: Crystal structure of the ideal perovskite ABO$_3$. Solid lines in the lower left mark the unit cell. An alternative description of the unit cell where the B-sites are located on the corners is obtained by a shift of the origin by 1/2 1/2 1/2 of the shown cell. The A-site ions are represented by turquoise spheres and the oxygen ions by red spheres. The B-site ions are drawn as green spheres and the corresponding BO$_6$ octahedra are also colored green. It has to remarked that the size of the drawn spheres does not reflect the real relation between the ionic radii. In the front top row the octahedral coordination is shown in more detail by grey B–O bonds.

leads to layered structures.

Although the crystal structure appears to be very rigid due to its stability, a certain flexibility is possible by rotating/tilting of the BO$_6$-octahedra. This effect depends strongly on the geometric relation of the ionic radii forming the structure, which was described by Goldschmidt [Gol26] as the ratio $t = (r_A + r_O) / \sqrt{2}(r_B + r_O)$. This ratio is close to unity for ideal cubic perovskites (e.g. SrTiO$_3$). When small A-site cations are incorporated ($t < 1$), the tensional stress leads to rotations and tiltings [Woo97a, Woo97b] of the octahedra (e.g. CaTiO$_3$). For $t > 1$ deformations of the octahedra are found according to Ref. [Jah37] (e.g. BaTiO$_3$). The deviations of bond lengths and angles from the original 180° B–O–B geometry (as shown in Fig. 1.1) as well as a varying number of valence electrons strongly influence exchange interactions.

Besides the (distorted) perovskites other crystal structures containing perovskite-like building blocks are known for their versatile physical properties. Especially layered compounds belonging to the Ruddlesden-Popper phases [Rud57, Rud58] or the [110]-phases [Lic01] show a strong dependence on distortions in the layers as well as on their thicknesses. Commonly a strong anisotropy of properties parallel and perpendicular to the layering is observed.

The physical effects observed for perovskite materials are typically a result of the interaction

between neighboring *B*-site cations since they possess (unpaired) *d* electrons in the valence shell in contrast to the *A*-site ions. These have either empty valence states like the alkali metals and the alkaline earths or, in the case of the rare-earth metals, energetically low lying *f* electrons. For this reason, and also because of the larger interatomic distances, the interaction of these ions with nearest neighbors is rather small, although they partly possess large magnetic moments (e.g. Gd and Dy). Concerning the *B*-site cations, a vast number of studies has been performed on the 3*d* metals, clearly outnumbering the investigations of compounds with 4*d* and 5*d* elements. However, due to their larger and more diffuse 4*d* and 5*d* orbitals deviating electric conductivities and changed magnetic interactions can be expected.

Especially ruthenium is a very interesting 4*d* element in the focus of the studies presented in this work. In ternary oxides Ru is found in three different oxidation states 3+, 4+, and 5+ and the corresponding ionic radii are comparable to the 3*d* elements, which easily allows substitutions. Ruthenates show metallic conductivity or semiconducting behavior depending on the varying itinerant or localized character of the 4*d* electrons in its oxides [Cav04]. Upon substitution the localization of electrons can be influenced and often result in electronic and/or magnetic phase transitions. Furthermore, substitutions with 5*d*- or 3*d*-ions offer the possibility to generate new interactions. The flexible valence of ruthenium helps to balance the charge of the substituent. Ti and Mn are good candidates to achieve new properties by substitution because of their similarity in size and oxidation state. For instance, superconductivity in Sr_2RuO_4 can be suppressed by replacing a small fraction of Ru by Ti [Mae94, Puc02]. On the other hand, some manganese substituted ruthenates show spin-glass behavior at low temperature and, moreover, a magnetoresistance effect is frequently observed, which can be used for data storage systems [Dag01].

To study of the relationship between composition, crystal structure, and physical properties, in this work two rather scarcely investigated compounds were chosen, which both possess perovskite related structures. The first one is La_2RuO_5 with a layered structure related to the [110]-phases [Bou03, Kha02]. The second system is of the $ACu_3B_4O_{12}$-type with a $2 \times 2 \times 2$ perovskite superstructure [Des67]. Both ruthenium-containing systems exhibit interesting and up to now rarely studied magnetic properties due to interactions of the 4*d* electronic states and resulting electronic correlations.

La_2RuO_5 has a unique crystal structure with alternating perovskite-related $LaRuO_4$- and LaO-layers [Bou03]. At room temperature a Curie-Weiss paramagnetic behavior of localized Ru spin moments is found together with a small band gap of roughly 0.15 eV characteristic for a narrow-gap semiconductor [Kha02]. At approximately 160 K a phase transition is observed, which affects structure, magnetic properties, and electrical conductivity. The low-temperature magnetic susceptibility drops to very small values and is almost temperature independent indicating the possible opening of a spin-gap as a result of an orbital-ordering process. This unusual low-temperature phase as well as the phase transition deserve a closer look and are therefore studied in detail in the course of this work.

Substitutions in La_2RuO_5 are expected to influence this magneto-structural transition either by local distortions of the crystal structure or by additional magnetic interactions. As mentioned previously, some of the rare-earth ions carry large magnetic moments, which may affect the dimer-

ization transition. Probably more effective are substitutions with $3d$ transition-metal cations, since they directly replace the ruthenium ions in the ordering network. Especially the redox-stable Ti^{4+} with its non-magnetic $3d^0$ configuration is suitable to substitute Ru^{4+} due to its comparable ionic radius. Furthermore, Mn is a good candidate for the partial replacement of Ru, because of its similar size. In addition, Mn is very flexible with respect to possible oxidation states. Depending on these, Mn-ions possess different magnetic moments that can lead to various magnetic exchange interactions and, hence, possible new magnetic phase transitions. Results of the systematic substitution with rare-earth elements, Ti, and Mn are documented in this work.

Oxides of the $ACu_3B_4O_{12}$-structure type are known for $B = $ tetravalent Ti, Ru, Fe, Mn, Ge, Ir, Pt, and pentavalent Ta, Nb, Sb [Vas07, Yam08, Lon09, Och13]. $CaCu_3Ti_4O_{12}$ has gained considerable interest because of its dielectric properties [Sub00, Sub02, Kro10]. The replacement of Ti by Ru leads to a complete solid-solution series for La, Pr, and Nd on the A-site, which affects the magnetic ordering and electronic structure. The pure titanates are insulators with colossal dielectric constants in a broad frequency and temperature range, whereas the ruthenates are heavy-fermion metals. This outstandig variety of properties in one solid-solution series raises the question of emerging phase transitions depending on the substitution level. In combination with the valence evolution of Ru and Cu it was possible to propose a detailed phase diagram of the investigated physical properties.

In this work different synthesis approaches are shown because many of the introduced compounds cannot be prepared by classical solid-state reactions. The crystal structures of the various samples are investigated in detail by x-ray and neutron diffraction techniques, as well as by x-ray absorption spectroscopy. The oxidation states of the redox-active ions as well as the chemical composition of the samples are determined. The observed structural changes are linked with the physical properties and especially become evident by magnetization and specific-heat measurements. For the investigated systems the experimental findings are compared to modelled electronic band structures. Starting from *ab-initio* density-functional theory (DFT) many of the measured properties can be explained.

The thesis starts with a chapter describing the applied methods for synthesis and structural characterization as well as the interpretation of the investigated physical properties (Chapter 2). This chapter is followed by a short introduction to the band-structure calculations using DFT and a description of the used FPLO-code package (Chapter 3). The studies of the magneto-structural transition in La_2RuO_5 are given in Chapter 4 including investigations under high pressure and with dielectric spectroscopy. In Chapter 5 the influence of different substitutions on the physical properties of La_2RuO_5 is reported. This chapter is divided according to the three systematic substitution series using rare-earth elements, Ti, and Mn, respectively. In the subsequent chapter 6 the $ACu_3B_4O_{12}$-type solid solutions are described. The first part deals with the structural influence of the A-site substitution on the magnetic and electronic properties of the titanates ($B = $ Ti) and the second part of the chapter is dedicated to the effect of Ru substitution on the electronic structure and magnetic properties giving rise to a rich phase diagram. The results are summarized and concluded in chapter 7.

2. Experimental Methods

In this chapter the experimental methods used for this work are briefly introduced. The synthesis methods applied for the sample preparation of the different compounds are described first. For the powder samples the solid-state synthesis as well as slightly varying soft-chemistry reactions are mentioned. In addition, the growth of single-crystalline samples is outlined. In Tabs. A.1 and A.2 in the appendix the chemicals used for the sample synthesis are listed.

The main part of this chapter introduces the characterization methods concerning the crystal structure and physical properties. Several diffraction techniques using x-rays and neutrons are described in combination with an introduction to the stuctural refinement processing. Furthermore, x-ray absorption spectroscopy (XAS) methods are introduced. Combined with this the determination of the cation valences from XAS data is described and discussed. The measurement techniques for physical properties like magnetism and thermal properties are presented as well as the treatment of the obtained experimental data.

2.1. Sample Preparation

2.1.1. Solid-State Synthesis

In the solid-state synthesis binary metal-oxide and carbonate powders are mixed, well ground, e.g. using agate mortar and pestle, and finally calcined in air at temperatures typically above $1000°C$ in muffle furnaces. The chosen calcination temperature determines the diffusion processes during the reaction (see e.g. Refs. [Wat07, Wes99]), but also strongly influences the morphology of the final product and, hence, the (physical) properties of the sample. The crucible material should be chosen carefully since a reaction between sample material and crucible, or the degeneration of the crucible material at the high temperatures is possible. For this work mainly highly densified Al_2O_3 crucibles are used for the synthesis of polycrystalline samples, while platinum crucibles were utilized for the single-crystal growth. In some cases reactions were carried out under argon gas flow in a tube furnace to ensure inert reaction conditions.

La_2RuO_5 (Chapter 4) and various $Ln Cu_3Ti_{4-x}Ru_xO_{12}$ samples (Chapter 6) were synthesized by classical solid-state reactions. The starting agents were weighed in corresponding molar ratio to receive approximately 2 g of the final material. To avoid errors, excess water and carbonates formed from the binary oxides due to their hygroscopic character had to be removed in advance. For this, the rare-earth oxides and RuO_2 were predried at $900°C$ for 6 hours. It has to be mentioned that during this step Pr_2O_3 reacted to non-hygroscopic Pr_6O_{11}, which was further used for the solid-state reactions. To improve homogeneity, the powders were wet ground under isopropanol,

which was allowed to evaporate after each grinding step.

For the La_2RuO_5 and rare-earth substituted powder samples ($La_{2-x}Ln_xRuO_5$, Ln = Pr, Nd, Sm, Gd, Dy) synthesis La_2O_3, the corresponding rare-earth oxides, and RuO_2 were used as agents. The mixed and ground powders were fired in covered aluminumoxide crucibles in air for at least 96 hours at 1175°C with intermediate regrinding steps each after 48 hours. An x-ray powder diffraction phase analysis was performed after each regrinding step. In contrast to the pure La_2RuO_5 the rare-earth substituted samples were not single phases but exhibited pyrochlores $Ln_2Ru_2O_7$ [Ken96, Yam94] as impurities. Therefore, co-precipitation and soft-chemistry methods described in the subsequent sections were applied to obtain single phase $La_{2-x}Ln_xRuO_5$ samples.

Polycrystalline samples of $LnCu_3Ti_{4-x}Ru_xO_{12}$ were prepared from a mixture of rare-earth oxide, TiO_2, RuO_2, and CuO in corresponding molar ratios to obtain 2 g of the final product. An excess of CuO (roughly 0.3 g per g of final product) was added as self-flux as explained below in more detail. This excess CuO was removed after the calcination using diluted hydrochloric acid (1N) [Ebb02]. The ground mixture was pelletized to avoid a reaction with the crucible material. The pellets were heated in air at between 1000°C and 1040°C for at least 96 hours with intermediate grindings after each 48 hours. The phase purity was checked by x-ray powder diffraction after each (re)grinding step. The required calcination temperature depends on the sample stoichiometry. Pure titanate samples ($x = 0$) were reacted at 1000°C, while Ru containing samples were heated to 1040°C to achieve single phases. The titanate powders exhibit an orange-brownish color, on the other hand, only a small adding of Ru ($x > 0$) turns the color of the sample powders to black.

2.1.2. Co-Precipitation

A co-precipitation route was tested to obtain single-phase polycrystalline La_2RuO_5. Stoichiometric amounts of La-nitrate hydrate and Ru-chloride hydrate (to obtain 0.5 g of La_2RuO_5) were dissolved under stirring in roughly 100 ml deionized water. By adding approximately 2 ml of 25% NH_3 to the solution a brownish precipitate was formed, which was filtered off and dried. This precipitate was calcined at 1175°C for 48 hours in covered aluminiumoxide crucibles in air. Powder x-ray diffraction revealed a mixture of La_2RuO_5 with distinct amounts of LaOCl [Bri83]. The LaOCl forms due to the use of Ru-chloride hydrate as an agent and cannot be removed by further calcination steps or changes of the amount of ammonia added to the solution. Thus, this method was found to be not suitable to obtain single phase (substituted) La_2RuO_5 and was not used for further sample synthesis.

2.1.3. Citrate-Reaction Route

The citrate-reaction route belongs to the soft-chemistry or "chimie douce" methods, which generally allow reactions under milder conditions compared to the solid-state synthesis. The synthesis started with a precursor solution containing the corresponding cations of the final oxide. For this either soluble starting agents like metal nitrates were used or non water-soluble binary metal oxides were dissolved using e.g. HNO_3. The dissolved cations were stabilized by establishing a framework of complexing organic molecules. Generally, citric acid was used for this purpose in

this work. The solutions were heated to remove the solvent until gels from the metal-organic matrix formed. These gels were dried and pyrolysed to remove the organics [Pec67]. Afterwards they were calcined at corresponding temperature to obtain the final oxide material. This method is widely used to obtain transition-metal oxides [Dou89] and the detailed physical and chemical properties of this method are described in Ref. [Bri90]. However, this approach was not reported before to synthesize La_2RuO_5.

For the preparation of polycrystalline $La_{2-x}Ln_xRuO_5$ (Ln = Pr, Nd, Sm, Gd, Dy) [Rie11] stoichiometric amounts of the rare-earth nitrate-hydrates and Ru-acetyle acetonate (Ru-AcAc) were dissolved in approximately 75 ml of ethanol (96%). For each mole of metal cations three moles of citric acid were added as the stabilizing organic fraction. The weights of the starting agents were calculated to obtain 0.75 g of final sample material. For the calculation the water contents of the nitrate-hydrates determined by thermogravimetry using a Q-500 thermobalance (TA-Instruments, Tab. A.2) and the Ru content between 22.4 % and 22.9 % of the Ru-AcAc had to be taken into account. The red solutions were stirred until all agents were solved completely and subsequently heated to roughly 90°C under stirring for four hours until gels formed. The gels were prepyrolysed for three hours at 180°C and afterwards pyrolyzed at 600°C for 12 hours in quartz crucibles. The obtained powder was ground with agate mortar and pestle and calcined in covered aluminumoxide crucibles in air at 1175°C for at least 96 hours with intermediate grindings after each 48 hours. The used calcination temperature is the same as in the solid-state reaction described above, which is rather unusual compared to assumptions described in Ref. [Bri90]. The synthesis was only successful in a narrow temperature range between 1150°C and 1200°C. Below 1150°C a mixture of different lanthanum-ruthenium oxides was present, which finally reacted to $La_{2-x}Ln_xRuO_5$ when heated above 1150°C. Above 1200°C impurities of La_3RuO_7 and pyrochlores were detected, which could not be removed by further calcination at lower temperatures. The synthesis conditions lead to single phase black powders for all rare-earth elements up to certain substitution levels depending on the lanthanide ionic radii. Detailed descriptions of the phase quality are given in Sec. 4.1.1 and Sec. 5.1.1.

The synthesis of manganese substituted $La_2Ru_{1-y}Mn_yO_5$ was similar to the above described reaction [Rie13c]. La-nitrate hydrate, Ru-nitrosyle acetate (Ru-NOAc), and Mn-nitrate hydrate were dissolved in appropriate amounts in roughly 50 ml of deionized water. The amount of the agents were calculated and weighed to obtain 0.5 g of final product. The precursors were heated under stirring to 120°C for four hours until gels formed. The gels were dried, pyrolyzed, and calcined at identical temperatures and for same durations. The phase purity of the obtained black powder samples was also checked intermediately and a maximal substitution level of $y = 0.25$ was found, which is described in more detail in Sec. 5.3.

For the synthesis of the polycrystalline Ti substituted La_2RuO_5 samples a Ti containing precursor had to be prepared [Rie13a]. The preparation route is described in detail in literature [Tad02]. 200 mg of titanium metal powder was dissolved in a mixture of 4 ml 25% NH_3 (Merck) and 18.7 ml H_2O_2 (Merck, not H_3PO_4 stabilized) using a water bath cooling. The mixture was stirred until a clear yellowish solution was obtained and the Ti powder was dissolved completely. By adding three moles of citric acid per mole Ti an orange colored citratoperoxotitanate-complex was

stabilized. The excess H_2O_2 was decomposed by boiling the solution for one hour. Afterwards the solution was diluted with deionized water to a volume of 250 ml to obtain a precursor with a defined Ti-concentration. This precursor was added to aquaeous solutions (50 ml of deionized water) of corresponding molar amounts of La-nitrate hydrate and Ru-NOAc to obtain 0.5 g of the final compounds. Citric acid was added to the precursors in a molar amount of three moles per mole metal cations. The solutions were heated under stirring at 150°C for three hours to remove the excess water until gels formed. The pyrolysis and calcination steps were the same as described above for the rare-earth and manganese substituted compounds. In addition to the solely titanium substitution a combination of simultaneous Ti and Pr substitution was performed by partly replacing La-nitrate hydrate by Pr-nitrate hydrate similar to the rare-earth substitution. Maximal substitution levels $y = 0.45$ for Ti and $x = 0.75$ for Pr were achieved for the $La_{2-x}Pr_xRu_{1-y}Ti_yO_5$ samples. The studies of the Ti substituted La_2RuO_5 are described in Sec. 5.2.

All obtained polycrystalline samples are black powders. It has to be mentioned that in the sol-gel reactions a small excess of roughly 2% La-nitratehydrate was required to obtain single-phased samples. This was neccessary due to the not exactly determined deviation of the metal-cation content to the nominal one in either the Ru or rare-earth metal containing agents.

2.1.4. Single-Crystal Growth

Single-crystalline materials bear the advantage of the angular-dependent investigation of physical-properties. Remarkable differences of the properties are usually found in anisotropic, for example layered, crystal structures.

A large number of crystal-growth methods are known for the single-crystal growth and described in detail e.g. in Ref. [Wil88]. For this work two methods were tested. The first one was the floating-zone technique using an optical heating by high-power halogen lamps and elliptical mirrors to locally melt densified rods of polycrystalline material. The rods were moved through the focus area of the mirrors resulting in large crystals of typically several centimeters in length and approximately 5 mm in diameter. A more detailed description of the floating-zone technique is given in Ref. [Goe06]. The floating-zone method unfortunately was not suitable for the Ru containing compounds, though. The rutheniumoxide in the polycrystalline rods thermally evaporated from the melt leading to strong Ru understoichiometries. Using an excess of Ru in this case did not lead to the desired products either.

The second method, which was applied successfully, is the flux growth. The flux itself either is one component of the final compound (self-flux) or a different material which is not incorporated in the crystals. Both flux variations were used for this work. The La_2RuO_5 single crystals were grown from a $BaCl_2$-flux [Kha02] and the $La_{2/3}Cu_3Ti_4O_{12}$ and $SrCu_3Ru_4O_{12}$ crystals from a CuO self-flux [Ebb02], respectively. The molten flux material dissolves the polycrystalline starting material. In the liquid phase little seed crystals of the final material start to grow due to oversaturation during cooling or partial evaporation of the flux. The flux reactions were carried out in non-reactive crucible materials. For this work highly densified aluminumoxide or platinum crucibles were used.

To obtain La_2RuO_5 crystals, the binary oxides La_2O_3 and RuO_2 (both previously dried at 850°C for 6 hours) were mixed in the stoichiometric ratio 0.5325 g : 0.2175 g and ground well using agate mortar and pestle [Rie12a]. 6.25 g $BaCl_2$ was added (also dried in advance at 120°C for several hours to remove excess water). The mixture was reacted in uncovered alumina crucibles in a tube furnace by heating to 1200°C in 4 hours, holding this temperature for 6 hours, and slow cooling down to 950°C with a cooling rate of 3 K/h to get below the melting point of $BaCl_2$. At this temperature the furnace was switched off and allowed to slowly cool down to room temperature. The chosen maximum temperature was high enough to both form La_2RuO_5 seeds and to melt $BaCl_2$ (melting point: 963°C, boiling point: 1560°C [Hay11]) without a too high evaporation rate. The excess $BaCl_2$ was dissolved in deionized water. The black La_2RuO_5 crystals had a plate or hexagonal shape and a size of 0.05×0.05 mm^2 with a thickness of less than 30 microns. They were separated from transparent LaOCl [Bri83] crystals under a microscope. In addition to the La_2RuO_5 crystals also black crystallites of $4H$-$BaRuO_3$ are formed due to the reaction of $BaCl_2$ with RuO_2 [Don65, Hon97]. These cannot be easily distinguished under the microscope, but were identified by magnetic susceptibility measurements and XRD (See Sec. 4.2.2 for more details). The observed La_2RuO_5 crystal shape is caused by a twinning, which is indicated by a fishbone like reflection pattern visible under a grazing angle with the microscope. A detailed description of the La_2RuO_5 single-crystal investigations is found in Sec. 4.1.2.

The $La_{2/3}Cu_3Ti_4O_{12}$ and $SrCu_3Ru_4O_{12}$ crystals were grown using a CuO-flux. Approximately 0.5 g previously reacted powder material was mixed with an equal weight of CuO, ground with agate mortar and pestle and reacted in platinum crucibles. The samples were heated to 1080°C in 3 hours and 40 minutes, this temperature was held for 12 hours followed by a slow cooling to 1000°C with a rate of 2 K/h. A final annealing step of 6 hours at this temperature was used before the furnace was switched off and allowed to cool down to room temperature. The excess CuO was removed utilizing diluted hydrochloric acid and deionized water. The obtained cubic black crystals with a size up to 1 mm^3 are large enough to be investigated by the Laue diffraction method in reflection mode described in more detail in Ref. [Spi05]. A temperature above 1050°C was used since the eutectic CuO/Cu_2O melts at this temperature. Details of the crystal-structure investigations are found in Secs. 6.1.1 and 6.2.1.

2.2. Structural Characterization Using Diffraction Techniques

In the following sections the applied methods for the crystal structure investigation are introduced briefly (detailed descriptions are given in e. g. Refs. [All03, Spi05]). All methods base on the diffraction of waves by the regular lattice of highly crystalline compounds. Since the scale of the ions in the lattice is in the range of Ångstroms (1 Å $= 10^{-10}$ m), the wavelength of the scattered radiation has to be in the same range to obtain diffraction patterns, which simply are projections of the crystal lattice in reciprocal space. The electromagnetic radiation with this wavelength is denoted x-radiation (named by its discoverer W. C. Röntgen). A description of the observed diffraction patterns is possible using the well known Bragg-equation, which is also illustrated in
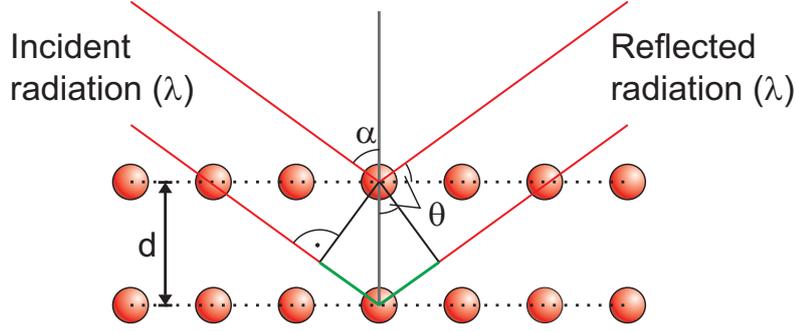
Figure 2.1.: Geometrical conditions of the Bragg equation (Eq. 2.1) for crystal planes of distance d. The angle between the incident (reflected) radiation and the surface is θ.

Fig. 2.1:

$$n \cdot \lambda = 2 \cdot d \cdot \sin \theta \quad (n \in \mathbb{N}) \; . \tag{2.1}$$

While x-rays interact with the electrons, neutrons are scattered at the atomic core providing a different kind of information, which is discussed in the subsequent sections.

2.2.1. X-ray Powder Diffraction

The most frequently used technique to investigate the powder samples in this work was powder x-ray diffraction (XRD) utilizing monochromatic radiation. The incident radiation is scattered and partially reflected at the planes of the crystal lattice of the powder sample. Positive interference conditions are fullfilled for each distance d of the planes applying a corresponding Bragg-angle θ of the incident beam with respect to the surface (Fig. 2.1). In other words, this is achieved when the geometrical (marked green in Fig. 2.1) and the optical path difference ($n \cdot \lambda$) are directly proportional (Eq. 2.1).

From the obtained distances d_{hkl} of the crystal-lattice planes (denoted with Miller indices hkl) the unit-cell parameters and the crystal system (triclinic, monoclinic, orthorhombic, tetragonal, trigonal, hexagonal and cubic) can be determined. For example, for an orthorhombic system ($\alpha = \beta = \gamma = 90°$) the relation between the unit-cell parameters a, b, and c and d_{hkl} is defined as:

$$\frac{1}{d_{hkl}^2} = \frac{h^2}{a^2} + \frac{k^2}{b^2} + \frac{l^2}{c^2} \; . \tag{2.2}$$

Further information about the space-group symmetry of the studied crystal powders is revealed by extinction rules of certain hkl index combinations. Finally, the exact atomic positions in the unit cell reflecting the specific crystal structure determines the structure factor F and in turn (relative) intensities of the diffraction peaks $I = |F|^2$. Detailed information about the solving of the crystal structure from powder-diffraction data as well as corresponding refinement methods are provided partly in the subsequent sections and in detail in literature, e. g. in Refs. [All03, Bor02, Mas07, Spi05].
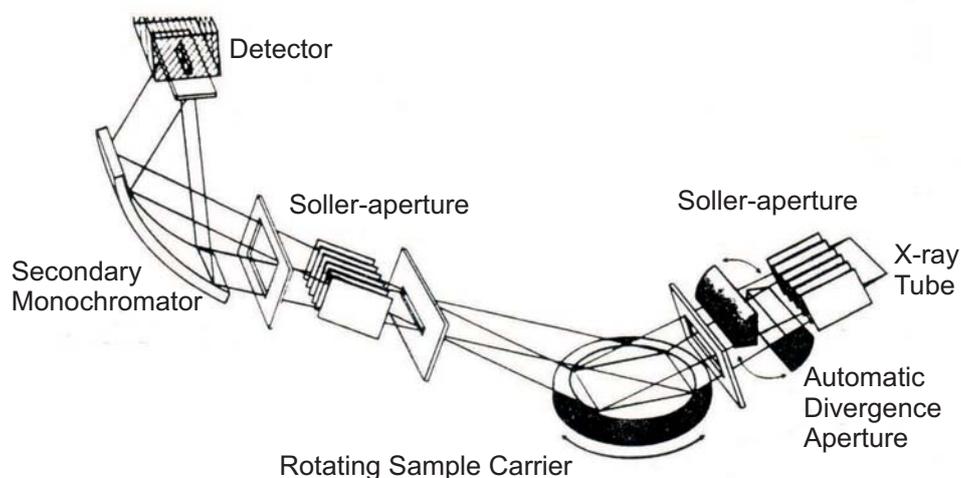
Figure 2.2.: Typical Bragg-Brentano x-ray diffractometer setup [All03]. For a detailed description see text.

The radiation sources used for the structural investigations were x-ray tubes of laboratory diffractometers or the synchrotron DORIS III at HASYLAB (Beamline B2). Most of the diffraction measurements were performed using a Seifert 3003-TT powder diffractometer. The radiation source was an x-ray tube with a copper anode providing Cu-$K_{\alpha1,2}$ radiation for the diffraction measurements. The general Bragg-Brentano setup is shown in Fig. 2.2. The measurements were carried out in reflection on the flat sample surface and the sampleholder was rotated with 1 Hz. Both the x-ray tube and the detector are moved simultaneously in steps $\Delta\theta$ to preserve the θ-θ geometry. The x-rays were collimated by Soller-apertures as well as slit apertures and a secondary monochromator was used to filter all wavelengths else than Cu-$K_{\alpha1,2}$, which was recorded using a scintillation detector.

During this work the Seifert 3003-TT was upgraded with a one-dimensional single-line semiconductor detector (METEOR 1D). An automatically varying entrance slit (i.e. a constant irradiated sample area) was used to enhance the intensities at high diffraction angles. To use the data in the Rietveld analysis, they were transformed to simulate a constant slit setup. With this detector the measuring time could be reduced to 3 h compared to 18 h for the scintilation counter while the signal to noise ratio and the angular resolution were even slightly better.

The diffraction patterns were recorded in an angular range $10° \leq 2\theta \leq 150°$ with a typical step width of $0.02°$ and 10 s integration time per data point for the scintillation counter. With the METEOR 1D detector a step width of $0.01°$ and a counting time of 300 s per data point were used. Applying the scintillation detector the angular range above $2\theta = 80°$ was measured additionally with a step width of $2\theta = 0.05°$ and 20 s per data point to increase the signal to noise ratio.

The x-ray diffraction measurements at low temperature were performed with a Philips X'Pert and a STOE STADI P diffractometer. The Philips X'Pert also operates with Cu-$K_{\alpha1,2}$ radiation
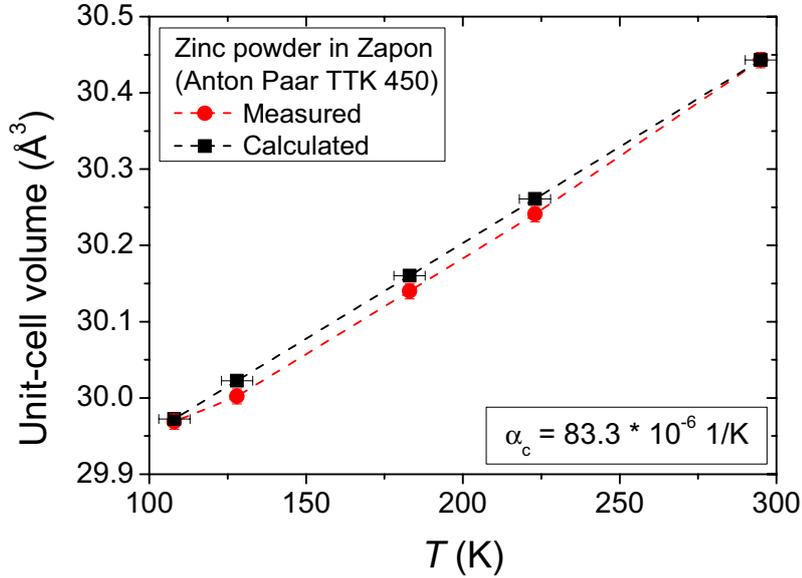
Figure 2.3.: Temperature calibration of the Anton Paar TTK camera. Red circles mark the unit-cell volume of zinc obtained for the setpoint temperature and black squares represent the calculated volumes.

and has Bragg-Brentano geometry with a scintillation detector according to Fig. 2.2. For the temperature variation an Anton Paar TTK450 camera was used. The sample-holder cavity of approximately $14 \times 10 \times 1$ mm^3 was filled with a mixture of the sample and Zapon varnish. The varnish improved the thermal conductivity between sample and sample holder, which was cooled by flowing cold nitrogen gas. The sample temperature was calibrated by studying the thermal change of the unit-cell volume of zinc-metal powder. For this the zinc diffraction pattern was measured at different temperatures and the obtained volume contraction was compared to the tabulated expansion factor $\alpha_c = 83.3 \cdot 10^{-6}$ K^{-1} [Lan64] as shown in Fig. 2.3. An acceptable agreement of measured and calculated values is observed corresponding to a deviation of 5 to 10 K between the set point and the actual sample temperature. The samples were measured at the corrected temperature of 128 K ($\cong -145°$C). The measured angular range was between $10°$ and $110°$ 2θ with a step width of $0.02°$ and an integration time of four seconds for each data point was used.

Additional temperature dependent x-ray diffraction measurements were performed using a STOE STADI P powder diffractometer with Cu-K$_{\alpha1}$ radiation in transmission mode. The sample powders were mixed with a threefold weight of ground charcoal to reduce absorption. The mixtures were filled in capillaries with 0.3 mm diameter. A STOE IP-PDS detector was used in combination with a flowing-nitrogen sample-cooling system (Oxford Cryosystems Cryostream 700) in the

angular range $15° \leq 2\theta \leq 130°$. For these measurements a temperature range between 100 K and 300 K was available. Ten patterns with an integration time of 600 s and a step width of 0.02° each were accumulated for the Rietveld analysis.

Synchrotron radiation x-ray diffraction patterns were recorded at the beamline B2 at HASYLAB [Kna04a] between 10 K and room temperature. The sample powders were filled in quartz capillaries with 0.3 mm diameter and measured in transmission mode using wavelengths of 0.499309 Å or 0.56285 Å (Si 311 monochromator) with a step width of 0.004° or 0.008°, respectively, in an angular range $2° \leq 2\theta \leq 75°$. The data were recorded with the on-site readable position-sensitive image-plate detector called OBI [Kna04b] with an integration time of roughly 15 minutes per scan. The exact values for the wavelength as well as the initial peak-profile function-parameters were obtained from the refinement of a LaB_6 standard.

2.2.2. Neutron Diffraction

Neutrons possess no electrical charge and do not interact with the electron shell of the atoms, but during the neutron-powder diffraction (ND) measurements are scattered at the atomic core. The neutron-scattering length does not change systematically with the atomic number but is characteristic for each nuclide. This offers the possibility to distinguish between neighboring elements in the periodic table or even isotopes of the same element. In addition, due to the similar scattering lengths of heavy and very light atoms - even hydrogen - the determination of the atomic positions of light elements in the unit cell is usually more precise than by the analysis of XRD patterns. On the other hand, absorption and incoherent scattering as well as radioactive activation of the sample are shortcomings of this method. The incoherent scattering increases the background noise and decreases the Bragg intensities thus reducing the signal to noise ratio. For example, hydrogen has a rather large incoherent scattering cross section of 80.27 bn, while the value for deuterium amounts to only 2.05 bn [Sea92].

The wavelength of neutrons is given by the de-Broglie equation according to:

$$\lambda_n(\text{Å}) = \frac{h}{m_n v_n} \approx \frac{0.286}{\sqrt{E_{kin} \text{ (in eV)}}} \quad . \tag{2.3}$$

Neutrons with a wavelength in the order of 1 Å are denoted "thermal" since their kinetic energy corresponds to roughly room temperature[1].

The ND measurements were performed at the PSI (Paul-Scherrer-Institute) in Villigen (Switzerland). The neutrons are generated in the spallation source SINQ (Swiss Spallation Neutron Source) in a continuous process, in which protons are accelerated in cyclotrons and brought to collision with a lead-Zircaloy target [Fis97, Bla09]. A reflector cooled with liquid D_2O moderates the neutrons and directs them to the beamlines through supermirror neutron guides (see left part of Fig. 2.4). With this method a high flux ($> 1 \cdot 10^{14}$ n/cm^2/sec/mA) of thermal neutrons could be provided continuously for the measurement application.

---

[1] $E_{kin}(300 \text{ K}) \approx 0.026$ eV;
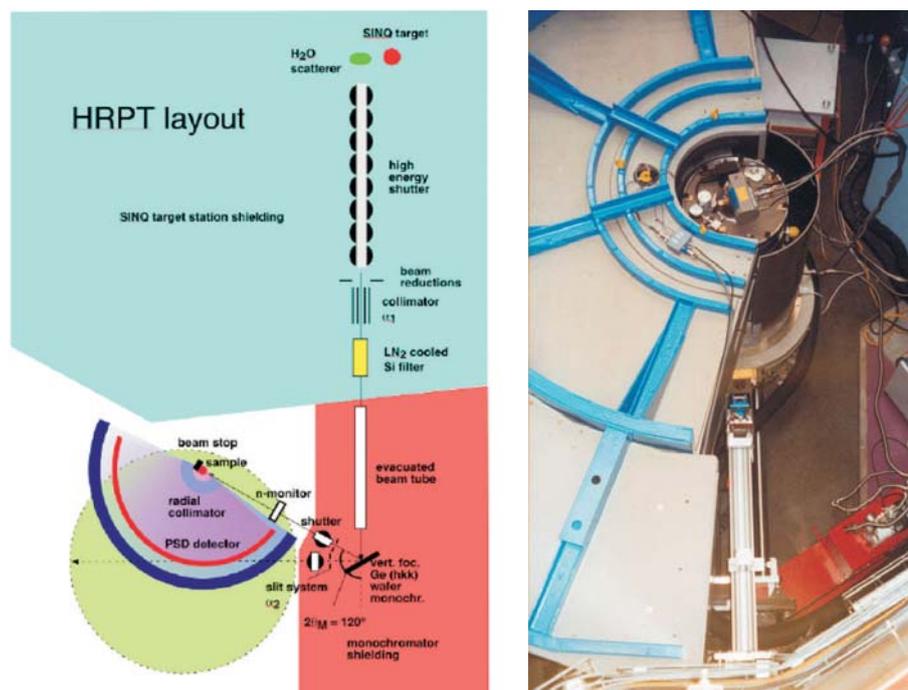
Figure 2.4.: Left: Sketch of the neutron spallation source and the HRPT experimental setup (PSI, Villigen, Switzerland). Right: Top view of the diffractometer showing the neutron waveguide, the sampleholder/cryostat, and the detector (taken from [Pom13]).

The powder diffraction measurements were performed at the HRPT (High Resolution Powder diffractometer for Thermal neutrons) diffractometer [Fis00]. The neutron beam is monochromatized using a Ge crystal monochromator (see right part of Fig. 2.4). The sample holder consists of a He cryostat equipped with an automatic changer for four vanadium sample containers. The available temperature range is $1.5K \leq T \leq 315$ K. The position sensitive He-3 detector (PSD) allows simultaneous measurements in an angular range of roughly $8° \leq 2\theta \leq 165°$ with a resolution of $0.1°$. By using air cushions the detector can be moved to intermediate positions, thus, reducing the step size to $0.05°$. A high intensity or a high resolution mode can be chosen for the measurement with respect to the available maximal resolution $\delta d/d \leq 0.001$ and the adjustable wavelength between 0.94 and 2.96 Å. The measurement parameters used in this work are a step width of $0.05°$, temperatures between 1.5 K and 300 K and a wavelength of 1.494 Å (Ge 533 monochromator) [Pom13].

2.2.3. Rietveld Analysis

In a Rietveld refinement the difference between the measured and calculated diffraction pattern is minimized by a least squares algorithm [Rie67, Rie69]. For the refinement the initial crystal structure has to be close to the final solution, else the method is often not able to find the absolute minimum. The Rietveld method is widely used to solve and refine crystal structures of

compounds, which are not available in single crystalline form. Based on the powerful computers nowadays the Rietveld analysis is implemented in ab-initio crystal-structure solution program-suites for polycrystalline samples. However, it is very complex to obtain the crystal structure from powder-diffraction data without available single-crystal information [All03, Spi05].

For the Rietveld analysis of the x-ray and neutron diffraction patterns the FullProf program suite and the WINPlotR graphical user interface were used [Car93]. Within FullProf even a simultaneous treatment of x-ray and neutron diffraction patterns is possible resulting in a higher accuracy of the structural data.

In the Rietveld method the intensities of all Bragg reflections contributing to one angular value i are summarized to the whole pattern information according to:

$$y_{ci} = S \cdot \sum_{hkl} L_{hkl} \cdot |F_{hkl}|^2 \cdot \Phi(2\theta_i - 2\theta_{hkl}) \cdot P_{hkl} \cdot A \cdot S_r \cdot E + y_{bi} \quad . \tag{2.4}$$

y_{ci} is the counting rate at point i and S is the scaling factor. The sum over all reflection contributions contains the Lorentz-factor L_{hkl} (including polarization correction and a factor regarding the multiplicity), the structure factor F_{hkl}, and the profile function Φ of the Bragg reflection. The width and shape of the profile function is depending on the diffraction angle 2θ. An occasional preferred orientation of the crystallites in the powder called texture effect is treated by a factor P_{hkl}. Other parameters concerning sample and preparation properties are the absorption A, the extinction E, and S_r, which is a measure for the roughness of the sample surface. Finally, the background signal y_{bi} is added to the intensity of each point i.

One important parameter is the choice of the profile function Φ for the refinement. The profile function is depending on the diffractometer, the type of radiation, the detector, and so on. For the refinement process also mathematical requirements have to be taken into account like the differentiability of the function. Thus, analytical functions are used, which are considering the different profiles yielded by x-ray and neutron diffraction. The pseudo-Voigt (pV) profile is generally used for x-ray diffraction patterns, while for the neutron-diffraction patterns a Thomson-Cox-Hastings pseudo-Voigt [Tho87] profile function is often more applicable. The pV profile is defined according to:

$$\Phi_{pV} = \eta \cdot L(x) + (1 - \eta) \cdot G(x) \quad (0 \leq \eta \leq 1). \tag{2.5}$$

Here the abbreviation $x = 2\theta_i - 2\theta_{hkl}$ is used. The mixture of the Lorentzian ($L(x)$) and Gaussian ($G(x)$) profile function is scaled with the mixing factor η, which for the pseudo-Voigt function can be expressed as:

$$\eta = \eta_0 + X \cdot 2\theta \quad . \tag{2.6}$$

For the Thomson-Cox-Hastings pseudo-Voigt profile, on the other hand, η is defined by:

$$\eta = \sum_{i=1}^{3} C_i (\Gamma_L / \Gamma)^i \quad . \tag{2.7}$$

For this profile the mixture parameter is linked to the full width at half maximum (FWHM) of the Lorentzian (Γ_L) and Gaussian (Γ_G) profile functions ($0 \leq C_i \leq 5$), which are calculated by a relation connected to real Voigt functions:

$$\Gamma = \sqrt[5]{\sum_{i=0}^{5} \Gamma_L^i \Gamma_G^{(5-i)}} \quad . \tag{2.8}$$

For the Lorentzian profile the FWHM is defined as:

$$\Gamma_L = X \cdot \tan \theta + Y / \cos \theta \quad . \tag{2.9}$$

The FWHM for the Gaussian profile can be expressed as a power series in $\tan \theta$:

$$\Gamma_G = \sqrt{W + V \cdot \tan \theta + U \cdot \tan \theta^2} \quad . \tag{2.10}$$

Starting values for the directly refineable parameters X, Y and U, V, W are often derived from calibration measurements of standards (e. g. LaB_6). Further refinement parameters are the unit-cell parameters, the fractional atomic coordinates (x_j, y_j, z_j), the (isotropic) displacement parameters B_{iso} and the site occupancies N_j. These parameters are connected to the structure factors according to:

$$F_{hkl} = \sum_{j=1}^{N} N_j \cdot f_j \cdot e^{-B_{iso,j} \cdot \sin^2 \theta / \lambda^2} \cdot e^{i2\pi(hx_j + ky_j + lz_j)} = |F_{hkl}| \cdot e^{i\phi} \quad . \tag{2.11}$$

Deviations from a full occupation are caused, for example, by defects or a changed stoichiometry due to substitution effects and thereby change N_j. In Eq. 2.11 the isotropic atomic displacement factor B_{iso} represents the thermal movement and static disordering of the single atoms. The atomic form factor for each atom f_j is taken from tables in literature. In the powder diffraction measurements the phase information (ϕ on the right side of Eq. 2.11) of the crystal structure cannot be determined since only the absolute values of the structure factor $|F_{hkl}|$ can be extracted from the measured intensities. For this reason a structure solution can become quite difficult and is usually not performed from powder data [All03, Spi05].

The background of the measured pattern is often either approximated by a polynomial function or a number of linearly interpolated points. Furthermore, the 2θ shift caused by a sample height deviating from the ideal geometric position is included. Additional parameters describe asymmetric peaks caused by the instrumentation, amorphous fractions, texture, absorption corrections, and a possible constant 2θ offset denoted zero-shift.

During the refinement the parameter χ^2 is minimized by a least squares algorithm:

$$\chi^2 = \sum_i w_i \cdot (y_i - y_{ci}(\mathbf{a}))^2 \quad . \tag{2.12}$$

Here, $\mathbf{a}$ denotes a vector in the parameter space. The weighting factor w_i is equal to the inverse value of the measured intensities y_i ($w_i = 1/\sigma^2 = 1/y_i$). A more detailed description of the mathematical treatment of the refinement process is given in Ref. [All03].

The progress of the refinement can be monitored by χ^2, which is also denoted "Goodness of fit" factor, or by using the residuals or R-values. Different variants of the R-values are defined, for example, commonly used are the profile residual R_P (Eq. 2.13) and the weighted profile residual R_{wP} (Eq. 2.14), both without additionally regarded background correction.

$$R_P = \frac{\sum_i |y_i - y_{ci}|}{\sum_i y_i} \qquad (2.13)$$

$$R_{wP} = \left(\frac{\sum_i w_i \cdot |y_i - y_{ci}|^2}{\sum_i w_i \cdot y_i} \right)^{1/2} \qquad (2.14)$$

Both χ^2 and R_{wP} are important indicators for the refinement quality. The smaller the residuals become the better is the refinement quality. The obtained values strongly depend on the instrumentation and the measurement parameters. Therefore, it is not possible to define absolute values. Nevertheless, values below 10 % for R_{wP} and a χ^2 value very close to unity are reasonable [All03, Spi05]. It has to be mentioned that the values can be below the criteria for a good refinement but still provide results which are physically not correct. As a consequence the obtained crystal structures have to be critically checked and other parameters reflecting the quality described in detail in Ref. [Hil87] are strongly recommended to be taken into account.

In addition to the structural information a quantitative phase analysis can be obtained from the Rietveld refinement. The weight W_j of each phase fraction j in the sample is connected to the scaling factor S_j:

$$W_j = \frac{S_j \cdot Z_j \cdot M_j \cdot V_j / t_j}{\sum_{k=1}^{N} S_k \cdot Z_k \cdot M_k \cdot V_k / t_k} \qquad . \qquad (2.15)$$

Z is the number of formula units in the unit cell, M and V are the corresponding molecular weight of the formula unit and the unit-cell volume. The different absorption corrections of the powders with respect to the particle sizes is described by the Brindley factor t [Bri45], but this correction is generally assumed to be unnecessary in a first approximation and t_j, t_k are usually set to one.

2.2.4. Single-Crystal Diffraction

The crystal-structure analysis for single crystals is performed in a similar procedure as the powder-diffraction methods. However, the data aquisition is different. Promising single crystals had to be preselected and were either measured on a four-cirle diffractometer equipped with a scintillation detector (Syntex P2$_1$) or a two-circle diffractometer with an image-plate detecting system (STOE IPDS 2T, see Fig. 2.5). Mo-K$_\alpha$ radiation was used on both diffractometers.

In case of the four-circle diffractometer (Fig.2.6) θ and ω describe the in plane angles of incident and reflected radiation. The angles ϕ and χ are used to align the different diffracting vectors, which are oriented normal to the set of lattice planes described by the Miller indices and which corrrespond to lattice points in reciprocal space. In the κ geometry of the IPDS 2T (Fig. 2.5) the circles of χ and ω are combined (more detailed information is given in Refs. [Spi05, Mas07]).
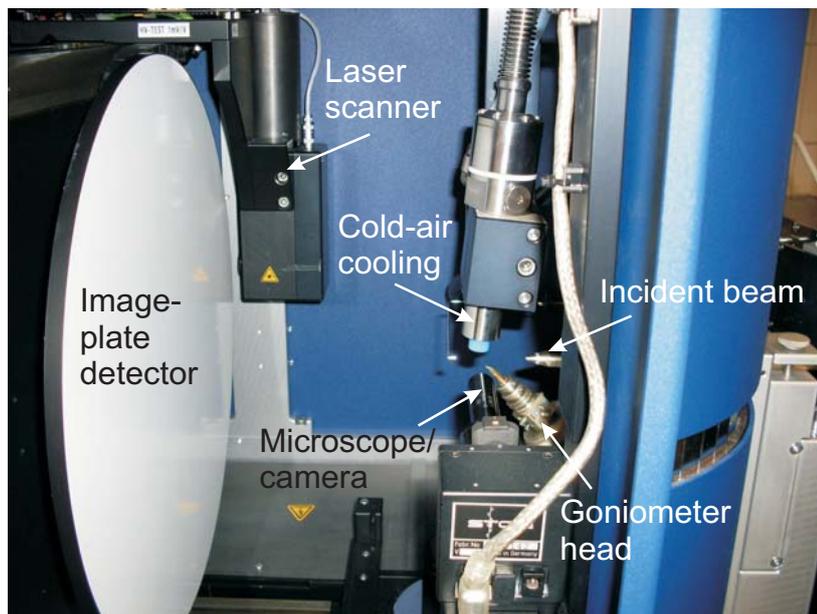
Figure 2.5.: Setup of the STOE IPDS 2T single crystal diffractometer equipped with image-plate detector (left) and cold air cooling system. The incident beam enters from the right via a collimator tube. The crystal is mounted on the goniometer head of the two-circle goniometer with κ geometry.

The preselected crystals with edge sizes between roughly 0.05 mm and 0.3 mm were glued on glass fibres using clear nail varnish. This crystallite size is required to obtain reasonable reflex intensities and low absorption losses. The glass fibre was fixed on a goniometer head with an Eulerian cradle, which was mounted on the goniometer of the single-crystal diffractometer.

First the unit-cell parameters are determined from a limited number of reflexes measured in a preliminary run. From this indexing step the Bravais type and the crystal orientation matrix are determined. With this information the measurement run of a large number of reflex intensities I_{hkl} is carried out using an optimized procedure to measure the complete available part of the Ewald sphere in reciprocal space. On the four-circle diffractometer often only one or two octants of the Ewald sphere are measured to reduce the data acquisition time to two days. Depending on the crystal symmetry more octants are required to obtain the necessary data for structure solution and refinement. In case of cubic systems the unique reflections are obtained measuring one octant only. Nevertheless, we measured the entire Ewald sphere because the intensities of symmetry-equivalent reflexes were used for the absorption correction. To enhance the (atomic) resolution, measurements are performed to high diffraction angles up to $2\theta = 90°$. For a good refinement quality the observed number of independent reflections should be ten times higher than the number of parameters used for the refinement.

From the measured reflex intensities the space group and Laue symmetry were determined by the investigation of systematic absence conditions using the program XPREP [She97a]. The mea-
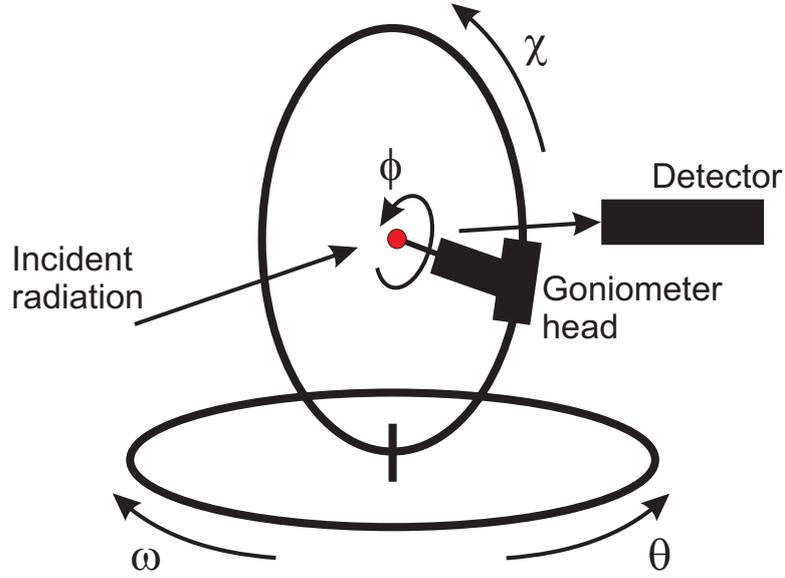
Figure 2.6.: Schematic geometry of the four-circle diffractometer with the crystal mounted on an Eulerian-cradle goniometer head.

sured intensities I_{hkl} were corrected[2] by the Lorentz- and polarization correction terms *LP* [Mas07] according to:

$$|F_o| = \sqrt{I_{hkl}/LP} \quad \left[LP = (1 + \cos^2 2\theta)/2\sin 2\theta\right] \quad . \tag{2.16}$$

For the absorption correction the measured shape of the crystal was optimized numerically with the XSHAPE suite based on the program HABITUS [Her97] to minimize the differences in the intensities of symmetry equivalent reflexes. Alternatively the surface planes can be indexed and used to describe the crystal shape. The final absorption correction of the data can be performed applying PLATON [Spe09].

The structure was solved using the program SHELXS-97 [She97b, She08]. The determination of the atom positions in the unit cell was performed applying so called "direct methods" or the Patterson method [Mas07]. The electron density ρ within the unit cell can be calculated from the structure factors F_{hkl} by Fourier transformation:

$$\rho_{XYZ} = \frac{1}{V} \sum_{hkl} F_{hkl} \cdot \exp[-i2\pi(hX + kY + lZ)] \quad . \tag{2.17}$$

XYZ are the coordinates describing ρ for each point of the real-space unit cell. The maxima of ρ_{XYZ} correspond to the coordinates of the atoms. However, the measured intensities do not provide the phase information as I_{hkl} is proportional to $|F_{hkl}|^2$. Structure factors calculated from the first structure model (F_c) are used in a Fourier sythesis and the obtained data are subsequently

---

[2]This is performed automatically by the diffractometers: P_{21} during the measurement of the reflexes, STOE IPDS 2T during the integration step.

subtracted from the ρ_{XYZ} data of the measurement. This differential Fourier analysis enables to locate atoms, which are not found in the first structure approximation. For oxides this is usually the case for the lighter elements like oxygen. The structure model can be considered to be correct if no strong maxima in the difference-electron density occur.

With the valid structural model the crystal structure is refined in a least-squares algorithm using the program SHELXL-97 [She97b, She08]. Similar to the Rietveld analysis of the powder-diffraction data, the atomic coordinates and the occupation factors were refined. In addition, the anisotropic displacement parameters U_{ij} are calculated, which are related to the anisotropic Debye-Waller factors β_{ij} according to:

$$\beta_{ij} = 2 \cdot \pi^2 \cdot a_i^* \cdot a_j^* \cdot U_{ij} \quad . \tag{2.18}$$

The displacement parameters are linked to the reciprocal axes a_i^* ($a_1^* = a^*$, $a_2^* = b^*$, $a_3^* = c^*$).

The refinement quality is described by R-values similar to the Rietveld analysis of powder data. However, the weighting factor w is generally applied, because during the refinement of the F_o^2 values the variance is less stable than for the F_o data. Therefore, a weighting scheme including a refineable empirical factor k is used [Mas07]:

$$w = 1/(\sigma^2 + k \cdot F_o^2) \quad . \tag{2.19}$$

The residuals are calculated in a different manner depending on the refinement of the F_o or the F_o^2 data. The R-values are then marked with the indices "1" or "2", respectively (the 1 is often neglected). The standard R-value is calculated according to:

$$R_1 = \frac{\sum_{hkl} \Delta_1}{\sum_{hkl} |F_o|} = \frac{\sum_{hkl} ||F_o| - |F_c||}{\sum_{hkl} |F_o|} \quad , \tag{2.20}$$

and the weighted wR-values of the refinement are calculated according to:

$$wR_1 = \sqrt{\frac{\sum_{hkl} w \cdot ||F_o| - |F_c||^2}{\sum_{hkl} w \cdot F_o^2}} \quad , \tag{2.21}$$

$$wR_2 = \sqrt{\frac{\sum_{hkl} w \cdot (F_o^2 - F_c^2)^2}{\sum_{hkl} w \cdot (F_o^2)^2}} \quad . \tag{2.22}$$

The residual values for a good refinement are recommended to amount well below 5% for R_1 and 10% for wR_2. In addition, a goodness of fit number, which should be close to unity, is defined:

$$S = \sqrt{\frac{\sum_{hkl} w \cdot ||F_o| - |F_c||^2}{m - n}} \quad . \tag{2.23}$$

m is the number of measured reflex intensities and n is the number of refined parameters.

2.3. X-ray Absorption Spectroscopy Measurements

In addition to the x-ray scattering methods, x-ray absorption spectroscopy (XAS) was used to investigate the samples. This technique bears different advantages. It is highly element specific for the investigated absorption edge of the studied element. This method can be used for the detailed investigation of the local structure neighboring or coordinating the central atom up to several Å. Since the structural resolution is limited to the nearest neighbors, besides highly crystalline materials also amorphous, liquid, or even gaseous samples can be investigated. Using a fast measurement technique the XAS spectra can be used to in-situ study the formation of a reaction product during the reaction process. Furthermore, the valence of different elements in the compounds can be determined by XAS measurements.

The passing of solid material attenuates the transmitted intensity of radiation according to the Lambert-Beer law [Kon88]:

$$I = I_0 \cdot exp(-\mu(E) \cdot \mathrm{d}) \quad . \tag{2.24}$$

The incident beam with intensity I_0 is damped exponentially depending on the sample thickness d and the absorption coefficient $\mu(E)$, which is in general a tensor of rank two, but in first approximation it can be considered as a material-specific parameter. The equation is only valid as approximation for low intensities and a one-dimensional case. In the energy range of x-radiation the coefficient is composed of different contributions, which are the result of inelastic (Rayleigh-) and elastic (Compton-) scattering and the photoionization of the inner shells of the atoms in the absorbing material. The scattering contributions are changing slowly and decrease with increasing energy. On the other hand, the element specific photoionization in comparison decreases more steeply with increasing energy. At certain energy values additional anomalies are appearing arising from the ionization of the inner shell (K, L, M,...) electrons.

The general behavior of the mass depending absorption coefficient ($\mu(E)/\rho$) without regarding the specifications of the atomic structural environment or the chemical properties of the neighboring atoms was calculated by Victoreen [Vic48]. The empirical formula

$$\frac{\mu(E)}{\rho} = C \cdot \left(\frac{hc}{E}\right)^3 - D \cdot \left(\frac{hc}{E}\right)^4 + \sigma_{KN} \cdot \frac{N_A Z}{A} \tag{2.25}$$

describes the decrease with increasing energy using terms which are weighted with element specific coefficients C and D for each separate absorption edge. The above mentioned inelastic and elastic scattering coefficients are included in Eq. 2.25 by the Klien-Nishina-coefficients σ_{KN}. N_A is the Avogadro constant and Z and A are the element specific atomic number and atomic weight, respectively.

Eq. 2.25 is a raw approximation due to the previously neglected element-specific photoionization, but it can still be used in a fit for the pre-edge background correction of the absorption measurement. A typical example of a measured Ru-K absorption edge is depicted in Fig. 2.7. It reveals a complex behavior around the absorption energy E_0, which is marked by a vertical red solid line. The appearing of a fine structure is mainly caused by two reasons. In the XANES
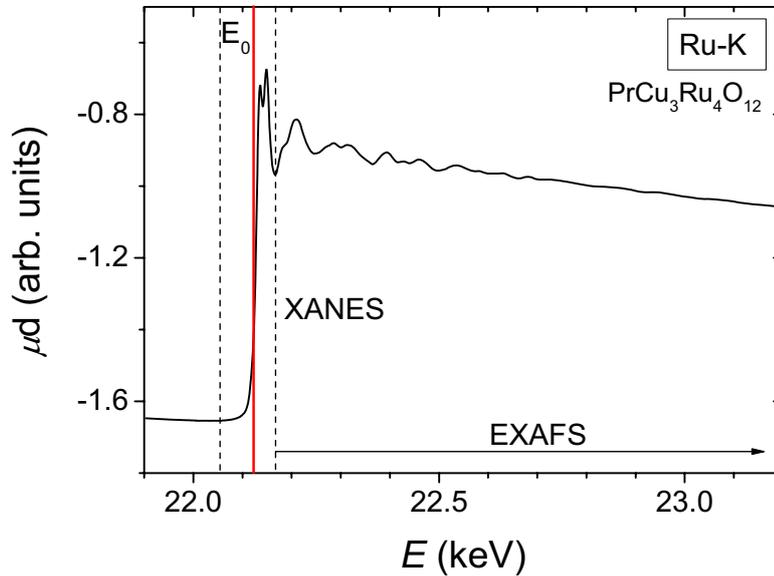
Figure 2.7.: Measured Ru-K absorption edge of $PrCu_3Ru_4O_{12}$. XANES and EXAFS regions are indicated by vertical dashed lines and the absorption-edge energy E_0 is marked with the solid red line.

(X-ray Absorption Near Edge Structure) region the electrons from the inner shells are excited into unoccupied bound or free levels close to the Fermi-energy. The EXAFS (Extended X-ray Absorption Fine Structure) region above the absorption energy results from electrons, which are photoionized but cannot be considered completely free as they are still moving inside the potential well of the neighboring atoms and are scattered within this potential. The interference of the scattered electrons results in the observed fine structure of characteristic oscillations above the absorption edge.

The information gained from these two regions are extracted by different approaches. The model to describe the XANES region is presented in section 2.3.1 in more detail, while the fitting and interpretation of the EXAFS region is described in section 2.3.2.

2.3.1. X-ray Absorption Near Edge Structure

The XANES region of the absorption spectrum is ranging from approximately 30 eV below E_0 to roughly 50 eV above the edge [Kon88]. It is difficult to define the exact range, because a clear separation of the XANES and EXAFS regions is not possible due to the strong sensitivity of the edge shape on the local coordination of the absorbing atoms. A rough estimate of the border between the XANES and the EXAFS regime is the similarity of the photoelectron wavelength and the distance to the next neighbors of the central atom.
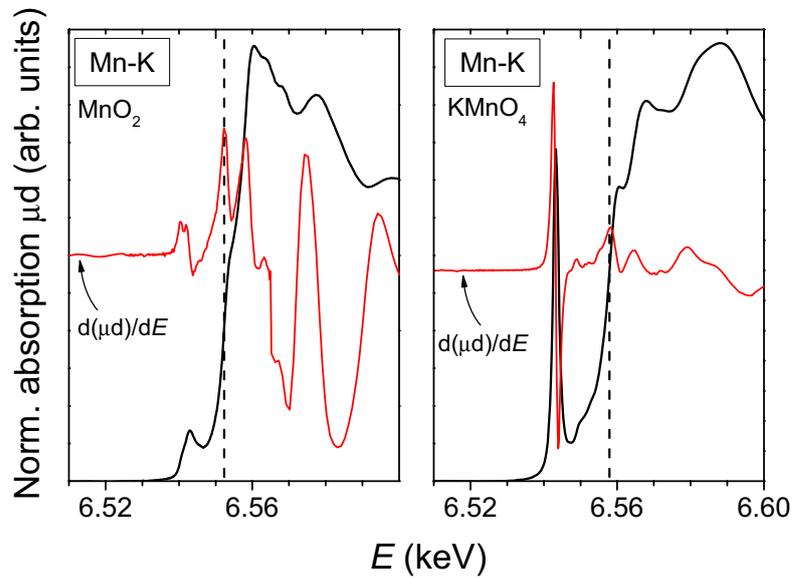
Figure 2.8.: Mn-K absorption edge spectra (black) and the corresponding first derivatives (red) of reference manganese oxides (Left: MnO_2, right: $KMnO_4$). The vertical dashed line marks the edge energy determined from the maximum in the derivative of the edge spectra.

In Fig. 2.8 an example of the correlation between the pre-edge shape and the local coordination is depicted using the normalized absorption spectra of the Mn-K edge of two different manganese oxides (black) and their first derivatives (red). In MnO_2 (left frame) the Mn^{4+} ions are coordinated octahedrally, while in $KMnO_4$ (right frame) a tetrahedral coordination of the Mn^{7+} ions is found. This results in a higher intensity of the pre-edge peak for $KMnO_4$ [Cha08], which is ascribed to usually forbidden transitions between s ($l = 0$) and d ($l = 2$) orbitals. Due to the breaking of the local inversion symmetry the transition becomes possible. The smaller pre-edge feature found in the absorption spectrum of MnO_2, on the other hand, is resulting from quadrupole contributions to the transition into $3d$ states at the absorption edge [Far05].

The observed fine structure in the XANES range is the result of the transitions of electrons from inner shell states into unoccupied electronic levels close to the Fermi-energy [Kon88]. The transitions to bound levels (usually d and p states) close to E_F are described as discrete and resonant processes. In addition, excitations into the free and unbound states as well as into contiunuous bands are possible. In transition and rare-earth metals the corresponding dipole-allowed transitions at the $L_{II,III}$ edges ($2p_{1/2,3/2} \rightarrow 3d, 4d$) appear as broad intense peaks denoted white lines.

The resonant excitations cause Lorentz-shaped peaks in the absorption spectra. The FWHM of these peaks is determined by the mean lifetime of the involved electronic states and their area is determined by the transition rate between those levels. The transition rate is resulting from a matrix element between the initial and final state of the many electron system and is calculated

from Fermi's Golden Rule (see e.g. in Ref. [Sch90]). The transition into the continuum is modelled by an arctangent function. The XANES is dominated by the contributions of multiple scattering in contrast to the EXAFS oscillation, which is predominantly formed by single scattered electrons [Reh00, Goe06].

The modelling of the near-edge structure can be performed by using band-structure calculations including a local-density approximation (LDA). The obtained density of states close to E_F reflects the measured absorption edge. It is recommended to start with a single-electron approximation since the solution of the quantum-mechanical equations could be considered as the product of single-particle wave functions. Alternatively in real-space approximations the scattering contributions in atomic clusters are calculated, which simulate the local environment of the absorbing atom. The pre-edge peaks can therefore be modelled by varying the number of atoms in the clusters or minor changes of the symmetry of the neighboring atoms. In these methods the single atom approximation is replaced by a multi-electron model, which is resulting in simulated absorption spectra very close to the measured data [Kon88].

In addition to the study of the local coordination of the absorbing atom its valence can be determined from the analysis of XANES spectra. This is the major use for the XANES analysis in this work, since the local geometry usually does not change significanty by substitution in the investigated samples. The edge position sensitively reacts on the oxidation state of the absorber ion, an effect called "valence shift". Higher valences increase the ionization energy, because the reduced number of valence electrons in the atomic shell decrease the screening of the core electric field. The edge position is also varied by the chemical nature of the ligands, for example, by a replacement of oxygen by nitrogen. This effect is called "chemical shift". The correlation between oxidation states and energy positions is done using reference materials with comparable coordination of the absorbing atom.

The valence determination was performed by the investigation of the first derivatives of the measured spectra. For the K-edges the inflection of the absorption edge defined as threshold energy E_0 is found as the first maximum in the derivative. This energy is marked by vertical dashed lines in the Mn-K example spectra in Fig. 2.8. The shift between the sample oxides MnO_2 (Mn^{4+}) and $KMnO_4$ (Mn^{7+}) is roughly determined to 5.5 eV, however, the octahedral and tetrahedral coordinations strongly influence to this value. For similar coordinations this method is accurate and the shift is typically linear with changing valence. In addition, the pre-edge feature can be investigated. From this the valence is determined by a rather complex modelling of the peak shape. Due to this elaborate fit and the often low intensity of the pre-edge peak this method is less accurate and was not used for this work.

The K-edge spectra were background corrected by subtracting a linear function which was determined from the pre-edge range and extrapolated for the entire measured energy range. After this background subtraction the spectra were normalized using a prominent region in the EXAFS part found for all investigated substances as reference. The value of the first maximum of the derivative was taken as energy value for the absorption edge.

For the Ru-L_{III} edge a slightly different approach was used. Since the L-edges are dominated by the very intense white lines, it is reasonable to use their energy positions in the determination
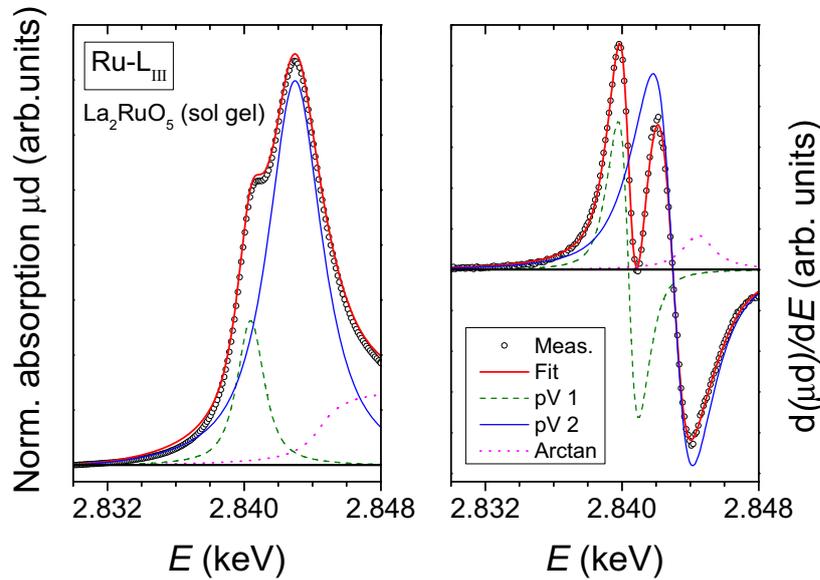
Figure 2.9.: Left: Ru-L$_{III}$ XANES spectrum of La$_2$RuO$_5$. Right: First derivative of the spectrum. In both frames the corresponding fit results with the two pseudo-Voigt and arctangent function contributions are shown. For details see text.

of the oxidation states as described in Refs. [Ebb98, Ebb01, Goe06]. In Fig. 2.9 the normalized absorption spectrum of the Ru-L$_{III}$ edge of La$_2$RuO$_5$ is depicted in the left frame. The two intense absorption peaks correspond to the $2p \rightarrow 4d$ transitions. The double peak structure is caused by the e$_g$–t$_{2g}$ splitting of the $4d$ orbitals in an octahedral crystal field. The peak at lower energies can therefore be assigned to the transition into the t_{2g} like states, while the peak at higher energies corresponds to the transition into e_g orbitals. The edge features can be modelled in a least square fit using two pseudo-Voigt (pV1 and pV2) and an arctangent function. The resulting fit curves are depicted in the left frame of Fig. 2.9. The pV functions simulate the transitions in the $4d$ levels (i.e. the white lines), while the arctangent is corresponding to the general egde jump. A better energy resolution is achieved by fitting the first derivatives of the spectra in the range between 2830 eV and 2848 eV as shown in the right frame of Fig. 2.9. The background correction, normalization, and the calculation of the derivative were performed similar to the K-edge analysis. The program WinXAS [Res97, Res98] was used for the data treatment and the least-squares fit.

2.3.2. Extended X-ray Absorption Fine Structure

The EXAFS region starts at approximately 50 eV above the absorption edge and ranges to the energy at which the oscillations cannot be distinguished optically from the background. This is usually the case between roughly 1000 eV and 1500 eV above E_0 (see Fig. 2.7). In this region the
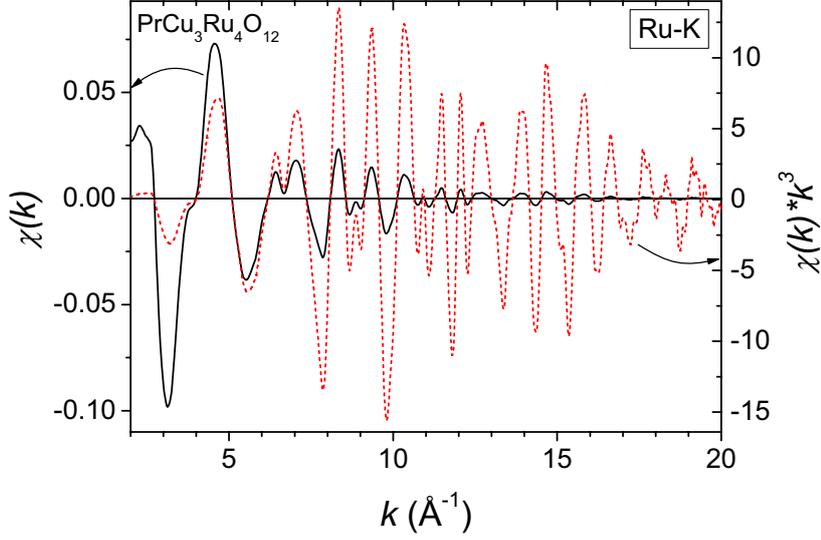
Figure 2.10.: $\chi(k)$ (solid) and k^3-weighted $\chi(k)$ (dashed) obtained from the Ru-K absortion spectrum of $PrCu_3Ru_4O_{12}$ (see Fig. 2.7).

electron excited from the absorber atom can be considered quasi-free and the oscillations are the result of scattering processes in the potentials of the neighboring atoms. Therefore, the electrons can be treated as wave packet with a wavevector according to [Teo81]:

$$k = \frac{2\pi}{\lambda} = \sqrt{\frac{2m_e}{\hbar}(E - E_0)} \quad . \tag{2.26}$$

The electron mass is denoted m_e and λ is the de-Broglie wavelength. The ionization energy E_0 is subtracted from the total energy E resulting in the kinetic energy of the free electron.

Because of the interference of the emitted and backscattered electron waves, a pattern emerges from wavelength dependent destructive and constructive interference giving rise to the EXAFS oscillations. In contrast to the XANES regime the EXAFS signal is dominated by single scattering processes [Reh00].

The oscillations in the EXAFS spectra can be modelled analytically by a pair of absorber atom and scattering atom [Lee75]. For this the function $\chi(k)$ was obtained from the measurement data utilizing the VIPER program [Kle01]. The pre-edge background was determined by fitting a polynomial function with coefficients x^{-3} and x^1 to the pre-edge region. After subtraction of this background the spectra were normalized using approximately the same part of the EXAFS region as reference for all samples resulting in $\mu(E)$. The atomic absorption coefficient μ_0 was obtained from a smoothing spline fit of the post-edge region. The subtraction of $\mu_0(E)$ from $\mu(E)$ and subsequent normalization by the edge jump $\Delta\mu_0$ results in the EXAFS function $\chi(E)$. Finally $\chi(E)$ was transformed to the k-scale according to Eq. 2.26 using the threshold energy E_0, which is the first maximum in the first derivative of the normalized spectra.

In Fig. 2.10 the obtained $\chi(k)$ of the Ru-K absorption edge of $PrCu_3Ru_4O_{12}$ is depicted as solid black line in the k-range between 2 Å^{-1} and 20 Å^{-1}. Since the oscillation amplitudes decline strongly with increasing k, $\chi(k)$ is weighted by a factor of k^n ($n = 1, 2, 3$) to emphasize the high energy region. The k^3 weighted $\chi(k)$ is shown Fig. 2.10 as red dotted line.

The theoretical description of the EXAFS function is a sum of analytical functions for pairs of central absorber and scattering atoms [Reh00, Kon88, Teo81] for each coordination sphere j according to:

$$\chi(k) = \sum_j S_0^2 \cdot \frac{N_j |f_j(k)|}{k R_j^2} \cdot \exp(-2k^2 \sigma_j^2) \cdot \exp\left[\frac{-2R_j}{\lambda(k)}\right] \cdot \sin[2kR_j + 2\delta_j(k) + \Phi] \quad . \tag{2.27}$$

Each summand in Eq. 2.27 represents one specific element, i. e. if the same coordination sphere is occupied by atoms of two different elements two individual functions have to be used in the sum to calculate the correct $\chi(k)$. l is the angular momentum quantum number and N_j (degeneracy) represents the number of identical backscattering atoms in shell j. S_0^2 is ascribed to the amplitude reduction of the backscattered intensity. R_j is the distance between the atoms in the jth coordination shell and the absorber atom. The function $f_j(k)$ describing the backscattering intensity is in more detail written:

$$f_j(k) = \frac{m}{2\pi\hbar^2 k} \cdot t_j(2k) \quad , \tag{2.28}$$

where the corresponding $t_j(2k)$ are the modelled amplitude functions for the scattering. The Debye-Waller factors σ_j^2 are describing the thermal displacement of the atoms or lattice phonons in harmonic approximation. The mean free path $\lambda(k)$ of the photoelectron in the sample is k-dependent due to the contributions from the electron-electron scattering. The sum of the central-atom partial-wave phase shifts is denoted $\delta_j(k)$, while Φ represents the phase factor of $f_j(k)$. The phase shift comprises contributions from the emission of the electron from the absorber atom potential, from the scattering process in the neighboring atom, and from the reentering of the electron in the absorber potential.

This theoretical description of the EXAFS function is valid for a small-atom approximation, i.e. the distance to the first backscattering shell is smaller than 0.5 Å, which is in turn corresponding to $k = 2$ Å^{-1}. Thus, the relevant EXAFS range is located above this k-value as indicated in Fig. 2.10. By adding more sophisticated approximations this lower border can be treated element specific, especially for larger distances as, for example, required for larger ions like the lanthanides [Kon88].

The theoretical amplitude functions and phase shifts were calculated using the program FEFF8 [Ank98]. The crystal structure obtained from x-ray and/or neutron diffraction were used as starting models.

The Fourier transformation of the EXAFS function back to real space results in the radial distribution function RDF, in which the backscattering shells are represented by peaks, whose intensities are depending on number, element, and thermal-displacement factors of the atoms in the shell. Since the borders of the EXAFS function are usually discontinuous, it is recommended to
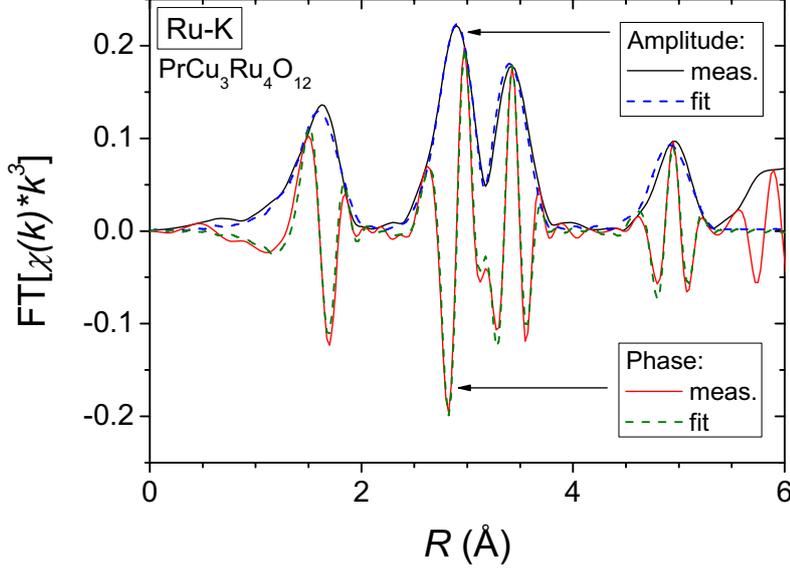
Figure 2.11.: Fit of the Fourier transformed k^3-weighted $\chi(k)$ obtained from the Ru-K edge absorption spectrum of $PrCu_3Ru_4O_{12}$.

use e.g. a Bessel-window function to suppress artificial satellite peaks in the resulting modified radial distribution function mRDF. The transformation to the mRDF is processed according to:

$$mRDF = FT[\chi(k) \cdot b(k) \cdot k^n] = \frac{1}{\sqrt{2\pi}} \int\limits_{k_{min}}^{k_{max}} \mathrm{d}(2k)\chi(k) \cdot b(k) \cdot k^n \cdot \exp(i2kR) \quad , \qquad (2.29)$$

where R is the distance to the backscattering atom and $b(k)$ is the Bessel-window function. The mRDF is more suitable to intuition due to its real-space character. It is, therefore, more comfortable to use it for the fitting process. The result for amplitude and phase-shift fit of the four closest shells in $PrCu_3Ru_4O_{12}$ is depicted in Fig. 2.11, a more detailed analysis is described in Sec. 6.2.2. It has to be mentioned that the peak-maxima positions are not identical with the real-space distance of the backscattering atoms due to the k-dependence of the phase shift $\delta_j(k)$. This phase shift results in a systematic reduction of roughly 0.2 Å - 0.5 Å [Goe06].

The fit of the $\chi(k)$ functions was performed utilizing the program WINXAS [Res97]. More details of the EXAFS data fitting and the interpretation of the results are presented in Secs. 5.1.1.2, 5.1.1.3, and 6.2.2.

2.3.3. Measurement of the X-ray Absorption Spectra

The x-ray absorption spectra were recorded at the synchrotron-radiation facility HASYLAB (Hamburger Synchrotron Laboratorium) of DESY (Deutsches Elektronen Synchrotron) in Hamburg. At
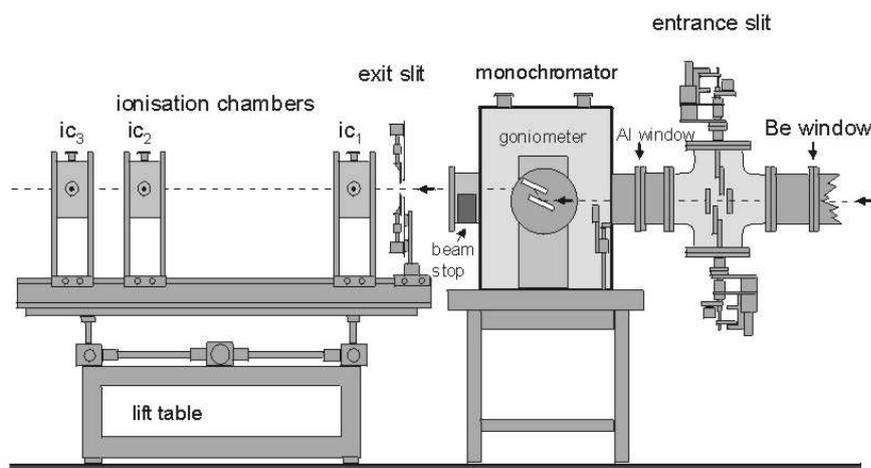
Figure 2.12.: Setup of the X1 beamline at HASYLAB [HAS12]. Incoming from the right, the incident beam passes the entrance slit, the Si-crystal double monochromator, the exit slits, and finally the ionization chambers (ic_{1-3}) with sample and reference in between.

the beamlines E4 and A1 energy ranges between approximately 2.5 keV and 10 keV were available and at beamline X1 radiation energies above roughly 6 keV and up to 80 keV could be achieved. The synchrotron ring DORIS III used positrons with 4.44 GeV energy and a beam current of up to 140 mA. The radiation for the beamlines was similarly branched off at different bending magnets. In Fig. 2.12 a sketch of a setup of the beamline X1 is shown [HAS12].

White synchrotron radiation from DORIS III passes the Si single-crystal double-monochromator to adjust the photon energy for the measurement [Kro84]. To suppress higher harmonics the monochromator is detuned by moving the second crystal to approximately 60 % of the maximum in the diffracted intensity. The large measured energy range from 2.8 keV (Ru-L_{III}) to 43.5 keV (Nd-K) was available due to the use of differently oriented Si monochromator crystals (111), (311), and (511). The samples were placed between the ionization chambers ic_1 and ic_2 and the absorption spectra were measured in transmission mode (Fig. 2.12). Metal foils as references were placed between the ionisation chambers ic_2 and ic_3 and measured simultaneously. The reference spectra were used for energy calibration of the sample spectra in the subsequent data analysis. In Tab. 2.1 the measurement parameters are listed. The ionization chambers were filled with different mixtures of nitrogen, argon, and xenon according to the edge energies in order to obtain high counting rates while keeping the absorption low. To obtain spectra of good quality, it is recommended to absorb 20% of the initial beam intensity in the first ionization chamber and roughly 50% of the correspondingly transmitted intensities in each of the other two chambers.

The samples were prepared by mixing appropriate amounts of the oxide powders with approx-imately 20 mg of organic material (e. g. cellulose or polyvinyl alcohol) and pressing this mixture

Table 2.1.: Elemental absorption-edge energies and measured EXAFS ranges used for this work.

Edge	Energy (keV)[Bea67]	Monochromator	EXAFS range (keV)	Δk (Å^{-1})
Ru-L$_{III}$	2.873	Si(111)		
Ti-K	4.966	Si(111)		
La-L$_{III}$	5.483	Si(111)	5.503 - 5.895	0.05
La-L$_{II}$	5.891	Si(111)		
La-L$_{I}$	6.266	Si(111)		
Mn-K	6.539	Si(111)		
Sm-L$_{III}$	6.716	Si(111)	6.736 - 7.310	0.055
Gd-L$_{III}$	7.243	Si(111)	7.263 - 7.390	0.056
Dy-L$_{III}$	7.790	Si(111)	7.810 - 8.585	0.05
Cu-K	8.978	Si(111)	9.010 - 10.000	0.05
Ru-K	22.117	Si(311)	22.160 - 24.000	0.05
La-K	38.925	Si(511)	38.970 - 40.000	0.04
Pr-K	41.991	Si(511)	42.030 - 43.100	0.04
Nd-K	43.569	Si(511)	43.620 - 44.800	0.04

in pellets of 13 mm diameter. Alternatively some milligrams of sample powder were glued on adhesive tape which can be assembled in several layers. As a rule of thumb, a $\Delta\mu$ of approximately 1 at the edge should be obtained. In the case of strongly absorbing samples lower values for $\Delta\mu$ were found and could be adjusted by e.g. the use of less sample material.

The measurement was divided in three regions or steps. In the pre-edge region the step width could be chosen wider since this region was only used for the background determination. The absorption edge itself was measured in fine steps and increased (doubled or tripled) integration times per data point. The EXAFS region was recorded using equidistant k-space steps of roughly 0.05 Å^{-1} (see Tab. 2.1) and a linear increasing integration time with increasing k to enhance the signal to noise ratio.

2.4. Magnetic Properties

This section is giving a brief introduction of investigated magnetic properties and measurement methods. A more detailed overview on magnetism in solid materials can be found in literature (see e.g. Refs. [Kit91, Lue99]).

Unpaired electrons in the valence shells of the atoms give rise to a paramagnetic moment, which can be influenced by external magnetic fields. In solid materials cooperative effects can occur due to exchange interactions. Three types of three dimensional (3D) magnetic cooperation are commonly found and ordering is characteristically emerging below specific phase transition temperatures. The magnetic moments of the atoms can align parallel to each other (Ferromagnetism).

In contrast, they can order antiparallel and compensate each other (Antiferromagnetism), or they only partly compensate due to aligned magnetic moments with different absolute values (Ferrimagnetism). Furthermore, magnetic ordering phenomena of lower dimensionality, 1D or 2D, can be observed, but these have to be described with more complex models. For these orderings also characteristic transition temperatures are found, however, the observed behavior below this temperature often strongly deviates from the ground-state properties of 3D ordered systems and is very specific for each of those systems. This lower dimensionality in magnetic ordering is strongly influenced by the crystal structure. Due to structural features like, for example, layered structures, the exchange interaction strength in one or two directions are disproportionally increased compared to the other directions and, thus, the 1D or 2D ordering can occur. In this section the analysis of the paramagnetic part of the susceptibility data and experimental details are introduced, while the specific investigations of the magnetic properties at low temperatures are discussed in the corresponding sections below.

The sum of the atomic magnetic moments μ per volume is the magnetization $\vec{M}$. In an isotropic material the magnetization vector either follows the external magnetic field $\vec{H}$ (paramagnetic) or turns into the opposite direction (diamagnetic). The field-dependence of the magnetization can be described by the introduction of the magnetic susceptibility χ, which acts as a dimensionless tensor according to:

$$\vec{M} = \chi \cdot \vec{H} \quad . \tag{2.30}$$

The Curie-law

$$\chi = \frac{C}{T} = \mu_0 \cdot \frac{N_A \mu^2}{3k_B T} \quad \text{and} \quad C = \mu_0 \cdot \frac{N_A \mu^2}{3k_B} \tag{2.31}$$

describes the thermal behavior of the susceptibility of a paramagnetic material. N_A is the Avogadro constant, μ_0 is the vacuum permeability, and k_B is the Boltzmann constant. Preconditions for the Curie law are a temperature indepent μ and a weak external magnetic field. For these conditions the equation is valid for adequate high temperatures. In many cases the Curie-law becomes invalid at lower temperatures due to magnetic correlations and ordering effects, which start to dominate the thermal fluctuations of the paramagnetic moments.

For a typical paramagnetic material, the measured temperature dependent susceptibility χ can be approximated by the Curie-Weiss law:

$$\chi_{mol} = \frac{C}{T - \Theta} + \chi_0 \quad , \tag{2.32}$$

where Θ takes into account local ferro- or antiferromagnetic interactions. The sign of Θ is positive in case of a ferromagnetic interactions and negative for antiferromagnetic ones. Contributions of the sample holder, possible Van-Vleck or Pauli-paramagnetism, and the diamagnetic moment of the paired electrons are included by the temperature independent term χ_0. From a fit of the experimental susceptibility data the parameters χ_0, Θ and C are obtained. Usually the inverse susceptibility $1/\chi$ is used for the fitting process, since an almost a linear temperature dependency

is observed, which allows a better optical check of the fit quality. The effective magnetic moment μ_{eff} is related to the Curie constant by Eq. 2.31. The equation is simplified by inserting the values of the constants to:

$$\mu_{\mathrm{eff}} = \sqrt{\frac{3k_B C}{\mu_0 N_A}} = \sqrt{4\pi \cdot C} \cdot 0.79773 \, (\mu_B) \quad . \tag{2.33}$$

The effective magnetic moment is frequently also denoted n_{eff}, which is the number of units of Bohr magnetons μ_B per magnetic ion. The obtained values for μ_{eff} and Θ are compared to theoretical values to investigate paramagnetic properties and possible correlation effects resulting from the magnetic exchange interactions.

The effective paramagnetic moment of a free atom or ion is calculated according to:

$$\mu_{\mathrm{eff}} = g \cdot \sqrt{J \cdot (J+1)} \quad . \tag{2.34}$$

For lighter atoms S is defined as the total spin $S = \sum_i s_i$ and L as the total orbital angular momentum ($L = \sum_i l_i$) of the compound. In case of a weak crystal field the coupling of spin and orbital momentum (LS-coupling) results in the total moment J. Due to the different possible couplings of S and L terms a multiplet with $2S+1$ levels emerges for J. Usually only the ground state J described by the term symbol $^{2S+1}L_J$ has to be taken into account due to the level splitting. The occupation of the electronic ground state occurs according to the three Hund's rules. The dimensionless Landé g-factor describes the contributions of spin and orbital angular momentum according to:

$$g = 1 + \frac{J \cdot (J+1) + S \cdot (S+1) - L \cdot (L+1)}{2J \cdot (J+1)} \quad . \tag{2.35}$$

For the rare-earth ions this model is a rather good approximation taking into account that the partly occupied f shells are determining the magnetic properties. These f states are only weakly influenced by the crystal field resulting in quasi free ions.

However, in the $3d$ and $4d$ elements the crystal field in most cases supresses the angular momentum. For this case the g-factor[3] obtained from Eq. 2.35 is 2 and the "spin-only" scenario simplifies Eq. 2.34 to:

$$\mu_{\mathrm{eff}} = 2 \cdot \sqrt{S \cdot (S+1)} \quad . \tag{2.36}$$

Measurements of magnetic properties were performed using a super-conducting quantum-interference device (SQUID) magnetometer (MPMS-XL by Quantum Design). The magnetometer bases on a superconducting ring with a Josephson contact as a weak link. The method is very sensitive, changes of the magnetic susceptibility in the range of 10^{-8} emu/mol can be detected. The measurement is performed by moving the magnetized sample through the superconducting ring with a certain number of steps and detecting the change of the magnetic flux. The Josephson effects (DC and AC) cause a changing amount of flux quanta $h/2e$ depending on the external

---

[3]For comparison: Experimental gyromagnetic factor for electrons $g \approx 2.0023$ [Odo06].

magnetic field and the magnetization of the sample. A more detailed description is, for instance, given in Ref. [Lue99].

From the measured magnetization data (M_sample and $M_\text{sampleholder}$) the magnetic susceptibility is derived according to:

$$\chi_{mol} = \frac{M_\text{sample} - M_\text{sampleholder}}{H} \cdot \frac{M}{m} \quad . \tag{2.37}$$

The external magnetic field H, the sample weight (m), and its molecular weight (M) are used to calculate the susceptibility according to Eq. 2.37. To obtain a good signal with low noise the sample weight was approximately 50 mg to 100 mg. The samples were filled in gel-capsules which were positioned in the magnetometer inside a plastic tube. The magnetization of this sample holder usually amounts to values well below 10^{-5} emu/mol, which is significantly smaller than the sample magnetization. Therefore, the correction could be neglected for this work. The used unit for χ in this work is the electromagnetic unit (emu) and the magnetic field is given in Oersted (Oe). Both are *cgs*-units and widely used to describe experimental findings in literature.

The measurements were performed with a constant external field (DC-measurement) either under field cooled (fc) or zero-field cooled (zfc) conditions. In the fc mode the sample is cooled within the static external field, while in the zfc mode the sample is cooled to the starting temperature without external field, which is switched on afterwards. Fc and zfc conditions lead to deviating magnetizations if specific ordering phenomena occur. This is, for example, the case for spin glasses, in which no well-defined spin arrangement can be achieved. Instead, the magnetic moments remain partly disordered showing a typical relaxation behavior similar to the glass state of a supercooled liquid. To investigate the relaxation properties, additional AC-magnetic field measurements are performed. For example, frequency dependent shifts of the emerging peak in the (zfc) data characterize a spin-glass phase [Bin86, Myd93].

2.5. Thermal Properties

To study the oxygen stoichiometry, thermogravimetric (TG) measurements were performed. Magnetic and structural phase transitions were investigated utilizing differential-scanning calorimetry (DSC) and specific-heat (C_p) measurement-techniques.

The thermogravimetric determination of oxygen stoichiometries is especially useful for oxides of noble metals since these can easily be reduced to the corresponding metals in e.g. forming gas (H_2/N_2 or H_2/Ar mixtures) [Osw85, Osw88, Ben90]. However, the method requires the knowledge of the exact composition of the final products. The obtained final products are usually noble metals (for example Cu, Ru) and binary metal oxides, which are highly stable at high temperatures in reducing atmosphere (for example TiO_2, La_2O_3). Reasonable weight losses are required to decrease the error range of the method. Therefore, the amount of starting material has to be chosen according to the expected weight loss. In addition, the sample morphology plays a role, which e.g. is reflected by the characteristic onset temperature of the weight reduction. A sample with larger grains usually shows a higher onset temperature, since the sample surface reacting with the reducing gas is considerably smaller compared to e.g. a nanoscaled powder.
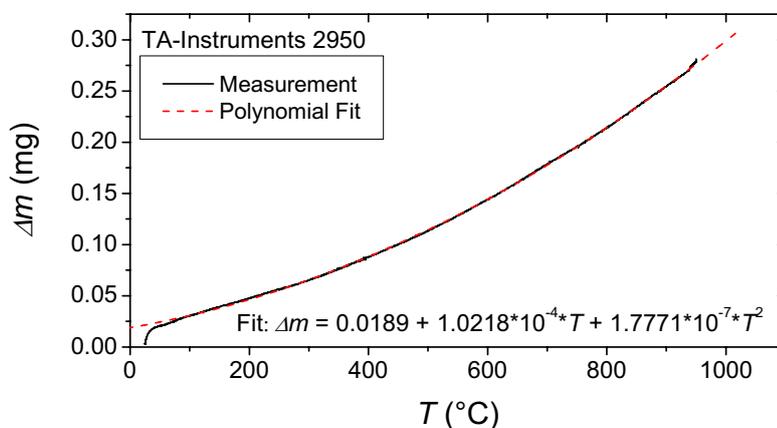
Figure 2.13.: Measured baseline of the platinum crucibles of the used TA-Instruments 2950 thermobalance (solid black line) and a polynomial fit of the curve (dashed red line).

For the TG measurements thermobalances model Q500 and 2950 from TA-Instruments were used. Approximately 50 mg of sample powder were heated in uncovered platinum crucibles with a constant rate of 10 K/min from room temperature to 950°C. This temperature was held for 15 min before the sample was allowed to cool down to room temperature. A gas flow of 70-80 ml/min forming gas (5%H_2 in N_2) through the balance was applied. A baseline measurement was performed to study the temperature-depending weight-change of the crucible during the heating process. The density of the atmosphere in the balance changes with temperature and convective flows occur, which causes a change of the crucible's buoyancy. This buoyancy variation has to be corrected in the sample-weight measurements. A small amount of dry Al_2O_3 (roughly 40 mg) was placed in the crucible for the baseline measurement, which is depicted in Fig. 2.13. The crucible weight seems to increase with increasing temperature in agreement with the crucible's decreasing buoyancy. Although the baseline can be reproduced by a quadratic polynom, which is also shown in Fig. 2.13 as dashed red line, the correction of the experimental data was done by a simple subtraction of the measured baseline.

The DSC measures the difference in heat between sample and reference due to their deviating thermal behavior. Sample and reference are heated simultaneously with a constant temperature rate and both temperatures are measured during the process. Since the sample has a different heat capacity than the reference, a difference of the sample temperature compared to the reference is observed. These differences are most pronounced during phase transitions, like, for example, the melting or crystallization of the sample material. The melting/crystallization process is a first order phase transition and, therefore, leads to the absorption/release of latent heat without a change of temperature. This causes a peak in the DSC curve, which is indicating the endothermal (or exothermal) process. Thus, crystal structure- or magnetic phase transitions are commonly object

of DSC studies [Hem89].

Approximately 15 mg of sample powder were sealed in aluminum crucibles and the DSC measurement was performed using a Netzsch F1 Phoenix calorimeter. A similar weight of Al_2O_3 was used as reference material. The low-temperature measurement routine was controlled by a liquid nitrogen cooling system. Starting at room temperature, the sample and reference were cooled down with a constant rate of 10 K/min to roughly 100 K. After a relaxation time of 5 minutes at this temperature the crucibles were heated to room temperature with 10 K/min. The measured DSC curves were analyzed using the Netzsch Proteus software. The transition temperatures were obtained by the determination of peak maxima and onset values of the observed transition peaks.

The specific heat reflects the energy required to increase the temperature of a defined amount of material by one degree. The applied measurement technique is strongly related to the DSC method, thus, the heat capacity can be obtained from DSC data analysis. The measurement of the specific heat of solid materials is used to investigate the contributions of electronic and lattice heat capacities and additional terms, for example, emerging from magnetic or crystallographic transitions. In general, the thermodynamic definition of C_p is given by [Tar03]:

$$C_p = -T \left(\frac{\partial^2 G}{\partial T^2} \right)_{p,B} = T \left(\frac{\partial S}{\partial T} \right)_{p,B} = \lim_{dT \to 0} \left(\frac{dQ}{dT} \right)_{p,B} \quad . \tag{2.38}$$

The indices p and B indicate that the measurement is performed at constant pressure and magnetic field. The values of the entropy S were be obtained from the specific heat by the integration of selected temperature ranges. The intrinsic energy of the system Q can also be determined from the measured C_p. Theoretical models (Einstein, Debye) are describing the heat capacity at constant volume C_v without regarding the thermal expansion of the crystal volume. Since in solids the thermal volume change is rather small, also the difference between C_p and C_v is small up to room temperature, which reasons the comparison of the measured C_p data with the C_v approaches.

The heat capacity was measured in the temperature range $1.8\text{K} \leq T \leq 300$ K using a physical property measurement system (PPMS by Quantum Design). The measurement technique is based on a relaxation method. For this the sample is heated for a short time interval and the exponential time constant of the temperature relaxation is measured [Las03]. From this value C_p is automatically calculated including further input parameters like the contribution of the sample platform (addenda) and the sample weight. The addenda of the PPMS was measured in a separate run of the empty sampleholder with a defined amount of the Apiezon N grease, which was the thermal coupling medium between sample and sampleholder. The step width for the measurement usually was 1 K and in the vicinity of observed phase transitions (±15 K) and below 30 K it was reduced to 0.2 K. For the measurements of the La_2RuO_5-related samples approximately 10 mg of the sample powder and 2 mg of polyvinyl alcohol (PVA) were mixed, ground in an agate mortar and pressed into pellets of 3 mm diameter.[4] To obtain C_p of the PVA, a pellet with roughly 5 mg was measured. This curve was multiplied by a factor regarding the PVA fraction in the mixed pellet and subtracted from the sample measurement data. This procedure can be used because

---

[4]Else pressed and sintered pellets without addings were used for the measurements of the specific heat.

of the Neumann-Kopp rule [Tar03], which describes the additive behavior of the specific heat of different materials measured simultaneously.

The lattice contribution to the C_p data was modelled with the program Mathematica 7 applying a three dimensional Einstein-Debye phonon model. The specific heat of the crystal lattice of solids results from vibrational modes of the atoms, which can be described as phonon quasiparticles. The phonon contributions can be deduced from a model of harmonic oscillators. The Einstein model for the heat capacity assumes a set of oscillators that are vibrating with the same frequency ω_E. Per formula unit consisting of Z atoms a specific heat of

$$C_{v,E} = 3RZ \left(\frac{\Theta_E}{T} \right)^2 \frac{\exp(\Theta_E/T)}{[\exp(\Theta_E/T) - 1]^2} \tag{2.39}$$

is obtained using this approximation. The Einstein-temperature Θ_E is a scaling factor and transforms the frequency to a temperature according to $\Theta_E = \hbar\omega_E/k_B$ (R is the gas constant). In solids the Einstein-model correctly describes the high-temperature limit, since at this temperatures the atoms vibrate independently and the Dulong-Petit limit $C_v = 3R$ per atom is almost reached.

In an improved approach Debye included a frequency distribution of the phonons. The Debye temperature $\Theta_D = \hbar\omega_D/k_B$ is defined analog to the Einstein temperature and the Debye frequency ω_D is linked to the acoustic velocity of the crystal lattice. For simple metals Θ_D is inversely connected to the unit-cell volume indicating the relationship of the acoustic velocity and the sample density. A cutoff wavelength has to be taken into account leading to:

$$C_{v,D} = 9RZ \left(\frac{\Theta_D}{T} \right)^3 \int_0^{x_D} \frac{x^4 \exp(x)}{[\exp(x) - 1]^2} \mathrm{d}x \quad . \tag{2.40}$$

The parameter x is defined by $x = \hbar\omega/k_B T$ and the upper limit x_D corresponds to the Debye frequency.

The Debye model describes a continuum of oscillations and lacks the discrete nature of the material. It was shown that in addition to the acoustic branches of the Debye model optical branches are appearing in ω vs. k of discrete materials (k is the propagation vector $2\pi/L$ of the wave in the crystal lattice). This deficit of the Debye model was overcome by the fusion of both models to the Einstein-Debye model, where the acoustic part is described by one three dimensional Debye term and the additional optical branch contributions are approximated utilizing the Einstein model [Tar03, Sin08, Kan10].

A significant contribution of the conduction electrons to the specific heat (denoted γ or Sommerfeld-coefficient) is only relevant for metallic systems, since its value is directly linked to the density of states at the Fermi-energy. As a consequence an insulating or semiconducting material theoretically provides $\gamma = 0$ due to the band gap at E_F. The Sommerfeld-coefficient can be determined by fitting the low-temperature region of C_p/T vs. T^2 with a Debye T^3 model defined according to $C_p = \gamma \cdot T + \beta \cdot T^3$. This fit also yields a maximal Debye-temperature for the compound, which can be calculated from the parameter β according to $\Theta_{D,max} = \sqrt[3]{12Z \cdot R \cdot \pi^4/5\beta}$. This model is valid for $T \ll \Theta_D$ and can be applied to most materials. However, for the low-temperature modelling of C_p of superconducting (BCS-model) and magnetically ordered (spin

excitations) systems additional terms are required. More relevant for this work are contributions emerging from crystal-field excitations, which are especially observed for lanthanide ions and are denoted as Schottky-type anomalies.

The magnetic entropy of an ordering transition can be determined from the experimental specific-heat data. At first the electronic and lattice contributions to C_p are subtracted. The remaining transition peak is integrated according to $S_{mag} = \int C_p/T \, dT$ to obtain the magnetic entropy S_{mag}. Using statistical thermodynamics, the magnetic entropy of magnetically ordered systems with a spin S amounts to $S_{mag} = R \cdot \ln(2S + 1)$, which will be described in detail for the special cases in the respective sections below.

3. Basics of the Density-Functional Theory and a Brief Introduction to FPLO

In this chapter the basics of density-functional theory (DFT) calculations and electronic band-structure investigations are outlined, but only as far as it is necessary concerning this work's results. The DFT calculations are basically used in this thesis to support the experimental results with theoretical models and conclusions. For this purpose, calculations with simplified models have been carried out to gain information on theoretical origins of observed physical effects by examination of the electronic band structure. A more detailed theoretical study is not taken into account in this work, since it would by far exceed the scope of this thesis, which is mainly focused on experimental work.

First, a brief general introduction of the density-functional theory as described by Kohn and Sham will be given in this chapter. The main section describes the local density approximation (LDA) and the local spin-density approximation (LSDA), which are used in this work. With these models a calculation of electronic band structures and the density of states (DOS) is possible. The modelling of the La_2RuO_5- and the $CaCu_3Ti_4O_{12}$-related compounds with these approximations is described in this chapter and the interpretation of the obtained results will be presented in the subsequent chapters 4, 5 and 6.

Since the La_2RuO_5 and the $CaCu_3Ti_4O_{12}$ related compounds are semiconducting oxidic materials and show electronic correlations, LDA and LSDA are not sufficient to completely describe the observed effects, which are mainly caused by the exchange interaction of electrons in $3d$, $4d$, and $4f$ orbitals. These interactions may better be described using e.g. LSDA+U or DMFT approaches. However, the results of the basic calculations described in this thesis can be used as a first benchmark for further investigations.

In the last section of this chapter an introduction to the used FPLO program and the description how the calculations were performed is given.

3.1. Introduction to Density-Functional Theory

Even for nearly free valence electrons in an ionic lattice the exact determination of the electronic structure by analytical or numerical methods is impossible, since roughly 10^{24} electrons are present in one mole of sample material [Eye00]. These electrons are exposed to Coulomb repulsion between them and attraction to the lattice ions with positive charge. The Born-Oppenheimer approximation allows to separate the modelling of the light electrons from the movement of the roughly 2000 times heavier ionic cores, which are considered stationary in an equilibriated state

compared to the fastly moving electrons [Bor27]. The electron dynamics is therefore defined by their kinetic energy, the potential caused by the ions, and the interaction between the electrons.

The energy eigenvalues of the electrons are given by the time independent Schrödinger equation ($H\psi = \varepsilon\psi$) with the Hamilton operator H rewritten as [Eye00]:

$$\left[\frac{\mathbf{p}^2}{2m} + V(\mathbf{r}) + U(\{n(\mathbf{r})\}, \mathbf{r})\right] \cdot \psi(\mathbf{r}) = \varepsilon \cdot \psi(\mathbf{r}) \tag{3.1}$$

(vectorial parameters are indicated by bold face). This Schrödinger equation cannot be solved exactly, except for the single electron systems like the hydrogen atom. Several approximations were therefore developed to calculate the electronic structure of the far more complex many electron systems.

In the DFT approach the energy functional $E(n)$ is minimized introducing $n(\mathbf{r})$ as the electron charge density. Results of the DFT calculations are ground state energy and the ground state electron charge density [Hoh64, Tem09]. The electron wavefunction $\psi(\mathbf{r}_1, \mathbf{r}_2, \ldots, \mathbf{r}_N)$ describing all N electrons on their positions $\mathbf{r}$ is replaced by $n(\mathbf{r})$ becoming the variable parameter in the calculation. Thus, the full solution of the many electron Schrödinger equation is replaced by the solution of a set of N single-electron equations known as Kohn-Sham functions [Koh65]. The exact value of $E(n)$ is not known, however it can be approximated by the above reported separation of the total energy-functional term and the addition of an exchange-correlation term $E_{xc}(n)$. The Hamilton operator or total energy functional is rewritten as

$$E(n) = T_0(n) + U(n) + V_{ext}(n) + E_{xc}(n) \quad , \tag{3.2}$$

where $T_0(n)$ is the kinetic energy of a non-interacting electron gas with charge density $n(\mathbf{r})$. The sum of the other three potential terms can be denoted as an effective potential. The electron-electron interaction term for electrons $\mathbf{r}$ and $\mathbf{r}'$ is given by:

$$U(n) = \int\int \frac{n(\mathbf{r})n(\mathbf{r}')}{|\mathbf{r}-\mathbf{r}'|} \mathrm{d}^3r\, \mathrm{d}^3r' \quad . \tag{3.3}$$

The external potential energy including electron-ion and ion-ion interactions is written as:

$$V_{ext}(n) = \int n(\mathbf{r})V_{ion}(\mathbf{r})\mathrm{d}^3r + E_{ion-ion} \quad . \tag{3.4}$$

The exchange correlation term $E_{xc}(n)$ is containing the functional of the electron-density approximation. The LDA is based on the assumption that each point in space contributes additively to $E_{xc}(n)$ and ε_{hom} is the exchange and correlation energy of a homogeneous electron gas according to:

$$E_{xc}^{LDA}(n) = \int n(\mathbf{r})\varepsilon_{hom}(n(\mathbf{r}))\mathrm{d}^3r \quad . \tag{3.5}$$

By using two spin densities (one for spin-up and one for spin-down, indicated by the arrows in the equation) the LSDA functional is given by:

$$E_{xc}^{LSDA}(n\uparrow, n\downarrow) = \int n(\mathbf{r})\varepsilon_{hom}(n(\mathbf{r})\uparrow, n(\mathbf{r})\downarrow)\mathrm{d}^3r \quad . \tag{3.6}$$

Even higher sophisticated functionals can be introduced to increase the calculation accuracy. For example the gradients of the electron charge density can be added in the generalized gradient approximation (GGA) according to:

$$E_{xc}^{GGA}(n\uparrow,n\downarrow) = \int n(\mathbf{r})\varepsilon_{hom}(n(\mathbf{r})\uparrow,n(\mathbf{r})\downarrow,\nabla n(\mathbf{r})\uparrow,\nabla n(\mathbf{r})\downarrow)d^3r \quad . \tag{3.7}$$

In literature a number of alternative models of electron-density functionals are reported, e.g. in Refs. [Per05, Esc03].

The $E(n)$ minimization is performed by solving a single particle Schrödinger equation for the effective potential including the exchange-correlation term [Tem09]. Initially a density $n(\mathbf{r})$ is calculated by the population of the lowest reasonable energy levels (eigenstates ε in Eq. 3.1). In a self-consistency run the energy is minimized and the density is again modelled by the same population procedure. This iterative process is performed until the deviation between the input $n(\mathbf{r})$ and the obtained simulated charge density is below the termination-criteria values set for e.g. the density and the total energy.

Additional spin-orbit interactions can only be modelled in a relativistic formalism [Tem09]. Often a scalar-relativistic approximation is used by adding a spin-orbit term acting like a pertubation to the total energy. However, in this simplification the angular momentum operator is supposed to act only in a defined region around each atom. Nevertheless, for many systems this approximation is very accurate and saves calculation time.

It is also reported that the LDA and LSDA methods are lacking accuracy when modelling simultaneously itinerant and localized electrons, which is especially the case for d and f electrons [Tem09]. The localization of d electrons in transition metal compounds is often underestimated and the existing band gaps are commonly too small or even not existing in LDA. The LSDA method improves the result accuracy, however often wrong magnetic ground states are found. The correlation of the f electrons in the screened core shell usually pins the very narrow f bands close to the Fermi level, which is not reasonable due to the required separation of occupied and empty states. This problem can be partly overcome, for example, by adding a scaling energy term to the E_{xc}^{LSDA} functional (OP scheme [Eri90]) or an on-site repulsion Hubbard-U term leading to the LSDA+U methods. They are completed by a double counting term, which is needed for correction of already included exchange interactions to avoid a double counting of them. However, the adding of the U and the double-counting term requires experience or several trials to find a reasonable value for correction, since the starting values are not known. Usually an estimation for U is determined from photoemission experiments and further refined during the calculations.

3.2. Introduction to the Code Package FPLO and the Performed Calculations

The DFT calculations of this work were performed with the full-potential non-orthogonal local-orbital minimum-basis program code FPLO 7.00-28 [Koe99, Opa99]. The input files were created

using the auxiliary editor "fedit". The crystal structure data including the space group, cell parameters and atomic positions were saved in a structure file "=.in" (all input data) including the crystal structure file "=.sym". The program is accessing this "=.in" file during the start of the modelling process.

The FPLO code is using a self-adjusting minimum basis consisting of an initially provided mixture of core and valence states for each element. For example, the used valence and semi-core states of Ru are $4s4p5s6s4d5d5p$ and the energetically lower lying states are treated as core states, which do not contribute to the chemical bonding properties. For oxygen respectively $1s2s3s2p3p3d$ valence and semi-core states are used. To avoid infinite contributions of those states a compression factor which is linked to the nearest-neighbor distance is introduced and optimized. The minimum-basis is an advantage since it reduces the numerical effort and hence computation time, however, the accuracy of the results is still comparable to alternative full-potential codes [Koe99].

The applied crystal potential in a regular lattice defined by $\mathbf{R} + \mathbf{s}$ ($\mathbf{R}$ is a Bravais-vector and $\mathbf{s}$ is a basis vector of the unit cell) is written as the sum of local potentials:

$$v(\mathbf{r}) = \sum_{\mathbf{R}+\mathbf{s},L} v_{\mathbf{s},L}(|\mathbf{r} - \mathbf{R} - \mathbf{s}|) \, Y_L(\mathbf{r} - \mathbf{R} - \mathbf{s}) \quad . \tag{3.8}$$

The terms Y_L are the spherical harmonics and the sum over $L = lm$ converges applying a cut-off L_{max}. The local potentials $v_{\mathbf{s},L}$ are achieved by utilizing a non-orthogonal local-orbital representation, which is resulting by a partition of unity. Thus, also the electron charge density has to be divided in the local densities of net (or on-site) and overlap contributions. For the density a one-dimensional shape function is used, while the decomposition of the non-linear exchange and correlation potential requires a three-dimensional function f_s. Due to the required overlapping of the shape functions so called "Voronoi cells" are used [Opa99], which are very efficient, since the function is a finite sum on sites where the cells overlap. Similarly to the potential the electron charge density can be obtained as a lattice sum of site densities according to:

$$n(\mathbf{r}) = \sum_{\mathbf{R}+\mathbf{s},L} n_{\mathbf{s},L}(|\mathbf{r} - \mathbf{R} - \mathbf{s}|) \, Y_L(\mathbf{r} - \mathbf{R} - \mathbf{s}) \quad . \tag{3.9}$$

The Hartree potential is evaluated with the Ewald method applied to all multi-pole components, the local part remains and the Fourier-transformed contributions are again partitioned equally to the density. Then a partial combination with the ion-ion Coulomb potential is performed, which leads to the localized potentials $v_{\mathbf{s},L}$ including the exchange and correlation term per unit cell written as [Koe99]:

$$E_{xc}(n) = \sum_{\mathbf{s}} \int d\mathbf{r} \, f_s(\mathbf{r} - \mathbf{s}) \, n(\mathbf{r}) \, \varepsilon_{xc}(n(\mathbf{r})) \tag{3.10}$$

(ε_{xc} are the exchange and correlation eigenvalues).

The local functions are represented on a radial mesh with some small (but nonzero) radius [Koe99]. For the calculation the radial functions are interpolated on the either logarithmic or power law spaced mesh. The determination of the on-site values of overlap, Hamiltonian matrix

elements, and total energy expressions is performed using radial integrations. The three dimensional integration of the two-site matrix elements is reduced to two dimensions by the application of the angular momentum operator and the rearrangement of the formulas, which reduces the number of needed calculation operation steps. Thus, the accuracy of the mesh point determination is $< 10^{-6}$ Hartree and the overlap integrals and densities are deviating with respect to the normalization below 10^{-6} [Koe99].

The resulting energy values, magnetic monents, and occupation factors were taken from a general output file. The density of states (DOS) was given orbital dependent with respect to the basis as a total sum and for each site separately. The band-structure results were plotted by the auxiliary application "bandplot", which is linked to the fedit editor.

The above mentioned use of an additional Hubbard-U on-site repulsion-term is also accessible with FPLO and described in detail in [Esc03a]. For this work this detailed investigation technique was not used due to the limited time, however, the obtained basic results could be improved by using this method in future works.

4. La$_2$RuO$_5$

The first two reports concerning La$_2$RuO$_5$ were published rather shortly after each other. The first publication by Khalifah *et al.* [Kha02] described the synthesis of polycrystalline material using the solid-state reaction of a stochiometric mixture of La$_2$O$_3$ and RuO$_2$. The crystal structure was obtained by Rietveld analysis of the neutron diffraction data for a high- (ht-) and a low-temperature (lt-) phase with a transition temperature T_d of roughly 160 K. The structural transition was found to be accompanied by interesting changes of different physical properties. Especially a dramatic reduction of the magnetic susceptibilty in the lt-modification was observed and its origin was discussed. In addition, the electric conductivity changes at the transition temperature, however, both modifications provide semiconducting properties. Using inelastic neutron-scattering data, the opening of a spin-gap of approximately 40 meV was described for the lt-phase. The second publication by P. Boullay *et al.* [Bou03] reported the detailed crystal structure obtained by the analysis of x-ray and selected-area electron-diffraction data. Further aspects concerning the exact composition and oxidation states were included to corroborate the structural data.

The detailed structural analysis of both phases by powder neutron diffraction was described in Ref. [Ebb05]. Further publications reported on the electronic conductivity and specific heat [Mal05], the local surrounding of the Ru-site and the Ru valence derived from x-ray absorption spectroscopy [Arc07]. The reduction behavior and the oxygen stoichiometry was studied in Ref. [Ben05]. From experimental results [Kha02, Kho05] and DFT calculations applying different models for the electron-density approximation [Eye06, Wu06, Eye07] an orbital-ordering mechanism was identified as the cause of the phase transition. The general occurrence of orbital ordering was previously predicted by Hotta *et al.* [Hot02] for single layered RP-ruthenates, which are structurally related to La$_2$RuO$_5$. For the strongly decreased lt-phase magnetic susceptibility Khalifah *et al.* [Kha02] assumed a quenched Ru spin moment ($S = 0$) induced by an energy splitting of the t_{2g} orbitals due to symmetry reduction. Alternatively, the formation of a two-leg spin ladder with rungs of antiferromagnetically coupled Ru $S = 1$ spin-moments was discussed and is favored by the DFT calculation results. The spin-ladder formation was further supported by the found changes of interatomic distances between ht- and lt-phase, which provide alternating long and short distances between the Ru ions [Ebb05], which also fits to a spin-Peierls like transition. Furthermore, by muon-spin rotation measurements Blundell *et al.* [Blu08] showed that the local $S = 1$ moment for the Ru ions is conserved in the lt-modification. This finding was supported by Moon *et al.* [Moo08] and Wu *et al.* [Wu08] using infrared spectroscopy due to a shift of the spectral weight at the absorption edge caused by the structural transition. In addition, Rivas-Murias *et al.* [Riv11] showed by thermal conductivity studies that the $S = 1$ is conserved in the lt-phase. Soares *et al.* [Soa12] found indications of $S = 1$ below T_d in the perturbed angular correlation of

Perovskite ABO_3 $ABO_{3.5}$ (n = 4) ABO_4 (n = 2) La_2RuO_5
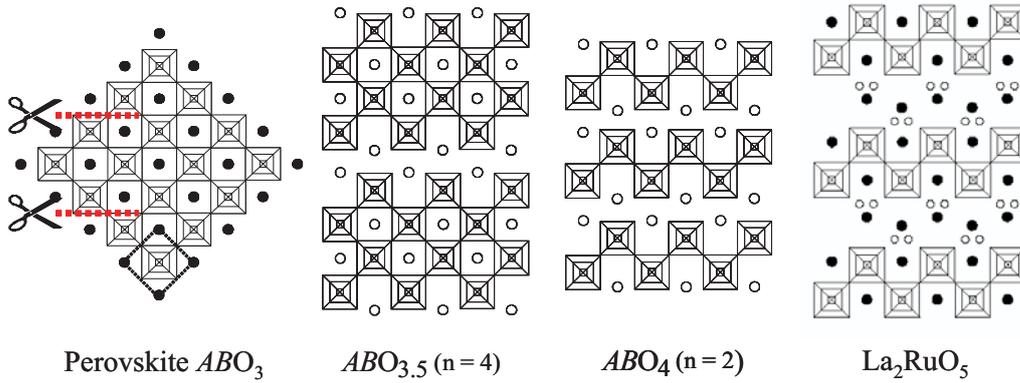
Figure 4.1.: Starting from the perovskite ABO_3 (unit cell marked with solid lines in the lower corner) structure on the left side a cut along the [110]-direction leads to $A_nB_nO_{3n+2}$ phases. In the center the examples for $n = 4$ and $n = 2$ are depicted. The La_2RuO_5 structure on the right side is achieved by a (formal) insertion of LaO-layers between the $LaRuO_4$-blocks ($n = 2$). For details see text.

hyperfine interactions obtained by measuring the $\gamma - \gamma$ cascade in the decay of diluted radioactive ^{111}In atoms ($\rightarrow$[111]Cd) added to the sample powder. In addition, Mössbauer spectroscopy proved the constant +4 oxidation state for Ru in combination with a preseved spin-moment of $S = 1$ between 4.9 K and 196 K [Hea07].

The diminishing magnetic susceptibility has to be explained taking into account the structural changes within the $LaRuO_4$-layers caused by the phase transition. Accordingly the transition can be described applying models for a two dimensional magnetic ordering with a singlet ground state, which is characterized by almost zero total magnetic susceptibility. The origin of the magnetic transition occurring at quite unusual high temperatures has not fully been solved. It is still questionable if the structural change induces the magnetic transition or if the magnetic exchange and the resulting orbital ordering forces the crystal lattice to the structural transition. Other alternative or sophisticated models like a spin-Peierls scenario have to be discussed to be able to explain the experimental results by one basic model.

One- or two-dimensional magnetic oxides providing low-temperature structural transitions with the formation of a non-magnetic singlet ground state are well known and intensively studied for $S = 1/2$ compounds [Has93, Iso96, Iwa96, Ono96, Pic97, Mat96, Kik99, Vas05]. However, there are only few examples for $S = 1$ systems with a singlet ground state, because usually 3D long-range order sets in due to residual interchain or interplane interactions [Yok95, Uch99, Vas04]. From the theoretical point of view the ground state of an ideal uniform antiferromagnetic Heisenberg chain with half integer spins is gapless, while in case of integer spins a non-zero excitation-gap is formed [Hal83]. Nevertheless, even in half-integer spin-chains an energy gap can open if pairs of neighboring spins dimerize forming a non-magnetic singlet ground state. Spin dimerization accompanied by structural modification is known as spin-Peierls transition [Pyt74] and sometimes observed in 1D systems. In 2D systems the magnetic ground state crucially depends on the anisotropy of the exchange with Ising spins exhibiting a long-range ordered state, while

Heisenberg spins show no magnetic phase transition at finite temperatures. *XY* systems provide no conventional long-range spin order but are characterized by the formation of vortex–anti-vortex pairs as described by Kosterlitz, Thouless, and Berezinskii [DeJ90]. Further complications arise from the fact that the transition from 1D to 2D is by no means smooth: The ground state of spin-ladder materials sensitively depends on the number of legs [Dag96].

La_2RuO_5 is a rare example for a low-dimensional magnetically ordered system providing a singlet ground state as well as a quite unique crystal structure. Therefore, it is very interesting to study this special compound with respect to its structural details and changing magnetic properties and to use more sophisticated models to describe the experimental data. A comparison of the obtained crystal structures for poly- and single crystalline La_2RuO_5 prepared by conventional solid-state reaction, soft-chemistry routes, and using a flux method is shown. Furthermore, the results of physical-property measurements (magnetic susceptibility, specific heat, optical and dielectric spectroscopy) and DFT calculations are discussed. Based on this, the origin of the magneto-structural phase transition is investigated and a new interpretation of the magnetic entropy change obtained from specific-heat data is provided, which nicely correlates to the results of the magnetic susceptibility and DFT calculations. This allows a first estimate of the change of the magnetic Ru–Ru exchange interaction caused by the phase transition.

The main part of the results shown in this chapter base on already published contributions in scientific journals [Rie11, Rie12a, Rie12b, Rie12c, Rie12d, Rie13a, Rie13b]. The data has been rearranged to soundly group the results with respect to the investigated samples and properties.

4.1. Crystal Structure

4.1.1. General Structural Description

As mentioned above, La_2RuO_5 crystallizes in two modifications, a monoclinic phase basically above $T_d = 161$ K denoted as ht-phase and a triclinic lt-phase below the transition temperature [Kha02]. The transition was observed in a broad temperature range of roughly 30 K around T_d as well as a complete mixing of both phases indicating a smooth change from ht- to lt- modification. The structure of a sample synthesized by solid-state reaction was studied earlier by ND at room temperature and 1.5 K [Ebb05]. Here the Rietveld analysis of x-ray diffraction data measured at varying temperatures are provided.

A model to describe the complicated structure of La_2RuO_5 is depicted in Fig. 4.1 as shown in Ref. [Ebb05]. The description is based on the perovskite ABO_3 structure depicted schematically in the left side of the figure. The BO_6 octahedra are represented by squares and the small circles mark the A cations. The perovskite unit cell is marked by solid lines in the lower corner. By formally cutting the perovskite along its [110]-direction a family of layered structures with the sum formula $A_nB_nO_{3n+2}$ ($n > 1$) is obtained, where the value of n denotes the perovskite-slab thickness. This structure family as well as the Ruddlesden-Popper layered structures are systematically described in Ref. [Lic01]. In the center of Fig. 4.1 the example $ABO_{3.5}$ for $n = 4$ is shown. Typical oxides crystallizing in this structure are $LaTiO_{3.5}$, $CaNbO_{3.5}$, $SrNbO_{3.5}$, and $SrTaO_{3.5}$, which are
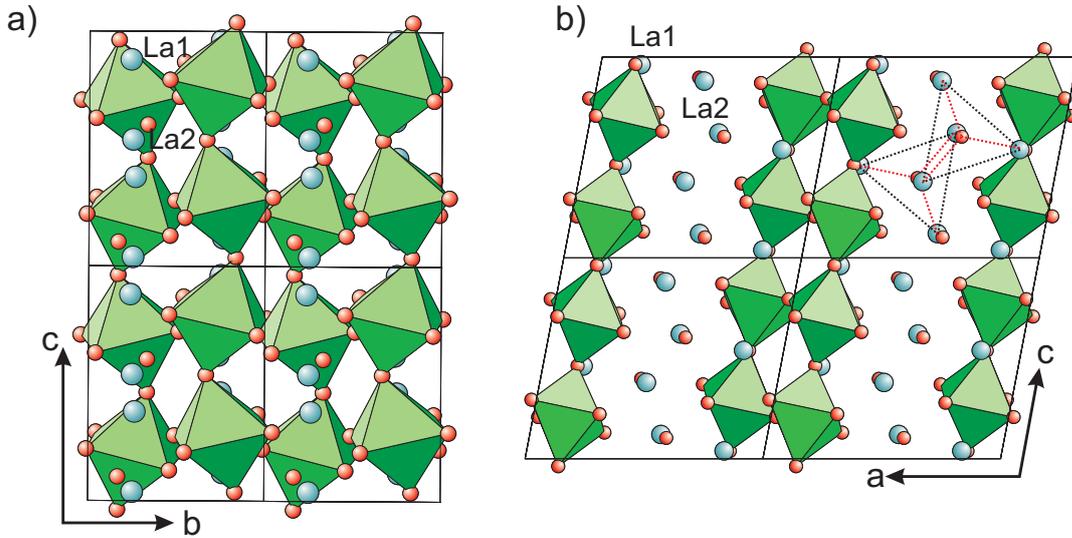
Figure 4.2.: La$_2$RuO$_5$ ht-phase crystal structure (2×2 unit cells) viewed along a) the *a*-axis and b) *b*-axis. The La ions are represented by turquoise circles, the oxygen ions by red circles and the RuO$_6$ octahedra are drawn in light green. In b) the terahedral coordination of oxygen by La in the LaO-layer is indicated by dashed lines.

all insulating high-T_c ferroelectrica [Lic01]. By an anionic substitution of oxygen by nitrogen so called oxynitrides are obtained which provide again a perovskite structure and the sum formula ABO$_2$N [Agu08, Ebb09]. The structure scheme second from right in Fig. 4.1 shows the resulting ABO$_4$ for $n = 2$. For this structure type only fluorides were reported in Ref. [Lic01], however, the oxide LaTaO$_4$ is an example for this structure type though the octahedra are slightly distorted [Cav81]. By increasing the slab thickness to infinity ($n \to \infty$) the original perovskite structure is again obtained.

The La$_2$RuO$_5$ crystal structure is achieved by taking the $n = 2$ representative ABO$_4$, corresponding to LaRuO$_4$-layers, and formally inserting buckled LaO-layers between the perovskite like slabs (right side of Fig. 4.1) leading to the overall sum formula La$_2$RuO$_5$ [Bou03, Ebb05]. The ht-modification crystallizes in the monoclinic space group P2$_1$/c with cell parameters $a \approx 9.185$ Å, $b \approx 5.83$ Å, $c \approx 7.95$ Å, and $\beta \approx 100.78°$. In contrast, the lt-phase has a triclinic structure (space group P$\bar{1}$) with slightly deviating cell parameters $a \approx 9.16$ Å, $b \approx 5.81$ Å, $c \approx 7.96$ Å, $\alpha \approx 89.8°$, $\beta \approx 101.1°$, and $\gamma \approx 91.8°$. In both the monoclinic and triclinic modifications all atoms are located on general Wyckoff-positions.

In the Figs. 4.2 and 4.3 the crystal structure of La$_2$RuO$_5$ is depicted projected along the three different unit-cell axes. In Fig. 4.2 only the ht-phase structure viewed along the *a*- and *b*-axis are shown, since the differences between ht- and lt-modifications are almost negligible. The light green RuO$_6$-octahedra are corner sharing, tilted, and twisted in opposite directions. The projection along the *b*-axis (Fig. 4.2b) is more useful to show the layered structure and the monoclinic angle β, which is distinctly larger than 90°. Due to the monoclinic angle the neighboring LaRuO$_4$-
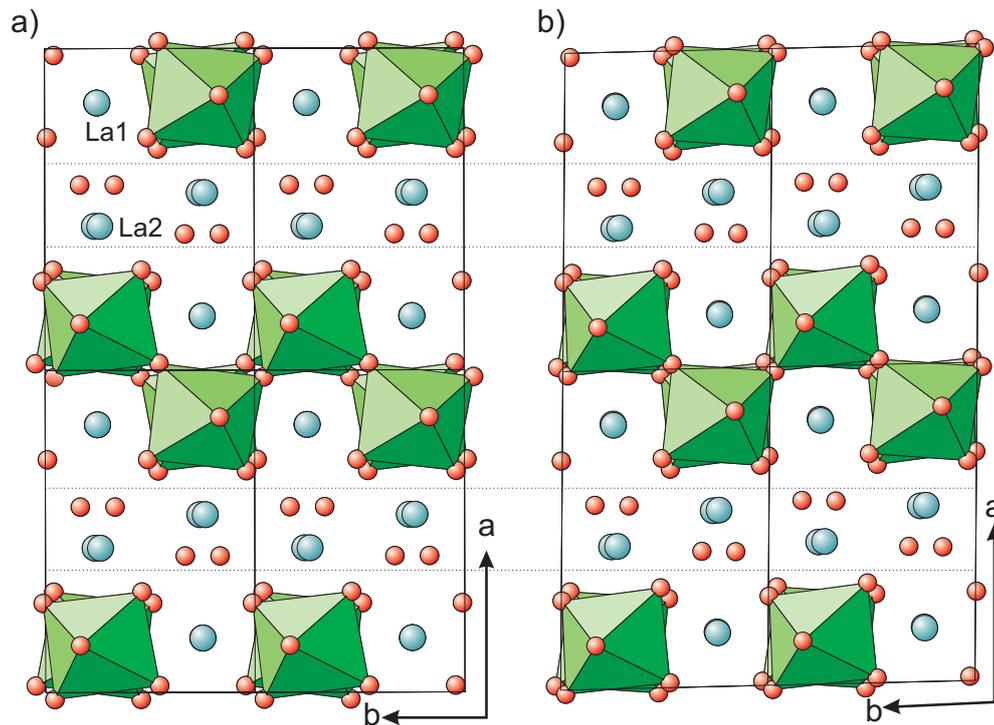
Figure 4.3.: La_2RuO_5 crystal structure of 2×2 unit cells viewed along the *c*-axis (a) ht- and b) lt-configuration). Color scheme as described in Fig. 4.2. The alternating layering of $LaRuO_4$- and LaO-layers is indicated by the horizontal dashed lines.

layers are shifted by roughly half of the height of one octahedron. Furthermore, in this projection the buckled LaO-layers are clearly visible. The site denoted La1 is located in the $LaRuO_4$-layers and the La2-site in the LaO-layers, respectively. The oxygens in the LaO-layer are coordinated tetrahedrally by La, i.e. each of these oxygens is connected to one La1 and three La2 [Bou03, Rie12b]. To illustrate this, two tetrahedra are marked in the top right unit cell by dashed lines.

The best perspective to illustrate the structure is the projection along the *c*-axis, which is depicted in Fig. 4.3. The alternating layering of $LaRuO_4$ and LaO is indicated by the horizontal lines. In the figure the difference between ht-phase and triclinic lt-phase can be seen. The deviation of γ by roughly 2 degrees is clearly visible and the twisting of the octahedra decreases slightly in the lt-phase. However, in general the differences in atomic positions and coordination between both phases are still very small. In Fig. 4.3 the sites La1 and La2 are well distiguishable, illustrating their different position in the layers of the crystal lattice. The zig-zag like arrangement of the RuO_6 octahedra along the *b*-axis is clearly visible and demonstrates the relationship to the [110]-phases like, for example, $LaTaO_4$.

In the ht-modification Ru is coordinated octahedrally with Ru–O bond lengths between 1.93 Å and 2.07Å. The varying distances show that the octahedra are distorted, reflecting an off-center position of the Jahn-Teller active Ru^{4+}. The La ions (La1 and La2) are coordinated by nine
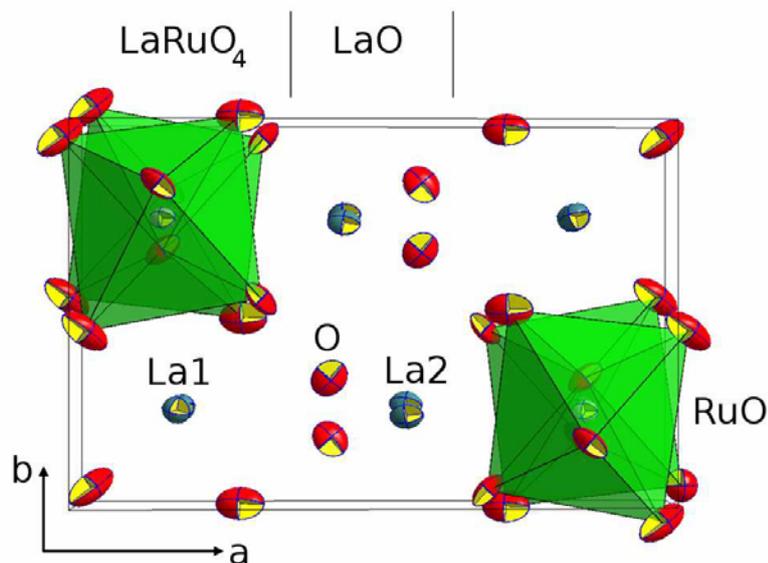
Figure 4.4.: La$_2$RuO$_5$ crystal structure viewed along *c*-direction. La is colored blue, oxygen red and Ru is represented light grey in the center of the green RuO$_6$ octahedra. The anisotropic displacement ellipsoids are shown with 90% probability. On the top the LaRuO$_4$ and LaO layering is indicated.

oxygen ions with varying La–O distances between 2.32 Å and 2.96 Å in irregular geometries. Bond valence sum (BVS) calculations of the ht-phase reveal the expected valences in the LaRuO$_4$-layers of +3.9 for Ru, +3 for La, and -1.9 for O. The valences of the ions occupying the LaO-layers amount to values of approximately +3.2 for La and in turn -2.4 for O. This reflects a difference in the ionic radii matching for the two sites. While La1 in LaRuO$_4$ provides an agreeable size for La^{3+}, in LaO the La2-sites are too small resulting in a considerable structural stress for these sites.

4.1.2. Single-Crystal X-ray Diffraction

Single crystals of La$_2$RuO$_5$ were obtained from a flux as described in Sec. 2.1.4. Several crystals were tested on a STOE IPDS-2T single-crystal diffractometer and all turned out to be twins. Nevertheless, a structure analysis was possible due to the partially merohedral nature of the twinning, which allowed the separation of the diffraction patterns of both twin domains. Overlapping peaks were omitted in the refinement. The data of the measurement conditions and parameters used for the refinement as well as the detailed obtained structural data are listed in Tabs. A.3 to A.5 in the appendix. Unit-cell values very close to the ones obtained from powder x-ray and neutron diffraction were found [Kha02, Bou03, Ebb05]. The single-crystal analysis also leads to similar atomic coordinates (Tab. A.4), therefore, the bond lengths and angles of the single crystal are very close to the results from the neutron powder diffraction.

In Fig. 4.4 the obtained crystal structure is depicted. The ellipsoids represent the anisotropic displacement factors (Tab. A.5) with 90% probability. Their shape illustratively reflects the possi-
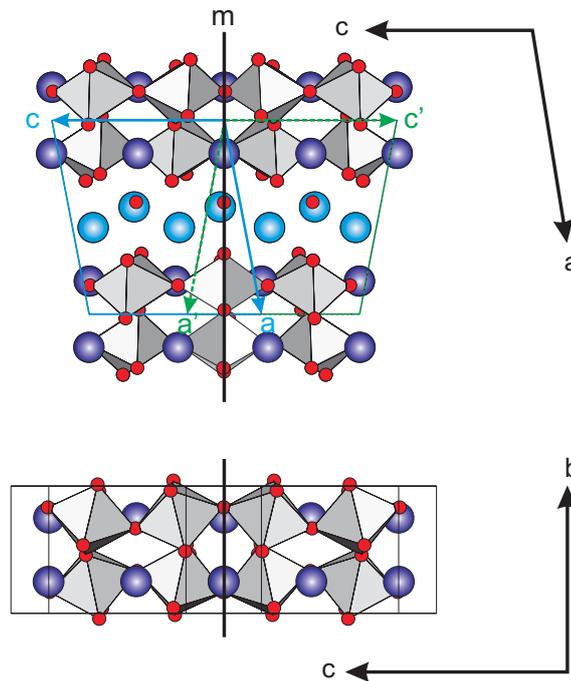
Figure 4.5.: Crystal structure of the La_2RuO_5 single crystals including the observed twin law. Top: View projected along *b*. Bottom: *a*-direction projection showing the detailed octahedral arrangement at the domain border. La are represented by large blue spheres, oxygen by small red spheres, and RuO_6 octahedra are colored grey.

ble displacement of the atoms caused by rotations and tilting of the RuO_6 octahedral and the La_4O tetrahedral units. The deviating Ru–O bond lengths listed in Tab. A.6 reflect the slightly off-center position of the Ru-site within the octahedra.

The mentioned twinning of the crystals can be described by the twin matrix (1 0 0.5, 0 -1 0, 0 0 -1). In Fig. 4.5 the crystal structure is depicted including the twinning law, which appears as a pseudo *ab* mirror plane (*m*). The obtained arrangement of the two domains is well describing the fishbone pattern observed by optical microscopy in grazing reflection since the intergrowth of the domains influences the reflection property by the formation of a lamellar superstructure.

4.1.3. Sample Morphology

In Fig. 4.6 SEM images of two different La_2RuO_5 samples are depicted to illustrate the differences between samples obtained from $BaCl_2$-flux or solid-state synthesis (left) and sol-gel synthesis (right). The crystallites from solid-state synthesis are distinctly smaller by roughly one order of magnitude than the shown crystals, however, their shape is very similar. On the surface of the plate-like and roughly hexagonally shaped crystals (left part of Fig. 4.6) the described fishbone structures are observable indicating twin-domain borders mentioned above. In the right part of Fig. 4.6 the characteristic sponge-like morphology of the samples obtained from soft-chemistry reactions can be seen. The porous structure results from the gaseous reaction products evolving
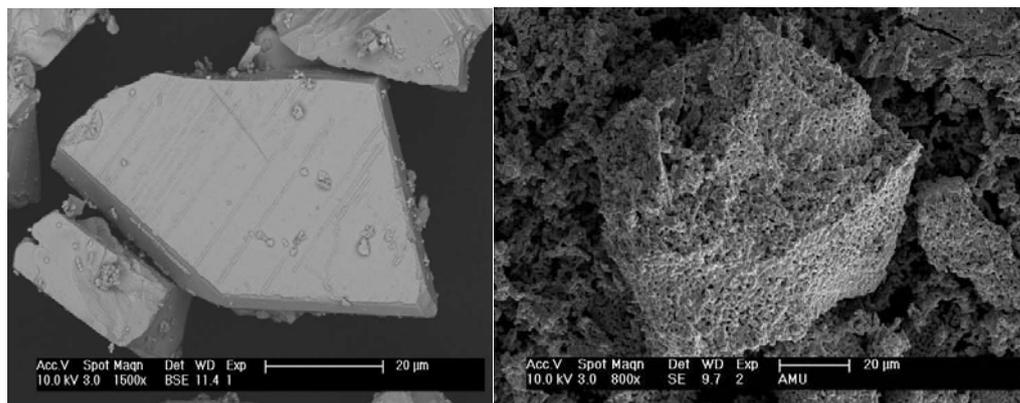
Figure 4.6.: SEM images of different La$_2$RuO$_5$ samples illustrating the different morphologies of single crystals (left) and samples obtained by sol-gel synthesis (right).

during the decomposition of the organic components. Therefore, a much larger surface results although the particles are comparable in size to the single crystals in the left frame.

4.2. Magneto-Structural Phase Transition

The origin and relationship of the structural changes and concomitant modifications of physical properties was investigated for pure La$_2$RuO$_5$ as well as for the rare-earth, Ti, and Mn substituted samples. The basic mechanism deduced for unsubstituted La$_2$RuO$_5$ is described and discussed in detail in this chapter. The results for the substituted samples are discussed in chapter 5.

4.2.1. Structural Phase Transition

Due to the limited neutron-diffraction beamtime most of the structural investigations were done using the Rietveld analysis of the x-ray diffraction data. In Fig. 4.7 the excellent agreement of the measured and Rietveld refined pattern is shown for the polycrystalline La$_2$RuO$_5$ sample obtained from the soft-chemistry reaction using Ru-NOAc. The high angle region above $80°$ is displayed in detail in the inset to illustrate the good fit quality in this part. The overall absence of additional peaks indicates the high phase purity of the sample.

The applied pseudo-Voigt peak profiles are in very good agreement with the measured data except for the $(h\,0\,0)$ reflections. In Fig. 4.7 the reflection $(3\,0\,0)$ is marked by an arrow. Its shape and intensity cannot be fit satisfyingly because the peak is broader and more asymmetric than the other reflections. The $(h\,0\,0)$ reflexes are linked to the layering in the crystal structure along the a-axis. Therefore, small irregular deviations of the stacking distances cause the broadening of the corresponding reflections and the by this changing interference conditions affect the peak intensity.

The differences between ht- and lt-phase crystal structure leads to clear changes in the diffraction patterns as shown in the synchrotron-radiation diffraction-patterns depicted in Fig. 4.8. In the left
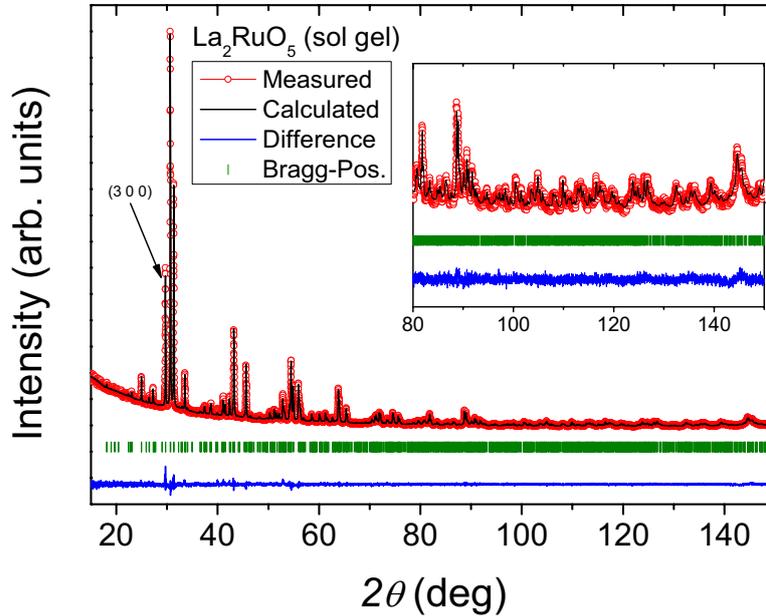
Figure 4.7.: X-ray diffraction pattern and result of the Rietveld refinement for polycrystalline La$_2$RuO$_5$ obtained from sol-gel synthesis with Ru-NOAc. The inset shows the 2θ range between 80 and 150° indicating the good fit quality.

panel the diffraction pattern (red circles) and refinement result (black solid line) for a measurement at 300 K is shown, while in the right frame the pattern recorded at 100 K is given. The bragg positions of both the ht- and the lt-phase crystal structure are marked by the green vertical dashes and the difference curves of measured data and refinement are drawn as a solid blue line in the bottom part of the panels. The most intense reflections in the vicinity of roughly $2\theta = 10°$ are slightly split in the lt-phase due to the lowered symmetry. Even more pronounced are the emerging intense additional reflections at approximately $2\theta = 14°$ and $16°$. The different angular range of the shown synchrotron-diffraction data compared to the laboratory x-ray diffraction data results from the wavelength of 0.499309 Å, which is approximately one third of the otherwise used Cu-K$_\alpha$ radiation. The rather pronounced backround is caused by the used glass capillary. The shown diffraction patterns of the single phases can be well refined. In contrast, in the vicinity of the phase transition temperature, where a mixture of both phases is observed, the refinement was only possible utilizing both the ht- and lt-modification structure models.

The high-resolution synchrotron-diffraction patterns recorded at different temperatures were used to study the unit-cell parameters in detail. Furthermore, a quantitative phase analysis of ht- and lt-fractions in the polycrystalline La$_2$RuO$_5$ sample (solid-state reaction) was performed. The results can be compared to earlier reported ND investigations [Kha02]. Measurements with
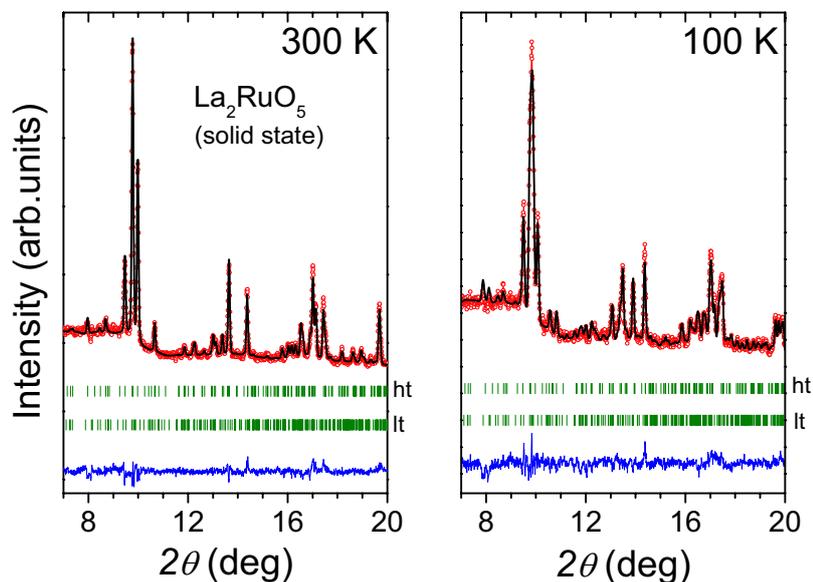
Figure 4.8.: Synchrotron x-ray diffraction patterns and results of the Rietveld refinements of the ht-(left) and lt-phase (right) of La$_2$RuO$_5$ synthesized by solid-state reaction. The wavelength of the used radiation was 0.499309 Å.

smaller temperature steps were performed here and were analyzed in more detail regarding the cell-parameter changes in the transition-temperature range.

The contributions of the monoclinic ht- and the triclinic lt-phases were determined from patterns recorded at temperatures between 50 K and 300 K. Starting at room temperature the sample was cooled down and roughly every 10 K a diffraction pattern was recorded. Afterwards, the sample was heated up again and patterns were recorded to check for a possible hystersis of the transition. The fractions of the ht- and lt-phases were calculated from Rietveld refinement at each temperature step and the result is shown in Fig. 4.9 for the patterns obtained from the cooling cycle. In the refinements the scaling factors, the cell parameters, and the overall displacement parameter were allowed to vary, while the atomic positions were fixed. The obtained result at a given temperature was used as starting point for the refinement of the next temperature step. To check whether or not this procedure leads to reliable results, both directions were tried for both cooling and heating, i.e. starting from 300 K going down and starting from the lowest temperature going up. Both ways yielded almost identical compositions as shown in Fig. 4.9. Obviously the phase transition itself is very broad, ranging over roughly 30 K. In this temperature interval the diffraction patterns can be described by a mixture of both phases. At higher or lower temperatures only the ht- or lt-phase is present, respectively. The (transition) temperature at which 50 % of each phase is present amounts to approximately 170 K. Comparing these results with the heating-cycle data (not shown
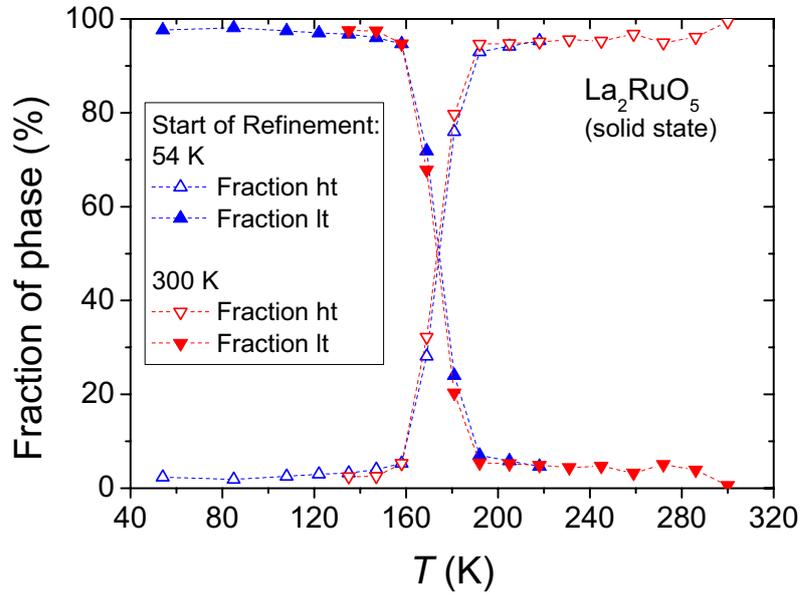
Figure 4.9.: Results of the quantitative phase analysis of La_2RuO_5 depending on temperature. Fractions of ht- and lt-phase were calculated from synchrotron-diffraction data for a stepwise cooling from 300 K to 54 K.

in Fig. 4.9) no thermal hysteresis was observed. A similar result was reported by Khalifah *et al.* on basis of neutron-diffraction data [Kha02]. These authors found a similar transition range and reported a structural transition temperature of 160 K. The deviations between the transition temperatures may be explained by different temperature calibrations. From the Rietveld analysis it can be concluded that the phase transition is fully reversible without dissipative character. The DSC data and magnetic properties discussed below support this finding. Only small differences (less than 2 K, which is in the error range of these measurements) between the heating and cooling measurements regarding methods and properties were observed for polycrystalline samples.

Details of the unit-cell parameter evolution depending on temperature are depicted in Fig. 4.10. In the left column the three axis lengths are shown, while the angles are shown in the three panels in the right column. For α and γ the ht-phase value is 90° due to the monoclinic symmetry and, therefore, omitted in the figure. The lt-phase is represented by the full symbols, while the open symbols mark the ht-modification, respectively. The data are taken from the cooling cycle. Results from the refinement start at 50 K are colored blue, the ones of the 300 K start are represented by red symbols, respectively. Only a very small difference between both sets is observed in agreement with the above described reversible character of the transition.

All parameters show a step-like or divergent behavior close to the transition temperature, which is indicated by the vertical solid line in each frame. This line represents the transition temperature
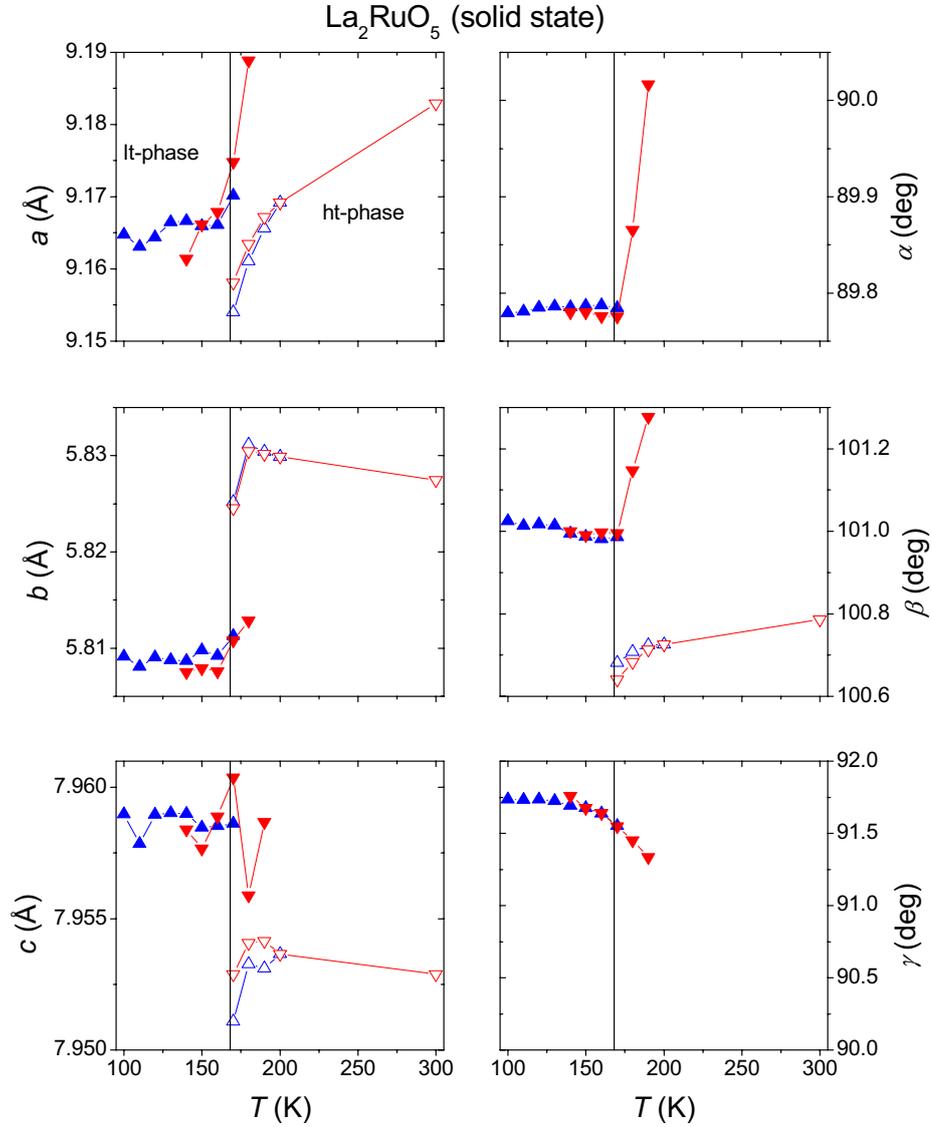
Figure 4.10.: Results from Rietveld analysis of synchrotron diffraction data of La_2RuO_5 recorded at different temperatures. Unit-cell parameters of the ht- and lt-phase were obtained from a stepwise cooling (and heating) between 300 K and 54 K. In the left column the unit-cell axes are shown, in the right column the unit-cell angles, respectively. Symbols according to Fig. 4.9 are used, i.e. full - lt-phase, empty - ht-phase, blue - start at 54 K, red - start at 300 K. The solid vertical lines mark the dimerization temperature T_d, as derived from magnetization measurements.

T_d determined by magnetization measurements and is roughly 10 K below the structural transition temperature, as derived from the phase distribution. Nevertheless, since the phase-transition regime is rather broad in temperature both values are in acceptable agreement with the visible
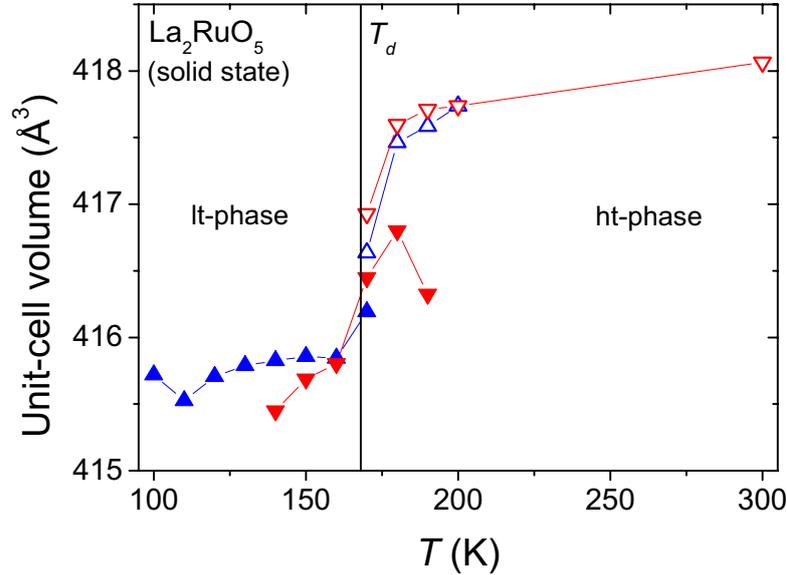
Figure 4.11.: Unit-cell volumes of the ht- and lt-phase were obtained from a stepwise cooling (and heating) between 300 K and 54 K during the synchrotron XRD measurement. Symbols according to Fig. 4.9 are used, i.e. full - lt-phase, empty - ht-phase, blue - start at 54 K, red - start at 300 K. The solid vertical line marks the dimerization temperature T_d, as derived from magnetization measurements.

changes of the cell parameters in Fig. 4.10. Especially for the parameters a and β a divergent behavior of ht- and lt-phase values are found, while the other ones are either showing a step-like or slightly convergent behavior. The values around the transition temperature provide a comparable high inaccuracy due to the lower fraction of the phase in the sample. In detail, below a fraction of 50 % the reliability of the cell-parameter refinement is not satisfying. Therefore, the obtained ht-values below the transition temperature and the lt-values above it are usually not shown. The changes between the ht- and lt-modification amount to less than 1 % except for γ where a difference of roughly 2 % is obtained. This deviation is in a reasonable range and even lower than found for e.g. $BaTiO_3$. This supports the reversibilty of the transition without dissipation and indicates low structural stress due to temperature variation.

The individual parameters show different temperature dependent behaviors. The ht-phase axis length a and the angle β decrease linearly with decreasing temperature, while the value of b and c provide a slightly increasing behavior. All lt-parameters remain almost temperature independent. This change of parameters is linked to the layered structure of La_2RuO_5 due to varying anisotropic temperature influences along or perpendicular to the stacking direction a. Furthermore, these deviating changes possibly induce the phase transition in order to reduce the evolving structural stress.

Table 4.1.: The Ru–Ru distances and Ru–O–Ru angles ϑ linked to the exchange couplings J_i as shown in Fig. 4.12.

J_i	d(Ru–Ru) (Å)	ϑ(Ru–O–Ru) (deg)
ht-phase		
J_0, J_3	3.975	155.4
J_1, J_2	3.978	152.8
lt-phase		
J_0	3.868	160.2
J_1	3.923	150.6
J_2	4.036	151.0
J_3	4.045	153.2

The overall behavior of the crystal structure is best represented by the evolution of the unit-cell volume, which is depicted in Fig. 4.11. While the unit-cell parameters can change individually due to the symmetry conditions as it was mentioned above, the volume is expected to decrease almost linearly upon cooling of the sample. This behaviour is observed for both the ht- and lt-phase of La$_2$RuO$_5$. At the transition temperature an additional step is found reflecting a volume reduction by 0.4 % from the ht- to the lt-modification. This small change is in agreement with the reversibility of the transition without very high structural stress.

4.2.2. Magnetic Phase Transition

As mentioned in the introduction the magnetic phase transition was observed in the same temperature range like the structural change [Kha02, Mal05]. This can be explained by the close structure-property relationship leading very probably to the dimerization of the Ru-spin moments in a spin-Peierls like transition [Eye06, Eye07, Wu06]. The magnetic susceptibility χ of the single- and polycrystalline samples was therefore studied in detail to characterize and discuss the origin of the strongly diminishing χ in the lt-phase related to the changes in the crystal structure.

While in the ht-phase the Ru–O–Ru angles (ϑ) and Ru–Ru distances[1] are almost equal in both directions b and c in the LaRuO$_4$-layers, in the lt-modification alternating short and long Ru–O–Ru distances are found. From literature Ru–Ru spin dimers are considered to form rungs of weakly interacting spin-ladders in the crystallographic c-direction. The situation becomes more complicated by the zig-zag square arrangement of Ru-ions and the alternating distances between the rungs in the ladders, which requires four exchange-interaction parameters J_i to describe the nearest-neighbor interactions. Possible next-nearest neighbour interactions are completely omit-

---

[1]To be correct, formally the Ru–O + O–Ru distances should be taken into account, since these are originally included in the superexchange considerations. However, the Ru–Ru distances are here recommended to use as simplification conserving the basic information, because their accuracy is higher in XRD analysis, which was mainly used to characterize the crystal structure in this thesis.
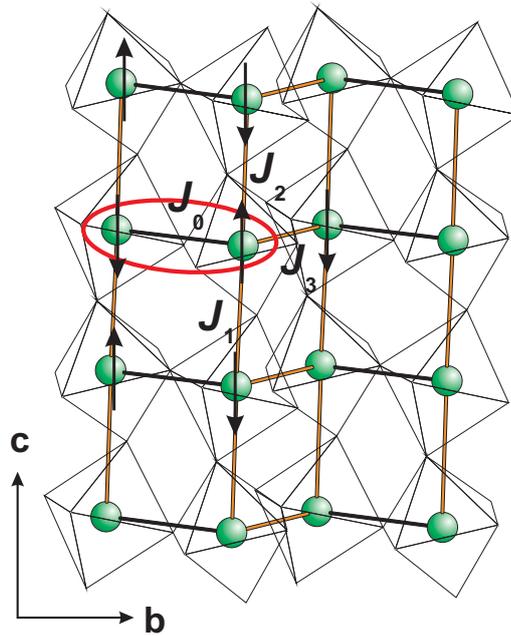
Figure 4.12.: RuO_6 octahedra network (transparent) in the *bc*-plane of the $LaRuO_4$-layers. One ruthenium (green spheres) spin-dimer is marked by a red ellipse and the exchange paths are denoted corresponding to the nearest Ru neighbors J_0 to J_3 (see also Tab. 4.1).

ted in the following. The spin-ladder model was mainly derived from the exchange values obtained from DFT calculations including spin polarized LDA and a Hubbard-U term [Wu06]. The corresponding Ru–Ru distances, Ru–O–Ru angles, and exchange paths denoted J_0 to J_3 for the ht- and lt-phase are listed in Tab. 4.1 and depicted in Fig. 4.12. For symmetry reasons J_0 and J_3, as well as J_1 and J_2 are identical in the monoclinic ht-modification. The crystal structure data shown in Tab. 4.1 are taken from ND experiments [Ebb05].

According to Tab. 4.1 the Ru–Ru distances in the ht-phase are almost identical and amount to roughly 3.975 Å. The Ru–O–Ru angles along the *b*-direction are slightly larger (155.4°) than in *c*-direction (152.8°). This arrangement already points to antiferromagnetic exchange interactions with smilar values for the corresponding constants J_i according to the Goodenough-Kanamori-Anderson rules [Goo63, Kan59, And59]. This point is discussed later in detail within the the ht-phase susceptibility analysis. In contrast, for the lt-modification the distances and angles are distinctly varying (Tab. 4.1). The structural changes are expected to lead to anisotropic variation of the J_i as deduced from the DFT calculations [Wu06] and, therefore, strongly support the dimerization of Ru-spins to nonmagnetic spin-dimers. From the inspection of the Ru–Ru distances and Ru–O–Ru angles it seems plausible that at 161 K a transformation takes place from an almost two-dimensional Heisenberg paramagnet into a spin ladder with spin-singlets along the rungs parallel to the *c*-axis. The dimer is most propbably found at the position marked by the red ellipse in Fig 4.12, which corresponds to the exchange path J_0 and the shortest Ru–Ru distance (3.868 Å)

and largest Ru–O–Ru angle (160.2 °).

To describe the electronic and magnetic configuration in La_2RuO_5, it is best to start from the strong crystal-field approach for the ht-phase. The octahedral crystal field splits the $4d$ electronic states of Ru in e_g and t_{2g} levels. The energetically lower lying configuration in Ru^{4+} is t_{2g}^4, which is equivalent to t_{2g}^2 in hole representation. As it was pointed out in Refs. [Eye06, Wu06], the distorted octahedral crystal field stabilizes the state $\{d_{xz}^\uparrow, d_{xz}^\downarrow\}$. The x- and y-axes are lying in the crystallographic ab-plane but are rotated by $45°$ with respect to the crystallographic axes a and b, while z and c are aligned parallel. Coulomb-repulsion between the remaining fourfold degenerate states $\{d_{xy}^\alpha, d_{yz}^\beta\}$ splits them into a singlet state ($S = 0$)

$$1/\sqrt{2}[\{d_{xy}^\uparrow, d_{yz}^\downarrow\} - \{d_{xy}^\downarrow, d_{yz}^\uparrow\}]$$

and a triplet ($S = 1$)

$$\begin{aligned}
|M_S = 1\rangle &= \{d_{xy}^\uparrow, d_{yz}^\uparrow\} \\
|M_S = -1\rangle &= \{d_{xy}^\downarrow, d_{yz}^\downarrow\} \\
|M_S = 0\rangle &= 1/\sqrt{2}[\{d_{xy}^\uparrow, d_{yz}^\downarrow\} + \{d_{xy}^\downarrow, d_{yz}^\uparrow\}] \quad .
\end{aligned}$$

According to Hund's rules the triplet state is energetically lower and can be described by the effective spin $S = 1$. The orbital momentum is considered to be quenched. This configuration is already energetically favored by the octahedral deformations in the ht-phase and becomes further stabilized by the structural changes occurring during the transition to the lt-phase. Since this scenario is found in both the ht- and lt-phase one can speculate that this effect could merely be ascribed to a Jahn-Teller deformation [Jah37] than a complete orbital-ordering process [Kug82] causing the structural changes, which was proposed in Ref. [Kha02] and later revised in Ref. [Wu06].

The superexchange interaction between cations with t_{2g}^n configuration via intermediate oxygens can be described according to [Mot70, Ere76]

$$J = J_{90}\sin^2\vartheta + J_{180}\cos^2\vartheta \quad , \tag{4.1}$$

where ϑ is the Ru–O–Ru angle listed in Tab. 4.1. J_{90} and J_{180} are the values of the superexchange coupling parameters at $\vartheta = 90°$ (ferromagnetic exchange) and $\vartheta = 180°$ (antiferromagnetic exchange), respectively. On the basis of the Goodenough-Kanamori-Anderson rules it is expected that $J_{180} > |J_{90}|$ [And59]. In addtiton, it should be noted that J_{180} should increase due to the slight shortening of the Ru–O distances during the magneto-structural transition, because its value is proportional to the Ru,O-transfer integral $t_{Ru,O}$ to the power of four: $J_{180} \sim [t_{(Ru,O)}^4/\Delta_{(Ru,O)}^2\,U]$, with $\Delta_{Ru,O}$ representing the charge transfer and the Mott-Hubbard gap U [Zak08]. Using Eq. 4.1 and the angles ϑ one can see that the superexchange coupling parameter J_0 increases due to the structural changes caused by the phase transition from the ht- to the lt-modification, while the values J_1, J_2, and J_3 decrease simultaneously. This finding strongly supports the model of the spin-ladder with rungs consisting of dimerized Ru-spins as indicated in Fig. 4.12. This model also implies a strong increase of J_0 in the lt-phase compared to the other exchange interactions in agreement with the rather high transition temperature of 161 K and the reported opening of a spin-gap, which

Table 4.2.: Results of the Curie-Weiss fit of $1/\chi$ above 200 K ($H = 1000$ Oe) for La_2RuO_5 samples prepared by various synthesis routes. Average exchange interactions calculated from Θ_{CW} using Eq. 4.2 are listed in the last two columns.

Reaction	χ_0 ($10^{-4} \frac{emu}{mol}$)	n_{eff} (μ_B)	Θ_{CW} (K)	$|J_0/k_B|$ (K)	$|J_0|$ (meV)
Solid State	0.4(1)	2.87(2)	- 122(10)	22.9(18)	2.0(2)
Soft chem. (Ru-AcAc)	0.7(1)	2.92(2)	- 177(12)	33.2(23)	2.8(2)
Soft chem. (Ru-NOAc)	1.0(1)	2.89(2)	- 162(10)	30.4(19)	2.6(2)
Flux grown	12.7(2)	2.62(2)	- 100(8)	18.8(16)	1.6(2)

is a measure of the intradimer exchange J_0 [Kha02]. This spin-gap can also be considered as an evidence for the existence of a low dimensional magnetic system consisting of $S = 1$ spins in the lt-phase [Hal83], however, this will be discussed below. The superexchange model is furthermore strongly supported by measurements of the magnetic susceptibility depending on applied pressure by Rivas *et al.* [Riv11]. These authors found that the transition temperature increases linearly with increasing pressure indicating the strong influence of the slightly changing crystal structure on the dimerization process by the variation of the magnetic exchange-interaction strength.

Samples of unsubstituted La_2RuO_5 were prepared by four different synthesis routes described in Sec. 2.1. Their susceptibilities were measured using a SQUID magnetometer applying an external field of 1000 Oe. As an example the susceptibilities (symbols) of poly- (Ru-AcAc) and a batch of single-crystalline La_2RuO_5 are shown in the top and bottom frame of Fig. 4.13. The transition step at approximately 160 K from the Curie-Weiss like ht-phase to the almost nonmagnetic lt-modification can be distinctly observed. Above 200 K $1/\chi$ was fitted using a Curie-Weiss law (Eq. 2.32) and the obtained parameters χ_0, n_{eff} and Θ_{CW} are listed in Tab. 4.2.

The temperature independent correction χ_0 amounts to a maximum of 10^{-4} emu/mol for poly-crystalline samples, which is in a common range for van-Vleck contributions in oxides. The susceptibility measured for the single crystals is remarkably higher by one order of magnitude and, therefore, cannot be explained by a simple van-Vleck correction. Very probably the large temperature-independent contribution stems from a considerable amount of $BaRuO_3$ resulting from the reaction with the $BaCl_2$ flux during the reaction. This is corroborated by the fact that a number of transparent $LaOCl$ [Bri83] crystals was found and removed after the flux reaction. Since the metallic $4H$-$BaRuO_3$ also forms plate-like black crystals [Hon97], it cannot be distinguished visually from La_2RuO_5. $4H$-$BaRuO_3$ shows a temperature-independent susceptibility in the range of 1×10^{-3} emu/mol [Rij99], which would be comparable to the observed shift in χ. However, such a stoichiometric amount of $4H$-$BaRuO_3$ which would explain the susceptibility shift was not directly observed. Only an increased intensity of a diffraction peak at $2\theta = 31°$ in an XRD pattern of the single-crystal batch points to the presence of $4H$-$BaRuO_3$. The origin of the shift is still not completely identified.

From a comparison of the susceptibilities for the poly- and single crystalline sample it could be concluded that the dimerization transition is of first order. This is especially documented by

the sharp step for the single-crystalline sample, while in the polycrystals the transition is smeared out. The first-order character of the transition in the single crystals is supported by the thermal hysteresis of χ shown in the inset of Fig. 4.13, where a shift of roughly 4 K between the heating and the cooling curve was observed. This is significant, since for the polycrystalline sample a shift of roughly 1 K was found. Similar to the description of the structural phase transition of the polycrystalline sample in the previous section the anomaly in χ is rather broad. For this sample neither in the susceptibility, DSC, or structure data a significant hysteresis was observed or it is below the experimental uncertainty. This smearing out may be caused by local inhomogeneities in stoichiometry or crystallinity, which could lead to a broader temperature distribution in the sample if the thermal conductivity between the crystallites is rather low. Thus, neighboring crystallites can reversibly adopt either the ht- or lt-modification in the vicinity of T_d similar to domains, while in the single crystal the in comparison good thermal conductivity leads to a sharp transition in the whole sample.

The experimental effective magnetic moments n_{eff} range between 2.62 μ_B and 2.92 μ_B. This is in good agreement with the value of 2.83 μ_B derived from the spin-only approximation for $S = 1$: $n_{\text{eff}} = g \cdot \sqrt{S(S+1)} \approx 2 \cdot \sqrt{2}$ μ_B. This magnetic moment corresponds to the t_{2g}^4 electron configuration of the Ru^{4+} ions. The small deviations from the theoretical value can be explained by the limited temperature range usable for the fit.

The corresponding Curie-Weiss temperatures amount to roughly -100 K for the single crystals and range between -122 K and -177 K for the polycrystalline samples. These values are in accordance with values for polycrystalline samples obtained from solid-state synthesis, for which Curie-Weiss temperatures between -70 K and -245 K were reported [Kha02, Mal05, Ebb06, Ebb10]. The high variation of Θ_{CW} is again caused by the rather narrow temperature range applicable for the Curie-Weiss fit, which significantly reduces the fit accuracy. The negative sign of Θ_{CW} indicates antiferromagnetic short-range interactions. A first estimate of the average exchange-interaction strength between two neighboring Ru-ions can be calculated according to [Kit91]:

$$\Theta_{CW} = \frac{2 \cdot z \cdot J_0 \cdot S(S+1)}{3k_B} \quad , \tag{4.2}$$

where z denotes the number of next neighbors, i. e. $z = 4$ reflecting the Ru square lattice shown in Fig. 4.12. The obtained interaction strenghts J_0 are listed in Tab. 4.2 in K and meV. The values amount to roughly 2 meV indicating only a weak coupling in the paramagnetic phase. However, it has to be mentioned that Eq. 4.2 and in turn also the values for $|J_0|$ are strictly valid only for a three-dimensional interaction. Clearly a two-dimensional model would be a more appropriate description of the magnetic interactions.

To check if the observed interactions strengths might be sufficient to explain the magnetic transition, two different models were fit to the ht-regime. The first one is a spin-dimer model with strongly antiferromagnetically coupled pairs of $S = 1$ spins, which are weakly interacting with neighboring dimers, e.g. in a spin-ladder. This model was successfully applied to Ba$_3$Mn$_2$O$_8$, for which a regular trigonal arrangement of $S = 1$ dimers and the existence of a spin-gap was reported characterized by the steep decrease of χ below the transition temperature. In this compound the spins of the Mn^{5+} ions with $3d^2$ configuration are paired and show a distinct interaction
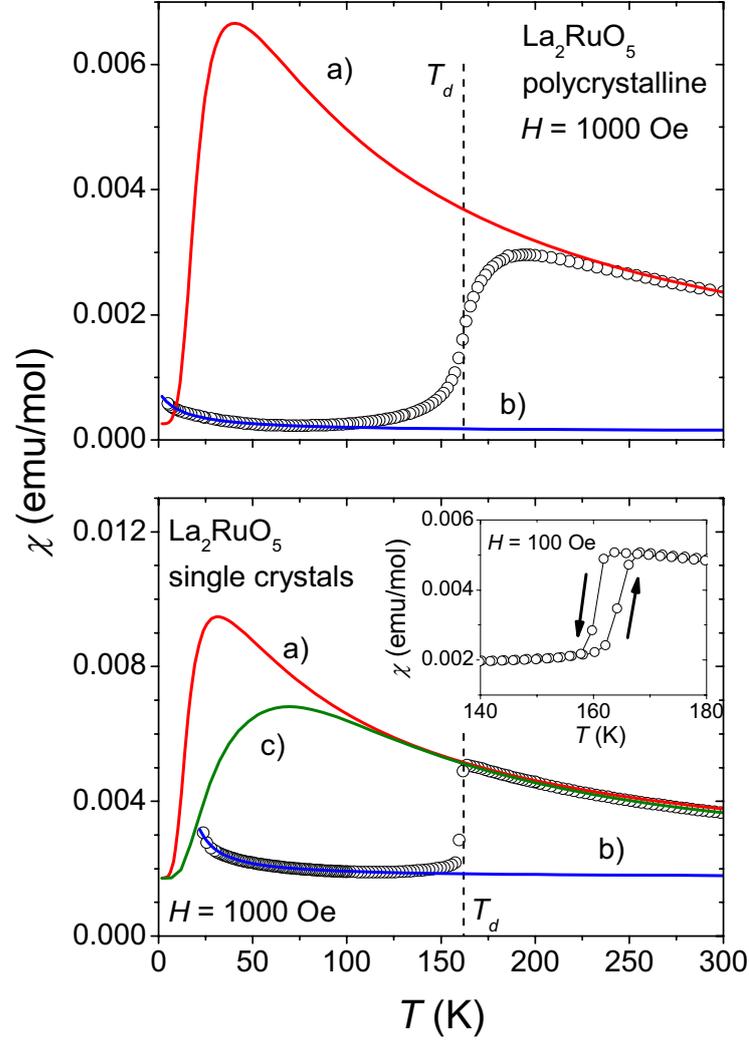
Figure 4.13.: Top frame: Magnetic susceptibility of polycrystalline La$_2$RuO$_5$ (Ru-AcAc) from sol-gel reaction (symbols). Bottom frame: Susceptibility of flux grown La$_2$RuO$_5$ single crystals (symbols). The solid red lines a) mark the 2D Heisenberg model, the solid blue lines b) indicate the Curie-Weiss fits of the low temperature Curie tails, and the solid green line c) shows the fit applying a spin-dimer model. The inset in the lower frame shows the thermal hysteresis of the dimerization transition in the susceptibility of single crystalline La$_2$RuO$_5$.

within the dimer-lattice [Uch02]. The solid green line denoted c) in the bottom frame of Fig. 4.13 represents the fit result of the $S = 1$ spin-pairs including a mean-field correction described in [Men06, Sam10, Sam11]:

$$\chi = \chi_0 + \frac{\chi'}{1 + \lambda \cdot \chi'} \quad . \tag{4.3}$$

The temperature independent χ_0 corresponds to the van-Vleck contributions and amounts to $1.72 \cdot 10^{-3}$ emu/mol for the single crystals. A fit carried out for the polycrystalline sample leads to a χ_0 of $2.6 \cdot 10^{-4}$ emu/mol. Both values are considerably higher than the ones obtained from the Curie-Weiss fit but still not unreasonably high. The second term of Eq. 4.3 corresponds to the spin-dimer model with intra-dimer exchange J_0 and including the additional interaction between neighboring dimers. The mean-field parameter λ represents the sum of exchanges J_1 to J_3 (Fig. 4.1). The susceptibility χ' of isolated dimers consisting of $S = 1$ moments is defined according to [Sam11]:

$$\chi' = \frac{2N_A g^2 \mu_B^2 (1 + 5\exp(-2J_0/k_B T))}{k_B T (3 + \exp(J_0/k_B T) + 5\exp(-2J_0/k_B T))} \quad , \tag{4.4}$$

where N_A is the Avogadro constant and μ_B is the Bohr magneton. $g = 2$ was used reflecting the spin-only approximation. The fit resulted in J_0/k_B values of roughly 67(1) K (5.8 meV) for both samples. Compared to the Curie-Weiss fits, the values for J_0 are slightly increased by a factor of two, which is still smaller than the expected intra-dimer coupling exchange in the lt-phase. The values for the mean-field correction λ are very small and negative (-0.35 K for the powder and -1.54 K for the batch of crystals), which strictly is not plausible for this model. In addition, the result of strongly deviating inter- and intradimer exchange strengths does not seem very plausible, since the corresponding Ru–Ru distances do not differ so much to justify the existence of a dominating coupling J_0 already in the ht-phase. One distinctive difference between La$_2$RuO$_5$ and Ba$_3$Mn$_2$O$_8$ is the phase-transition temperature reflected by the maxima in χ. The maximum found for Ba$_3$Mn$_2$O$_8$ at $T_{max} = 18$ K is much lower than the 190 K observed in polycrystalline La$_2$RuO$_5$ in Fig. 4.13. The position and width of the peak in the magnetic susceptibility correlates with the intradimer exchange and the ratio of intra- and interdimer exchange, respectively [Hei04]. The interdimer exchange can always be assumed significantly smaller than the intradimer value. While the width of the cusp for Ba$_3$Mn$_2$O$_8$ amounts to roughly 50 K, the peak in the fit c) with $T_{max} = 65$ K in the lower frame of Fig. 4.13 is more than 100 K wide. By extrapolation the width of the peak for $T_{max} = 190$ K is expected to range well above 200 K. Instead, the step in the susceptibility of the polycrystalline La$_2$RuO$_5$ looks very similar to the fit c), it is only shifted to a higher temperature. From this it seems reasonable that the shape of the step cannot be reproduced by this dimer model, also the much steeper transition step of the La$_2$RuO$_5$ single crystals reveals the different nature of the formed lt-dimerized state.

In a second approach a 2D-Heisenberg model was chosen to describe the magnetic interaction. The use of this model is justified due to the almost regular two-dimensional lattice of Ru^{4+} ions in the structurally isolated LaRuO$_4$-layers and the antiferromagnetic interactions derived from the Curie-Weiss temperature observed for the paramagnetic ht-modification. The calculated susceptibilities are marked by solid red lines a) in Fig. 4.13 and were obtained according to [Rus58]:

$$\chi = \chi_0 + \frac{N_A g^2 \mu_B^2 \mu_{eff}^2 S(S+1)}{3k_B T} \cdot \left(\sum_{n=0}^{6} a_n x^n\right)^{-1} \quad . \tag{4.5}$$

The constants amount to $a_0 = 1$, $a_1 = -5.333$, $a_2 = 9.778$, $a_3 = -9.481$, $a_4 = 6.420$, $a_5 = -42.923$, $a_6 = 269.313$, and $x = -J_0/k_B T$. The values for a_n were calculated from equations

and tables given in Ref. [Rus58], while J_0/k_B was derived from a fit using the temperature region above the transition step. The small values of $J_0/k_B = 9$ K (sol-gel) and $J_0/k_B = 7$ K (single crystal) reveal an antiferromagnetic exchange interaction between the Ru ions, which was also found in the dimer model. When multiplied with the number of neighboring centers ($z = 4$) the values of J_0/k_B are comparable to the exchange interactions determined from the Curie-Weiss temperatures. The 2D-Heisenberg model may probably provide a reasonable description of the susceptibility, if no structural changes occurred. Nevertheless, the Heisenberg model is obviously not suitable to explain the susceptibility in the phase transition range here.

Both models lead to similarly shaped theoretical susceptibilities, which are drastically deviating from the experimental data. The transition temperature for the ordered ground state is significantly smaller than the found 160 K and the peaks are rather broad compared to the sharp step observed for the single crystals. This shows that the exchange-interaction strength in the ht-phase, which determines the shape of the dimer- and the 2D-Heisenberg model, is not sufficiently high to drive the dimerization phase transition alone. Thus, the dimerization transition is strongly coupled to the structural changes occurring at roughly 170 K.

From Fig. 4.13 it can be seen that the susceptibility increases at lowest temperatures. This points to the presence of paramagnetic centers, which do not take part in the dimerization. To estimate the concentration of these paramagnetic centers, the susceptibilities below 50 K were fit using a Curie-Weiss law. The fits are marked by solid blue lines b) in both frames of Fig. 4.13. The Curie constant of the polycrystalline sample amounts to $8.13(50) \cdot 10^{-3}$ emu K/mol, which corresponds to roughly 1% of the Curie constant of the ht-phase. This finding can be explained by a small number of non-dimerized Ru spins due to the structural distortions, e.g. at grain boundaries. On the other hand, the presence of an impurity phase cannot be completely ruled out, because its concentration would be close to the detection limit of x-ray powder diffraction. Θ_{CW} of the lt-fit is negative (-12.6(8) K) and χ_0 is roughly reduced by a factor of two compared to the value calculated above ($1.3 \cdot 10^{-4}$ emu/mol). The absolute values are slightly smaller than reported by Khalifah *et al.* [Kha02] for a sample obtained by solid-state reaction. For the single crystals a slightly increased value for the Curie constant ($16.38(60) \cdot 10^{-3}$ emu K/mol, roughly 2% of ht-phase Curie constant) was obtained and χ_0 amounts to $1.72 \cdot 10^{-3}$ emu/mol, which is close to the value found for the Curie-Weiss fit in the high-temperature region. A small positive Curie-Weiss temperature ($\Theta_{CW} = 10.5(5)$ K) is found for the lt-fit of the single-crystalline sample.

To investigate the unexpected uprise found in the susceptibility of the single crystals at low temperatures, additional field-dependent measurements were performed for selected temperatures. The *M* vs. *H* curves are depicted in Fig. 4.14. In the ht-phase a linear paramagnetic behavior is observed up to the highest available external field of 50 kOe. A paramagnetic behavior is also found in the lt-phase down to 50 K reflecting the absence of a ferro- or ferrimagnetic impurity in the sample with an ordering temperature above 50 K. At 2 K, a broad and irregular shaped hysteresis is observed (Fig. 4.14) indicating a ferro- or ferrimagnetic phase with a very small ordered moment of roughly 60 emu/mol (0.01 μ_B/mol) as derived from the remanence. The shape at small fields is similar to the ones observed for layered thin antiferromagnetically ordered films (see e.g. [Hel03, Moc03, Lei01]). The layered structure of La_2RuO_5 leads to twinned crystals, i.e.
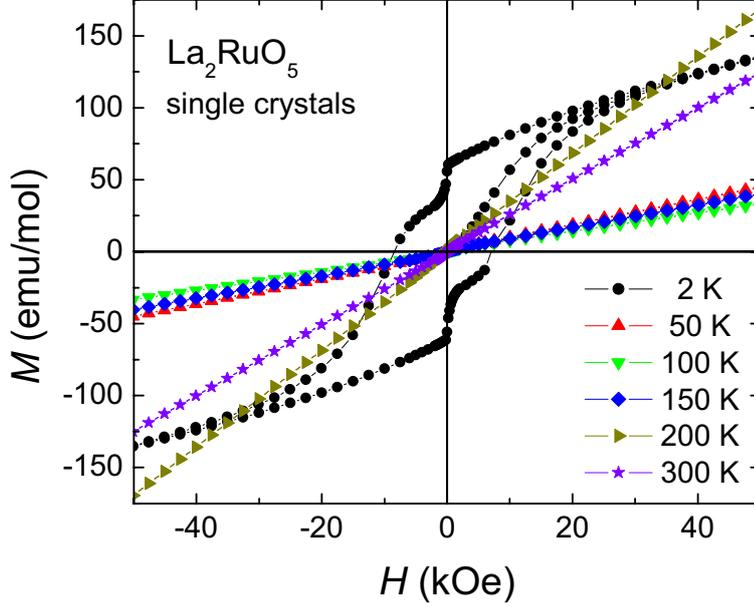
Figure 4.14.: Magnetization hysteresis curves at selected temperatures of the batch of single crystals of La$_2$RuO$_5$.

domains with alternating orientations. The interaction between the crystal domains is comparable to the coupling between the thin films. Therefore, it can be assumed that the interaction of the domain layers causes the hysteresis at low temperature as an intrinsic effect in the crystals. In polycrystalline samples the hystersis cannot be observed because the size of the domains becomes too small for a cooperative ordering.

To obtain further information from the magnetic susceptibilities in the dimerized phase, the low-temperature Curie-Weiss fits including a constant χ_0 were subtracted from the experimental results leading to a corrected susceptibility χ_{korr}. As the temperature independent susceptibility was significantly enhanced for the batch of the single crystals when compared to the results obtained for the polycrystalline sample, the former results bear a larger experimental uncertainty. From the residual magnetic susceptibilities the derivatives $d\chi_{korr}/dT$ were calculated. The results are depicted in Fig. 4.15. Both data sets show a rather symmetric peak with a maximum close to the dimerization transition. The peaks for both samples can well be fit assuming Lorentzian profiles. The fits for both samples yield similar transition temperatures $T_{d,sc} = 160.7(1)$ K, and $T_{d,pc} = 161.9(2)$ K), but significantly different widths. For all four polycrystalline samples an average T_d of 161 K is obtained in good agreement with literature [Kha02, Mal05]. T_d is marked by the vertical dashed lines in Fig. 4.13. The widths amount to FWHM$_{sc} = 1.9(3)$ K, FWHM$_{pc} = 11.8(6)$ K reflecting the transition step in Fig. 4.13.
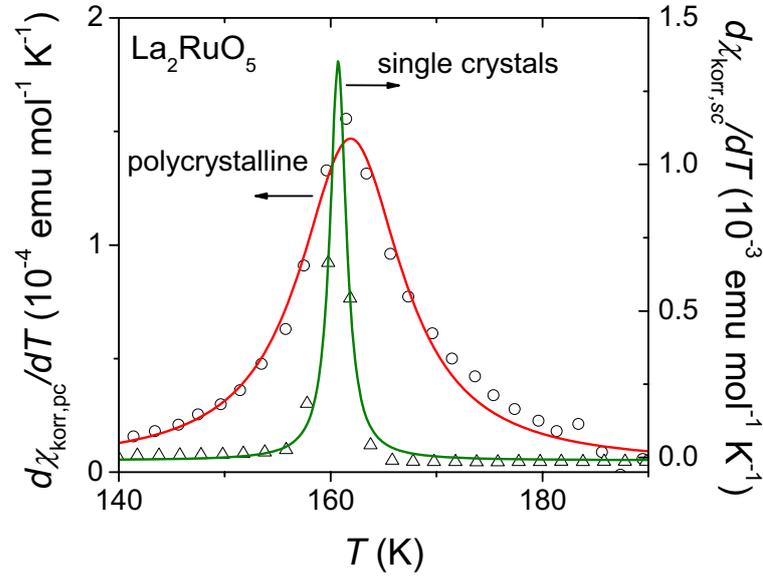
Figure 4.15.: Derivatives of the magnetic susceptibilities for polycrystalline (open circles) and single crystalline La$_2$RuO$_5$ (open triangles). The susceptibilities were corrected for the low-temperature Curie-Weiss contributions as indicated by the blue lines in Fig. 4.13. The solid lines correspond to Lorentzian-fits, centered at the phase transition temperature.

As mentioned above, from the very small susceptibility below the phase transition typically a spin gap can be expected for the lt-phase. This means that besides the spin dimers representing the ground state excited states at certain energies can be assumed (see inset of Fig. 4.18), which are increasingly populated with increasing temperature according to a Boltzmann-distribution. This thermal excitation can be described by a simple exponential temperature dependence of $\chi \propto \exp[\Delta/(k_B T)]$ close to the phase transition (see for example Ref. [Hal83]). The corrected susceptibilities χ_{korr} are therefore shown in an Arrhenius-type plot in Fig. 4.16, i.e. the logarithm of the magnetic susceptibility is plotted as a function of the inverse temperature. Between approximately 150 K and 70 K in the polycrystalline sample and down to roughly 100 K in the single crystals both susceptibilities reveal a strictly linear behavior. But the different slopes indicate significantly different spin-gap energies. The deviations at low temperatures reflect errors due to corrections of the lt-Curie-Weiss fits and the temperature independent susceptibilities. The spin-gaps as derived from the linear fits amount to $\Delta_{pc} = 48(1)$ meV for the polycrystals and $\Delta_{sc} = 112(1)$ meV for the single crystals. The result for the polycrystalline sample is close to the spin-gap value of 40 meV obtained from inelastic neutron scattering [Kha02]. The corresponding Arrhenius behavior is indicated as dashed line in Fig. 4.16. However, the spin-gap for the single crystals is significantly larger. The fact that the results of poly- and single crystalline samples differ significantly has already been observed in the determination of the charge gap from resistivity
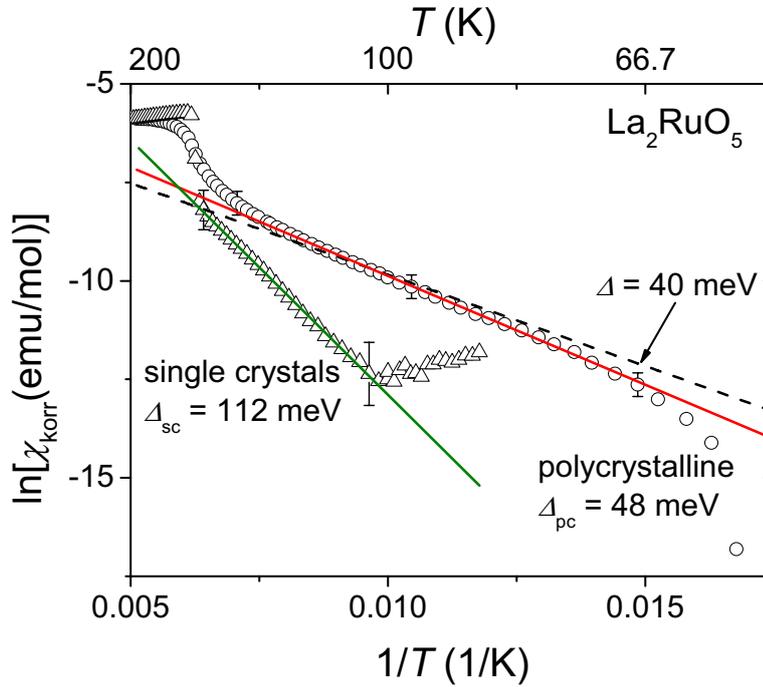
Figure 4.16.: Arrhenius plots of the corrected susceptibilities in the low-temperature phase for poly-(open circles) and single (open triangles) crystalline La_2RuO_5. The solid lines are linear fits assuming an Arrhenius behavior, resulting in spin-gaps of $\Delta_{pc} = 48$ meV and $\Delta_{sc} = 112$ meV for the poly- and single-crystalline sample, respectively. The Arrhenius behavior characteristic for a spin-gap of $\Delta = 40$ meV as observed by inelastic neutron scattering is shown as dashed line.

measurements [Kha02], where values of roughly 0.21 eV are observed for single crystals, while a value of 0.32 eV for polycrystalline samples is found. Malik *et al.* [Mal05] reported a charge gap of even only 0.16 eV for the polycrystals. Thus, it may be concluded that the gaps in La_2RuO_5 are extremely sensitive to even small structural variations between samples. This can be already anticipated regarding the strong increase of the exchange constant J by two orders of magnitude at the dimerization transition, which is dominantly driven by the structural changes, reflecting only weakly modified bond angles and interatomic distances. Different preparation routes and internal strains in the twinned single crystals certainly provide slight variations of the structural parameters. It should also be noted that the inelastic peak in the neutron data [Kha02] extends up to 120 meV reflecting the broad distribution of gap values in polycrystalline material.

Neither changes of the phase-transition temperatures nor of the obtained J_0 values were observed upon varying the external magnetic field H between 100 Oe and 50 kOe. Such a shift was reported to be typical for an $S = 1/2$ spin-Peierls transition [Bul78], which was observed, e.g., in $CuGeO_3$ [Has93]. In agreement with the shown findings the transition in La_2RuO_5 is expected
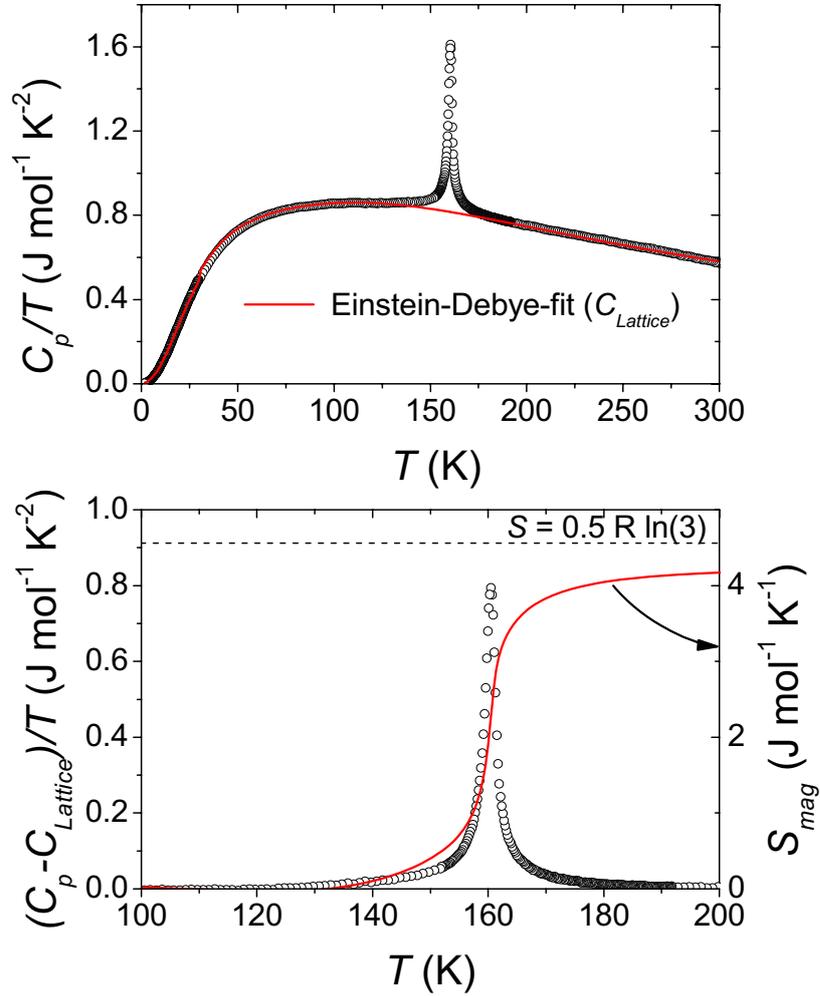
Figure 4.17.: Top frame: Specific heat of polycrystalline La_2RuO_5 in C_p/T representation (symbols) and Einstein-Debye fit (solid red line). Bottom frame: Data after subtraction of the Einstein-Debye fit $((C_p - C_{Lattice})/T$; symbols) and S_{mag} obtained from integration of the residual curve (solid red line).

to be unconventional for $S = 1$ from both theoretical calculations [Guo90] and our experimental results similar to the 1D antiferromagnetically ordered chains with $S = 1/2$ and $S = 1$ described by Haldane [Hal83].

4.2.3. Specific-Heat Investigations of the Phase Transition

The specific heat of the polycrystalline La_2RuO_5 in C_p/T representation is depicted in the top frame of Fig. 4.17. The solid red line in the top frame marks the Einstein-Debye-fit, which was performed according to Sec. 2.5 to model the lattice contribution to C_p. For the fit one tempera-

ture term was used for each atom per formula unit, i.e. $1 \times \Theta_D$ (Debye-temperature) and $7 \times \Theta_E$ (Einstein-temperature). To reduce the number of parameters, four of the Einstein-terms were set equal, reflecting the oxygen octahedra in the $LaRuO_4$-layers. According to the low electrical conductivity of La_2RuO_5 a very small constant c_0 of roughly 2.2 mJ mol^{-1} K^{-2} was used in agreement with previously reported results [Mal05]. In metals c_0 is known as the Sommerfeld coefficient and describes the contribution of the conduction electrons to C_p. However, since La_2RuO_5 is semiconducting the influence of conduction electrons to the specific heat is expected to be negligible. Thus, the small c_0 is merely considered an additional parameter to improve the fit quality. The following values for the five fitting parameters corresponding to the number of independent lattice sites were obtained: $\Theta_D = 132(1)$ K, $\Theta_{E1} = 175(1)$ K, $\Theta_{E2} = 217(2)$ K, $\Theta_{E3} = 325(3)$ K, and $4 \times \Theta_{E4} = 520(3)$ K (see also Tab. 5.7).

To determine the contribution of the phase transition, the Einstein-Debye fit was subtracted from the experimental data. The residual $(C_p - C_{Lattice})/T$ depicted in the bottom frame of Fig. 4.17 shows a sharp peak indicating a first-order transition. This transition can be attributed to the abrupt change of magnetic exchange interaction due to the structural transition, which is clearly observable in the bottom frame of Fig. 4.13. To obtain the excess entropy, $(C_p - C_{Lattice})/T$ was integrated between 75 K and 250 K according to $S_{exc} = \int C_p/T dT$. The integral is depicted in the bottom frame of Fig. 4.17 (solid red line). A value of $S_{exc} = 4.2(3)$ J mol^{-1} K^{-1} was obtained.

For the antiferromagnetic ordering of $S = 1$ spins a magnetic entropy of $S_{mag} = R \cdot \ln(2S+1) = 9.13$ J mol^{-1} K^{-1} is expected. Values of 8.3 J mol^{-1} K^{-1} [Mal05] and 8.56 J mol^{-1} K^{-1} [Riv11] were reported in literature for La_2RuO_5 but rather simple approaches were used to model the lattice contributions. The Einstein-Debye fit applied in this work is more sophisticated and the smaller value is therefore considered to be more reliable. The large deviation of the experimentally found and the expected value can be explained taking into account the spin pairing of the lt-phase. The molar entropy is defined $S_{mag} = k_B \cdot \ln(\Omega)$, where k_B is the Boltzmann constant and Ω is the partition function. In the lt-phase the entropy is deviating from zero due to the dimerization. The entropy change at T_d is therefore calculated according to $\Delta S = |R \ln(3) - 0.5 \cdot S_{dimer}|$ (see Fig. 4.18). The latter term represents the entropy of the dimers according to $S_{dimer} = \bar{E}/T + k_B \ln(Z)$ and is multiplied by 0.5 due to the half number of dimers compared to the single spins. Z is the partition function of the energy spectrum of the dimers with a singlet ground state which is shown as inset in Fig. 4.18. The first and second excited state of the dimers are a triplet and a quintuplet state, respectively. At T_d the partition function Z of this spectrum is given by:

$$Z = \sum_i g_i \exp(-\frac{E_i}{k_B T_d}) \quad , \tag{4.6}$$

where g_i is the degeneracy and E_i the energy of the corresponding state with respect to the ground state ($i = 0$). The averaged energy $\bar{E}$ of the spectrum is calculated according to:

$$\bar{E} = \frac{\sum_i g_i E_i \exp(-\frac{E_i}{k_B T_d})}{\sum_i g_i \exp(-\frac{E_i}{k_B T_d})} \quad . \tag{4.7}$$

The energies E_i in the spectrum in first approximation are determined by the intradimer exchange
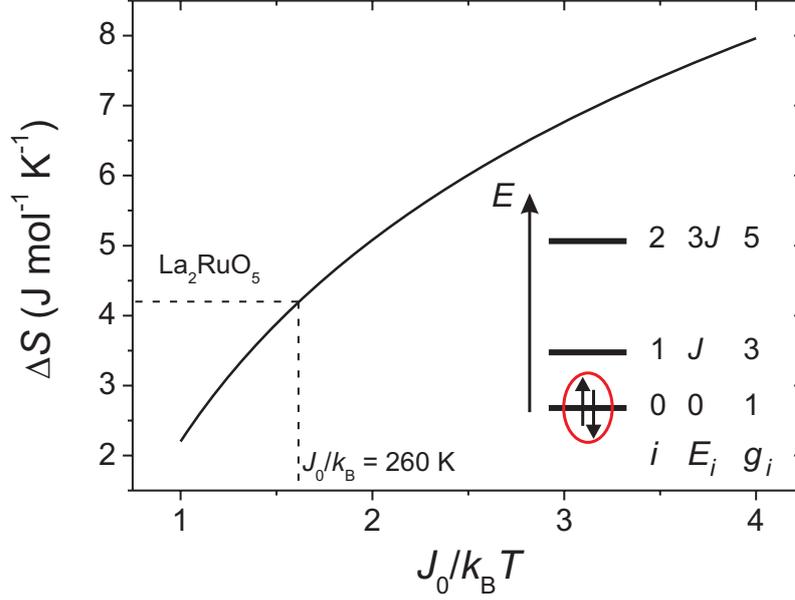
Figure 4.18.: Entropy change ΔS of La_2RuO_5 at T_d depending on the intradimer exchange J_0/k_BT. Inset: Energy-level scheme of the dimer state consisting of $S = 1$ spins.

J_0 and therefore the entropy change is depending on the ratio of J_0 and the dimerization temperature T_d leading to the simplified averaged energy for the dimer state:

$$\bar{E}_{dimer} = \frac{3J_0}{k_B} \cdot \frac{\exp(-\frac{J_0}{k_BT_d}) + 5\exp(-\frac{3J_0}{k_BT_d})}{1 + 3\exp(-\frac{J_0}{k_BT_d}) + 5\exp(-\frac{3J_0}{k_BT_d})} \quad . \tag{4.8}$$

Using these equations the entropy change can be calculated as a function of J_0/k_BT_d, which is depicted as solid black line in Fig. 4.18. The obtained value of 4.2 J mol^{-1} K^{-1} for pure La_2RuO_5 (marked by the dashed lines) corresponds to an intradimer exchange of $J_0/k_B \approx 260$ K (23.5 meV), which is smaller than the 40 meV obtained by inelastic neutron scattering. From DFT calculations a value of 65.5 meV was derived, which is somewhat larger but still in the same range as our finding [Kha02, Wu06]. It should be mentioned that, on the one hand, DFT calculations usually overestimate the exchange values and, on the other hand, 23.5 meV is a lower estimate of the exchange since interactions between the dimers are neglected in this model.

For a more precise description also the contribution of the structural transition to the change in C_p has to be regarded. However, it is impossible to separate its contribution since both transitions are coupled. The above described good agreement of the magnetic entropy with the theoretical estimate indicates that the change of C_p caused by the structural transition is rather small.
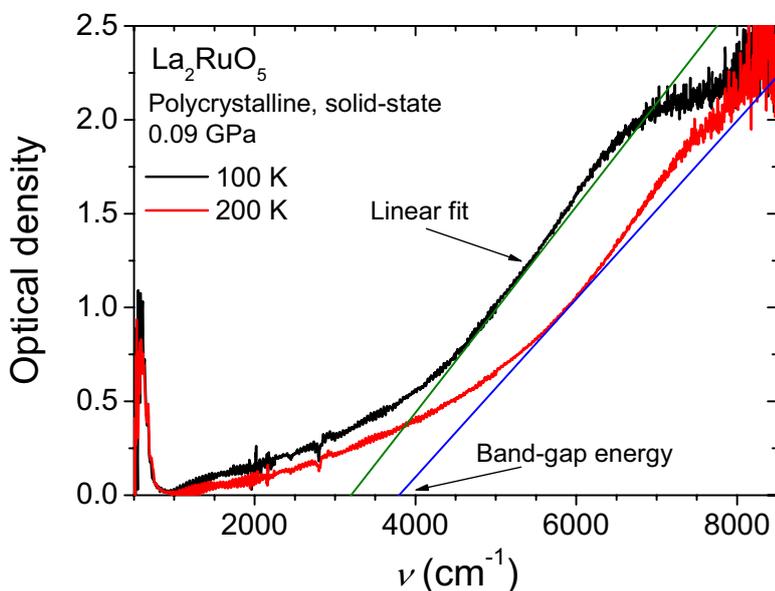
Figure 4.19.: Absorption spectra of polycrystalline La$_2$RuO$_5$ at 100 K and 200 K recorded applying a pressure of 0.09 GPa in absorption mode. The solid lines are linear fits in the vicinity of the inflection point to determine the absorption-edge positions.

4.3. High-Pressure Spectroscopic Investigations

The observed narrow band gap and electronic correlation in La$_2$RuO$_5$ lead to the idea of pressure depending studies. Pressure might induce an insulator to metal transition, since the interatomic distances decrease and in turn the overlap and hybridization of orbitals increases [Kun10]. This simplified model of a Mott-insulator [Mot49] is valid for compounds, in which the strong electronic correlations lead to an increased localization of the electrons resulting in the creation of a band gap and an insulating behavior [Ima98]. The by the correlation narrowed bands can be broadened either by chemical (substitution) or physical pressure.

The electrons in the lt-phase of La$_2$RuO$_5$ are strongly correlated as reflected by their singlet ground state. However, in the paramagnetic ht-phase weak antiferromagnetic interactions between the $S = 1$ spin moments are present. These properties can be described by strongly localized Ru $4d$ electrons in (compared to $3d$ orbitals) rather diffuse $4d$ states [Cav04]. To reduce the localization by increased band overlap and hybridization at E_F, and to suppress the dimerization, pressure was applied. The measurements were performed by E. A. Francis and L. Baldassare in the group of Prof. C. A. Kuntscher at the University of Augsburg.

The polycrystalline sample obtained from solid-state reaction was investigated by pressure-dependent transmittance and reflectance experiments in the infrared (IR) frequency range 550 cm^{-1}
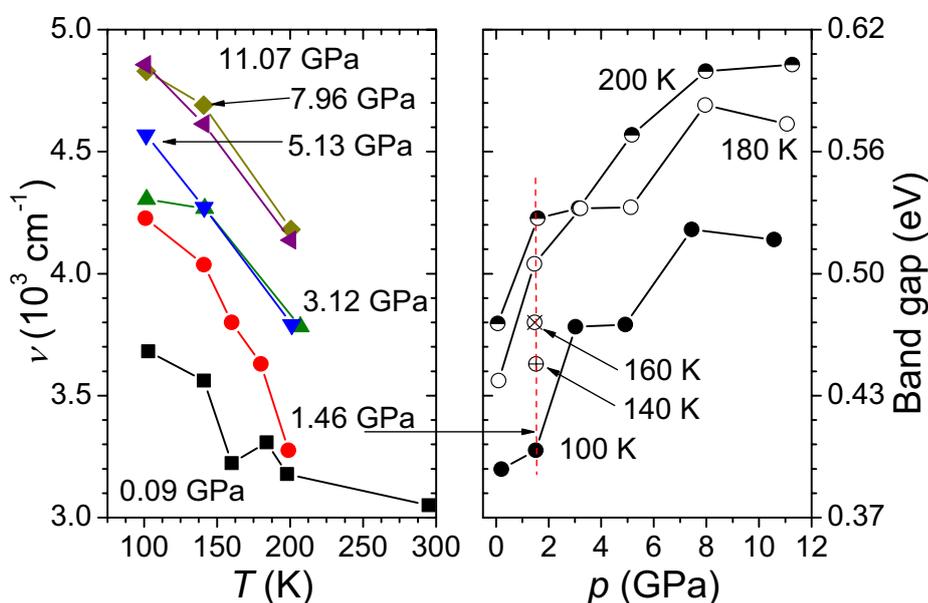
Figure 4.20.: Temperature dependent (left) and pressure dependent (right) band-gap energies of La$_2$RuO$_5$ determined from absorption-edge spectra.

- 8500 cm^{-1} between 100 K and room temperature. A Bruker IFS 66v/S FT-IR spectrometer with an infrared microscope (Bruker IRscope II) was used to measure the transmittance and reflectance [Kun10]. The pressure was generated by a diamond anvil cell with CsI as pressure transporting medium and a ruby crystal as reference [Hub77]. The ruby luminescence wavelength varies as a function of pressure in the applied range up to 15 GPa. For frequency calibration this is measured alternatingly with the sample [Kun10].

In Fig. 4.19 the measured absorption spectra of La$_2$RuO$_5$ are shown for 100 K and 200 K and a pressure of 0.09 GPa. The solid lines represent linear fits in the vicinity of the inflection point, which were used to determine the absorption edge positions. The band gap is determined as intersection point with the x-axis. Unfortunately the quality of the fits is quite low, because only the tail of the absorption edge was observed up to 1 eV above E_F. The shape is very similar to experimental data reported in Refs. [Moo08, Wu08], where a range up to 3 eV was measured at ambient pressure. Furthermore, the anomalies observed in the low energy range are almost identical and comparable to the density of states close above E_F obtained by DFT calculation (see Sec. 4.5). Apart from this the absolute value of the gap cannot be determined precisely by the linear fits but the relative change of the spectra and, hence, the band gap evolution provides promising results.

The small frequency shift and relative change of the band gap indicates a very low compressibility of the La$_2$RuO$_5$ crystal structure. The obtained temperature and pressure depending change

of the band gap is depicted in Fig. 4.20. The frequency units of the y-axis are transformed to the eV energy scale for better comparability with other investigations. The band gap increases with decreasing temperature and increasing pressure and ranges between 0.37 eV and 0.6 eV for the applied conditions. The temperature-depending behavior is similar to the resistivity measurements reported in Refs. [Kha02, Mal05]. The value increases continuously in both the ht- and lt-modification and shows a broad step of approximately 0.06 eV height at the phase-transition temperature. However, the band gaps determined here are by roughly a factor two larger than the ones reported earlier [Kha02, Mal05]. As it is shown in the left frame of Fig. 4.20, the temperature depending behavior is shifted almost linearly by the increasing pressure up to roughly 12 GPa. Similar, a shift caused by the temperature change is observed in the pressure dependency of the band gap (right frame of Fig. 4.20).

For all applied pressures only a gradually change of the band gap was found at the phase-transition temperature. Furthermore, an insulator to metal transition was not observed in the available pressure and temperature range. The pressure induces a quite unexpected increase of the band gap, which can be explained by the shift of electronic bands above the fermi edge. Thus a larger gap between conduction and valence band is the result instead of an increasing orbital overlap. Deduced from this behavior the application of chemical pressure by substitution promises to be more successful influencing the electronic band structure around E_{F} and to possibly induce an insulator to metal transition (see chapter 5).

4.4. Electrical AC-Conductivity Investigations

It has to be mentioned in advance that the polycrystalline La$_2$RuO$_5$ samples are very brittle even after pelletizing and long sintering times. Therefore, dc-resistivity measurements could not be carried out, since a bar of pressed (and sintered) powder is required for the 4-point measurement. It was only possible to obtain cylindrical pellets with a diameter of 3 mm and a thickness of roughly 1 mm, which were stable after a long sintering process. The pellets were contacted using silver-paint and a pseudo-four-point setup was applied, in which voltage and current contacts were attached on the top and the bottom side of the pellet. The AC-conductivity measurements were carried out by Stephan Krohns utilizing a Novocontrol α-analyzer. The principles of the measurement technique are described in detail in Refs. [Kro10, Lun10].

The results from dielectric spectroscopy reflected the brittle property of the sample material. Observed high dielectric constants (ε' up to 10^4 at 300 K) for frequencies below 10 kHz are very probably caused by grain-boundary effects or reflect the zone of the measurement contacts. The corresponding dielectric losses are very high due to the additional capacitances emerging from the sample morphology. The observable relaxations of Maxwell-Wagner type can be reasoned by the large additonal barrier-layer capacities of the grain-boundaries or sample contacting. Details to this principle properties are found in Refs. [Kro10, Lun10]. Furthermore, the rather good conductivity and in turn significant charge-carrier concentration also causes this large Maxwell-Wagner relaxation step and, thus, the data merely represent the zone in the samples close to the electric
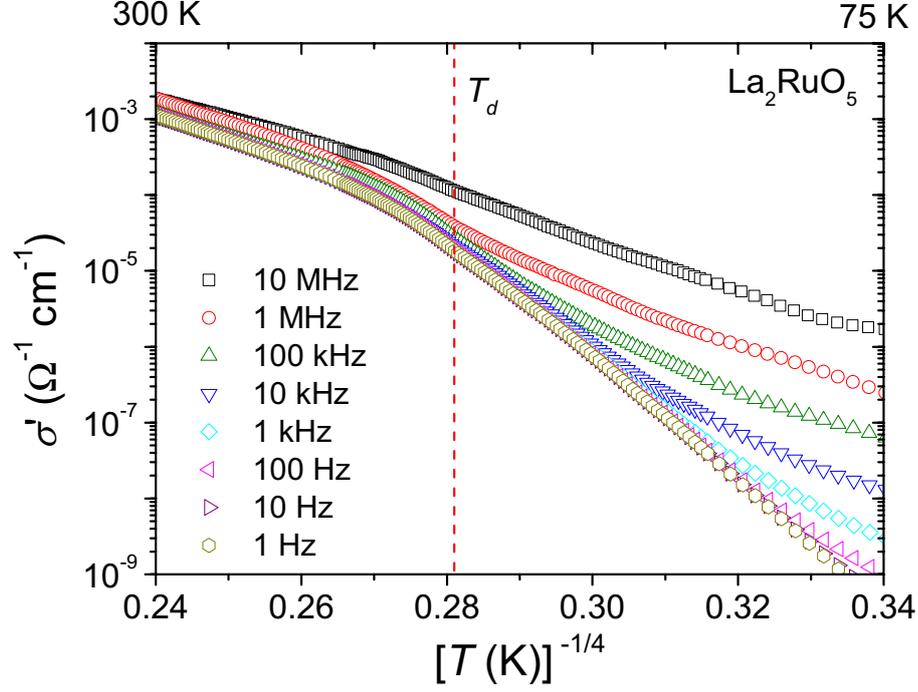
Figure 4.21.: Temperature dependence of the AC-conductivity σ' of La_2RuO_5 between 1 Hz and 10 MHz versus $T^{-1/4}$ according to the 3D-variable-range hopping model. The dashed red vertical line marks the phase-transition temperature obtained from the magnetic susceptibility.

contacts for the measurements.

Despite of these experimental problems intrinsic values can be extrapolated from high-frequency or low-temperature data. The intrinsic dielectric constant amounts to a range between 10 and 20, which is typical for badly conducting oxide materials. As a sign of the dimerization transition anomalies at T_d could be expected in the large relaxation steps, however, no significant changes caused by the phase transition were observed.

From the measured data the real part of the conductivity σ' was calculated according to Refs. [Kro10, Lun10] and is depicted in Fig. 4.21 for a frequency range between 1 Hz and 10 MHz and temperatures between 75 K and 300 K. The data are drawn on a logarithmic scale for σ' vs. $T^{-1/4}$ according to 3D-variable-range hopping (VRH) behavior $\sigma(T) \propto \exp\left[-\left(\frac{T_0}{T}\right)^{-1/4}\right]$. The almost linear course of σ' for all measured frequencies agrees with the hopping-charge transport mechanism. Close to the phase-transition temperature (marked by the vertical dashed line) a change of the slope occurs due to the changing crystal structure, and, hence, the changing potential for the hopping charge-carriers. In the lt-phase σ' increases with increasing frequency by approximately three orders of magnitude. This is in accordance with the universal dielectric-response phenomenon [Kro10, Lun10] characterized by a power law behavior according to $\sigma' = \sigma_0 \cdot v^s$

with frequency v and a material-specific constant $s < 1$.

However, the observed VRH behavior is very probably only showing the behavior of the contact zone in the sample and not valid for the bulk metrial itself, although a similar behavior can be expected. A more detailed analysis of the overall dielectric properties of pure and substituted La$_2$RuO$_5$ polycrystalline samples showed very similar results for all investigated Pr and Ti substituted samples.

In an alternative approach the conductivity of La$_2$RuO$_5$ may be described as a classical semiconductor. Using this simple thermal excitation model according to $\sigma' \propto \exp(-\Delta/k_B T)$ a value of $\Delta \approx 0.15$ eV is obtained. This value is comparable to the DC-conductivity results shown in Refs. [Kha02, Mal05]. On the other hand, we could not find any significant difference between the ht- and the lt-phase.

4.5. DFT Calculation

Density-functional theory calculations for the ht- and the lt-phase of La$_2$RuO$_5$ were performed to investigate the changes of the electronic band structure due to the phase transition. Additional DFT calculations for substituted compounds was carried out and the results are discussed with respect to the unsubstituted La$_2$RuO$_5$ in chapter 5.

Previous calculations by Eyert *et al.* [Eye06, Eye07] and Wu *et al.* [Wu06] revealed a spin-Peierls like transition in La$_2$RuO$_5$ conserving the local $S = 1$ spin-moment of the Ru^{4+} ions in accordance with the experimental results mentioned above. In this model the structural changes lead to anisotropic magnetic exchange interactions. This results in a pairing of the spin moments by alternating short and long distances in the Ru lattice. Due to this a spin-gap opens as deduced from the magnetic susceptibility of the lt-phase in Sec. 4.2.2. In an alternative totally antiferromagnetically ordered model the diminishing susceptibility and the opening of a small spin-gap would also be possible [Wha81]. However, this model does not explain the size of the gap and the entropy change observed in specific-heat measurements.

For the DFT calculations the crystal-structure data from ND measurements [Ebb05] were used as input data. Initially the symmetry reduction from the original monoclinic (respectively triclinic) structure to space group P1 was performed. Test calculations with the original and P1 symmetry lead to almost identical results, which justifies the symmetry reduction. The reduction was required to enable a replacement of single atoms for the modelling of substituted compounds. The number of k-points was adapted to the reciprocal unit cell and set to $3 \times 6 \times 4$. These numbers were chosen considering the upper limit of matrix elements available in the program code by simultaneously minimizing the required memory space and in turn the calculation time. A scalar relativistic setting was applied for the calculations and convergence criteria concerning the minimization of changes of the atomic density and total energy were used. Several iterations of the modelling had to be performed using the previously obtained density-map file as starting parameter to further reduce the calculation duration to several days.

In the top frame of Fig. 4.22 the obtained electronic band structure of the ht-phase La$_2$RuO$_5$
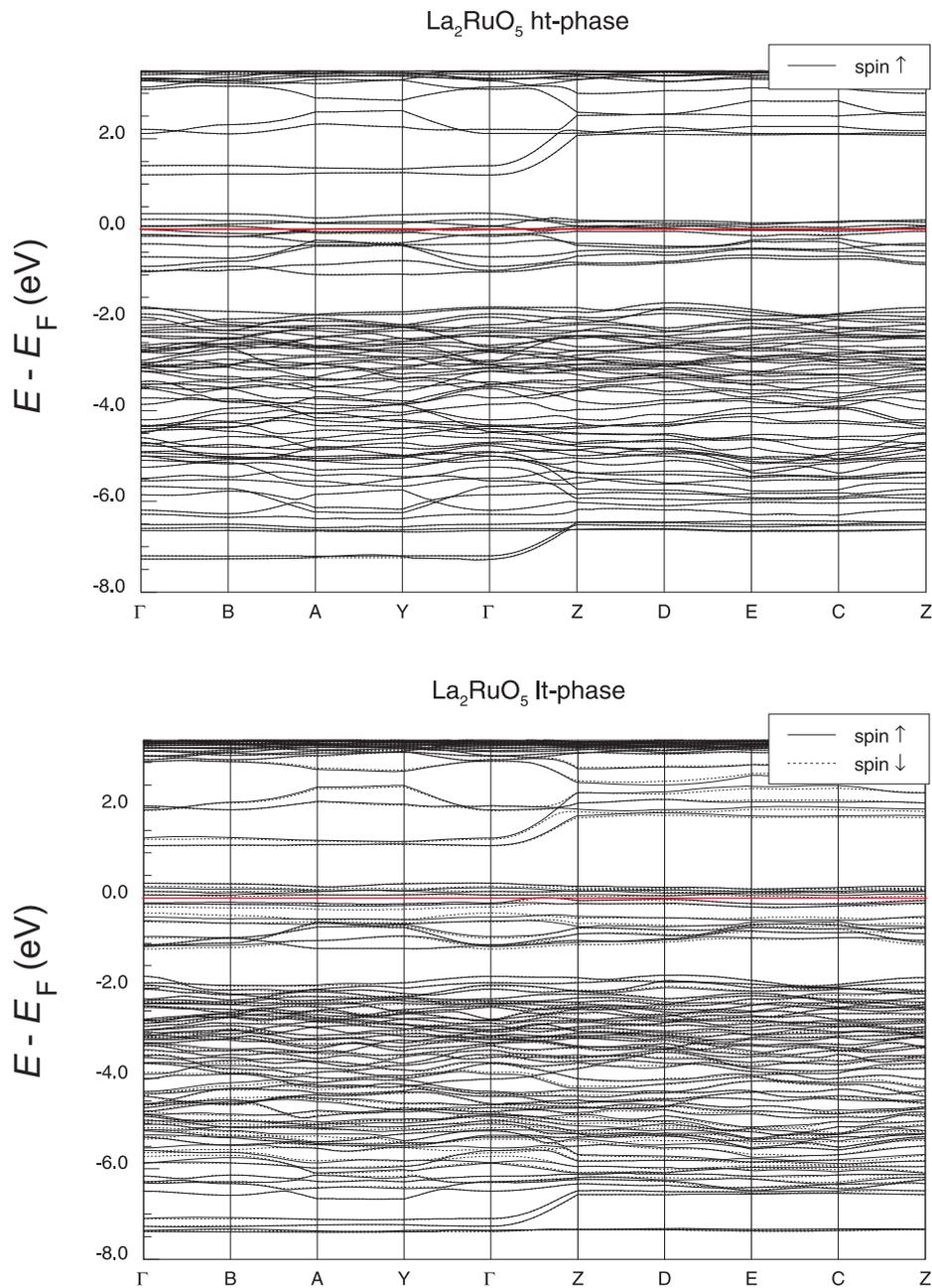
Figure 4.22.: Electronic band structure of the ht-phase (top) and the lt-phase (bottom) of La_2RuO_5. The ht-phase band structure was calculated using LDA and the lt-phase results were obtained from a spin polarized LSDA calculation, in which the solid and dashed lines represent the spin-up (majority) and the spin-down (minority) channel respectively. The horizontal solid red lines mark the Fermi energy.

is depicted in the energy range 8 eV below and 3.5 eV above the Fermi energy E_F. Due to the application of LDA without a spin polarization the resulting band structure contains only one spin
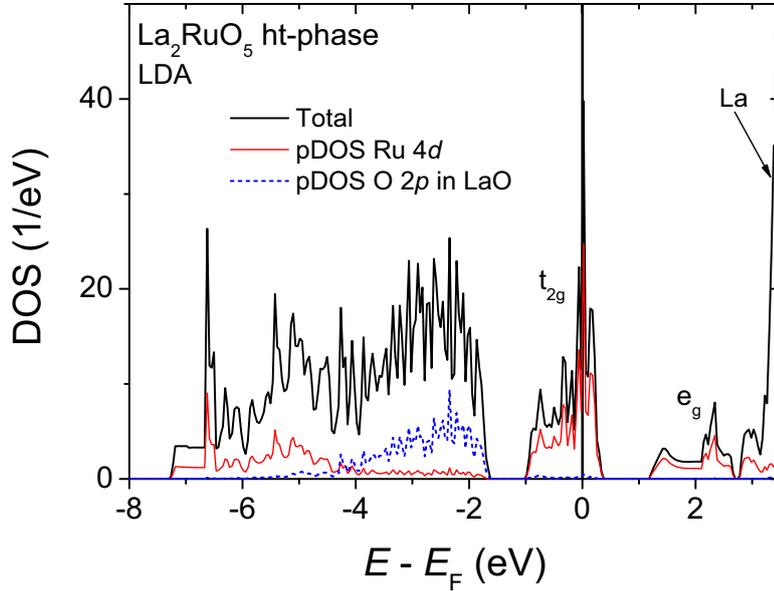
Figure 4.23.: Density of states for the ht-phase of La_2RuO_5 applying LDA.

channel. For the modelling of the lt-phase band-structure LSDA was used and the obtained DOS for both spin channels (spin ↑, spin ↓) are depicted in the bottom frame of Fig. 4.22 for the same energy range as the ht-phase. Furthermore, the same path in reciprocal space is shown for both phases as reflected by the notation of the reciprocal lattice points. The paths start at the Γ-point, which is corresponding to the origin (0 0 0), and make a loop in the $x' - y'$-plane (approximately corresponding to the *ab*-plane). Then the paths lead in z' direction (corresponding to *c*), followed by a second loop in the $x' - y'$-plane shifted to the first one by half of the unit-cell parameter. The horizontal solid red lines mark the position of E_F.

A great number of bands is located between -2 eV and -7.5 eV. These are almost exclusively oxygen 2*p* and Ru 4*d* bands. In the vicinity of E_F (-1 eV to 0.5 eV) the band structure is dominated by Ru 4*d* and hybridized O 2*p* bands. In the range above 1 eV the e_g levels of Ru and above 3 eV the unoccupied La 4*f* states are located. In general, the bands are rather flat. Exception are few Ru bands, which are showing a greater change of their slope between Γ and Z due to the changing direction of the path between *ab*-layer loop and perpendicular to it, i.e. parallel to the LaRuO₄-LaO-layering. The band structures of the ht- and lt-phase are very similar, which is expected considering the only slight changes in the crystal structure. Furthermore, both spin channels of the lt-modification are very similar reflecting an antiferromagnetic character.

While for the ht-modification no gap at E_F was observed (Fig. 4.22) for the lt-phase a small gap can be assumed. Only one, rather flat band crosses the Fermi energy between Γ and Z, which
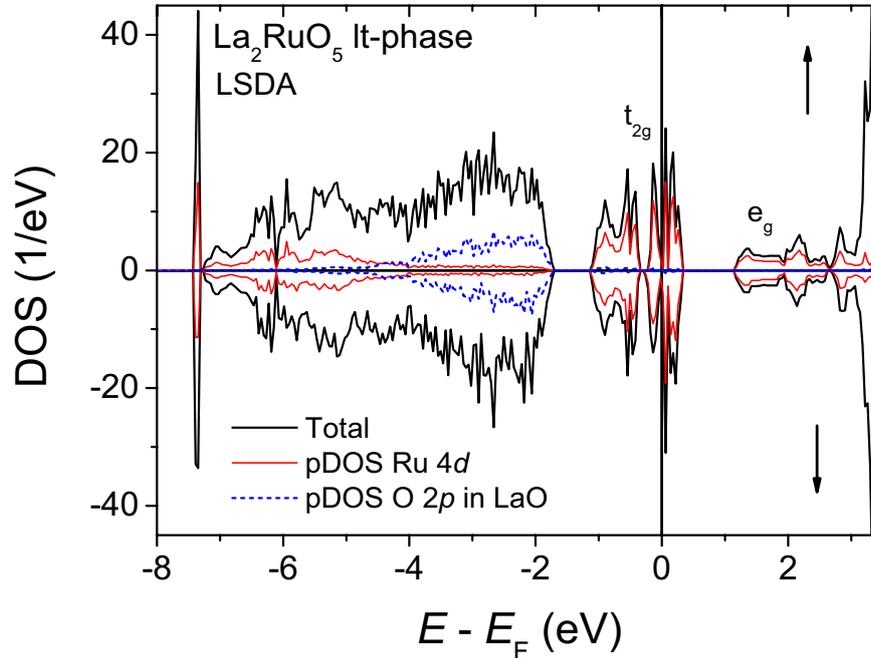
Figure 4.24.: Density of states of the spin-up (top) and the spin-down (bottom) channel for the lt-phase of La₂RuO₅ using LSDA.

in turn means that the gap is strongly anisotropic corresponding to the two-dimensionality of the crystal structure and the strongly anisotropic spin-dimer formation. The gap is opening for the zig-zag arrangement of RuO_6 octahedra in the $LaRuO_4$-layers, but becomes closed in c-direction. This assumption is reasonable since the axes in both real and reciprocal space are pointing in almost the same directions. It has to be reminded that the results of the basic DFT calculation have to be interpreted with some caution. As a result of the structural phase transition the bands are slightly shifted in energy. This is more obvious roughly between -0.3 eV and -1 eV, where a second gap opens due to the structural transition. The shift of some of the relatively flat bands is in agreement with the findings from the pressure related band gap determination above (Sec. 4.3). The pressure leads to deviations in the crystal structure, which in turn can shift some of the electronic bands and the observed band gap.

The DOS of the ht-modification is shown in Fig. 4.23 for the same energy interval as the electronic band structure. The calculation is in reasonable agreement with literature [Eye06, Eye07]. In particular, the same contribution of Ru 4d and O 2p orbitals around E_F was found. The oxygen contribution in this range explicitly stems from the RuO_6-octahedra in the $LaRuO_4$-layers. The t_{2g} levels of Ru are also located there, while the e_g levels are observed above 1 eV. Furthermore,
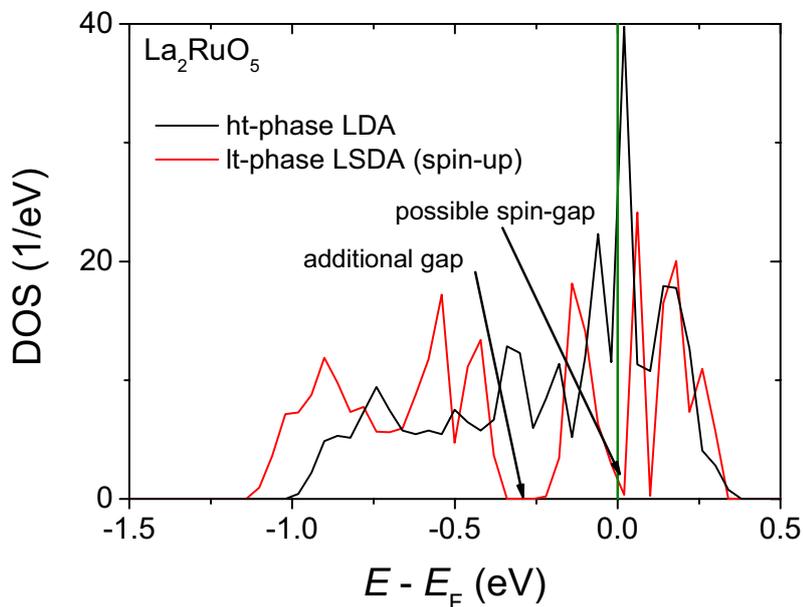
Figure 4.25.: Density of states DOS for the ht- and lt-phase (spin-up) of La$_2$RuO$_5$ close to the Fermi energy. The solid vertical green line marks the Fermi energy.

the distance between the centers of t$_{2g}$ and e$_g$ bands of approximately 2.5 eV is very similar to the corresponding value derived from the maxima of the white lines in the Ru-L$_{III}$ XANES spectra (see Fig. 2.9). The rather large partial DOS of La is located roughly 4 eV above E_F reflecting unoccupied 4f states. The O 2p contribution from the LaO-layers is only found in the range -2 eV to -4 eV and shows an increased negative charge compared to the other oxygens in the LaRuO$_4$-layers. This finding is consistent with the BVS calculations discussed above in Sec. 4.1.1.

To investigate the magnetic interactions in the ht-phase, additional spin-polarized modelling was performed. Different initial settings, including a ferro- and various antiferromagetic spin arrangements were tested. The lowest energy was obtained for the antiferromagnetic arrangement with local Ru spin moments of $S \approx \pm 1.15$ (the sign only represents the relative orientation of the spins). This setting is energetically favored by roughly 0.1 eV compared to the nonmagnetic LDA result. The negative Curie-Weiss temperature supports the antiferromagnetic interaction of the Ru spin-moments. Of course the ht-phase of La$_2$RuO$_5$ does not show a collective spin ordering but a paramagnetic behavior. It should be kept in mind though that the DFT calculations were performed under the precondition of $T = 0$ K. Therefore, thermal breaking of magnetic interactions is not taken into account.

The DOS for the lt-phase is depicted in Fig. 4.24. In the top frame the spin-up and in the bottom frame the spin-down channels are shown. Since the polarization was found to be antiferromagnetic
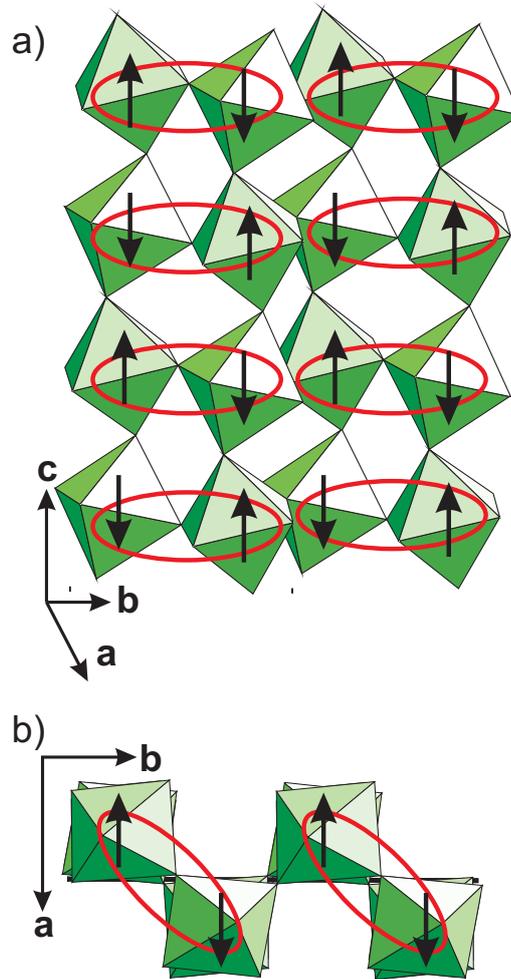
Figure 4.26.: Ru spin ordering in the lt-phase of La_2RuO_5. RuO_6 octahedra of the $LaRuO_4$-layer are drawn within a $2 \times 2 \times 2$-unit cell. Lanthanum ions are not shown for clarity. Black arrows indicate the $S = \pm 1$ spin ordering of the Ru^{4+}-ions, but do not represent an absolute orientation. The spin-dimer arrangement is indicated by the red ellipses. a) perspective viewing, b) projection along the c-axis.

both spin channels provide almost the same structure of the DOS. A ferromagnetic moment would cause a shift in energy of the Ru $4d$ and O $2p$ bands against each other in the vicinity of E_F. The general shape of the DOS is similar to the ht-phase and in agreement with literature [Eye06, Eye07]. A completely antiferromagnetically ordered state was found to be energetically favored by roughly 0.01 eV compared to the LDA model without magnetic settings. Different initial spin-ordering arrangements were tried as starting points. The corresponding calculations lead to the same ordered state for all initial arrangements and, therefore, proves the stability of this solution. Two very small band gaps at roughly −0.2 eV and approximately E_F originating from the ordering are found in contrast to the ht-phase or to unpolarized calculations. The DOS in the vicinity of E_F is shown in more detail in Fig. 4.25 for both ht- and lt-phase (spin-up channel) in comparison. While only a very small gap opening at E_F is found, the second gap at −0.2 eV provides a width of

approximately 0.1 eV and originates from the shift of the energetically lower part of the Ru and O bands towards lower energies. It has to be mentioned that band gaps are typically underestimated by the LDA or LSDA method and due to the strongly correlated electrons more sophisticated calculations introducing additional (exchange) interaction parameters would be required. The gap at E_F may alternatively be explained as a result of the antiferromagnetic arrangement according to Ref. [Wha81]. The local Ru spin moments were found to be approximately $S = +0.95$ and $S = -0.98$ for neighboring sites perfectly fitting to this model. However, the results of the experimental investigations shown above strongly prefer a singlet ground state formed by almost isolated spin dimers in the lt-phase.

The complete antiferromagnetic arrangement of the Ru spin moments found in the lt-phase of La$_2$RuO$_5$ is depicted schematically in Fig. 4.26. To increase clarity, only the RuO$_6$ zig-zag-like octahedra double layers of the LaRuO$_4$-unit are shown. Black arrows represent the Ru^{4+}-ion $S = \pm 1$ spin moments with spin-up and down orientation. It should be noted, that the shown directions are only the relative orientation of the spins with respect to each other and do not represent an absolute orientation with respect to the crystallographic axes. Fig. 4.26a illustrates the formation of the Ru-Ru dimers in the LaRuO$_4$-layers by red ellpises, which mark the antiferromagnetically coupled spins. In a projection along the c-axis the dimers are better recognizable (Fig. 4.26b). According to the obtained results each dimer is also antiferromagnetically interacting with the neighboring ones. However, taking into account the experimental results discussed above this interaction can only be very weak.

Starting from the DFT modelling for the pure La$_2$RuO$_5$ additional calculations for selected substituted samples were performed. The results are presented in the following sections and related to the results described here.

5. Influence of Substitution on La$_2$RuO$_5$

5.1. Lanthanide Substitution: La$_{2-x}$Ln$_x$RuO$_5$

While the undoped compound has been comparatively well examined, little is known about substituted La$_2$RuO$_5$. To the best of our knowledge there is only a short note on Pr-substituted La$_2$RuO$_5$ in literature found in Ref. [Mal05]. Due to the decreasing ionic radii of the lanthanides, rare-earth substitutions should result in a reduction of the interatomic distances. It can be expected that a smaller Ru–Ru distance increases the magnetic interaction resulting in higher dimerization temperatures. In addition, the interaction of the magnetic moments of the lanthanide ions with the magneto-structural coupling of the Ru spin moments may occur. In this context also the distribution of the rare-earth ions in the crystal structure has to be taken into account. Since the *Ln*–Ru distances are expected to become shorter, an additional magnetic moment in the LaRuO$_4$-layers may have a stronger impact on the dimerization transition than a substitution which takes place mainly in the LaO-layers. Furthermore, the varying magnitude of the magnetic moment of the different rare-earth metal ions has to be considered. If an interaction exists, a large magnetic moment, e.g. for Gd^{3+} or Dy^{3+}, should affect the dimerization transition stronger than a very small moment, like e.g. found for Sm^{3+}. As will be shown in this chapter, the influence of the lanthanide's moments are very small while their varying size has a pronounced effect.

A full substitution of the diamagnetic La^{3+} ions by other rare-earth ions (Pr, Nd, Sm, Gd, Dy) leads to the sum formula *Ln*$_2$RuO$_5$. Some of these compounds have actually been prepared from the binary oxides in the absence of oxygen [Cao01, Koc82, Dix80]. However, the *Ln*$_2$RuO$_5$ oxides crystallize in a completely different orthorhombic structure, which is isostructural to Y$_2$TiO$_5$ [Mum68]. In an oxygen-containing atmosphere, the smaller lanthanides are known to form ruthenates with pyrochlore structure (*Ln*$_2$Ru$_2$O$_7$) [Yam94, Ken96]. For this reason a complete substitution was not achieved in this work, but a partial replacement of La was successfully carried out up to a certain maximum substitution level at which the structure becomes unstable. First attempts to prepare rare-earth substituted samples by classical solid-state synthesis were not successful. No single-phase compounds could be obtained, instead the reaction products contained significant amounts of pyrochlore impurities. Thus, a soft-chemistry sythesis-method based on the thermal decomposition of citric-acid stabilized precursors [Dou89] has been developed to prepare single-phase powder samples (see Sec. 2.1.3).

The obtained La$_{2-x}$Ln$_x$RuO$_5$ samples were investigated with respect to their crystal structure by powder x-ray-, synchrotron-, and neutron-diffraction measurements. The location and distribution of the incorporated lanthanide ions in the layered crystal structure was studied by EXAFS. A detailed investigation of the magnetic properties was performed. Moreover, the phase-transition
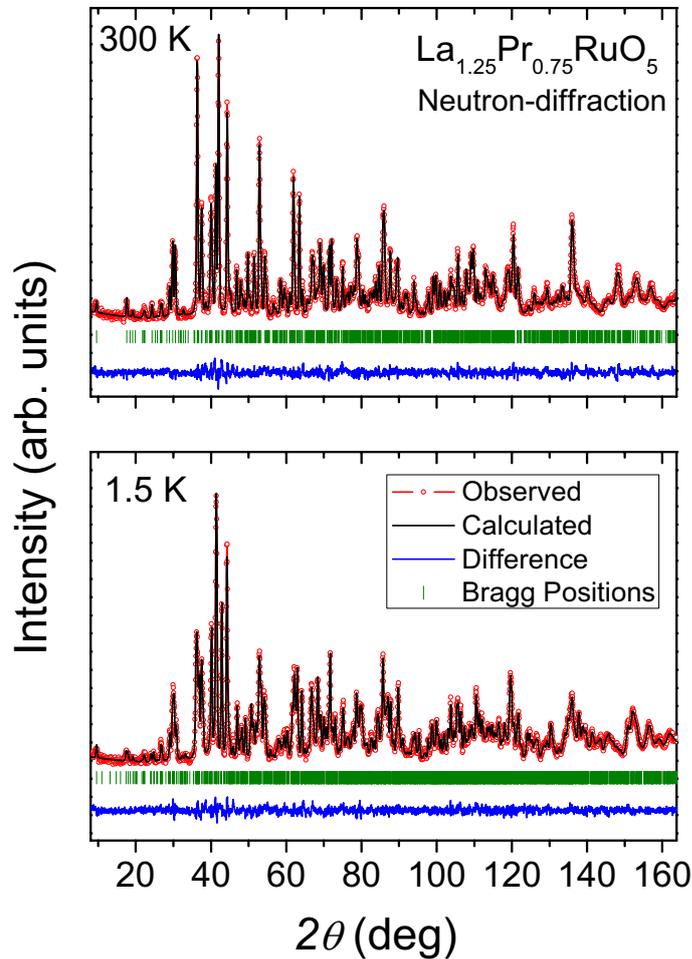
Figure 5.1.: Rietveld refinement of the La$_{1.25}$Pr$_{0.75}$RuO$_5$ neutron-diffraction patterns ($\lambda = 1.4940$ Å) measured at 300 K (top) and 1.5 K (bottom).

temperature was determined from DSC and compared to values derived from magnetic susceptibility data. Specific-heat measurements have been performed as well as DFT calculations to investigate the Ru spin-dimerization transition. The results presented in this section are mainly based on already published data in Refs. [Rie11, Rie12a, Rie12c].

5.1.1. Crystal Structure

X-ray powder diffraction revealed phase purity for almost all rare-earth substituted compounds presented in this work. Only for the samples with the highest substitution levels marginal traces of LaRuO$_3$ were found. The maximum substitution level can be linked to the ionic radii of the used lanthanides. The partial replacement of La^{3+} by smaller rare-earth metal ions causes an increasing

structual stress, which finally results in the formation of impurity phases. This stress increases with decreasing ionic radius (caused by the lanthanide contraction) and in turn the maximum achievable substitution level was higher for the larger lanthanides. The maximum concentration of rare-earth metal ions (x) in La$_{2-x}$Ln$_x$RuO$_5$ was found to be 0.75 for Pr, 0.6 for Nd, 0.5 for Sm, 0.3 for Gd and 0.2 for Dy. For substitution levels beyond these values significant amounts of the above mentioned other phases (e.g. pyrochlores) were observed. These impurities were very stable and could not be removed by further thermal treatment of the sample at 1175°C, which was found to be the optimum synthesis temperature. It has to be mentioned that single phase La$_2$RuO$_5$ is only formed in a small temperature range from 1150°C to 1200°C. At lower temperatures different other lanthanum ruthenate compounds like La$_3$Ru$_3$O$_{11}$ [Abr78, Cot78], LaRuO$_3$ [Bou72], La$_3$RuO$_7$ [Kha00], and La$_{3.5}$Ru$_4$O$_{12}$ [Abr80] were observed which finally reacted to La$_2$RuO$_5$ at T $\geq$ 1150°C. Above 1200°C the pyrochlores and other, still unidentified oxides were formed in an irreversible reaction. The Y$_2$TiO$_5$-type ruthenates Ln_2RuO$_5$ were not observed since they only form under pressure in an oxygen-free atmosphere.

As one representative example for the Rietveld refinements Fig. 5.1 shows the fits of the ND data of La$_{1.25}$Pr$_{0.75}$RuO$_5$ recorded at 300 K (top) and 1.5 K (bottom). A very good agreement of measurement and modelled patterns is achieved. Similar to the synchrotron XRD patterns (Fig.4.8) slight deviations between ht- and lt-modification are observable in the patterns. The experimental room-temperature XRD data of the rare-earth substituted samples are not shown here, because due to the only very small differences to the pattern of pure La$_2$RuO$_5$ they provide almost no significant additional information. Numerical values obtained from the Rietveld refinements of the La$_{2-x}$Ln$_x$RuO$_5$ samples are listed in the tables in Ref. [Rie11].

5.1.1.1. Structural Analysis Using Diffraction Data

In Fig. 5.2a - c the room-temperature cell parameters of all La$_{2-x}$Ln$_x$RuO$_5$ samples are shown for different substitution levels. A strong dependence on x is observed: All three axis lenghts a, b and c decline almost linearly for all rare-earth elements. The shrinkage of the three axis lengths also results in a decreasing volume of the unit cell. The effects are increasing with decreasing size of the lanthanide ion, i.e. the slopes of the curves develop in the order Pr < Nd < Sm < Gd < Dy. This behavior reflects the lanthanide contraction. The changes in the axis lengths can directly be linked to the maximum substitution levels mentioned above implying a structural stress limit, i.e the general limit is reached for $a \approx 9.12$ Å, $b \approx 5.81$ Å and $c \approx 7.93$ Å.

The evolution of the monoclinic angle β is shown in Fig. 5.2d. The changes of the angle are small, but they also clearly depend on the rare-earth substitution. The bigger rare-earth metal ions Pr and Nd cause a continuous decrease with increasing x, the effect of Pr being stronger than for Nd. For Sm β remains almost constant, while for the small ions Gd and Dy even enlarged angles are found. The influence of the smaller Dy is stronger than the one of Gd.

A more detailed insight in the evolution of the different cell parameters depending on x is obtained by a plot of the relative changes as presented in Fig. 5.3. The relative values were calculated by dividing the cell parameters of La$_{2-x}$Ln$_x$RuO$_5$ by their corresponding values of unsubstituted
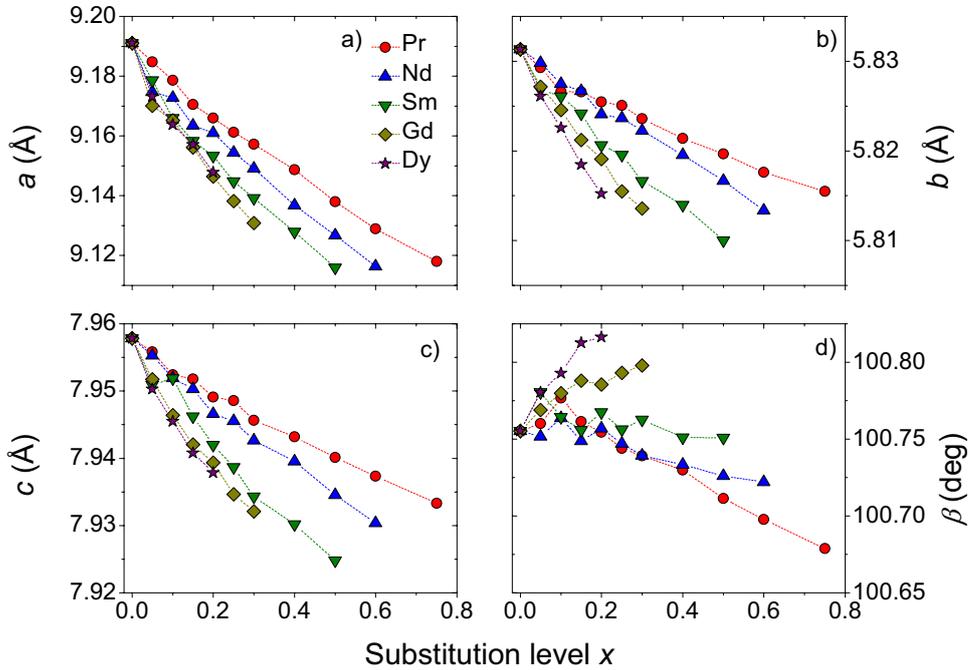
Figure 5.2.: Cell parameters for La$_{2-x}$Ln$_x$RuO$_5$ derived from powder XRD data at room temperature. In frames a, b, and c the cell parameters *a*, *b*, and *c* are displayed, respectively, while the monoclinic angle *β* is shown in frame d. Error bars are smaller than the size of the symbols.

La$_2$RuO$_5$, which makes the changes better comparable for the different lanthanides and for the cell parameters themselves. Since the behavior is similar for all rare-earth elements, only the values for *Ln* = Pr (left) and Gd (right) are given as examples in Fig. 5.3. All cell parameters change linearly with *x*, but a highly anisotropic behavior is observed. The axis *a* shows the strongest decrease with *x* while the axes *b* and *c* behave almost identically and show a significantly smaller decrease than *a*. Since *β* does not change very much, the unit-cell volume also decreases with *x* for all rare-earth elements. Although the changes in the cell parameters are clearly significant, the relative values deviate by less than 1.3 % from La$_2$RuO$_5$, which is a surprisingly small value taking into account that substitution levels up to *x* = 0.75 were achieved.

Regarding the crystal structure and the alternating stacking of LaRuO$_4$- and LaO-layers along the *a*-axis, the anisotropic behavior gives a first hint for the location of the substituting ions. If the smaller lanthanide ions were placed in the LaRuO$_4$-layer, a more or less isotropic change in structure would be expected, i.e. the relative decrease of the three axes lengths should be similar. A substitution in the LaO-layers, on the other hand, is expected to predominantly shorten the interlayer distance and, therefore, mainly affect the *a*-axis, in accordance with the experimentally observed behavior. A preferred occupation of the smaller lanthanide ions in the LaO-layer
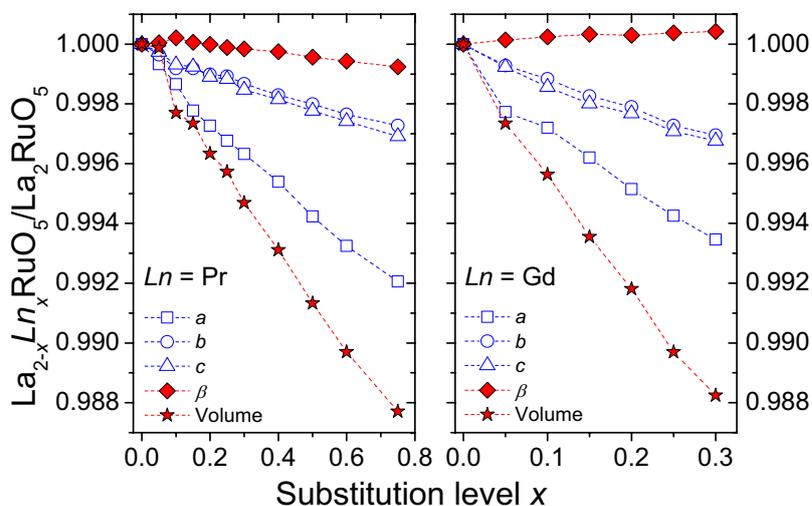
Figure 5.3.: Relative change of the cell parameters for the Pr- (left) and the Gd- (right) substituted samples. The cell parameters of $La_{2-x}Ln_xRuO_5$ were divided by their correspondng values for pure La_2RuO_5. Error bars are smaller than the size of the symbols.

is reasonable since the La–O distances in this layers are significantly shorter than those in the $LaRuO_4$-layer [Bou03, Ebb05]. A detailed study of the rare-earth metal ion distribution will be discussed later.

A broad choice of compositions was investigated by additional low-temperature x-ray diffraction at 128 K, i.e. well below the phase transition temperature. As a main result of the low-temperature XRD data, the triclinic lt-phase was observed for all rare-earth substituted compounds under investigation. In Fig. 5.4 the cell parameters obtained from the Rietveld refinement of the low-temperature XRD data (128 K) and neutron data (1.5 K) are shown for the series of Pr-substituted samples. The values were divided by their corresponding room-temperature values for better comparability. As can be seen the results from neutron diffraction and x-ray diffraction yield almost identical values. Small deviations (especially for the *a*-axis) may be due to the different temperatures (XRD 128 K, ND 1.5 K). From Fig. 5.4 it is evident that the phase transition leads to an increase of *b*, a smaller increase of *a*, a barely significant decrease of *c* and a clear decrease of β. In the triclinic lt-phase α is slightly decreased while γ is increased compared to the value of $90°$ for both angles in the monoclinic ht-phase (not shown in Fig. 5.4). It is noteworthy that the relative changes associated with the phase transtition are almost independent of the substitution level *x*. In addition, it has to be mentioned that in Fig. 5.4 the data for $x = 0.5$ (marked by the arrow) were obtained for the Nd substituted sample, not for Pr.

Bond-valence sum (BVS) calculations [Bro85] based on the Rietveld refinements of XRD and ND data yielded valences that are close to the formal charge of the ions, i.e. in the $LaRuO_4$-layer
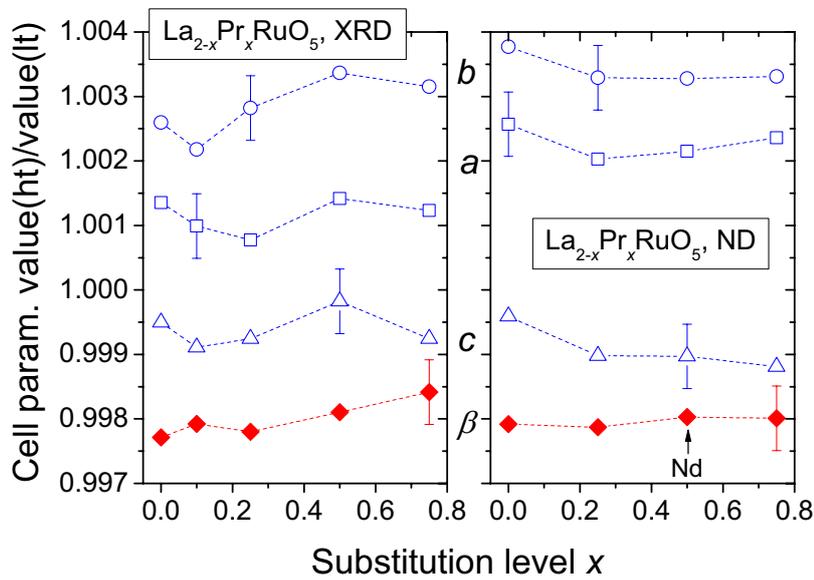
**Figure 5.4.:** Comparison of the cell parameters for the high- and low-temperature phases of La$_{2-x}$Pr$_x$RuO$_5$. Comparable room-temperature parameters have been divided by their correspondng lt-data. Left: Data from XRD, right: Data from neutron diffraction.
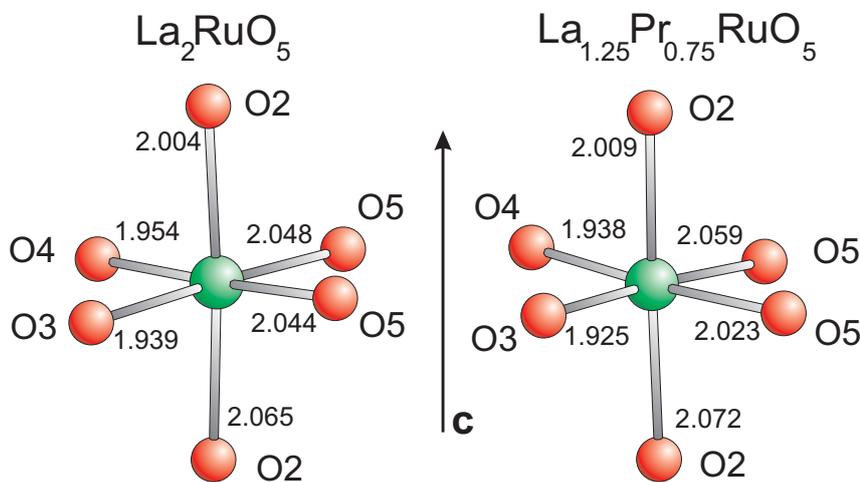
Figure 5.5.: Comparison of the octahedral coordination of Ru in La$_2$RuO$_5$ (left) and La$_{1.25}$Pr$_{0.75}$RuO$_5$ (right) from room-temperature ND data. The bond lengths are given in Å.

approximately -1.9 for oxygen, $+3.0$ for lanthanum and $+3.8$ for ruthenium. However, in the LaO-layer oxygen exhibits a larger negative valence of -2.4 while the value for La is shifted to $+3.2$ caused by the shortened La–O bonds. In addition, a valence of roughly $+2.9$ is found for Pr
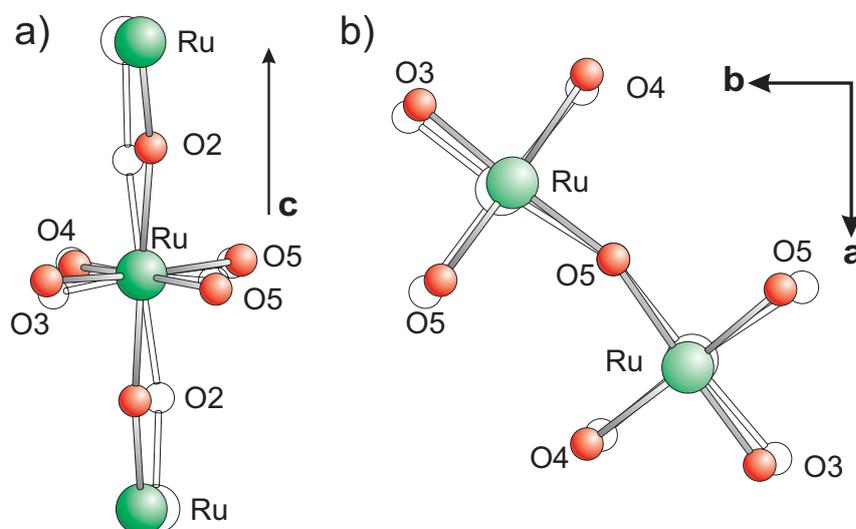
Figure 5.6.: Comparison of the Ru–O2–Ru angles along the *c*-direction (a) and the local oxygen coordination in the *ab*-plane in La$_2$RuO$_5$ (transparent) and La$_{1.25}$Pr$_{0.75}$RuO$_5$ (opaque) from room-temperature ND data. For better comparability of the changes, the central atoms [Ru in a) and O5 in b)] were placed on the same position.

which is slowly decreasing for Nd, Sm, and Gd to roughly +2.5, and finally dropping to +2.0 for Dy. These valences were found to be almost constant for all substitution levels *x*. This indicates that the La–O bonds are shorter than predicted by the BVS approach while the *Ln*–O distances are too long. Apparently, structural restrictions do not allow the bonds in the (La/*Ln*)O-layers to take their preferred values.

The bond lengths, especially those between the metal ions, reveal the same dependence on the substitution level as the cell parameters. While the intralayer La–Ru distance remains almost constant, the interlayer distance between La/*Ln* and Ru decreases slightly. This effect is even more pronounced for the La–La/*Ln* distance, which is highly related to the value of the axis *a*.

As will be described later, the rare-earth substitution leads to significant changes in the physical properties of the samples, especially differences in the temperature of the magneto-structural transition. It is well known that in perovskites such changes can be induced by even small variations of bond distances and/or angles. While the former can result in distortions of the metal-oxygen octahedra, which affect the energies of the *d* orbitals and may cause phenomena like orbital ordering, the latter directly influence the metal-oxygen-metal superexchange interaction due to variations in the overlap of the corresponding orbitals [Kan59]. For this reason a thorough inspection of the geometry of the RuO$_6$ octahedra and the Ru–O–Ru angles was performed. Since the atomic coordinates of oxygen can more accurately be determined by neutron than by x-ray diffraction, only the ND data is considered in the following.

For the monoclinic high-temperature phase small changes caused by the substitution were observed. This is shown in detail in Fig. 5.5 for the octahedra in La$_2$RuO$_5$ and La$_{1.25}$Pr$_{0.75}$RuO$_5$. O3 and O4 are directing towards the LaO-layers while O2 is connecting the RuO$_6$-octahedra along
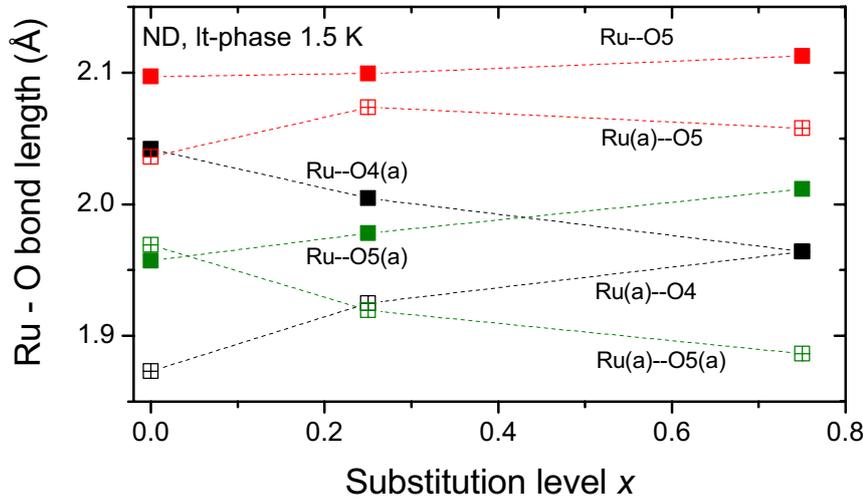
Figure 5.7.: Selected Ru–O bond lengths for the lt-phase of $La_{2-x}Pr_xRuO_5$ derived from ND-data (1.5 K) refinements.

the *c*-axis. O5 links the RuO_6-octahedra within the *ab*-plane. The O2–Ru–O2 angles are close to 178° for all samples under investigation and also the Ru–O bond lengths are almost constant. Ru–O5 is an exception, here a distinct elongation of one of the bonds and simultaneous shortening of the second one is observed. Apart from this, the tilting of the RuO_6-octahedra was found to increase, when La is substituted by Pr. The angle Ru–O2–Ru (i.e. parallel to the *c*-axis) is reduced from 152.8° for $x = 0$ to 152.3° for $x = 0.75$ in the Pr substituted samples. This smaller bond angle results in a slightly shortened Ru–Ru distance and a small torsion of the octahedra along *c*, as shown in Fig. 5.6a for La_2RuO_5 (transparent) and $La_{1.25}Pr_{0.75}RuO_5$ (opaque). In the *ab*-plane the Ru–O5–Ru angle remains almost unchanged, while on the other hand the O5–Ru–O5 angle decreases from 95.1° to 94.1° causing an elongation of the Ru–Ru distance by 0.015 Å. This is illustrated in Fig. 5.6b for La_2RuO_5 (transparent) and $La_{1.25}Pr_{0.75}RuO_5$ (opaque) for the Ru–O coordination in the *ab*-plane.

The low-temperature (1.5 K) ND data of the samples $La_{1.75}Pr_{0.25}RuO_5$, $La_{1.25}Pr_{0.75}RuO_5$, and $La_{1.5}Nd_{0.5}RuO_5$ reveal the same structural phase transition to the triclinic space group P$\bar{1}$ as found for the unsubstituted La_2RuO_5. Due to the symmetry reduction the number of crystallographic sites doubles [indicated by the index (a) in the following], but corresponding atoms and bonds can be discussed simultaneously. Again, similar alternating elongations and shortenings of the Ru–Ru distances are observed and the Ru–O–Ru angles show only minor changes with increasing substitution level similar to the situation in the ht-phase discussed above. In contrast, we observed a deviation of two Ru–O bond lengths. First, the Ru–O bond, which is bridging the RuO_6 octahedra
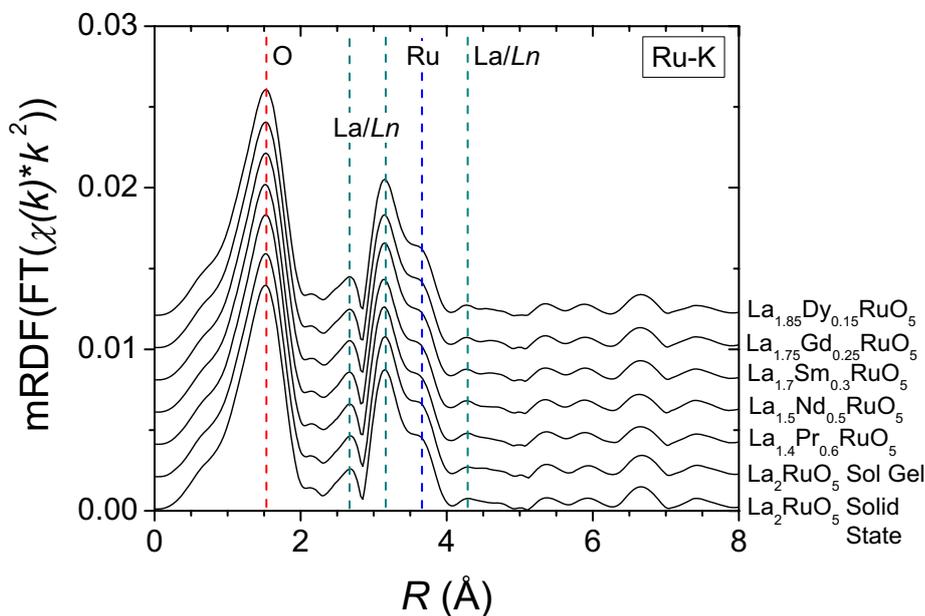
Figure 5.8.: Modified radial distribution function from the k^2-weighted Ru-K EXAFS spectra (curves are shifted by 0.002). The vertical dashed lines mark the different coordination shells of Ru.

in the *ab*-plane (Ru(a)–O5 and Ru(a)–O5(a)) shows an increasing dispersion of bond length with increasing *x* from 1.96 Å ($x = 0$) to 1.88 Å ($x = 0.75$, Ru(a)–O5(a)), respectively 2.04 Å ($x = 0.75$, Ru–O5(a)) (see Fig. 5.7). Second, the Ru(a)–O4 and Ru–O4(a) bonds directing to the LaO-layer act in the opposite way. The rather different values for $x = 0$ (1.88 Å, 2.04 Å) change to an almost identical distance of 1.96 Å for $x = 0.75$. For comparison the bond lengths of Ru–O5 and Ru(a)–O5 are shown in Fig. 5.7 representing the almost constant values of the other Ru–O bonds for increasing *x*.

In summary, a variation of the shape of the RuO_6-octahedra and a reduction of the Ru–O–Ru tilting angle resulting in a torsion of the octahedra along the *c*-axis with increasing substitution level was detected. This finding is important for the interpretation of the magnetic data presented in Sec. 5.1.2.

5.1.1.2. Ru-K EXAFS

In Fig. 5.8 the modified radial distribution functions of the Ru-K EXAFS for the $La_{2-x}Ln_xRuO_5$ compounds with a high substitution level for each rare-earth element are shown. The corresponding curve for unsubstituted La_2RuO_5 (solid-state and sol-gel synthesis) are additionally displayed for comparison. All EXAFS spectra were weighted by k^2 and oscillations for $2\,Å^{-1} \leq k \leq 15\,Å^{-1}$ were used for the Fourier transformation.

Table 5.1.: Ru-K EXAFS fit results for polycrystalline La$_2$RuO$_5$ obtained by sol gel reaction. With the simplified fit-model described in the text a residual of 13.10 % was achieved. The EXAFS function $\chi(k)$ was k^2-weighted, the E$_0$ shift was -2.58(1) eV and S$_0^2$ amounted to 0.910(1).

Coordination	N	R (Å)	σ^2 (Å^2)
Ru–O	1.96(1)	1.909(1)	0.0013(1)
Ru–O	4.01(1)	2.042(1)	0.0013(1)
Ru–La	0.98(1)	3.280(1)	0.0047(1)
Ru–La	3.94(1)	3.477(1)	0.0047(1)
Ru–La	1.98(1)	3.574(1)	0.0047(1)
Ru–La	0.95(1)	3.640(1)	0.0047(1)
Ru–Ru	4.11(1)	4.013(1)	0.0080(1)
Ru–La	0.98(2)	4.694(1)	0.0039(1)
Ru–La	0.90(2)	4.838(1)	0.0039(1)

Up to 4 Å, well defined peaks according to the different coordination spheres can be identified in the mRDF (Fig. 5.8). The peaks at roughly 1.8, 2.7/3.2, 3.7, and 4.3 Å represent the neighboring O, La/*Ln*, Ru, and a second shell of La/*Ln*, respectively. The peak positions of the unsubstituted La$_2$RuO$_5$ are marked with dashed lines for better comparability. Since the Ru–O bond lengths vary between 1.933 Å and 2.067 Å, the peak resulting from the backscattering of the oxygens is broadened and asymmetric. With FEFF8 the amplitudes and phase shifts for the backscattering atoms were modelled and used for fitting the measured data of La$_2$RuO$_5$ prepared by the sol-gel method. Using the scattering paths for the coordinating atoms up to roughly 5 Å distance, the result is in very good agreement with the experimental data (Fig. 5.9). In Tab. 5.1 the obtained values from the fit are listed. Arcon *et al.* reported an EXAFS fit using a more complex model [Arc07]. After a first attempt with this model, it was found that reducing the number of fit parameters by combining several backscattering paths with similar interatomic distances leads to more stable results. During the refinement of the undoped La$_2$RuO$_5$ the coordination numbers N were kept fix and the Debye-Waller factors σ^2 were constrained to be equal for the backscattering atoms of the same element in equivalent coordination shells. In a second refinement step S$_0^2$ and σ^2 were fixed to the values previously obtained and N and the distances were refined. The model was further improved by neglecting all Ru–O paths above approximately 3.5 Å. Their contribution is of minor relevance for the fit and the obtained values in the first attempts were not reliable. Multiple scattering was not taken into account since its contribution was negligible compared to the direct scattering. Multiple scattering occurs for collinear arrangements, i.e. bond angles close to 180° [Ebb97], which are not present in La$_{2-x}$*Ln*$_x$RuO$_5$ [Ebb05, Rie11]. The Ru–O–Ru bonding angles of $\approx$ 155° in the *ab*-plane (resp. $\approx$ 153° along *c*) are comparable to *A*Cu$_3$Ru$_4$O$_{12}$ with Ru–O–Ru $\approx$ 140°, in which the multiple scattering could also be neglected [Ebb02].

By combining several backscattering shells as described above a reasonable simplification was achieved, which lead to a stable fit. For this the single backscattering paths listed in Tab. 5.1 are
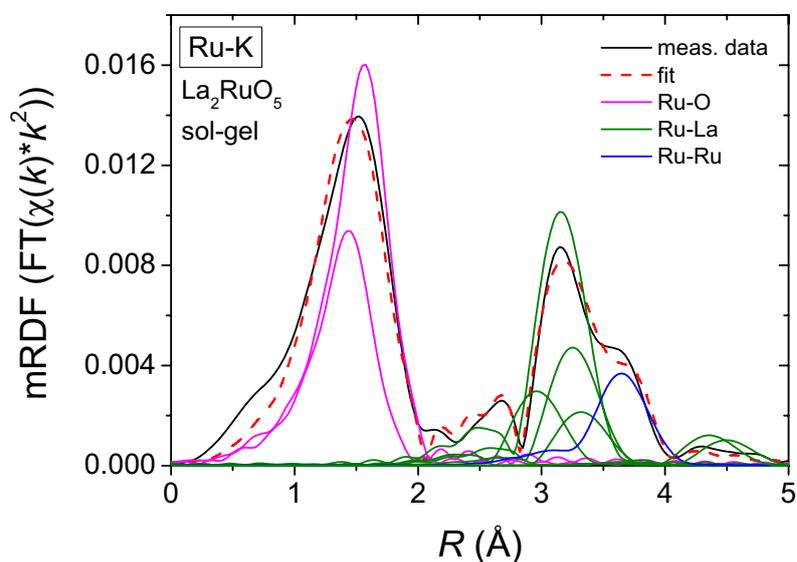
Figure 5.9.: Fit (dashed red line) of the mRDF of the k^2-weighted $\chi(k)$ measured at the Ru-K absorption edge of La$_2$RuO$_5$ (solid black line) prepared by the sol-gel route. Furthermore, the fit curves for the individual coordination shells according to Tab. 5.1 are shown in different colors: Ru–O in magenta, Ru–La in green, and Ru–Ru in blue, respectively.

shown in Fig. 5.9 and colored according to the element in the coordination shell (Ru–O in magenta, Ru–La in green, and Ru–Ru in blue, respectively). The Ru–O distances were rearranged in two shells, which represent the two shorter bond lengths of O3 and O4, which are pointing to the LaO-layers (see Fig. 5.5), and the four longer bond lengths of O2 and O5, respectively. The obtained distance of 1.909 Å for the two shorter bonds is slightly smaller than the values of the single-crystal results (see Tab. A.6). On the other hand, the second distance representing the four oxygen atoms crosslinking the RuO$_6$ octahedra in the LaRuO$_4$-layer gave an averaged distance of 2.042 Å, which is in good agreement with the single-crystal data (between 2.001 and 2.067 Å, averaged distance 2.041 Å). From the distribution of the distances it can be seen that the eight Ru–La distances can be grouped into four sets with a degeneracy of 1, 4, 2, and 1. Therefore, four scattering shells were used to fit the first two La-related peaks. The obtained distances from the EXAFS spectra are only slightly larger by between 0.01 Å and 0.04 Å than the ones shown in Tab. A.6. For the Ru–Ru backscattering a single shell with a coordination number of four was sufficient, while two different distances were used to model the third Ru–La peak. The obtained EXAFS distances are again distincly larger by 0.04 Å to 0.1 Å than expected from the single-crystal data. In general, the obtained interatomic distances from EXAFS spectroscopy agree well (better than 0.2 Å) with the values derived from the diffraction results. The small deviations observed are most likely due to the simplified model applied. The deviations of the coordination numbers from the EXAFS fit

Table 5.2.: Distribution of Pr in the two different types of layers in La$_{2-x}$Ln$_x$RuO$_5$.

La$_{2-x}$Pr$_x$RuO$_5$	Pr in LaO	Pr in LaRuO$_4$	sum of Pr
300 K			
$x = 0.25$	0.19(2)	0.09(2)	0.28(2)
$x = 0.75$	0.51(2)	0.27(2)	0.78(2)

to the the expected values are small, which proves that the used model is applicable and leads to stable results.

The fitting procedure described above was applied to all spectra and resulted in very similar values. Thus, it can be concluded that substitution by rare-earth ions does not lead to a considerable distortion of the local Ru environment. This corresponds well to the findings obtained from x-ray and neutron powder diffraction. Also with these diffraction methods only very small deviations of bond lengths and angles in the RuO$_6$ octahedra were observed for La$_{2-x}$Ln$_x$RuO$_5$.

The XANES region of the Ru-K edge was used for the determination of the Ru valence. The first maximum of the derivative of the spectra was taken as energy measure. A comparison showed that all compounds exhibit very similar absorption-edge energies. Thus the Ru valence is +4 for all La$_{2-x}$Ln$_x$RuO$_5$ compounds in agreement with results on La$_2$RuO$_5$ reported by Arcon *et al.* [Arc07].

5.1.1.3. Detailed Analysis of the Lanthanide Distribution Using ND and EXAFS

Neutron diffraction was used to investigate the distribution of the rare-earth metal ions in the two distinct layers of the crystal structure. The Pr substituted samples were measured since the scattering lengths of La (8.24 fm) and Pr (4.58 fm) are very different, while their absorption cross sections are similar [Sea92]. As shown in Tab. 5.2 both in the high- and the low-temperature phase roughly $65 - 70\%$ of the Pr^{3+} ions are found to be placed in the LaO-layers. This preferred occupation of the La-sites is in accordance with the structural data discussed above. It is reasonable to assume that for the even smaller lanthanide ions Nd^{3+}, Sm^{3+}, Gd^{3+}, and Dy^{3+} the same or even an enhanced enrichment in the LaO-layers occurs. Unfortunately, these cationic orderings could not be investigated due to very similar neutron scattering lengths and/or huge absorption cross sections (e.g. Sm: 5922 bn, Gd: 49700 bn) [Sea92].

In the triclinic lt-structure, both La positions split into two different sites. Due to a strong correlation of the corresponding fit parameters it was not possible to refine the occupation factors of the four positions independently. Therefore, the distribution of La/Pr derived from the room temperature ND data were fixed in the refinement of the data recorded at 1.5 K. This procedure is justified by the immobility of the rare-earth metal ions at room temperature and below, i.e. the cationic ordering is frozen in at these temperatures. Detailed structural data obtained from the ND measurements are given in the tables in Ref. [Rie11].

Since XAS is highly element specific, it allows the investigation of the surrounding of the sub-
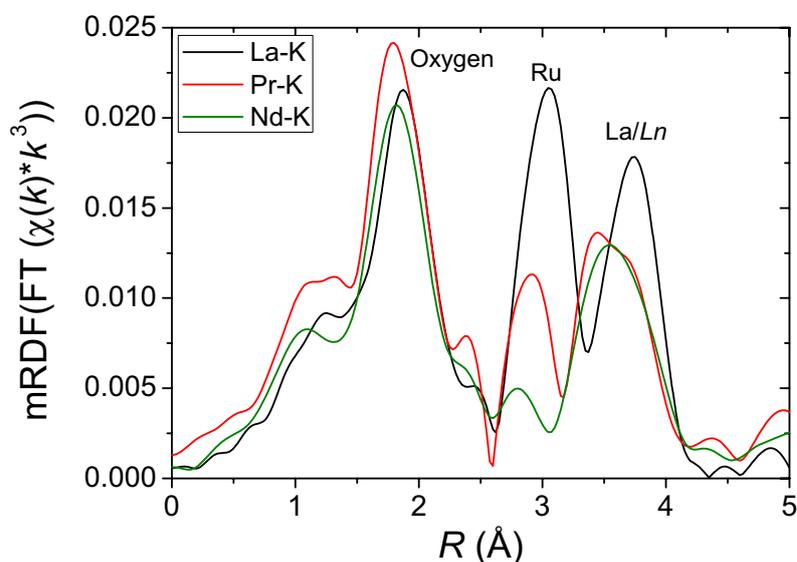
Figure 5.10.: Fourier transforms (mRDF) of the k^3-weighted EXAFS function $\chi(k)$ of the La-K-, Pr-K-, and Nd-K-absorption edge.

stituting elements selectively. In Tab. 2.1 the K- and L$_{III}$-absorption-edge energies of the used lanthanides are listed. The L$_{III}$-edge energies of La, Pr, and Nd are too similar in energy to be evaluated separately. Thus, the strong overlapping of the EXAFS regions of La and Pr/Nd demands the investigation of the K-edges of these elements. The larger energy difference of the K-edges enables a clear separation of the EXAFS spectra. However, for the late $4f$ elements like Sm, Gd, and Dy the energy finally becomes so high that the EXAFS oscillations are of very low amplitude, e.g. at the Sm-K edge no significant oscillations were observed anymore. For these elements the L$_{III}$-edges were investigated instead.

The fitting of the *Ln*-EXAFS data is complicated by the fact that the rare-earth elements under investigation can occupy both crystallographic La-sites, i.e. the one in the LaRuO$_4$-layers and the one in the LaO-layers. Thereby, the obtained spectra contain contributions from both sites. Looking at the interatomic distances listed in Tab. A.6 it is obvious that for both La positions a large number of different backscattering paths have to be considered. Therefore, certain simplifications were applied to reduce the number of fitting parameters with a conservation of accuracy. First of all, all backscattering rare-earth elements were treated as lanthanum. This simplification is justified by almost identical backscattering amplitudes and phases for the used *Ln* calculated with FEFF8. As a second simplification the La-oxygen coordination sphere was not considered. The oxygen environment is composed of the contributions of many different oxygen neighbors with strongly varying La–O distances. In addition, the coordination numbers are very similar for both La-sites. La1 in the LaRuO$_4$-layer is surrounded by twelve oxygen atoms and La2 in the LaO-
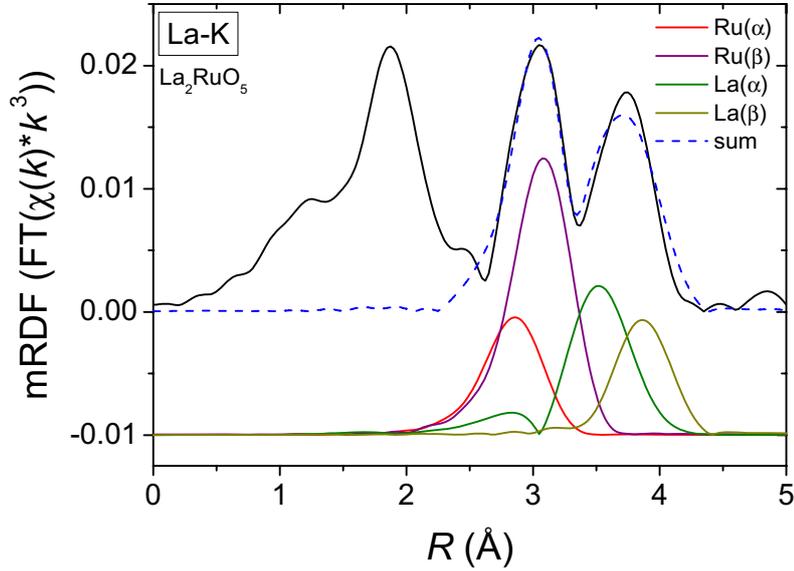
Figure 5.11.: Fit results for the La-K mRDF. Ru(α), Ru(β) and La(α), La(β) indicate scattering paths for the two different crystallographic La-sites (see text for details).

Table 5.3.: Averaged distances calculated from La$_2$RuO$_5$ single-crystal data. The values in brackets represent the variance of the coordination shells.

EXAFS path	Atoms	Average distance d(Å)
Ru(α)	La2–Ru	3.35(7)
Ru(β)	La1–Ru	3.52(5)
La(α)	La–La	3.87(15)
La(β)	La1–La1	4.22(2)

layers has ten oxygen neighbors. For both sites the distances vary in the range R(La–O) $\approx$ 2.35 Å to 2.98 Å with a quite regular length-distribution. Thus, a fit of the oxygen coordination sphere does not help to distinguish the two La-sites and was, therefore, not considered in the fits.

From the single-crystal structure results it was found that the La1-site in the perovskite like LaRuO$_4$-layers is surrounded by six Ru ions (3.4588 Å $\leq$ R $\leq$ 3.5703 Å). In contrast, the La2-site in the LaO-layer is well separated from the Ru ions. As a result, only two La–Ru distances with shorter lengths of R = 3.2690 Å and 3.4364 Å need to be considered for this site. In the following the Ru coordination sphere of La2 is denoted as Ru(α) due to the shorter distances and Ru(β) is used for the La1-site. Ru(α) thus consists of 2 Ru ions with an average distance of 3.35 Å, while Ru(β) contains 6 Ru ions at an average distance of 3.52 Å. The values of the average distances

derived from the single crystal analysis and the variance of the distribution range of distances, which reflects the "thickness" of the coordination shell, are listed in Tab. 5.3.

The La/*Ln* coordination of the La1- and La2-sites requires a more detailed discussion. La1 is surrounded by eight La/*Ln* atoms, which can be divided in six shorter distances with values between 3.80 Å and 4.02 Å and two clearly longer distances of ≈ 4.21 Å. In contrast, the La2-site has a tenfold La-coordination with distances between 3.59 Å and 4.02 Å. The coordination spheres are therefore rather similar for both La-sites. Although this backscattering shell is not very well suited for distinguishing La1 and La2, it had to be included in the fitting procedure due to the overlap of the Ru- and La/Ln-shells clearly visible in Fig. 5.10. To describe these coordination shells the nomenclature La(α) for the 16 shorter bonds and La(β) for the two longer bonds was chosen. The combined backscattering of both La-sites contributes in the fitting process of the La-K spectrum. This situation is expected to be different for the *Ln*-K spectra due to the preferred localization described below.

The distribution of the *Ln*$^{3+}$ ions was derived from the combined fitting of the Ru(α)/Ru(β) and the La(α)/La(β) coordination spheres. If the substituting rare-earth element *Ln* was occupying solely the La2-site, the following coordination numbers would result: Ru(α) 2, Ru(β) 0, La(α) 10, and La(β) 0. On the other hand, for a completely random distribution of *Ln* the expected coordination numbers are Ru(α) 2, Ru(β) 6, La(α) 16, and La(β) 2. These numbers are given as N$_{theo}$ (total) and N$_{theo}$ (La2-site) in the second and third line of Tabs. 5.4. Because of these different coordination numbers the intensity ratio of the Ru and La/*Ln* peak are expected to change compared to the La-K-edge spectrum if a (partial) cation ordering is present. In Fig. 5.10 the mRDF for the three recorded K-edges are shown in comparison. The peaks are indicating the coordination shells of oxygen at approximately 1.8 Å, Ru at ≈ 3.0 Å and La/*Ln* at ≈ 3.7 Å. For La-K the intensity of the Ru-related peak is larger than the one of the La/*Ln*-shell, while for Pr-K and Nd-K the Ru peak is explicitly smaller than the La/*Ln* peak. This is already a hint for a non-statistical site distribution.

For a quantitative analysis the fitting of the La-K spectra was carried out using the four shell model described above. In this model the scattering paths of Ru and La/*Ln* ions with similar distances are unified to a single backscattering shell with an averaged interatomic distance. This approach is commonly used to reduce large numbers of scattering amplitudes and phases. For example for the compound Ce$_{1-x}$La$_x$O$_{2-x/2}$ averaged coordination spheres of O and La/Ce were used to fit the EXAFS spectra in a similar procedure [Deg03].

The fit applying this four shell model for the unsubstituted La$_2$RuO$_5$ is depicted in Fig. 5.11. The calculated and measured mRDF match very well in the fitting region (2.5 Å to 4.2 Å). The contributions of the four shells are shown as colored solid lines (shifted for clarity) and the summation is depicted as dashed line.

In Tab. 5.4 the results of the fitting parameters for the La-K, Pr-K, and Nd-K spectra are listed. In the first step of the fitting procedure the amplitude reduction factor S$_0^2$ and the energy shift E$_0$ of the La-K spectra were refined while averaged values of the distance (R) taken from single-crystal data and the Debye-Waller factors (σ^2) were kept fixed. In addition, the theoretical values N$_{theo}$ (total) were used as coordination numbers. The same shift of the threshold energy E$_0$ was used

Table 5.4.: EXAFS refinement results for the K- and L$_{\text{III}}$-edge measurements [Rie12a].

Edge	S$_0^2$	E$_0$ (eV)		Ru(α)	Ru(β)	La(α)	La(β)
			N$_{\text{theo}}$ (total)	2	6	16	2
			N$_{\text{theo}}$ (La2 site)	2	0	10	0
La-K (La$_2$RuO$_5$)	0.56(1)	-7.28(5)	N	2	6.07(7)	16.29(20)	1.99(3)
		Res = 9.72 %	R (Å)	3.245(1)	3.480(1)	3.905(1)	4.234(1)
			σ^2($\times 10^{-3}$Å^2)	8.77(7)	8.90(5)	15.88(7)	5.21(6)
Pr-K (La$_{1.4}$Pr$_{0.6}$RuO$_5$)	0.34(1)	-8.68(11)	N	2	4.14(6)	13.34(16)	1.58(2)
		Res = 12.46 %	R (Å)	3.194(1)	3.439(1)	3.852(1)	4.232(1)
			σ^2($\times 10^{-3}$Å^2)	6.90(6)	9.20(4)	10.71(4)	3.13(4)
Nd-K (La$_{1.5}$Nd$_{0.5}$RuO$_5$)	0.25(1)	-9.76(21)	N	2	4.68(16)	19.89(38)	2.72(6)
		Res = 7.19 %	R (Å)	3.145(1)	3.378(2)	3.846(2)	4.227(2)
			σ^2($\times 10^{-3}$Å^2)	6.36(7)	12.67(6)	11.58(10)	3.85(10)
Sm-L$_{\text{III}}$ (La$_{1.70}$Sm$_{0.30}$RuO$_5$)	0.49(1)	6.17(1)	N	2	3.96(1)	14.18(2)	1.44(1)
		Res = 11.64 %	R (Å)	3.294(1)	3.394(1)	3.939(1)	4.225(1)
			σ^2($\times 10^{-3}$Å^2)	7.37(2)	10.82(2)	13.06(2)	5.43(2)
Gd-L$_{\text{III}}$ (La$_{1.75}$Gd$_{0.25}$RuO$_5$)	1.17(1)	5.97(3)	N	2	3.91(15)	19.67(17)	2.84(4)
		Res = 11.88 %	R (Å)	3.276(2)	3.392(2)	3.925(5)	4.141(11)
			σ^2($\times 10^{-3}$Å^2)	14.21(25)	13.98(25)	29.61(31)	8.39(34)
Dy-L$_{\text{III}}$ (La$_{1.85}$Dy$_{0.15}$RuO$_5$)	0.68(1)	5.59(1)	N	2	4.60(2)	11.65(2)	1.45(1)
		Res = 17.28 %	R (Å)	3.257(1)	3.373(1)	3.983(1)	4.304(1)
			σ^2($\times 10^{-3}$Å^2)	7.23(3)	7.48(3)	14.13(3)	4.10(3)

for all backscattering shells. In a next step R and σ^2 were refined with fixed E$_0$ and N. Finally, only the coordination numbers and S$_0^2$ were refined resulting in the values shown in Tab. 5.4. In all runs the coordination number N(Ru(α)) was fixed to 2 in order to enhance the stability of the refinement and because this value is the same for both a statistical and a completely ordered distribution of *Ln*.

The obtained residuals (denoted "Res" and defined according to [Ank98]) given in Tab. 5.4 indicate a good fit quality. The rather high values for Debye-Waller factors of Ru(β) (12.67$\times$10^{-3} Å^2 for Nd-K) and La(α) (15.88$\times$10^{-3} Å^2 for La-K) result from the large spreading of the interatomic distances unified to one backscattering shell in the fit. The σ^2 of the remaining two paths is significantly smaller (roughly 7$\times$10^{-3} Å^2 for Ru(α) and resp. 3$\times$10^{-3} Å^2 for La(β)), because only two quite similar distances were averaged here.

For the La-K edge of La$_2$RuO$_5$ the obtained coordination numbers agree well with the expected values and prove that the simplified model (Tab. 5.4) can in fact be used for data analysis. This is illustrated in Fig. 5.11, where the resulting sum matches the experimental mRDF very well. The obtained distances of the backscattering shells are in good agreement with the merged values listed in Tab. 5.3. Only the distance for Ru(α) was approximately 0.1 Å shorter than expected from the single-crystal analysis.

The same fitting procedure was used for the Pr-K and Nd-K spectra, leading to the values listed in Tab. 5.4. The obtained distances are distinctly smaller than the values calculated from the single-crystal data listed in Tab. 5.3. These shorter interatomic distances correspond well with the observed decrease of the unit-cell parameters upon rare-earth substitution (see Sec. 5.1.1.1). The obtained values are quite similar for La$_{1.4}$Pr$_{0.6}$RuO$_5$ and La$_{1.5}$Nd$_{0.5}$RuO$_5$ (in detail the distances are slightly smaller for the latter one), which agrees with the similar unit-cell parameters for both compounds.

Comparing the coordination numbers for the Pr-K and Nd-K edge spectra, it can be seen that the obtained number of backscattering atoms in the Ru(β) shell is clearly smaller than expected for a random distribution of Nd or Pr on the two La-sites. For the La(α) and La(β) shells the differences of the coordination numbers are less reliable mostly due to the quality of the absorption spectra, which became rather noisy at high *k*-values because of the high absorption of lanthanum. In fact, coordination numbers even larger than expected for a statistical distribution were in some cases observed (see Tab. 5.4). These may of course be avoided by appropriate constrains, which were not applied to avoid biases in the results. N(Ru(β)) was found to be the most reliable measure for the distribution of the substituting rare-earth elements and values of 4.14 for Pr and 4.68 for Nd correspond to 65% and 61% of the substituting lanthanide on the La2-site. This is in very good accordance with the 65 - 70% for Pr derived from neutron diffraction.

The EXAFS spectra of the *Ln*-K-edge of Sm, Gd and Dy did not exhibit evaluable oscillations, therefore, we used the L$_{III}$-edges of these elements. The Sm-L$_{III}$ absorption edge has a sufficiently higher energy than the La-L$_I$ edge (Tab. 2.1). Gd and Dy possess even higher L$_{III}$-edge energies, thus, an overlapping with the La-L$_I$-edge is not required to be considered.

The spectra were recorded and evaluated similar to the the procedure described above for *Ln*-K-edges. The mRDFs of the *Ln*-L$_{III}$-edge spectra are depicted in Fig. 5.12. It is noteworthy that
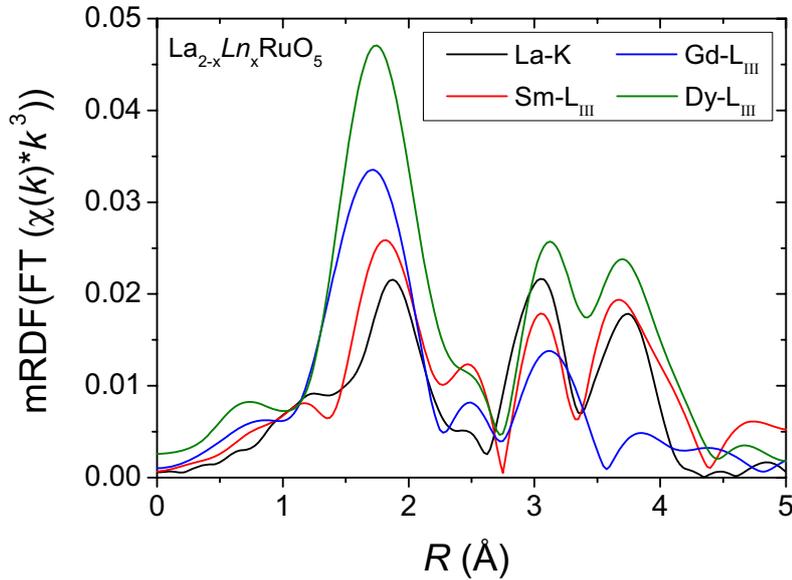
Figure 5.12.: Fourier transforms (mRDF) of $\chi(k) \cdot k^3$ at the *Ln*-L$_{III}$-absorption edges of La$_{2-x}$*Ln*$_x$RuO$_5$. The corresponding mRDF from the La-K EXAFS is shown for comparison.

the signal-to-noise ratio at the L$_{III}$-edges of Sm, Gd, and Dy was by far worse that for the K-edge spectra of Pr and Nd (see Fig. 1 in [Rie12a]). Due to the smaller maximum substitution levels for the late lanthanides (e.g. $x_{max} = 0.2$ for Dy in comparison to $x_{max} = 0.75$ for Pr) rather small $\Delta\mu$ values were observed at the L$_{III}$-edges. Because of the high absorption of the compounds, the thickness of the samples had to be small. For these reasons, only edge jumps of $\Delta\mu \leq 0.1$ could be achieved. As a consequence the useful k range was limited to roughly 7 Å^{-1} (Gd) or 10 Å^{-1} (Sm, Dy). Among the mRDF of the rare-earth substituted compounds the curve for Gd shows the smallest peak for the La/*Ln* coordination shells due to the comparable low quality of the measured spectra and the smallest k-range, which was evaluable. Additionally, the small k-region results in an overall broadening of the peaks in the L$_{III}$-edge mRDFs [Kon88].

Calculation of the scattering amplitudes and phases at the L$_{III}$-edges was again performed with FEFF8. Similar scattering paths were combined and the same four coordination spheres introduced for the K-edge were used for the fit. A similar approach was previously described e.g. for investigations of the L$_{III}$-edge of *Ln*$_2$O$_3$ [Ali97, Mal94].

For the edge-energy correction E$_0$, the intense white lines at the L$_{III}$-edges cause an increased shift. The fit of the data was done according to the above described procedure for the K-edges. First the distances R and the energy shifts were refined and in a second step the weighting of scattering paths was refined leaving R and N(Ru(α)) = 2 fixed.

The fit values are listed in the lower part of Tab. 5.4 for La$_{1.70}$Sm$_{0.30}$RuO$_5$, La$_{1.75}$Gd$_{0.25}$RuO$_5$,

and La$_{1.85}$Dy$_{0.15}$RuO$_5$. As was expected for the overall smaller *k*-range, the Debye-Waller factors of all four backscattering shells are slighty increased compared to the K-edge.

The obtained coordination shell distances agree well with the merged values in Tab. 5.3. For Ru(α) the accordance is excellent with approximately 3.3 Å, for Ru(β) the distances of roughly 3.4 Å are slightly shorter than the expected 3.52 Å, while the La backscattering shells show an increased distance compared to the merged values. With increasing distance the deviation between the expected and observed values increases. Taking into account the above described quality of the data such deviations are not surprising.

The obtained coordination numbers show a decrease for N(Ru(β)), which is very similar to the one for the Pr and Nd substituted samples. The preferred occupation of *Ln* on the La2-site in the LaO-layers is therefore clearly supported by the EXAFS results. The reduction from N = 6 to 3.96 for Sm, 3.91 for Gd and 4.60 for Dy corresponds to roughly 68%, 69%, and, respectively, 57% of the *Ln*-ions occupying the La2-site. Again, these findings are in very good agreement with the neutron diffraction result for the Pr-substituted compounds (65 - 70% of the Pr ions in the LaO-layer). Only for Dy no clear site preference was found in the EXAFS analysis.

5.1.2. Magnetic Properties

5.1.2.1. Paramagnetic ht-phase

In combination with the structural changes discussed in Sec. 5.1.1.1 La$_{2-x}$Ln$_x$RuO$_5$ exhibits an anomaly at approximately 161 K in the magnetic susceptibility. This observation was explained by a dimerization of neighboring Ru^{4+} $S = 1$ spin moments in the *ab*-plane leading to a spin-singlet state. This spin pairing is linked to the structural phase transition. As mentioned in the introduction of this chapter the investigation of the magnetic properties was performed to examine whether the rare-earth substitution affects or even completely suppresses this magnetic transition, while preserving the structural changes as shown in Sec. 5.1.1.

In the top frame of Fig. 5.13 the temperature dependent magnetic susceptibilities $\chi(T)$ of La$_2$RuO$_5$ and La$_{1.9}$Ln$_{0.1}$RuO$_5$ ($H = 1000$ Oe) are depicted. The results for La$_{1.9}$Ln$_{0.1}$RuO$_5$ are dominated by the additional magnetic moments of the rare-earth metal ions. All curves possess a clear step at the transition temperature with a reduced susceptibility. This reduction is of similar magnitude for all samples. In the bottom frame the inverse magnetic susceptibility $1/\chi(T)$ shows the influence of the magnetic lanthanide ions more clearly. The higher the value of $1/\chi$ below T_d, the smaller is the additional magnetic moment of the rare-earth metal ion. The order of reduction is "no substitution" > Sm > Pr $\geq$ Nd > Gd > Dy, which reflects the values listed in Tab. 5.5.

For a quantitative analysis a fit of the inverse susceptibility in the temperature range 200 K to 300 K with a Curie-Weiss law was performed (see Eq. 2.32). χ_0 was found to be in the range of 10^{-4} emu/mol for all samples and is therefore not explicitly discussed here. The values for n_{eff} derived from *C* are shown in Fig. 5.14 for each lanthanide ion. The solid lines represent the calculated $n_{\text{eff,total}}$ according to a summation of the Ru^{4+} and the *Ln*$^{3+}$ magnetic moments

$$n_{\text{eff,total}} = \sqrt{n_{\text{eff}}^2(\text{Ru}) + x \times n_{\text{eff}}^2(Ln)} \,, \tag{5.1}$$
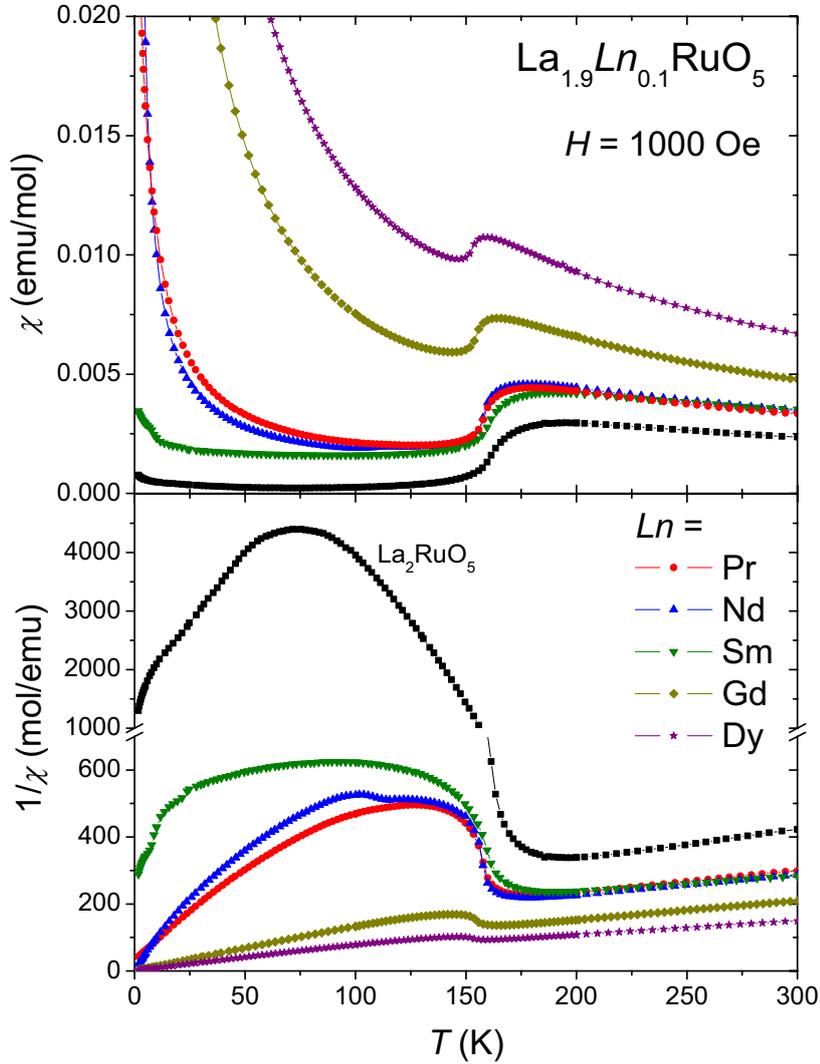
Figure 5.13.: Top frame: Temperature dependent magnetic susceptibility of La$_2$RuO$_5$ and La$_{1.9}Ln_{0.1}$RuO$_5$ at $H = 1000$ Oe. Bottom frame: Corresponding inverse magnetic susceptibility $1/\chi$.

where x represents the substitution level. With this model an excellent agreement is achieved as can be seen from Fig. 5.14. Only the unsubstituted sample La$_2$RuO$_5$ shows a slightly increased moment of $2.91\mu_B$ compared to the theoretical $2.83\mu_B$ for Ru^{4+} obtained from the spin-only approximation (see Sec. 4.2.2). For the calculation of the additional magnetic moments of the rare-earth metal ions the free-ion approximation is a well-suited description [Lue99].

In Fig. 5.15 the Curie-Weiss temperatures Θ_{CW} derived from the same fits are shown. The negative signs indicate an antiferromagnetic interaction in the paramagnetic ht-phase. The strength of this interaction is represented by the absolute value of Θ_{CW}. The value of the Curie-Weiss temper-

Table 5.5.: Electron configuration, ground state term symbol and effective magnetic moments of Ln^{3+} from the free-ion approximation.

Ln^{3+}	$4f^N$	$^{2S+1}L_J$	n_{eff} (μ/μ_B)
Pr^{3+}	$4f^2$	$^3H_4$	3.578
Nd^{3+}	$4f^3$	$^4I_{9/2}$	3.618
Sm^{3+}	$4f^5$	$^6H_{5/2}$	0.845
Gd^{3+}	$4f^7$	$^8S_{7/2}$	7.937
Dy^{3+}	$4f^9$	$^6H_{15/2}$	10.646
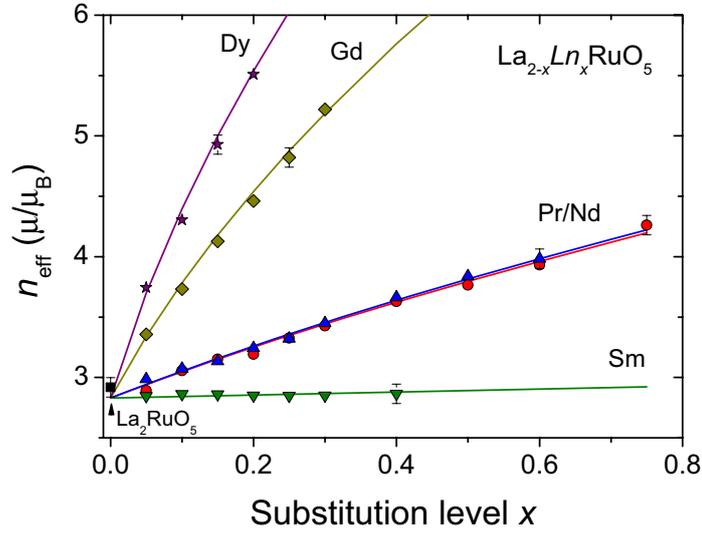
Figure 5.14.: Effective magnetic moments in Bohr magnetons of $La_{2-x}Ln_xRuO_5$ from Curie-Weiss fits of $1/\chi$ in the temperature range 200 - 300 K. The solid lines represent the summation according to Eq. 5.1 of the Ru^{4+} and Ln^{3+} spin moments calculated from the spin-only and free-ion approximation, respectively.

ature is reduced from -177 K for La_2RuO_5 by the incorporation of the lanthanide ions. Clearly the changes in the Curie-Weiss temperatures depend on the magnetic moment of the substituting rare-earth element. Dy^{3+} with the highest moment leads to the strongest change in Θ_{CW} with values ranging from roughly -85 K at $x = 0.05$ to -40 K at $x = 0.2$. The Gd-substituted samples, in which Gd^{3+} possesses a comparable magnetic moment, exhibit a very similar behavior. Pr^{3+} and Nd^{3+} reveal almost identical magnetic moments and also the Curie-Weiss temperatures of the Pr- and Nd-substituted compounds are very similar for all substitution values x. Starting from -110 K for $x = 0.05$ Θ_{CW} declines slowly to around -80 K for $x = 0.75$. A very interesting ex-
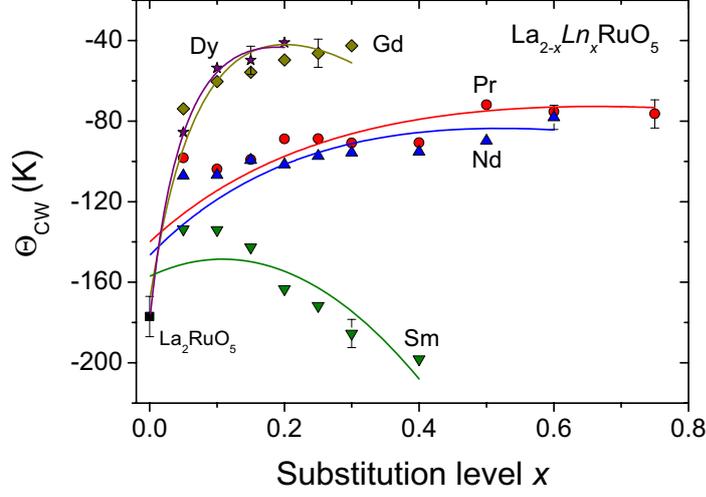
Figure 5.15.: Curie-Weiss temperatures Θ_{CW} from the fit of $1/\chi$ in the temperature range 200 - 300 K. The solid lines represent Θ_{CW} values calculated with equation 5.2.

ception are the Sm-containing compounds, which reveal a different behavior, with Θ_{CW} increasing from -130 K to about -200 K for La$_{1.6}$Sm$_{0.4}$RuO$_5$.

Theoretical Θ_{CW} values can be calculated using a model assuming an antiferromagnetically interacting system consisting of two different magnetic sublattices of atoms *A* (Ru^{4+}) and *B* (*Ln^{3+}*) according to [Goo63]:

$$\Theta_{CW} = \frac{2\lambda_{AB}C_AC_B - \lambda_{AA}C_A^2 - \lambda_{BB}C_B^2}{C_A + C_B} \quad . \tag{5.2}$$

In this equation C_A and C_B are the Curie constants of Ru^{4+} and *Ln^{3+}*, respectively. λ_{AA} and λ_{BB} represent the fitting parameters of the two sublattices and λ_{AB} the effective coupling between the two systems. The interaction strengths *W* according to Ref. [Goo63] in and between the lattices could be calculated from the fitting parameters, starting with $\lambda_{AB} = -W_{AB}$. For the two different lattices the internal coupling values are calculated according to $W_{AA} = W_{AB} \times \lambda_{AA}$ and $W_{BB} = W_{AB} \times \lambda_{BB}$, respectively.

The Curie constants C_A and C_B were obtained from the theoretical effective magnetic moments of *Ln^{3+}* and Ru^{4+} ions (Eq. 5.1). λ_{AB}, λ_{AA}, and λ_{BB} were obtained from a least-square fitting. As a starting point for λ_{AA} (i.e. the interaction of the Ru-moments) the value for undoped La$_2$RuO$_5$ was used, which can derived from $\Theta_{CW} = -\lambda_{AA} \times C_A$. The calculated data for the Curie-Weiss temperatures according to Eq. 5.2 are drawn as solid lines in Fig. 5.15 using the same colors as for the measured values (shown as symbols). In general, a satisfying agreement between the experimental Θ_{CW} values and the calculated ones is observed. All coupling strengths *W* possess a negative sign indicating an antiferromagnetic interaction and for the Pr-, Nd-, Gd-, and Dy-
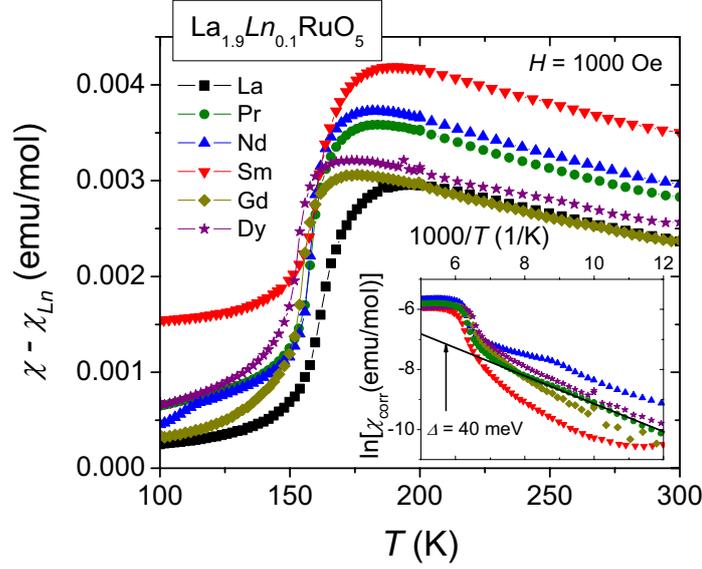
Figure 5.16.: Temperature dependence of the magnetic susceptibility of La_2RuO_5 and $La_{1.9}Ln_{0.1}RuO_5$ after subtraction of the corresponding trivalent rare-earth metal ion susceptibility χ_{Ln}. The inset shows Arrhenius-plots of the additionally χ_0-corrected susceptibilities χ_{corr}. The solid black line corresponds to a 40 meV spin-gap.

substituted compounds an ascending order of absolute values $W_{AB} << W_{BB} < W_{AA}$ was found. In contrast, for the Sm containing samples the Sm–Sm interactions are strongly dominating ($W_{AB} << W_{AA} << W_{BB}$) which leads to the decrease of Θ_{CW} values and the appearance of a maximum at very low substitution levels. In summary, the weakest interaction for all compounds was found between the two sublattices and the strongest coupling was obtained within the Ru^{4+} sublattice (except for Sm) in accordance with the observed Ru-spin dimerization below approximately 161 K. Crystal-field effects (especially for Pr and Nd [Pen32]) and the different nature of the interaction between the two crystallographic Ln-sites and the Ru^{4+} sublattice should be included for a more detailed explanation of the Θ_{CW} behavior. The crystal-field effects are reflected by the values of λ_{AA}, which are deviating at $x = 0$ for the Pr-, Nd-, and Sm-substituted compounds, strongest observed for Pr followed by Nd and weakest for Sm.

The quality of the fit may be improved by a more complicated model which accounts for the two Ln^{3+}–Ru^{4+} exchange-interaction terms for each site which have to be weighted since their occupancies are different as shown in the previous section 5.1.1.3. In the case of Sm-substituted samples the obtained results should be treated with caution since the magnetic moment of Sm^{3+} is small (see Tab. 5.5) and n_{eff} is temperature dependent as a result from the energetically close $4f$ multiplet levels [Lue99].

From the above discussed results it can be concluded that the influence of the lanthanide ions, which are preferably occupying the LaO intermediate layer, on the Ru–Ru dimerization is very

small. The reduction of the Curie-Weiss temperature with higher substitution level and different Ln^{3+} moments as well as the observed interaction strengths are confirming the assumption of an only weak interaction between the two sublattices. A similar situation was recently found for $Ln_{2/3}$Cu$_3$Ti$_4$O$_{12}$ [Dit11] which also can be considered as consisting of two nearly independent magnetic systems.

5.1.2.2. Magnetic Properties of the Low-Temperature Phase

To investigate the magnetic behavior of La$_{2-x}Ln_x$RuO$_5$ in the lt-phase, the experimental susceptibilities were evaluated with respect to the rare-earth contribution by subtracting the susceptibility of unsubstituted La$_2$RuO$_5$. The residuals were fit with the sum of a Curie-Weiss law and a constant contribution as described above in the temperature interval 10 K $\leq T \leq 300$ K. Very small χ_0 values in the order of 10^{-4} emu/mol were obtained which are in the range of the observed temperature independent shifts visible in Figs. 5.16 and 5.17. The χ_0 values will be discussed in more detail below. Applying the free-ion approximation, the expected values for the lanthanide moments are $n_{\text{eff,theo}} = \sqrt{x} \cdot n_{\text{eff}}(Ln)$. In Tab. 5.6 the experimentally obtained ($n_{\text{eff,fit}}$) and expected ($n_{\text{eff,theo}}$) values are listed for the compounds with substitution level $x = 0.1$ and for selected Pr substituted compounds ($x = 0.25, 0.5, 0.75$). The results for $n_{\text{eff,fit}}$ are in reasonable agreement with the expected values. On the one hand, this reflects the correct stoichiometry of rare-earth ions in the compounds and, on the other hand, it also proves that the summation of the lanthanide and the Ru magnetic moment is a reasonable approximation to describe the magnetic behavior of the samples, both below and above the magnetic transition. Only at temperatures below roughly 30 K this model cannot be applied, because crystal-field effects and interactions between the $4f$ electrons of the rare-earth metal ions become important. This effect correlates with the specific-heat data described in Sec. 5.1.3. The Curie-Weiss temperatures $\Theta_{CW,Ln}$ are close to zero for most of the samples, indicating a negligible magnetic interaction of the lanthanide ions. In the Pr-doped compounds slightly negative $\Theta_{CW,Ln}$ values are caused by the crystal-field splitting of the Pr ground state [Pen32].

In Figs. 5.16 and 5.17 modified susceptibilities for La$_{1.9}Ln_{0.1}$RuO$_5$ and La$_{2-x}$Pr$_x$RuO$_5$ are depicted. To derive these curves, the contribution of the rare-earth metal ions was calculated using n_{eff} and $\Theta_{CW,Ln}$ from Tab. 5.6 and subtracted from the experimental data. The results are denoted in the following as $\chi - \chi_{Ln}$ and $\chi - \chi_{\text{Pr}}$, respectively. The susceptibility of pure La$_2$RuO$_5$ is shown in both figures for comparison. The remaining susceptibilities for La$_{2-x}Ln_x$RuO$_5$ are very similar to the one of the unsubstituted material. Especially the strongly reduced low-temperature susceptibility and the transition step between 150 K and 170 K are clearly visible for all compounds. Also the shift of the transition temperatures depending on the rare-earth element and the substitution level x is evident. The values of $\chi - \chi_{Ln}$ above the magnetic transition change in the order Sm > Nd, Pr > Dy, Gd $\geq$ La$_2$RuO$_5$. This temperature independent shifts can partly be explained by the van-Vleck paramagnetism χ_0 of the rare-earth metal ions, which is here unexpectedly strong for Sm, intermediate for Nd and Pr, and negligible for Gd and Dy according to the crystal-field multiplet-level splitting [Lue99].
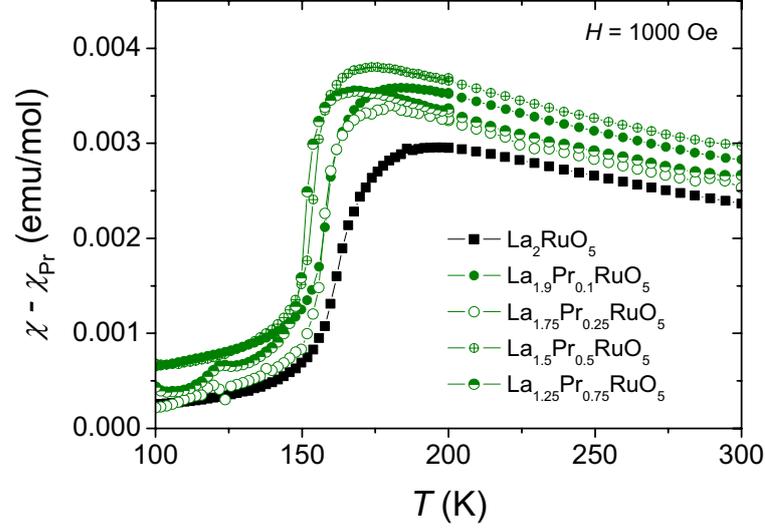
Figure 5.17.: Temperature dependence of the magnetic susceptibility of La$_2$RuO$_5$ and La$_{2-x}$Pr$_x$RuO$_5$ after subtraction of the Pr^{3+} susceptibility χ_{Pr}.

Table 5.6.: Effective magnetic moments n_{eff} and Curie-Weiss temperatures $\Theta_{CW,Ln}$ of the Ln^{3+} ions in selected La$_{2-x}$Ln$_x$RuO$_5$ compounds. See text for details.

Compound	$\Theta_{CW,Ln}$ (K)	$n_{\text{eff,fit}}$ (μ/μ_B)	$n_{\text{eff,theo}}$ (μ/μ_B)
La$_{1.9}$Sm$_{0.1}$RuO$_5$	-3.61(5)	0.27(2)	0.26
La$_{1.9}$Nd$_{0.1}$RuO$_5$	0.19(5)	0.81(2)	1.14
La$_{1.9}$Gd$_{0.1}$RuO$_5$	-0.08(5)	2.44(2)	2.50
La$_{1.9}$Dy$_{0.1}$RuO$_5$	-0.24(5)	3.05(2)	3.36
La$_{1.9}$Pr$_{0.1}$RuO$_5$	-3.74(5)	1.03(2)	1.13
La$_{1.75}$Pr$_{0.25}$RuO$_5$	-6.71(5)	1.60(2)	1.78
La$_{1.5}$Pr$_{0.5}$RuO$_5$	-7.10(6)	2.34(2)	2.53
La$_{1.25}$Pr$_{0.75}$RuO$_5$	-16.63(8)	3.03(2)	3.09

According to Sec. 4.2.2 the derivatives of the susceptibilities yield a peak, which can be fit using a Lorentzian profile. For this χ_{corr} without the lanthanide moment was taken, since these data undisturbtly show the dimerization transition. The temperatures of the peak centers are in good agreement with T_d reported in Sec. 4.2.2, but are shifted to lower temperatures by approximately 4 K. This is to be expected since in Sec. 5.1.2.3 the onset temperatures were used. The FWHM of the peaks vary between 6 K and 10 K and the peak areas remain almost constant for all samples reflecting the identical spin-dimerization occurring in the samples.
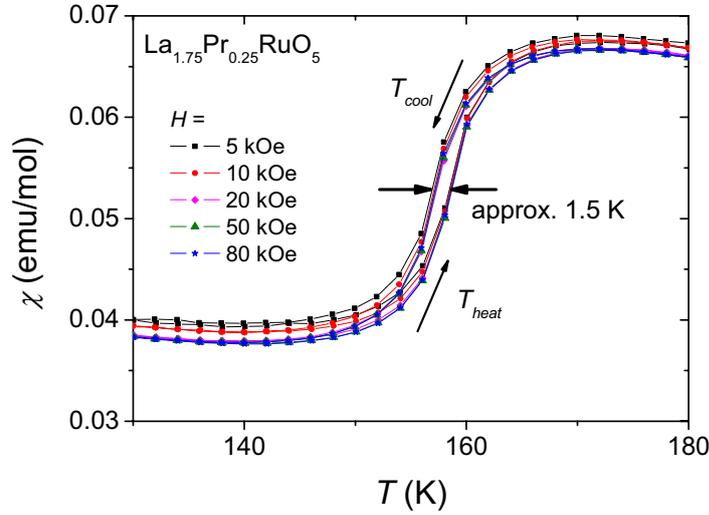
Figure 5.18.: Temperature dependent magnetic susceptibility of La$_{1.75}$Pr$_{0.25}$RuO$_5$ for different external magnetic fields. Cooling and heating cycles are marked by arrows.

To investigate the size of the spin-gaps, χ_0 was additionally subtracted from the susceptibilities and the residuals are denoted as χ_{corr}. In the inset of Fig. 5.16 the logarithm $\ln[\chi_{corr}]$ is depicted as a function of the inverse temperature in an Arrhenius-plot providing spin-gaps of 40 ± 10 meV for the samples with $x = 0.1$. This constant value is also found for the Pr substitution series and therefore it can be concluded that a constant spin-gap of roughly 40 meV is characteristic for all polycrystalline La$_2$RuO$_5$ samples. This indicates that the the rare-earth substitution has only a negligible influence on the spin-gap in accordance with the weak influence of the lanthanides on the physical properties and crystal structure. Furthermore, the almost constant spin-gaps are behaving similar to the related J_0 values obtained from the peak in the specific heat (Sec. 5.1.3).

As reported in Sec. 4.2.2 the change in the susceptibility takes place in a very narrow temperature interval for single crystals of La$_2$RuO$_5$ and exhibits a thermal hysteresis of roughly 4 K. For polycrystalline samples, on the other hand, the transition is broadened to a range of roughly 30 K without a visible hysteresis. This large temperature interval can be explained by minor inhomogeneities in the polycrystalline material. Since no broadening of the x-ray or neutron-diffraction peaks was observed, the proposed inhomogeneities must be limited to a very local scale. This interpretation is supported by the fact that a La$_2$RuO$_5$ sample synthesized by solid-state reaction with 24 hours calcination [Ebb05] showed a broader transition compared to the sample prepared by the soft-chemistry route. It can be seen in Figs. 5.16 and 5.17 that the lanthanide substitution does not additionally change the width of the transition step, which is in agreement with the above described independency of the magnetic sublattices and the identical sample morphology expected for the sol-gel prepared samples.

The occurrence of a possible transition hysteresis in the La$_{2-x}$Ln$_x$RuO$_5$ samples was studied, and as an example, Fig. 5.18 shows temperature cycles of the susceptibility of La$_{1.75}$Pr$_{0.25}$RuO$_5$ for various magnetic fields between $H = 5$ kOe and 80 kOe. The difference between the heating and cooling curves amounts to roughly 1.5 K, which is comparable to the difference obtained by DSC measurements (see Sec. 5.1.2.3). For the other compounds similar values were obtained, in most cases the temperature deviation was well below 1 K. Although in La$_2$RuO$_5$ single crystals the hysteresis of 4 K suggests a first-order character, the broadening of the transition due to inhomogeneities in the polycrystalline samples induces a more second-order like behavior.

5.1.2.3. Effect of *Ln*-Substitution on the Phase-Transition Characteristics

The influence of the substitution on the phase transition was investigated by temperature dependent magnetic susceptibility and DSC measurements [Rie11].

For the determination of the transition temperature from the susceptibility data the paramagnetic contribution of the ht-phase was calculated using the above obtained parameters for C, Θ_{CW} and χ_0 and subtracted from the $1/\chi$ data. The obtained results are shown in Fig. 5.19a for selected Pr-substituted compounds. The dimerization temperature (T_d) was taken from the onset, i.e. the intersection point of the tangent of the $1/\chi$ curve with the temperature axis. A remarkable temperature change can be observed in Fig. 5.19a. The onsets of the curves are shifted towards lower temperatures with increasing rare-earth substitution level. Numerical values are shown in Fig. 5.20a and discussed below.

Transition-temperature data were also derived from DSC-measurements by heating the samples controlled from 100 K to room temperature. In Fig. 5.19b a typical DSC-measurement is depicted. The small sharp peaks below the transition temperature are instrumental artifacts. In analogy to the magnetic measurements the onset temperature for the transition was determined as shown in Fig. 5.19b. As a second characteristic the temperature of the DSC peak was used. The transition leads to an endothermic signal caused by the breaking up of the Ru–Ru dimers during heating.

In Fig. 5.20a the transition temperatures derived from the susceptibility data and the DSC measurements are shown for the Pr- (left) and the Nd- (right) substituted compounds. The results from the different methods agree very well with deviations of only a few K. The agreement is slightly better for Nd than for Pr. As a general behavior a linear shift of the dimerization temperatures to lower values with increasing substitution level x was observed.

For the Sm-, Gd-, and Dy-substituted samples T_d values could not be obtained from DSC data because they range below the available temperature regime of the instrument. Thus, only the magnetization results are shown in Fig. 5.20b for all compounds investigated. Comparing the temperature changes from Fig. 5.20b with the structural data of the unit-cell axis lengths a depicted in Fig. 5.2, a remarkably similar behavior is found. Obviously the decrease of T_d is directly correlated to the structural compression, which confirms the strong linkage between the structural and magnetic phase transitions. On the other hand, no significant influence of the magnetic moments of the substituting lanthanides on the temperature change of T_d was detected. This again proves the weakly coupled magnetic moments of Ru^{4+} and the Ln^{3+} ions.
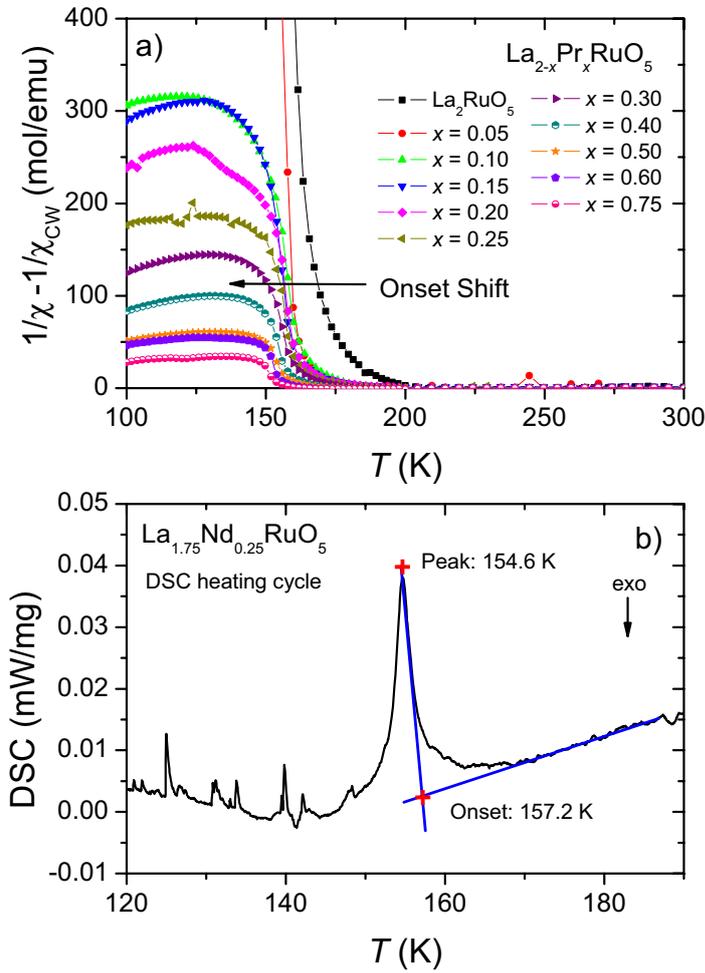
Figure 5.19.: a) Inverse magnetic susceptibility of the Pr-substituted samples calculated after subtraction of the high-temperature paramagnetic susceptibility deduced from Curie-Weiss fits (χ_{CW}). See text for details. b) DSC curve from the heating of La$_{1.75}$Nd$_{0.25}$RuO$_5$. The onset temperature was taken from the intersection of the two blue tangents.

The dimerization temperatures shown in Fig. 5.20 can be compared with the values of $|\Theta_{CW}|$ from the Curie-Weiss fit of the inverse susceptibility. In La$_2$RuO$_5$ and the Sm-substituted compounds T_d and $|\Theta_{CW}|$ are comparable (around 170 K). The Pr- and Nd-substituted compounds show $|\Theta_{CW}|$ values which are roughly half of T_d. For Gd and Dy the ratio $f = |\Theta_{CW}|/T_d$ is even less than one third. This indicates the absence of untypical magnetic frustration e.g. due to geometric reasons, because frustration is generally indicated by a considerably higher ratio of at least ten [Ram94]. On the other hand, (geometric) magnetic frustration is not be expected considering the almost square-planar arrangement of the Ru ions in the LaRuO$_4$-layers.
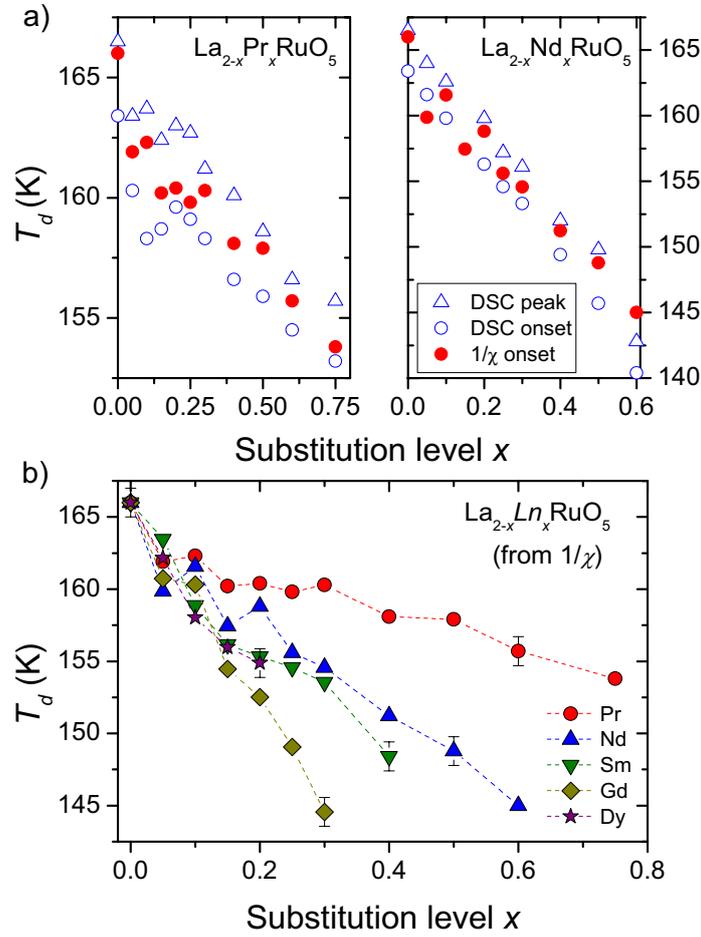
Figure 5.20.: a) Comparison of the transition temperatures obtained by DSC and magnetic measurements for the Pr- and Nd-substitution series. b) Dimerization temperatures T_d obtained from magnetic suceptibility data for La$_{2-x}$Ln$_x$RuO$_5$.

From the above given results it can be summarized that the phase transition is not considerably influenced by the magnetic moments of the lanthanides. In contrast, the evolution of the transition temperature is obviously directly correlated to the structural changes caused by the smaller radii of the rare-earth metal ions. It has to be noted that the effect of the substitution turned out to be opposite to what originally was expected. The incorporation of the smaller *Ln*-ions leads to a reduction of the cell parameters. Therefore, the distance between the paramagnetic Ru^{4+} centers in the *a*-direction becomes shorter, while the intralayer distances in the LaRuO$_4$-layers remain merely constant. One would expect that this shorter distance results in a stronger interaction and, in turn, to an increase of the magnitude of T_d. In contrast, T_d and also $|\Theta_{CW}|$ decrease, revealing a weaker antiferromagnetic exchange interaction. This reduced antiferromagnetic cou-

pling may partly be caused by the increasing deformation of the RuO$_6$ octahedra with increasing *x*. Probably more important are the observed changes in the Ru–O–Ru angles with respect to the Goodenough-Kanamori-Anderson rules (see Sec. 4.2.2). As discussed in detail in Sec. 5.1.1 we found a small decrease of the Ru–O–Ru angles along *c* as a result of the introduction of the smaller lanthanide ions. This smaller bond angle is expected to result in a weakening of the antiferromagentic coupling parallel to this crystallographic direction. However, the observed reduction of the tilting angle is maybe too small to explain the lower transition temperatures only by the superexchange mechanism. Another possible explanation comes from the unit-cell volume-contraction with increasing *x* itself. The contraction causes an enhanced overlap of orbitals which results in a broadening of the electron bands near the Fermi-level. This broadening is leading to a less localized nature of the electrons [Hof87]. This effect causes a weakening of the antiferromagnetic exchange within the dimers and, hence, a decrease of T_d.

5.1.3. Specific Heat

Similar to the undoped La$_2$RuO$_5$, the specific heat was measured for the rare-earth substituted samples with the highest achievable substitution level of each rare-earth element. The experimental data of C_p/T are depicted in Fig. 5.21, shifted in equidistant steps for clarity. All samples provide very similar heat capacities and reach a value of $C_p \approx 180$ J mol^{-1} K^{-1} at 300 K. Thus, the expected Dulong-Petit limit $C_p = 3z \cdot$ R ≈ 199.54 J mol^{-1} K^{-1} (*z* is the number of atoms per f.u. and R is the gas constant) is not yet reached at room temperature. A peak between 130 K and 170 K was observed for all samples mirroring the magneto-structural phase transition. The peaks show an increasing asymmetric broadening with increasing atomic number of the lanthanide.

The fit of the lattice contribution was carried out according to the description in Sec. 4.2.3 using the same weighting scheme. The resulting Debye- and Einstein-temperatures are listed in Tab. 5.7. The individual temperatures are increasing from La$_2$RuO$_5$ to La$_{1.8}$Dy$_{0.2}$RuO$_5$ following the atomic number and in turn the weight of the rare-earth element. This behavior possibly reflects the increasing rigidity of the crystal lattice according to the smaller unit-cell volumes, which were observed for increasing substitution level and decreasing size of the lanthanide ion.

For the rare-earth metals the influence of the crystal-field excitations is increasing the heat capacity below roughly 15 K as shown in Fig. 5.22 using a representation C_p/T^3 vs. *T* according to a Debye T^3 model. A logarithmic scale for the ordinate axis was chosen to increase clarity in the low-temperature range. The rise observed for the rare-earth substituted samples can be described as Schottky-type anomaly caused by crystal-field splitting of the 4*f* levels [Sin08, Lay09]. The crystal-field Schottky anomaly is proportional to T^{-2} (for $T \gg \Delta_{CF}$) in C_p [Tar03]. Correspondingly, this behavior is proportional to T^{-5} in C_p/T^3, which is marked by the solid line in Fig. 5.22. The expected T^{-5} behavior is observed for the Nd-, Sm-, and Gd-substituted samples, which could even be improved by subtraction of the La$_2$RuO$_5$ experimental data. For La$_{1.25}$Pr$_{0.75}$RuO$_5$ the data below 4 K seem to be unreliable and for La$_{1.8}$Dy$_{0.2}$RuO$_5$ the crystal-field excitations appear to be weaker in this temperature range. Measurements in different magnetic fields yield behaviors consistent with Schottky-type anomalies. The appearance of an uprise for La$_{1.7}$Gd$_{0.3}$RuO$_5$
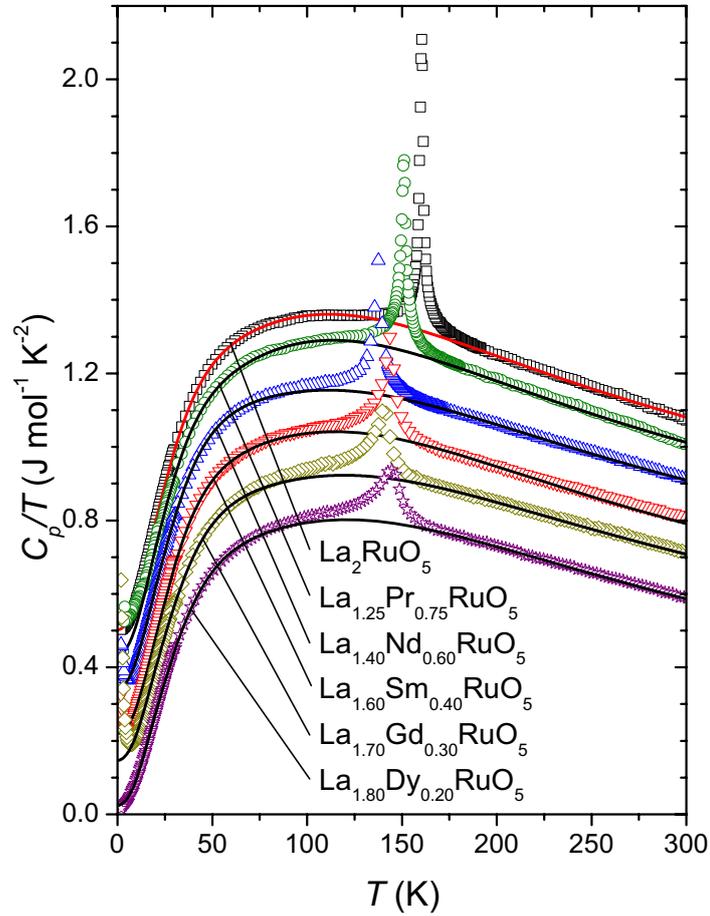
Figure 5.21.: Temperature dependence of the specific heat in the representation C_p/T vs. T for La$_2$RuO$_5$ and La$_{2-x}$*Ln*$_x$RuO$_5$ with the highest available substitution level for each rare-earth element (symbols). For clarity the curves were shifted by a constant value. The solid lines mark the Einstein-Debye fits. For more details see text.

was rather surprising with respect to its intensity, but is in agreement with similar findings for e.g. Gd$_{1-x}$Sr$_x$TiO$_3$ [Hei01]. As expected, for the pure La$_2$RuO$_5$ no significant increase of C_p is observed.

Using a single Debye T^3 term for the low-temperature region, a first estimate of the Debye temperature of La$_2$RuO$_5$ was obtained. As can be seen from Fig. 5.22 this simplified model is not sufficient to describe the specific heat due to the temperature dependent behavior of C_p/T^3. For the more sophisticated fit of C_p/T an additional term c_0 was required to improve the fit quality. In metals c_0 is known as Sommerfeld-coefficient representing the contribution of the conduction electrons, which is proportional to the density of states at the Fermi energy. For semiconducting

Table 5.7.: Results of the heat-capacity fits of La$_{2-x}$Ln$_x$RuO$_5$ (see text for details). The magnetic entropy S_{mag} was calculated by the integration of C_p/T after the subtraction of the lattice contribution.

Sample	Θ_D (K)	Θ_{E1} (K)	Θ_{E2} (K)	Θ_{E3} (K)	Θ_{E4} (K)	S_{mag} $\left(\frac{J}{mol\,K}\right)$
La$_2$RuO$_5$	132	175	217	325	520	4.2(3)
La$_{1.25}$Pr$_{0.75}$RuO$_5$	132	175	222	335	515	3.9(3)
La$_{1.4}$Nd$_{0.6}$RuO$_5$	135	182	219	330	564	4.0(3)
La$_{1.6}$Sm$_{0.4}$RuO$_5$	139	177	223	341	547	3.8(3)
La$_{1.7}$Gd$_{0.3}$RuO$_5$	140	192	231	358	583	4.0(3)
La$_{1.8}$Dy$_{0.2}$RuO$_5$	140	192	238	354	580	3.6(3)
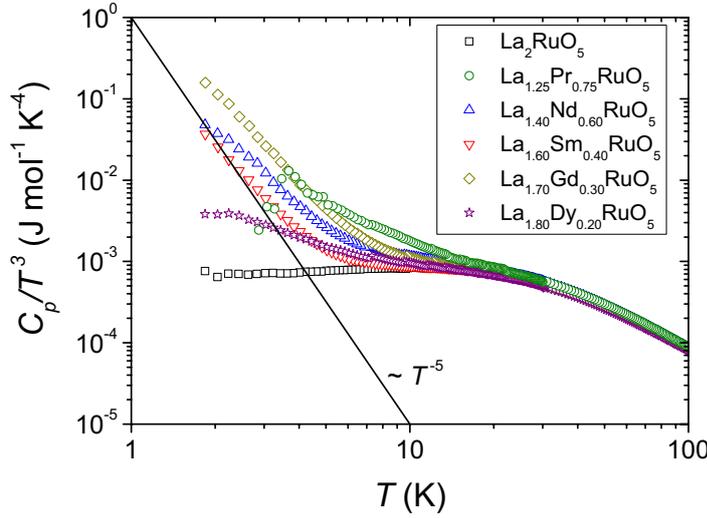
Figure 5.22.: Low-temperature specific heat on a double logarithmic scale in the representation C_p/T^3 vs. T of La$_2$RuO$_5$ and selected La$_{2-x}$Ln$_x$RuO$_5$ samples.

oxides, however, a value of zero is expected because of the existing band gap. Here c_0 is only a parameter, which accounts for any additional temperature-independent contribution to the specific heat, like e.g. the higher crystal-field levels of the rare-earth metal ions, which can extend up to energies corresponding to room temperature. These contributions will not be further discussed due to their general complexity and they provide no significant information on the dimerization transition.

In Fig. 5.21 the Einstein-Debye fit results are shown as solid lines and they are in good agreement with the measured data (symbols). This adequate description of the phonon contribution is required for reliable results since even small deviations strongly influence the subsequent calcula-
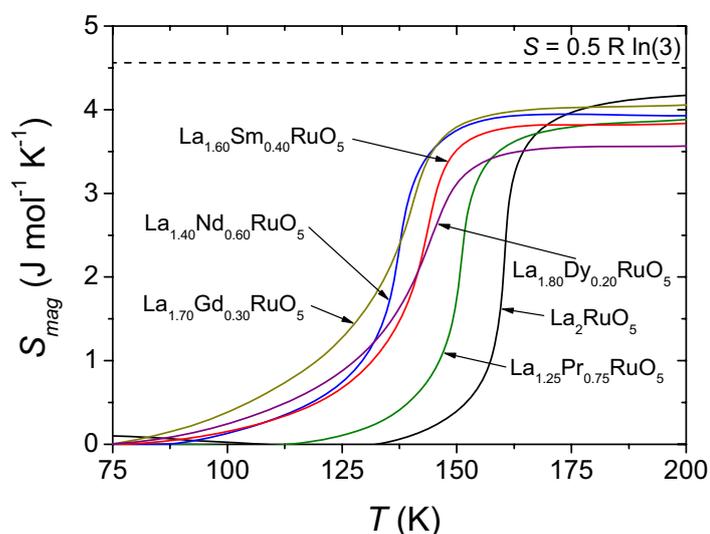
Figure 5.23.: Magnetic entropy obtained from integration of the La$_{2-x}$Ln$_x$RuO$_5$ specific-heat residuals after subtraction of the lattice contribution. The value of $0.5R\ln(3)$ is a first approximation showing the significant contribution of the dimer state to the total entropy.

tions. To obtain the magnetic contribution to C_p, the Einstein-Debye fits (parameters in Tab. 5.7) were subtracted from the experimental data. The residuals $C_p - C_{lattice}$ were integrated between approximately 75 K and 250 K according to $S_{mag} = \int (C_p - C_{lattice})/T \, dT$. The results for the entropies S_{mag} are depicted in Fig. 5.23 and show very similar constant excess entropies between 3.6 and 4.2 J mol^{-1} K^{-1} (Tab. 5.7) for all samples. These values corroborate the pure spin dimerization occurring at the magnetic transition and they are ruling out any kind of long-range order in agreement with ND experiments, in which no additional magnetic peaks were observed in Ref. [Ebb05] and Fig. 5.1.

The very similar values obtained for S_{mag} reveal the same nature of the phase transitions and spin dimerization in all La$_{2-x}$Ln$_x$RuO$_5$ compounds in accordance with the results described in Sec. 5.1.2.2. Furthermore, the slight variation of the entropies correlates to some extend with the varying dimerization temperatures of the rare-earth substituted samples reflecting a slightly reduced intradimer exchange J_0 as a result of the substitution.

On the other hand, besides the magnetic entropy also the effect of the structural transition has to be regarded. However, it is impossible to separate its contribution since both transitions are coupled. The above described good agreement of the magnetic entropy with the theoretical estimate indicates that the change of C_p caused by the structural transition is very small.
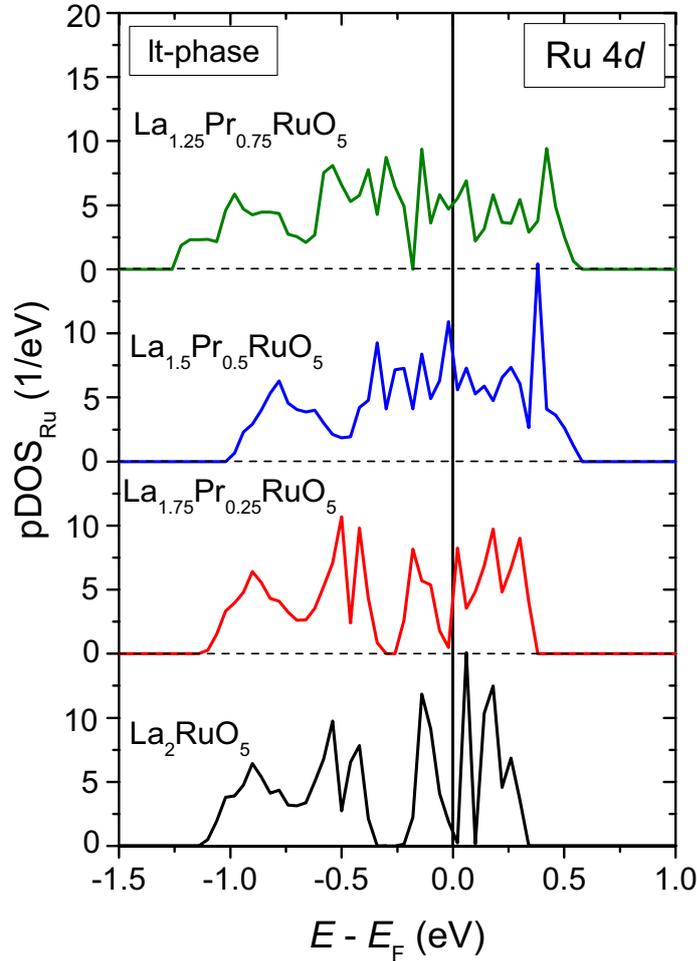
Figure 5.24.: Sum of the Ru contributions (spin-up channel) to the partial density of states (pDOS) close to E_F in the lt-phase of selected $La_{2-x}Pr_xRuO_5$ compounds applying LSDA.

5.1.4. DFT Calculation

To investigate the effect of the rare-earth substitution, one, two, and three La ions within the unit cell in P1 setting were replaced by Pr ions, respectively, reflecting the substitution levels $x = 0.25$, 0.50, and 0.75. Different arrangements of Pr in the crystal lattice were tested. The lowest total energy was achieved for the different substitutions as follows: For $x = 0.25$ when the single rare-earth metal ion was placed in the LaO-layer, for $x = 0.50$ when the two Pr ions were divided to occupy both layers, and for $x = 0.75$ one Ln had to be placed in the $LaRuO_4$- and two in the LaO-layer. In the ht-modifications the same lanthanide-ion distribution had to be applied to obtain minima in total energy. These lanthanide-ion distributions are in very good accordance with

neutron-diffraction results of Pr-substituted compounds and EXAFS investigations (Sec. 5.1.1.3). Studies of the spin-singlet state (consisting of dimers of antiferromagnetically arranged Ru ($S = 1$) spins) in the lt-phase were performed for Pr-substituted compounds with the same lanthanide-distribution scheme like in the ht-phase.

A comparison of the Ru contribution to the DOS close to E_F for different Pr substitution levels in the lt-phase of $La_{2-x}Pr_xRuO_5$ is shown in Fig. 5.24. As can be seen, the Ru $4d$ bands are broadening [Hof88] and slightly shifting with increasing Pr content. The decreasing absolute values of the Ru spin moments correlate with the declining transition temperature in $La_{2-x}Ln_xRuO_5$ with increasing x. In contrast the DOS below $E_F - 2$ eV remains almost unchanged since the structural changes are barely influencing the oxgen $2p$ bands. As expected, the $4f$ states of Pr are located around the Fermi-energy in very narrow bands, however, the hybridization with the other bands seems to be negigible.

For all lt-modifications different starting models for the magnetic arrangement and the Pr-substitution were used. The completely antiferromagnetic arrangement shown in Fig. 4.26 is slightly favored by up to 0.14 eV per unit cell for the Pr substituted compounds, compared to the unpolarized LDA calculations or the LSDA results obtained for other magnetic arrangements, independent of the magnetic moments of the Pr ions. The obtained local Ru spin moments in the favored magnetic arrangment were found to be approximately $S_\uparrow = +0.95$ and $S_\downarrow = -0.98$ for neighboring sites in La_2RuO_5, reflecting the antiferromagnetic pairing. The absolute values of the localized moments are strongly decreasing with increasing Pr substitution level mirroring a possible higher delocalization of the Ru spin moments, which explains the observed change in transition temperature. Alternatively, this could be an artifact of the modelling. Possibly a part the Ru $4d$ electron density is simply shifted into the Pr $4f$ bands located at E_F. For $x = 0.25$ spin moments $+0.85$ and -0.79 are found, for $x = 0.50$ they amount to ±0.32, and for $x = 0.75$ only $+0.05$ and -0.07 remain. This evolution of the absolute values of the local magnetic Ru moments at first sight seems to contradict the above described similar magnetic pairing in all rare-earth substituted compounds. However, the dimerization character is preserved by constant exchange interactions although the local magnetic moments distinctly decrease.

5.2. Ti Substitution and Combined Ti-Pr Substitution: La$_{2-x}$Pr$_x$Ru$_{1-y}$Ti$_y$O$_5$

5.2.1. Ti Substitution

In perovskite-related ruthenates titanium substitution previously was carried out for e.g. SrRuO$_3$ and the layered Sr$_2$RuO$_4$. The (partial) replacement of Ru by Ti typically leads to a metal to insulator transition and an increased thermal stability of the compounds [Puc02, Osw93]. Sr$_2$RuO$_4$ has been investigated extensively due to the occurrence of unconventional superconductivity at 0.93 K [Mae94], which is suppressed already by traces of Ti [Puc02]. The ruthenates LnCu$_3$Ru$_4$O$_{12}$ (Ln = La, Pr, Nd) are heavy-fermion compounds, which show a change of various physical properties including a metal to insulator transition and the change from itinerant magnetism to local moments upon increasing Ti substitution [Ram04, Ebb10, Bue10]. This will be described in more detail in chapter 6.

As shown in the previous section, for all rare-earth substituted compounds La$_{2-x}Ln_x$RuO$_5$ the structural phase transition from the monoclinic ht- to the triclinic lt-modification was observed, always occurring in combination with the antiferromagnetic Ru–Ru dimerization and concomitant spin-singlet formation. This indicates that the stuctural changes caused by the substitution and additional magnetic moments of the rare-earth metal ions do not significantly influence the singlet ground state of the Ru spin system. Starting from this consideration it was planned to more directly affect the magnetic coupling by substituting Ru with Ti. Ti^{4+} is non-magnetic due to its $3d^0$ configuration and, therefore, interrupts the magnetic exchange between the Ru $S = 1$ spins. Furthermore, the Ti incorporation should affect the crystal structure because La$_2$TiO$_5$ crystallizes with an orthorhombic unit cell isostructural to Y$_2$TiO$_5$ and Ln_2RuO$_5$ (Sec. 5.1), which is completely different from the La$_2$RuO$_5$ structure [Gui66, Pet03, Mum68].

It was not possible to synthesize polycrystalline La$_2$Ru$_{1-y}$Ti$_y$O$_5$ samples by a conventional solid-state reaction. Thus, an adapted sol-gel route was developed to obtain single phase samples up to $y = 0.45$, which is described in detail in Sec. 2.1.3. The samples are investigated in detail with respect to their crystal structure and the impact of emerging structural changes on the spin-Peierls like transition. To deepen the understanding of the phase-transition behavior the Ru and Ti oxidation states were determined by XANES spectroscopy. Furthermore, the entropy of the dimerization transition was investigated with specific-heat measurements to study the exchange interaction strength. DFT calculations were performed to support the interpretation of the experimental results of the magneto-stuctural transition. The results presented in this section are descibed in detail in Refs. [Rie13a, Rie13b].

5.2.1.1. Crystal Structure

By x-ray diffraction no traces of impurities were detected for $y < 0.3$. However, for $y \geq 0.30$ an increasing amount of La$_3$RuO$_7$ [Kha00] up to roughly 1.5 % ($y = 0.45$) was observed. The occurance of this phase can be ascribed to the small excess of La(NO$_3$)$_3$, which had to be applied to obtain single-phase samples at lower substitution levels. The most intense reflex of the La$_3$RuO$_7$
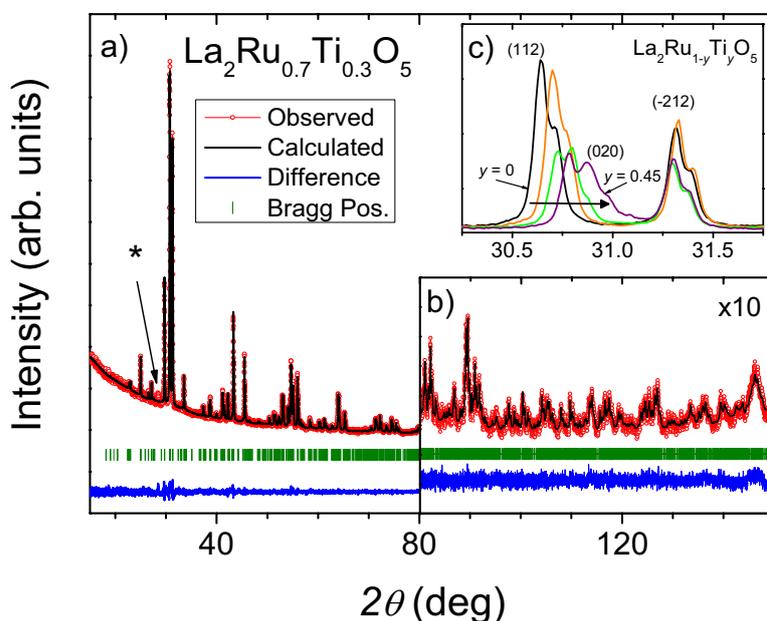
Figure 5.25.: a) Rietveld refinement of the $La_2Ru_{0.7}Ti_{0.3}O_5$ x-ray diffraction pattern measured with Cu-$K_{\alpha1,2}$ radiation at room temperature. The asterisk marks a trace of La_3RuO_7. The inset b) shows a magnification (10×) of the angular range $80° \leq 2\theta \leq 150°$ to illustrate the good fit quality even at high diffraction angles. c) Room temperature Cu-$K_{\alpha1,2}$ x-ray diffraction patterns of La_2RuO_5 and Ti-substituted compounds with $y = 0.15, 0.30, 0.45$ in the region $30.25°$ to $31.75°$ showing the angular evolution of selected Bragg-reflections due to structural changes caused by the Ti substitution.

pattern at roughly $2\theta = 28°$ is marked with an asterisk in Fig 5.25a. The beginning appearance of the reflex can be related to an amount of roughly 0.5 % in this sample. No further additional peaks are observed, indicating that no superstructure with long-range ordered Ru and Ti occurs, and that the two elements are distributed statistically on the Ru-sites.

The replacement of the Ru^{4+} ions (ionic radius: 0.620 Å) by slightly smaller Ti^{4+} ions (0.605 Å) [Sha76] in the octahedra of the $LaRuO_4$-layers causes structural stress and, as a consequence, only a partial substitution can be achieved. Remarkably, although almost half of the Ru is substituted, no indications for the formation of the La_2TiO_5 crystal structure is observed. For $y \geq 0.5$ the amount of impurity phases increased dramatically. Therefore, these samples are not discussed in the following.

At room temperature the $La_2Ru_{1-y}Ti_yO_5$ powder samples crystallize in the monoclinic space group $P2_1/c$ in accordance with the unsubstituted La_2RuO_5. The Rietveld analysis of the x-ray diffraction pattern of $La_2Ru_{0.7}Ti_{0.3}O_5$ recorded at room temperature is depicted in Fig. 5.25a and b as an example for the very good agreement of calculated pattern and measurement. Numeri-

cal values of the XRD Rietveld analysis results for all samples are listed in the supplementary information in Ref. [Rie13a].

In Fig. 5.25c the angular range $30.25° \leq 2\theta \leq 31.75°$ of the XRD patterns of pure La$_2$RuO$_5$ and selected Ti-substituted compounds with $y = 0.15, 0.30, 0.45$ are shown in more detail. The (0 2 0) peak is shifted with increasing y to higher 2θ values reflecting a shortening of the unit-cell parameter b. For the other two axes the influence of the substitution is by far less pronounced. This observation is in clear contrast to the structural changes caused by rare-earth substitutions. In La$_{2-x}$Ln$_x$RuO$_5$ the a-axis was found to become particularly shorter mirroring the incorporation of the smaller lanthanide ions in the LaO-layers.

The values for the room temperature unit-cell parameters obtained from the Rietveld refinements are depicted in Fig. 5.26a for a, b, and c and in Fig. 5.26b for β as a function of the substitution level y. The length of the a-axis slightly decreases up to $y = 0.25$ and then significantly increases. Upon substitution the b-axis decreases linearly by approximately 0.04 Å and, in contrast, the c-axis increases linearly with y. The most significant changes concern the b-axis ($\approx 0.75\%$). Linked to the increase of c, the monoclinic angle β also increases linearly from approximately $100.75°$ to $101.2°$ (Fig. 5.26b). The behavior of β is similar to observations in La$_{2-x}$Ln$_x$RuO$_5$ with smaller rare-earth metal ions like Gd and Dy in Sec. 5.1.1. The limit of the structural changes upon Ti substitution is reached at ≈ 9.192 Å for a, at ≈ 5.79 Å for b, and at ≈ 7.975 Å for c.

The changes of the unit-cell axis lengths detected for the Ti-substituted samples are clearly different from the ones caused by rare-earth substitution, where all three unit-cell axes were found to decrease with increasing substitution level. This behavior was assigned to the ionic radii of the smaller lanthanide ions compared to the La^{3+} ion. Consequently, the shrinkage of the cell parameters becomes stronger with decreasing ionic radius of Ln^{3+}. The rare-earth metal ions are preferably incorporated in the LaO-layer, therefore, in these compounds the a-axis shows the strongest decrease. Titanium, on the other hand, can only occupy the Ru-site within the LaRuO$_4$-layers. This affects the Ru–O distances, as reflected by the b- and c-axis variation. The a-axis which is related to the interlayer distance, therefore, is rather undistorted.

The relative changes of the unit-cell parameters are shown in Fig. 5.26c. The values were calculated by normalizing the cell parameters of the substituted samples to the corresponding cell parameters of La$_2$RuO$_5$. A linear behavior is observed for all cell parameters except for a and the unit-cell volume. These show a significant kink at $y = 0.25$. β, c, and a increase by roughly 0.4%, 0.2%, and 0.1%, respectively. In contrast, b decreases strongly by approximately 0.75% in turn causing a decrease of the unit-cell volume. The anomalies detected close to $y \approx 0.25$ might indicate that for $y \geq 0.3$ the characteristics of the magnetostructural transition are changing. Despite these clearly observable changes, it is noteworthy that the maximum relative changes are rather small (below 1 %), which is not surprising considering the minor difference of the ionic radii of Ru^{4+} and Ti^{4+}.

In Sec. 4.1.2 and 5.1.1.1 the ruthenium-oxygen distances in La$_2$RuO$_5$ obtained by powder neutron diffraction and single-crystal x-ray diffraction [Ebb05, Rie11, Rie12a] have already been discussed. The distances range between 1.933 Å and 2.067 Å. The shorter Ru–O bonds (O3, O4) are pointing to the LaO-layers, while the longer bonds (O2 and O5) are crosslinking the corner
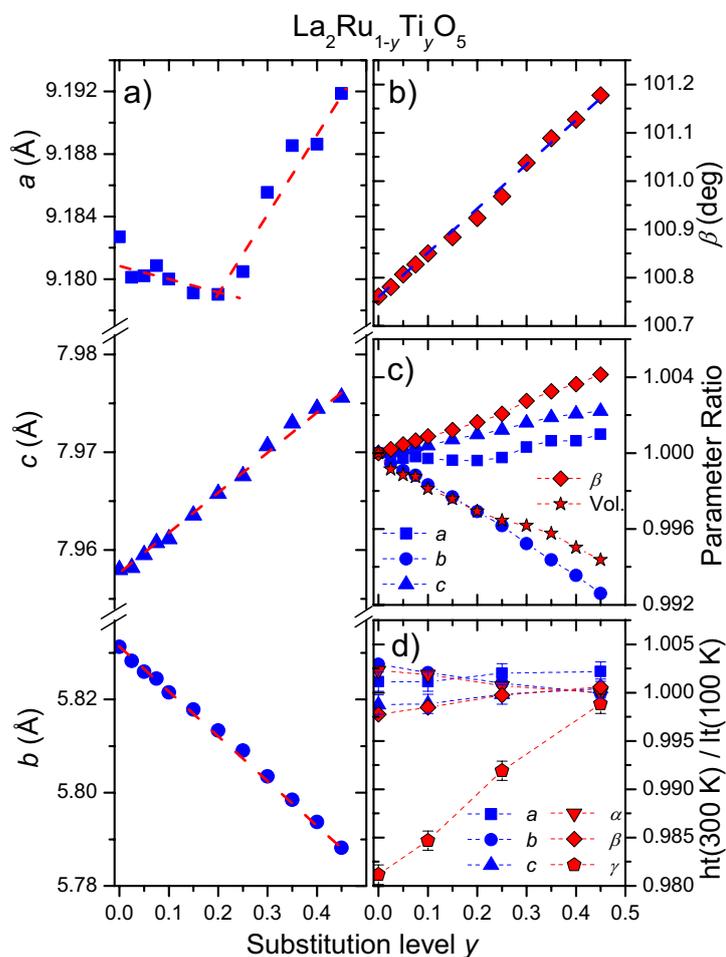
Figure 5.26.: Cell parameters for La$_2$Ru$_{1-y}$Ti$_y$O$_5$ derived from Rietveld analysis of powder XRD data at room temperature. a) Cell parameters a, b, and c. b) Monoclinic angle β. Error bars are below the size of the symbols. c) Relative change of the cell parameters. The cell parameters of La$_2$Ru$_{1-y}$Ti$_y$O$_5$ were divided by their corresponding values for La$_2$RuO$_5$. d) Comparison of the cell parameters for the high-temperature (300 K) and low-temperature phases (100 K) of La$_2$Ru$_{1-y}$Ti$_y$O$_5$. Values of α and γ are 90° in the ht-phase.

sharing octahedra in the LaRuO$_4$-layer. For La$_2$Ru$_{1-y}$Ti$_y$O$_5$ similar values are obtained from the powder XRD data, i.e. the shape of the octahedra is barely influenced by the substitution and the observed changes of the unit-cell parameters b and c are correlated to the angles between the octahedra. Although the Rietveld analysis of XRD measurements yields structural information for the oxygen atoms with a somewhat broader error range than ND data, the accuracy is sufficient to monitor the evolution of the corresponding bond angles upon Ti substitution. It was found that the O5–Ru–O5 and the O2–Ru–O2 angles in the octahedra remain almost constant with values of approximately 95° and 178°, respectively, which is in good agreement with ND results for

La$_2$RuO$_5$ [Ebb05]. Furthermore, the Ru–O2–Ru angles along the *c*-axis of La$_2$Ru$_{1-y}$Ti$_y$O$_5$ are similar 153(1)° to the ones of La$_2$RuO$_5$ (152.5°). In contrast, the angles for Ru–O5–Ru increase significantly from 155.4° for La$_2$RuO$_5$ to roughly 160° with increasing Ti substitution level *y*. This results in a reduced tilting of the octahedra in the *ab*-plane, which causes the observed decrease of the unit-cell parameter *b* and also explains the slightly increasing values of *a* at higher substitution levels.

Bond-valence sum (BVS) calculations based on the XRD data were performed, from which the formal valences of the ions were derived [Bro85]. In the LaRuO$_4$-layers of the Ti-substituted compounds valences of +3.0 for La, -2.0 for O and +4.0 for Ru were found in perfect agreement with the formal charges. The slightly smaller Ti ion radius compared to Ru results in a smaller value for the oxidation state of roughly +3.9. In the LaO-layers deviations of the valences due to the shortened La–O distances are observed. Oxidation states of approximately +3.3 and -2.5 for lanthanum and oxygen, respectively, are obtained. This effect has already been observed for pure and rare-earth substituted La$_2$RuO$_5$ and corresponds to smaller La-sites in the LaO-layers compared to the LaRuO$_4$-layers (Sec. 5.1.1.1).

For the low-temperature modification the evolution of the unit-cell parameters was investigated by XRD at 100 K. Samples with *y* = 0, 0.1, 0.25, and 0.45 were used for the measurements. For a better comparability the room-temperature cell parameter data were divided by their corresponding values obtained at 100 K. The results are shown in Fig. 5.26d. For the unsubstituted La$_2$RuO$_5$ (i.e. *y* = 0), the angle γ increases distinctly by approximately 1.8 % due to the phase transition, while all other cell parameters remain basically constant (changes below 0.3 %). From Fig. 5.26d it can be seen that the ratio for γ approaches unity with increasing titanium-substitution level. This indicates that the structural phase transition is progressively supressed by the Ti incorporation. A comparison of the patterns of La$_2$Ru$_{0.55}$Ti$_{0.45}$O$_5$ obtained by XRD using synchrotron radiation (λ = 0.56285 Å) at 50 K and 300 K shows no significant difference implying that the structural transition is completely supressed for this substitution level. The results from magnetic measurements discussed in the following clearly support this finding.

The thermal contraction of the unit-cell volume for La$_2$Ru$_{0.55}$Ti$_{0.45}$O$_5$ from room temperature down to 50 K was additionally determined. The thermal expansion coefficient $\alpha_c = 24.2(2) \cdot 10^{-6}$ K^{-1} derived from the fit according to $V = V_{300K} \cdot \exp\left(-\alpha_c \cdot \Delta T\right)$ is in the usual range for inorganic oxide materials [Hay11]. Below 100 K the contraction and, hence, α_c decreases, which is a commonly observed behavior since the thermally activated vibration of the ions in solids freezes in with decreasing temperature [Kri09, Ebb98].

### 5.2.1.2. X-ray Absorption Spectroscopy

To investigate a possible influence of the substitution on the oxidation states of Ru and Ti, XANES measurements at the Ru-L$_{III}$ and Ti-K absorption edges were performed. In Fig. 5.27a the normalized Ru-L$_{III}$ XANES spectra of selected samples (La$_2$Ru$_{0.9}$Ti$_{0.1}$O$_5$, La$_2$Ru$_{0.75}$Ti$_{0.25}$O$_5$, and La$_2$Ru$_{0.55}$Ti$_{0.45}$O$_5$) and references are depicted. The intense white lines at roughly 2.84 keV resulting from $2p \rightarrow 4d$ excitations were modelled according to Sec. 2.3.1. For comparison,
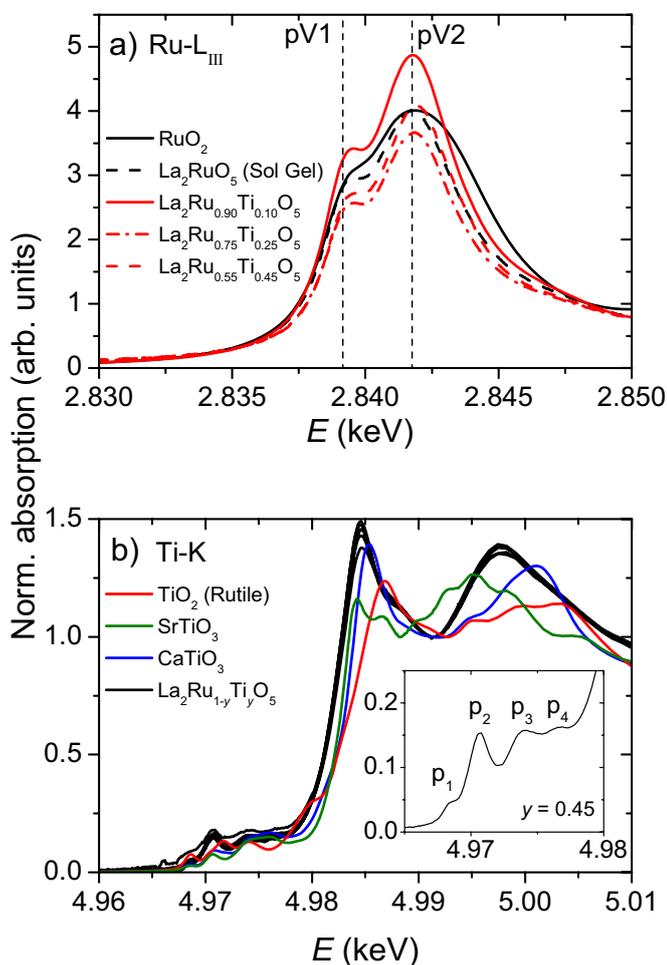
Figure 5.27.: a) Normalized Ru-L$_{III}$ absorption spectra of RuO$_2$, La$_2$RuO$_5$, and La$_2$Ru$_{1-y}$Ti$_y$O$_5$ samples. The dashed vertical lines mark the positions of the two pseudo-Voigt fit maxima of the La$_2$RuO$_5$ reference sample obtained from solid-state reaction. b) Normalized Ti-K absorbtion spectra of TiO$_2$, (Ca,Sr)TiO$_3$ and La$_2$Ru$_{1-y}$Ti$_y$O$_5$. The inset shows the characteristic pre-edge region for La$_2$Ru$_{0.55}$Ti$_{0.45}$O$_5$.

La$_2$RuO$_5$ and RuO$_2$ were used as Ru^{4+} reference materials [Rie12a, Ebb01, Arc07], which yield edge energies in agreement with previously determined values [Ebb98, Ebb06, Goe06]. The energy positions of the two peaks are shown in comparison in the right frame of Fig. 5.28. From the almost identical values for the samples and references an oxidation state of Ru^{4+} for all samples can be deduced.

At the Ru-L$_{III}$ edge the ratio of the pseudo-Voigt peak areas (pV2/pV1) decreases from 6.57 ($y = 0, 0.10$) to 5.16 for $y = 0.45$. This can possibly be explained by energetically closer $4d(e_g)$ states (d$_{z^2}$ and d$_{x^2-y^2}$) and, therefore, would point to a less distorted octahedral symmetry than
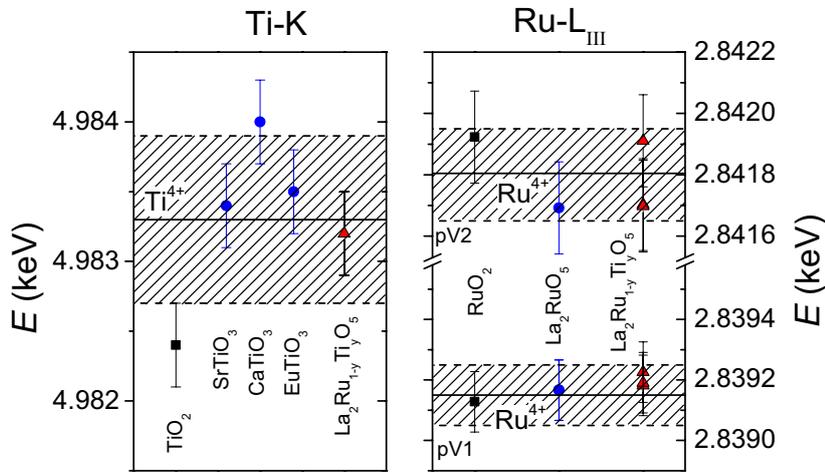
Figure 5.28.: Left: Ti valence determined from the maxima of the first derivatives of the Ti-K XANES spectra. Right: Ru valence determined from the fit of the first derivative of the Ru-L$_{III}$ XANES, the symbols represent the pseudo-Voigt maxima. Horizontal solid lines indicate the average Ti^{4+} and Ru^{4+} energies determined from the reference compounds. Dashed horizontal lines mark the estimated error window.

described for e.g. La$_{2-x}$Sr$_x$Cu$_{1-y}$Ru$_y$O$_{4-\delta}$ [Ebb01]. The crystal structures obtained from XRD and ND are in agreement with this explanation. Furthermore, the energy difference between the two pseudo-Voigt peaks is almost identical for all samples and in good agreement with the value of 2.6(1) eV typically found for tetravalent Ru in oxide materials [Ebb01].

The normalized spectra of the Ti-K edge measurements are depicted in Fig. 5.27b. Reference samples were TiO$_2$ and the perovskite compounds (Ca, Sr, Eu)TiO$_3$, in which titanium is tetravalent. The spectra of all La$_2$Ru$_{1-y}$Ti$_y$O$_5$ samples are almost identical, which reflects a constant Ti valence and oxygen coordination in the TiO$_6$ octahedra. In addition, the BVS calculations revealed almost constant Ti–O distances for all substitution levels y, which is also in agreement with this finding. The first maximum of the derivatives of the spectra was taken as a measure for the edge energy. In the left frame of Fig. 5.28 the obtained energies of the tetravalent references and the samples are depicted. All La$_2$Ru$_{1-y}$Ti$_y$O$_5$ samples contain Ti ions with oxidation state +4 within the error bars, as expected.

The inset of Fig. 5.27b shows the pre-edge region of the Ti-K edge of La$_2$Ru$_{0.55}$Ti$_{0.45}$O$_5$. Four separate peaks (p1 - p4) can be distinguished, which belong to the quadru- and dipolar transitions from the 1s to the higher 3d and 4p states [Yam05]. In addition, the spectra are very similar to the Ti pre-edge region found for BaTiO$_3$, which is known for the off-center located Ti in the octahedra at room temperature [Yam05]. This observation is in agreement with the deviating Ru/Ti–O distances within the octahedra derived from the Rietveld refinements. The pre-edge feature shapes were almost identical for all titanium contents indicating that the metal-oxygen coordination re-
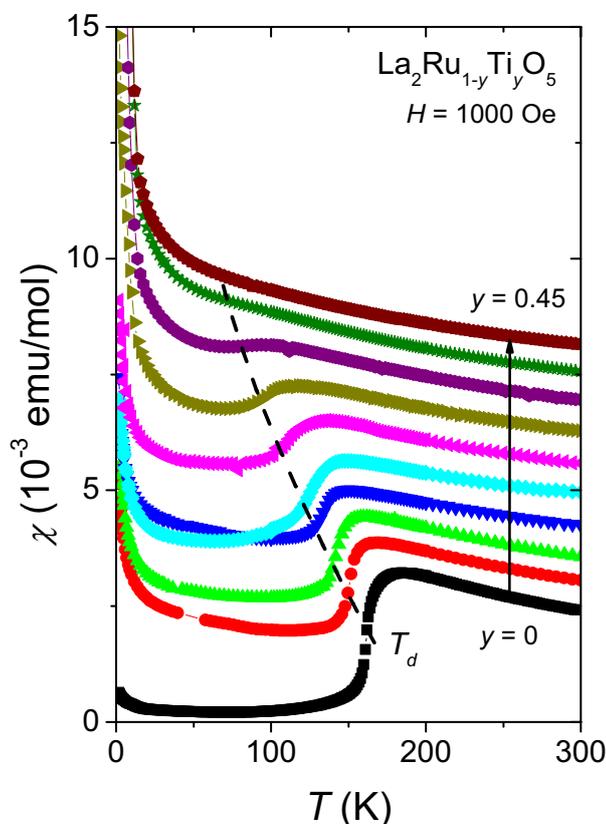
Figure 5.29.: Magnetic susceptibilities of $La_2Ru_{1-y}Ti_yO_5$ samples with steps of $y = 0.05$ increasing from bottom to top (indicated by vertical arrow). The χ curves are shifted by a constant value for clarity. The dashed line indicates the change of T_d with increasing substitution level.

mains basically identical for all $La_2Ru_{1-y}Ti_yO_5$ samples. However, first dielectric spectroscopy measurements do not provide an ordered polar ground state comparable to the ferroelectric transition in $BaTiO_3$ (see Sec. 4.4).

5.2.1.3. Magnetic Properties

As described above, pure and rare-earth substituted La_2RuO_5 exhibit a paramagnetic behavior above the dimerization transition. In the lt-modification the magnetic susceptibility χ drastically decreases reflecting the (quasi) non-magnetic spin-singlet ground state. Due to their $3d^0$ electronic configuration, the Ti^{4+} ions have no paramagnetic moment. A substitution of Ru^{4+} ions ($S = 1$) by Ti ($S = 0$) is expected to strongly influence the magnetic properties of $La_2Ru_{1-y}Ti_yO_5$ according to the increased dilution of the Ru–Ru magnetic exchange.

In Fig. 5.29 the magnetic susceptibilities of $La_2Ru_{1-y}Ti_yO_5$ samples with steps of $y = 0.05$ are depicted. For clarity the curves are shifted in χ by a constant value. The increase of χ at very
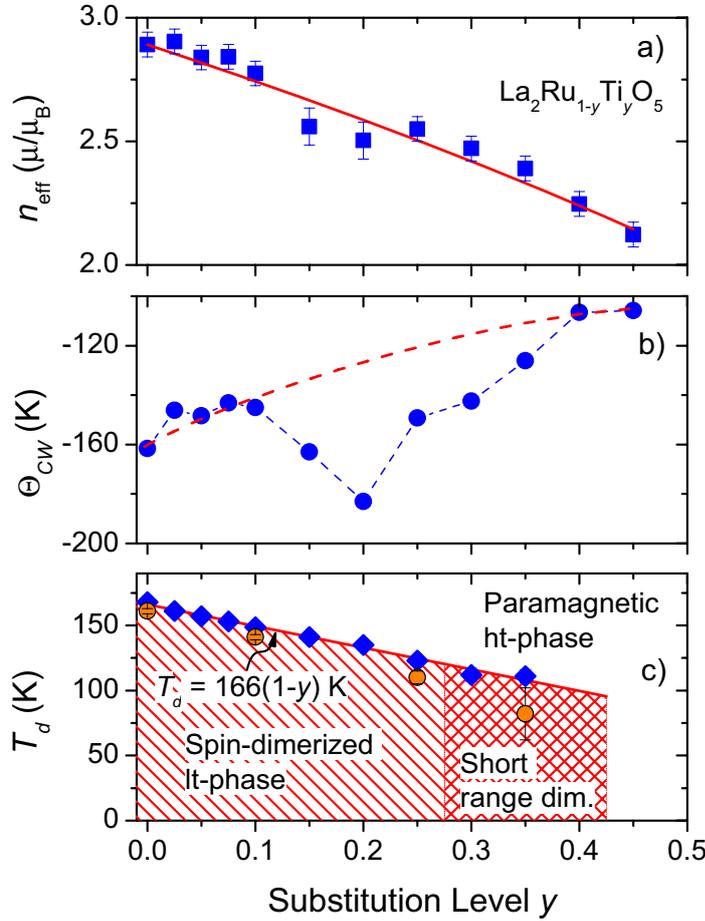
Figure 5.30.: a) Effective magnetic moments n_{eff} and b) Curie-Weiss temperatures Θ_{CW} of La₂Ru$_{1-y}$Ti$_y$O₅ determined from the high-temperature range fit of $1/\chi$. The solid line in a) marks the theoretical values for n_{eff} and the dashed red line in b) represents the assumed evolution for Θ_{CW}. For details see text. c) Transition temperatures of La₂Ru$_{1-y}$Ti$_y$O₅ obtained from magnetic susceptibility data. The solid red line is a linear fit between $y = 0$ and $y = 0.25$ (and continued to $y = 0.425$). The shaded red area marks the region of the spin-dimerized phase for $y \leq 0.25$ and a short-range dimerized phase for $y \geq 0.3$ (cross shaded). Orange circles represent the peak-maxima temperatures obtained from specific-heat data analysis described in Sec. 5.2.1.4.

low temperatures (i.e. below 50 K) is caused by remaining unpaired (e.g. by substitution, grain boundaries, vacancies or twin boundaries) Ru^{4+} spin moments with a paramagnetic behavior. The susceptibility in this range was fit with an additional Curie-Weiss function. The obtained Curie constants amount to approximately 1 % for pure La₂RuO₅ (Sec. 4.2.2) and slightly increase to a few percent with increasing Ti substitution level. Using the same Ru moments to describe C in the function for χ in both temperature ranges, the relation between the two Curie constants directly

describes the fraction of unpaired spins.

Obviously, the magnetic transition temperatures are strongly shifted (as indicated by the dashed line) and the reduction of χ below the transition temperature becomes less pronounced with increasing substitution level. For $y > 0.3$ the step in χ becomes increasingly smeared out and for $y \geq 0.45$ the step has completely vanished, indicating that the Ti substitution locally inhibits the Ru–Ru dimerization. This is the first hint that a long-range dimerized ground state cannot be established for $y \geq 0.3$ and becomes completely supressed for $y > 0.4$. This simply is a consequence of the statistical dilution of Ru dimers in the zig-zag chains of the $LaRuO_4$-layers and the decreasing magnitude of the structural transition with increasing y.

By fitting $1/\chi$ above 200 K with a modified Curie-Weiss law (Eq. 2.32) the effective magnetic moment n_{eff} and the Curie-Weiss temperature Θ_{CW} in this paramagnetic range were calculated. The obtained values for n_{eff} are depicted in Fig. 5.30a in units of the Bohr-magneton μ_B. A decrease of the magnetic moment with increasing Ti substitution level is observed, in agreement with the dilution effect caused by non-magnetic Ti^{4+} ions. The theoretical effective magnetic moments of the $La_2Ru_{1-y}Ti_yO_5$ samples were calculated using the spin-only value for Ru^{4+} and the Ru-substitution $(1-y)$ according to the equation $n_{eff} = \sqrt{(1-y)} \cdot n_{eff}(Ru^{4+})$. The corresponding result is drawn as solid red line in Fig. 5.30a. A good agreement of the calculation and the fit values is observed, therefore, the model of non-magnetic Ti ions diluting the paramagnetic Ru^{4+} centers provides an appropriate description for the ht-phase of $La_2Ru_{1-y}Ti_yO_5$.

The Curie-Weiss temperatures Θ_{CW} obtained from the fits are depicted in Fig. 5.30b. Starting from approximately -160 K for La_2RuO_5, Θ_{CW} increases to roughly -105 K for $La_2Ru_{0.55}Ti_{0.45}O_5$ reflecting a successive reduction of the antiferromagnetic exchange in the paramagnetic phase. This effect again is caused by the dilution with the non-magnetic Ti^{4+} ions and is assumed to lead to a smooth change as indicated by the dashed red line, which is just a guide to the eye. However, an unexpected minimum is observed at roughly $y = 0.2$ at which Θ_{CW} reaches approximately -185 K. At the same substitution level the step in the magnetic susceptibility changes from a sharp to a smoother and broader shape (Fig. 5.29) and n_{eff} shows a local minimum (Fig. 5.30a). The occurring minima can be explained by two antagonistic effects, namely the increasing antiferromagnetic exchange interaction due to the decreasing interatomic distances in the crystal structure and, on the other hand, the dilution caused by the diamagnetic Ti^{4+}. For small substitution levels the first effect apparently dominates. However, above $y = 0.2$ the effect of dilution becomes stronger than the increase of (nearest-neighbor) antiferromagnetic exchange and, hence, a rapid increase of Θ_{CW} is observed (Fig. 5.30b). More interestingly, this behavior correlates to the starting significant increase of cell parameter a for $y > 0.2$ (Fig. 5.26a), which can be ascribed to changes in the crystal structure caused by the Ti substitution. This once more reemphasizes the close relationship between crystal structure and physical properties.

The dimerization temperature T_d corresponding to the transition from the ht- to the lt-phase was obtained from the inverse susceptibility according to the procedure described in Sec. 5.1.2.3. In Fig. 5.30c T_d is depicted as blue diamonds as a function of the Ti concentration. The transition temperatures reveal a linear decrease, which can be fit by $T_d = 166 \cdot (1-y)$ K (solid red line in Fig. 5.30c). Above a substitution level of 0.25 the transition-temperature determination becomes

increasingly uncertain due to the decreasing step height in $1/\chi$. For this reason the values for $y = 0.3$ and 0.35 were omitted in the fit. The corresponding area of the spin-dimerized phase below T_d is shaded red for $y < 0.3$ to separate the paramagnetic and the dimerized phase in the diagram. Furthermore, a cross-shaded area representing short-range ordered clusters of Ru–Ru dimers is shown for $0.3 \leq y \leq 0.425$. The reasons for defining this additional region are described below. T_d decreases linearly and, thus, would become zero for a complete substitution of Ru by Ti and the subsequent structural changes according to Vegard's law [Veg21]. Due to the dilution the cooperative structural distortion is weakened and, hence, the intradimer exchange decreases.

Taking into account the observed linear T_d decrease and the vanishing of the transition step for $y = 0.45$, the absence of the structural transition also needs to be discussed in this context. The Rietveld analysis of the diffraction pattern recorded at 100 K leads to similar cell-parameter values and almost equal fit quality regardless of the starting model (i.e. when the monoclinic ht- or the triclinic lt-structure is used). Most prominently, the ratio of γ is changing from ≈ 0.982 for $y = 0$ to roughly unity for $y = 0.45$ as shown in Fig. 5.26d. Even in the high-resolution synchrotron data no structural changes were detectable down to 50 K. Thus, the sample La$_2$Ru$_{0.55}$Ti$_{0.45}$O$_5$ does not undergo the structural phase transition in accordance with the magnetic susceptibility data (Fig. 5.30c). This finding indicates that the spin-Peierls transition is actually driven by structural changes at T_d in the La$_2$RuO$_5$ compounds. Without additional energetical stabilization of the Ru orbitals by the structural modifications the resulting increased Ru–O–Ru superexchange and, hence, the spin-dimerization cannot be observed.

5.2.1.4. Specific Heat

In Fig. 5.31 the specific heat in C_p/T vs. T representation is depicted for five selected titanium substitutions. To increase the comparability the curves are shifted by 0.125 J mol^{-1} K^{-2}. All samples show similar phononic contributions, but significant differences at the phase transition. The shape of the peak changes with increasing substitution level. A broadening from La$_2$RuO$_5$ to La$_2$Ru$_{0.75}$Ti$_{0.25}$O$_5$ is observed, however, the peak is less asymmetrically broadened as found for the rare-earth substituted samples (Sec. 5.1.3). The observed broadening may be caused by local inhomogeneities of the Ti substitution, minor impurities (La$_3$RuO$_7$), and the different crystallinity of the samples due to different calcination durations. With increasing Ti substitution level the peak successively diminishes and cannot be clearly detected for $y \geq 0.35$. At lower substitution levels the transition temperature obtained from the onset point of the high-temperature side of the peak complies well with the temperature derived from the magnetic susceptibility measurements described above as can be seen from Fig. 5.30c.

The lattice contributions for samples up to $y = 0.25$ were fit using the Einstein-Debye phonon model introduced in Sec. 4.2.3. In Tab. 5.8 the obtained values for the Debye- and Einstein-temperatures are summarized. These temperatures are very similar for all investigated compounds and they agree well with values obtained for the rare-earth substituted compounds (Sec. 5.1.3). To improve the fit quality a small constant offset value of approximately 2.3(2) mJ mol^{-1}K^{-2} is added. This small contribution to the specific heat, which is linear in T, would be due to free
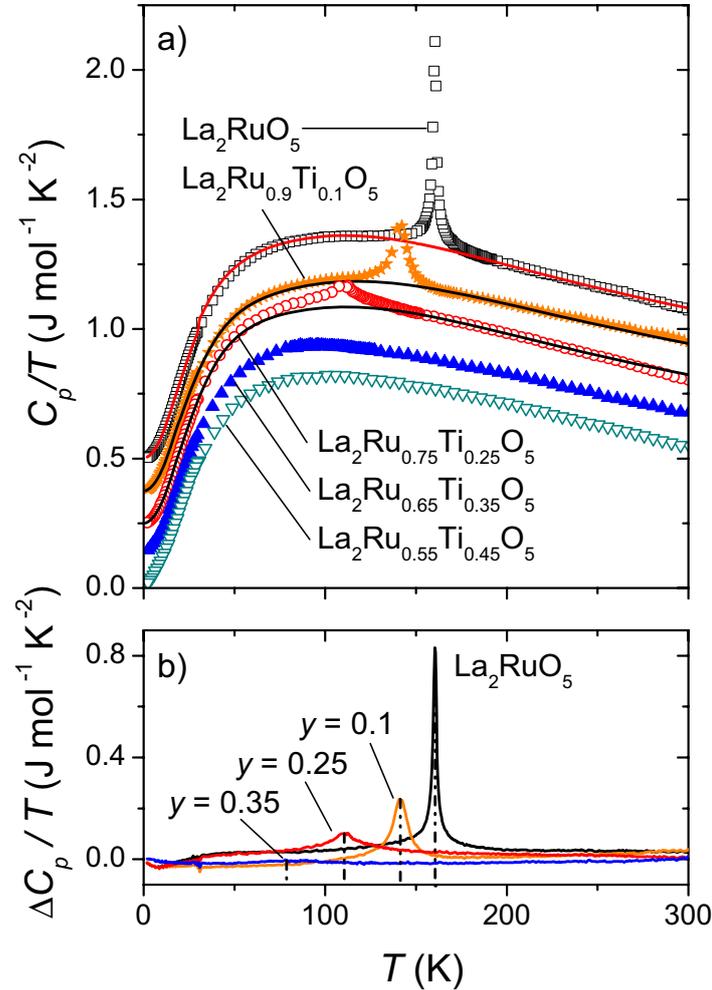
Figure 5.31.: a) Temperature dependence of the specific heat in representation C_p/T vs. T for La_2RuO_5 and selected $La_2Ru_{1-y}Ti_yO_5$ samples (symbols). For clarity the curves were shifted by $0.125\,\text{J}\,\text{mol}^{-1}\,\text{K}^{-2}$. The solid lines mark the Einstein-Debye fit results. b) Excess specific heat $\Delta C_p/T$ after subtraction of the $La_2Ru_{0.55}Ti_{0.45}O_5$ heat-capacity curve. The vertical dash dotted lines mark the T_d values shown in Fig. 5.30c.

charge carriers, but in the doped samples rather stem from local disorder resulting in a linear glass-like contribution. The calculated parameters are in agreement with previously reported specific-heat data of La_2RuO_5 and, thus, indicate a semiconducting behavior for all Ti-substitution levels [Mal05, Rie12b].

To obtain the magnetic entropy S_{mag} the Einstein-Debye fit curves were subtracted from the experimental data. The remaining residual peak was integrated between approximately 50 K and 250 K according to $S_{mag} = \int C_p/T\,dT$. To simplify the interpretation of the values for S_{mag}, they

Table 5.8.: Results of the heat-capacity fit for La$_2$Ru$_{1-y}$Ti$_y$O$_5$ (see text for details). The excess entropy contribution S^*_{mag} was calculated from the integrated residual peak after the subtraction of the lattice contribution and normalized to the Ru content.

Sample	Θ_D (K)	Θ_{E1} (K)	Θ_{E2} (K)	Θ_{E3} (K)	Θ_{E4} (K)	S^*_{mag} ($\frac{\mathrm{J}}{\mathrm{mol\,K}}$)
La$_2$RuO$_5$	132	175	217	325	520	4.2(3)
La$_2$Ru$_{0.9}$Ti$_{0.1}$O$_5$	131	182	231	351	552	4.0(3)
La$_2$Ru$_{0.75}$Ti$_{0.25}$O$_5$	134	176	219	328	542	4.4(3)

are normalized with respect to the substitution level (i.e. divided by $1 - y$) and listed as S^*_{mag} in Tab. 5.8. The entropy of pure La$_2$RuO$_5$ is expected to be $\Delta S = \mathrm{R}\ln(3) - 0.5 \cdot S_{dimer}$ according to Sec. 4.2.3. Due to the increasing Ti incorporation the number of dimers decreases, because each single Ti impedes the formation of one spin dimer. The prefactor 0.5 should therefore decrease due to the lower number of remaining dimers. However, it is assumed constant, because this number is considered by a certain degree applying the normalization. According to the description of S_{mag} depending on $J_0/k_\mathrm{B}T_d$ as introduced in Sec. 4.2.3, where J_0 represents the exchange interaction strength within the dimers. Since the normalized entropy values of the three samples are very similar, the intradimer exchange decreases with higher Ti incorporation according to the lower transition temperatures T_d.

In an alternative, more straightforward analysis the measured heat capacity of La$_2$Ru$_{0.55}$Ti$_{0.45}$O$_5$ was subtracted from the experimental data of the other samples. The residual curves are depicted in Fig. 5.31b. While for the samples with low Ti substitution the transition peak is clearly observable, for La$_2$Ru$_{0.65}$Ti$_{0.35}$O$_5$ the peak is severely smeared out and almost not detectable. This might be explained by the absence of a true structural phase transition. On the other hand, the magnetic measurements reveal a reduction of the susceptibility even at this substitution level. This finding can be explained assuming that for $y \geq 0.3$ only short-range dimerization occurs with local clusters of Ru-Ru dimers, which do not lead to a sharp peak in C_p. The transition temperatures determined by the peak maxima (shown as orange circles in Fig. 5.30c) agree fairly well with the above described transition temperatures of the dimerization transition.

The results of the x-ray diffraction investigations, the magnetic as well as the C_p measurements clearly prove the close correlation between structural and physical features in Ti-substituted La$_2$RuO$_5$. With increasing titanium content the structural changes occuring at the phase transition become gradually smaller and for $y = 0.45$ they cannot be detected at all (Fig. 5.26d). Simultaneously, the step-like decrease in the magnetic susceptibility diminishes and also the peak in C_p is suppressed. Already for $y = 0.3$ it is difficult to identify a sharp step at all. The variation of χ and C_p can be understood by a dilution of the interacting Ru moments by the non-magnetic Ti ions. This dilution reduces the number of remaining Ru spin dimers by the statistical distribution of Ru and Ti on the same crystallographic sites. Therefore, the reduced interaction only allows the formation of local dimers for $y > 0.25$. Also, it has to be noted that the formation of spin-singlets

is closely linked to the crystallographic phase transition, which results in alternating short and long Ru–Ru distances within the RuO_4-zig zag chains. At the critical level of $y \approx 0.3$ the Ru–Ru interaction becomes therefore too small and/or the strain due the incorporated Ti ions becomes too large to allow the crystallographic transformation and, hence, the formation of spin dimers is reduced stronger than derived from only the Ru/Ti distribution and becomes fully suppressed for $y = 0.45$.

5.2.1.5. DFT Calculation

Calculations of the electronic band structures of Ti-substituted La_2RuO_5 were performed as described in Sec. 4.5 using the crystal stuctures obtained by x-ray powder diffraction as input data. Due to the reduction of the symmetry to space group P1 (No. 1) the replacement of one or two Ru ions by Ti was possible and allowed to study the changes in the density of states (DOS) and the electronic band structure. The replacement of one or two Ru ions by Ti per unit cell corresponds to the compositions $La_2Ru_{0.75}Ti_{0.25}O_5$ and $La_2Ru_{0.5}Ti_{0.5}O_5$, respectively. The crystal structure of the latter one was calculated by a linear extrapolation of the cell parameters and by using the atomic coordinates of the sample with the highest available substitution level $y = 0.45$. Several configurations of Ru and Ti on the four sites in the crystal structure were modelled and in addition the signs of the initial magnetic moments were changed for different spin-polarized calculations to investigate their possible influences on antiferromagnetic and ferromagnetic nearest-neighbor exchange interactions.

In Fig. 5.32 the obtained DOS for the ht-modifications of La_2RuO_5 (c), $La_2Ru_{0.75}Ti_{0.25}O_5$ (b), and $La_2Ru_{0.5}Ti_{0.5}O_5$ (a) are shown. In the modelling of the ht-phase the LDA was used, because of the absence of magnetic ordering. The overall DOS and the partial DOS (pDOS) of Ru (red) and Ti (green) are shown in the range between -8 eV and 3.5 eV with respect to the Fermi level (E_F).

The DOS related to the LaO-layers is barely influenced by the Ti substitution, which is in agreement with the absence of Ti in this layers and the comparably small changes of the interatomic distances and coordinations. The charge of the corresponding oxygen is found to be higher than -2 for the three compounds in agreement with the BVS calculations described above in Sec. 5.2.1.1. The charges of the other ions are roughly in agreement with their respective values from the BVS calculation, as well.

With increasing Ti substitution changes are observed especially in the range above the Fermi-energy by the appearance of unoccupied Ti $3d$ levels between 1 eV and 2 eV. In addition, the Ru contributions at E_F and below -4 eV are considerably reduced according to the decreasing Ru amount in the compounds. The energy range of the Ru $4d$ oribitals near E_F is significantly reduced from 1.5 eV for La_2RuO_5 to 0.8 eV for $y = 0.5$ reflecting the increasing localization of the Ru spin moments. This effect is in contrast to the broadening of the Ru bands observed for rare-earth substitutions, where the broadening was explaining the lowering of T_d due to the delocalization of the Ru spin moments [Wha81]. In the present $La_2Ru_{1-y}Ti_yO_5$ samples the strongly reduced value of T_d merely reflects the decreasing number of Ru–Ru spin-singlets. Furthermore, it can be seen
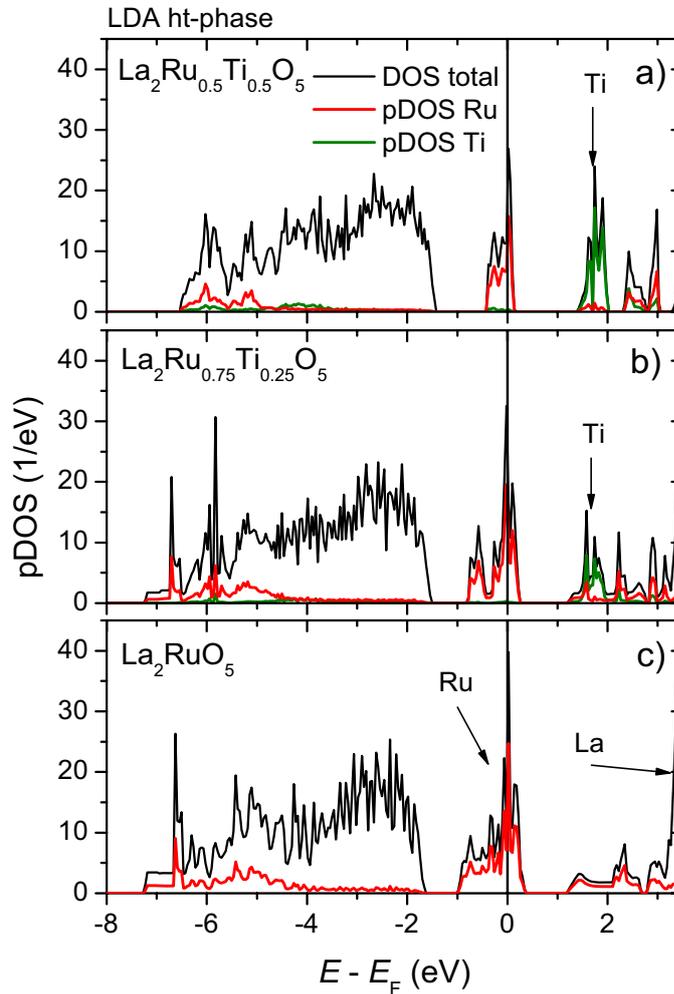
**Figure 5.32.:** Comparison of the density of states of a) La$_2$Ru$_{0.5}$Ti$_{0.5}$O$_5$, b) La$_2$Ru$_{0.75}$Ti$_{0.25}$O$_5$, and c) La$_2$RuO$_5$ using LDA.

that the distance between the centers of the Ru e_g and t_{2g} bands amounts to approximately 2.5 eV identical for all three Ti substitution levels. This finding is in good agreement with the Ru-L$_{III}$ XANES fit results, where also aconstant energy difference of 2.6 eV between the pseudo-Voigt peaks at the absorption edge is determined, which can be ascribed to excitations into the 4d e_g and t_{2g} states.

In space group P1 there are four possible Ru-sites per unit cell, on which the Ti atoms can be placed for the modelling. A comparison of the four possibilities of replacing one Ru atom by Ti in La$_2$Ru$_{0.75}$Ti$_{0.25}$O$_5$ was executed. All LDA calculations of the ht-phase lead to almost identical results in total energy and DOS, which shows that the Ti ion can statistically occupy any of the Ru-sites. Since all possible arrangements lead to identical energy values, no long range cationic
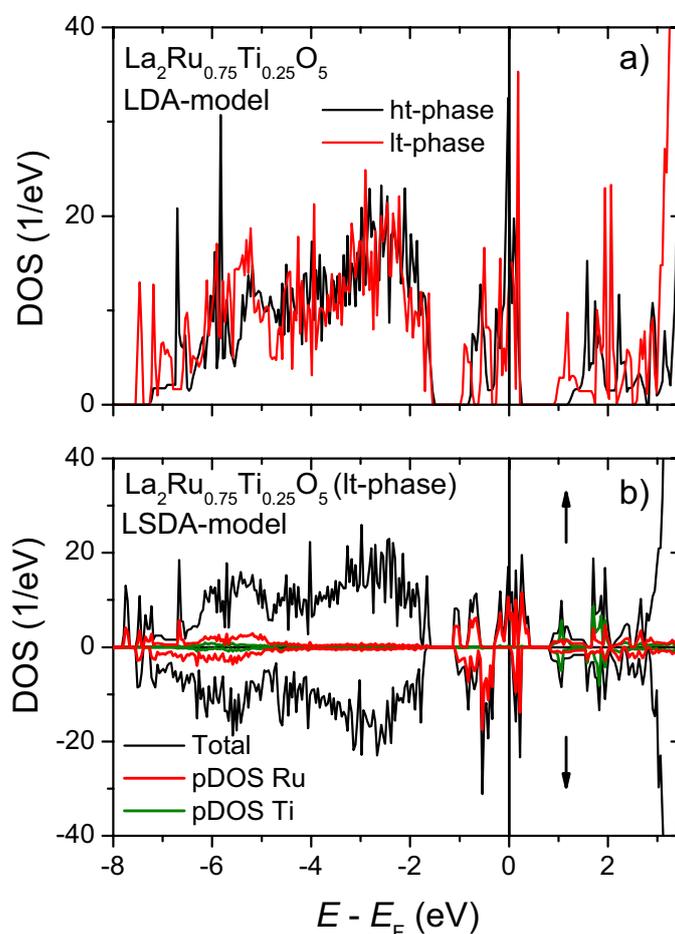
Figure 5.33.: Comparison of the density of states for the ht- and lt-phase of $La_2Ru_{0.75}Ti_{0.25}O_5$ using a) LDA and b) LSDA, for more details see text.

ordering and in turn no crystallographic superstructure is expected, which is in agreement with the XRD results. Similar investigations were performed for the ht-phase of $La_2Ru_{0.5}Ti_{0.5}O_5$, however, in this case a slightly preferred Ti distribution was found. The most stable result with lowest total energy (by less than 0.1 eV) was a checkerboard-like distribution of Ru and Ti ions, i.e. all Ru ions are surrounded by Ti and vice versa, which, however, is not found by XRD but possibly might reflect an ordering on local scale. The DOS of this arrangement is shown in Fig. 5.32a.

In addition, a number of different types of calculations using LDA and LSDA were carried out for the modelling of the lt-modification of $La_2Ru_{0.75}Ti_{0.25}O_5$. In Fig. 5.33 the results of the calculation using LDA (top frame) and LSDA (bottom frame) are depicted. The LDA results of the ht- and lt-phase are similar and the small deviations are simply caused by the slightly different crystal structures (Fig. 5.26d) as already observed for unsubstituted La_2RuO_5 [Eye06, Wu06, Rie11].

The similarity to the dimerized lt-phase of pure La$_2$RuO$_5$ was checked for La$_2$Ru$_{0.75}$Ti$_{0.25}$O$_5$ by spin-polarized calculations, which showed a preference of roughly 0.3 eV in total energy when an antiferromagnetic setting was used. The local spin moments of Ru amount to $S_\uparrow \approx 1.3$ and $S_\downarrow \approx 1.2$ with an obtained total magnetic moment of $\pm 2\mu_B$ per f.u. with respect to the initial random orientation of the Ru spin moments. The resulting DOS according to $-2\mu_B$ per f.u. is shown in the bottom frame of Fig. 5.33. The obvious changes are mainly concerning the partial DOS (pDOS) of Ru and (in a lower amount) the one of Ti. The observed shift between the spin-up and spin-down channels reflects a remaining ferromagnetic moment from the uncompensated Ru-spin moment per f.u. as a result of the next-nearest neighbor interactions. The bands corresponding to Ru and Ti are showing a stronger mixing in the LSDA model, which reflects the increased interactions in the lt-modification. In general it was found that antiparallel oriented Ru moments are favored for La$_2$Ru$_{0.75}$Ti$_{0.25}$O$_5$ as was already found for the lt-phase of unsubstituted La$_2$RuO$_5$. The only difference between these two compounds is the incorporation of non-magnetic Ti ions within the antiferromagnetically arranged net of Ru spins. The increase of the local spin moments could result from the stronger overlapping of Ru $4d$, Ti $3d$ and O $2p$ orbitals due to the structural changes. The result of the preserved antiparallel alignment in the lt-phase is in excellent agreement with the above described results obtained from the magnetic and specific-heat measurements.

For La$_2$Ru$_{0.5}$Ti$_{0.5}$O$_5$ identical crystal structures were applied for the ht- and lt-modification according to the XRD results discussed above. Different spin-polarized scenarios were tested. It was found that the total energies are only slightly favored to the LDA results and all different sets of the Ru/Ti distribution representing the magnetic nearest-neighbor interactions lead to similar results. Using the above mentioned preferred checkerboard Ru/Ti distribution, the resulting Ru spin moments amount to $S \approx 1.4$ and a total magnetization of $+4\mu_B$ per f.u. was obtained caused by ferromagnetic next-nearest neighbor interactions. Thus, for $y = 0.5$ (respectively 0.45) the ferromagnetic next-nearest-neighbor interactions seem to dominate the antiferromagnetic nearest-neighbor interactions when the checkerboard arrangement is present. A detailed study of the lt-phase may be performed by the introduction of e.g. an on-site repulsion term or by using a larger supercell with a less regular modulation of the Ru and Ti distribution.

The DFT calculations strongly support the above described findings for the dimerized state of lt-La$_2$Ru$_{0.75}$Ti$_{0.25}$O$_5$ and the absence of the spin-singlets for La$_2$Ru$_{0.5}$Ti$_{0.5}$O$_5$. Furthermore the character of the magnetic exchange interactions between nearest neighbors and next-nearest neighbors can be estimated and used to interpret the experimental results for χ and C_p.

5.2.2. Ti and Pr Co-Substitution

As described in the previous chapter, the rare-earth substitution was found to have only a small influence on the spin-Peierls transition. The Ln^{3+} ions remain as isolated paramagnetic centers and their interaction with the magnetic Ru sublattice is very weak. In contrast, the Ti substitution effectively disturbs the magnetic Ru–Ru dimerization. With increasing substitution level the transition temperature decreases and the drop in the magnetic susceptibility becomes smaller until the spin-dimerization completely vanishes for $y = 0.45$ in combination with the suppression of the structural transition.

Based on these findings the question arose whether the simultaneous substitution on both the La- and Ru-sites might result in unexpected new effects. For example, due to magnetic fluctuations caused by the Ti substitution and the remaining unpaired Ru spin moments, new interactions with the magnetic moments of the Pr ions seem possible. Reasoned by this samples with a partial replacement of La by Pr and an additional subsitition of Ru by Ti were synthesized and their magnetic susceptibilities were measured to study the possibly different magnetic behavior. The crystal structures of the $La_{2-x}Pr_xRu_{1-y}Ti_yO_5$ samples were investigated by x-ray powder diffraction in order to reveal possible correlations between the two different types of substitution (for more details see Ref. [Rie13b]).

The polycrystalline samples were synthesized similar to the $La_2Ru_{1-y}Ti_yO_5$ compounds (see Sec. 2.1.3). $Pr(NO_3)_3$-hydrate was added in corresponding stoichiometric amounts to the precursor solutions to obtain $La_{2-x}Pr_xRu_{1-y}Ti_yO_5$. The same heat treatment as for the solely Ti-substituted samples was applied.

5.2.2.1. Crystal Structure

According to the x-ray diffraction data, single-phase polycrystalline samples were obtained for $0 \leq x \leq 0.75$ and $0 \leq y \leq 0.4$. Only trace impurities of $LaRuO_3$ or La_3RuO_7 (with contents well below 1% according to Rietveld refinement) were detected for the highest substitution levels. Both substitutions with Pr and Ti cause structural stress due to the slightly smaller ionic radii of the inserted ions compared to La and Ru. However, the crystal structure changes differently for each kind of the substitutions. Since the location of the Pr ions is expected to be mainly in the LaO-layers and Ti can only be incorporated in the $LaRuO_4$-layers, a simultaneous substitution is expected to reach a limit at certain maximal levels x_{max} and y_{max} before the structural stress is impeding further substitution.

In Fig. 5.34 the measured pattern of $La_{1.5}Pr_{0.5}Ru_{0.8}Ti_{0.2}O_5$ is depicted as a representative example along with the result of the Rietveld refinement. An excellent concordance of the refinement is obtained for all samples applying the ht-phase crystal structure of La_2RuO_5 with monoclinic $P2_1/c$ symmetry as starting model. Details of the refinements are found in the supplement of Ref. [Rie13b].

The evolution of the cell parameters for $La_{2-x}Pr_xRu_{1-y}Ti_yO_5$ is depicted in Fig. 5.35. The obtained values for the parameters a, b, c, and the values for the monoclinic angle β are shown in the panels a), b), c), and d), respectively. To illustrate the dependence on the two different
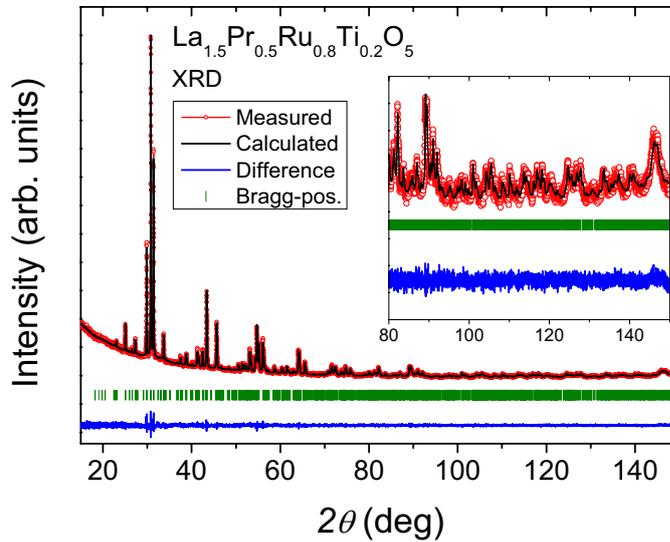
Figure 5.34.: Rietveld refinement of the x-ray diffraction pattern for $La_{1.5}Pr_{0.5}Ru_{0.8}Ti_{0.2}O_5$, measured with Cu-K$_{\alpha1,2}$ radiation at room temperature. In the inset a magnification of the range $80° \leq 2\theta \leq 150°$ is shown to illustrate the fit quality even for low intensities and overlapping reflexes at higher diffraction angles.

substitution levels *x* and *y*, quasi three-dimensional plots are shown with a color-coding depending on the cell-parameter value. Black arrows indicate increasing substitution levels.

For the *a*-axis (Fig. 5.35a), the doping effect of the smaller Pr ion compared to La is observed for all samples causing a linear decrease of *a* with increasing *x*. In contrast, the *a*-axis length is barely affected by the value of *y*, i.e. the titanium-substitution level. The weak dependence on the Ti concentration can be seen in the projection of the data points onto the x-z-plane in the graph, where basically a linear decrease with increasing *x* can be observed. The smallest values for *a* are found for $x = 0.75$ and establish a limit of ≈ 9.12 Å, which is comparable to values obtained for pure rare-earth substitutions.

The *b*-axis (Fig. 5.35b) is decreasing linearly with both increasing Pr- and Ti-substitution level. The effect of Ti substitution is more pronounced than for Pr substitution. The interplay between both substitutions generates an almost planar relation (Fig. 5.35b). The limit of structural stress is dominated by the Ti substitution, which impedes the synthesis of samples with both high Pr and Ti-substitution levels. The smallest *b*-axis value was obtained for $La_{1.75}Pr_{0.25}Ru_{0.6}Ti_{0.4}O_5$ and corresponds to the limit ≈ 5.787 Å. This value is roughly 0.02 Å below the shortest obtained length for Sm substituted $La_{1.5}Sm_{0.5}RuO_5$ (see Sec. 5.1.1.1).

For the *c*-axis evolution (Fig. 5.35c) opposing effects for the two kinds of substitutions are observed. While with increasing Pr concentration the axis length is reduced, Ti substitution increases
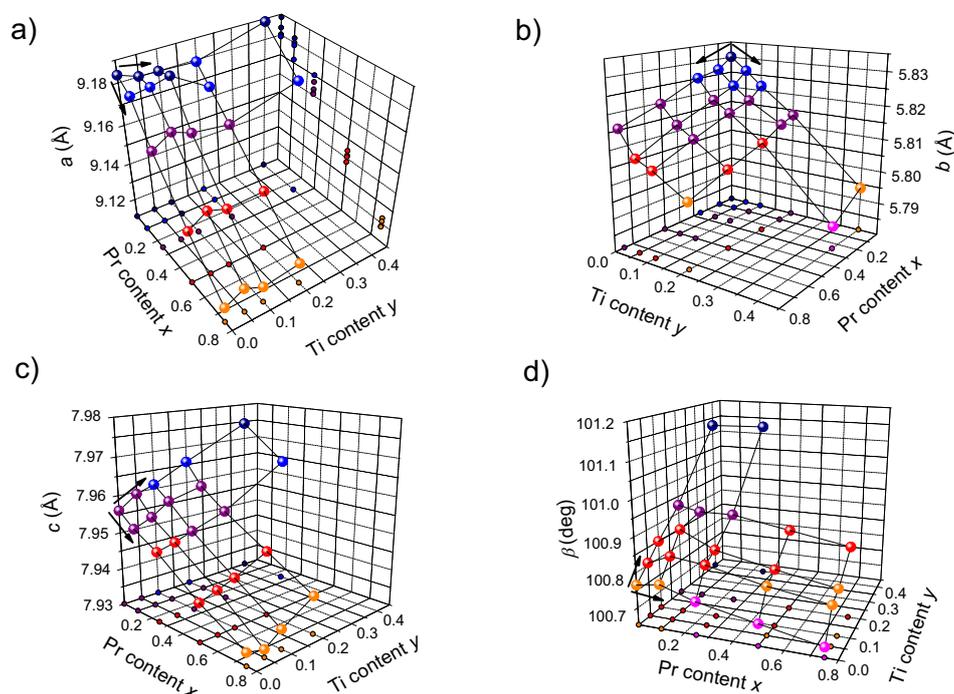
Figure 5.35.: Cell parameters for $La_{2-x}Pr_xRu_{1-y}Ti_yO_5$ derived from Rietveld analysis of powder XRD data measured at room temperature. The color-coded symbols represent the values of a) length of the *a*-axis, b) length of the *b*-axis, c) length of the *c*-axis, and d) monoclinic angle β. Error-bars are smaller than the size of the symbols.

the *c*-axis values. Since the two effects almost compensate each other, very similar values for *c* are obtained when $x = y$. The *c*-axis values are limited between the Pr and Ti borders of ≈ 7.93 Å and ≈ 7.98 Å.

The monoclinic angle β (Fig. 5.35d) decreases for increasing Pr substitution, but, in contrast, increases for increasing Ti contents. The upper limit is given by the value obtained for the sample with highest Ti-substitution level $La_2Ru_{0.55}Ti_{0.45}O_5$ and amounts to $\approx 101.18°$.

The maximal and minimal values of the cell parameters define a stability regime, in which the La_2RuO_5 structure can be synthesized. However, additional effects have to be taken into account. The rare-earth substitution provides more pronounced decreases of the unit-cell axes for the smaller lanthanide ions. In contrast, the monoclinic angle shows an opposite behavior, it decreases for Pr and Nd, remains almost constant for Sm and even increases for Gd and Dy. The limiting cell parameter for the maximum substitution is the *b*-axis length, because both the Pr and the Ti substitution induce a decrease. For the Ru–O distances and Ru–O–Ru bond angles only small changes in the range of 0.05 Å and below 2° compared to the values of Pr or Ti substituted La_2RuO_5 are observed. These deviations are barely significant since the accuracy of the XRD

Rietveld refinements is assumed to be in a similar range as these changes, which are therefore not discussed in detail.

In summary, the effects of substitutions of La by Pr and Ru by Ti show an additive behavior resulting in planar relationships of the cell parameters. On the one hand, the Pr substitution mainly affects the LaO-layers, where roughly two thirds of the Pr is incorporated, while the lower fraction of Pr is occupying the La-sites in the LaRuO$_4$-layers. This is leading to the observed strong reduction of the *a*-axis compared to the moderate decrease of the *b*- and *c*-axis. On the other hand, the Ti substitution does not significantly influence the *a*-axis due to the incorporation of the inserted Ti ions in the LaRuO$_4$-layers.

It should be mentioned that the relative changes of the cell parameters are within 1.5% compared to La$_2$RuO$_5$. This is a surprisingly small value and shows that the stability range of the La$_2$RuO$_5$ structure type is rather limited. But even these minor differences of the cell parameters are causing distinct changes of the physical properties of the substituted compounds, as shown for the magnetic properties in the following section.

5.2.2.2. Magnetic Properties

The effect of the simultaneous substitution on the magnetic phase transition was investigated by measurements of the magnetic susceptibility. For pure La$_2$RuO$_5$ a magneto-structural transition caused by the Ru^{4+} ($S = 1$) spin pairing at 161 K was observed, which leads to the formation of non-magnetic singlets driven by the structural changes at T_d. This transition is preserved in the rare-earth substituted samples, but is progressively suppressed by increasing Ti substitution. For $y > 0.25$ the observed magnetic properties and the absence of a peak in the specific heat were ascribed to the appearance of only short-range ordered clusters of dimers in the low-temperature phase.

In Fig. 5.36a the magnetic susceptibilities for a constant Pr concentration ($x = 0.25$) are depicted. The χ data were shifted by a constant value for better comparability. The strong increase at very low temperatures can be ascribed to both the paramagnetic Pr^{3+} ions and emerging unpaired Ru^{4+} spin moments in the range of a few percent depending on y similar to Sec. 5.2.1.3. In the paramagnetic range above T_d the curves for La$_{1.75}$Pr$_{0.25}$Ru$_{1-y}$Ti$_y$O$_5$ indicate a slightly reduction of the paramagnetic moment and changes of the Curie-Weiss temperature with increasing Ti-substitution level. A diminishing of the transition step is observed in agreement with the findings for La$_2$Ru$_{1-y}$Ti$_y$O$_5$. The transition step becomes broader with increasing y and its height declines progressively until it vanishes for $y = 0.40$. This value is slightly lower than obtained for La$_2$Ru$_{1-y}$Ti$_y$O$_5$, i.e. samples without Pr substitution. Due to the Pr incorporation the borders of the phase diagram (y, T) introduced above are shifted to lower y-values.

The suppression of the susceptibility step as a consequence of the Ti doping is also visible in the inverse susceptibility, which is depicted in Fig. 5.36b. The $1/\chi$ data for the two Ti substitutions $y = 0.05$ and $y = 0.20$ are shown for different Pr-substitution levels x. In the paramagnetic range above 200 K a linear behavior in agreement with a Curie-Weiss law is observed. The increasing Pr contribution to the total magnetic moment is reflected by the decreasing slope of the linear
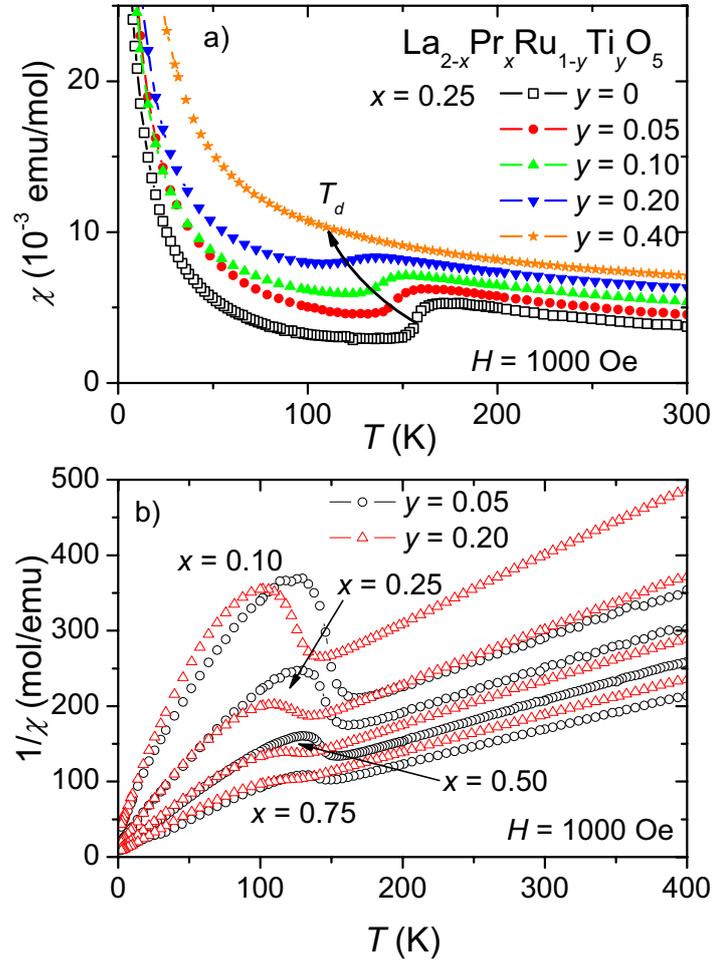
Figure 5.36.: a) Temperature depending magnetic susceptibility $\chi = M/H$ of La$_{1.75}$Pr$_{0.25}$Ru$_{1-y}$Ti$_y$O$_5$ applying an external field of $H = 1000$ Oe. The curves are shifted by a constant value for better comparability. The arrow marks the shift of the transition temperature T_d upon Ti substitution. b) Thermal behavior of the inverse magnetic susceptibilities $1/\chi$ of La$_{2-x}$Pr$_x$Ru$_{0.95}$Ti$_{0.05}$O$_5$ and La$_{2-x}$Pr$_x$Ru$_{0.8}$Ti$_{0.2}$O$_5$ at $H = 1000$ Oe.

regions. Furthermore, the higher Ti-substitution level generates a stronger splitting of the curves for the ht-phase. In turn, the decreasing upturn caused by the dimerization transition is correlating with the behavior observed for the solely Ti-substituted samples reflecting the suppression of the singlet formation.

The high-temperature regions above 200 K of the inverse susceptibilies were fit using a modified Curie-Weiss function (Eq. 2.32). The value of χ_0 was found to decrease from roughly 10^{-4} emu/mol to 10^{-5} emu/mol with increasing substitution levels x and y, which indicates either
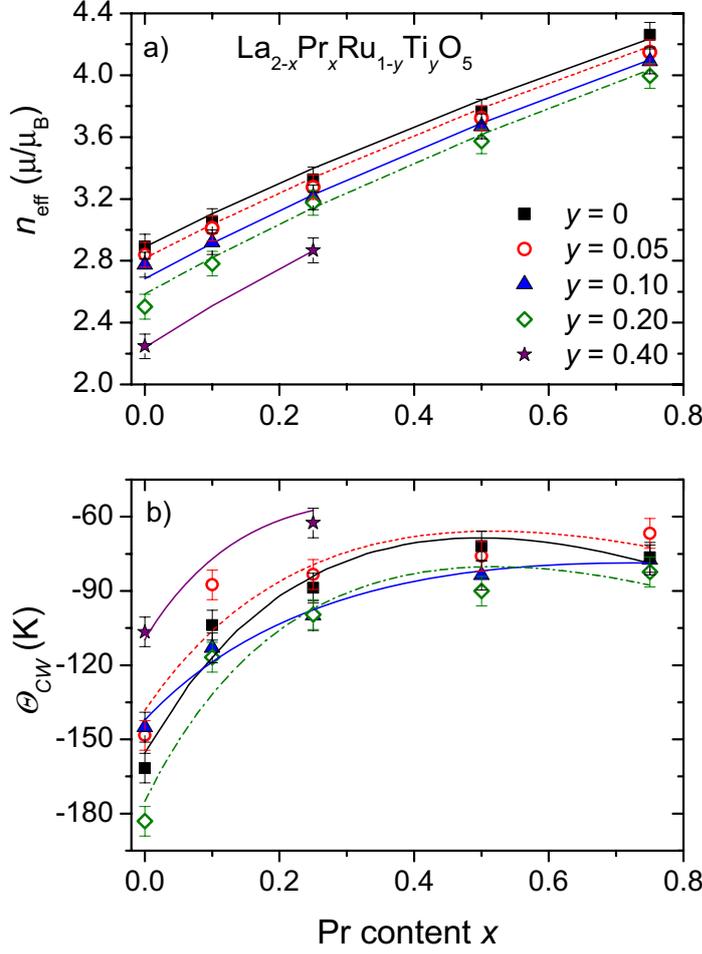
Figure 5.37.: a) Effective magnetic moments in Bohr magnetons derived from Curie-Weiss fits of $1/\chi$ in the temperature range 200 - 400 K. The lines represent the sum of the moments according to Eq. 5.3 using the spin-only value for Ru^{4+} and the free-ion approximation value for Pr^{3+}. b) Curie-Weiss temperatures obtained from the fit of $1/\chi$ in the temperature range 200 - 400 K. The solid and dashed lines represent Θ_{CW} values calculated with Eq. 5.2.

rising diamagnetic and/or decreasing van-Vleck contributions. The effective magnetic moments n_{eff} are shown in Fig. 5.37a in units of μ_B. The solid and dashed lines represent the calculated $n_{\text{eff,}total}$ according to

$$n_{\text{eff,}total} = \sqrt{(1-y) \cdot n_{\text{eff}}(\text{Ru})^2 + x \cdot n^2_{\text{eff}}(\text{Pr})} \quad , \tag{5.3}$$

where x and y are the corresponding Pr- and Ti-substitution levels. This equation implies completely independent contributions of the two types of paramagnetic ions. The good agreement of the magnetic moments obtained from the Curie-Weiss fit with the calculated values is evident from

Fig. 5.37a. The deviations are within the range of the error bars proving that the assumed additive behavior of the contribution of Ru^{4+} and Pr^{3+} to the total magnetic moment is correct.

The Curie-Weiss temperatures Θ_{CW}, which are depicted in Fig. 5.37b, were used to investigate in more detail the magnetic character of the paramagnetic ht-phase. The negative sign of Θ_{CW} indicates the occurrence of antiferromagnetic interactions, as e.g. $\Theta_{CW} \approx -162$ K for the above mentioned La_2RuO_5 sample. The absolute value is mirroring the interaction strength, which was found to decrease with increasing substitution level x, i.e. with a higher content of paramagnetic rare-earth metal ions. On the other hand, the Ti substitution leads to a change of the interaction strength due to structural deformations and the dilution of the interacting Ru-spin moments by the diamagnetic Ti^{4+}. In detail, the Ru–O bond lengths get reduced with increasing Ti concentration and, in turn, the exchange interactions between the Ru-centers become stronger. This effect is increasing the absolute value of Θ_{CW} in the range $0.1 < y < 0.25$ reaching a minimum of approximately -185 K at $y = 0.25$. Upon higher Ti doping levels a decrease of the absolute value is found. Starting at $y = 0.25$ the increasing dilution of the Ru-centers begins to dominate the magnetic exchange and, hence, explains the strong decrease of $|\Theta_{CW}|$. For the co-substituted samples the obtained Θ_{CW} values are shown in Fig. 5.37b. They reveal a decreasing absolute value for increasing x and constant y. Furthermore, for constant x the Curie-Weiss temperatures behave according to the solely Ti substitution, i.e. for $y = 0.2$ a minimum is always observed in the graph. This behavior of Θ_{CW} indicates the above proposed change from a long-range dimerized lt-phase with singlet ground state to a phase with only short-range ordering of dimers in clusters.

The curves in Fig. 5.37b represent fits of Θ_{CW} for two antiferromagnetically interacting sublattices A (Ru^{4+}) and B (Pr^{3+}) according to Eq. 5.2. The values of the λ parameters were obtained from least-squares fits of the Curie-Weiss temperatures for constant Ti substitution level. The results are the solid and dashed curves shown in Fig. 5.37b. Since only a limited number of data points were available for the fit, the absolute values are just taken as a measure of the involved interactions. For $y = 0.40$ only two data points were available. Therefore, the parameters λ_{AB} and λ_{BB} were taken from the $y = 0.05$ fit and only λ_{AA} was refined. The fit for $y = 0$ is in good agreement with the result shown in Sec. 5.1.2 but not identical, since in compliance with the substituted samples the Curie-Weiss temperature for pure La_2RuO_5 synthesized with Ru-NOAc was used (see Tab. 4.2).

Good agreements of measured Θ_{CW} values and the fit curves were found. The sign of all interaction strengths W was negative, which is characteristic for antiferromagnetic interactions both within the sublattices and between them, in agreement with the results given in Sec. 5.1.2 and also in accordance with the negative Curie-Weiss temperatures. The absolute values of the interaction strength behave according to $W_{AA} > W_{BB} >> W_{AB}$. Thus, the interactions within the sublattices are much stronger by roughly two orders of magnitude than between them. It is therefore justified to describe the overall magnetic behavior by two almost independent sublattices. The values of W show a local maximum for the Ti substitution level $y = 0.2$ and a strong decrease for $y = 0.40$. This reflects the above mentioned behavior for the pure Ti substitution, where a maximum of Θ_{CW} is found close to $y = 0.25$. In general, the (antiferro-)magnetic interactions are diminishing in accordance with the decreasing absolute values of Θ_{CW}. Simultaneous doping of Pr ions into the
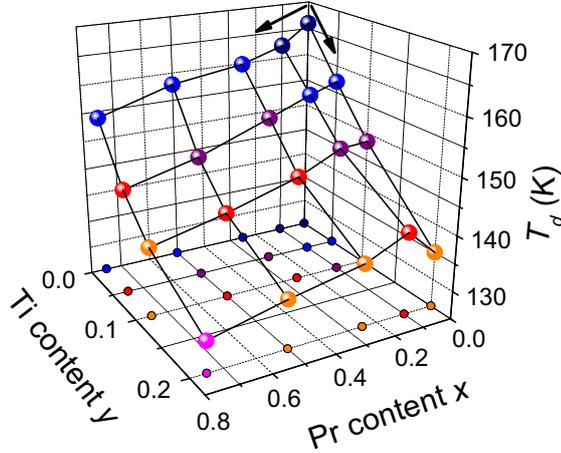
Figure 5.38.: Dimerization temperatures T_d obtained from the magnetic susceptibility data of La$_{2-x}$Pr$_x$Ru$_{1-y}$Ti$_y$O$_5$.

LaRuO$_4$-layers does therefore not change the impact of the Ti substitution on the system.

From the inverse susceptibilities, the dimerization temperatures were obtained using the onsets of the transition anomalies (Fig. 5.38). Since no transition was observed for the sample La$_{1.75}$Pr$_{0.25}$Ru$_{0.60}$Ti$_{0.40}$O$_5$, T_d is only shown for $y \leq 0.20$. Within this range the transition temperature decreases linearly in both directions with increasing substitution levels. The effect of the Ti substitution is more pronounced than of the Pr substitution (steeper slope in y direction in Fig. 5.38). This can be explained by different origins for the T_d reduction. The Pr substitution leads to a decrease by the increasing delocalization of the Ru electrons. This delocalization is caused by an electronic band broadening resulting from slight changes of the crystal structure. On the other hand, the Ti substitution directly impedes the Ru dimerization by the dilution of the magnetic Ru centers and, therefore, provides a more pronounced influence on the phase transition. Since the structural parameters change according to Vegard's law, a linear decrease of T_d is very reasonable. The simultaneous replacement of La and Ru leads to the obtained change of T_d depending on the particular substitution levels x and y, because both substitutions alter the structural and magnetic properties almost independently.

In summary, the cell parameters exhibit a completely additive behavior with respect to the changes obtained for the pure Pr and Ti substitution. This finding can be explained by taking into account the layered structure of La$_2$RuO$_5$. While Pr ions are predominantly occupying the LaO-layers, Ti ions are located on the Ru-sites in the LaRuO$_4$-layers. The simultaneous substitution leads to a certain degree of compensation of cell-parameter changes, which results in a large regime of x and y. Only the b-axis is shortened by both substitutions, which limits the range of

simultaneously high substitution levels for Pr and Ti ($x \leq 0.5$ and $y \leq 0.3$).

The magnetic susceptibilities can be described assuming a coexistence of two only very weakly interacting magnetic sublattices formed by the Pr^{3+} and Ru^{4+} ions, respectively. The Curie-Weiss temperature Θ_{CW} exhibits largest negative values for medium Ti contents. Increasing values found for $0 \leq y \leq 0.2$ are caused by increasing antiferromagnetic interactions due to the decrease of inter-atomic distances. The decrease of $|\Theta_{CW}|$ for $y > 0.2$ can be explained by the dominating dilution of the magnetic Ru-centers by non-magnetic Ti-ions and the formation of short-range ordered clusters of dimers as observed for the pure Ti substition. A magnetic phase transition reflecting a Ru–Ru spin pairing in the lt-phase was observed for the samples with $y \leq 0.4$ independent of the Pr-content. While the rare-earth substitution has no direct effect on the Ru-Ru dimerization, the Ti ions impede this process for substitution levels $y \geq 0.4$. The values of T_d change with respect to the individual Pr or Ti concentration. As the Pr and the Ti substitutions do not mutually affect each other, linear changes with both x and y were found for all investigated parameters.

## 5.3. Mn Substitution: La$_2$Ru$_{1-y}$Mn$_y$O$_5$

The substitution of Ru by Mn in perovskite-related oxides leads to a large variety of structural modifications and concomitant changing physical properties. Especially various magnetic phases are observed due to the diversity of possible exchange interactions of Mn and Ru spin moments in these compounds. Furthermore, Ru and Mn can adopt various oxidation states and by this further increase the variability of exchange interactions and magnetic arrangements.

For example, perovskitic SrRu$_{1-x}$Mn$_x$O$_3$ shows a complex magnetic phase diagram [Zha07]. This phase diagram involves a phase transition from a paramagnetic high-temperature phase to a ferromagnetically ordered low-temperature state at low substitution levels x with itinerant Ru 4d electrons and metallic conductivity. In contrast, on the Mn rich side an antiferromagnetically ordered and insulating phase with localized moments with a Néel temperature of approximately 200 K is observed. For intermediate x values spin-glass and cluster-glass phases are found. Cao *et al.* reported a possible quantum critical point (QCP) for $x \approx 0.39$, at which the ferromagnetic ordering turns into an antiferromagnetic arrangement at zero temperature [Cao05]. In addition, a weak external magnetic field-dependent magnetoresistance at low temperatures was reported for the samples with intermediate substitution levels [Zha07]. The partial replacement of Sr by Ca shifts the QCP to $x = 0.2$ and a substitution using trivalent La decreases in general the magnetic phase-transition temperatures [Ohn10, Man98].

A Ru/Mn-substitution series was recently reported for CaCu$_3$Ru$_{4-x}$Mn$_x$O$_{12}$ ($0 \leq x \leq 3$), which belong to the $AA'_3B_4O_{12}$ family of distorted perovskites [Vas07, Cal11]. In this series the ruthenate CaCu$_3$Ru$_4$O$_{12}$ is a Pauli-paramagnet with itinerant charge carriers showing heavy-fermion behavior. For this compound non-Fermi liquid and an intermediate-valence behavior were reported [Kri08, Kri09, Kob04] and further discussed in more detail in Sec. 6.2. On the other hand, the manganite CaCu$_3$Mn$_4$O$_{12}$ is a half-metallic ferromagnet and provides colossal-magnetoresistance properties up to 280 K [Weh01]. The Mn substitution leads to a progressive change of structural and magnetic properties from the ruthenate to the manganite. The Curie temperature behaves proportional to the Mn content.

Layered manganites of lower dimensionality based on the perovskite-related Ruddlesden-Popper phases have also been substituted with Ru. The manganites (La,Sr)$_{n+1}$Mn$_n$O$_{3n+1}$ provide different giant-magnetoresistance properties depending on n, which reflects the dimensionality of the MnO$_6$-octahedra network [Uru95, Mor96]. For $n = 1$ (Sr$_2$Mn$_{0.5}$Ru$_{0.5}$O$_4$) and $n = 2$ (Sr$_3$MnRuO$_7$) the partial substitution of Mn by Ru was reported and phase transitions from a paramagnetic phase with ferromagnetic Curie-Weiss temperature to a cluster-glass and spin-glass phase were observed [Gal02]. Lanthanum containing compounds La$_{1.2}$Sr$_{1.8}$Mn$_{2-x}$Ru$_x$O$_7$ ($n = 2$) with Ru-substitution levels up to $x = 0.5$ show a complex antiparallel magnetic-ordering behavior [Wei02, Sch04].

Magnetic ordering in these compounds is basically caused by the different valence states of Ru^{4+}/Ru^{5+} and Mn^{3+}/Mn^{4+} and by the fact that the electrons behave somewhat in between localized and itinerant. The various d electron configurations lead to a large number of magnetic interactions between the ions and to the reported magnetoresistance effects. The ferromagnetic double-exchange mechanism competes with the antiferromagnetic superexchange resulting in dif-
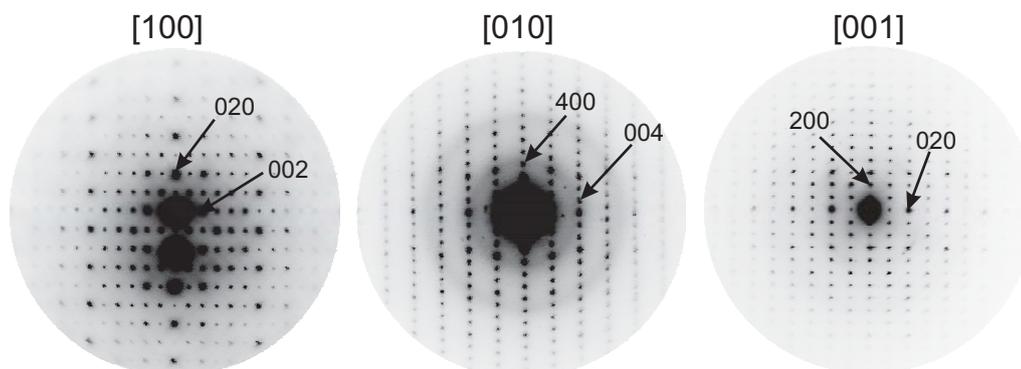
Figure 5.39.: SAED patterns observed for the zone axes [100], [010], and [001] of La$_2$Ru$_{0.75}$Mn$_{0.25}$O$_5$.

ferent magnetic ground states depending also on structural changes.

Motivated by the complex changes of the physical properties caused by Mn substitution in Ru-based oxides, the influence of a partly replacement of Ru by Mn on the singlet ground state of La$_2$RuO$_5$ was investigated and in parts already reported in Refs. [Rie13c, Rie13d]. Similar to the Ti- and rare-earth substitutions a full replacement was not expected, since an isostructural La$_2$MnO$_5$ was not reported yet.

The crystal structure of La$_2$Ru$_{1-y}$Mn$_y$O$_5$ was investigated by XRD and ND at varying temperatures to study in detail the changes caused by the Mn doping and the phase transition. Possible charge ordering of Ru^{4+}/Ru^{5+} and Mn^{3+}/Mn^{4+} was studied using XAS. Based on this the experimental data of the specific heat and magnetic properties were analyzed. In addition, the structural changes correlated to the magnetic dimerization transition were studied to further characterize the different magnetic phases.

5.3.1. Crystal Structure at Room Temperature

The polycrystalline samples were obtained via the citrate route described in Sec. 2.1.3. Traces below 0.5% of LaRuO$_3$ or La$_3$RuO$_7$ impurities were found in analogy to the Ti- and rare-earth substitutions. For $y > 0.25$ distinct amounts of MnO$_2$ were detected indicating the upper limit of Mn incorporation in the La$_2$RuO$_5$ crystal structure. This upper limit will be discussed below with respect to the values obtained from the Ti substitution and the deviations of the ionic radii depending on the Ru and Mn oxidation states.

To investigate the possible existence of superstructures caused by cationic ordering of Ru and Mn, selected area electron diffraction (SAED) patterns were recorded. In Fig. 5.39 the zone axes [100], [010], and [001] of La$_2$Ru$_{0.75}$Mn$_{0.25}$O$_5$ are depicted. The absence of additional reflexes excludes the possible occurrence of Ru/Mn cationic ordering. The extinction rules derived from the patterns are the same as found for pure La$_2$RuO$_5$ and correspond to space group P2$_1$/c. The unit-cell parameters agree with the values found by XRD and ND.

The XRD patterns recorded at room temperature were analyzed by Rietveld refinement. The results show that La$_2$Ru$_{1-y}$Mn$_y$O$_5$ crystallizes in the monoclinic (P2$_1$/c) modification, isostruc-
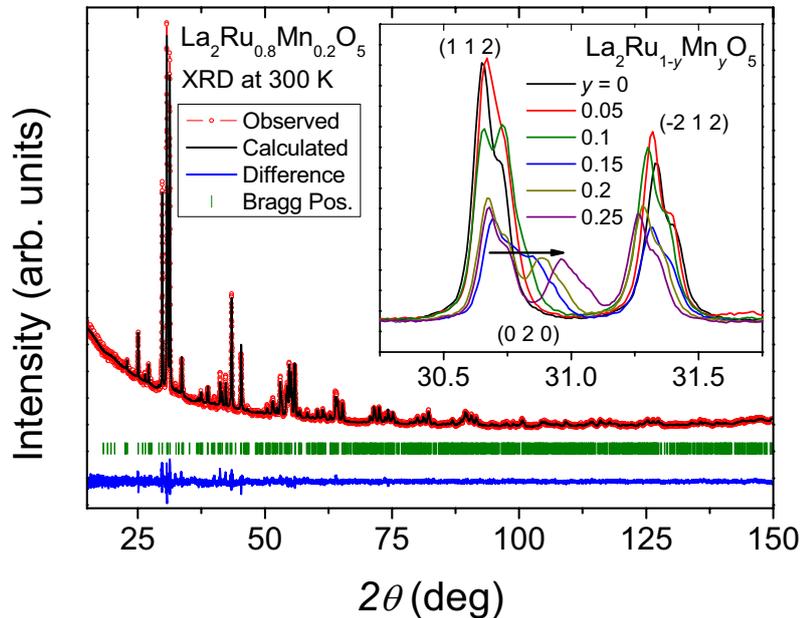
Figure 5.40.: Rietveld refinement of the La$_2$Ru$_{0.8}$Mn$_{0.2}$O$_5$ x-ray diffraction pattern measured with Cu-K$_{\alpha1,2}$ radiation at room temperature. Inset: Detail of the patterns for $y = 0$, 0.05, 0.1, 0.15, 0.2, and 0.25 in the angular range $30.25° \leq 2\theta \leq 31.75°$.

tural to pure La$_2$RuO$_5$ and in agreement with the SAED patterns. As an example of the fit quality, the refinement of La$_2$Ru$_{0.8}$Mn$_{0.2}$O$_5$ is depicted in Fig. 5.40. In the inset the angular range $30.25 \leq 2\theta \leq 31.75°$ is shown in detail for the y values 0, 0.05, 0.1, 0.15, 0.2, and 0.25. The observed peaks at approximately $30.7°$ corresponding to the *hkl* values (1 1 2) and (0 2 0) show an increasing splitting with y. This effect is caused by the decrease of cell parameter b, which shifts the (0 2 0) peak to higher 2θ values. In contrast, the overall change of the cell parameters almost compensates for (1 1 2) and (-2 1 2), which explains the almost constant 2θ values for those peaks. This observation is very similar to the Ti substitution (Sec. 5.2) but differs strongly from the rare-earth substitution (Sec. 5.1) illustrating the different influence of the substituted site on the crystal-structure evolution.

Fig. 5.41 shows the Rietveld refinement of the ND pattern of La$_2$Ru$_{0.75}$Mn$_{0.25}$O$_5$ recorded at 300 K. The very good agreement of the fit verifies that La$_2$Ru$_{1-y}$Mn$_y$O$_5$ is isostructural to pure La$_2$RuO$_5$ at room temperature. Furthermore, no additional peaks belonging to possible superstructures from a cationic ordering were observed. This indicates a completely statistical occupation of Mn on the Ru-sites. The refinement of the Mn occupancy yielded a value of 0.24(2) which is very close to the nominal concentration $y = 0.25$. The Ru/Mn occupation can be obtained with high reliability due to the strongly different scattering lengths of Ru (7.02 fm) and Mn (-3.75 fm),
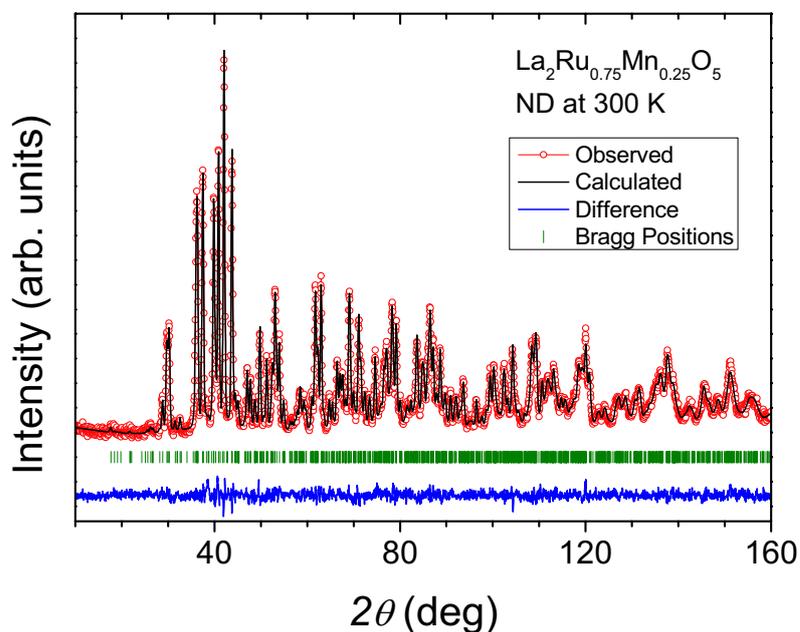
Figure 5.41.: Rietveld refinement of the $La_2Ru_{0.75}Mn_{0.25}O_5$ neutron diffraction pattern measured at 300 K with $\lambda = 1.494$ Å.

while their absorption cross sections are similar [Sea92]. Further detailed results of the Rietveld fits are given in the supplementary information of Ref. [Rie13c].

The cell parameters obtained from the Rietveld analysis of the XRD data are depicted in Fig. 5.42. The unit-cell axes are shown in the left frame (Fig. 5.42a), while the values of β are displayed in the top right frame (Fig. 5.42b). The evolution of the unit-cell parameters of $La_2Ru_{0.75}Mn_{0.25}O_5$ is similar as for the Ti substitution (Sec. 5.2). The a-axis as well as the cell parameter b decrease linearly for increasing y, however, for b the decrease is significantly larger. In contrast, the c-axis and the monoclinic angle β are increasing linearly with y. The most significant changes of the axis lengths are found for the axes b and c due to the Mn incorporation in the $LaRuO_4$-layers, which also induces the increase of β. On the other hand, the observed slight decrease of a results from slightly shorter Ru–O bond lengths in the ab-plane, which is discussed below in more detail.

The distinct changes for b and c are caused by the smaller ionic radius of the Mn ions compared to the Ru ions. A structural stress limit for the b-axis can be assumed to determine the stability of the compound according to $La_{2-x}Ln_xRuO_5$. For $y = 0.25$ the extreme values for all cell parameters are found. The lowest value of ≈ 5.77 Å for b is even smaller than observed for the rare-earth substitution. The largest value for the c-axis is ≈ 8.02 Å, for β it is $\approx 101.1°$, and the values for a remain within the boundaries determined from $La_{2-x}Ln_xRuO_5$ and $La_2Ru_{1-y}Ti_yO_5$ (Sec. 5.1.1 and 5.2.1.1).
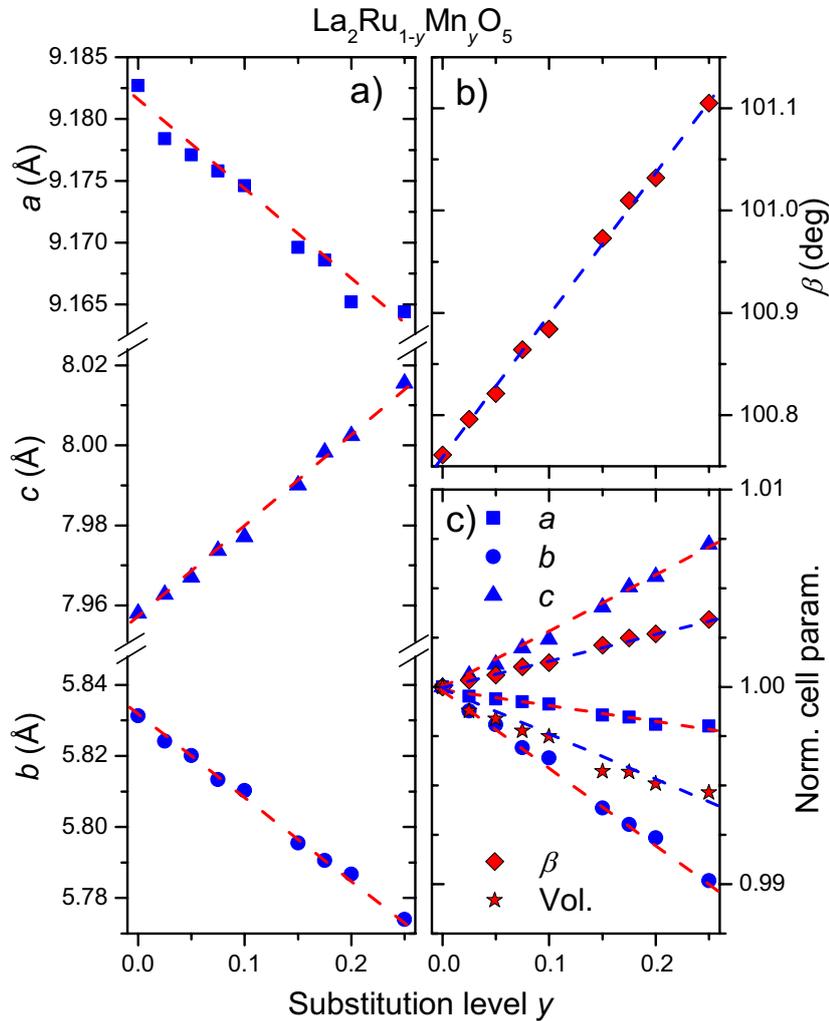
Figure 5.42.: Cell parameters for $La_2Ru_{1-y}Mn_yO_5$ derived from Rietveld analysis of room-temperature powder XRD data. a) Cell parameter a, c, and b. b) Monoclinic angle β. Error-bars are smaller than the size of the symbols. c) Relative change of the unit-cell parameters. The cell parameters of $La_2Ru_{1-y}Mn_yO_5$ were normalized to their corresponding values of La_2RuO_5. All dashed lines are guides to the eye.

The relative changes of the unit-cell parameters are shown in Fig. 5.42c. The values were obtained by normalizing the cell parameters of $La_2Ru_{1-y}Mn_yO_5$ to their corresponding value for pure La_2RuO_5. As discussed above, the parameters b and c show the strongest y dependency with changes of roughly ± 1 %, while a only slightly decreases by 0.2 %. The rather small changes ranging below 1 % indicate the minor effect of differences between the Ru and Mn ionic radii. The small decrease of the unit-cell volume by 0.5 % is mainly due to the slightly increasing monoclinic angle β. The described changes are different to the unit-cell evolution of $La_{2-x}Ln_xRuO_5$,
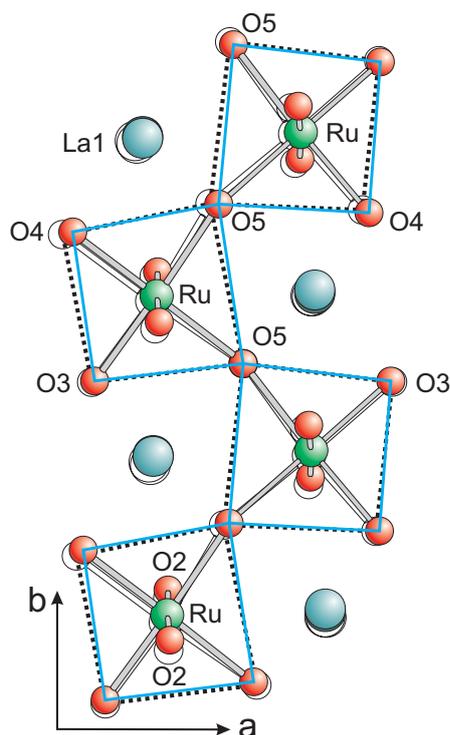
Figure 5.43.: Ru-O coordination in the $LaRuO_4$-layers projected along the c-axis for La_2RuO_5 (transparent) compared to $La_2Ru_{0.75}Mn_{0.25}O_5$ (opaque) as derived from ND data. The dashed ($y = 0$) and cyan solid ($y = 0.25$) lines mark the ab-plane of the RuO_6 octahedra.

where the volume decrease is mainly caused by the a-axis shortening. On the other hand, in $La_2Ru_{1-y}Ti_yO_5$ the volume reduction is determined by the shortening of the b-axis and the simultaneous increase of β.

A detailed discussion of the structural changes caused by the Mn-substitution can be based on the results from the Rietveld-analysis of the ND data. The values for the ht-phase of La_2RuO_5 were taken from [Ebb05] and are compared to $La_2Ru_{0.75}Mn_{0.25}O_5$. The observed changes of the crystal structure are displayed in Fig. 5.43. The notation of the oxygens introduced earlier in Sec. 5.1.1 is used to compare the Ru–O bond lengths and angles. The octahedra of La_2RuO_5 (transparent) and $La_2Ru_{0.75}Mn_{0.25}O_5$ (opaque) are shown projected along the c-axis and fixed on the same central oxygen ion (O5) to increase the comparability of structural deviations. The distorted square-shaped Ru–O coordination in the ab-plane is marked by the dashed (La_2RuO_5) and solid cyan ($La_2Ru_{0.75}Mn_{0.25}O_5$) lines. It shows that the ab-plane coordination within the octahedra changes only very little. Nevertheless, it is obvious that the distance between top and bottom O5 atoms is shorter for the Mn substituted sample reflecting the b-axis decrease. This is supported by the increase of the Ru–O5–Ru angle by roughly $2°$ from $155.4°$ to $157.5°$, which becomes visible between the top two octahedra in Fig. 5.43. The La atoms remain on almost identical positions in the rhombic-shaped space between the rows of octahedra along the c-direction.
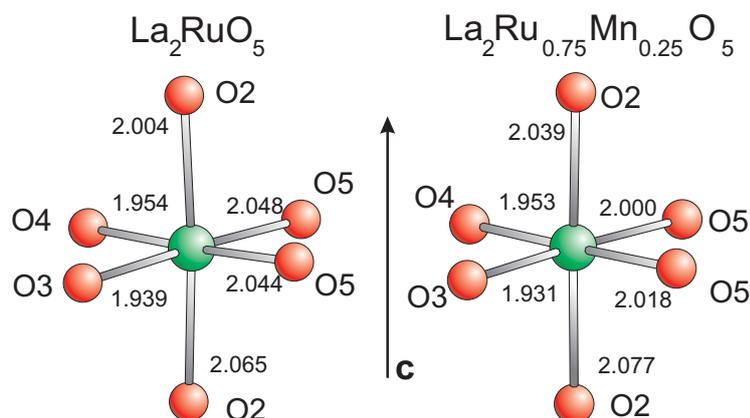
Figure 5.44.: Comparison of the octahedral coordination of Ru in La$_2$RuO$_5$ (left) and Ru/Mn in La$_2$Ru$_{0.75}$Mn$_{0.25}$O$_5$ (right). The oxygen atoms are labelled corresponding to the previous sections. Bond lengths are given in Å.

Furthermore, while the O2–Ru–O2 angle remains constant at roughly 178.5°, the Ru–O2–Ru angle increases slightly from 152.8° ($y = 0$) to 153.6° ($y = 0.25$). This explains the observed increase of the c-axis for La$_2$Ru$_{0.75}$Mn$_{0.25}$O$_5$ compared to pure La$_2$RuO$_5$.

The (Ru/Mn)O$_6$ octahedra are depicted in Fig. 5.44 for La$_2$RuO$_5$ (left) and La$_2$Ru$_{0.75}$Mn$_{0.25}$O$_5$ (right). To increase clarity only the label Ru is used in the following for the mixed occupation of Ru and Mn on the Ru-site. In the ab-plane O3 and O4 are pointing towards the LaO-layers, while the two O5 ions connect the corner sharing octahedra in a zig-zag arrangement. Parallel to the c-direction the octahedra are linked by the two O2 ions. The Ru–O bond-length modifications are in agreement with the changes observed for the cell parameters b and c. The Ru–O2 distances increase according to c and the Ru–O5 distances decrease following the evolution of b. The obtained changes of Ru–O bond lengths result in a stronger tetragonal distortion of the octahedra for La$_2$Ru$_{0.75}$Mn$_{0.25}$O$_5$. This behaviour would be expected for the Jahn-Teller active Mn^{3+} ions, but is not anticipated for Mn^{4+} with a $3d^3$ configuration in octahedral coordination, which is expected to favor a higher symmetry. In addition, the bond lengths for Ru–O3 and Ru–O4 also become slightly shortened in the range of several mÅ.

The incorporation of Mn also affects the Ru–Ru distances. For $y = 0$ similar values of approximately 3.98 Å for the Ru–Ru distance in c-direction and ab-plane were reported [Ebb05]. For $y = 0.25$ the Ru–Ru distance parallel to c is elongated to roughly 4.01 Å, while the one in the ab-plane is shortened to 3.94 Å. These values are close to the Ru–Ru distances in the lt-phase of La$_2$RuO$_5$ (1.5 K), where values of 3.87 Å/3.92 Å and 4.04 Å/4.05 Å were observed. On the other hand, in the lt-modification of La$_2$RuO$_5$ the bond lengths are alternating in both b- and c-direction (see Sec. 4.1.1), while in La$_2$Ru$_{0.75}$Mn$_{0.25}$O$_5$ no alternations occur due to the higher crystallographic symmetry. It has been argued in the previous sections that the alternating short and long Ru–Ru distances are closely related to the spin-dimerization phenomena in lt-La$_2$RuO$_5$. Thus, the magnetic exchange interactions are expected to vary and probably cause a different magnetic
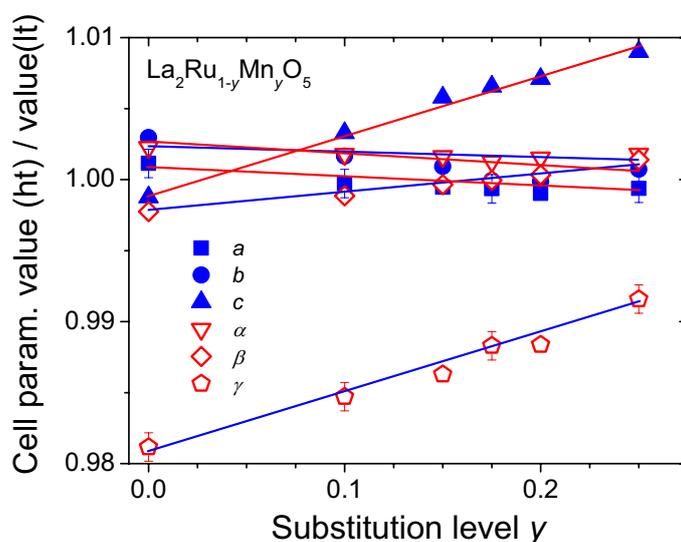
Figure 5.45.: Comparison of the unit-cell parameters of the high-temperature (300 K) and the low-temperature (100 K) phase of La$_2$Ru$_{1-y}$Mn$_y$O$_5$. Values of α and γ are 90° in the ht-phase.

phase transition for Mn-substituted samples.

BVS calculations were performed using the neutron-diffraction data for La$_2$Ru$_{0.75}$Mn$_{0.25}$O$_5$. The obtained valences of the ions in the LaO-layers amount to +3.2 for La and -2.4 for oxygen caused by smaller La-sites than calculated from typical interatomic distances of La^{3+} and O^{2-} in agreement with the results for pure, rare-earth, and titanium substituted La$_2$RuO$_5$. For the LaRuO$_4$-layers the valences were slightly smaller than the expected nominal ones, Ru provides +3.9, La +2.9, and O -1.9, respectively. It has to be mentioned that by the BVS calculation the Mn oxidation state was determined to +3.1, which can be explained by the comparable ionic radius of the high-spin state of Mn^{3+}: 0.645 Å to the Ru^{4+} ion (0.62 Å) in octahedral coordination [Sha76]. Assuming a constant oxidation state of +4 on the Ru-site, which was already reported for the Ti substitution (Ti^{4+}: 0.605 Å), the Mn^{4+} ion radius is significantly smaller: 0.53 Å. As mentioned above, the valence is determined from a comparison of the bond lengths between Mn and the coordinating O atoms. In La$_2$Ru$_{0.75}$Mn$_{0.25}$O$_5$ larger distances than expected for Mn^{4+}–O are present and, thus, artificially reduce the oxidation state. However, with respect to the described local changes in the crystal structure upon substitution, which are similar to the Ti substitution, a +4 oxidation state of Mn seems to be more plausible. This is discussed in the sections 5.3.3 and 5.3.4, in which the XANES and magnetic susceptibility measurements are outlined.

### 5.3.2. Low-Temperature Crystal Structure

As a consequence of the structural phase transition to the triclinic space group P$\bar{1}$, changes of the interatomic distances and unit-cell parameters were observed for pure La$_2$RuO$_5$. Due to bond-
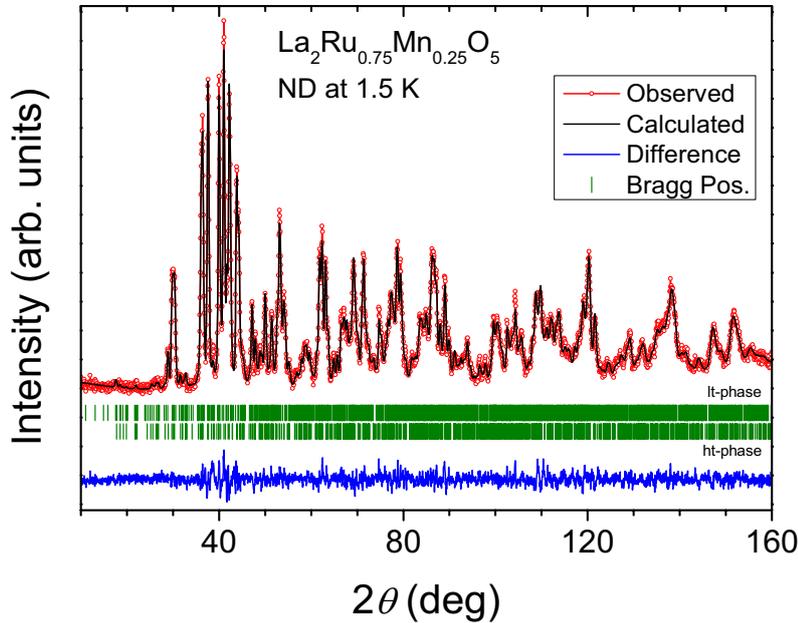
Figure 5.46.: Rietveld refinement of the La$_2$Ru$_{0.75}$Mn$_{0.25}$O$_5$ ND pattern measured at 1.5 K with $\lambda =$ 1.494 Å. Bragg positions for both ht- and lt-phase are marked by green vertical dashes.

length and angle variations, the magnetic exchange between the Ru ions is influenced and leads to the singlet ground state with dimerized neighboring Ru $S = 1$ spins. In the previous section the influence of the Mn substitution on the ht-phase structure was discussed. From the observed changes it can be expected that also the low-temperature crystal structure as well as the phase transition are affected.

To study the effect of the Mn substitution on the structural phase transition, the cell parameters at room temperature and 100 K were compared. In pure La$_2$RuO$_5$ the values for a, b, and α decrease during the transition from ht- to lt-modification and, in turn, c, β, and γ increase. Except for γ, which decreases by 2 % during the phase transition, all other parameters show small deviations of less than 0.3 %. In Fig. 5.45 the ht-phase data at 300 K normalized to the lt-phase values at 100 K are shown as a function of the Mn concentration y. For $y = 0, 0.1$, and 0.175 the values were obtained from patterns recorded on a laboratory diffractometer (STOE STADI P), while for $y = 0.15, 0.2$, and 0.25 synchrotron-radiation diffraction patterns were used. All parameter ratios change linearly with increasing substitution level. In the case of a, b, α, and β for concentrations $y \geq 0.15$ the values are close to unity indicating that the phase transition barely affects these parameters. On the other hand, for c and γ a different behavior is observed. Similar to the Ti substitution the low-temperature value of γ is reduced. With increasing Mn content the differences between ht- and lt-modifications become smaller, but do not vanish completely like in the case
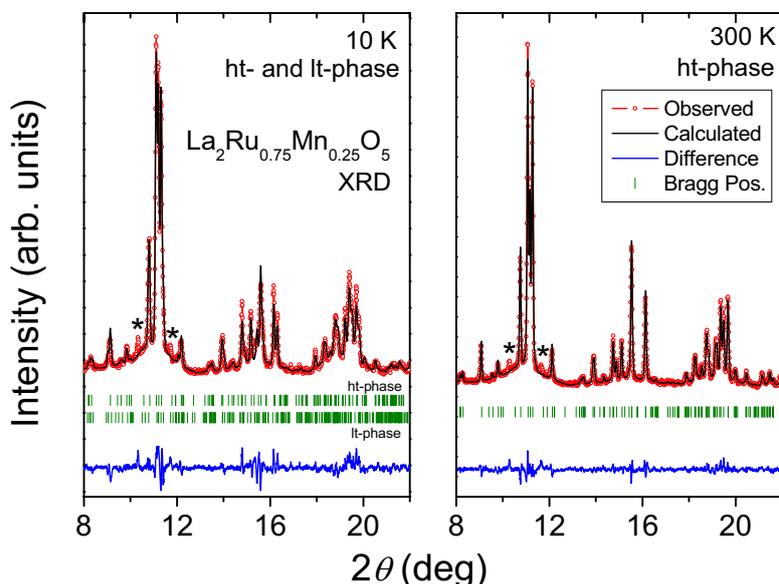
Figure 5.47.: Rietveld refinement of the $La_2Ru_{0.75}Mn_{0.25}O_5$ XRD pattern measured at 10 K (left) and 300 K (right) at the beamline B2 of HASYLAB using $\lambda = 0.56285$ Å. The asterisks mark an impurity phase.

of Ti doping. For the *c*-axis the differences between ht- and lt-phase increase with higher Mn concentration from roughly 1.00 to 1.01 for $y = 0.25$. It should be noted that although the observed changes seem to be rather small, they are clearly significant as indicated by the error-bars shown in Fig. 5.45. Despite the difference in the behavior to the Ti substituted samples, the smaller Mn^{4+} ions similarly affect the crystal structure, but these changes do not suppress the structural transition in total. More reasonably the emerging structural modifications determine a solubility limit for Mn in La_2RuO_5.

The structural changes between the ht- and lt-phase were also determined by Rietveld-analysis of ND data for $La_2Ru_{0.75}Mn_{0.25}O_5$. In Fig. 5.46 the refinement result of the data recorded at 1.5 K is shown. A good agreement of measured data and Rietveld-fit is achieved, but surprisingly a mixture of both the monoclinic ht- and the triclinic lt-modification is found at 1.5 K. This is in contrast to the other Mn substituted samples, where roughly 20 K below the transition temperature only the lt-phase is present. For $La_2Ru_{0.75}Mn_{0.25}O_5$ a ratio of approximately 55 % ht- and 45 % lt-modification was found at 1.5 K. Very similar results were obtained from the synchrotron XRD data analysis. The same ratio of ht- and lt-phase was observed for the data recorded at 10 K, which was the lowest temperature applied for the synchrotron XRD measurements. In Fig. 5.47 the refinement results for 10 K (left) and 300 K (right) are depicted. While at room temperature only the ht-phase is present, at 10 K data a mixture of both modifications is observable as indicated

by additional peaks, which are characteristic for the lower symmetry of the triclinic unit cell. The fit quality of the low-temperature patterns is slightly worse, as can be seen by the larger amplitude of the difference curve and, in turn, higher residual values. This is not surprising taking into account the significantly increased number of fit parameters and strong correlations.

From the ND data at 1.5 K a Mn occupancy of 0.27(2) is obtained for the ht-phase and 0.20(2) for the lt-phase. Weighted with their fractions 55 % and 45 %, respectively, an average occupancy of 0.24(2) is achieved in excellent agreement with the nominal value of 0.25 and also the room-temperature results. The fraction of 20 % Mn probably indicates an upper substitution limit, which allows the transformation to the lt-modification and, hence, drives the dimerized state. But strikingly, at 300 K no remarkable splitting or broadening of the diffraction peaks can be observed in the ND and XRD pattern. Such a splitting would indicate the presence of two fractions with slightly varying Mn occupancy. Furthermore, the crystallites investigated with SAED showed no additional reflexes or a noticeable broadening and energy dispersive x-ray spectroscopy did not yield varying Mn incorporation within one crystallite, either.

To study the temperature-depending phase evolution, the relative fractions of the ht- and lt-phase for La$_2$Ru$_{0.75}$Mn$_{0.25}$O$_5$ from the Rietveld analyses are depicted in Fig. 5.48. The ND patterns were recorded during continuous cooling. In addition, synchrotron XRD patterns were analyzed. The values for both datasets are in good agreement and show smooth changes starting at 120 K, which saturate below 50 K with a fraction of roughly 45 % lt-phase. At 150 K a fraction of approximately 11 % lt- and 89 % ht-phase was found in the ND patterns. In contrast, the XRD data document the absence of the lt-modification above 130 K. Due to the better signal-to-noise ratio for the XRD patterns this result is more reliable.

The incomplete phase transition for La$_2$Ru$_{0.75}$Mn$_{0.25}$O$_5$, which is apparently completed at 50 K, is not easy to explain. A inhomogeneous distribution of the Mn-ions comes to mind. On the other hand, such a chemical inhomogeneity should result in detectable splittings or at least broadening of the diffraction peaks (especially since the cell parameters were found to significantly change with *y*). Surprisingly no sign of such features were observed, not even in the synchrotron data. This finding indicates that possible inhomogeneities can only exist on a very local scale. It is likely that due to the Mn incorporation the formation of Ru-Ru spin dimers becomes locally suppressed (similar to the Ti substitution in Sec. 5.2.1) as discussed later. If the formation of such dimers is the driving force for the structural transition it is reasonable that it remains incomplete.

The observed phase separation is rather unusual and, therefore, a detailed structural analysis was carried out using the ND pattern of La$_2$Ru$_{0.75}$Mn$_{0.25}$O$_5$ recorded at 1.5 K and 300 K. This offers the opportunity to derive bond lengths and angles for both modifications simultaneously at low temperatures and compare the values to the results of the room-temperature measurements. The values for the Ru–O bond lengths, the Ru–Ru distances, and the O–Ru–O and Ru–O–Ru bond angles of the 1.5 K measurement are listed in Tab. 5.9. The oxygens O3 and O4 are pointing towards the LaO-layers. In addition, the O2 bridge the octahedra in *c* direction and the O5 connect them in the *ab* plane. The denotation of the oxygen sites deviates from the previously used ones in Sec.4.1. However, to increase comparability a similar notation used in [Ebb05] for pure La$_2$RuO$_5$ was applied, where the in the lt-phase splitted Ru-site is labelled Ru and Ru(a).
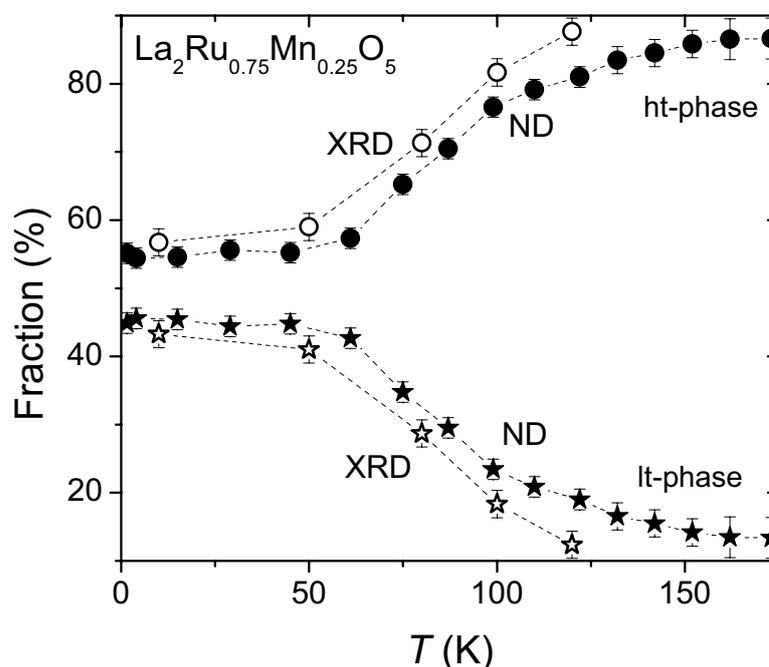
Figure 5.48.: Temperature dependence of the fraction of the ht- and lt-modification in $La_2Ru_{0.75}Mn_{0.25}O_5$ from synchrotron XRD and ND data sets.

In the ht-modification the $(Ru/Mn)O_6$ octahedra document a typical thermal contraction from 300 K to 1.5 K characterized by slightly shortened Ru–O bonds and almost constant angles. In the lt-phase distinct deviations in the coordination of the emerging two Ru-sites (Ru and Ru(a)) can be observed. In comparison with the structural data of pure La_2RuO_5 the octahedral deformation is even more pronounced due to the Mn substitution. The O2–Ru–O2 angle of 179.02° indicates a small degree of deformation of the octahedra for the ht-phase of $La_2Ru_{0.75}Mn_{0.25}O_5$. In the lt-phase, on the other hand, the angle decreases to 175.83° for Ru and even more drastically to 166.03° for Ru(a) due to the pronounced off-center Ru-site in this octahedron. In agreement with the off-center position of Ru the Ru–O bond lengths in the *ab*-plane become systematically shorter for O3 and O4 by approximately 0.1 Å, while they elongate by the same value for O5. The smaller ionic radius of Mn^{4+} compared to Ru^{4+} allows a such larger displacement of the central ion in the octahedra.

With respect to the distinctly reduced O2–Ru(a)–O2 angle, the shortest Ru–Ru distance is also found along *c* (marked with ** in Tab. 5.9), however, this is not the superexchange path corresponding to the Ru singlet formation. According to Anderson, Kanamori, and Goodenough the superexchange-interaction strength strongly depends on the metal-oxygen-metal bonding angles, which can be expressed by Eq. 4.1. As mentioned above the ferromagnetic exchange J_{90} is con-

Table 5.9.: Ru–O bond lengths and Ru–O–Ru bond angles in the ht- and lt-modification of La$_2$Ru$_{0.75}$Mn$_{0.25}$O$_5$ at 1.5 K. Errors amount to roughly 30 mÅ for the bond lengths and to 0.8° for the bond angles, respectively.

ht-phase		lt-phase	
Bond	d(Å)	Bond	d(Å)
Ru–O2	2.044	Ru–O2	2.024
Ru–O2	2.075	Ru–O2(a)	2.164
Ru–O3	1.915	Ru–O3	2.002
Ru–O4	1.936	Ru–O4(a)	1.956
Ru–O5	1.978	Ru–O5	2.003
Ru–O5	2.003	Ru–O5(a)	1.884
		Ru(a)–O2	1.921
		Ru(a)–O2(a)	2.070
		Ru(a)–O3(a)	1.762
		Ru(a)–O4	1.854
		Ru(a)–O5	2.152
		Ru(a)–O5(a)	2.167
Ru–Ru (*ab*)	3.897	Ru–Ru(a)	4.001 (*)
		Ru–Ru(a)	4.060
Ru–Ru (*c*)	4.006	Ru–Ru(a)	3.799 (**)
		Ru–Ru(a)	4.144
Angle	ϑ (°)	Angle	ϑ (°)
O2–Ru–O2	179.02	O2–Ru–O2(a)	175.83
		O2–Ru(a)–O2(a)	166.03
O5–Ru–O5	96.86	O5–Ru–O5(a)	93.17
		O5–Ru(a)–O5(a)	91.58
Ru–O2–Ru	153.12	Ru–O2–Ru(a)	148.78 (**)
		Ru–O2(a)–Ru(a)	156.45
Ru–O5–Ru	156.45	Ru–O5–Ru(a)	155.47
		Ru–O5(a)–Ru(a)	162.13 (*)

sidered to be significantly smaller than the antiferromagnetic J_{180}. The corresponding angle ϑ for Ru–O2–Ru for the shortest Ru–Ru distance (**) is decreasing from 153.6° at room temperature to 148.78° at 1.5 K, reflecting a strongly decreasing antiferromagnetic superexchange compared to the other Ru–O–Ru paths. In contrast, in the *ab*-plane one Ru–O–Ru angle increases to 162.13° (marked with * in Tab. 5.9) and additionally corresponds to the second shortest Ru–Ru distance of 4.001 Å. Along this Ru–O–Ru path the singlet formation is very likely preferred due to the increasing antiferromagnetic superexchange similar to the results of pure La$_2$RuO$_5$. This finding shows that the singlet formation depends stronger on the Ru–O–Ru angle than on the Ru–O–Ru
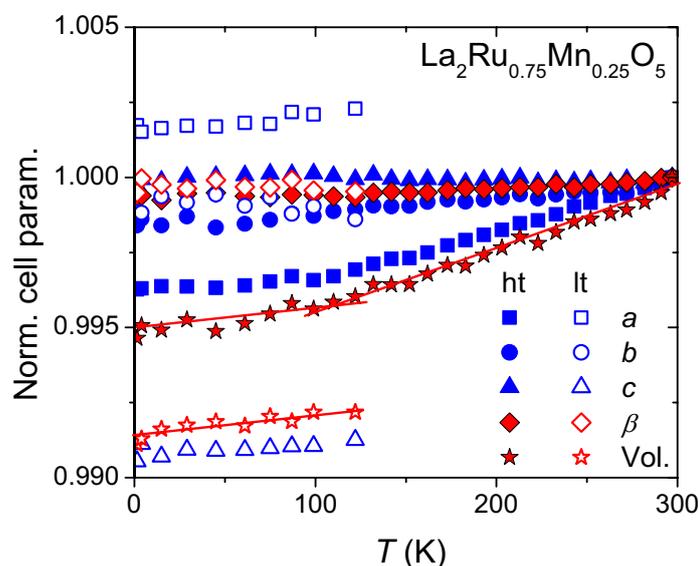
Figure 5.49.: Relative change of the ht- (full symbols) and lt-phase (open symbols) unit-cell parameters of La$_2$Ru$_{0.75}$Mn$_{0.25}$O$_5$ from ND pattern analysis. For better comparability the values at each temperature step are normalized to their corresponding ht-modification values at 300 K. Error-bars are smaller than the size of the symbols.

distances, which do not change enough to explain the effect. Applying the superexchange description, the observed magnetic properties concerning the dimerization transition in La$_2$Ru$_{1-y}$Mn$_y$O$_5$ can be well explained. The more complex Ru-Mn interactions can only be interpreted together with detailed magnetic studies shown in Sec. 5.3.4.

Based on the ND patterns, the temperature-dependent changes of the cell parameters were investigated for La$_2$Ru$_{0.75}$Mn$_{0.25}$O$_5$. Due to the incomplete phase transition the unit-cell parameters of the ht-modification are available for the entire temperature range from 300 K to 1.5 K. The lt-phase data were obtained for $T < 120$ K. To improve comparability, the different parameters for ht- and lt-phase were normalized to the room-temperature values as depicted in Fig. 5.49. The data for α and γ were omitted, since in the ht-modification these amount to 90° by definition of the unit-cell symmetry. For the ht-phase the thermal contraction of the unit-cell volume by 0.5° is mainly a result of the shortening of the a-axis (i.e. along the alternating layering of the LaO- and the LaRuO$_4$-layers). This preferred contraction direction is understandable since similar to the rare-earth substitution it is easier to change the interlayer distance than to stretch or compress a layer of corner-sharing octahedra. The unit-cell volume decreases almost linearly between 300 K and 50 K with a slightly reduced slope down to 1.5 K (marked by dashed lines in Fig. 5.49). This is a typical behavior caused by the increasing rigidity of solids at low temperatures as already observed for La$_2$Ru$_{0.55}$Ti$_{0.45}$O$_5$ (Sec. 5.2.1.1). From the linear part above 80 K the thermal expansion
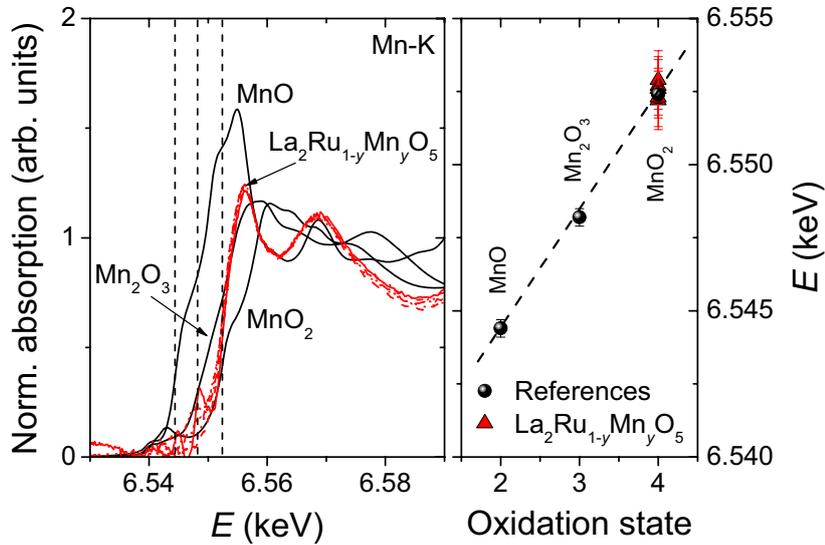
Figure 5.50.: Left: Normalized Mn-K absorption spectra of reference manganese oxides and selected La$_2$Ru$_{1-y}$Mn$_y$O$_5$ samples ($y = 0.05, 0.1, 0.15, 0.2, 0.25$). The dashed vertical lines mark the edge energy of the reference oxides reflecting the valences +2, +3, and +4. Right: Mn valence of the samples as determined from the first derivative of the Mn-K XANES spectra.

was determined to $\alpha_c = 20 \cdot 10^{-6}$ K^{-1}, which is in a typical range for oxides and almost identical to La$_2$Ru$_{0.55}$Ti$_{0.45}$O$_5$. For the lt-modification the increases/decreases of the corresponding cell parameters caused by the structural transition is visible. For both phases similar relative changes of the cell parameters are observed with decreasing temperature. Below 100 K the slope of the lines indicate the volume change, which reduces the thermal expansion factor to $\alpha_{c,\mathrm{lt}} = 5 \cdot 10^{-6}$ K^{-1}.

5.3.3. Ru- and Mn-Valence Determination Using XANES

For the interpretation of the magnetic properties and structural changes the determination of the oxidation states of Mn and Ru in La$_2$Ru$_{1-y}$Mn$_y$O$_5$ is required, since both elements can adopt different valences in oxides (e.g. Mn^{2+}, Mn^{3+}, Mn^{4+}, and Ru^{3+}, Ru^{4+}, Ru^{5+}). This would allow charge ordering in La$_2$Ru$_{1-y}$Mn$_y$O$_5$. Very often mixed valences of Mn^{3+}/Mn^{4+} and Ru^{4+}/Ru^{5+} are found in Mn substituted ruthenates explaining the observed complex magnetic phase diagram and phase segregation. Alternatively, both Mn- and Ru-ions may be tetravalent.

XANES measurements for selected La$_2$Ru$_{1-y}$Mn$_y$O$_5$ samples and reference oxides with known oxidation states and similar octahedral coordination were performed. In Fig. 5.50 the normalized absorption spectra at the Mn-K edge are shown in the left frame. The spectra of the reference oxides MnO (Mn^{2+}), Mn$_2$O$_3$ (Mn^{3+}), and MnO$_2$ (Mn^{4+}) are depicted and dashed lines mark the corresponding edge energies, which were determined from the first maxima of the first
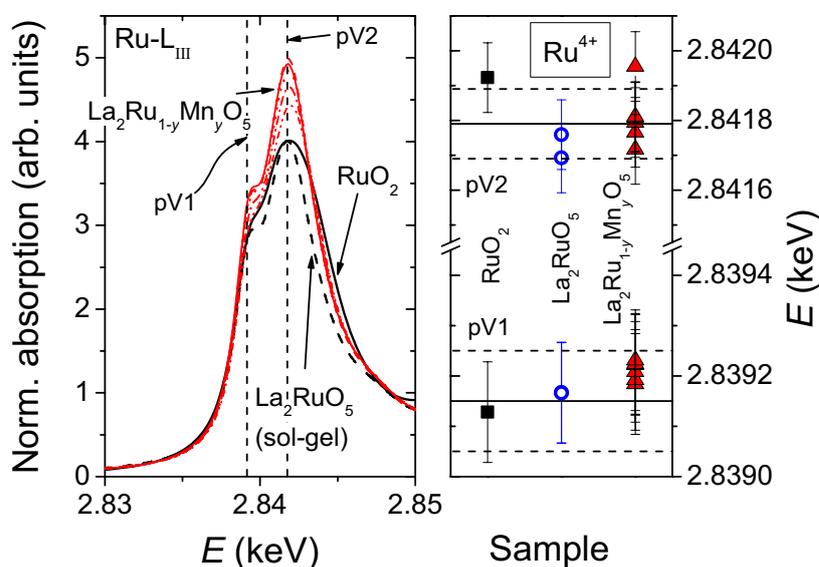
Figure 5.51.: Left: Normalized Ru-L$_{III}$ absorption spectra of reference oxides and selected La$_2$Ru$_{1-y}$Mn$_y$O$_5$ samples ($y = 0.025, 0.05, 0.1, 0.15, 0.2, 0.25$). The dashed lines mark the positions of the two pseudo-Voigt fit maxima (pV1 and pV2). Right: Ru valence determined from the fit of the first derivative of the Ru-L$_{III}$ XANES. The symbols represent the energies of the pseudo-Voigt peak-fit maxima. The horizontal solid lines indicate the Ru^{4+} energy determined from the references (see text).

derivatives of the spectra [Gar10, Bri01]. The measurements of the La$_2$Ru$_{1-y}$Mn$_y$O$_5$ samples ($y = 0.05, 0.1, 0.15, 0.2, 0.25$) were repeated four times and averaged to improve the signal-to-noise ratio. This averaging was necessary due to the low Mn content of some samples and the high absorption caused by the La-L$_I$ edge (6266.3 eV) that is leading to a high background at the Mn-K edge (6539.0 eV) [Bea67].

In the right frame of Fig. 5.50 the obtained edge energies for La$_2$Ru$_{1-y}$Mn$_y$O$_5$ are compared with the values of the reference compounds. The energy increases linearly with the Mn oxidation state with a slope of roughly 4 eV per oxidation number. The edge positions of La$_2$Ru$_{1-y}$Mn$_y$O$_5$ agree well with the one of the Mn^{4+} reference. No significant difference between the spectra of the different Mn substituted samples could be found. In conclusion, the Mn-ions in La$_2$Ru$_{1-y}$Mn$_y$O$_5$ clearly have the oxidation state +4.

For the Ru valence determination RuO$_2$ and unsubstituted La$_2$RuO$_5$ (from sol-gel and solid-state synthesis) were used as reference material as well as a number of other ruthenates, all possessing an oxidation number of +4 (see e.g. Sec. 5.2.1.2 and Sec. 6.2.3). In the left frame of Fig. 5.51 normalized spectra of the Ru-L$_{III}$ absorption edge are shown. In contrast to the Mn-K edge spectra the Ru-L$_{III}$ absorption edge needed to be recorded only once. The determination of the edge energy was performed by fitting the first derivative of the XANES spectra (see Sec. 2.3.1). For
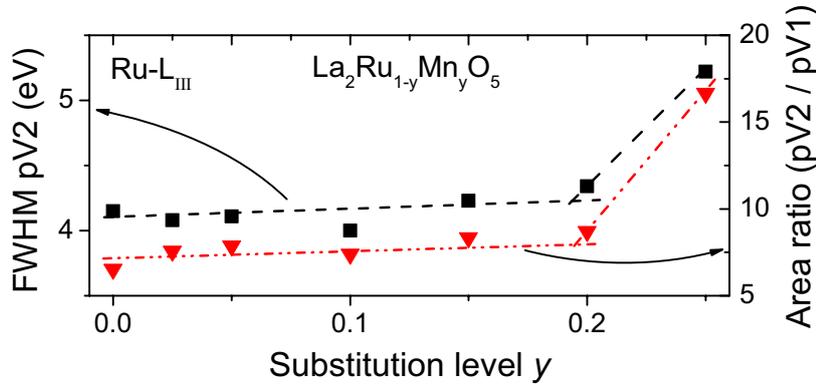
Figure 5.52.: FWHM of the second pseudo-Voigt peak and area ratio of both peaks obtained from the fit of the normalized Ru-L$_{III}$ absorption spectra.

the reference compounds the obtained energies of the maxima of the two pseudo-Voigt functions are marked by the dashed lines in the left frame of Fig. 5.51 (denoted as pV1 and pV2). The peak maxima of all spectra visibly exhibit very similar energies.

In the right frame of Fig. 5.51 the horizontal solid lines mark the peak positions for the references. The obtained values are within experimental uncertainties (shaded area) in agreement with the data reported in Sec. 5.2.1.2 and Sec. 6.2.3. The peak energies for the La$_2$Ru$_{1-y}$Mn$_y$O$_5$ samples ($y = 0.025, 0.05, 0.1, 0.15, 0.2, 0.25$) reveal a valence of +4 within the determined error range of the references. In addition, similar to the results for the Ti substitution shown in Sec. 5.2.1.2 the energy spacing between the two pseudo-Voigt maxima is in good agreement with the value of 2.6(1) eV typically found for Ru^{4+} [Ebb01].

For La$_2$Ru$_{0.75}$Mn$_{0.25}$O$_5$ absorption spectra for both edges Mn-K and Ru-L$_{III}$ were also measured for lower temperatures down to 110 K, which is significantly below the transition temperature. The spectra remain almost identical for all temperatures indicating constant valence and the absence of a charge ordering due to the phase transition. It should be mentioned that the edge shape was not influenced by the minor structural changes occurring during the cooling, an effect which was also observed for pure La$_2$RuO$_5$.

As described for La$_2$Ru$_{1-y}$Ti$_y$O$_5$ (Sec. 5.2.1.2) and La$_{2-x}$Sr$_x$Cu$_{1-y}$Ru$_y$O$_{4-\delta}$ [Ebb01], the full width at half maximum of the two pV peaks utilized for the Ru-L$_{III}$ fit can be used to estimate the distortion of the RuO$_6$ octahedra. While the FWHM of pV1 (which can be assigned to a transition into empty orbitals of predominantly t_{2g}-character) remains almost constant (≈ 1.8 eV), the second pV peak (transition to e_g-type orbitals) broadens with increasing Mn substitution level. The FWHM of pV2 (squares in Fig. 5.52) of pure La$_2$RuO$_5$ amounts to roughly 4.2 eV, which is significantly smaller than the approximately 6 eV observed for RuO$_2$ and La$_{2-x}$Sr$_x$Cu$_{1-y}$Ru$_y$O$_{4-\delta}$ [Ebb01]. With increasing Mn substitution level, the FWHM of La$_2$Ru$_{1-y}$Mn$_y$O$_5$ increases slightly

until $y = 0.2$, while for $y = 0.25$ a strong broadening is observed. In addition, the ratios of the peak areas pV2/pV1 (red circles in Fig. 5.52) increase slowly between $0 \leq y \leq 0.2$ from approximately 6.5 to 8.7 and then reveals a strong increase to 16.7 for $y = 0.25$. For comparison, the La$_{2-x}$Sr$_x$Cu$_{1-y}$Ru$_y$O$_{4-\delta}$ samples provide a ratio of roughly 30 similar to e.g. RuO$_2$ [Ebb01]. The increased ratio for La$_2$Ru$_{0.75}$Mn$_{0.25}$O$_5$ corresponds to the larger distortion of the octahedra. The Ru–O bonds in c-direction were found to be elongated compared to the very similar bond lengths in the ab-plane. The increasing quasi-tetragonal distortion can be explained taking into account the size of the Mn^{4+} ion (0.53 Å), which is too small for the Ru-site (Ru^{4+}: 0.62 Å) and, therefore, leads to a displacement similar to the situation found e.g. in BaTiO$_3$.

In summary, the oxidation states of both Mn and Ru were determined to be +4 without a charge ordering. This result is used for the interpretation the magnetic properties discussed in the subsequent section.

5.3.4. Magnetic Properties

The substitution of Ru by Mn directly affects the observed magnetic properties in La$_2$Ru$_{1-y}$Mn$_y$O$_5$. The almost completely suppressed magnetic susceptibility in the lt-phase of pure La$_2$RuO$_5$ originates from the compensation of the magnetic moments by an antiparallel pairing of the $S = 1$ spin moments of the Ru^{4+} ions forming a singlet ground state. The Mn ions are also tetravalent with a $3d^3$ electron configuration and a magnetic spin moment of $S = 3/2$. The incorporation of Mn^{4+} with its larger magnetic moment leads to new magnetic features as shown in Fig. 5.53.

In the top and middle frame of Fig. 5.53a, respectively b, the temperature depending magnetic susceptibilities $\chi = M/H$ are depicted for field cooled conditions at $H = 1$ kOe. In Fig. 5.53c the corresponding inverse susceptibility is shown. Above 190 K all samples exhibit a paramagnetic behavior. The characteristic step of the Ru-spin dimerization transition for La$_2$RuO$_5$ denoted as (1) in Fig. 5.53b is evident for the samples with lower Mn substitution levels. With increasing y it becomes somewhat narrower and the step height decreases. The low temperature paramagnetic Curie-like increase of χ denoted (2) can very probably be ascribed to a small fraction of uncoupled Ru and Mn spin moments or maybe the residual moment of an Ru-Mn pair. The unusual (ferromagnetic) increase of χ (3) for the samples with higher substitution levels ($y \geq 0.15$) is best visible in Fig. 5.53a. The curves (3) display an increasing transition temperature with y for this feature indicated by the horizontal arrow. The increase possibly stems from the rresidual moment of uncompensated antiparallel aligned and unequal Ru and Mn spin moments. In the susceptibility for $y = 0.10$ besides the dimerization step (1) an anomaly ascribed to effect (3) at roughly 40 K can be seen in Fig. 5.53b. Furthermore, the Ru-spin dimerization becomes increasingly suppressed with y until it is completely vanishing for La$_2$Ru$_{0.75}$Mn$_{0.25}$O$_5$. In Fig. 5.53c the upturn below 170 K in $1/\chi$ indicating the dimerization decreases strongly with increasing y until for $y = 0.25$ a ferrimagnetic shape is observed and the anomaly caused by the dimerization vanishes completely.

Before the three low-temperature magnetic phases are discussed, the ht-phase susceptibility is investigated to possibly extrapolate information on the magnetic interactions to the low temperature behavior. Above the dimerization temperature T_d all compounds display a linear slope in $1/\chi$
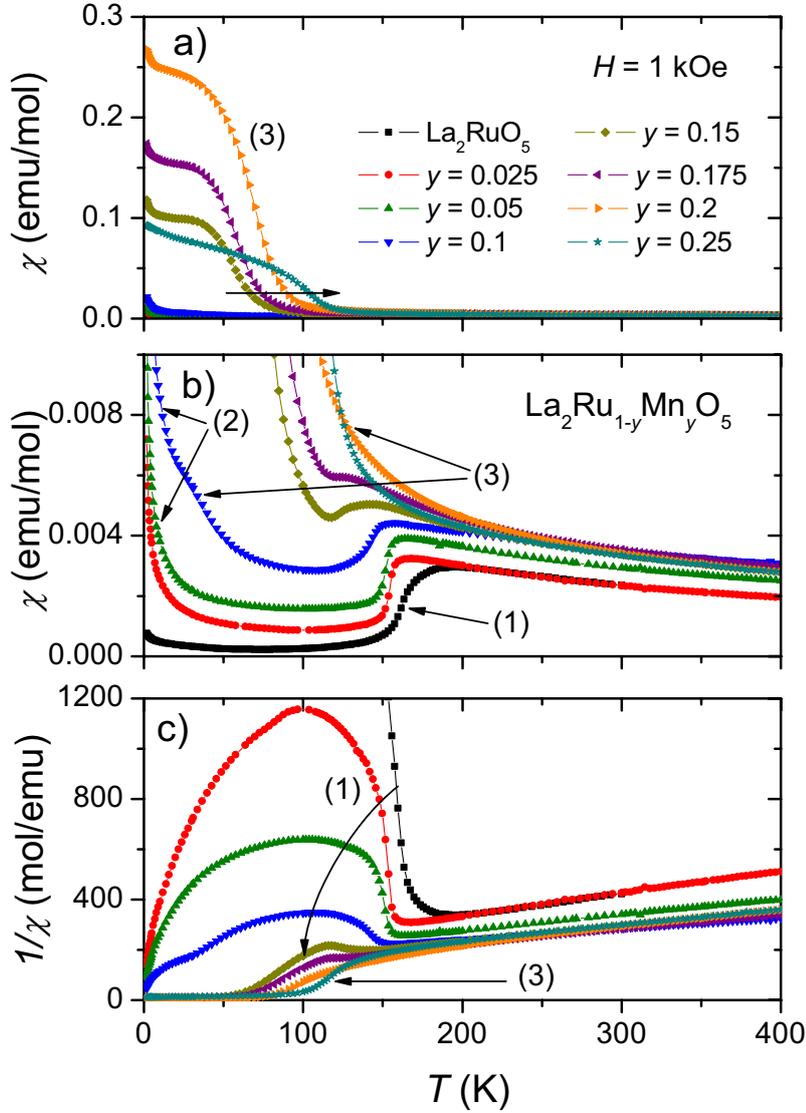
Figure 5.53.: a) Temperature dependent magnetic susceptibility of La$_2$Ru$_{1-y}$Mn$_y$O$_5$. b) Detailed susceptibilities up to 0.01 emu/mol. c) Corresponding temperature dependent inverse magnetic susceptibilities. The numbers correspond to the different magnetic phases according to: (1) Ru-Ru spin dimerization, (2) Paramagnetic Curie-tail (of not dimerized Ru and Mn spin moments), and (3) Other Ru and Mn spin interactions. For details see text.

indicating a paramagnetic behavior, which was fit using the Curie-Weiss law (Eq. 2.32) between 190 K and 400 K. For all samples the additional parameter χ_0 was found to be negligibly small ($\leq 10^{-4}$ emu/mol) and is therefore not further discussed. From the fitting parameter C the effective magnetic moment n_{eff} was calculated.
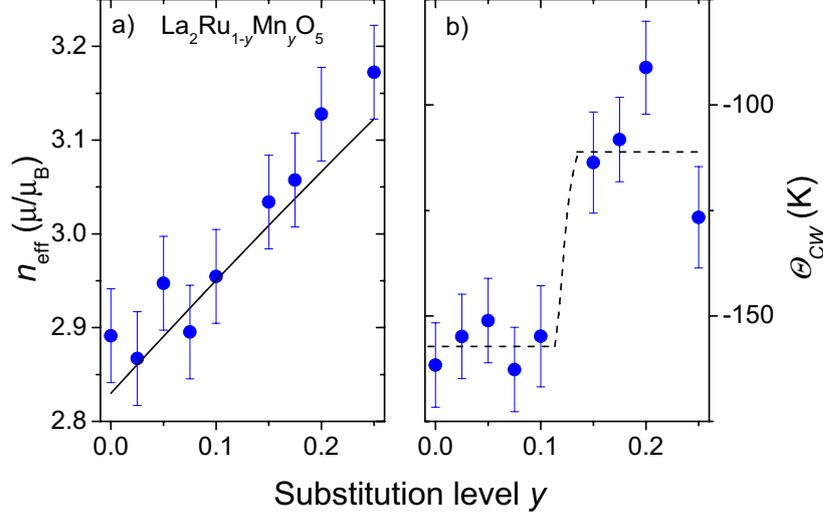
Figure 5.54.: a) Effective magnetic moments n_{eff} and b) Curie-Weiss temperatures Θ_{CW} for La₂Ru₁₋ᵧMnᵧO₅ determined from fits to the high temperature range of $1/\chi$ (190 - 400 K). The solid line in frame a) indicates the theoretically expected paramagnetic moments (Eq. 5.4). The dashed line in frame b) is drawn to guide the eye. For details see text.

In Fig. 5.54a the n_{eff} values for the La₂Ru₁₋ᵧMnᵧO₅ samples are depicted. They increase with the Mn substitution level. This behavior can very well be described by the combination of the spin moments for Mn^{4+} and Ru^{4+} applying the oxidation states obtained by XANES. Since Mn^{4+} has an larger spin moment $S = 3/2$ in contrast to Ru^{4+} with $S = 1$, the magnetic moment is expected to increase with y. The sum of the Mn^{4+} and Ru^{4+} spin moments is indicated by the solid line and was calculated according to:

$$n_{\text{eff},total} = \sqrt{(1-y) \cdot n_{\text{eff}}^2(\text{Ru}^{4+}) + y \cdot n_{\text{eff}}^2(\text{Mn}^{4+})} \quad . \tag{5.4}$$

Values $n_{\text{eff}}(\text{Ru}^{4+})$ and $n_{\text{eff}}(\text{Mn}^{4+})$ were derived from the spin-only approximation as $2.83\mu_B$ for Ru^{4+} ions and $3.87\mu_B$ for Mn^{4+}. As seen in Fig. 5.54a, with this approach the experimental values can well be reproduced within the range of the estimated standard deviations. It has to be mentioned, though, that also the combination of Mn^{3+} ($3d^4$: $S = 1$) and Ru^{5+} ($4d^3$: $S = 3/2$) reported for other Ru/Mn compounds would lead to the same values for n_{eff}. However, the XANES measurements clearly prove the +4 oxidation states for both ions.

The Curie-Weiss temperatures Θ_{CW} obtained from the fit are shown in Fig. 5.54b. The negative signs indicate that antiferromagnetic exchange interactions are dominant in the paramagnetic ht-phase. For $0 \leq y \leq 0.1$ Θ_{CW} is close to -155 K and indicates a step-like increase to -110 K for higher Mn concentrations. This abrupt change of Θ_{CW} by roughly 30 % is not easy to explain. It cannot be ascribed to structural changes, since for these only gradual changes without a step

are observed. On the other hand, the change in Θ_{CW} for $y = 0.15$ is in good agreement with the distinctly changing shape of the susceptibility curves in Fig. 5.53 reflecting the onset characteristic for a ferrimagnetic or canted antiferromagnetic spin arrangement. This is probably caused by a percolation effect, since at this Mn substitution level any ruthenium ion has a manganese ion at a neighboring site. This decreases the average exchange-interaction strength, because due to the more extended $4d$ orbitals the Ru-Ru interaction can be assumed to be stronger than the Ru-Mn interaction. The replacement of Ru^{4+} by Mn^{4+} ions with a higher spin moment on the Ru-site is expected to heavily disturb the local magnetic ordering. This explains the progressive suppression of the Ru-dimerization contribution in the magnetic susceptibility curves with increasing substitution level similar to the Ti substitution. In the $1/\chi$ curve of La$_2$Ru$_{0.75}$Mn$_{0.25}$O$_5$ no signature of the dimerization is observable anymore.

To gain further insight in the lt-ordered state, detailed field cooled (fc) and zero field cooled (zfc) measurements of χ applying a small external field of $H = 100$ Oe were performed. In Fig. 5.55 the experimental data of χ and corresponding inverse susceptibilities are shown from top to bottom for a) La$_2$Ru$_{0.95}$Mn$_{0.05}$O$_5$, b) La$_2$Ru$_{0.85}$Mn$_{0.15}$O$_5$, and c) La$_2$Ru$_{0.75}$Mn$_{0.25}$O$_5$. Below $y = 0.1$ the fc and zfc values are very similar, only a small shift of the step reflecting the dimerization of less than 2 K is observed, which is in agreement with the temperature hysteresis reported for pure and rare-earth substituted La$_2$RuO$_5$. For $y = 0.1$ a splitting of fc and zfc susceptibility occurs just below the Ru-dimerization temperature. In Fig. 5.55b the results for $y = 0.15$ indicate the presence of two transitions at roughly 120 K and 80 K. The $1/\chi$ signal shows the typical uprise caused by the spin-Peierls transition. This increase is already dominated by the onset of the Ru-Mn interaction leading to a smeared out cusp at approximately 100 K. At roughly 80 K a splitting of fc and zfc measurement is observed, which is indicating a second magnetic transition due to Ru-Mn interactions.

No dimerization peak was observed in $1/\chi$ for La$_2$Ru$_{0.75}$Mn$_{0.25}$O$_5$, instead, solely the fc-zfc splitting is found (Fig. 5.55c). The Ru spin pairing is already hardly observable for $y \geq 0.175$, however a small peak in the $1/\chi$ curves shown in Fig. 5.53 indicates the existence at least up to $y = 0.2$. Nevertheless, at low temperatures the susceptibilities of the samples with $y \geq 0.15$ are clearly dominated by the Ru-Mn interaction. Since the shape is similar to a ferrimagnetic system, a canted antiferromagnetic arrangement of the magnetic moments is a possible model. Alternatively, a spin-glass would also cause this observed shape of $1/\chi$ as reported in Ref. [Zha07]. The large increasing low temperature part of the susceptibility is contradictory to a spin-glass behavior, for which the zfc-susceptibility should decrease to almost zero at lowest temperature. The observed increase can very probably be ascribed to unpaired paramagnetic spin-moments (2).

To further investigate the origin of the magnetic features denoted (3), isothermal measurements of M vs. H were performed for La$_2$Ru$_{0.75}$Mn$_{0.25}$O$_5$. The experimental data are depicted in Fig. 5.56 for various temperatures above and below the different transitions. The top frame of Fig. 5.56 shows the full range of the external field, while in the bottom frame the low field region is depicted for a better comparability. At high temperatures a linear paramagnetic behavior of M is observed. Below the first phase-transition temperature, i.e. at 80 K, the appearance of a hysteresis is found with a small remanence of $M_R \approx 14$ emu/mol and a coercive mag-
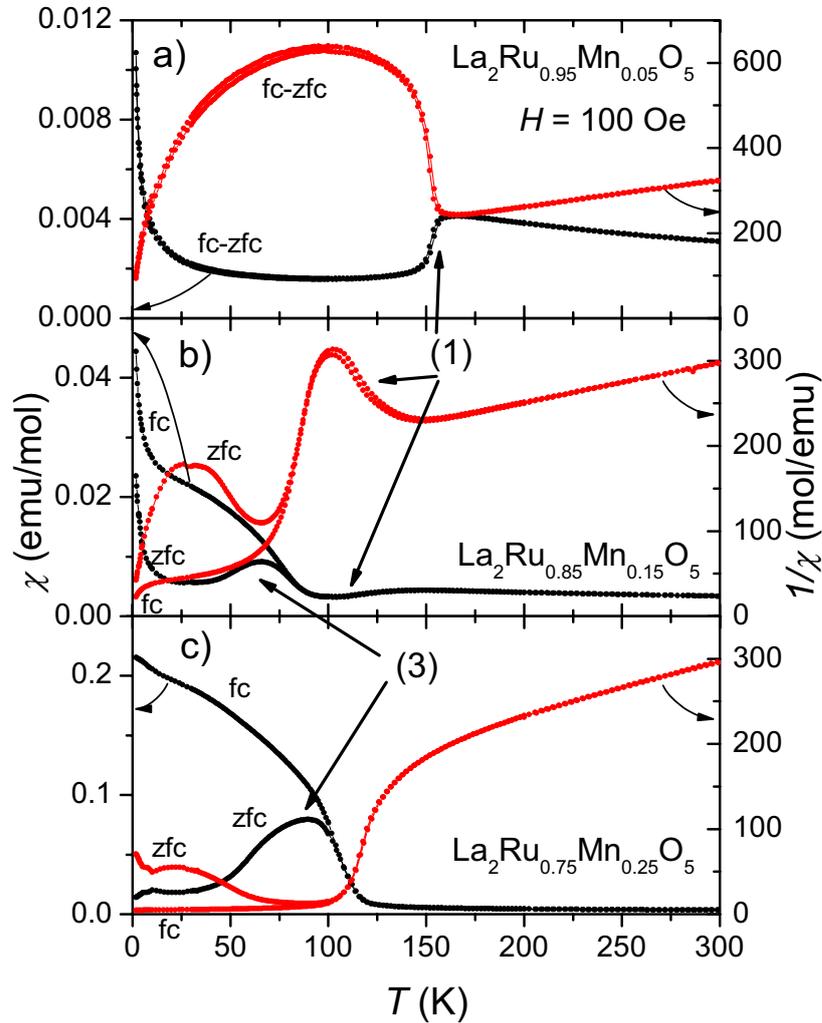
Figure 5.55.: Temperature dependent magnetic susceptibility (black, left scale) and corresponding inverse susceptibility (red, right scale) measured in fc and zfc mode at $H = 100$ Oe for a) $La_2Ru_{0.95}Mn_{0.05}O_5$, b) $La_2Ru_{0.85}Mn_{0.15}O_5$, and c) $La_2Ru_{0.75}Mn_{0.25}O_5$.

netic field $H_c \approx 0.1$ kOe. At 30 K H_c increases to roughly 1.2 kOe and the remanence at this temperature is $M_R \approx 51$ emu/mol. These values further increasse at 2 K to $M_R \approx 93$ emu/mol and $H_c = 2.8$ kOe. This residual magnetization at 2 K is more than 15 times smaller than expected for a classical ferrimagnetic arrangement of Mn^{4+} and Ru^{4+} moments with a remaining single electron-spin moment ($S = 1/2$, corresponding to $1\mu_B \approx 5584$ emu/mol), which amounts to 0.25×5584 emu/mol $= 1396$ emu/mol. However, this limit could be achieved in saturation by extrapolating the data for $y = 0.25$ to higher fields. The small and broad hysteresis is characteristic for either a soft ferrimagnetic (canted antiferromagnetic) or a spin-glass. The area increases
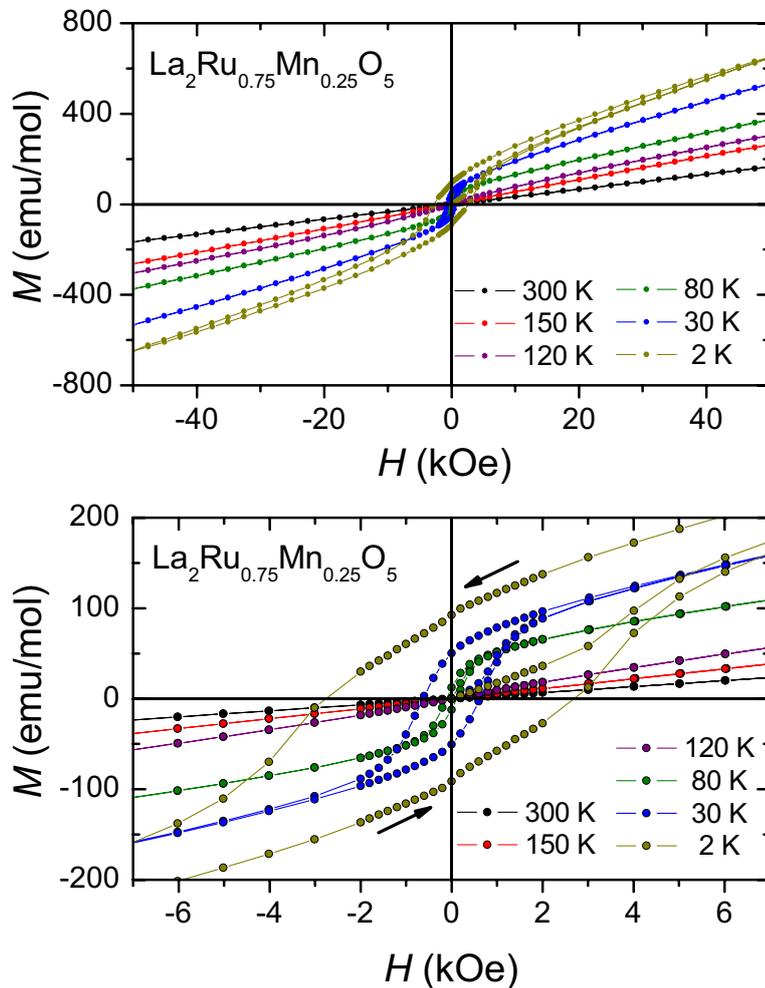
Figure 5.56.: Magnetic hysteresis curves of La$_2$Ru$_{0.75}$Mn$_{0.25}$O$_5$ at 300 K, 150 K, 120 K, 80 K, 30 K and 2 K. In the top frame the complete measurement range and in the bottom frame the part close to the origin are shown. Arrows indicate the direction of the change of the external field H during the measurement.

with decreasing temperature indicating an increased ordering or freezing of the spin-orientations. Furthermore, no saturation of M was found up to the maximal available external magnetic field. This behavior as well as the s-shaped hysteresis are characteristic for a spin-glass phase. Similarly, a canted antiferromagnetic arrangement would provide a superposed paramagnetic behavior in addition to the hysteresis since the spins are further rotated against each other with increasing field.

In addition, isothermal measurements of M vs. H were performed for $y = 0.15$ in the same temperature range. Between 300 K and 100 K a linear paramagnetic behavior is found. At 80 K

in agreement with the fc-zfc splitting a small s-shaped anomaly at the origin is observed indicating the onset of canting/spin-glass formation which distinctly increases at lower temperatures. Furthermore, a similar deformation of the hysteresis is observed, but a smaller hysteresis area compared with identical temperature data for $y = 0.25$ is found.

The origin of the fc - zfc splitting as well as the emerging hysteresis at low temperatures was studied in more detail. A spin-glass is characterized by an increase of the transition temperature with increasing frequencies in an ac-zfc susceptibility measurement. To investigate this behavior, the real (χ') and imaginary (χ'') part of the susceptibility for $0.1 \leq y \leq 0.25$ were measured for varying frequencies in the range between 1 Hz and 1000 Hz ($H_{ac} = 2.00$ Oe and $H_{dc} = 0$ Oe). The measurements exhibit a double peak in χ' and an even more complex temperature dependent behavior of two overlapping peaks in χ''. For $y = 0.15$ and $y = 0.25$ significant shifts of the peak maxima to higher temperatures by approximately 2.3 K and 2.6 K, respectively, were observed for the peak closer to the transition anomaly. This frequency dependent shifts in the imaginary (and real) part are characteristic for spin-glasses [Bin86, Myd93], although the overlapping peaks behave rather unusual. Such peak shifts can be described by a Vogel-Fulcher-Tammann law known from canonical glass dynamics of supercooled liquids [Lun99]. This law was also applied for the observed shift for the insulating spin-glass system Eu$_{1-x}$Sr$_x$S [Mal79, Tho80]. Nevertheless, the interpretation of the double peak structure becomes rather complex due to the occurring interactions of Ru-Ru, Ru-Mn, and Mn-Mn spin moments, as well as the existence of a cluster-phase (see Ti-substituted La$_2$RuO$_5$ in Sec. 5.2.1.3) and a possible blocking of the cluster- or spin-glass arrangement. A further detailed study on the properties of the spin-glass phase seems to be promising for this semiconducting system and will be performed in future works.

From the measurement results the magnetic phase diagram shown in Fig. 5.57 is proposed. The dimerization temperatures T_d from the paramagnetic to the Ru–Ru spin pairing phase were determined from the inverse susceptibilities. The obtained values (black circles) are depicted in Fig. 5.57 together with a linear fit (solid red line). The fit corresponds to a linear decrease of T_d down to 0 K for full substitution of Ru by Mn ($y = 1$) identical to the Ti substitution: $T_d = [166 \cdot (1 - y)]$ K (see Sec. 5.2.1.3). While up to $y = 0.15$ the T_d values can be well determined by the tangent method (solid black circles), for $0.15 < y \leq 0.2$ the characteristic jump in $1/\chi$ is very small but still recognizable (indicated by the empty grey circles). Thus, the solid line is extrapolated until $y = 0.2$. The second set of temperatures (blue triangles) in Fig. 5.57 are the freezing temperatures T_f of the Mn/Ru spin-glass transition. These values were obtained from the onset temperatures, where the fc and zfc susceptibilities split into two branches. This point reflects the varying ordering dynamics of the two spin systems and their different magnetic interactions. The three regions in Fig. 5.57 are the paramagnetic phase above T_d, the Ru-spin dimerization phase between T_d and T_f (shaded red), and a spin-glass state involving Mn and Ru spin moments below T_f (light cyan). The samples with $y < 0.1$ only show the spin-Peierls transition, while for $y \geq 0.1$ they undergo both transitions. On the other hand, La$_2$Ru$_{0.75}$Mn$_{0.25}$O$_5$ probably only shows the transition to the spin-glass phase. This temperature-dependent occurrence of several magnetic transitions for one substitution level is a typical property caused by the Ru/Mn mixing. Similar behaviors were also reported for other perovskite-like and layered compounds with mixed Ru/Mn
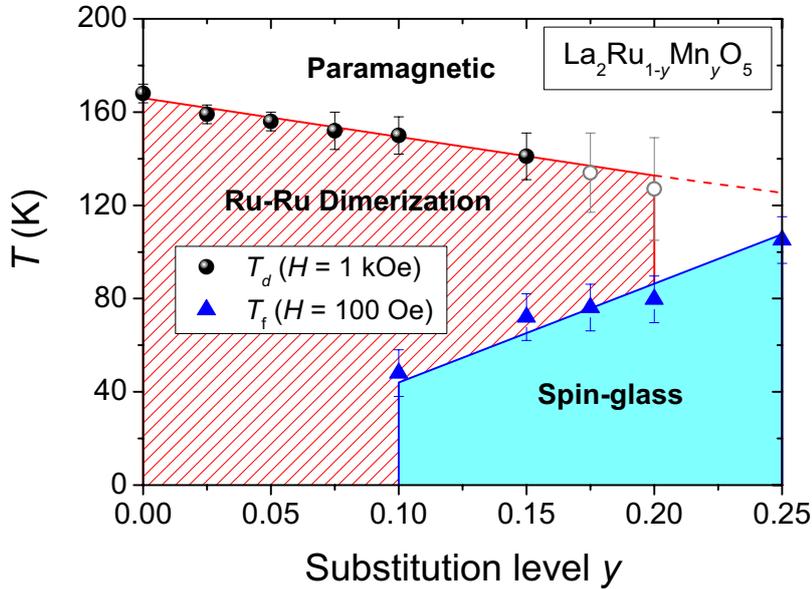
Figure 5.57.: Transition temperatures T_d (solid black and empty grey circles) and T_f (blue triangles) of La$_2$Ru$_{1-y}$Mn$_y$O$_5$ determined from magnetic susceptibility data. The solid red line marks the linear fit of $T_d = [166 \cdot (1-y)]$ K, while the dashed red line is an extrapolation of the fit. The solid blue line indicates the transition to the spin-glass phase to guide the eye. The red shaded area marks the Ru-spin dimerized phase while the light cyan colored area indicates the spin-glass phase.

occupation on the Ru or Mn-site, see e.g. Refs. [Zha07, Gal02, Sch04, Zha08]. But it has to be mentioned that the incomplete structural transition for $y = 0.25$ plays an important role and is difficult to explain in combination with the observed magnetic transition properties. This demands further investigations of the magneto-structural correlations for these samples.

5.3.5. Specific Heat

To further characterize the magnetic phase transitions described above, the specific heat of unsubstituted La$_2$RuO$_5$ was compared to experimental data of selected La$_2$Ru$_{1-y}$Mn$_y$O$_5$ samples (y in steps of 0.05). From the magnetic susceptibility measurements it is known that for $y \leq 0.1$ only the dimerization transition is present, while for $y \geq 0.1$ an additional spin-glass transition at lower temperatures occurs. For $y = 0.25$ only the latter one was found. The heat capacities of the samples are depicted in Fig. 5.58 in C_p/T representation as a function of the temperature. The peak emerging from the Ru-spin dimerization transition at 161 K is clearly observed for unsubstituted La$_2$RuO$_5$ and shifted linearly to lower temperature for increasing Mn concentration. For $y \geq 0.15$ the peak significantly broadens indicating increasing disorder in the low-temperature phase. This broadening and smearing out of the heat-capacity anomaly increases with increasing
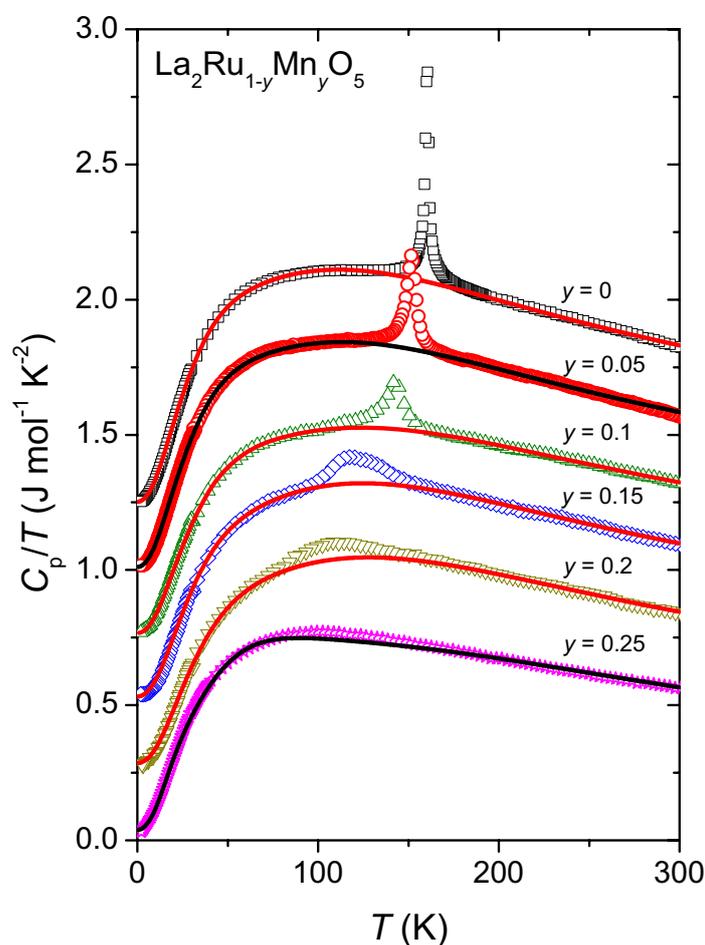
Figure 5.58.: Specific heat in C_p/T representation for $La_2Ru_{1-y}Mn_yO_5$ with selected substitution levels (y in steps of 0.05). To increase the comparability the data were shifted in equidistant steps. The corresponding Einstein-Debye fits of the phononic contribution are shown as solid lines.

Mn substitution level until for $y = 0.25$ a clear peak cannot be observed anymore and can only be recognized by a slight change of curvature at approximately 100 K. The peak maxima are in reasonable agreement with the spin-dimerization transition temperatures obtained form the onset in the susceptibility data.

The fit of the specific-heat data was carried out using an Einstein-Debye phonon model with one Debye- and four Einstein-terms to describe the phononic contribution to C_p. The obtained fit values for La_2RuO_5 (already shown in previous sections) and the other substitution levels are listed in Tab. 5.10. The fits are shown as solid lines in Fig. 5.58 and are in reasonable agreement with the experimental data. The Debye temperatures for all compounds are similar. Also the four Einstein terms used for the fitting procedure are similar and of comparable size. However,

Table 5.10.: Results of the heat-capacity fit of La$_2$Ru$_{1-y}$Mn$_y$O$_5$ (see text for details). The excess entropy contribution S_{mag} was calculated from the integrated residual peak after the subtraction of the lattice contribution.

Sample	c_0 ($\frac{mJ}{molK^2}$)	Θ_D (K)	Θ_{E1} (K)	Θ_{E2} (K)	Θ_{E3} (K)	Θ_{E4} (K)	S_{mag} ($\frac{J}{molK}$)
La$_2$RuO$_5$	2.2	132	175	217	325	520	4.2(3)
La$_2$Ru$_{0.95}$Mn$_{0.05}$O$_5$	11	132	179	221	335	540	3.9(3)
La$_2$Ru$_{0.9}$Mn$_{0.1}$O$_5$	16.5	144	190	233	359	592	3.1(3)
La$_2$Ru$_{0.85}$Mn$_{0.15}$O$_5$	32	148	185	263	348	558	3.2(3)
La$_2$Ru$_{0.8}$Mn$_{0.2}$O$_5$	36	154	197	267	352	583	3.4(3)
La$_2$Ru$_{0.75}$Mn$_{0.25}$O$_5$	39	136	195	291	291	720	3.6(3)

it was not possible to derive a stable and reliable fit for the compound with the Mn concentration $y = 0.25$. In this case a constraint, i.e. $\Theta_{E2} = \Theta_{E3}$ had to be used. In addition, Θ_{E4} is rather large when compared to the results of the other concentrations. This probably results from the smeared out dimerization transition and a hidden spin-glass peak, which is expected in the same temperature range.

At very low temperatures an increasing offset in C_p/T was observed, which was included into the fit using a constant c_0. This constant increases from 2.2 mJ mol^{-1} K^{-2} to roughly 39 mJ mol^{-1} K^{-2} and can be explained by an increasing importance of the spin-glass contribution to the specific heat (see Sec. 5.2.1.4). However, there is no simple scaling of c_0 with the manganese concentration. Also no significant contribution of the spin-glass state to the heat capacity at about $1.2 \cdot T_f$ can be distinguished [Myd93]. For high substitution levels this contribution is expected close to 100 K, where phonon contributions dominate the heat capacity and it might well be that these spin-glass contributions merge with the smeared out peak of the dimerization transition.

Fig. 5.59 shows the experimental specific heat after subtraction of the lattice contribution in C_p/T versus T representation. For increasing Mn concentration a shift of the peak ascribed to the Ru dimerization to lower temperatures is observed. With increasing y the peak height strongly decreases and the dimerization transition becomes significantly smeared out.

In the upper frame of the inset in Fig. 5.59 the temperatures of the peak maxima are depicted as a function of the substitution level. The solid red line corresponds to $T = 166 \cdot (1 - y)$ K, which stems from the linear fit of the spin-dimerization transition temperatures up to $y = 0.175$ obtained from the magnetic susceptibility data. For $y \geq 0.15$ the peak broadens significantly and the maximum shifts constantly to values 20 K below the extrapolated ordering temperatures. This shift could be caused by additional contributions of the spin-glass transition just below the dimerization temperature in the lt-phase. From the peak areas the magnetic entropy contribution S_{mag} was obtained via $S_{mag} = \int (C_p - C_{lattice})/T \mathrm{d}T$ between 50 K and 250 K. The obtained entropies are listed in the last column of Tab. 5.10 and are depicted in the lower frame of the inset in Fig. 5.59.
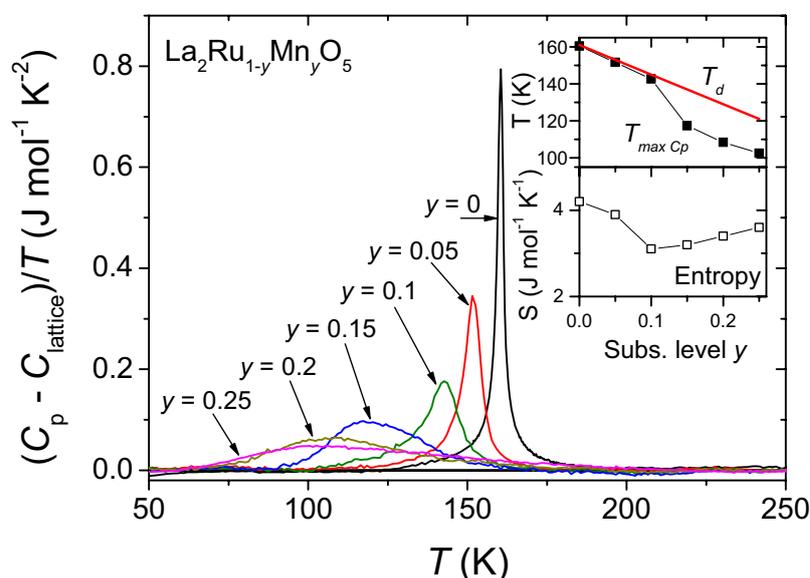
Figure 5.59.: Residual specific heat in $(C_p - C_{lattice})/T$ of $La_2Ru_{1-y}Mn_yO_5$ for the samples shown in Fig. 5.58. The insets give the temperatures of the peak maxima and the entropy changes from the peak integration as a function of the Mn concentration.

In the pure compound La_2RuO_5 the entropy is 4.2 J mol^{-1} K^{-1}, which is approximately 50% of the entropy for spin $S = 1$ systems due to a residual degeneration of the dimerized ground state. The decreasing entropy with increasing Mn concentration for $y \leq 0.1$ results from the dilution of Ru centers and further appearing Ru-Mn exchange interactions, which compete with the Ru-Ru exchange. However, for $y \geq 0.15$ the entropy is increasing due to the increasing contribution of the spin-glass to the transition peak, while the fraction of the dimerization transition is expected to rapidly decrease above $y = 0.1$ because the structural changes very strongly reduce the intradimer interaction strength.

5.3.6. DFT Calculation

According to the magnetic susceptibility and specific heat the increasing Mn substitution drastically changes the magnetic properties especially for $La_2Ru_{0.75}Mn_{0.25}O_5$. The Mn $3d$ states are therefore expected to mix strongly with the Ru $4d$ main contribution to the local density of states at the Fermi-energy. In the vicinity of E_F the Ru $4d$ and the O $2p$ levels located in the LaRuO$_4$-layers dominate the DOS (see Sec. 4.5). Therefore, DFT calculations were performed for $La_2Ru_{0.75}Mn_{0.25}O_5$ for the ht-phase crystal structure obtained from the Rietveld-analysis of the ND measurements. For the modelling the symmetry was reduced to space group P1 to exchange a single Ru atom by Mn in the unit cell.
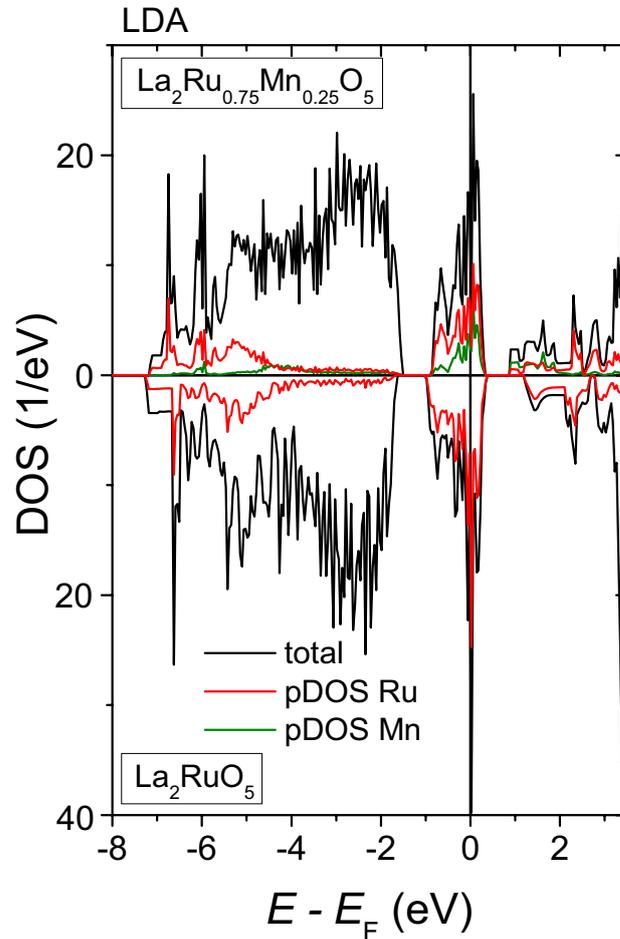
Figure 5.60.: DOS of La$_2$Ru$_{0.75}$Mn$_{0.25}$O$_5$ (top frame) and La$_2$RuO$_5$ (bottom frame) using LDA.

In Fig. 5.60 the DOS for La$_2$Ru$_{0.75}$Mn$_{0.25}$O$_5$ is shown in the upper frame and pointing downwards the DOS of pure La$_2$RuO$_5$ is depicted in the bottom frame for comparison. The calculations were performed using the local density approximation (LDA), since for the ht-phase the absence of ordering does not require spin-polarized modelling. Only small deviations between both DOS are observed, the Mn contribution is found very close to the partial DOS of Ru. The same result is obtained for all four replacement possibilities of one Ru by one Mn atom in the unit cell in agreement with almost identical total energies. The range between -1.5 eV and -4 eV, which is corresponding to the O $2p$ states of LaRuO$_4$- and LaO-layers is not significantly influenced by the Mn substitution. The barely observable deviations below -4 eV and above 1 eV are explained by the small changes of interatomic distances caused by the substitution.

Futher investigations were performed by spin-polarized calculations applying the local spin density approximation (LSDA). The results of magnetic and heat-capacity measurements exhibited

the existence of strong magnetic interactions in the lt-phase of $La_2Ru_{0.75}Mn_{0.25}O_5$. In contrast to the pure and rare-earth substituted La_2RuO_5 no antiparallel arrangement of the Ru spin moments was found [Rie12c]. Due to the replacement of Ru by Mn the magnetic exchange results from a summation of nearest-neighbor (AFM) and next-nearest neighbor (FM) interactions. To study this exchange correlation, the LSDA calculations were performed with different ferro- and anti-ferromagnetic initial spin settings using the same crystal-structure data as described above. For the Mn^{4+} ion the initial spin moment $S = 3/2$ and for Ru^{4+} the moment $S = 1$, respectively, were used in agreement with the XANES results. The LSDA modelling lead to a more than 1 eV lower total energy than the unpolarized LDA calculation, which shows that the magnetic interactions are required to more accurately model the band structure of the ht-phase.

An ferromagnetic ordering of the Ru and Mn spin moments lead to the result with the lowest total energy. In detail, its energy was roughly 0.02 eV lower than for the calculation applying anti-ferromagnetic ordering. This finding to some extend explains the observed magnetic susceptibility which is obviously reflecting a residual ferromagnetic exchange interaction in $La_2Ru_{0.75}Mn_{0.25}O_5$. It appears to be impossible to model the lt-phase behavior due to the coexistence of the two crystal structures with deviating Mn content. Nevertheless, the ht-phase results of unpolarized and polarized setting already provide results corroborating the experimentally found complex behavior of the magnetic properties. The DFT calculations require more effort to better describe the experimental data at this point. However, first the complex correlations and magnetic properties should be understood in more detail before the DFT calculations can help to develop more accurate models to describe the experimental findings.

5.4. Thermogravimetric Analysis and Oxygen Stoichiometry

In general, the physical properties of oxides are strongly influenced by variations of the oxygen stoichiometry. Especially the electrical conductivity changes due to additional charge carriers created by off-stoichiometric oxygen contents. Furthermore, the magnetic properties are affected by changed valences of the transition-metal cations. For (substituted) La$_2$RuO$_5$ no large oxygen non-stoichiometries were expected due to the +4 valence of Ru, Ti, and Mn and the trivalent lanthanide ions. In addition, from neutron diffraction no hints for e.g. oxygen vacancies were obtained. To exclude oxygen non-stoichiometries as origin of the observed physical properties, selected pure and substituted La$_2$RuO$_5$ samples were investigated by thermogravimetric measurements. Some of the results were already reported in Ref. [Rie12d].

The relative weight changes for three La$_2$RuO$_5$ samples synthesized by different reaction routes are depicted in Fig. 5.61. The sample notation refers to the applied Ru-agent as mentioned in Sec. 2.1. Two distinct and well separated weight reduction steps of approximately 2% and 5% are observed for all samples. The first reduction step is completed at roughly 550°C and results in a stable intermediate state, as already noticed by Benčan *et al.* [Ben05]. This new phase was described by the sum formula La$_2$RuO$_{4.6}$ but despite of unit-cell parameters no structural information was given. The own thermogravimetric measurements correspond rather to the sum formula La$_2$RuO$_{4.5}$ and rather distinct deviations from the La$_2$RuO$_5$ crystal structure were found. Since the structural investigations of this intermediate phase are not finished yet, it is not further discussed here.
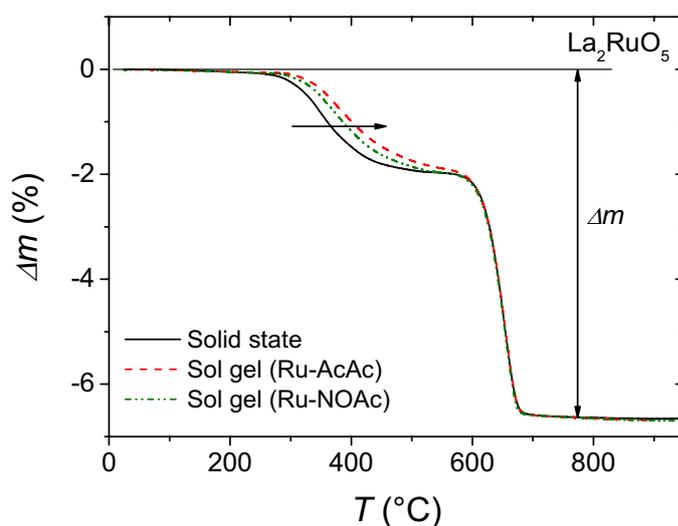

Figure 5.61.: Relative weight changes for La$_2$RuO$_5$ samples synthesized by different reaction routes and varying calcination times.
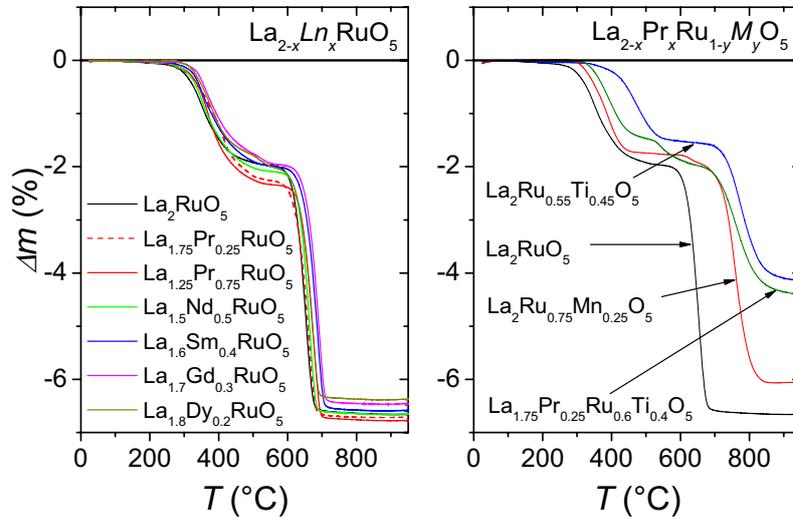
Figure 5.62.: Relative weight changes for selected La$_{2-x}$Ln$_x$RuO$_5$ (left frame) and La$_{2-x}$Pr$_x$Ru$_{1-y}$M$_y$O$_5$ (M = Ti, Mn; right frame) samples.

The inflection point of the first step differs by roughly 50°C for the three samples shown in Fig. 5.61. This very likely is due to the different calcination time. The sample synthesized in a sol-gel reaction using Ru-AcAc was calcinated 120 hours, the one with Ru-NOAc 96 hours, and the solid-state reacted sample was heated for only 48 hours. Thus, an increased crystallinity might reason the higher onset temperatures. In contrast, the second step is very similar for all three samples and occurs in a narrow temperature range of roughly 620-680°C. At 700°C the reduction is completed and the final weight loss is apparently identical for all three samples.

The obtained total weight losses of 6.64-6.70% are slightly smaller than the value of 6.9% reported in Ref. [Ben05]. Assuming that La$_2$RuO$_5$ is decomposed to La$_2$O$_3$ and metallic Ru during the reaction, a theoretical weight loss of 6.97% is calculated for two released oxygen atoms ($z = 2$) according to the reaction:

$$La_2RuO_{3+z} + z \cdot H_2 \longrightarrow La_2O_3 + Ru + z \cdot H_2O(\uparrow) \quad . \tag{5.5}$$
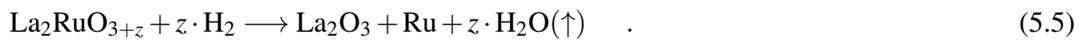
From the experimentally found weight losses the oxygen content z was calculated using:

$$z = \left(\frac{1}{1 - \Delta m} - 1 \right) \cdot \frac{M_f}{M(O)} \quad , \tag{5.6}$$

where Δm denotes the measured relative weight loss determined in the temperature range 110°C to 755°C, $M(O)$ is the molecular mass of oxygen and M_f is the sum of the molecular masses of the non-volatile products of the reaction (Eq. 5.5). The values determined for Δm and the corresponding oxygen contents for all investigated samples are given in Tab. 5.11. For convenience

Table 5.11.: Relative weight losses and oxygen contents of selected pure and substituted La$_2$RuO$_5$ samples. Estimated standard deviations are 0.05 for Δm and 0.03 for the oxygen contents/deficiencies.

Compound	Δm (%)	Oxygen content	Oxygen deficit δ
La$_2$RuO$_5$ (solid state)	6.64	4.90	0.10
La$_2$RuO$_5$ (sol gel Ru-AcAc)	6.69	4.91	0.09
La$_2$RuO$_5$ (sol gel Ru-NOAc)	6.70	4.91	0.09
La$_{1.75}$Pr$_{0.25}$RuO$_5$	6.85	4.93	0.07
La$_{1.25}$Pr$_{0.75}$RuO$_5$	6.84	4.94	0.06
La$_{1.5}$Nd$_{0.5}$RuO$_5$	6.70	4.93	0.07
La$_{1.6}$Sm$_{0.4}$RuO$_5$	6.65	4.92	0.08
La$_{1.7}$Gd$_{0.3}$RuO$_5$	6.53	4.89	0.11
La$_{1.8}$Dy$_{0.2}$RuO$_5$	6.44	4.86	0.14
La$_2$Ru$_{0.75}$Mn$_{0.25}$O$_5$	6.07	4.94	0.06
La$_2$Ru$_{0.55}$Ti$_{0.45}$O$_5$	4.15	5.03	-0.03
La$_{1.75}$Pr$_{0.25}$Ru$_{0.6}$Ti$_{0.4}$O$_5$	4.41	5.01	-0.01

also the (apparent) deficiencies $\delta = 5 - (3+z)$ are listed. It is striking that for all three samples of La$_2$RuO$_5$ significant deficiencies in the range of $\delta \approx 0.09$ were found. Such high values cannot be explained by instrumental errors. From experience a general reproducibilty of roughly 10 μg for the single measurements can be estimated. Taking into account an additional uncertainty of 10-20 μg for the baseline correction, a standard deviation of $\delta \pm 0.03$ can be assumed for the oxygen content [Ebb98, Goe06]. The values listed in Tab. 5.11 are well above the 2σ-limit for most of the samples.

In the left frame of Fig. 5.62 the thermogravimetric results for selected rare-earth substituted La$_2$RuO$_5$ compounds are shown. The lanthanide incorporation does not change the absolute shape of the curves, i.e. the two steps are still observable. The relative weight losses change depending on the atomic weight of the lanthanide and the substitution level. Due to the rare-earth substitution a slightly modified reaction equation has to be used to calculate the oxygen content:

$$\text{La}_{2-x}Ln_x\text{RuO}_{3+z} + z \cdot \text{H}_2 \longrightarrow (2-x) \cdot \text{La}_2\text{O}_3 + x \cdot Ln_2\text{O}_3 + \text{Ru} + z \cdot \text{H}_2\text{O}(\uparrow) \ . \tag{5.7}$$
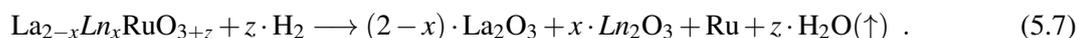
The M_f used in Eq. 5.6 change according to the content of $Ln_2\text{O}_3$. The oxygen contents/deficiencies for La$_{2-x}Ln_x$RuO$_5$ calculated using Eq. 5.6 are also listed in Tab. 5.11. The obtained deficiencies determined from Δm between 110°C and 755°C range between 0.06 and 0.14 (Tab. 5.11) and are, thus, significantly larger than the calculated error of ± 0.03.

Furthermore, in the right frame of Fig. 5.62 the relative weight losses of selected samples substituted on the Ru-site by Ti and Mn (denoted as M) are depicted. The two weight-reduction steps are also observable for these samples but are progressively shifted to higher temperatures with

increasing substitution level y. This is known as shielding effect described in Ref. [Osw93]. In addition, very obviously the relative weight losses are decreasing with increasing y. This can be explained by the formed products of these compounds by the reaction. The incorporated Ti^{4+} ions are not reduced at all, instead, reduction stable TiO_2 remains after the reaction. Similarly, Mn is not fully reduced from the +4 state to metal. In this reaction usually MnO is formed as reduction product corresponding to Mn^{2+} ions [Wur96]. Reasoned by this significantly lower weight losses between 4.15% and 6.07% were obtained. For Ti- and Mn-substitutions Eq. 5.6 was further modified to calculate the appropriate M_f:

$$La_2Ru_{1-y}Ti_yO_{3+2y+z} + z \cdot H_2(g) \longrightarrow La_2O_3 + (1-y) \cdot Ru + y \cdot TiO_2 + z \cdot H_2O(\uparrow) \ , \quad (5.8)$$

$$La_2Ru_{1-y}Mn_yO_{3+y+z} + z \cdot H_2(g) \longrightarrow La_2O_3 + (1-y) \cdot Ru + y \cdot MnO + z \cdot H_2O(\uparrow) \ . \quad (5.9)$$
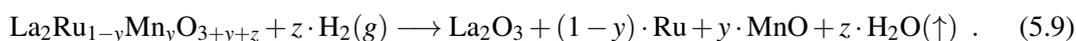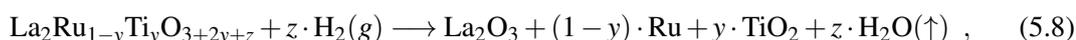
The correspondingly used reaction for simultaneously Pr- and Ti-substituted samples is a hybrid of Eq. 5.7 and Eq. 5.8, and, therefore, not given explicitly. Using Eq. 5.6 the oxygen content was determined. The obtained values for δ of the Ti containing samples are given in Tab. 5.11. Surprisingly, only for the Ti-substituted samples the values for δ are zero in the σ range indicating the expected oxygen content of five oxygens per f.u.. For the Mn substituted sample still a significantly larger oxygen deficiency of 0.06 was calculated. This might be explained by a trace of remaining Mn(III)- or Mn(II)/Mn(III)-oxide after the reduction as described in Ref. [Wur96]. On the other hand, this explanation is obviously not valid for the rare-earth substitution, which thus has to be investigated in more detail.

The reduction products were examined by powder XRD. In Fig. 5.63a the pattern of La_2RuO_5 after the TG measurement is shown. All peaks can be identified as α-La_2O_3 and $La(OH)_3$, which is formed by the reaction of the hygroscopic La_2O_3 with the air moisture. Strikingly, the expected Ru-metal was not detected for any of the samples. A similar finding was reported by Benčan *et al.* [Ben05], where the Ru-metal was not observed in the XRD patterns either, but was identified by selected area electron diffraction. These authors explained the absence of Ru-metal diffraction peaks by very small particle sizes.

This interpretation is rather unlikely, because in other ruthenium oxides investigated, Ru-metal could clearly be detected by XRD in the TG reaction products. In Fig. 5.63b the pattern of the ruthenate $NdSr_3RuO_{7+\delta}$ after reduction (same reaction conditions as for La_2RuO_5) is shown as one example. The Ru-metal reflections can be clearly identified. The other peaks can be explicitly ascribed to Nd_2O_3 and $Sr(OH)_2$, which are the other expected TG reaction products for this compound.

For the (substituted) La_2RuO_5 samples the oxidation states of Ru and the substituting elements were determined by XANES investigations and magnetic susceptibility measurements. For Ru, Ti, and Mn a valence of +4 was found. For selected Mn-substituted samples additional low-temperature XAS investigations were carried out. No changes in the oxidation states of the involved elements were observed. The calculated oxygen deficiencies according to Tab. 5.11 correspond to oxidation states well below +4 for the transition metals, in clear contradiction to the
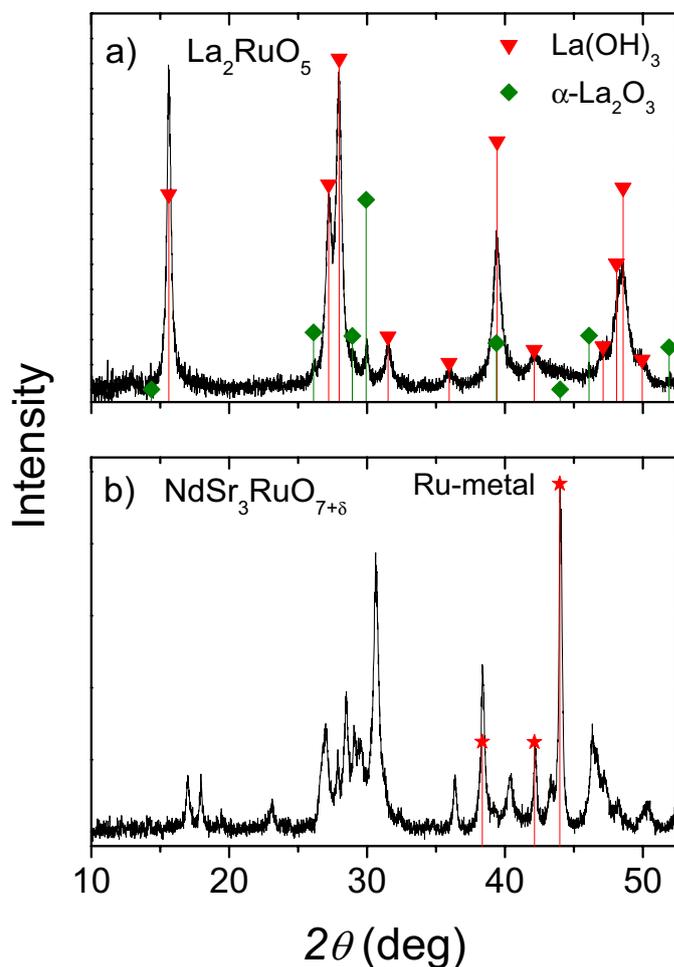
Figure 5.63.: XRD patterns of a) La$_2$RuO$_5$ and b) NdSr$_3$RuO$_{7+\delta}$ after thermogravimetric measurement in reducing atmosphere. a) The markers indicate the 2θ-values and intensities of La(OH)$_3$ (PDF 036-1481) (red) and α-La$_2$O$_3$ (PDF 071-4953) (green). b) The red markers represent the 2θ-values and intensities of Ru-metal (PDF 065-1863).

results of the XAS and magnetic measurements. Furthermore, neutron diffraction experiments gave no indications for vacancies on the oxygen sites [Rie11, Ebb05]. The absence of Ru-metal peaks in the XRD are a hint that this apparent contradiction might be caused by an incomplete reaction.

To gain a better insight in the nature of the ruthenium-related reduction products, XAS measurements at the Ru-L$_{\text{III}}$ and Ru-K edges were carried out. XAS is highly element specific and not restricted to crystalline samples. For these reasons (possibly amorphous) Ru compounds can be investigated while by-products like *Ln*(OH)$_3$ do not interfere.
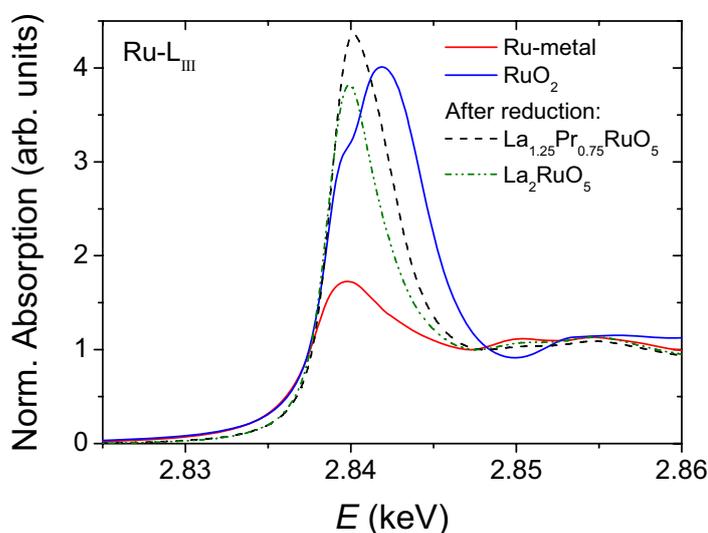
Figure 5.64.: Normalized Ru-L$_{\text{III}}$ absorption spectra of reduced La$_{1.25}$Pr$_{0.75}$RuO$_5$ (at 950°C) and La$_2$RuO$_5$ (at 1100°C) in comparison with the references Ru-metal and RuO$_2$.

The normalized XANES spectra at the Ru-L$_{\text{III}}$ absorption edges are shown in Fig. 5.64. The so-called "white line" observed at the Ru-L$_{\text{III}}$ edge is caused by transitions form the $2P_{3/2}$ core state to unoccupied states with predominatly $4d$ character. The intensity, fine structure and energy position of the white line is affected by several parameters, like the number of available states (which reflects the oxidation state), coordination geometry and hybridization of the Ru $4d$ orbitals with ligand orbitals. The Ru-metal reference shows a single, broad absorption peak with a rather low intensity. On the other hand, RuO$_2$ provides the typical edge shape of ruthenium-based oxides with two very intense white lines. These two white lines correspond to excitations into the $4d\ t_{2g}$ and e_g levels of Ru in an octahedral oxygen coordination [Ebb01]. The same structure of the white lines was also observed for the original (i.e. not reduced) La$_2$RuO$_5$ samples. The XANES spectra of the reduced samples are clearly different from the one of ruthenium metal, indicating that the reduction is not fully completed. It has to be noted, that the reduction products of other ruthenium oxides like RuO$_2$ show XANES spectra that are identical with the Ru-metal reference. Thus, the reduction behavior of (substituted) La$_2$RuO$_5$ is obviously different from the one of other ruthenates. On the other hand, the XANES spectra of the reduced La$_2$RuO$_5$ samples also show clear differences compared to "normal" ruthenium-based oxides, see e.g. Refs. [Agu09, Ebb04, Ebb07, Goe05]. An obvious difference is that only one intense peak is observed for the reduced samples. This peak indicates the presence of some bonded oxygen, i.e. the hybridization of Ru $4d$ and O $2p$ orbitals, but only in such small amounts that a splitting of the Ru-d orbitals into sets of different energy does not occur. For the different samples the peak exhibits a different shape, which is strongly depending on the type of the substitution and the final temperature of the TG measurement. The
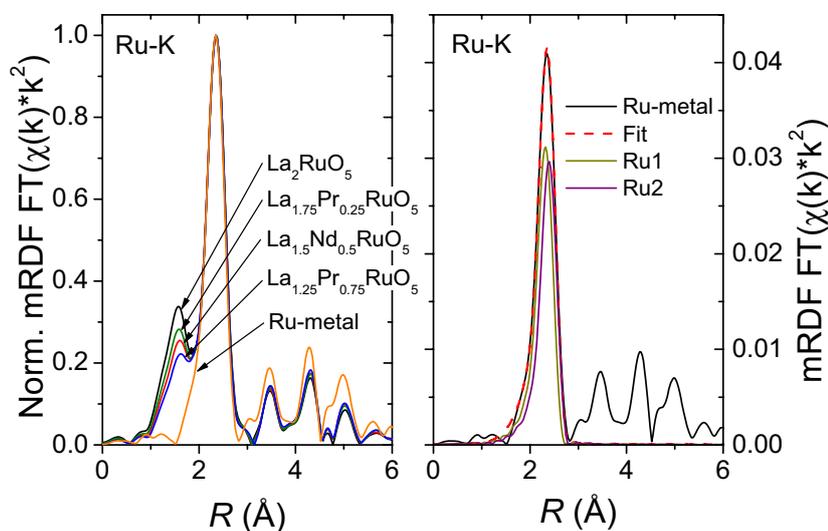
Figure 5.65.: Left frame: Normalized mRDF of the Ru-K absorption spectra of La$_{2-x}$Ln$_x$RuO$_5$ samples after TG reduction and of metallic Ru powder. Right frame: Fit of the first coordination shell of the Ru-metal powder mRDF.

pure La$_2$RuO$_5$, which was reduced up to 1100°C (dash dot dot line) and samples with Mn or Ti incorporation show a narrower and smaller peak compared to the rare-earth substituted samples (dashed line) and the La$_2$RuO$_5$ sample only reacted to 950°C. The peak maxima of the Ru-metal and the Mn- and Ti-substituted samples are in good agreement, whereas the maximum for the other samples is slightly shifted to higher energies by roughly 0.1 eV indicating a small valence shift effect. This is also a sign of traces of oxidized Ru remaining in the TG reacted samples.

From the Ru-L$_{III}$ absorption spectra a quantitative analysis of a correlation between δ and the peak intensity was impossible, therefore, additional Ru-K EXAFS spectra were recorded and analyzed.

From the Ru-K absorption spectra of selected samples the corresponding mRDFs were obtained by the Fourier-transformation of the k^2-weighted EXAFS regions. They are depicted in the left frame of Fig. 5.65 together with the Ru-metal reference. For better comparability the mRDFs were normalized to the maximum of the main peak at roughly 2.2 Å. In the mRDF of the Ru-metal four distinct peaks at approximately 2.2 Å, 3.5 Å, 4.3 Å, and 5 Å are observed. The shown pattern is typical for metals with (cubic or hexagonal) closed packings. These four peaks were also found for the reduction products of the (rare-earth substituted) La$_2$RuO$_5$ samples, indicating that a reduction actually took place. Interestingly, for the reduced samples an additional peak at approximately 1.5 Å was found. This additional peak at the left side of the most intense peak, which corresponds to the first Ru coordination shell in the metal, was only found for the reduced samples of La$_2$RuO$_5$-related compounds. The distance of 1.5 Å from the x-ray absorbing atom is
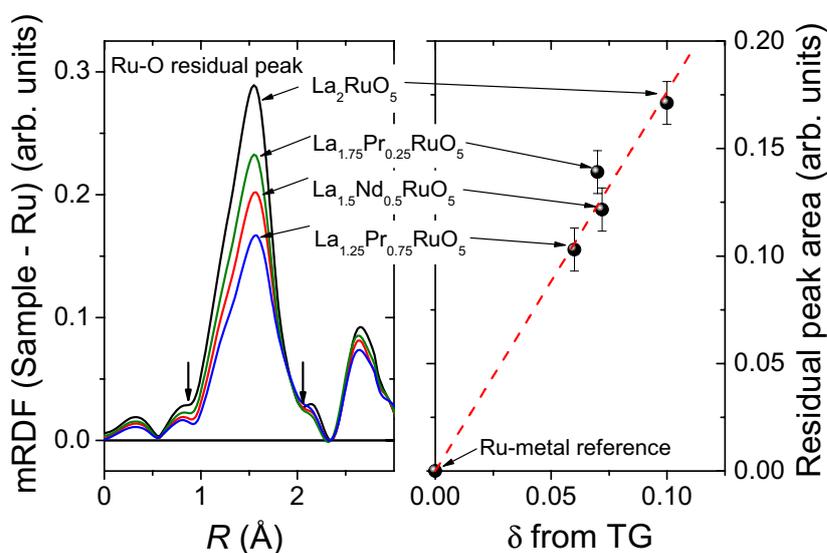
Figure 5.66.: Left: Residuals of the Ru-K mRDF after subtraction of the fit of the first Ru coordination shell. Right: Residual peak area vs. oxygen deficiency obtained from TG measurements. The dashed line represents a linear regression.

typical for the ruthenium-oxygen bond-length taking into account that due to phase shifts during the absorption/backscattering process the interatomic distances seen in the mRDFs are systematically too small. In fact, the same peak distance of roughly 1.5 Å was found for all ruthenium oxides including e.g. La_2RuO_5 or RuO_2, and is a clear proof that a small fraction of oxidized ruthenium is preserved in the reduced samples after the TG treatment.

From Fig. 5.65 and Tab. 5.11 it is very obvious that the peak intensity correlates with the obtained oxygen deficiency δ. For a quantitative analysis the peak areas were determined to study this correlation in detail. For this the first coordination peak of the Ru-metal mRDF was fit to obtain a smooth, well-defined reference curve, which can be subtracted from the other samples' mRDFs. In this fit two Ru backscattering paths were used reflecting the two slightly distinct nearest-neighbor sites of the hexagonal lattice. The corresponding amplitudes and phase shifts were modelled by FEFF8. The distances of the shells amounted to 2.64(1) Å (Ru1) and 2.71(1) Å (Ru2) with a fixed degeneracy of N = 6 for each backscattering path according to the hexagonal crystal structure of Ru-metal. In addition, equal Debye-Waller factors $\sigma^2 = 0.0033(1)$ Å^2 were used. The excellent agreement of mRDF and fit is shown in the right frame of Fig. 5.11. The fit curve was subtracted from the mRDFs of the reduced samples leading to the residuals mRDF shown in the left frame of Fig. 5.66.

The Ru–O related peaks were integrated between the markers shown in the left frame of Fig. 5.66 to obtain numerical values for the peak intensities. The obtained values are drawn vs. the corresponding oxygen deficits δ (from Tab. 5.11) in the right frame of Fig. 5.66. The Ru-metal sample

was determined to have a zero peak area and $\delta = 0$. As clearly visible in the right frame of Fig. 5.66, the peak areas show a linear correlation to the (apparent) oxygen deficits as indicated by the red dashed line, which represents a linear fit.

The correlation of δ and the Ru–O peak area illustratively reflects the incomplete reduction of pure and rare-earth substituted La$_2$RuO$_5$ samples due to a remaining small fraction of oxidized Ru. One might assume that the applied reduction temperature of 950°C is not sufficient to obtain a complete reduction. For this reason additional reductions on a Netzsch STA 409 up to a temperature of 1100°C were performed. Even at this much higher temperature the reduction remained incomplete as deduced from the weight loss of 6.81% related to an (apparent) oxygen deficiency of $\delta = 0.05$. The fact that δ was found to be smaller than for the samples heated to only 950°C but neither an additional reduction step nor a slow continous weight loss were observed indicate that the reduction process becomes very slow at temperatures above approximately 800°C. Furthermore, it can be seen from Fig. 5.66 that the reduction gradually proceeds to a higher degree with increasing *Ln*-substitution level. One possible reason may be the structural stress induced by the substitution.

The incomplete reduction of the investigated Ru-oxides is very unusual. It was found that the observed additional peak in the mRDFs of the reduced samples can be ascribed to typical Ru–O bond lengths for e.g. RuO$_2$. The peak corresponding area is correlated to the oxygen deficit obtained from the thermogravimetric measurements, which in turn means that the samples have not been completely reduced by the TG treatment. Thus, the observed deviation of theoretical and experimental oxygen content can be explained by these findings and the (apparent) oxygen deficiencies amount to $\delta = 0$ for the pure and rare-earth substituted La$_2$RuO$_5$. For the Ti- and Mn-substituted samples also $\delta = 0$ can be reasonably assumed with respect to the changed reduction reactions and, hence, different oxidized but well-defined products.

6. $Ln_y\text{Cu}_3\text{Ru}_x\text{Ti}_{4-x}\text{O}_{12+\delta}$

Besides the layered La_2RuO_5 a second group of oxides was investigated. These are based on a $2 \times 2 \times 2$ superstructure of the perovskite $AB\text{O}_3$ unit cell and is achieved by a cooperative rotation of the $B\text{O}_6$ octahedra around $\langle 111 \rangle$ corresponding to a threefold tilting according to $a^+a^+a^+$ in the Glazer notation [Gla72, Woo97a]. As a consequence, three quarters of the A-site show a strongly deformed coordination changing the cuboctahedral symmetry to an almost square-planar coordination with a changed notation A'. Due to this coordination the ions occupying the A'-sites have to be Jahn-Teller active. On the B-sites usually $3d$ and $4d$ transition metals are found in accordance with the perovskites. This results in a general sum formula $AA'_3B_4\text{O}_{12}$ for these oxides, which crystallize in the space group $\text{Im}\bar{3}$ (No. 204). The A-site corresponds to the Wyckoff-site $2a$ (relative coordinates: 0 0 0), the A'-site to $6b$ (0 1/2 1/2), the B-site to $8c$ (1/4 1/4 1/4), and the oxygen-site to $24g$ ($x\ y\ 0$, where x is typically 0.18 and y is 0.31) [Hah05, Boc79]. This structure type was first described for $\text{CaCu}_3\text{Ti}_4\text{O}_{12}$ in Ref. [Des67]. The Jahn-Teller active A'-site cations for this structure type are usually Cu^{2+} and Mn^{3+} [Vas07, Boc74, Boc79].

To illustrate the close relationship of the $AA'_3B_4\text{O}_{12}$ structure to the perovskite (see in detail in Sec. 1) both are depicted in Fig. 6.1. On the left side (Fig. 6.1a) an arrangement of $2 \times 2 \times 2$ (ideal) cubic-perovskite unit cells (e.g. SrTiO_3) is depicted with green corner sharing $B\text{O}_6$ octahedra and turquoise spheres as A-site cations. The unit cell is marked in the lower left corner similar to Fig. 1.1. The cubic structure of $AA'_3B_4\text{O}_{12}$ is shown in Fig. 6.1b. The $B\text{O}_6$ octahedra are also green to emphasize the relationship, while the A-site and A'-site cations are colored turquoise and brownish, respectively, to visually distinguish between both sites. To highlight the $A'\text{O}_4$ square plaquettes, several of them are marked by purple lines. It should be mentioned that each octahedron is linked to six plaquettes, of which always the two opposing ones are oriented the same way perpendicular to the three crystallographic axes. The open faced octahedron in the top right of Fig. 6.1b illustrates the equivalent B–O bond lengths within the octahedra similar to the perovskite, while the B–O–B angle deviates distinctly from $180°$ for the perovskite.

A remarkable number of compounds showing this specific crystal structure was synthesized and reported [Vas07]. Furthermore, a rich variety of physical properties was found depending on the used element composition. Similar to the perovskites already small substitutions can lead to significant changes of the properties. This is due to the strong correlation of the electrons of the A'- and B-site cations caused by B–O–B and A'–O–B exchange interactions, which mutually can affect each other via the A'–O–B–O–A' exchange path (colored yellow in Fig. 6.1b). Besides the doping of only one site, a co-substitution on both sites A' and B can be performed and usually results in more complex correlation phenomena.

In this chapter several new or up to now rarely described compounds and their physical prop-
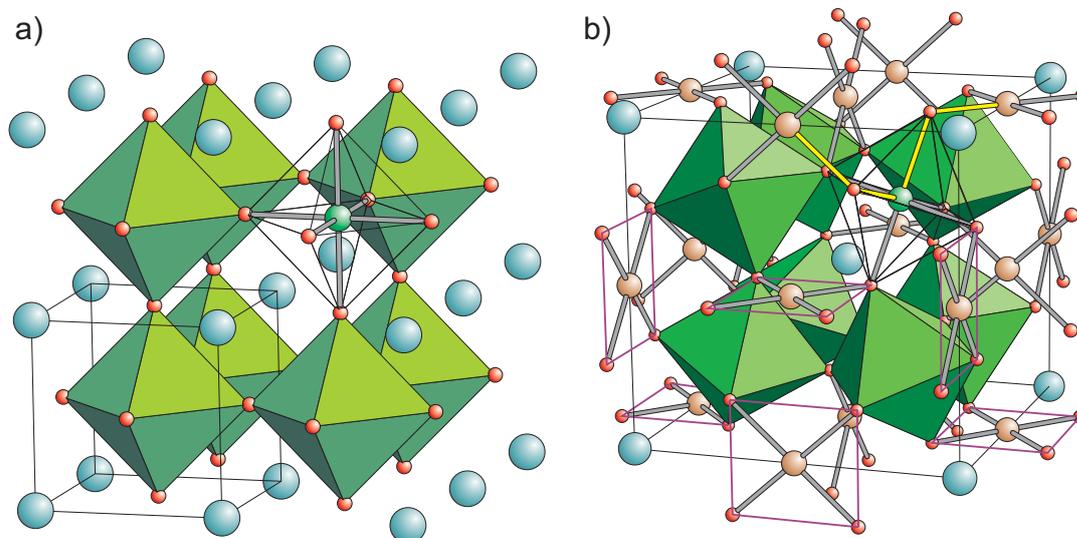
Figure 6.1.: a) Crystal structure of an ideal perovskite ABO_3 in an arrangement of $2 \times 2 \times 2$ unit cells (One cell is marked in the lower left corner in accordance with Fig. 1.1) with the *A*-site ions on the corners of the cells. The *A*-site ions are represented by large turquoise spheres, the oxygen ions are drawn as red spheres, and the BO_6 octahedra are colored green. The top right octahedron is shown with transparent faces to illustrate the regular octahedral coordination of the green *B*-site ion by grey *B*–O bonds. b) Crystal structure of $AA'_3B_4O_{12}$. The *A*-site ions are represented by turquoise spheres like in a), while the A'-site ions are colored brownish. The top right octahedron is shown with transparent faces and the grey *B*–O bonds. A possible superexchange path of two A'-sites via an octahedral center (A'–O–*B*–O–A') is illustrated by yellow bonds. For several A' ions the square-planar oxygen coordination is highlighted by purple lines.

erties are studied. The recently intensively investigated titanates of the $CaCu_3Ti_4O_{12}$-type are introduced regarding their crystal structure and physical properties. In addition, the results for the compounds with substitution on the *A*-site using rare-earth elements are described. The results of the crystal-structure analysis and magnetic properties are supported by UV-Vis spectroscopy and electronic band-structure calculations.

The second part of the chapter contains the study of the *B*-site Ru substitution effects on the titanates and the observed phase transitions. The composition was expected to strongly influence the crystal structure as well as the physical properties in $Ln_yCu_3Ti_xRu_{4-x}O_{12}$. To further investigate the relationship of structure and physical properties, the oxygen stoichiometry in combination with XANES for the cation-valence determination was studied. DFT-calculations were performed to support the experimental results.

6.1. $ACu_3Ti_4O_{12}$

Recently, the members of the $AA'_3B_4O_{12}$ oxides with copper on the A'-site and titanium on the *B*-site ($ACu_3Ti_4O_{12}$) have been of high interest. These titanates exhibit very large values for

the dielectric constant ε'. The discovery of values above 10^4 for ε' in a frequency range up to several MHz and between 100 K and 300 K was reported for CaCu$_3$Ti$_4$O$_{12}$ and the rare-earth substituted $Ln_{2/3}$Cu$_3$Ti$_4$O$_{12}$ (Ln = La, Pr, Nd, Sm - Yb) for example in Refs. [Sub00, Hom01, Sub02, Kro10, Seb10]. The large permittivity depends strongly on the sample morphology and on the quality of the electric contacts, which lead to the conclusion of several non-intrinsic effects increasing ε'. The two effects called surface barrier layer capacity (SBLC) and internal barrier layer capacity (IBLC) were suggested to describe the experimental data. The SBLC can be caused by the external contacting of the sample and, therefore, effects similar to a Schottky diode are increasing ε'. On the other hand, e.g. grain boundaries and twinning are reported as reasons for the IBLC effects. Both capacity increasing effects are found in single crystals and polycrystalline samples of CaCu$_3$Ti$_4$O$_{12}$ and have been discussed in Ref. [Kro10].

6.1.1. Crystal Structure and Magnetic Properties

The titanates ACu$_3$Ti$_4$O$_{12}$ synthesized for this work crystallize in the cubic space group $Im\bar{3}$ and provide a cell parameter of roughly 7.4 Å [Des67, Boc79]. Reference samples with divalent A-site cations (Ca, Sr) were synthesized since their properties are well studied and reported in literature. Charge neutrality is achieved assuming the typical valences +2 for Cu and +4 for Ti. These references are required, since the substitution of the A-site by trivalent rare-earth metals (Y, La, Pr, Nd, Sm, Eu, Gd, Tb, Dy, Ho, Er, Tm, Yb) reduces the occupancy to 2/3 on this site and results in the sum formula $Ln_{2/3}$Cu$_3$Ti$_4$O$_{12}$. In the same way the replacement with Ce^{4+} ions reduces the occupancy of the A-site to 1/2, i.e. Ce$_{1/2}$Cu$_3$Ti$_4$O$_{12}$. The remaining unoccupied A-sites are treated as vacancies and show no additional ordering which would lead to superstructural reflexes.

In Fig. 6.2 the Rietveld-refinement results of the x-ray diffraction patterns of CaCu$_3$Ti$_4$O$_{12}$ (top), SrCu$_3$Ti$_4$O$_{12}$ (center), and Pr$_{2/3}$Cu$_3$Ti$_4$O$_{12}$ (bottom) are depicted. All figures display good agreement of the measured data and the refinement. In addition, high crystallinity of the samples can be estimated from the small FWHM of the reflex peaks. The result for Pr$_{2/3}$Cu$_3$Ti$_4$O$_{12}$ is shown as a representative for the rare-earth substitutions. If observable, only small amounts of impurities were detected for all samples. For example, a small fraction ($\leq$ 1%) of SrTiO$_3$ in SrCu$_3$Ti$_4$O$_{12}$ was already reported in Ref. [Sub02] and results from the thermodynamically preferred formation of this phase at this temperature. Another typically found impurity is TiO$_2$. For Ce$_{1/2}$Cu$_3$Ti$_4$O$_{12}$ and Yb$_{2/3}$Cu$_3$Ti$_4$O$_{12}$ traces of the rare-earth oxides CeO$_2$ and Yb$_2$O$_3$ can be observed, respectively.

Since only the element on the A-site is varied in the substitution, the a-axis length directly depends on the ionic radii of the A-cations. This correlation is shown in Fig. 6.3 for all investigated samples. The circles mark the values obtained from Rietveld analysis of the x-ray diffraction data for the samples synthesized for this work. The red diamonds are the corresponding values reported in literature for samples obtained from a similar synthesis method [Boc79]. A good agreement of own and reported sample parameters is observed with deviations of less than 0.003 Å except for Ce and Pr, where the literature data are roughly larger by 0.01 Å compared to the own samples. The yellow downward pointing triangles indicate the corresponding A-cation size taken
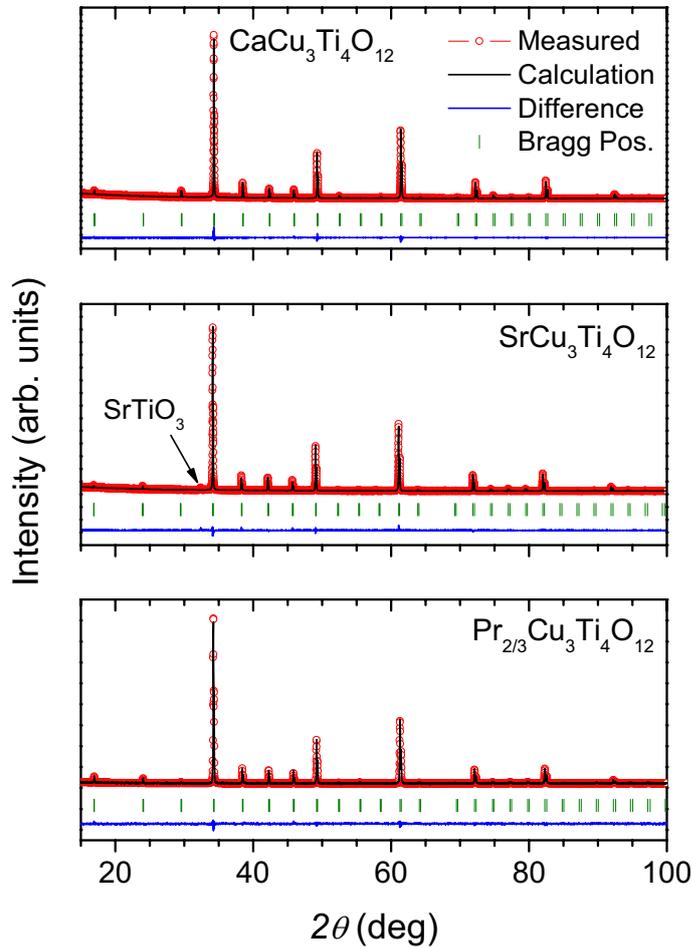
Figure 6.2.: Rietveld refinement results of the $CaCu_3Ti_4O_{12}$ (top), $SrCu_3Ti_4O_{12}$ (center), and $Pr_{2/3}Cu_3Ti_4O_{12}$ (bottom) x-ray diffraction patterns.

from literature [Sha76] for equalized coordination numbers[1]. From the ionic radii and the *a*-axis data the lanthanide contraction from La to Yb is observed. Ce is an exception, since its valence amounts to +4 compared to the Ln^{3+} of the other compounds. This can be concluded by a closer look on the Ce^{3+} ionic radius, which amounts to 1.196 Å (CN 9) and is lineary placed between trivalent La and Pr. However, the observed value for *a* is significantly smaller than expected for $Ce_{2/3}Cu_3Ti_4O_{12}$ with assumed trivalent Ce, which can be basically explained by tetravalent Ce. $SrCu_3Ti_4O_{12}$ provides the largest *a*-axis length of approximately 7.425 Å. The values for *a* of

---

[1]The majority of the data in Ref. [Sha76] are only given for ninefold coordinated ions (CN 9), however, in the $AA'_3B_4O_{12}$ crystal structure the *A*-site is coordinated cuboctahedrally by twelve oxygens (CN 12). Therefore, the data for CN 9 have been scaled to CN12 to obtain data for all used *A*-site ions. This is reasonable, since a comparableness of the ionic size for all used elements is required to discuss the correlation with the obtained cell parameters.
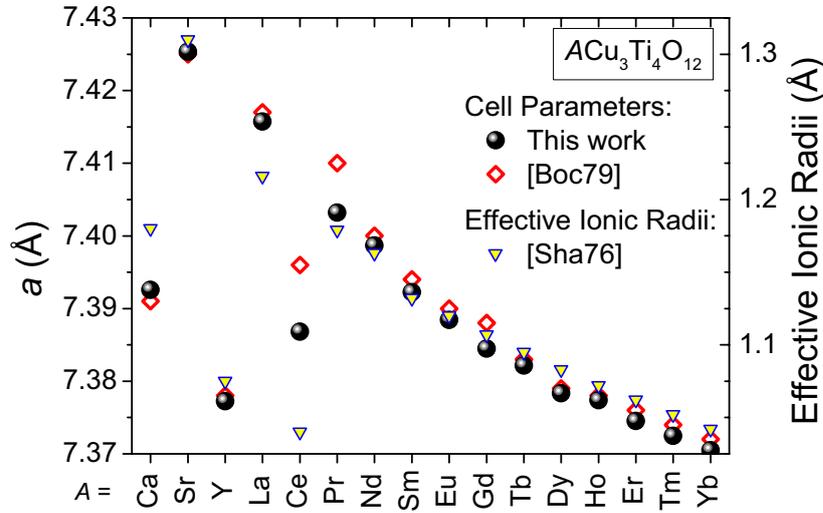
Figure 6.3.: Comparison of the cell parameters *a* of the $ACu_3Ti_4O_{12}$ samples from this work (circles) and literature (open red diamonds). Effective ionic radii of the corresponding *A*-site cations are shown as yellow downward pointing triangles.

$CaCu_3Ti_4O_{12}$ and $Sm_{2/3}Cu_3Ti_4O_{12}$ are very similar, also the *a* axis lengths of $Y_{2/3}Cu_3Ti_4O_{12}$ and $Ho_{2/3}Cu_3Ti_4O_{12}$ are mutually in good agreement as expected from the *A*-site ionic radii. The obtained values for *a* of $Pr_{2/3}Cu_3Ti_4O_{12}$ and $Ce_{1/2}Cu_3Ti_4O_{12}$ are fitting better to the course of the ionic radii than the data in Ref. [Boc79].

In Fig. 6.4 selected parameters of the $AA'_3B_4O_{12}$ crystal structure are displayed for a more detailed analysis of the Rietveld refinement results. The *Ln*–O distance shown in Fig. 6.4a is almost unaffected by the size of the *A*-site cation. It remains almost constant at roughly 2.59 Å, which is comparable to $CaCu_3Ti_4O_{12}$ with 2.6 Å [Sub02]. The constant *Ln*–O distance can be explained by the concomitant increase of the relative *x* and *y* coordinates of the oxygen-site due to the observed decrease of the *a*-axis.

The Ti–O–Ti bonding angle depicted in Fig. 6.4b is a measure of the octahedral tilting in the crystal structure. For $CaCu_3Ti_4O_{12}$ a value of approximately 141° was reported in Ref. [Sub02], which is very close to the constant 141.2° found for the $Ln_{2/3}Cu_3Ti_4O_{12}$ samples. This constant value for the $ACu_3Ti_4O_{12}$ compounds should be kept in mind, because it affects the *B*–O–*B* exchange interaction as well as the electronic band structure.

In Fig. 6.4c the evolution of the Ti–O bond length in $Ln_{2/3}Cu_3Ti_4O_{12}$ is shown. The values decrease linearly from approximately 1.965 Å for La to 1.954 Å for Tb and remain constant until Yb. This behavior is unexpected since the Ti–O distances are assumed to be almost fixed and not to be influenced by the unit-cell contraction caused by the *A*-site substitution. Furthermore, the Cu–O bond length shown in Fig. 6.4d decreases almost linearly from 1.98 Å for La to approximately 1.965 Å for Yb. These Ti–O and Cu–O bond-length reductions can be explained by
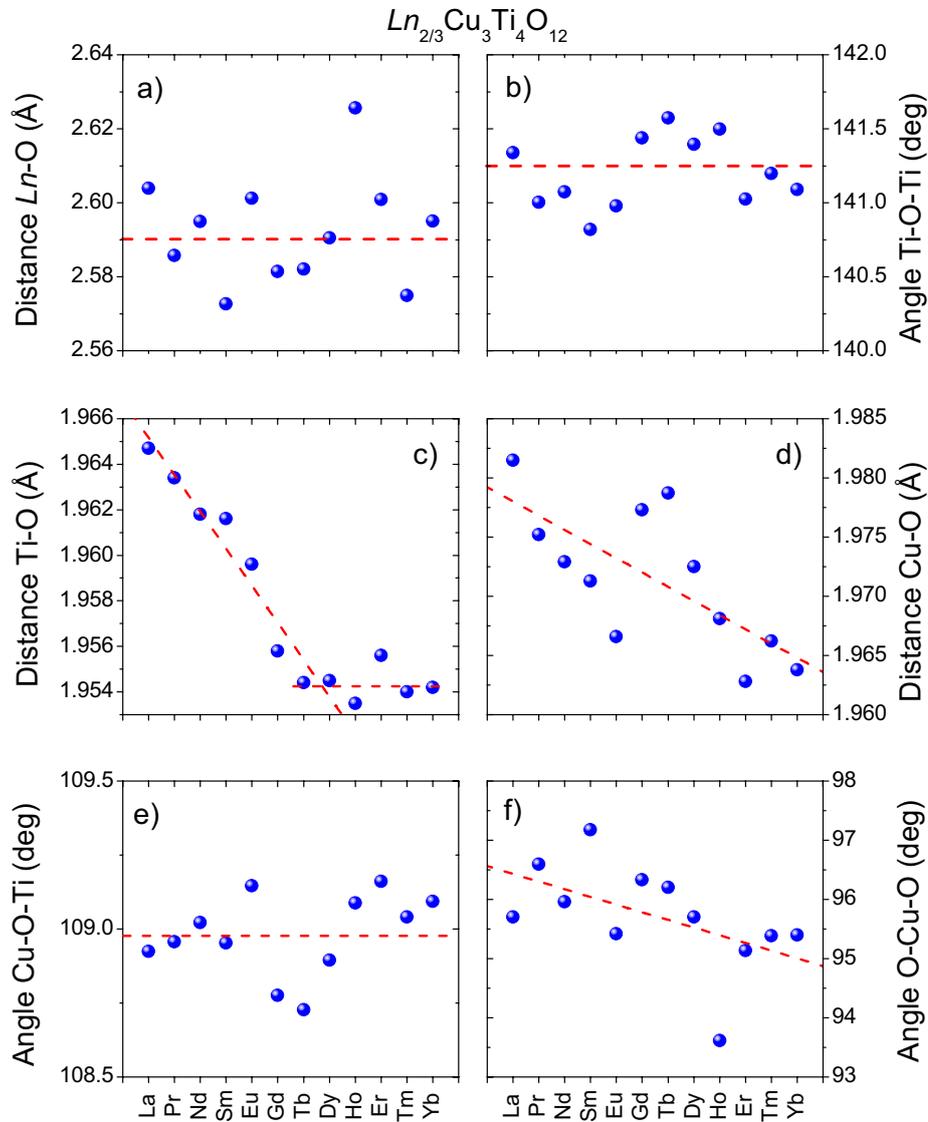
Figure 6.4.: Detailed structural data of the $Ln_{2/3}Cu_3Ti_4O_{12}$ samples. a) Ln–O distances, b) Ti–O–Ti angles, c) Ti–O bond lengths, d) Cu–O bond lengths, e) Cu–O–Ti angles, and f) O–Cu–O angles. Dashed red lines are drawn to guide the eye and particularly represent linear regressions.

the compression of interatomic distances to a minimum value caused by the unit-cell contraction. For comparison, from literature [Bro85] the minimal distances obtained for BVS calculations of ACu$_3$Ti$_4$O$_{12}$ amount to 1.815 Å for Ti–O and significantly smaller 1.679 Å for Cu–O. Since the achieved minimum for Ti–O is relatively close to this value this explains the constant value between Tb to Yb. However, the theoretical Cu–O bond is much shorter than the experimental, which, in turn, reflects the ability of further decrease until Yb in this crystal structure.

Fig. 6.4e displays the obtained values for the Cu–O–Ti angle. Although the values are spreaded significantly, the angles amount constantly to roughly 109°. The O–Cu–O angle, which is a measure of the square planar geometry of the CuO_4 plaquettes, is depicted in Fig. 6.4f. From this it can be seen that the plaquettes are not perfectly shaped squares, since the angles deviate significantly from 90°. From $La_{2/3}Cu_3Ti_4O_{12}$ to $Yb_{2/3}Cu_3Ti_4O_{12}$ an almost linear decrease from roughly 96.5° to 95° is found, which, in turn, yields an increasingly squared shaping with decreasing unit-cell volume. The described behavior of the detailed structural properties depending on the A-site cation radii can be used to interpret the change of the physical properties of the samples, since already small variations of the interatomic distances and angles strongly influence the cationic exchange interaction. Apart from this, the obtained interatomic distances of $Nd_{2/3}Cu_3Ti_4O_{12}$ and $Tb_{2/3}Cu_3Ti_4O_{12}$ are in good agreement with data given in Ref. [Mul86] and reveal the good comparability of the new and already reported data. A closing remark has to be given on the scattering of the data points. This can be explained by performing structural analysis based on XRD data, which are known for the rather low scattering intensity of the oxygen ions. Nevertheless, the accuracy is absolutely sufficient for a qualitative analysis.

In addition, the temperature dependent magnetic susceptibilities of $ACu_3Ti_4O_{12}$ compounds were investigated. In the case of non-magnetic A-cations (A = Ca, Sr, Y, La) the susceptibility is paramagnetic and shows an antiferromagnetic ordering at roughly 25 K (indicated by the vertical red dashed line in Fig. 6.5a and b). The obtained magnetic moments from Curie-Weiss fits above 50 K are well in agreement with the calculated values from a spin-only approximation of the sum of three Cu^{2+} ions with $S = 1/2$ due to the $3d^9$ electron configuration [Kro09, Kro10, Dit11]. The antiferromagnetic ordering of the Cu spin moments is clearly observed at $T_N \approx 25$ K. The ordering was described as the alternating antiferromagnetic stacking of planes of ferromagnetically coupled Cu moments along the crystallographic [111]-direction [Kim02]. The main exchange path is presumed along Cu–O–Ti–O–Cu by results from linear spin-wave calculations [Kim02]. An example for this path is indicated by the yellow bonds in the upper right corner of Fig. 6.1b.

According to the free-ion approximation, the magnetic moment carried by the rare-earth metal ions in $Ln_{2/3}Cu_3Ti_4O_{12}$ varies strongly between almost zero for Eu^{3+} and roughly 10 μ_B for Dy^{3+} [Lue99]. In the paramagnetic region a good agreement of experimental data and the Curie-Weiss fit using the sum of the Cu and Ln moments from literature is achieved [Kro10]. The Curie-Weiss temperatures obtained from the fit could also be described by a model of two weakly interacting magnetic sublattices (Cu^{2+} and Ln^{3+}) [Dit11, Kro10] similar to the rare-earth substituted La_2RuO_5 compounds described in Sec. 5.1.2. The varying Ln^{3+} specific moments strongly influence the susceptibility curves illustrated in Fig. 6.5 for selected lanthanides. While in the description of the very similar susceptibilities of $SrCu_3Ti_4O_{12}$ and $La_{2/3}Cu_3Ti_4O_{12}$ only Cu is required, the adding of an additional intermediate moment like, for example Yb^{3+} (4.536 μ_B), shifts χ significantly. This shift increases for large moments of e.g. Gd^{3+} (7.937 μ_B). The susceptibility of $Gd_{2/3}Cu_3Ti_4O_{12}$ becomes that strongly dominated by the rare-earth moment that the anomaly of the AFM ordering of Cu cannot be observed. Thus, the magnetic properties of the $Ln_{2/3}Cu_3Ti_4O_{12}$ compounds were distributed into three groups depending on the value of the A-site cation magnetic moment [Dit11, Kro10]. In the first one the weakly or non-magnetic cations
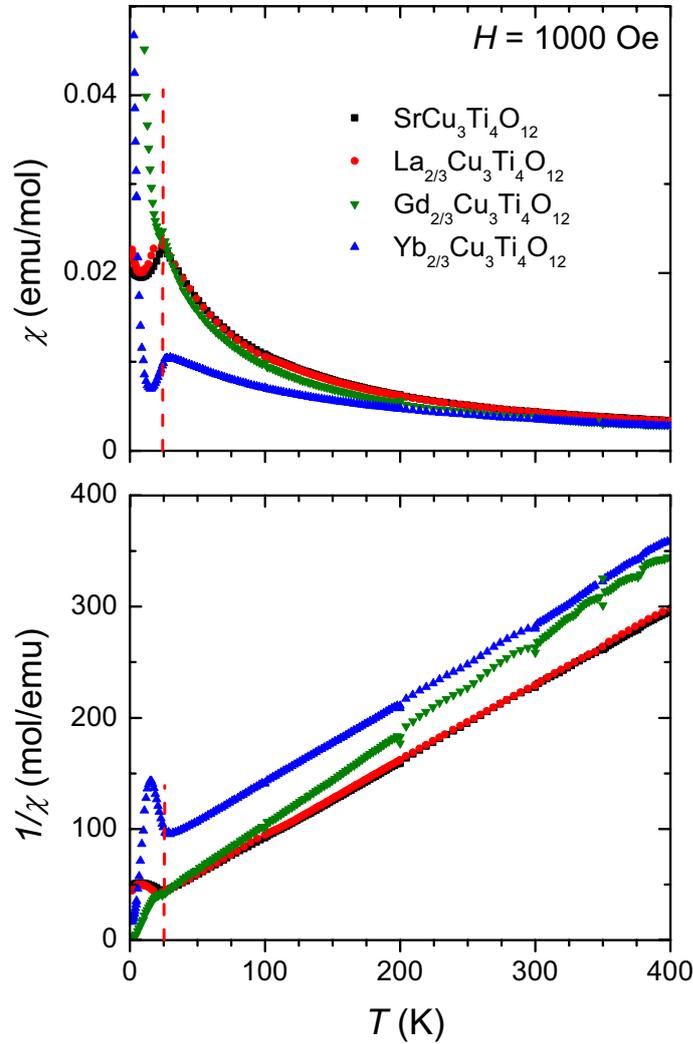
Figure 6.5.: a) Magnetic susceptibilities χ of selected $ACu_3Ti_4O_{12}$ samples (A = Sr, La, Gd, Yb) corrected by the paramagnetic contribution of the rare-earth metal ions. b) The corresponding inverse susceptibilities $1/\chi$. The vertical dashed red line marks the Néel temperature of the antiferromagnetic Cu^{2+} spin-moment ordering, for details see text.

Ca, Sr, Y, La, Sm, and Eu are grouped. They show the Cu dominated χ and a clearly visible kink at T_N. The second group contains the lanthanides with intermediate magnetic moment between roughly 3.5 μ_B and 4.5 μ_B, in detail Pr, Nd, and Yb. For these compounds the AFM ordering could hardly be observed in χ, but it is observable in $1/\chi$ at roughly 25 K. In the susceptibilities of the third group with lanthanides possessing large magnetic moments like Gd, Tb, Dy, Ho, Er, and Tm (≈ 7.5 μ_B to ≈ 10.6 μ_B) the AFM Cu ordering in both χ and $1/\chi$ is apparently covered.

This vanishing of the transition anomaly in *Ln$_{2/3}$*Cu$_3$Ti$_4$O$_{12}$ motivated a more detailed investigation of the antiferromagnetic Cu ordering. It either is suppressed by the large magnetic moments of the rare-earth metal ions, or the effect is simply hidden in the susceptibility curve due to the strongly dominating lanthanide moments. Therefore, electron spin resonance (ESR) spectroscopy was performed investigating the Cu^{2+} moment [Dit11]. It was shown that the antiferromagnetic ordering is preserved for all samples and the rare-earth metal ions yield an almost undisturbed paramagnetic behavior over the whole temperature range. With respect to this finding the rare-earth contribution was subtracted from the experimental susceptibilites similar to the rare-earth substituted La$_2$RuO$_5$ (Sec. 5.1.2.1). The resulting susceptibilities for Gd and Yb are shown in Fig. 6.5. They are very similar to the ones with non-magnetic *A*-site cations and, more interestingly, they reveal the expected anomaly at T_N. The strong increase of χ at very low temperatures can be ascribed to impurities, not ordering Cu spins, and, if present, magnetic moments of the lanthanide ions. The deviating slope of Gd$_{2/3}$Cu$_3$Ti$_4$O$_{12}$ can maybe be explained by the electronic correlation of Cu and Gd, which reduce the Cu spin moment by increasing spin-obit coupling. The observed behavior exhibits the strong influence of the crystal structure on this ordering phenomena, since the simultaneous decrease of Ti–O and Cu–O bond length along with the constant Cu–O–Ti angle are the only relevant parameters for the AFM ordering of the Cu^{2+} moments, while the magnetic moment of the lanthanides almost do not matter.

The rather large variety of the *A*-cation size and, linked to this, of the unit-cell parameter values (see Fig. 6.3) motivated the synthesis of *A*Cu$_3$Ti$_4$O$_{12}$ compounds with a mixed *A*-site occupation. Polycrystalline samples were successfully synthesized and neither yield two separate phases nor a cationic ordering and, therefore, a resulting superstructure. In the top frame of Fig. 6.6 the cell-parameter data of (La$_{1-x}$Pr$_x$)$_{2/3}$Cu$_3$Ti$_4$O$_{12}$ are depicted which are obtained from the Rietveld analysis of XRD measurements. The parameter x describes the fraction of Pr substituting La on the $A_{2/3}$-site. The linear decrease of the cell parameter is in excellent agreement with Vegard's law for the occupancy variation of two differently sized ions on one crystallographic site [Veg21]. For similar reasons the mixture of Ca and a lanthanide ion on the *A*-site was investigated. To preserve charge neutrality the fraction of *Ln^{3+}* was multiplied with 2/3. The corresponding cell-parameter evolution for (*Ln$_{2/3\cdot(1-x)}$*Ca$_x$)Cu$_3$Ti$_4$O$_{12}$ is depicted in the bottom frame of Fig. 6.6 and x is the fraction of Ca on the *A*-site. The selected trivalent rare-earth metal ions either possess a larger ionic radius (Pr^{3+}), a similar radius (Sm^{3+}), or a smaller radius (Dy^{3+}) compared to Ca^{2+}. The partly substitution of Ca by La was reported by Shao *et al.* [Sha07], however, there the La substitution was assumed to replace Cu, which is unreasonable due to the distinct difference of the ionic radii of Cu^{2+} and La^{3+}. The cell parameters of our samples obey Vegard's law and show a linear dependency on x (bottom frame of Fig. 6.6). This available mixture of two differently sized cations on the *A*-site proves the stability of the initial Cu$_3$Ti$_4$O$_{12}$ crystal structure, which can be described simply to "breathe" depending on the *A*-site cationic size. The structure is even stable with completely vacant *A*-sites, which was reported for Cu$_3$Ti$_2$Ta$_2$O$_{12}$ and Cu$_{2+x}$Ta$_4$O$_{12+\delta}$. This is possible due to the (partial) replacement of the tetravalent Ti by pentavalent Ta ions to preserve the charge neutrality [Ebb10].
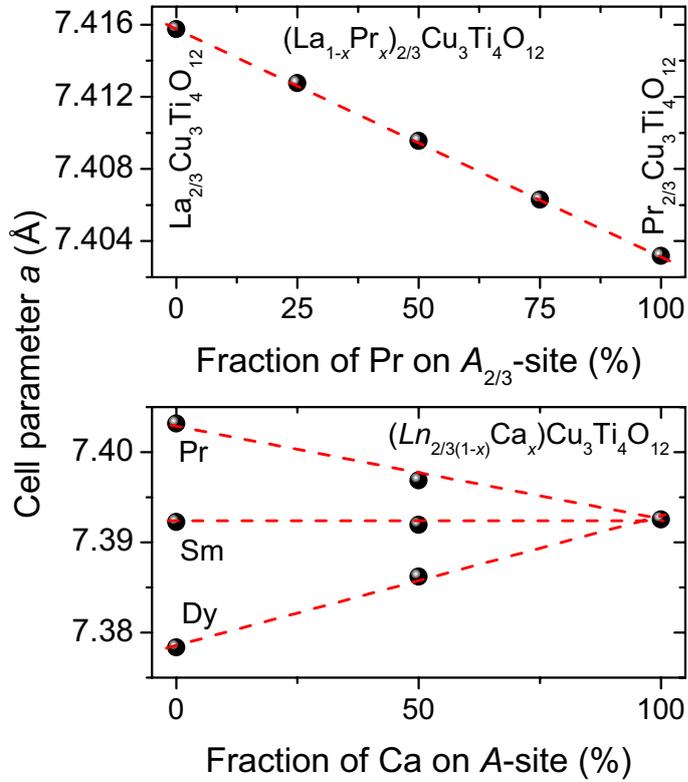
Figure 6.6.: Cell-parameter data of $(La_{1-x}Pr_x)_{2/3}Cu_3Ti_4O_{12}$ (top frame) and $(Ln_{2/3\cdot(1-x)}Ca_x)Cu_3Ti_4O_{12}$ (bottom frame) obtained from Rietveld analysis of x-ray diffraction measurements.

6.1.2. Single-Crystal Structure

Single crystals of $La_{2/3}Cu_3Ti_4O_{12}$ were obtained from a CuO flux reaction (see Sec. 2.1.4) and investigated by single-crystal x-ray diffraction utilizing a $P2_1$ diffractometer (Syntex) with Mo-K_α radiation. Shape of the black crystal is a truncated pyramid. For the absorption correction the crystal faces were indexed and both the indices and corresponding measures were added to the input file for the refinement. The detailed parameters of the measurement, given in Tab. A.7 in the appendix, reveal the high refinement quality characterized by the low residuals and well equilibrated remaining electron density. To summarize, the obtained data are very similar to the $CaCu_3Ti_4O_{12}$ single crystals described in Refs. [Hom01, Kro07], as expected.

The cell parameter a amounts to 7.4361 Å, which is significantly larger by 0.02 Å than the value obtained from the Rietveld analysis of the polycrystalline sample ($\approx$ 7.416 Å). A small deviation of several mÅ is normal and can be explained by the different synthesis conditions and the lower accuracy of the unit-cell parameters of the single-crystal measurement data. Nevertheless, the
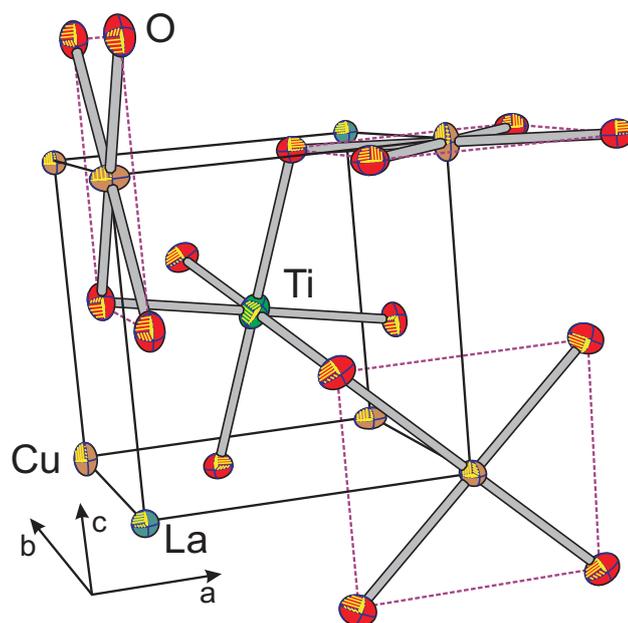
Figure 6.7.: Detail of the crystal structure of single crystalline $La_{2/3}Cu_3Ti_4O_{12}$ (La: blue, Cu: brown, O: red, Ti: green ellipsoid). One octant of the $AA'_3B_4O_{12}$ structure corresponding to a perovskite unit cell is shown to illustrate specific structural features. The central TiO_6 octahedron is marked by the grey Ti–O bonds. To exemplify their orientation and connection to the octahedra, three of the six coordinating CuO_4 plaquettes are shown. The anisotropic displacement ellipsoids are drawn with 90% probability.

found difference may result from additional copper ions incorporated on the *A*-site due to the used flux and long reaction duration. This is reasonable since the occupation factor refines to a slightly larger value than the expected formal 2/3. The atomic coordinates and displacement factors are listed in Tabs. A.9 and A.10. The values are very similar to the results of the Rietveld analysis of the polycrystalline sample. Furthermore, the characteristic interatomic distances and angles listed in Tab. 6.1 are in rather good agreement with the results for the polycrystalline $La_{2/3}Cu_3Ti_4O_{12}$, which are shown above in Fig. 6.4.

To illustrate specific parts of the crystal structure of $La_{2/3}Cu_3Ti_4O_{12}$, one representative octant vaguely corresponding to a perovskite unit cell is depicted in Fig. 6.7. Three of the six CuO_4 plaquettes connected to the TiO_6 octahedra are shown, one example for each orientation perpendicular to the unit-cell axes. Each two opposing plaquettes on the corners of the octant align parallel to each other. While the blue La ions display almost isotropic displacement factors the brown Cu ions provide a preferred oscillation direction perpendicular to the plaquette plane (marked by grey Cu–O bonds and dashed purple lines), which is indicated by the correspondingly elongated ellipsoids. The green Ti ions also show slightly deformed ellipsoids, which are elongated along the space diagonal [111]. The TiO_6 octahedron (grey Ti–O bonds) only indicates a slight rotation, since the red oxygen ellipsoids preferrably are elongated perpendicular to the Cu–O–Ti bonds.

Table 6.1.: Interatomic distances (in Å) and angles for the $La_{2/3}Cu_3Ti_4O_{12}$ and $SrCu_3Ru_4O_{12}$ single crystals.

$La_{2/3}Cu_3Ti_4O_{12}$		$SrCu_3Ru_4O_{12}$	
Ti–O	1.9698(4)	Ru–O	1.9897(10)
Cu–O	1.9847(9)	Cu–O	1.9322(27)
La–O	2.6272(10)	Sr–O	2.6426(28)
Ti–O–Ti	141.38(5)°	Ru–O–Ru	138.46(5)°
O–Cu–O	94.77(5)°	O–Cu–O	94.93(5)°
Ti–O–Cu	109.02(5)°	Ru–O–Cu	110.49(5)°

The quality of the crystal-structure refinement is high since absolute values of the displacements are relatively small and provide reasonable thermal oscillation movements in agreement with the crystal structure.

Besides the titanate cubic $SrCu_3Ru_4O_{12}$ single crystals with typical edge lengths of roughly 0.08 mm were obtained from a similar flux reaction. The single crystal x-ray diffraction measurement was performed with a STOE IPDS 2 diffractometer (Mo-K_α radiation). The cubic crystal shape was studied by a scanning electron microscope (SEM) and is shown in Fig. 6.8. The crystal faces can be indexed in agreement with the {100} planes as expected for the cubic crystal structure. Small pores or holes are observed on the surface resulting from the flux-removing process using diluted hydrochloric acid. This porous surface explains the lower refinement quality compared to the $La_{2/3}Cu_3Ti_4O_{12}$ crystal. Due to the resulting inhomogeneous crystal density the simple absorption correction using the crystal shape and face indexing is overestimating the absorption and therefore not accurately correcting the reflex intensities. The detailed parameters of the measurement are listed in Tab. A.8 in the appendix.

The cell parameter a amounts to 7.4418 Å, which is only slightly larger than the value found for single crystalline $La_{2/3}Cu_3Ti_4O_{12}$ although the replacement of Ti by Ru is expected to stronger increase the unit-cell volume. The atomic coordinates and displacement factors shown in Tabs. A.9 and A.10 provide similar values compared to the $La_{2/3}Cu_3Ti_4O_{12}$ crystal. The x-coordinate for the oxygen site for $SrCu_3Ru_4O_{12}$ is slightly smaller with a value of 0.1755 whereas the y-coordinate is slightly increased to 0.3088 indicating the small changes of the octahedra tilting angle caused by Ru incorporation.

By comparing the interatomic distances of $SrCu_3Ru_4O_{12}$ with the ones of $La_{2/3}Cu_3Ti_4O_{12}$ (Tab. 6.1), the Ru–O distance is expectedly larger than for Ti–O by approximately 0.02 Å due to the slightly larger Ru ion. On the other hand, the Cu–O bond length in $SrCu_3Ru_4O_{12}$ is distinctly reduced to compensate the growth of the octahedra volume, since the O–Cu–O angles of the CuO_4 plaquettes remain constant for both samples. The Ru–O–Cu angle is slightly increased by roughly 1.5° compared to the corresponding Ti–O–Cu angle, which could be indication for a varying magnetic exchange of Cu and Ru simply caused by the structural changes. Further physical properties have not yet been investigated on the single crystals. Nevertheless it can be expected
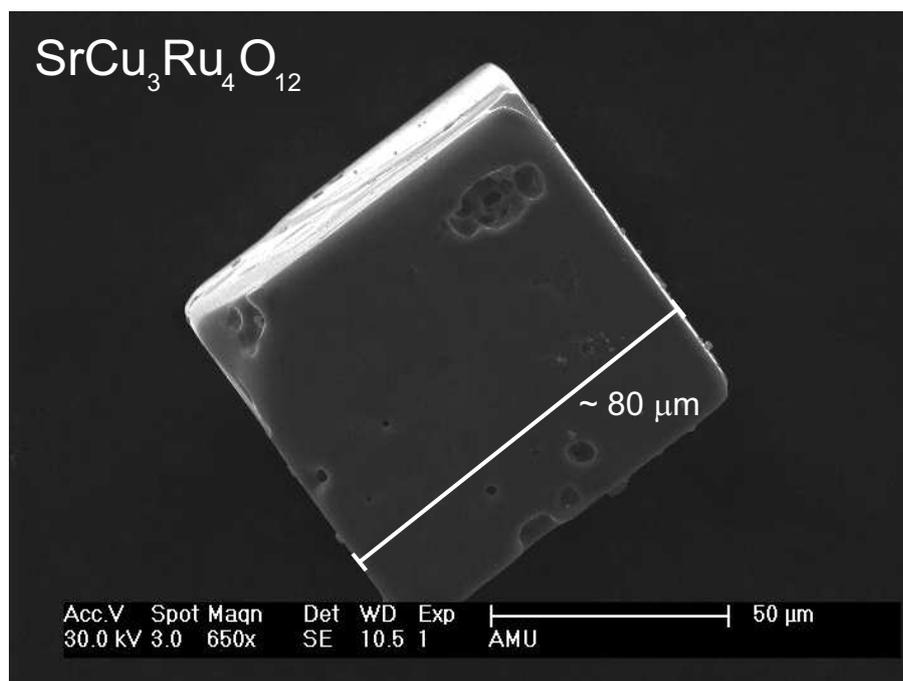
**Figure 6.8.:** SEM image of a SrCu$_3$Ru$_4$O$_{12}$ cubic single crystal.

that measurements depending on the crystallographic direction will yield isotropic results due to the cubic symmetry, however, for example, electric conductivity measurements are assumed to be more accurate, since grain boundary caused effects can be neglected.

The shown data are in good agreement with the structural data reported for NdCu$_3$Ru$_4$O$_{12}$ single crystals grown from a Cu/Cu$_2$O flux [Mul86]. The interatomic distances of NdCu$_3$Ru$_4$O$_{12}$ are very similar to the corresponding ones listed in Tab. 6.1 for SrCu$_3$Ru$_4$O$_{12}$. A more detailed study of the Ru containing AA'_3B_4O$_{12}$ compounds is presented below in Sec. 6.2.

6.1.3. UV-Vis Spectroscopy

The ACu$_3$Ti$_4$O$_{12}$ samples are colored orange-brownish indicating a significantly large band gap. This observation is supported by the low electrical conductivity measured for the samples studied by dielectric spectroscopy [Kro10]. The conductivity behaves typically for a semiconducting material close to an insulator, i.e. the band gap is expected to be in the range of roughly 3 eV.

The band gap was determined from the absorption-edge position measured by diffuse-reflectance spectroscopy in a range 250 nm $\leq \lambda \leq$ 1000 nm using a UV-Vis-IR spectrometer (Lambda 19 by Perkin Elmer). For the UV range a deuterium lamp is used in combination with a tungsten lamp (showing the radiation maximum in the visible and near infrared wavelength range) to cover the whole wavelength range. The samples or the white standard (LiF) were prepared in a circular depression with approximately 2 mm diameter on the sample holder. Samples were mixed with an equivalent amount of white standard. This leads to a constant background, which was subtracted
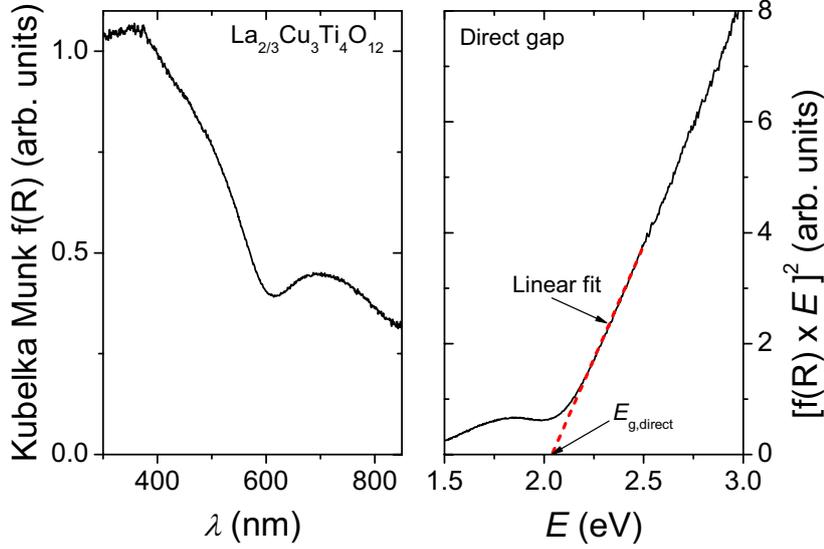
Figure 6.9.: Left: Kubelka-Munk function f(R) calculated from experimental reflectance of polycrystalline La$_{2/3}$Cu$_3$Ti$_4$O$_{12}$. Right: Determination of the direct band gap $E_{g,direct}$ from $[f(R) \times E]^2$ by a linear fit marked by the red dashed line.

from the measured spectra. The spectra yielded a large absorption edge as a consequence of the band gap as well as several additional small edge like features at higher wavelengths, which are neglected in the following.

The wavelength λ was transformed to an energy scale according to $E = hc/\lambda$ (*h*: Planck's constant, *c*: speed of light). Using the experimental reflectances (R) the Kubelka-Munk functions were calculated according to f(R) = (1-R)^2/(2R) [Kub31]. The result is shown in the left frame of Fig. 6.9 for La$_{2/3}$Cu$_3$Ti$_4$O$_{12}$, which is similar to the result in Ref. [Cla11] for CaCu$_3$Ti$_4$O$_{12}$. To determine the gap energy, f(R) was weighted according to $[f(R) \times E]^r$, which can be used for displaying a direct gap for $r = 2$ or an indirect gap for $r = 1/2$ [Loc07, Cla11]. The existence of both a direct and an indirect gap with similar values is reasoned by the obtained band structure discussed in Sec. 6.1.4, where the bands close to E_F are relatively flat. In the right frame of Fig. 6.9 $[f(R) \times E]^2$ is shown for the energy range between 1.5 and 3 eV and the linear increase above 2.2 eV indicates the direct gap. A linear fit drawn as the solid red line is used to determine $E_{g,direct}$ from the intersection point with the E-axis. The obtained value amounts to approximately 2.06 eV for $E_{g,direct}$ of La$_{2/3}$Cu$_3$Ti$_4$O$_{12}$. For CaCu$_3$Ti$_4$O$_{12}$ 2.01 eV is obtained, which is slightly smaller than 2.21 eV reported by Clark *et al.* [Cla11]. The indirect gap was reported to be 1.93 eV ($E_{g,indirect}$) [Cla11], which is significantly larger than the obtained average (1.2 ± 0.2) eV for the ACu$_3$Ti$_4$O$_{12}$ samples. This is reasoned by the small available linear regime for the fit when $r = 1/2$ is used to weight the Kubelka-Munk function. Therefore, the indirect gap is not further considered
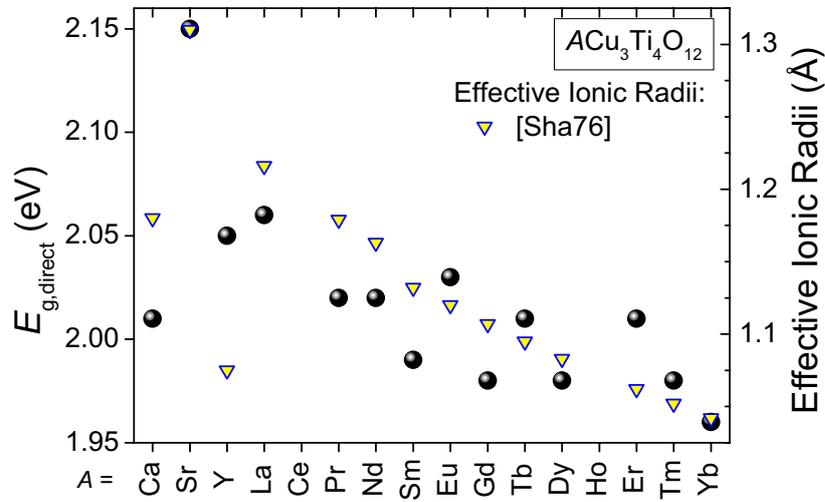
Figure 6.10.: Comparison of the $E_{g,direct}$ values (circles) and the corresponding A-site cation size (yellow triangles) of $ACu_3Ti_4O_{12}$.

in the investigation at this point.

Different values for $E_{g,direct}$ were reported previously for $CaCu_3Ti_4O_{12}$. Homes *et al.* [Hom03] determined the optical gap to a value larger than 1.5 eV, while Ning *et al.* [Nin08] found 2.88 eV from a measurement of a thin film prepared on a $LaAlO_3$ substrate in transmission mode. The values of the direct gaps of all investigated $ACu_3Ti_4O_{12}$ samples amount to $1.96eV \leq E_{g,direct} \leq$ 2.15 eV, which is in the range of the literature data and fits nicely to the observed orange-brownish color of the powder samples. In Fig. 6.10 the $E_{g,direct}$ values (circles) of all investigated $ACu_3Ti_4O_{12}$ samples are shown in comparison with the A-site cationic size (yellow triangles), which is correlated to the unit-cell parameter a (see Fig. 6.3). From this figure it can be carefully assumed that the band-gap value is linked to the A-site ion radii, which is reasonable, since the interatomic distances Ti–O and Cu–O are also correlating with this size. As was mentioned above (Sec. 5.1.4) shorter bond-lengths cause the broadening of the electronic bands [Hof88], which may result in a change of the band gap. Due to the very similar optical properties also the electronic structure for all $ACu_3Ti_4O_{12}$ samples can be considered similar. In combination with the only slightly varying crystal structures similar physical properties are expected, as already reported, for example, in Refs. [Kro10, Seb10, Dit11].

6.1.4. DFT Calculation

Using DFT calculations it is possible to directly compare the different $ACu_3Ti_4O_{12}$ compounds with one consistent method. While for $CaCu_3Ti_4O_{12}$ the results of several electronic band-structure calculations using different functionals for the treatment of the electron density were reported in literature, for $SrCu_3Ti_4O_{12}$ and $La_{2/3}Cu_3Ti_4O_{12}$ this is not the case. Basic *ab initio* LDA and
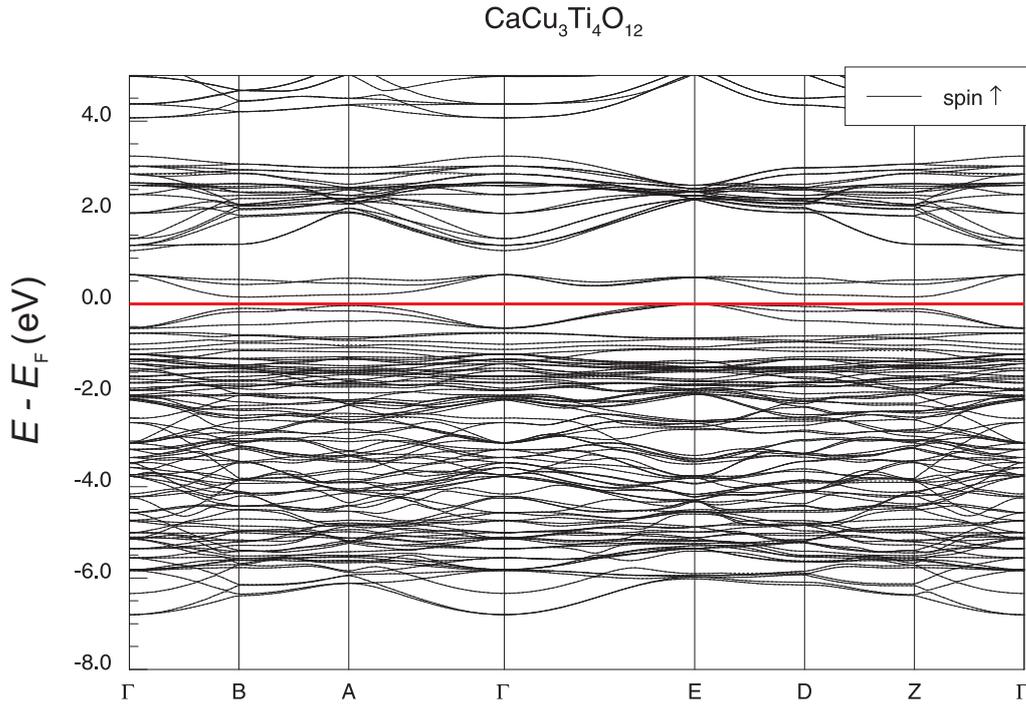
$CaCu_3Ti_4O_{12}$

Figure 6.11.: Electronic band structure of $CaCu_3Ti_4O_{12}$ calculated with FPLO applying LSDA. The solid lines mark the bands of the spin-up channel, which is congruent with the spin-down channel due to the antiferromagnetic result. The horizontal solid red marks the Fermi energy.

LSDA calculations for $CaCu_3Ti_4O_{12}$ were performed in Ref. [He02, He03, Fag05], GGA was used in Ref. [Li05, Shi07], and from Hückel crystal-orbital overlap-population (COOP) models the DOS was derived in Ref. [Mat06]. The results of various methods LDA, LSDA+U and GGA were compared by Zheng *et al.* [Zhe10], who also reported on the nanoscale disorder effects in detail concerning the Ca and Cu site and the resulting change of the electronic band structure. The most sophisticated LSDA+U calculation results were reported by Clark *et al.* in combination with diffuse-reflectance measurements [Cla11]. These calculations based all on crystal-structure data obtained from Rietveld analysis results of powder XRD data, which reasoned to use the obtained own structure data for the DFT calculations of the titanates.

For this work the LSDA model was used for the band-structure modelling of $CaCu_3Ti_4O_{12}$, $SrCu_3Ti_4O_{12}$, and a hypothetical $LaCu_3Ti_4O_{12}$ using the FPLO code. Similar to the DFT-LSDA calculations of La_2RuO_5 (Sec. 4.5) the symmetry was reduced to P1 to vary single initial spin-moments of the atoms in the lattice. Initially the results for the original cubic $Im\bar{3}$ and the transformed triclinic P1 symmetry were compared and were found to agree well. In reciprocal space $4 \times 4 \times 4$ *k* points were chosen for the calculation similar to the literature. The La-site in $LaCu_3Ti_4O_{12}$ was set fully occupied, since it was not possible to obtain reasonable results simulating a 2/3rd occupied site with a coherent-potential approximation (CPA) due to the large difference of the "atom" chemical properties, i.e. La and empty site [Koe97].
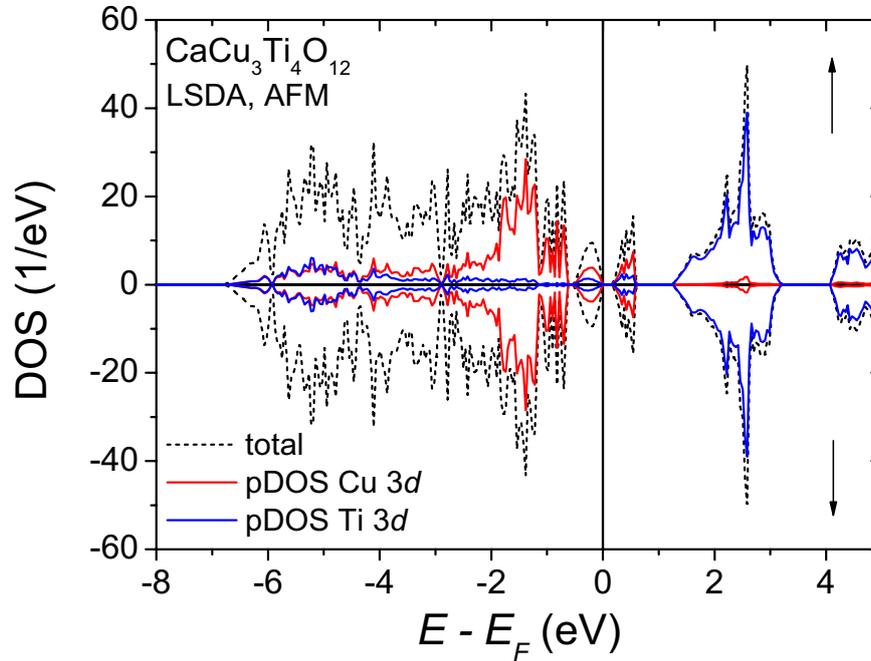
Figure 6.12.: Density of states of CaCu$_3$Ti$_4$O$_{12}$ calculated with FPLO applying LSDA (top frame: spin-up channel, bottom frame: spin-down channel).

The spin-polarized modelling was used since the Cu spin moments order antiferromagnetically below roughly 25 K in all three compounds, which was shown above in Sec. 6.1.1 by magnetic susceptibility data. The obtained band structure yields semiconducting property in accordance with the experimental results (Sec. 6.1.3), which are indicating a significant band gap of approximately 2 eV. In Fig. 6.11 the obtained electronic band structure of CaCu$_3$Ti$_4$O$_{12}$ using LSDA is depicted. The resulting bands for the spin-up and the spin-down channel are identical, which is expected for a completely antiferromagnetically ordered compound. The valence band below E_F is rather broad with roughly 6 eV and consists mainly of Cu 3d and O 2p bands. Slightly above E_F a narrow region containing empty Cu 3d and O 2p bands is observed and roughly between 1.5 eV and 3 eV the unoccupied Ti 3d and O 2p bands forming the conduction band are found.

The obtained CaCu$_3$Ti$_4$O$_{12}$ band structure is in good agreement with literature for DFT calculations using similar density functionals [He02, Fag05]. The resulting DOS is depicted in Fig. 6.12 for both spin channels indicated by the arrows. An antiferromagnetic arrangement was used for the initial spin orientations of the Cu atoms, which refined to the shown symmetrical DOS. The region between -6 eV and E_F consists of hybridized Cu 3d and O 2p states and some additionally mixing Ti 3d orbitals. The narrow contribution above E_F in Fig. 6.12 stems from antibinding Cu 3d_{xy} orbitals which geometrically form direct σ-bondings to the oxygens in the CuO$_4$ plaquettes.
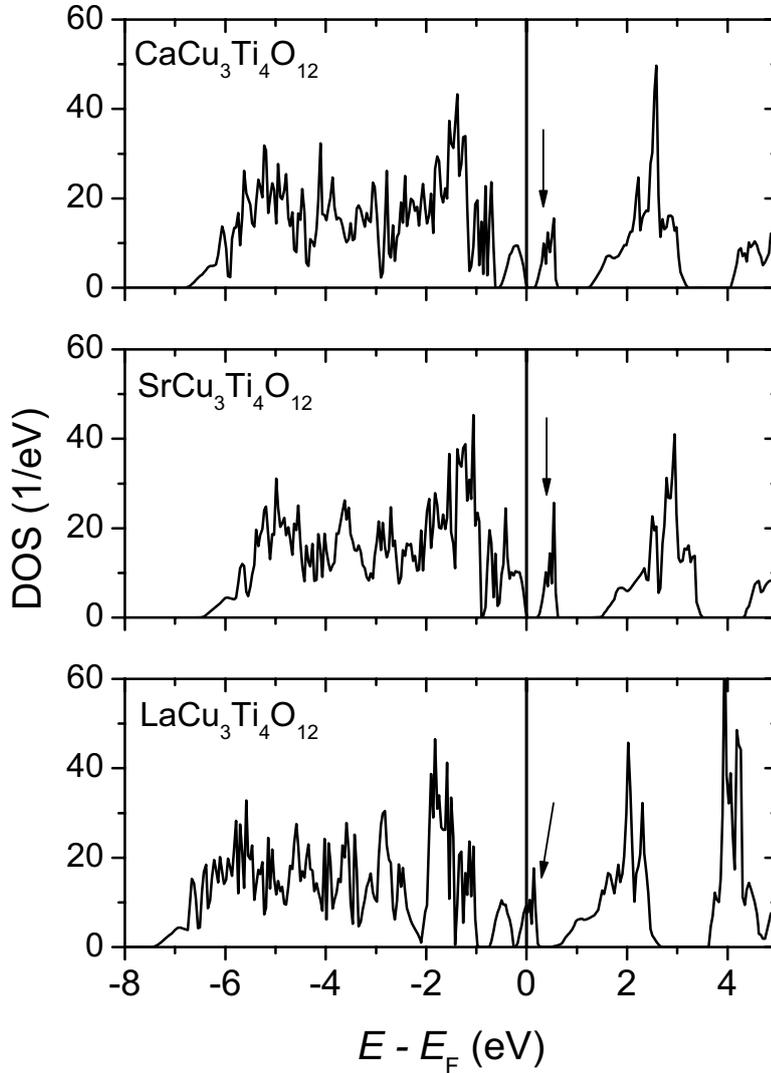
Figure 6.13.: Comparison of total DOS (spin-up channel) of $CaCu_3Ti_4O_{12}$ (top), $SrCu_3Ti_4O_{12}$ (center), and $LaCu_3Ti_4O_{12}$ (bottom) calculated with FPLO.

This reflects the strongly localized character of the Cu $3d$ electrons in these titanates. The DOS between roughly 1.5 eV and 3 eV only contains the unoccupied Ti $3d$ and O $2p$ orbitals similar to the region above 4 eV. The Ca, Sr, and La contributions are found well above 4 eV, respectively.

From the k-space band plot in Fig. 6.11 two different band gaps were obtained similar to the UV-Vis spectroscopy experiments, a direct gap of $E_{g,direct} \approx 0.25$ eV (at A) and an indirect gap of $E_{g,indirect} \approx 0.19$ eV (between A and B) were determined. These values are comparable to the reported ones for calcuations applying LSDA [He02, Fag05, Zhe10]. For GGA a value of roughly

0.51 eV for the indirect gap and 0.58 eV for the direct gap were described [Li05]. Applying the GGA method the general band structure is preserved, only the narrow region in the DOS with the Cu $3d_{xy}$ orbital contribution is slightly shifted upwards in energy. The introduction of an Cu onsite repulsion Hubbard-U (≈ 6 eV) to the LSDA leads to a further pushing of those bands close to the Ti $3d$ bands at roughly 2 eV above E_F. By this the band gap energies are shifted to $E_{\mathrm{g,direct}} \approx 2$ eV in agreement with the UV-vis spectroscopy data and results of DFT calculations in Refs. [Zhe10, Cla11].

Since the absorption edges are very similar for all investigated ACu$_3$Ti$_4$O$_{12}$ samples, only minor deviations of the band structure were expected for those compounds. This was already shown for isostructural CdCu$_3$Ti$_4$O$_{12}$ by LSDA calculations [He03]. Therefore, the band stucture modelling was performed applying LSDA for SrCu$_3$Ti$_4$O$_{12}$ and LaCu$_3$Ti$_4$O$_{12}$. The obtained total DOS is shown in Fig. 6.13 for all three compounds with A = Ca, Sr, La from top to bottom. SrCu$_3$Ti$_4$O$_{12}$ provides a DOS structure very similar to CaCu$_3$Ti$_4$O$_{12}$ and, thus, the band-gap values are only slightly increased: $E_{\mathrm{g,direct}} \approx 0.32$ eV, $E_{\mathrm{g,indirect}} \approx 0.23$ eV. This fits to the results from the UV-Vis spectroscopy (Sec. 6.1.3), where also the size of the gap depends on the A-site ionic radius. For LaCu$_3$Ti$_4$O$_{12}$ the DOS appears to be shifted by roughly 0.5 eV downwards in energy while the shape is in general preserved, except the La $4f$ bands appearing at approximately 4 eV. Due to the additional electron caused by the changed stoichiometry for the calculation the Fermi-level is shifted to higher energy and, by this, the contribution of Cu $3d_{xy}$ slides below the Fermi energy. With respect to this artifical shift, the sample color and the UV-vis spectroscopy data, which are rather similar for all ACu$_3$Ti$_4$O$_{12}$ samples, a similar gap can be expected and is actually observed in the band structure (Fig. 6.13). The gap values amount to $E_{\mathrm{g,direct}} \approx 0.11$ eV and $E_{\mathrm{g,indirect}} \approx 0.07$ eV, which is distinctly smaller than the band gaps for CaCu$_3$Ti$_4$O$_{12}$ and SrCu$_3$Ti$_4$O$_{12}$ due to the artificial shifts caused by the formal excess electron.

From the DFT calculations very similar values of the Cu spin moments and valences were obtained for CaCu$_3$Ti$_4$O$_{12}$ and SrCu$_3$Ti$_4$O$_{12}$. For both the Cu moment amounted to $S_{\mathrm{Cu}} = \pm 0.50(1)$, which is in excellent agreement with the $3d^9$ configuration of Cu^{2+}. In addition, a small spin moment was also found for oxygen $S_\mathrm{O} = \pm 0.06(1)$, which indicates the magnetic exchange interaction via the oxygen ions in the crystal structure. In contrast, Ca, Sr, and Ti do not carry a significant residual magnetic moment as can be expected for their electron configuration deduced from their corresponding valences. For LaCu$_3$Ti$_4$O$_{12}$ a smaller value was obtained $S_{\mathrm{Cu}} = \pm 0.38(1)$, which can be explained by the formally varied La-site occupancy.

The compliant results of the DFT calculations using the same model for the ACu$_3$Ti$_4$O$_{12}$ compounds corroborate the almost identical experimental results. Therefore, the DFT calculations based on experimental crystal-structure data and magnetic properties are reliable and will be used for the investigation of the properties of the Ru substituted Ln_yCu$_3$Ru$_x$Ti$_{4-x}$O$_{12}$ compounds (Ln = La, Pr, Nd, Sm) in the following sections.

6.2. *B*-site Substitution Influence in $Ln_y\mathbf{Cu}_3\mathbf{Ru}_x\mathbf{Ti}_{4-x}\mathbf{O}_{12+\delta}$

In the previous section the influence of the *A*-site substitution on the crystal structure and the resulting changes of the physical properties were discussed for the $ACu_3Ti_4O_{12}$ compounds. More promising is the substitution of the non-magnetic Ti by Ru on the *B*-site to investigate the influence on the crystal structure, the electronic system, and the resulting changes of the magnetic properties. As metioned above, the titanates provide an insulating behavior in combination with large dielectric constants ε. The magnetic behavior is determined by the localized valence electrons of the Cu^{2+} ions, showing a paramagnetic behavior until roughly 25 K followed by an antiferromagnetic ordering (see Sec. 6.1.1). On the other hand, the pure ruthenates $ACu_3Ru_4O_{12}$ (A = Na, Ca, Sr, Cd, La, Pr, Nd [Lab80]) possess a metallic conductivity and yield an almost temperature-independent magnetic susceptibility, which was explained by typical Pauli paramagnetism of the itinerant electrons in metallic compounds. In addition, properties which are typical for "heavy fermion compounds" were observed in the specific heat and by resonance-spectroscopical methods. This is unusual since heavy fermions are more typically observed for compounds containing $4f$ or $5f$ elements (e.g. Ce and U). The $ACu_3Ru_4O_{12}$ compounds are rare examples with heavy d electrons, and moreover exhibit a non Fermi liquid behavior at low temperatures [Kob04, Kri09]. This outstanding variety of physical properties in the same system with only varying *B*-site cation occupancies reasoned the study of the change of physical properties by mixing Ti and Ru on the octahedrally coordinated site.

Although the possibility of a full substitution in the system $CaCu_3Ru_xTi_{4-x}O_{12}$ was reported in literature [Ram04], it was not possible to obtain single phase samples for the range $1.5 < x < 4$. This was also reported in Refs. [Kob04, Tsu09]. Alternatively, the same Ru substitution was tested for Sr instead of Ca on the *A*-site to study the influence of the *A*-cation radius. In literature with *A* = Sr only the pure titanate or the pure ruthenate compound was described [Sub02, Boc79, Lab80]. Nevertheless, the partly substitution of the titanate with Ru and vice versa failed, which can be explained reasonably by the Sr^{2+} ion radius. The mixture of the two slightly differently sized Ti^{4+} and Ru^{4+} on the *B*-site causes major structural stress, which is probably too high to be stabilized by the too large Sr ion. Thus, only the compounds with homogeneous *B*-site occupation are available for Sr. In contrast, the Ca^{2+} ion is probably too small, which causes in turn the observed miscibility gap $1.5 < x < 4$.

Considering these assumptions on the size of the *A*-site, trivalent rare-earth metal ions were taken into account for the occupation, because their size ranges between Ca^{2+} and Sr^{2+}. Similar to Ca^{2+} and Sr^{2+}, La^{3+} does not provide an additional magnetic moment to the system due to the absence of unpaired electrons and an empty f shell. On the other hand, the trivalent La with its increased positive valence is expected to influence the electronic structure by correspondingly changing the valences of Cu and Ru. Due to the stable $3d^0$ electronic state of the Ti^{4+} ions it can be expected that these remain tetravalent. Therefore, the oxygen content and in turn the valences of the *B*-site cations were studied and based on these results the physical properties are interpreted. Single phase samples of $LaCu_3Ru_xTi_{4-x}O_{12}$ for the complete x range between 0 and 4 were prepared for this work according to the synthesis reported in Refs. [Ram04, Ebb06, Ebb10, Bue10]

and in detail in Sec. 2.1.1. Furthermore, using the *A*-site cations Pr and Nd [Mul86] samples for the complete *x*-range were synthesized. In addition, for Sm it was possible to obtain samples up to $x = 0.5$ in accordance with Ref. [Ter10], where compounds were reported for various rare-earth elements (Y, La, Nd, Sm, Gd, Dy, Ho, Er) and a Ru substitution level of $x = 0.4$. Due to the 3+ valence of the rare-earth metal ion, the samples with $x \leq 1/3$ had to be prepared with an *A*-site deficiency. As described above, in the titanates 1/3 of the *A*-sites remain unoccupied leading to the sum formula $Ln_{2/3}Cu_3Ti_4O_{12}$. The increase of *x* was compensated by the same amount of *y* according to $y = 2/3 + x$ (for $x \leq 1/3$). Thus, starting with the compounds $LnCu_3Ru_{0.33}Ti_{3.67}O_{12}$ ($x = 0.33$) the fully occupied *A*-site was kept until $x = 4$. To indicate these complex rules the samples were in general denoted as $Ln_yCu_3Ru_xTi_{4-x}O_{12}$, where *y* marks the (deficient) *A*-site occupancy.

6.2.1. Crystal Structure

The crystal structure of the $Ln_yCu_3Ru_xTi_{4-x}O_{12}$ samples remains very similar over the whole substitution range since all samples crystallize in space group Im$\bar{3}$ (No. 204).

In Fig. 6.14 the measured patterns and the results of the Rietveld refinement are depicted for the three examples $LaCu_3Ru_{0.33}Ti_{3.67}O_{12}$ (top), $LaCu_3Ru_{2.25}Ti_{1.75}O_{12}$ (center), and $LaCu_3Ru_4O_{12}$ (bottom). The corresponding diffraction pattern of the pure titanate is shown above in Fig. 6.2 in Sec. 6.1. A very good agreement of experimental data and the Rietveld-refinement curves was achieved for all samples and in very few cases neglibible traces (≤ 0.5 %) of TiO_2 impurities were detected, which in turn proves the high purity of the synthesized samples.

The unit-cell parameters *a* obtained from Rietveld analysis of the x-ray diffraction patterns are depicted in Fig. 6.15 as a function of the Ru-substitution level *x*. The data for $Ln_yCu_3Ru_xTi_{4-x}O_{12}$ (*Ln* = La, Pr, Nd, Sm) are shown using different colors and symbols. Starting from the titanates the cell parameter *a* sharply increases by roughly 0.03 Å for increasing *x* until $Ln_1Cu_3Ru_{0.33}Ti_{3.67}O_{12}$ due to the simultaneous increase of the *A*-site occupancy *y*. Since then the *A*-site is fully occupied, the slope in the substitution range $0.33 \leq x \leq 4$ of the still linearly increasing *a* becomes smaller, which is explained by the pure Ru substitution in this range. The Ru^{4+} ions possess a slightly larger ionic radius compared to Ti^{4+} (see Sec. 5.2.1.1), providing the linear increase in agreement with Vegard's law. The solid lines are added to the figure to guide the eye.

The general evolution of the cell parameter is very similar for all substitution series, only the varying size of the *A*-site cation (Pr, Nd, Sm) causes a constant shift. Therefore, the slopes are identical for the corresponding substitution ranges and the shift is in accordance with the *A*-site ion size similar to the pure titanates as shown in Fig. 6.3. In addition, the obtained values for the pure ruthenates are in good agreement with literature data [Lab80]. The values for the samples with *A* = Sm are shown for completeness (empty circles) although no further investigations are considered in this work.

The changes of the cell parameter reported by Ramirez *et al.* [Ram04] for $La_yCu_3Ru_xTi_{4-x}O_{12}$ are strongly deviating from the data obtained for the own samples. A significant difference of 0.01 Å was reported for the samples, which can be explained by the fact that the calcination time
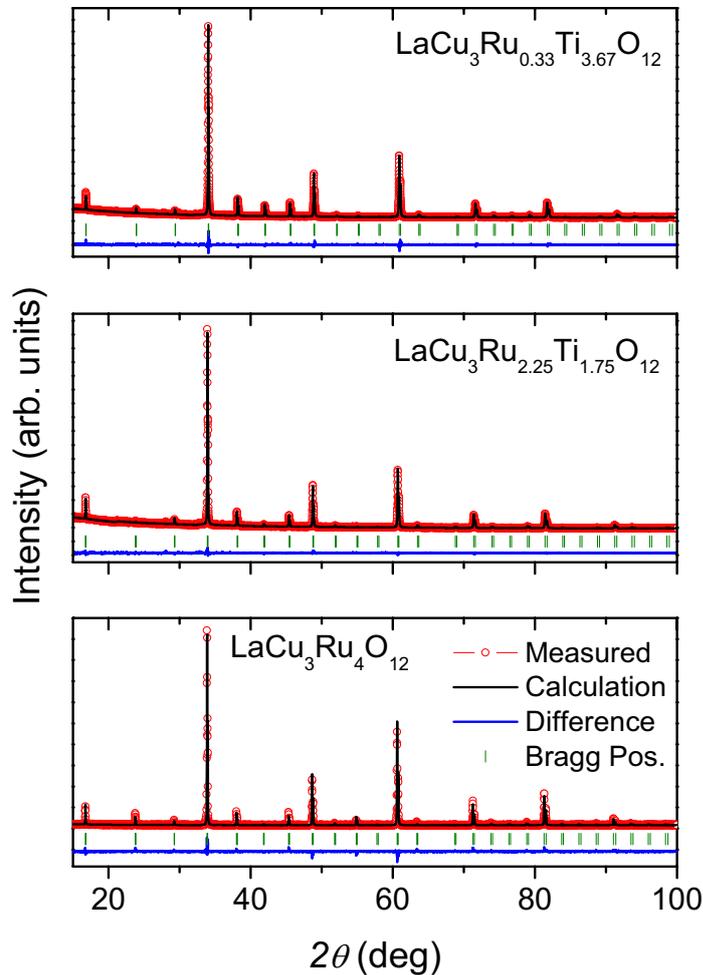
Figure 6.14.: Rietveld-refinement results of the $LaCu_3Ru_{0.33}Ti_{3.67}O_{12}$ (top), $LaCu_3Ru_{2.25}Ti_{1.75}O_{12}$ (center), $LaCu_3Ru_4O_{12}$ (bottom) x-ray diffraction patterns.

was only half as long as for our own samples. On the other hand, the cell-parameter values for $Nd_yCu_3Ru_xTi_{4-x}O_{12}$ by Muller *et al.* [Mul86] are in very good agreement with the results of the Rietveld analysis of the own samples.

The detailed structural properties were also determined to study a possible correlation with the physical-property changes. Similar to the investigations carried out for the rare-earth substituted titanates in Fig. 6.16a the *A*–O distances are shown. The values are slightly decreasing with *x* indicating the concomitant decrease of the *A*-site coordination sphere with the growing volume of the BO_6-octahedra. This shows a higher compressibility of the *A*–O bonds compared to the *B*–O bonds and corroborates the breathing effect of the $AA'_3B_4O_{12}$ structure caused by the *A*-site cation size described in the section above.
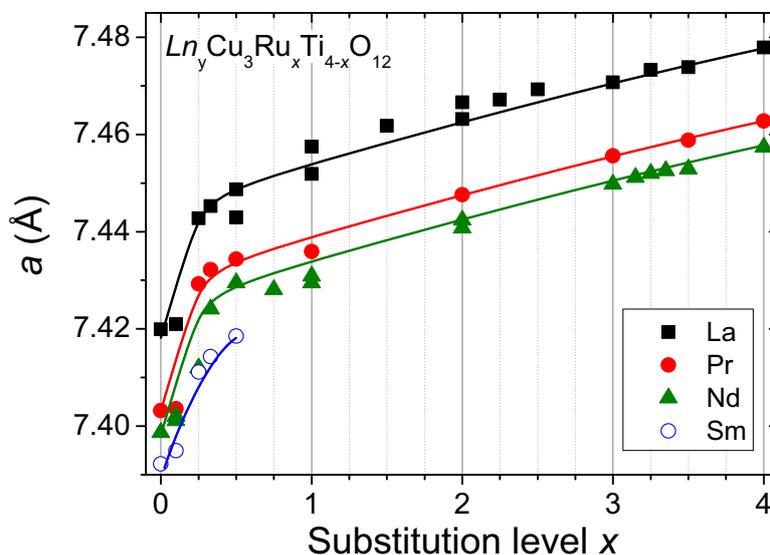
Figure 6.15.: Cell parameter a of $Ln_yCu_3Ru_xTi_{4-x}O_{12}$ (Ln = La, Pr, Nd, Sm) obtained from Rietveld analysis of x-ray diffraction patterns. The solid lines are drawn to guide the eyes.

The magnitude of octahedral tilting is characterized by the B–O–B angle, which is shown denoted as Ru–O–Ru in Fig. 6.16b. Below $x = 0.5$ the angle decreases linearly by approximately $1.2°$ due to the distinct increase of a for the same region in x. Above $x = 0.5$ the decrease is slower but still linear until $139.5°$ is reached for $x = 4$, which is comparable to the value of roughly $138.5°$ for single crystalline $SrCu_3Ru_4O_{12}$. A decrease of the Ru–O–Ru angle leads in general to a reduction of the antiferromagnetic superexchange interaction according to Anderson, Kanamori, and Goodenough [And59, Kan59, Goo63]. The behavior of the Ru–O–Ru as well as the Ru–O–Cu angles is used to interpret the changes of the physical properties obtained for the $La_yCu_3Ru_xTi_{4-x}O_{12}$ compounds.

Very similar to the change of a the B–O distance varies as a function of the substitution level, which is depicted in Fig. 6.16c. The bond length increases from 1.96 Å by roughly 0.02 Å for $x \approx 0.33$ and further increases to approximately 1.99 Å for $x = 4$. This evolution is reasonable because of the slightly larger ionic radius of Ru^{4+} compared to Ti^{4+}. The value for the Ru–O distance in the pure ruthenate is comparable to other compounds containing RuO_6 octahedra including La_2RuO_5 and $SrCu_3Ru_4O_{12}$. The A-site substitution is a further cause for the varying B–O distance, especially below $x = 0.33$. It has to be mentioned that the observed decrease of the Ti–O bond length in the A-site substituted $Ln_{2/3}Cu_3Ti_4O_{12}$ is correlated with the size of the A-site cation (Sec. 6.1.1). Here this effect is especially observable for the Nd substituted samples, since they yield in general slightly shorter B–O distances compared to the rather similar values of La-
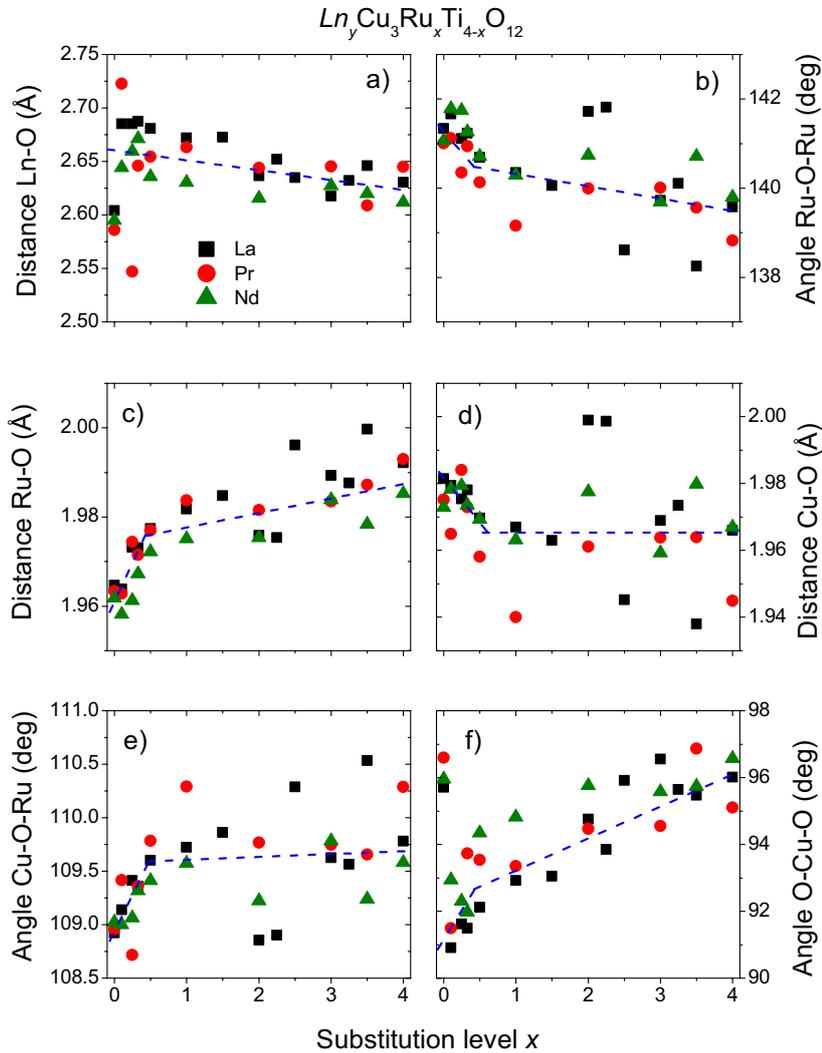
Figure 6.16.: Detailed structural data of the $Ln_yCu_3Ru_xTi_{4-x}O_{12}$ (Ln = La, Pr, Nd, Sm) samples. a) Ln–O distances, b) Ru–O–Ru angles, c) Ru–O bond lengths, d) Cu–O bond lengths, e) Cu–O–Ru angles, and f) O–Cu–O angles. Dashed blue lines are drawn to guide the eye.

and Pr-substituted samples.

In contrast, the Cu–O distances decrease linearly below $x = 0.33$ by roughly 0.02 Å (Fig. 6.16d). Above this substitution level they remain almost constant, because this value possibly is the minimal Cu–O distance for these compounds. The lower limit of 1.963 Å agrees well with the minimal value obtained for the $Ln_{2/3}Cu_3Ti_4O_{12}$ sample with the smallest used rare-earth element Yb.

The exchange interaction between the B- and A'-site cations is clearly influenced by the Cu–O–B angle, which is shown in Fig. 6.16e. According to the filling of the A-site the angle increases linearly by approximately 1° from the titanate to $x = 0.33$. For higher substitution levels with fully

occupied *A*-sites the angle seems to remain constant at 109.5° due to the large observed scattering of the data points.

The square-planar coordination of Cu is also slightly changing during the Ru substitution, which is possibly influencing the localized character of the Cu electrons. In Fig. 6.16f the evolution of this angle is shown and provides an unusual behavior. While for the pure titanates the O–Cu–O angle amounts to roughly 96°, it drastically drops to 91° at $x = 0.1$ and increases again similar to *a* to approximately 96° for the pure ruthenates. Furthermore, for this parameter a quite clear dependence on the size of the lanthanide ion can be observed. The overall behavior is similar for La and Pr, while for Nd the change is less pronounced.

For the parameters depicted in Fig. 6.16c to f in general a similar behavior depending on the substitution level is observed. Below roughly $x = 0.5$ a steeper slope for the parameter change is found compared to the region $0.5 \leq x \leq 4$. This can be explained by the simultaneously changing cell parameter *a*, which follows the substitution on the *A*- and *B*-site as was shown above. Due to the weak scattering of the oxygen ions in x-ray diffraction data the standard deviations of the of the atomic coordinates are quite large. Therefore, for some parameters the error bars are apparently larger than the changes shown in Fig. 6.16, however, from the data a general evolution still can be derived and discussed.

In general, the rather similar behavior of the crystallographic changes are directly linked to the evolution of the unit-cell parameter and the increasing averaged size of the *B*-site cation (merged Ru^{4+} and Ti^{4+} radius according to the occupancy). The absence of sharp step-like transitions leads to the conclusion that the combination of the smoothly changing parameters is causing the physical property changes at certain threshold values with increasing Ru substitution level. Therefore, rather broad transition regimes depending on *x* should be expected.

6.2.2. EXAFS Results for $PrCu_3Ru_4O_{12}$

The EXAFS measurements of $PrCu_3Ru_4O_{12}$ at the Ru-K and Cu-K edge are discussed in this section as an example and for completion of the data in Ref. [Ebb02]. The local geometry of the A'- and the *B*-site in the $AA'_3B_4O_{12}$ crystal structure is obviously different, which is demonstrated in Fig. 6.17a for $B = $ Ru and 6.17b for $A' = $ Cu. This difference is also evident in the EXAFS spectra and can be used to study the details of the structural properties. The sample was measured at the beamline X1 at HASYLAB. With a k^3 weighting oscillations are observable up to 20 Å^{-1} at the Ru-K edge as shown in Fig. 2.10.

In Fig. 6.18 the mRDF (solid black line) and the result of the EXAFS fit of the Ru-K absorption edge (red dashed line) are depicted. Four peaks are clearly identified up to roughly 5 Å. The first one at roughly 1.7 Å is ascribed to the six oxygens in octahedral coordination and the second one at approximately 3 Å represents the *A*- and *A'*-site cation neighbors Cu and Pr, which have a total number of eight. The third peak at roughly 3.5 Å corresponds to the six next neighboring (nn) Ru and the fourth one is assigned to the twelve next nearest neighboring (nnn) Ru ions in a distance of 5 Å. These different coordination shells are shown for a single Ru-atom in Fig. 6.17. The refined fit parameters are listed in Tab. 6.2. The data are in good agreement with earlier data for $A = $ Na,
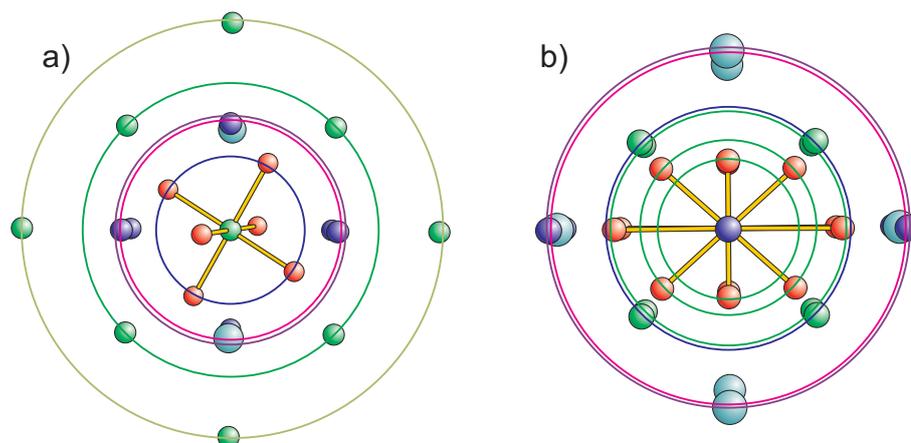
Figure 6.17.: Local coordination of a) Ru and b) Cu in $PrCu_3Ru_4O_{12}$. The Ru atoms are represented by green spheres, oxygen by small red spheres, copper atoms are drawn blue, and Pr atoms turquoise. The circles mark the corresponding coordination shells in the same color used in figures 6.18 and 6.20. The closest oxygens are linked to the central atom (Ru or Cu) by yellow bonds.
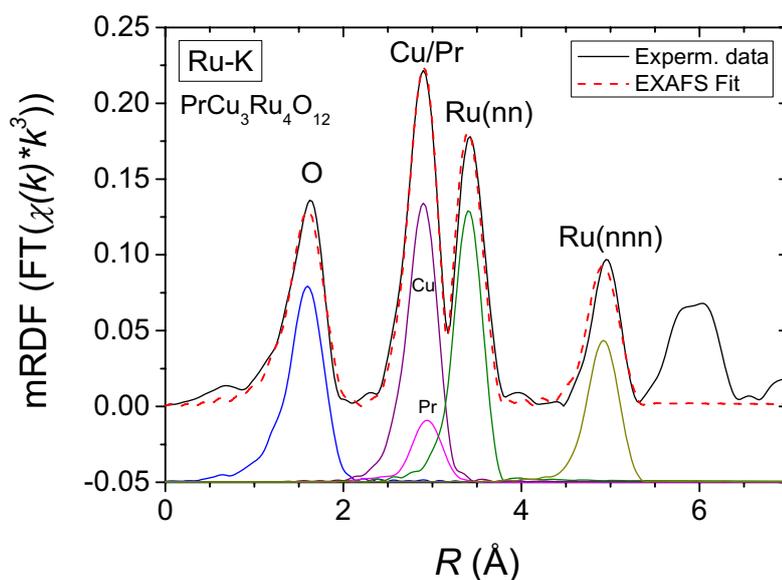

Figure 6.18.: Experimental data and fit results of k^3-weighted Ru-K mRDF of $PrCu_3Ru_4O_{12}$. The single contributions of the scattering paths in Tab. 6.2 are shifted downwards by 0.05 and colored individually for better comparability.

Ca, Sr, La, Nd [Ebb02], completing the list of lanthanide based $ACu_3Ru_4O_{12}$ compounds. The distances of the coordination shells to the central Ru are very similar to the structural data obtained

Table 6.2.: Ru-K EXAFS fit results for polycrystalline $PrCu_3Ru_4O_{12}$. The model from Ref. [Ebb02] was used and a residual of 8.94 % was achieved. A k^3 weighting was applied. The E_0 shift was -0.83(8) eV and S_0^2 amounted to 0.806(5).

| Coordination	N	N (theo)	R (Å)	σ^2 (Å^2)
Ru–O	6.18(3)	6	1.994(1)	0.0032(1)
Ru–Cu	6.43(7)	6	3.229(1)	0.0040(2)
Ru–Pr	1.56(7)	2	3.229(1)	0.0058(4)
Ru–Ru (nn)	5.88(3)	6	3.737(1)	0.0037(3)
Ru–Ru (nnn)	11.81(9)	12	5.282(1)	0.0048(4)
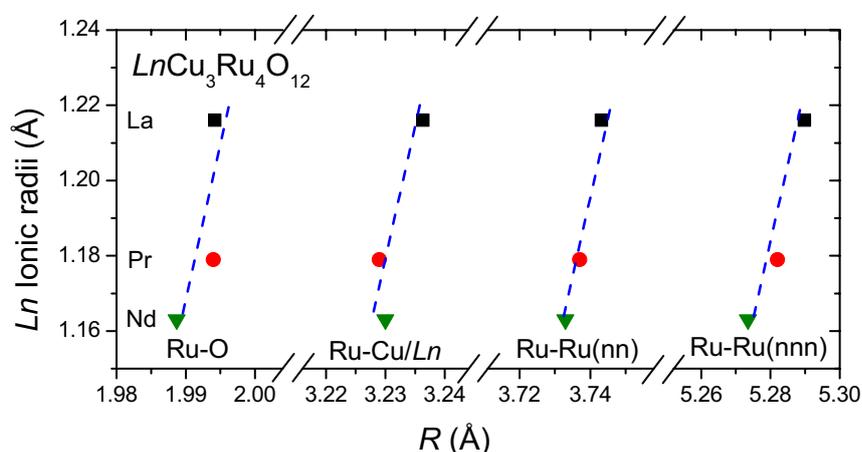
Figure 6.19.: Comparison of the interatomic distances from Ru-K EXAFS fits for $ACu_3Ru_4O_{12}$. Data for $A =$ La and Nd are taken from Ref. [Ebb02]. The parallel dashed lines are guides to the eye.

by the Rietveld analysis of XRD data (see Sec. 6.2.1). The Debye-Waller factors refine to slightly larger values than referred in literature, which can be explained by the smaller measured k-range leading to slightly broadened peaks in the mRDF. The refined coordination numbers N agree well with the expected ones N(theo), the deviations are in the same range as reported in Ref. [Ebb02]. To illustrate the contribution of the single coordination shells, the separate peaks are depicted in Fig. 6.18. Multiple scattering paths were not included in the Ru-K EXAFS modelling since a Ru–O–Ru angle of approximately 140° strongly decreases their intensity [Ebb02].

To illustrate the good agreement of the EXAFS fit results with the data given by Ebbinghaus *et al.* [Ebb02], the refined distances of the used backscattering shells for $ACu_3Ru_4O_{12}$ ($A =$ La, Pr, Nd) are shown in Fig. 6.19. Due to the direct relation of the distances to the ionic radii of the A-site cations, these are used for the ordinate scaling of the data for the corresponding rare-earth
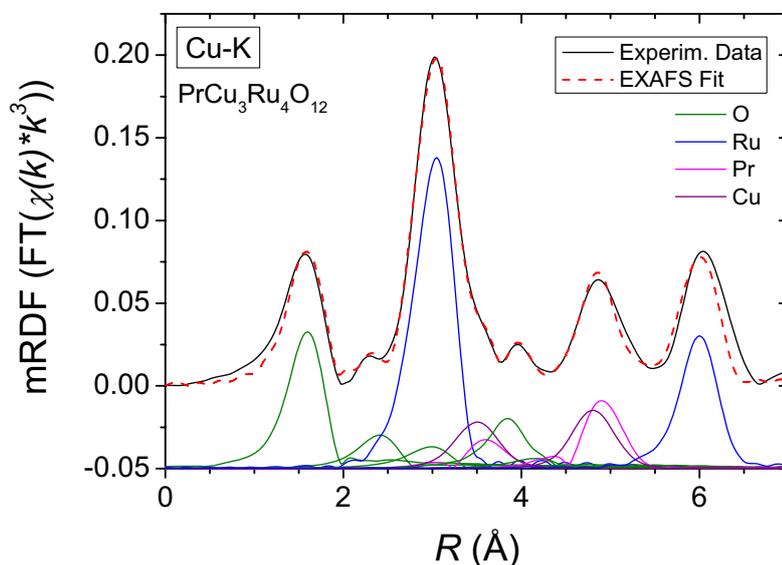
Figure 6.20.: Experimental data and fit results of k^3-weighted Cu-K mRDF of $PrCu_3Ru_4O_{12}$. The single contributions of the scattering paths in Tab. 6.3 are shifted downwards by 0.05 and colored individually for better comparability.

element. The parallel dashed lines indicate a similar decrease of the interatomic distances with decreasing A-site ion radius similar to the titanates.

In the right part of Fig. 6.17 the corresponding coordination of Cu in the $ACu_3B_4O_{12}$ structure is shown for distances up to 4 Å. Further coordination shells are not considered since they contain a large number of atoms and by this would severely reduce clarity. Thereby the expected difference of the coordination compared to Ru is clearly visible. The coordination of the Jahn-Teller active Cu^{2+} ions gives rise to three separate oxygen shells, each containing four atoms.

The mRDF obtained from the Cu-K EXAFS spectra is depicted in Fig. 6.20 (solid black line). Peaks reflecting the corresponding shells can be clearly identified up to roughly 6 Å. The peaks at roughly 1.7 Å and 2.3 Å reflect the two closest oxygen spheres. The intense peak at approximately 3 Å corresponds to the eight Ru neighbors plus the third oxygen coordination sphere and the shoulder on the right side reflects the nearest Cu/Pr sphere. The further peaks are identified as next nearest neighboring shells of oxygen ($R \approx 4$ Å), Cu/Pr ($R \approx 5$ Å), and Ru ($R \approx 6$ Å) (not shown in Fig. 6.17).

The fit result of the Cu-K EXAFS is shown in Fig. 6.20 as dashed red line. It shows a good agreement with the experimental data. It has to be noted that although the fit contains a large number of coordination shells, it is possible to model the Cu-K EXAFS data up to the comparably large distance of 6 Å. Furthermore, it has to be mentioned that the fit only considers single scattering paths and also neglects oxygen coordination shells above 4.7 Å due to their weak backscattered

Table 6.3.: Cu-K EXAFS fit results for polycrystalline $PrCu_3Ru_4O_{12}$. A residual of 10.50 % was achieved. A k^3-weighting was applied. The E_0 shift was 12.63(3) eV and S_0^2 amounted to 0.889(4).

Coordination	N	N (theo)	R (Å)	σ^2 (Å^2)
Cu–O	3.91(3)	4	1.966(1)	0.0067(1)
Cu–O	3.37(7)	4	2.815(1)	0.0098(3)
Cu–Ru	7.65(4)	8	3.249(1)	0.0061(1)
Cu–O	4(fixed)	4	3.438(1)	0.0135(15)
Cu–Cu	3.55(6)	4	3.783(1)	0.0106(1)
Cu–Pr	2.45(6)	2	3.783(1)	0.0106(1)
Cu–O	9.20(14)	8	4.248(1)	0.0046(2)
Cu–O	4.61(34)	8	4.665(1)	0.0124(13)
Cu–Cu	8.21(11)	8	5.088(1)	0.0083(1)
Cu–Pr	7.78(11)	4	5.088(1)	0.0083(1)
Cu–Ru	23.70(15)	24	6.233(1)	0.0070(1)

intensity. The Cu–Pr–Cu or Cu–Cu–Cu angles amount to 180° in certain crystallographic directions and multiple scattering maybe influences the data at larger distances, where in contrary the backscattered intensity is very low unless a magnifying effect is observed [Teo81]. Since these effects were not detected by unproportionally increased intensities in the mRDF, they were neglected in the fit. Again, the contributions of the single backscattering paths are shown in Fig. 6.20 shifted downwards by 0.05 and colored according to Fig. 6.17.

The obtained parameters for the Cu-K edge fit are listed in Tab. 6.3. The distances are in good agreement with the data from the XRD analysis and the Debye-Waller factors σ^2 are comparable to the Ru-K EXAFS fit. Nevertheless, several parameters had to be constrained to obtain a stable fitting result. The distances of the Cu and Pr backscattering paths were set equal due to crystallographic relations. The degeneracy N of the third oxygen coordination shell had to be fixed to 4 because of the dominating contribution of the next-neighbor Ru backscattering intensity. Finally, the sum of Cu and Pr coordination number was fixed to six corresponding to the crystal structure. The resulting degeneracy values for the oxygen shells at $R = 3.438$ Å and $R = 4.665$ Å are strongly deviating from the theoretical values 8, which is caused by the weak backscattered intensity. Thus, the coordination numbers for these shells are meaningless. However, the distance to the central atom and the Debye-Waller factors refined to stable and reasonable values.

The fit of the EXAFS data with the used simplified and constrained structural models shows the possibility of gaining additional information on the crystal structure like bond lengths and coordination. At least the high accuracy of the fit parameters for the closer neighboring atoms allows the investigation of possible oxygen vacancies and the distribution of elements on one crystallographic site. The latter is based on the high element-specific character of the XAS data.
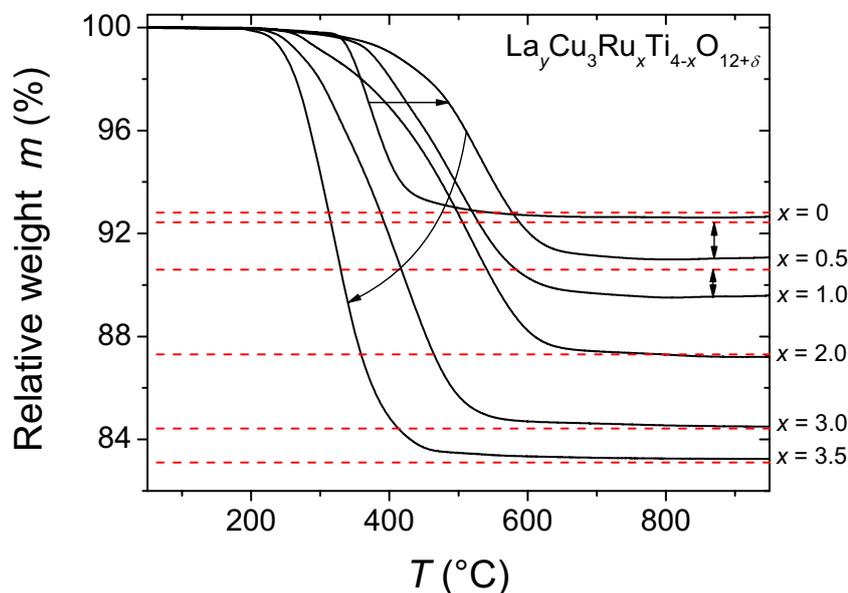
Figure 6.21.: Relative sample-weight curves from thermogravimetric measurements of $La_yCu_3Ru_xTi_{4-x}O_{12+\delta}$ for selected x. The horizontal dashed lines mark the theoretical weight after the reduction considering tetravalent Ru and divalent Cu.

6.2.3. Oxygen Stoichiometry and Cation Valences

Physical properties like electrical conductivity, superconductivity, and magnetism react very sensitively on the oxygen content and, in turn, the cation valences in the samples. To be able to reasonably discuss the observed variation of the investigated properties, the accurate determination of both parameters is required.

The oxygen content was obtained by thermogravimetric measurements under reducing conditions. The measured weight reduction of the samples during heating in reducing atmosphere is used to calculate the oxygen content, for which a deviation is denoted δ in the sum formula $Ln_yCu_3Ru_xTi_{4-x}O_{12+\delta}$. The late (noble) transition-metal cations of Cu and Ru are commonly reduced to the metals completely. On the other hand, La^{3+} and Ti^{4+} are stable under reducing conditions up to the maximum temperature of 950 °C used for the measurements. Thus, after the TG measurement the oxides La_2O_3 and TiO_2 are remaining besides the metals, which was confirmed by powder XRD.

In Fig. 6.21 the obtained relative weight changes are depicted for selected substution levels. The observed weight-reduction step is located at different temperatures depending on x. Above approximately 700 °C the reaction is completed for all samples visible by the constant value up to the maximum temperature. For the titanate a steep decrease is observed at roughly 375 °C
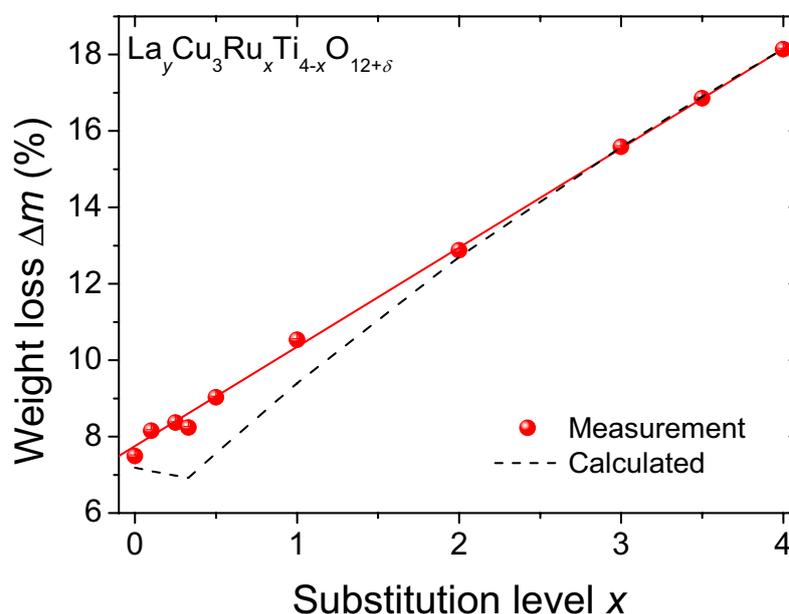
Figure 6.22.: Experimental weight loss of $La_yCu_3Ru_xTi_{4-x}O_{12+\delta}$ from TG measurement (symbols) and linear interpolation (solid line). The dashed line marks the theoretical weight loss considering constant Ru^{4+} and Cu^{2+} valence.

continuing slowly until 700 °C. Upon Ru substitution the reduction step becomes much smoother for $x = 0.5$ and its inflection point is shifted by roughly 150 °C to higher temperature, which is an unexpected behavior since it is contradictory to the shielding effect for the ruthenates substituted with Ti [Osw93]. By further increasing Ru content the weight reduction increases correspondingly and the temperature of the reduction step is almost linearly shifted to lower temperatures (300 °C). This behavior, on the other hand, is in agreement with the decreasing shielding effect with respect to the lower Ti incorporation. The TG data for the pure ruthenate $LaCu_3Ru_4O_{12+\delta}$ were taken from literature [Ebb02]. It has to be mentioned that the absence of clearly separated steps indicates the simultaneous reduction of Cu and Ru. The horizontal dashed lines in Fig. 6.21 mark the expected final relative weight after the reduction. Especially for low Ru concentrations significant deviations can be observed, which are indicated by the arrows.

To illustrate the unexpected deviations in Fig. 6.21 the relative weight-loss values are depicted as red circles in Fig. 6.22 as a function of the substitution level. The experimental data are increasing linearly with x, which is marked by the red solid line resulting from a linear regression. The value for Δm was determined as the difference between 50°C and 900°C. An error of $\pm 0.06\%$ can be estimated as standard deviation. For comparison the theoretical weight loss was calculated
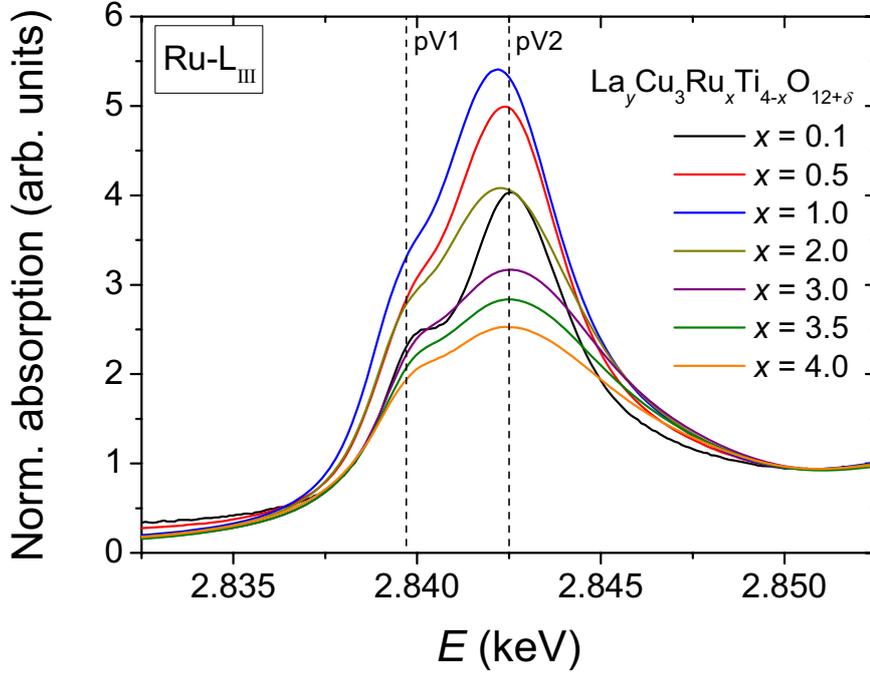
Figure 6.23.: Normalized Ru-L$_{III}$ edge XANES spectra of LaCu$_3$Ru$_x$Ti$_{4-x}$O$_{12}$ for selected substitution levels x. The dashed vertical lines mark the maxima positions of the two pseudo-Voigt peaks of the edge fit for RuO$_2$ as Ru^{4+} reference.

assuming constant Cu^{2+} and Ru^{4+} valences according to:

$$Ln_y\text{Cu}_3\text{Ru}_x\text{Ti}_{4-x}\text{O}_{12+\delta} \longrightarrow y/2\,Ln_2\text{O}_3 + (4-x)\text{TiO}_2 + 3\text{Cu} + x\text{Ru} + (4+2x+\delta-1.5y)\text{O}(\uparrow)\,.$$
$$(6.1)$$
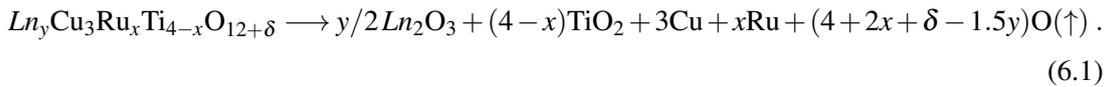
The calculated Δm assuming $\delta = 0$ are drawn as dashed line in Fig. 6.22. The deviation between the experimental and the calculated data is usually denoted as excess or deficit (depending on the sign) oxygen content δ. In this case a large value of apparent excess oxygen is observable for low Ru substitution levels, since the expected values are significantly smaller than the measured data. In addition, the strongly varying shape of the two curves is unusual, because the kink in the black curve caused by the changing occupation of the Ln-site for $x \leq 0.33$ does not appear for the measured weight-loss values. The difference between both curves would lead to unreasonable oxygen excesses of more than 0.7 per formula unit.

In order to investigate the found oxygen stoichiometry more critically, the Ru and Cu valence was determined by XANES. Assuming a constant 2+ valence for the Cu ions the Ru valence is forced to reduce from +3.75 for LnCu$_3$Ru$_4$O$_{12}$ to +3 for LnCu$_3$RuTi$_3$O$_{12}$ to preserve charge neutrality. However, for even lower Ru content the Ru valence has to decrease to almost a metallic
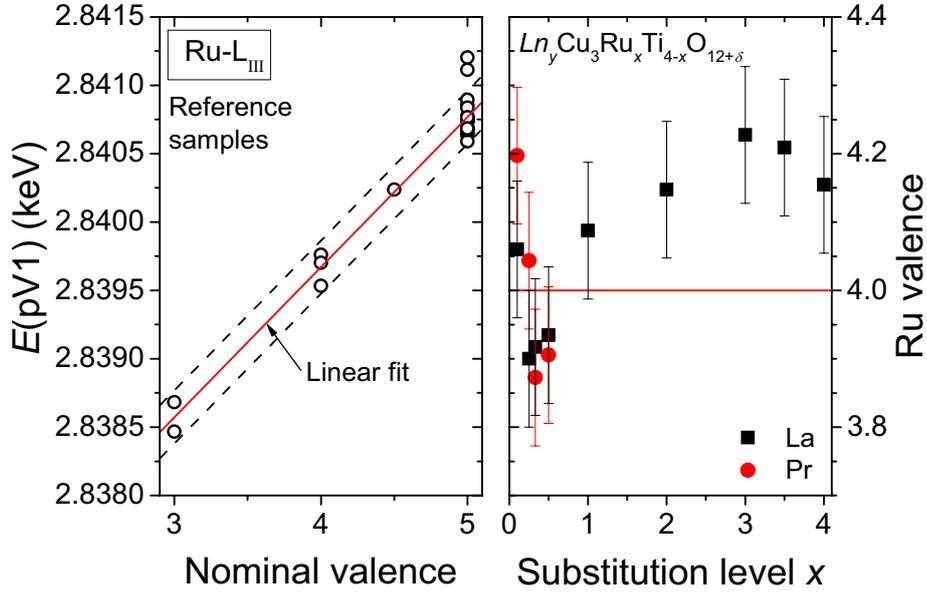
Figure 6.24.: Left: Fit of the energy position of the first pseudo-Voigt peak in the Ru-L$_{III}$ absorption spectra of Ru reference oxides according to Eq. 6.2. Right: Ru valence of $Ln_yCu_3Ru_xTi_{4-x}O_{12+\delta}$.

state for $x = 0.1$, which is highly unlikely. Furthermore, a constant Ru valence close to +4 was reported in Refs. [Ebb06, Ebb10].

The normalized spectra of the Ru-L$_{III}$ absorption edges are depicted in Fig. 6.23. Two white lines indicating the transition from the $2p_{3/2}$ level into the $4d$ states can be seen. They are splitted by the octahedral crystal field and can be fit utilizing two pseudo-Voigt functions. Obviously the shape of the edge changes from two sharp and distinct peaks to a smoother shape of two strongly overlapping broad peaks. However, all spectra were fit and the results for the LaCu$_3$Ru$_x$Ti$_{4-x}$O$_{12}$ samples (and selected samples with Ln = Pr) are shown in Fig. 6.24. In the left frame the absorption-energy positions obtained for the first pseudo-Voigt peak of the reference ruthenium oxides are displayed. The valence of a sample can be determined from an equation according to a linear fit:

$$E_{pV1}(keV) = 2.8353 + 0.0011 \cdot (\text{nominal Ru valence}) \quad, \tag{6.2}$$

similar to the one shown in Ref. [Ebb01]. The valence shift of the edge energy amounts to 1.1 eV per integer step in oxidation state for Ru between 3+ and 5+. The error range of the energy determination amounts to ± 0.2 eV, which corresponds to a valence error of ± 0.18. This is accurate enough to obtain the oxidation state for the samples. The Ru valences calculated with Eq. 6.2 using the energy of the maximum of the first pseudo-Voigt peak are depicted in the right frame of Fig. 6.24. The solid horizontal line marks the energy of the +4 oxidation state. From this figure it
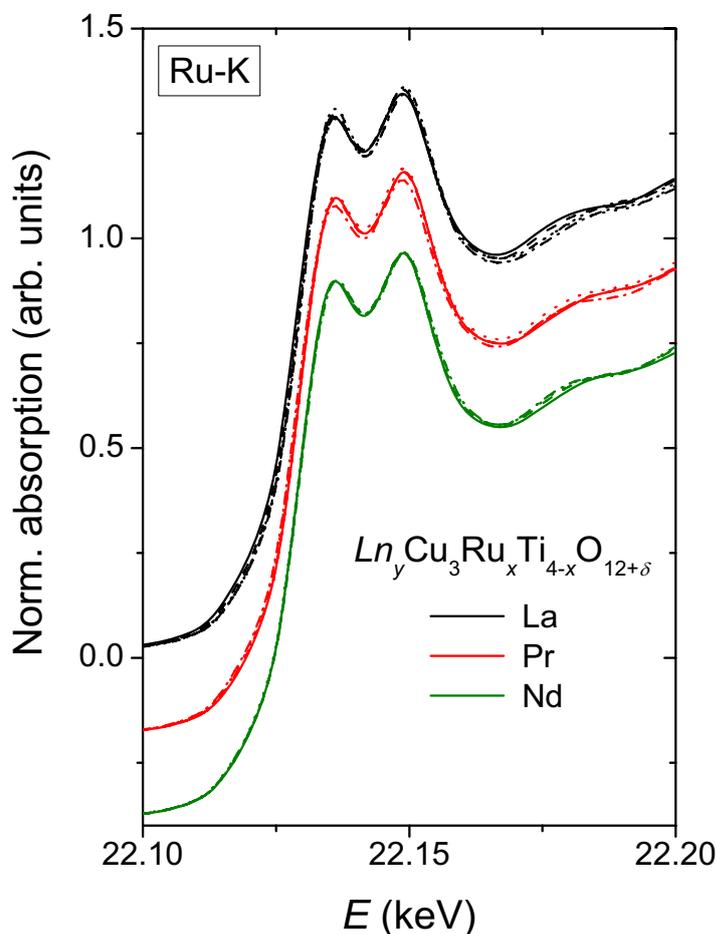
Figure 6.25.: Ru-K edge XANES spectra of LnCu$_3$Ru$_x$Ti$_{4-x}$O$_{12+\delta}$ for the three investigated A-site rare-earth elements: La (top), Pr (center), Nd (bottom).

can be concluded that tetravalent Ru is present in all $Ln_yCu_3Ru_xTi_{4-x}O_{12+\delta}$ samples in agreement with Refs. [Ebb06, Ebb10].

To corroborate this finding, XANES measurements were also performed at the Ru-K absorption edge. Due to the higher energy (≈ 22.1 keV) of the radiation and the therefore increased transmission it was possible to measure the absorption spectra of the samples and the Ru-metal reference simultaneously. Thus, a highly reliable energy calibration was possible for each spectrum. The normalized spectra of the Ru-K edge of selected $Ln_yCu_3Ru_xTi_{4-x}O_{12}$ are shown in Fig. 6.25. To increase the comparability, the spectra for $Ln =$ Pr and Nd were shifted vertically. The general shape is similar to the Ru-L$_{\text{III}}$ edge showing two distinct peaks. However, the distance in energy between the peak maxima is in comparison much larger and, therefore, these do not directly reflect the transitions to the 4d e_g and t_{2g} like orbitals. The spectra grouped for one rare-earth element
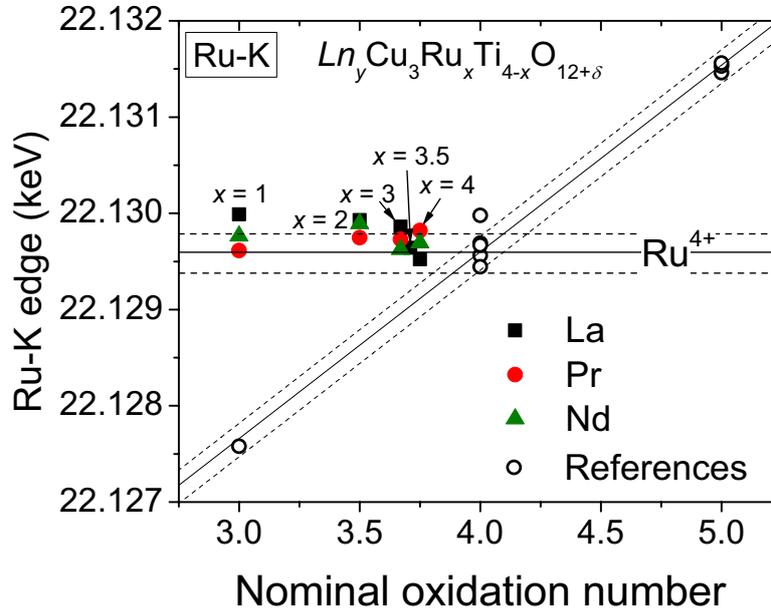
Figure 6.26.: Ru valence of $Ln_yCu_3Ru_xTi_{4-x}O_{12+\delta}$ from Ru-K edge XANES spectra.

are very similar and significant deviations caused by the increasing Ru concentration cannot be observed. The *A*-site substitution does not remarkably influence the shape of the XANES spectra either.

As usual for the K-edges the inflection point of the absorption edge was determined as the first maximum in the first derivative (see Sec. 2.3.1). In Fig. 6.26 the obtained edge energies are shown depending on the nominal oxidation state. The empty circles correspond to the edge energies of the same reference oxides, as used for the L_{III}-edge calibration. The observed valence shift is linear (≈ 1.9 eV per oxidation state) as marked by the diagonal solid line and follows the relation.

$$E_{Ru-K}(keV) = 22.1219 + 0.0019 \cdot (\text{nominal Ru valence}) \tag{6.3}$$

The dashed lines indicate the error range. The edge energies of the $Ln_yCu_3Ru_xTi_{4-x}O_{12+\delta}$ samples are shown with respect to the calculated valence assuming a constant Cu^{2+} oxidation state. In agreement with the L_{III}-edge results the ruthenium oxidation state remains constantly +4 for all samples.

In contrast to the Ru-K edge, the Cu-K edge spectra show a visible dependency on the substitution level. The spectra depicted in Fig. 6.27 are equidistantly shifted to increase clarity. For $La_{2/3}Cu_3Ti_4O_{12}$ a well detailed and sharp structure of the absorption edge is visible, which is remaining almost unchanged up to $x = 2.0$. A small pre-edge feature denoted P is visible as well as
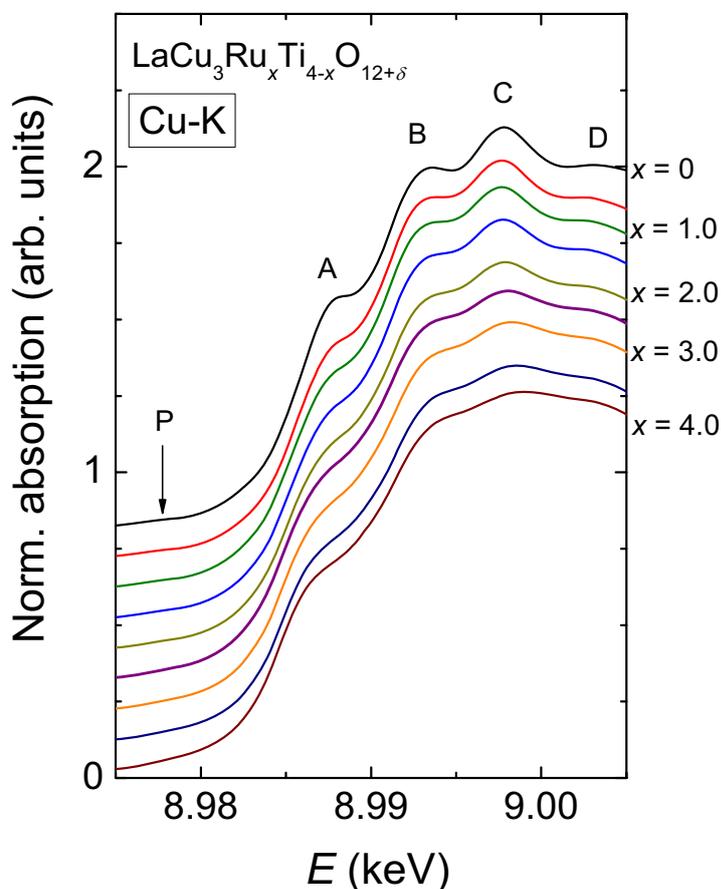
Figure 6.27.: Normalized Cu-K edge XANES spectra of $LaCu_3Ru_xTi_{4-x}O_{12+\delta}$ for selected substitution levels x in steps of 0.5. The spectra were shifted by 0.1 to increase clarity.

four distinct peak-like structures denoted A to D. Starting with the spectrum of $LaCu_3Ru_{2.5}Ti_{1.5}O_{12}$ these peaks become significantly broader and the shape of the absorption edge of the pure ruthenate becomes much smoother.

The derivative of the Cu-K edge spectra is shown in Fig. 6.28 to study in detail the evolution of the relevant peak for the valence determination. The small pre-edge feature of the excitation into the $3d^{10}\underline{L}$ hole state decreases slightly with increasing x. This is reflecting the reducing number of holes due to a possibly decreasing average valence. In addition to this pre-edge feature, four distinct peaks are observable, which correspond to the transition into the $4s$ and $4p$ levels [Kos89, Pan91, Cho94, Wu96]. In agreement with the softening of the absorption-edge shape in Fig. 6.28 the peaks are broadening and their maximum is decreasing upon increasing Ru substitution. More interestingly, only the maxima of the first peak corresponding to the $4s$ and part of the $4p_\pi$ excitations are affected. The energy shift is observed in combination with a decreasing shape
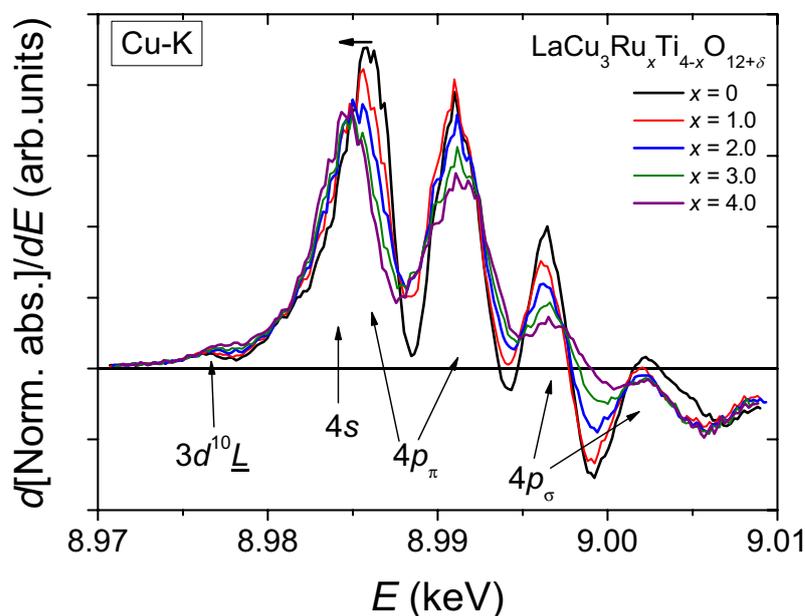
Figure 6.28.: Derivative of the normalized Cu-K edge XANES spectra of $LaCu_3Ru_xTi_{4-x}O_{12+\delta}$ for selected substitution levels x.

asymmetry. Above $x = 2$ the peak is symmetric indicating an increasing overlap of the orbitals in general.

For the accurate determination of the oxidation state by the valence shift a similar coordination of the central cation in the references is required. In addition, the coordinating anions have to be of the same element as in the sample, otherwise the occurring chemical shift of the absorption-edge energy would strongly overlap the investigated valence shift. This entanglement makes it very complicated to obtain a reasonable valence behavior of the cations when both valence and chemical shift have to be considered. In this case, Cu is in all samples surrounded by oxygen only. In $Ln_yCu_3Ru_xTi_{4-x}O_{12+\delta}$ the coordination is almost square planar in contrast to the most reference oxides, where copper is usually octahedrally coordinated by oxygen. Due to this specific coordination simple oxides like Cu_2O (Cu^{1+}) and CuO (Cu^{2+}) are not suitable for the direct comparison of the edge energies. However, the relative shift of the absorption edge caused by the changing valence is taken into account, since the effect of varying Cu–O bond lengths on the edge energy as a reason for the shift can be ruled out due to the comparable distances in CuO and $Ln_yCu_3Ru_xTi_{4-x}O_{12+\delta}$ [Pan91].

Resulting from these considerations $CaCu_3Ti_4O_{12}$ and $SrCu_3Ti_4O_{12}$ were used as references, because the Cu valence of +2 can be very reasonably assumed as derived from charge neutrality and magnetic properties (see Tab. 6.4). The edge energies of these two compounds and the pure
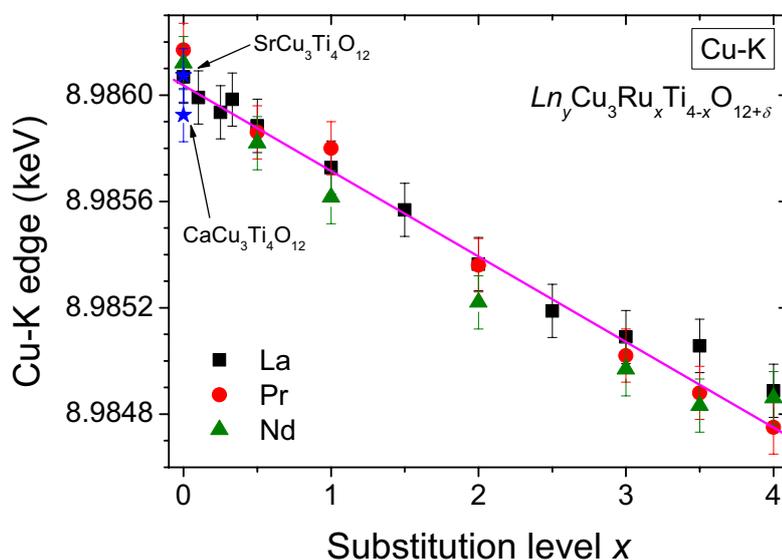
Figure 6.29.: Cu-K edge energies of $Ln_yCu_3Ru_xTi_{4-x}O_{12+\delta}$ and selected references from XANES measurements. The dashed line represents the linear regression of the data points.

Table 6.4.: Cu-K XANES absorption-edge energies of selected samples and references.

Compound	Cu-K edge (keV)	Literature value (keV)	Reference
Cu_2O (Cu^{1+})	8.98041(10)	8.9804(1)	[Hsu03, Wan05, Bij11]
CuO (Cu^{2+})	8.98355(10)	8.9837(2)	[Hsu03, Wan05, Bij11]
$CaCu_3Ti_4O_{12}$ (Cu^{2+})	8.98592(10)		
$SrCu_3Ti_4O_{12}$ (Cu^{2+})	8.98607(10)		
$Y_{2/3}Cu_3Ti_4O_{12}$ (Cu^{2+})	8.98604(10)		
$La_{2/3}Cu_3Ti_4O_{12}$ (Cu^{2+})	8.98607(10)		
$Pr_{2/3}Cu_3Ti_4O_{12}$ (Cu^{2+})	8.98617(10)		
$Nd_{2/3}Cu_3Ti_4O_{12}$ (Cu^{2+})	8.98612(10)		
$Gd_{2/3}Cu_3Ti_4O_{12}$ (Cu^{2+})	8.98595(10)		

titanate samples $Ln_{2/3}Cu_3Ti_4O_{12}$ (Ln = La, Pr, Nd) are in good agreement, which justifies the assumption of divalent copper in the pure titanates with $A = Ln$. The obtained edge energies for $Ln_yCu_3Ru_xTi_{4-x}O_{12+\delta}$ are depicted as a function of the Ru-substitution level in Fig. 6.29. It can be seen that the edge energies linearly decrease from the pure titanates to the pure ruthenates with increasing x.

To determine the absolute valences of the Ru-substituted samples the difference of the absorp-

tion edge energies of Cu_2O and CuO was used as reference. The difference amounts to roughly 3.1 eV, which is in good agreement with the average difference of 3.3 eV reported in literature (see Tab. 6.4). From the linear regression in Fig. 6.29 a decrease of the edge energy of $\Delta E \approx 1.3$ eV between $x = 0$ and $x = 4$ is obtained, which corresponds to a Cu valence of approximately +1.6 for the pure ruthenates $(\Delta E/[E(CuO) - E(Cu_2O)] = 1.3/3.1 \approx 0.42)$. This in turn can be expressed by the variation of the Cu valence by 0.1 per integer value of x upon substitution.

The oxidation state is an average value, which could be explained by the existence of a statistical distribution of mono- and divalent Cu ions in the samples. However, in Fig. 6.28 the presence of only a single peak at the absorption-edge energy shows that all Cu ions possess the same average valence.

To verify the decreasing Cu valence with increasing Ru substitution, the theoretical oxidation state was calculated from the TG weight loss based on Eq. 6.1 assuming fixed tetravalent Ru and $\delta = 0$. The obtained valences per Cu ion are depicted in Fig. 6.30. The solid red line marks the oxidation state resulting from the energy shift of the Cu-K absorption edge. The TG data and the linear fit are in good agreement except of the samples with low Ru substitution level $x \leq 0.25$ which show a slightly higher valence than expected. This can either be explained by a small oxygen excess or more probably by a small additional off-stoichiometric amount of Cu in the sample, which is incorporated on the unoccupied A-sites due to the sample preparation using a CuO flux. The latter reason is corroborated by the fact that from the structure analysis of single and polycrystalline samples of the pure titanates a slightly higher A-site occupancy than 2/3 was received. The good complementarity of the results again shows that the combination of TG and XAS is very useful to study basic material properties similar to the investigations on La_2RuO_5 described in Sec. 5.4 and Ref. [Rie12c].

The found average shift of the valence for all Cu ions is in contrast to the observation for thermally quenched isostructural $Cu_{2+x}Ta_4O_{12+\delta}$ compounds [Ebb10]. For these the appearance of a clearly visible shoulder was reported on the low energy side of the peak in the first derivative of the absorption edge pointing to the coexistence of Cu^{2+} and Cu^{1+} ions in quenched $Cu_{2+x}Ta_4O_{12+\delta}$. This was corroborated by x-ray photoelectron spectroscopy and the formation of a partial charge ordering derived from the structural analysis of neutron-diffraction data [Ebb07a]. Although for $Ln_yCu_3Ru_xTi_{4-x}O_{12+\delta}$ the peak shape is changing upon variation of x, a similarly clear splitting into two separate peaks cannot be observed. The peak shape becomes slightly more symmetric and broadens with increasing x (Fig. 6.28). The findings for the $Ln_yCu_3Ru_xTi_{4-x}O_{12+\delta}$ are also different to the results of the valence evolution observed for $La_{2-x}Sr_xCu_{1-y}Ru_yO_{4-\delta}$ with mixed Ru/Cu-site. These compounds provided almost constant divalent copper and a change of the Ru valence depending on the substitution levels [Ebb98, Ebb01].

The result of the constant +4 oxidation state of Ru and the variation of the Cu valence between +2 and +1.6 in combination with the assumed $\delta \approx 0$ can now be used to interpret the magnetic properties of the $Ln_yCu_3Ru_xTi_{4-x}O_{12+\delta}$ samples. This will be topic of the subsequent section and furthermore the overall observed physical properties of these compounds will be discussed with respect to these results. On the other hand, from the XANES spectra more information on the electronical properties than the cation oxidation states can be obtained, which will be discussed in
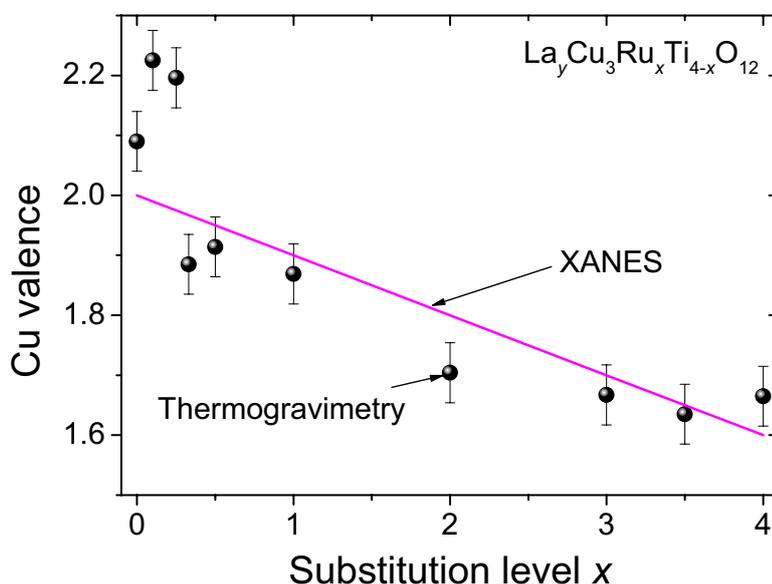
Figure 6.30.: Cu valence of $La_yCu_3Ru_xTi_{4-x}O_{12}$ calculated from the measured weight loss assuming a constant Ru^{4+} oxidation state and $\delta = 0$. The solid line is corresponding to the line in Fig. 6.29.

Sec. 6.2.5.

6.2.4. Magnetic Properties and Phase Diagram

The interpretation of the magnetic susceptibilities of the $Ln_yCu_3Ru_xTi_{4-x}O_{12+\delta}$ samples is rather difficult due to the manifold and complex magnetic exchange interactions between the different cations. Taking into account the importance of the bond angles for the character of the superexchange interaction the different paths can be examined. For example, the Cu–O–*B* angle amounts to 110° with expected ferromagnetic exchange, while the *B*–O–*B* angle with 140° ranges close to the border between ferro- and antiferromagnetic superexchange. The ordering of the Cu spin moments in the titanates was described by ferromagnetically coupled moments in the {111}-planes, which are antiferromagnetically coupled with each other resulting in the negative Curie-Weiss temperature [Kim02]. This ordering should be influenced by the Ru substitution, since the Ru ions (with *d* electrons) are inserted into the main exchange path Cu–O–*B*–O–Cu between the planes. The magnetic susceptibility of selected $La_yCu_3Ru_xTi_{4-x}O_{12}$ samples is depicted in Fig. 6.31a for $x = 0$, $x = 2$, and $x = 4$. These are typical representatives for the three types of observed susceptibilities.

For the pure titanates an antiferromagnetic ordering of the Cu $S = 1/2$ moments below roughly 25 K was reported, while up to 400 K a paramagnetic behavior was observed in agreement with
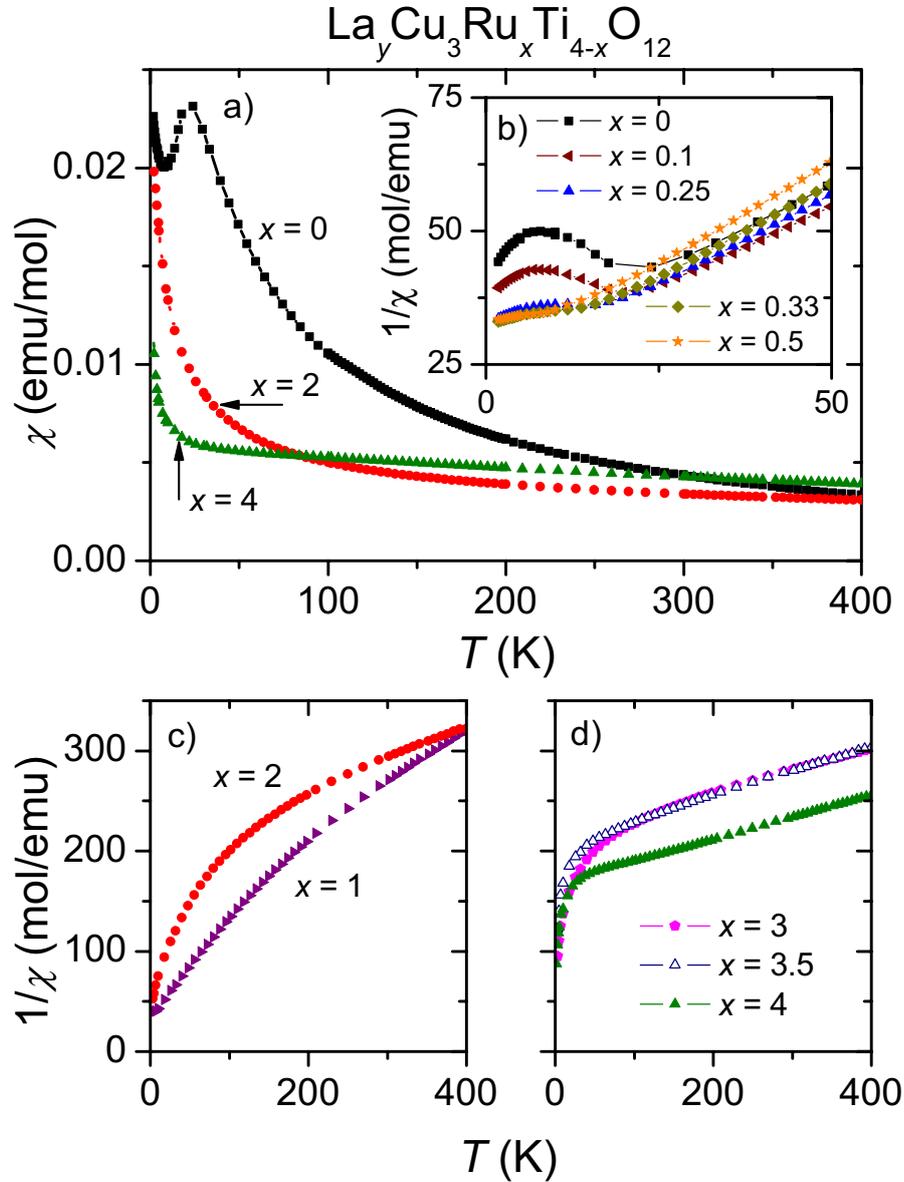
Figure 6.31.: a) Temperature dependent magnetic susceptibility of $La_yCu_3Ru_xTi_{4-x}O_{12}$ for selected x. b) Inverse susceptibilities for $x \leq 0.5$, c) for $x = 1$ and $x = 2$, and d) for $x \geq 3$.

the Curie-Weiss law (see Sec. 6.1.1). The anomaly at roughly 25 K in the inverse susceptibility (Fig. 6.31b) indicates the antiferromagnetic ordering at least up to $x = 2$, however, T_N decreases gradually with increasing x. The effective magnetic moment obtained from the Curie-Weiss fit of the paramagnetic part can be explained by the addition of the moments of Cu^{2+} and Ln^{3+}. The almost constant Curie-Weiss temperature of roughly -30 K indicates a dominating antiferro-
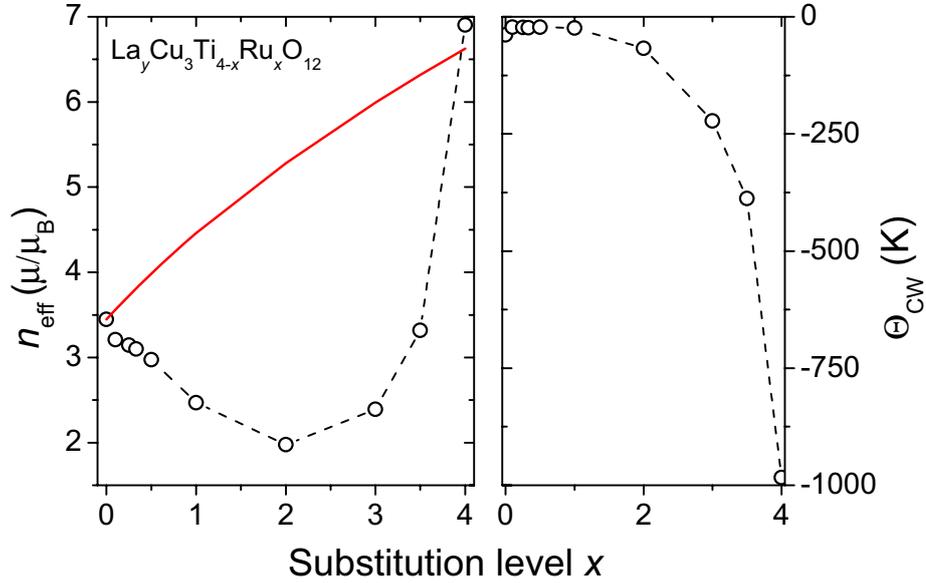
Figure 6.32.: Left: Effective magnetic moment n_{eff} of $La_yCu_3Ru_xTi_{4-x}O_{12}$ obtained from a Curie-Weiss fit of the inverse magnetic susceptibilites. The solid red line marks the theoretical sum of Cu^{2+} and Ru^{4+} spin moments. Right: Corresponding Curie-Weiss temperatures Θ_{CW}.

magnetic exchange and only weak interactions between the Cu and *Ln* sublattices [Kro10, Dit11]. The antiferromagnetic ordering is observed up to a Ru content of $x = 0.33$. For Ru substitution levels $0.5 \leq x \leq 1.5$ in $CaCu_3Ru_xTi_{4-x}O_{12}$ a spin-glass behavior was described [Tsu09], which is also present for $La_yCu_3Ru_xTi_{4-x}O_{12}$ up to $x \approx 2$ characterized by the kink in the zero-field cooled susceptibility at low temperatures [Bue10]. Furthermore, the transformation from the paramagnetic-insulator to the heavy-fermion phase is indicated by visible changes of the curvature of the (inverse) susceptibility, as shown in Fig. 6.31c for $x = 1.0$ and $x = 2$. The non-Curie-Weiss behavior is reflected by the increasing deviation from a straight line. The pure ruthenates, which are described as metallic and heavy-fermion compounds, and the samples with $x \geq 3$ show a susceptibility characteristic for metals over a broad temperature range, i.e. temperature independent Pauli-paramagnetism can be assumed [Kob04, Ebb06, Ebb10]. Only at low temperatures a steep increase can be observed. This results in a ferrimagnetic-like shape of $1/\chi$ as can be seen in Fig. 6.31d, which is possibly caused by the changing magnetic interactions. Therefore, the steep decrease to the origin below 50 K is apparently no further sign of long-range magnetic ordering.

From the high temperature part (roughly 100 K to 400 K) of the inverse susceptibilites the effective magnetic moment and the Curie-Weiss temperatures were derived for $La_yCu_3Ru_xTi_{4-x}O_{12}$ using a Curie-Weiss fit according to Eq. 2.32. In Fig. 6.32 the obtained values for n_{eff} and Θ_{CW} are shown in the left and right frame, respectively. For the effective magnetic moments an unex-

pected evolution is observed. A minimum is found at $x \approx 2$ and the experimental values are partly strongly deviating from the theoretical sum of the spin-only values for the three Cu $S = 1/2$ and the corresponding fraction of Ru $S = 1$ spin moments, which is represented by the solid red line. For $x = 0$ an average Cu moment of 1.99 μ_B was obtained, which is larger than expected for $S = 1/2$ in the spin-only approximation (1.73 μ_B). This deviation is probably caused by contributions of the spin-orbit coupling, which is neglected in this simplified model. However, the found value is in excellent agreement with literature data comparing experimental results in Ref. [Lue99]. The decrease of the total magnetic moment for increasing x can only be explained by the electronic correlations in $Ln_yCu_3Ru_xTi_{4-x}O_{12}$ and the changing Cu valence. But the decrease is much stronger than the effect caused by the decreasing Cu valence. Thus, other effects like the gradual delocalization/localization of the Cu/Ru valence electrons have to be taken into account and will be discussed in detail later. Furthermore, the Curie-Weiss temperature in the right frame of Fig. 6.32 exhibits unusual high absolute values for $x > 2$ indicating that the application of the Curie-Weiss law for the susceptibility fit is probably not recommended for this substitution range.

As suggested by [Tsu09, Bue10] and investigated by S. Widmann in his diploma thesis [Wid12], the observed different shapes of the susceptibilities (Fig. 6.31) can be ascribed to several magnetic phases. In Fig. 6.33 the temperatures indicating of the upturn in the susceptibilities obtained for the $Ln_yCu_3Ru_xTi_{4-x}O_{12}$ samples are depicted (circles) and corresponding phase boundaries are marked by dashed lines. For $x \leq 0.5$ the anomaly indicates the antiferromagnetic ordering similar to the pure titanates and the transition temperature is represented by the Néel temperature. Above T_N the samples are paramagnetic insulators. Upon increasing x the transition temperature is shifted linearly from 25 K to roughly 10 K simultaneously for Ln = La, Pr, Nd. In the range between $x = 0.5$ and $x = 2.25$ the ordering temperature (freezing temperature T_f) reflects the border to a spin-glass phase, since the peak position in the ac-susceptibility becomes frequency dependent, as typically observed for spin glasses [Tsu09, Bue10, Bin86, Myd93]. The decrease of this freezing temperature is less steep in x and finally the magnetic phase transition vanishes above $x = 2.25$. The borders $x = 0.5$ and $x = 2.25$ of the described phases are identical for all three A-site cations. The interpretation of the magnetic properties in the range above $x = 2.25$ is complicated due to the entanglement of the correlating Cu and Ru electrons, which is becoming more complex by the addition of the A-site ions Pr and Nd with significant magnetic moments. Due to this, crystal-field effects become relevant for lower temperatures, which further increases the complexity.

Basically, the susceptibilities of the Pr and Nd containing samples are comparable to the ones of $La_yCu_3Ru_xTi_{4-x}O_{12}$ for the same x. The ordering temperatures (T_N and T_f) are almost identical for all three lanthanides for the same substitution levels as can be seen in Fig. 6.33. Nevertheless, χ of $La_yCu_3Ru_xTi_{4-x}O_{12}$ cannot be easily obtained by the subtraction of the paramagnetic susceptibility of the lanthanide ions like it was possible for the $La_{2-x}Ln_xRuO_5$ samples shown in Sec. 5.1.2. The deviations of the residual susceptibility to the samples containing La after subtraction of a paramagnetic rare-earth metal ion contribution from the measured susceptibilities cannot be neglected. Thus, the correlation in the Cu–Ru system is apparently affected by the additional rare-earth metal ion moments.

For $x \geq 2.5$ the Pauli-paramagnetic behavior of the susceptibility as well as results of electrical
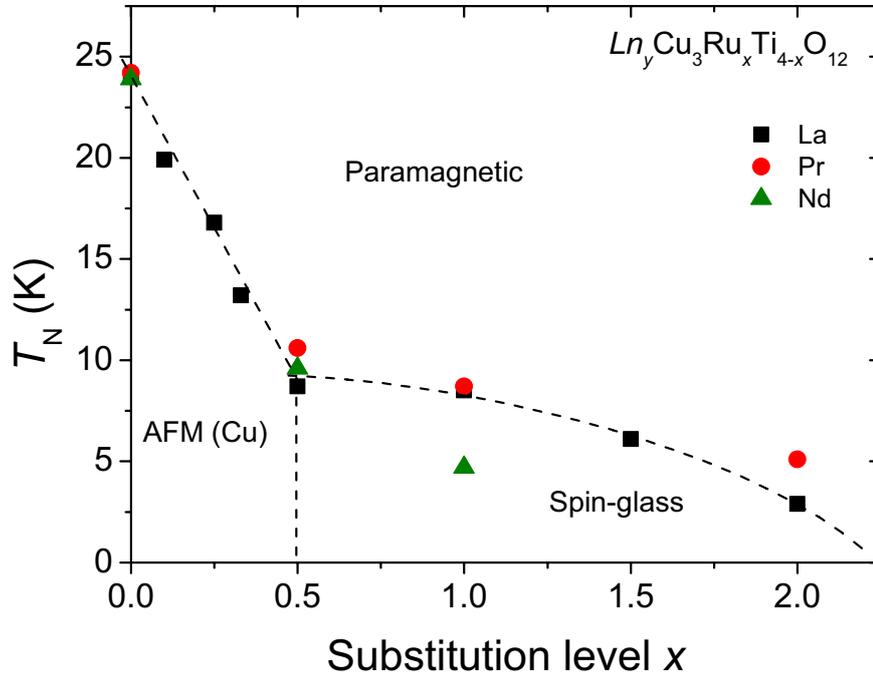
Figure 6.33.: Néel temperatures of $Ln_yCu_3Ru_xTi_{4-x}O_{12}$ as a function of the substitution level until $x = 2.25$. The dashed lines mark the phase boundaries of the different observed magnetic phases.

resistivity measurements [Ebb06, Ebb10] let expect an insulator to metal transition at $x = 2.25$. The phase transition was assumed in a first approximation for the substitution level where the sign of the slope in the temperature dependent resistivity changes to positive. From Ref. [Ebb10] this was expected at roughly $x = 3$. Recent electron spin resonance (ESR) measurements on Gd doped $LaCu_3Ru_xTi_{4-x}O_{12}$ ($1 \leq x \leq 4$) samples revealed that the transition is occurring close to $x = 2.25$ [Sch12]. The width of the measured resonance line is typically broadening linearly with increasing temperature in metallic systems (Korringa-effect [Kor50]). Starting from the pure ruthenate the broadening effect decreases with increasing Ti incorporation and vanishes for $x = 2.25$, where the insulating spin-glasses become evident. This finding is not in contrast to the resistivity results of Ebbinghaus *et al.* [Ebb06, Ebb10], though a heavy-fermion like behavior for a broader range $2.25 \leq x \leq 4$ can be interpreted from more recent resistivity (ρ) data. Despite the behavior of the electrical resistivity of the pressed and sintered pellets is very sensitive on the contact resistivity, cracks, and grain boundaries within the sample, the overall behavior can be used to study the transition. The resistivities for $x > 3$ follow a T^2 behavior, which characterizes the metallic heavy-fermion state of a Kondo-system. In this system intinerant electrons are screened by localized ones resulting in a virtual increase of the electron mass, which is deduced from the

increased Sommerfeld-coefficient in the specific heat. For $2 \leq x \leq 3$ ρ is partly proportional to $\ln(T)$ indicating a disturbed Kondo-lattice with still a heavy-fermion like behavior of the electrons [Wid12].

The metal-insulator transition seems to be linked to a transition from the heavy-fermion to the spin-glass behavior, which is probably coupled with a quantum-critical point (QCP) at $x = 2.25$ [Bue10]. Very probably this QCP is not fixed to a narrow concentration x but it can be located between $x = 2$ and $x = 2.5$ due to the results described up to this point. From the smooth change of the crystal-structure data also a sudden transition at a sharp substitution level is not expected. To further study the magnetic phase transitions and the QCP the XANES data were investigated in detail.

In addition to the valence determination the XANES spectra of the Ru-L$_{\text{III}}$ and Cu-K absorption edges provide further characteristics of the electronic structure at the Fermi-energy. The shape of the absorption edge is composed by allowed excitations of electrons of states close to the core into unoccupied valence states and transitions, which are forbidden by quantum-mechanical selection rules but become allowed by breaking the local inversion symmetry. Therefore, the near-edge structure is reflecting the influence of the nearest neighbor atoms by, for instance, crystal-field or valence changes.

The spectra of the Cu-K edge are shown in Fig. 6.27. The excitation of the core electrons into localized valence states leads to a sharp transition peak in the absorption spectra since due to the Born-Oppenheimer approximation the spatial movement of the ions can be neglected. In the case of increasingly diffuse orbitals or itinerant electrons in the valence states the absorption energy varies stronger and therefore causes a distinct broadening of the peak. Thus, the loss of the clear features in the absorption-edge spectra is very well in agreement with the increasing itineracy of the Cu valence electrons, which can be deduced from the decreasing valence depending on x. In addition, the spin moment per Cu obtained from the integration of the transition peak in the specific-heat data decreases from approximately $S = 0.42$ for the titanate to $S = 0.12$ for $x = 2.25$ [Wid12]. For $x > 2.25$ the transition anomaly cannot be detected either since the transition is suppressed in agreement with the susceptibility data or the peak is becoming to broad to be recognized or the peak maximum is shifted below the lowest available temperature of roughly 2 K for the measurement.

Moreover, the shape of the Ru-L$_{\text{III}}$ edge spectra provides detailed information of the electronic states in the LaCu$_3$Ru$_x$Ti$_{4-x}$O$_{12}$ samples. The double-peak structure shown in Fig. 6.23 was fit using two pseudo-Voigt functions. Fit parameters like the FWHM and the intensity can be used as a measure for the degree of hybridization. Two sharp peaks with small FWHM as observed for low substitution levels intuitively provide a small overlap and in turn broad peaks result in a large overlapping area, which should indicate increasing hybridization and, therefore, itineracy of the 4d electrons. For the La$_2$RuO$_5$ compounds it was discussed that the lower symmetry of the octahedra as a result of the deformation decreases the FWHM values. This was suggested since compared to e.g. RuO$_2$ with tetragonally elongated octahedra broad peaks were observed. However, this structural argument is not valid for LaCu$_3$Ru$_x$Ti$_{4-x}$O$_{12}$, where by definiton from symmetry the octahdera are regular with equal B–O bond lengths. In this case a different origin
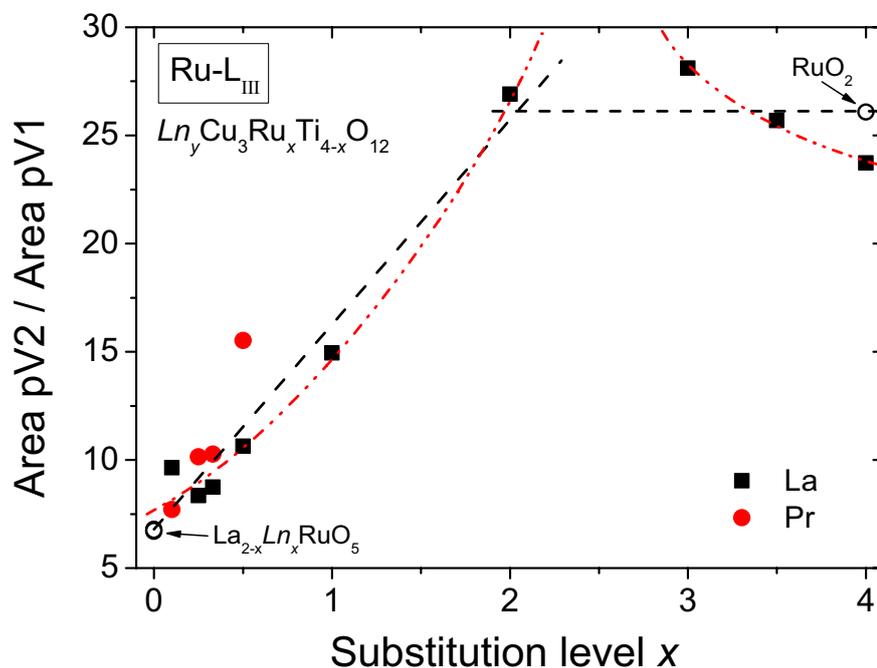
Figure 6.34.: Ratio of the pseudo-Voigt peak areas (pV2/pV1) used for the Ru-L_{III} edge XANES fit of $LaCu_3Ru_xTi_{4-x}O_{12}$ and reference ruthenates.

has to be discussed for the broadening of the white lines. At low substitution levels $x \leq 1.0$ clearly the two maxima are separated and pV1 is distinctly smaller than pV2. Beginning with $x = 2$ both peak intensities are increasingly becoming equal and the FWHM is broadening similar to the peak in the derivative of the Cu-K spectra. This behavior probably is also caused by the increasing itineracy of the electrons in the system and the stronger hybridization, which results in an increased conductivity of the compounds and, hence, agrees with the insulator to metal transition for increasing x. Moreover, the results of the ESR spectroscopy on the Gd-doped $LaCu_3Ru_xTi_{4-x}O_{12}$ samples show that the Ru electrons are not fully localized (especially in the range $2 \leq x < 4$), but also contribute to the itinerant behavior of the total electronic system [Sch12].

The ratio of the peak areas of pV2 and pV1 is shown in Fig. 6.34 for the $La_yCu_3Ru_xTi_{4-x}O_{12}$ and several $Pr_yCu_3Ru_xTi_{4-x}O_{12}$ samples. For the pure La- and Pr-titanates and the $La_{2-x}Ln_xRuO_5$ samples comparable values are found and as expected the values are increasing with increasing substitution level due to the stronger delocalized character of the electrons. The almost linear increase is marked by the dashed line in the figure rising from approximately 6 for the titanates to 27 for $x = 2.0$. Then the pV2/pV1 ratio remains almost constant until $x = 4$. The high value is in good agreement with the ratio obtained for RuO_2, which yields a metallic conductivity. This peak broadening reflects the closing of the electronic band gap and increasing hybridization with the O-

$2p$ orbitals. This pV2/pV1 ratio method is maybe useful to get a first approximation of the electric conductivity of ruthenate compounds to decide between semiconducting and metallic behavior. Nevertheless, this has to be studied systematically in future using fully characterized samples and probing their electrical conductivity. Alternatively the dashed line can be used to guide the eyes through the data points. Its shape reminds of a volcano with a maximum at approximately $x = 2.5$, which is surprisingly close to the QCP. This interpretation illustratively shows the divergence of an ordering parameter at the QCP, which is expected around $x = 2.25$. Nevertheless, a correlation between physical parameters still has to be found for this volcano-like shape.

6.2.5. DFT Calculation

The above described phase transitions and, therefore, resulting changes of the electronic structure were additionally investigated by DFT-calculations. The same LSDA modelling parameters which which were presented for the titanates in Sec. 6.1.4 were used to calculate the electronic band structures for $LaCu_3Ru_xTi_{4-x}O_{12}$. The crystal-structure data obtained from powder XRD were taken as input data. To model the mixing of Ru and Ti on the B-site in the symmetry reduced P1 unit cell, several combinations of Ru and Ti were placed on the eight available sites. Thus, the substitution levels $x = 0.5, x = 1, \ldots, x = 3.5, x = 4$ correspond to the replacement of one, two, $\ldots$, seven or eight Ti ions by Ru, respectively. The modelling of varying combinations of the site occupations, which are not equal by using a symmetry operation, was reqired from two to six replaced ions to study the energetical preference of ordering on the B-site by taking the solution with lowest total energy. For example, in the case of $x = 2$ four Ti and four Ru ions are distributed on the eight available sites, which can result in layered arrangements of alternating Ti and Ru containing layers or stripes or a checkerboard type ordering, in which each nearest neighbor is of the other element.

Summarized, no preference for long-range ordered arrangements was found. This result was expected, since if such highly symmetrical orderings would be present, they would be observable by superstructural reflections in the XRD patterns. Nevertheless, all possible combinations neglecting the symmetry equivalent ones were modelled, because the obtained difference to the minimum energy can be used to argue on the probability of the existence of these arrangements averaged over the whole crystal structure. Since the modelled unit cell is only the smallest super-cell available for this compound, more sophisticated algorithms generating larger supercells with a random distribution of the B-cations would lead to more reliable results, but such large cells would require impractibable long computational times. However, the results already agree very well with the experimental data and motivate more detailed studies in future.

Due to the correlation between the electrons of the Cu and Ru ions, the calculations converged only up to a maximum substitution level of $x = 2.5$. Above this value the repetition of the calculations basing on the output data of the previous run were performed until the energy criteria for convergence was achieved and the deviation within the electron density was below 10^{-4}. Upon using the spin-polarized LSDA the magnetic ordering of the cations was investigated by different initial spin settings. As shown above for $LaCu_3Ti_4O_{12}$ in Sec. 6.1.4 the AFM setting of the Cu
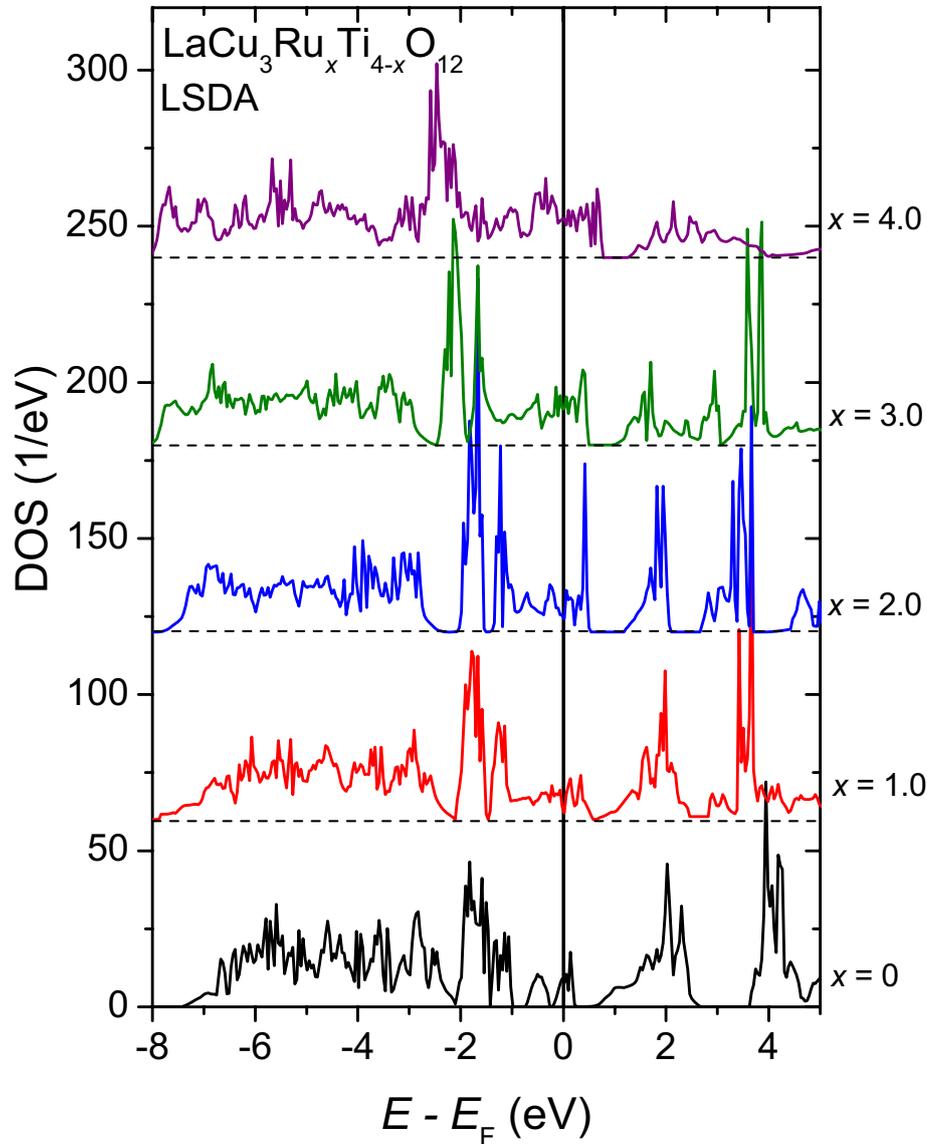
Figure 6.35.: DOS of $LaCu_3Ru_xTi_{4-x}O_{12}$ obtained by DFT-calculation using LSDA (spin-up channel is shown). The curves were shifted by a constant value to increase clarity.

spin moments leads to a converging solution providing almost the expected $S = \pm 0.38$ moment per copper ion. Thus, with respect to the magnetic properties discussed above the Cu spins were all set to this AFM configuration before the LSDA calculation was started. The Ru spins $S = 1$ were initially set in a ferromagnetic arrangement.

In Fig. 6.35 the resulting density of states for the calculation result with lowest total energy for

integer x are depicted. The DOS of $LaCu_3Ti_4O_{12}$ is shown at the bottom (see also Fig. 6.13) while the DOS of the substituted compounds are each shifted by a constant value to increase clarity. The typical structure of the DOS described above for the titanates is conserved (Sec. 6.1.4). The unoccupied Ti $3d$ bands are found above 1.5 eV, between 0.5 and 2.5 eV the Cu and Ti $3d$ bands are mixing and the main contribution of the Cu states is located from -2 to 0.3 eV. The remaining part is dominated by the large number of oxygen $2p$ bands. The Ru $4d$ bands are appearing for $x = 0.5$ at approximately 3 eV and close to the Fermi energy. Basically these contributions increase with increasing substitution level, as expected. Especially at E_F the increased number of states would close of the band gap and a higher electrical conductivity is expected. This is also indicated by the change of the sample color from brownish to black and by resistivity measurements [Ebb10, Mul86, Ram04].

The former Ti-dominated sharply peaked pDOS above 3.5 eV is only slightly shifted upon the Ru substitution. On the other hand, for $x = 4$ the DOS in this region is smeared out to a broad structure reflecting the Ru $4d$ e_g bands of the RuO_6 octahedra similar to La_2RuO_5. In this structure also Cu $3d$ bands are found indicating hybridization. The whole structure of the main contribution of the Cu bands located between -2 and -1 eV in the valence band is shifted by roughly -1 eV in $LaCu_3Ru_4O_{12}$ compared to the titanate. This shift is almost linear in x and is probably linked to the linear decrease of the Cu valence described in Sec. 6.2.3. In general, the region dominated by O $2p$ bands below roughly -2 eV becomes strongly broadened and smoothened upon the increasing substitution level reflecting once more the observed delocalization of electrons in the compounds.

In Fig. 6.35 only the spin-up channel of the DOS is shown since the almost perfect AFM ordering results in symmetrical DOS of both majority and minority spin channels. The band gap like structure observed for $LaCu_3Ru_4O_{12}$ results from the ferromagnetic ordered Ru spin moments, which cause a minor visible shift of the Ru pDOS. In contrast, the spin-down data yield a very low number of states at E_F typical for a half-metallic system. This finding is not in agreement with the experimental data and shows that more detailed modelling is required for the Ru-rich compounds due to the strongly correlated electrons of Cu and Ru.

The local spin moments of the ions for each site are additionally obtained from the DFT-calculations. The averaged moments for Cu and Ru are depicted in Fig. 6.36 versus the substitution level. The Cu moments posses both positive and negative signs due to the AFM ordering, while for Ru only positive signs were found reflecting a ferromagnetic arrangement. The AFM ordering is constantly the same alternation of ferromagnetically ordered layers along the [111]-direction like the one reported for $CaCu_3Ti_4O_{12}$ [Kim02]. The Cu spin values decrease gradually from approximately 0.38 for $x = 0$ to almost zero at $x = 2.5$. This finding is in agreement with the Cu spin moments obtained from the entropy change during the transition in experimental specific-heat data [Wid12]. In contrast, the Ru moment increases for $x \geq 2.5$. This behavior of the local spin moments agrees well with the above described increasing delocalization of the Cu $3d$ electrons, which become itinerant above $x = 2.5$. On the other hand, (itinerant) Ru $4d$ electrons start to increasingly localize into Ru spin moments of $S_{Ru} \approx 0.83$, which is close to the $S = 1$ expected for the $4d^4$ low spin configuration of Ru^{4+} ions in octahedral coordination. Formally for Ru a va-
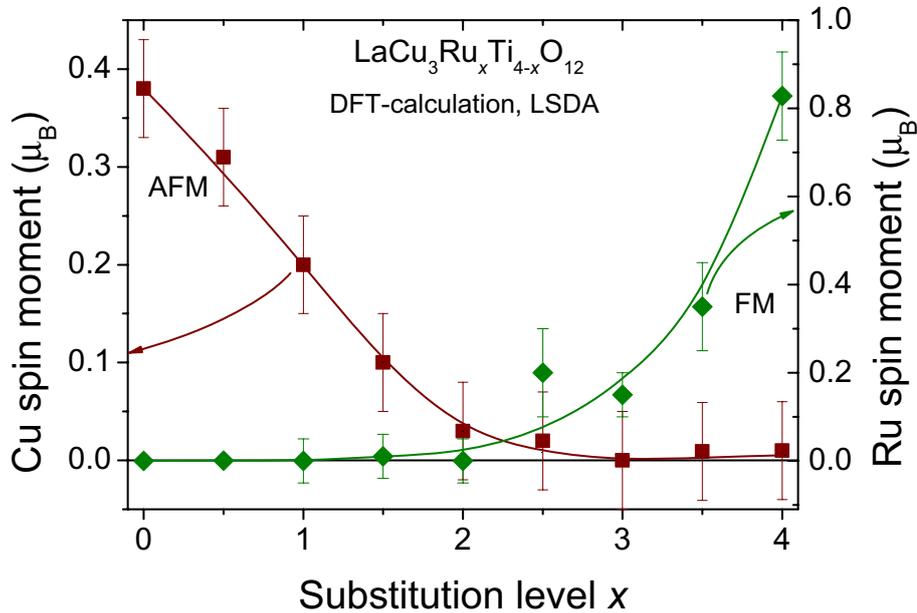
Figure 6.36.: Spin moments of Cu and Ru in $LaCu_3Ru_xTi_{4-x}O_{12}$ obtained by DFT-calculation using LSDA. The Cu moments are found antiferromagnetically arranged, while the Ru moments order ferromagnetically.

lence of +3.75 is expected,[2] which would also result in a slightly smaller spin moment per Ru ion. The findings imply that the heavy-fermion properties are generated by the itinerant Cu electrons, which are interacting according to the Kondo effect with the localized Ru electrons leading to the increased electron mass observed in the specific-heat data of the pure ruthenates.

Additional DFT calculations for the $ACu_3Ru_4O_{12}$ (A = Ca, Sr, Pr, Nd) compounds using LSDA were performed to compare this finding with the other related heavy-fermion compounds using the same method. While for Pr and Nd no convergence was achieved and only local moments for the rare-earth metal ions were obtained, the results for Ca and Sr reflect almost identical findings as obtained for $LaCu_3Ru_4O_{12}$. Both compounds yield an itinerant character of the Cu electrons and local Ru spin moments of $S \approx 0.45$ for A = Ca and $S \approx 0.5$ for A = Sr, respectively. The smaller local moment is surprising since this means that the Ru electrons are less localized in the compounds with divalent A-site ions than in the ones with the rare-earth metal ions. On the other hand, a changed Ru valence to +3 with t_{2g}^5 configuration would result in a total $S = 1/2$ spin moment, however, this scenario is in strong contrast to the observed tetravalent Ru in this compounds and the absence of trivalent Cu to preserve charge neutrality for this case [Ebb02]. Probably this finding fits to the opposite explanation of delocalized Ru electrons interacting with

---

[2]This is the case when only divalent Cu is assumed.

the Kondo lattice as proclaimed for $CaCu_3Ru_4O_{12}$ to increase the electron mass [Tra06].

The finding of localized Ru moments and itinerant Cu electrons was quite unexpected, because the rather diffuse Ru $4d$ orbitals seem to be more suitable for the delocalization in contrast to the more localized character of the $3d$ orbitals. However, a strongly varying nature of the Ru d electrons has been reported in Ref. [Cav04]. Furthermore, the crystal structure has to be considered. Goodenough [Goo01] reported on an increasing localized character of electrons in octahedral BO_6 coordination when the average B–O bond length increases, which is the case for increasing x in $LaCu_3Ru_xTi_{4-x}O_{12}$. In comparison, the Cu–O bond length either slightly decrease or remain almost constant in agreement with the observed changes of the electronic character. Moreover, due to the empty Ti $3d$ orbitals and the square planar coordination of the Cu ions in $CaCu_3Ti_4O_{12}$ the localization of the Cu $3d$ electrons is increased [Cla11]. The slight changes of the local crystal structure and the rising number of Ru–O–Cu exchange interaction paths with increasing Ru incorporation seem to support the mobility and itineracy of the Cu electrons.

In conclusion, it was shown that the substitution on the B-site in $Ln_yCu_3Ru_xTi_{4-x}O_{12}$ strongly influences the physical properties including a number of magnetic transitions to an antiferromagnetically ordered state, a spin-glass phase and a heavy-fermion behavior although the structural changes are very small. Thus, the transitions are not caused by abrupt changes of the unit-cell symmetry crossing the phase boundaries as it was shown in the previous chapter for (substituted) La_2RuO_5 compounds. Still the entanglement of the slight structural changes and the electronic structure variation requires investigations to get a more detailed overview of the correlations between Cu and Ru electrons. Therefore, more sophisticated DFT calculations and ESR spectroscopy measurements are planned to gain a deeper understanding of the complex relationships of composition - structure - physical property in the $AA'_3B_4O_{12}$ related compounds.

7. Summary

In this work the complex relationships of composition, crystal structure, and physical properties were investigated for perovskite-related oxides containing ruthenium. It was shown that the changes of structure and properties can be modified in detail by specific substitutions. For the presented studies substitution series were performed for the parent compounds La_2RuO_5 with a layered structure and $ACu_3B_4O_{12}$ of the $CaCu_3Ti_4O_{12}$-type with a $2 \times 2 \times 2$ perovskite superstructure.

La_2RuO_5 is interesting due to its magneto-structural transition at an unusual high temperature ($T_d = 161$ K) including the formation of a non-magnetic singlet ground state, which is rarely observed in 3D crystal structures. Poly- and single crystalline samples were synthesized applying different techniques, inter alia were solid-state and varying soft-chemistry syntheses as well as a flux method. The high- and low-temperature phases were characterized by studies of the crystal structure, the magnetic susceptibility, and the specific heat. Basically, the crystal structure can be described by an alternating stacking of LaO- and $LaRuO_4$-layers along the crystallographic a-axis. Above the transition temperature La_2RuO_5 adopts a monoclinic ($P2_1/c$) structure and is paramagnetic yielding a Curie-Weiss behavior corresponding to $S = 1$ spin moments of the Ru^{4+} ions. The Curie-Weiss temperature ranges between -100 and -180 K (depending on the applied synthesis route) reflecting significant antiferromagnetic exchange interactions between the Ru moments. For the low-temperature modification ($T < T_d$) a triclinic structure (space group $P\bar{1}$) was found. Due to the structural changes a variation of Ru–O–Ru bond lengths and angles emerges in the RuO_6-octahedra. The structural parameters were investigated in detail by analysis of diffraction data of single crystals and powder samples. Very interestingly, in the powder samples a rather broad regime of 20 K in the vicinity of T_d is observed, in which both phases coexist. A singlet-formation of the Ru spin moments is occurring in the lt-phase characteristically leading to the observed step-like decrease of the magnetic susceptibility to roughly $1 \cdot 10^{-4}$ emu/mol.

In the specific heat of La_2RuO_5 a peak is observed at T_d. The symmetric shape of the peak reflects a first-order transition, which is corroborated by the instant drop in the susceptibility of the single-crystalline sample. After subtraction of the lattice contribution the entropy change caused by the transition can be determined to approximately 4.2 J mol^{-1} k^{-1}. This value is approximately one half of what is expected for a classical model of the transition into an antiferromagnetically ordered ground state formed by the Ru ($S = 1$) spin moments. Therefore, a model to estimate the entropy for the transition from a paramagnetic to the dimerized state was developed. A typical energy spectrum for the singlets (with coupling J_0) in the lt-phase was used and depending on $J_0/k_B T_d$ the entropy could be calculated. From this the exchange parameter was determined to

$J_0/k_B \approx 260$ K ($J_0 \approx 23.5$ meV). In addition, from the susceptibility data a spin-gap of approximately 48 meV in polycrystalline samples and 110 meV in single crystals was found in agreement with inelastic neutron scattering, where a broad peak around 40 meV was observed [Kha02]. A strong anisotropy of magnetic exchange in the lt-phase was deduced from the structural deviations compared to almost regular Ru–O bond lengths and angles in the ht-phase. Thereby a dimer model consisting of almost isolated Ru spin singlets was established in accordance with theoretical results in literature describing the exchange anisotropy obtained from DFT calculations [Eye06, Wu06]. A spin-ladder like arrangement along c (within the $LaRuO_4$-layers) with rungs formed by the Ru–Ru spin singlets was proposed.

Ab-initio DFT calculations using LDA and LSDA were performed for both the ht- and lt-phase. The results are in accordance with previous calculations applying an augmented-spherical-wave approach [Eye06] as well as with the experimental results. More sophisticated calculations should include Mott-Hubbard U electron-repulsion terms to model the anisotropic exchange parameters.

The investigation of the band-gap evolution under pressure up to 12 GPa did not reveal the expected semiconductor to metal transition. An energy shift of the bands close to E_F was found instead of the expected broadening due to decreasing interatomic distances. These findings point to a strong rigidity of the crystal structure. Dielectric spectroscopy revealed a very small anomaly at T_d in the permittivity ε' and pointed to a variable range hopping mechanism, which is slightly different in ht- and lt-phase reflecting the change in crystal structure, electrical conductivity, and band gaps of the phases. However, the results were strongly influenced by contact effects, which only allowed a comparison of the relative changes.

For further studies on the dependence of the physical properties on the structural changes systematic substitutions were carried out. Lanthanum was substituted by trivalent rare-earth metal ions (Ln = Pr, Nd, Sm, Gd, Dy) of different sizes and magnetic moments up to 10 μ_B. In addition, ruthenium was partly substituted by the $3d$ metals Ti and Mn. To check a mutual influence of the substitution on both sites, a co-substitution of La by Pr and Ru by Ti was performed. A large number of polycrystalline samples was synthesized by an adapted soft-chemistry route, which had to be applied since by the classical solid-state synthesis no single-phase samples could be obtained.

Depending on the ionic radii of the rare-earth metal ions - result of the lanthanide contraction - different maximum substitution levels were obtained for $La_{2-x}Ln_xRuO_5$. For Pr the upper limit was $x = 0.75$ and was found to decline to $x = 0.2$ for Dy. The single-phase polycrystalline samples were investigated by x-ray and neutron diffraction in combination with Rietveld analysis. All samples show the transition from the monoclinic ht-phase to the triclinic lt-phase like the unsubstituted La_2RuO_5 including a similar change of the cell parameters during the transition. Besides the cell axes, the monoclinic angle β decreases linearly with x for Pr and Nd, for Sm it remains almost constant, while for Gd and Dy the angle increases slightly. This effect can be explained by the different sizes of the lanthanide ions and the (mis-)matching of the ions into the two available La-sites in the structure. In general, the unit-cell volume decreases linearly with x by up to 1.8 % due to the reduction of the axis lengths. This effect is highly anisotropic and mainly caused by

the reduction of the axis a, which is directed perpendicularly to the layers in the compound. This anisotropy results from the fact that the smaller rare-earth ions are preferably occupying the La-sites in the LaO-layers. From Rietveld analysis of ND patterns it was found that roughly 65-70 % of the Pr ions are incorporated in the LaO-layers. Neutron diffraction could only be used for the Pr-containing samples due to the highly different scattering lengths of La and Pr (while the absorption cross sections are very similar). For the other lanthanides the scattering lengths are either too similar to the one of La (like for Nd) or they have huge absorption cross sections (especially Sm, Gd, and Dy). Therefore, EXAFS spectroscopy at the L_{III}- and K-absorption edges was applied as an alternative method to examine the occupation of the two La-sites in the $La_{2-x}Ln_xRuO_5$ crystal structure. For Pr, Nd, Sm, and Gd a preferred occupation within the LaO-layers was found, while for Dy no significant preference could be observed.

The magnetic susceptibility data showed the characteristic step-like decrease at the dimerization temperature for all the rare-earth substituted samples. The ht-phase susceptibilities can be well described by Curie-Weiss fits. The effective magnetic moments correspond to the sum of the $S = 1$ moment of Ru^{4+} and the moments of the trivalent lanthanide ions (from the free-ion approximation) weighed with x. In addition, the evolution of the Curie-Weiss temperatures can well be described assuming two weakly coupled magnetic sublattices corresponding to the Ru and Ln ions. Furthermore, it was shown that the susceptibility of the lt-phase can be described by the sum of the susceptibilities of La_2RuO_5 and the paramagnetic lanthanide ions. Only below roughly 50 K additional contributions due to emerging crystal-field effects and interactions of electrons within the f orbitals of the rare-earth metal ions were observed.

The dimerization temperature T_d was determined from differential-scanning calorimetry (DSC), specific heat, and the magnetic susceptibility data. The values of the three methods are in good agreement and yield a linearly decreasing dimerization temperature with increasing lanthanide substitution level. Furthermore, it can be generalized that T_d decreases with decreasing unit-cell volume. This behavior reflects a strong correlation of the singlet-formation transition with the crystal-structure variation. The strongest decrease of approximately 20 K was observed for Gd ($x = 0.3$) and Nd ($x = 0.6$), i.e. for maximal substitution levels.

The specific heat of selected $La_{2-x}Ln_xRuO_5$ samples revealed very similar lattice contributions as derived from fits using an Einstein-Debye model. The magnetic entropy was also almost identical for all investigated compounds. The average value of roughly 3.9 J mol^{-1} K^{-1} is very close to the entropy change in pure La_2RuO_5. The constant entropy together with the decreasing T_d indicate a slightly decreasing intradimer exchange J_0 for the Ln-substituted samples. For these samples also the C_p/T peak at T_d broadens, which very likely results from local inhomogeneities affecting the distribution of the rare-earth substitution.

DFT calculations for Pr substituted compounds using LSDA indicate that the magnetic moment of the Pr ions has only a minor influence on the spin ordering found for pure La_2RuO_5. The broadening of the Ru d bands close to E_F with increasing Pr substitution level in the lt-phase explains the lowering of the transition temperature by increasing delocalization of the Ru d electrons.

In summary, the observed features in crystal structure, specific heat, and magnetic susceptibility as well as the performed spin-polarized DFT calculations indicate the spin-singlet formation in

the lt-phase of $La_{2-x}Ln_xRuO_5$ with a quite large exchange-coupling parameter J_0/k_B of ≈ 260 K (23.5 meV). The rare-earth substitution barely affects the phase-transition properties.

Partially Ti-substituted $La_2Ru_{1-y}Ti_yO_5$ was successfully synthesized up to the substitution level $y = 0.45$ using a soft-chemistry route based on the thermal decomposition of a citrate-stabilized precursor. Rietveld analysis of powder XRD data recorded at room temperature reveals that the a-axis slightly increases for $y > 0.2$, whereas the length of the b-axis decreases continuously. The c-axis as well as the monoclinic angle β increase linearly with y. The rotation of the RuO_6 octahedra causes larger Ru–O–Ru angles in the ab-plane, while the angle in c-direction increases only slightly. Decreasing deviations between the ht- and the lt-structures are observed with higher Ti contents in measurements performed at 300 K and 100 K. For $y = 0.45$ the structural phase transition is completely suppressed, as evidenced by diffraction measurements using synchrotron radiation down to 50 K.

XANES measurements at the Ru-L_{III} and Ti-K absorption edges reveal oxidation states of +4 for both Ti and Ru in all samples. A detailed study of the white line at the Ru-L_{III} edge and the pre-edge region of the Ti-K edge indicates very similar (distorted) octahedral oxygen coordinations for all samples up to $y = 0.45$ in agreement with the results of the XRD investigations.

With increasing substitution level a distinct change of the magnetic susceptibility was observed. The strong suppression of χ below the phase-transition temperature becomes less pronounced with increasing y and finally vanishes for $y > 0.4$. The magnetic moments derived from a Curie-Weiss fit of $1/\chi$ above 190 K are in agreement with the sum of the remaining Ru^{4+} paramagnetic moments. For low substitution levels the negative values of Θ_{CW} first increase with y. However, after reaching a maximum for $y = 0.2$, which indicates increasing antiferromagnetic exchange due to the shorter interatomic distances, the values decrease again for higher substitution levels. In this substitution range the Ru dilution dominates Θ_{CW} due to the decreasing magnetic exchange. The transition temperatures obtained from $1/\chi$ decrease linearly with higher substitution levels according to $T_d = 166 \cdot (1 - y)$ K.

The phase transition is clearly observable by a peak in the specific heat up to $y = 0.25$ and with increasing substitution level the peak broadens. The entropy change at the phase transition decreases with increasing y, reflecting the smaller number of emerging Ru spin dimers and also a decreasing intradimer exchange J_0. No transition anomaly can be observed in C_p for $y > 0.3$ due to the breakdown of the antiferromagnetic nearest-neighbor interaction. This results in the suppression of the long-range ordered singlet ground state, yielding only isolated spin-dimer clusters on a local scale. XRD, as well as magnetic and C_p measurements show the close correlation between structural and physical properties. Both the structural phase transition and the changes in χ and C_p are successively suppressed with increasing Ti content and completely vanish for $y = 0.45$. However, it still remains to be clarified in detail if the structural changes are driven by magnetic exchange interactions or vice versa.

The comparison of DFT calculations for $La_2Ru_{0.75}Ti_{0.25}O_5$ and $La_2Ru_{0.5}Ti_{0.5}O_5$ with unsubstituted La_2RuO_5 shows a strong contribution of the Ti states at roughly 1.5 eV above E_F and in turn a decrease of the Ru-pDOS at E_F. Spin-polarized calculations for the lt-phase of $La_2Ru_{0.75}Ti_{0.25}O_5$

reveal that the antiferromagnetic arrangement known from lt-La_2RuO_5 is preserved, despite of the incorporated non-magnetic Ti ions. This finding is in agreement with the specific-heat and susceptibility results, both indicating the transition to a long-range dimerized state. For $y = 0.5$ the weak ferromagnetic exchange interactions of Ru–Ru next-nearest neighbors seem to be stronger than the antiferromagnetic exchange leading to the dimerization in calculations using LSDA, which is in agreement with the absence of the singlet state for this substitution level.

The simultaneous substitution of La by Pr and Ru by Ti in La_2RuO_5 ($La_{2−x}Pr_xRu_{1−y}Ti_yO_5$) was successfully carried out for a large composition range $0 \leq x \leq 0.75$ and $0 \leq y \leq 0.4$. The upper substitution limits reflect increasing structural stress caused by the different ionic radii of the substituents in agreement with solely Pr- or Ti-substitution studies.

The polycrystalline samples were investigated by powder XRD at room temperature in combination with Rietveld analysis. The cell parameters reflect a completely additive behavior with respect to the changes observed for the solely Pr and Ti substitution. This finding can be explained taking into account the layered structure of La_2RuO_5. While the Pr ions are predominantly occupying the LaO-layers, the Ti ions are located on the Ru-sites in the $LaRuO_4$-layers. The simultaneous substitution leads to a certain degree of compensation of the cell-parameter changes, which results in the large available range of x and y. Only the b-axis is shortened by both substitutions, which limits the range of concomitantly high substitution levels for Pr and Ti ($x \geq 0.5$ and $y \geq 0.3$).

The magnetic susceptibilities of the ht-phase can be explained assuming a coexistence of two only weakly interacting magnetic sublattices formed by the Pr^{3+} and Ru^{4+} ions, respectively. The Curie-Weiss temperature Θ_{CW} exhibits largest negative values for medium titanium contents. Its increasing absolute value found for $0 \leq y \leq 0.2$ is caused by increasing antiferromagnetic interactions due to the decrease of interatomic distances as a result of small structural modifications. The decrease of $|\Theta_{CW}|$ for $y > 0.2$ can be explained by the dominating dilution of the magnetic Ru-centers by non-magnetic Ti.

A magnetic phase transition with Ru–Ru spin pairing in the lt-phase is observed for all samples with $y < 0.4$. Correspondingly, a linearly decreasing dimerization temperature is found for both substitutions, however, the slopes deviate according to the effects found for the solely Ti and Pr replacement. As the Pr and the Ti substitutions do not mutually affect each other, linear changes with both x and y are obtained for all investigated parameters.

Samples with partial substitution of Ru by Mn in La_2RuO_5 could also be obtained by the sol-gel reaction outlined above. An upper limit of the substitution level is reached at $y = 0.25$. By XRD and ND it was found that the $La_2Ru_{1−y}Mn_yO_5$ samples crystallize in the same monoclinic structure as unsubstituted La_2RuO_5 without any cationic ordering. Additional SAED data support the statistical distribution of Mn on the Ru-site by the absence of superstructure reflections in the zone-axis patterns. The unit-cell parameters a and b decrease while c and the monoclinic angle β increase with increasing substitution level. The parameters remain within the boundaries determined from $La_{2−x}Ln_xRuO_5$ and $La_2Ru_{1−y}Ti_yO_5$. Due to the replacement of Ru^{4+} by smaller Mn^{4+} ions with $3d^3$ configuration the local coordination in the $(Ru/Mn)O_6$ octahedra changes

distinctly, resulting in a tetragonal elongation of the octahedra along c. Furthermore, the Ru–O–Ru bond angles change with y. The angles along the c-axis increase by roughly 1° to 153.6°, while in the ab-plane a more significant increase of 2° to roughly 156° was found compared to pure La_2RuO_5.

XANES measurements proved the oxidation state of +4 for both Ru and Mn ions. Thus, the magnetic properties of the lt-phase described in the following are not caused by a mixture of Mn^{3+}/Mn^{4+} and Ru^{4+}/Ru^{5+} valences, as it is typically observed in other Ru/Mn oxides.

The sum of the magnetic moments of Ru^{4+} ($S = 1$) and Mn^{4+} ($S = 3/2$) is in good agreement with the n_{eff} values obtained from the Curie-Weiss fit of the experimental susceptibilities between 190 K and 400 K. The values of Θ_{CW} are remaining almost constant at -160 K up to $y = 0.1$. For $y = 0.15$ $|\Theta_{CW}|$ increases in a step-like manner to roughly -110 K. This effect is accompanied by the appearance of a second magnetic phase transition. The usual transition step for the spin dimerization at T_d was also observed in the Mn-substituted samples for $y \leq 0.2$. The second magnetic phase found for $y \geq 0.1$ in fc-zfc-measurements can be ascribed to the occurrence of a spin-glass from the $S = 1$ and the $S = 3/2$ moments characterized by the freezing temperature T_f. The observed ferro-(or ferri-)magnetic like increase in χ below 110 K for $y \geq 0.1$ was studied in detail by field-dependent magnetization measurements. The obtained absolute value of the remanence of the hysteresis formed at 2 K is much smaller than expected for a ferrimagnet and, therefore, strongly supports a spin-glass phase below T_f. In addition, the typical s-shaped hysteresis and further AC-susceptibility measurements at the second transition at T_f corroborate the spin-glass transition. A cusp with maximum at T_f appears in the AC-susceptibility and these maxima shift considerably by several K to higher temperatures with increasing frequency, which is characteristic for a spin-glass state.

Up to the substitution level $y = 0.2$ the structural transition to the triclinic lt-phase was observed in combination with the typical change in the magnetic susceptibility, which is ascribed to the dimerization transition of the Ru spin moments. The observed fc-zfc splitting of χ in the lt-phase is not related to a second structural change. From the comparison of χ of the different samples with the appearance of the structural transition it was found that the spin-glass phase emerges in the lt-modification at temperatures just below the Ru dimerization. Surprisingly, $La_2Ru_{0.75}Mn_{0.25}O_5$ shows an incomplete structural transition, i.e. even at 1.5 K roughly 55 % of the ht-phase is still found by quantitative Rietveld analysis of (synchrotron) x-ray- and neutron-diffraction data. Even more interestingly, the (apparently homogeneous) ht-phase splits at 120 K into an lt-phase with lower Mn content ($y \approx 0.2$) and a ht-phase with higher Mn content ($y \approx 0.27$). This observation is unusual taking into account that at room temperature no sign of a mixture of two phases with varying Mn substitution was observed.

The specific heat of the Mn-substituted compounds yields a decreasing magnetic entropy at the dimerization transition with higher manganese contents. Above $y = 0.15$ the dimerization peak has vanished, mirroring that only short-range exchange remains. For $La_2Ru_{0.75}Mn_{0.25}O_5$ no reliable fit of the phonon contributions to the heat capacity was obtained, possibly reflecting smeared out contributions from the spin-glass transition.

Unpolarized and spin-polarized DFT calculations for $La_2Ru_{0.75}Mn_{0.25}O_5$ were used to inter-

prete the magnetic Ru-Mn interaction. The found scenarios of parallel and antiparallel spin moments fit to the spin-glass behavior. On the other hand, the absence of a complete structural transition makes it impossible to study the low-temperature behavior in detail by DFT modelling.

$La_2Ru_{1-y}Mn_yO_5$ is a descriptive example for the strong influence on macroscopic physical properties by even very small structural changes caused by substitution. Especially the unusual mixing of two crystallographic phases with different substitution level in the lt-phase of $La_2Ru_{0.75}Mn_{0.25}O_5$ requires a more detailed investigation. Furthermore, the strongly off-center displacement of the Ru/Mn site in the octahedra in the lt-modification possibly results in a dipole moment, which may be interesting for dielectric investigations and the possible occurrence of ferroelectricity.

The reduction behavior of pure and substituted La_2RuO_5 was studied by thermogravimetry in order to derive the exact oxygen stoichiometry. Surprisingly, the observed weight losses lead to (apparent) oxygen deficiencies $0.06 \leq \delta \leq 0.14$ in clear contradiction to the results from neutron diffraction, XAS, and magnetic measurements. Ru-L_{III}-XANES measurements show that the structure of the absorption edge does not resemble the one of metallic ruthenium. The presence of a very intense white line indicates a Ru $4d$–O $2p$ hybridization, i.e. the presence of oxidized ruthenium. Ru-K EXAFS measurements clearly indicate Ru–O coordination shells revealing an incomplete reduction of the transition metal. It was possible to quantify the amount of remaining oxygen and a linear correlation with the apparent oxygen deficiency of the samples was found. This linear relation proves that the calculated oxygen deficiencies are actually artifacts, resulting from an incomplete reaction even at temperatures up to 1100 °C. The incomplete reduction of the La_2RuO_5-type samples is an unusual exception for an oxide containing noble-metal ions.

The relationship between crystal structure and physical properties of $CaCu_3Ti_4O_{12}$-related samples was also investigated in this thesis. The titanates $Ln_{2/3}Cu_3Ti_4O_{12}$ (Ln = trivalent rare-earth element), $Ce_{0.5}Cu_3Ti_4O_{12}$, and $(Sr,Ca)Cu_3Ti_4O_{12}$ have already been intensely studied because of their very high (colossal) dielectric permittivities in the range of $\varepsilon' \approx 10^4$. For additional investigations of these oxides polycrystalline samples were synthesized by solid-state reaction leading to single phase samples of orange-brownish color. It was shown earlier that the dielectric properties of the samples are very similar [Sub02], which summoned a detailed study of their crystal structure and physical properties (e.g. magnetic properties and band-gap tuning).

The crystal structures of these titanates are basically identical, only the length of the lattice parameter a was found to directly depend on the effective ionic radii of the A-site cation. With respect to this the Ti–O bond length decreases linearly from 1.965 Å for La to 1.954 Å for all A-site ions smaller than Dy. Similarly, the Cu–O distance is almost linearly reduced from 1.98 Å (La) to 1.965 Å (Yb). While the Ti–O–Ti bond angles remain constant at 141.2°, the O–Cu–O angle decreases from 96.5° to 95° resulting in a more regular square shape of the CuO_4 plaquettes, which should slightly influence the d level splitting of the Jahn-Teller active ion. The Cu–O–Ti bond angle is assumed to have the strongest influence on the magnetic exchange interaction between the Cu spin moments on the path Cu–O–Ti–O–Cu. For all samples an antiferromagnetically ordered state below 25 K was found. Since the Cu–O–Ti angle amounts to identical 109° for all

$ACu_3Ti_4O_{12}$ samples, this explains the very similar values and temperature/frequency depending behavior of ε' as found by dielectric spectroscopy measurements. The structural analysis of $La_{2/3}Cu_3Ti_4O_{12}$ single crystals yielded a good agreement with the results of the Rietveld analysis of powder-diffraction patterns.

Besides the compounds with a single element on the *A*-site, it was possible to synthesize poly-crystalline samples as solid solutions with mixed *A*-site occupation. A number of samples with La/Pr and Pr/Nd mixture of neighboring elements were synthesized as well as several mixtures of divalent Ca and trivalent lanthanides (Pr, Sm, Dy) with strongly deviating ionic radii and va-lences. From this and the corresponding structural investigations it can be concluded that due to the flexibility of the structure a rather large variation of the ionic size and valence of the A-cation can be compensated. As a consequence similar physical properties can be expected for all these titanates, since the electronic structure relevant for the physical properties is assumed to remain almost identical independent of the *A*-site occupation.

This interpretation was corroborated by detailed investigations of the dielectric properties (shown in detail in Ref. [Kro10]), the magnetic susceptibility, and by UV-Vis spectroscopy. By ESR it was furthermore shown that the antiferromagnetic ordering of the Cu spin moments is similarly occur-ring at 25 K for all samples and that the paramagnetic rare-earth metal ions are only very weakly coupled to the magnetic Cu sublattice [Dit11]. As already mentioned, dielectric spectroscopy yields a high permittivity for all samples and an almost identical temperature and frequency vari-ation of ε' [Seb10]. Furthermore, the shape of the absorption-edge and the band-gap position measured by UV-Vis spectroscopy are also very similar for all titanate samples.

DFT calculations of $CaCu_3Ti_4O_{12}$ using LSDA in the FPLO code are resembling the results given in literature. Additional calculations were performed for $SrCu_3Ti_4O_{12}$ and $La_{2/3}Cu_3Ti_4O_{12}$. The latter were previously not investigated using DFT and were found to possess very similar band structures and DOS compared to $CaCu_3Ti_4O_{12}$. An antiferromagnetic ordering of the Cu moments was found for all three compounds. In addition, the local spin moments are similar and amount to $S = 0.5$ for A = Ca and Sr, and to $S = 0.38$ for A = La, respectively, in agreement with the $3d^9$ configuration of Cu^{2+}.

For the solid-solution systems $Ln_yCu_3Ru_xTi_{4-x}O_{12}$ (Ln = La, Pr, Nd) a large number of phase-pure samples with different values of x were prepared applying a solid-state synthesis route. For very low Ru contents the *A*-site occupancy was set to $y = 2/3 + x$ ($x \leq 1/3$), while for $x \geq 1/3$ samples with completely occupied *A*-site could be prepared because of the conservation of charge neutrality by the trivalent lanthanide ions. For $x \geq 1/3$ it was assumed that the incorporated Ru ions can balance the gradually changing total *A*-site valence from +2 to +3 by variation of the Ru oxidation state. The unit-cell volume increases with rising Ru content according to Vegard's law. In detail, two effects have to be taken into account for the behavior of the axis length, namely the gradually increasing occupation of the *A*-site (for $x \leq 1/3$) and the replacement of Ti^{4+} by slightly larger Ru^{4+} ions. The latter effect results in smaller changes than the first. The increase of *a* for A = La ranges from 7.42 Å ($x = 0$) to 7.48 Å ($x = 4$). This relative change of approximately 0.06 Å is found for La, Pr, and Nd, while the absolute values of *a* are shifted by a constant amount according

to the different *A*-site cation size.

In detail, the structural changes mainly affect the *B*–O–*B* bond angle, which slightly decreases from 141° to 139.5° with *x*, and the *B*–O distances, which linearly increase with *x* from 1.96 Å by 0.03 Å due to the larger Ru ions compared to Ti. The Cu–O distances (1.965 Å) as well as the Cu–O–*B* angles (109.5°) remain constant for $x \geq 0.33$, while the changes observed below this substitution level are caused by the filling of the empty *A*-sites. The O–Cu–O angle, on the other hand, shows a significant correlation with the substitution level. From 96° for pure titanate the value drops drastically to 91° for $x = 0.1$ and increases linearly back to 96° for the pure ruthenates. This angle reflects the (distorted) square-planar geometry of the Cu-oxygen plaquettes. It can be assumed that a more symmetric plaquette results in more localized *d* electrons due to the reduced Jahn-Teller distortion and vice versa. Thus, changes in the electronic structure of $Ln_y Cu_3 Ru_x Ti_{4-x} O_{12}$ were expected and further investigated.

The oxygen stoichiometry of $La_y Cu_3 Ru_x Ti_{4-x} O_{12+\delta}$ was studied using thermogravimetry under reducing conditions. Only one reduction step was observed, i.e. Cu and Ru are reduced simultaneously. In addition, it was observed that the weight reduction step is shifted to higher temperature with increasing titanium content in agreement with the increased shielding effect of the incorporated Ti. Especially for lower Ru contents ($x \leq 1$) the measured weight loss was significantly higher than expected, which can be explained either by unreasonably high oxygen deficiencies in the range of 0.3 or by varying cationic valences. Therefore, the valences of Cu and Ru were determined using XANES. Tetravalent Ru was found for all substitution levels, while the Cu valence decreases linearly by approximately 0.1 per integer *x* from +2 for the titanates ($x = 0$) to +1.6 for the ruthenates ($x = 4$). This finding is quite surprising because it is to be expected that Ru changes its valence more easily than Cu, which should provide localized electrons due to the plaquette coordination. However, the valence variation may be ascribed to the mentioned deformations of the plaquettes and the changing *B*–O bond lengths. Using the experimentally found oxidation states in the interpretation of the thermogravimetric weight losses, oxygen contents very close to the nominal value of 12 were calculated. However, it should be mentioned that a possible occupation of Cu on parts of the vacant *A*-sites for $y \leq 0.33$ would also explain the observed deviations in this substitution range.

With respect to these surprising results, the dependence of the magnetic phase transitions on the Ru substitution level was studied in detail. From the magnetic susceptibility three different phases can be identified. Below $x = 0.33$ an antiferromangnetic ordering of the Cu spin moments below 25 K is observed, which is typically found for the titanates as described above. The transition temperature decreases linearly with *x*. Above $x = 0.33$ a spin-glass phase becomes evident, which is most significant around $x = 1$ and vanishes in the range $2.0 < x < 2.5$. For substitution levels $x \geq 2.5$ no low-temperature ordering is found. From the Curie-Weiss fits of the high temperature part (100 - 400 K) of the susceptibilities of $La_y Cu_3 Ru_x Ti_{4-x} O_{12}$ local spin moments were obtained, which are in general agreement with the XANES results. For low Ru contents the total moment decreases according to the reduced Cu oxidation state and beginning at $x = 2.5$, the Ru moment dominates the again increasing total magnetic moment. The negative Curie-Weiss temperatures amount to roughly -25 K for the titanates and increase slowly with increasing *x* until at

$x = 2.5$ this model cannot be applied anymore as reflected by the unreasonable value of roughly $\Theta_{CW} = -1000$ K for the pure ruthenate. It was also found that the susceptibilities of the Pr and Nd containing samples cannot simply be considered as sum of the $La_yCu_3Ru_xTi_{4-x}O_{12}$ data and the paramagnetic moment of the rare-earth metal ions as it was found for rare-earth substituted La_2RuO_5. Thus, a more complex correlation of the magnetic and electronic structures has to be assumed.

It was shown by ESR on Gd doped $La_{0.95}Gd_{0.05}Cu_3Ru_xTi_{4-x}O_{12}$ with $x \geq 1.0$, as well as specific heat and resistivity measurements that the $La_yCu_3Ru_xTi_{4-x}O_{12}$ samples with high Ru contents ($x \geq 2.5$) are metallic heavy-fermion compounds. The origin of the heavy-fermion state was further investigated using XANES measurements and DFT calculations. A metal to insulator transition was found by resistivity measurements. The metallic heavy-fermion phase above $x = 2.25$ transforms into a semiconducting spin-glass for lower substitution levels. This is due to the increasing delocalization of the Cu 3d electrons with increasing x, which is correlated to the observed decrease of oxidation state and local spin moment (from DFT: $S = 0.38$ for $x = 0$ and $S = 0$ for $x \geq 2$) of the Cu ions, as well as the distinct softening of the XANES structure at the Cu-K absorption edge for $x \approx 2.25$, while the shape of the Ru-K absorption edge remains unchanged. The changing Cu moment was also obtained from the entropy of the antiferromagnetic ordering transition in the specific heat. The DFT modelling shows an almost unchanged Ru pDOS, while the Cu pDOS at E_F becomes broader in energy with increasing x.

In conclusion, the complementary experimental methods used in this work provide a deeper insight in the characteristics of the rich and complex phase diagram of the $ACu_3B_4O_{12}$-type compounds. It was shown that the observed heavy-fermion behavior of the ruthenates is caused by itinerant Cu electrons, which are interacting with the localized Ru 4d electrons resulting in the Kondo-like increase of the fermion mass. This model is in contrast to the scenario proposed for $CaCu_3Ru_4O_{12}$ [Kob04], where the Ru electrons are considered itinerant and the Cu electrons are supposed to form the centers of the Kondo-lattice.

The close relationship between composition, crystal structure, and physical properties is a crucial parameter to be studied especially when phase transitions are occurring. By carefully chosen substitutions both the structure and physical properties like magnetic-ordering phenomena and electrical conductivity can be affected. It has to be mentioned, though, that additional parameters like oxygen stoichiometry and cation valence can also play an important role in the studied parameter relationships. Therefore, a generalized statement on the evolution of electronic, magnetic, and thermodynamic properties based on structural and physical property investigations is still not simply available due to the complex interplay of different factors strongly correlated with each other.

Besides the described results further interesting questions arose during the course of this thesis. For example, an unusual fragility of the spin-glass phase in Mn substituted La_2RuO_5 was observed, or the analysis of the structure and properties of $La_4Ru_2O_9$ obtained from the intermediate in the thermal reduction of La_2RuO_5 is planned, or further ESR studies on the heavy-fermion

state in $CaCu_3Ru_4O_{12}$ related compounds based on the presented results should be applied. Very interesting is also the prediction of Dagotto and Rice [Dag96] that a hole-doping of the spin-ladder could induce a superconduting phase, which in the case of La_2RuO_5 would emerge at a very high temperature of possibly $T_d = 161$ K. This could be promisingly tested by e.g. substituting the trivalent La by divalent Sr. These questions may be addressed in future works revealing the power of the fundamental correlation between structure and physical properties in solid-state chemistry and physics.

Concluding Summary

For this work a considerable number of pure and substituted (rare-earth elements, Ti, and Mn) La_2RuO_5 samples with an unconventional layered perovskite-related structure were synthesized by a new soft-chemistry approach. Besides the crystal structure investigated by x-ray and neutron diffraction as well as x-ray absorption spectroscopy, the magneto-structural phase transition was studied in detail by measurements of the magnetic susceptibility and specific heat. Below the transition temperature $T_d = 161$ K a rare spin-singlet ground-state was identified consisting of Ru^{4+} ($S = 1$) spin dimers, which can be imagined as the rungs of a ladder-like arrangement parallel to the crystallographic c-axis. In this low-temperature state a spin gap of approximately 48 meV opens as derived from the magnetic susceptibility. This was corroborated by modelling the entropy changes of the transition observed as peak in the specific heat using the intradimer exchange $J_0 = 23.5$ meV. Furthermore, it was found that rare-earth substitution merely influences the structure rather than the magnetic properties, while titanium suppresses both the structural and magnetic phase transition when almost half of the ruthenium becomes replaced. Manganese substitution leads to a second magnetic phase transition at lower temperatures than the dimerization. It was characterized as spin-glass state but the type of exchange between Mn^{4+} ($S = 3/2$) and Ru^{4+} ($S = 1$) driving this spin-glass state within the dimerized Ru matrix has still to be clarified.

Polycrystalline samples of a second group of ruthenates with a $2 \times 2 \times 2$ - perovskite superstructure ($ACu_3Ru_xTi_{4-x}O_{12}$) were also synthesized as solid-solution series with $A =$ La, Pr, Nd. The complex phase diagram depending on the Ru content was studied in detail. Pure titanates (known for their colossal dielectric permittivities) show an antiferromagnetically ordered ground-state below 25 K even remaining for small Ru doping. For $0.25 \leq x \leq 2.25$ a spin-glass phase was found, while above $x = 2.25$ a heavy-fermion phase with a behavior characterized by a disturbed Kondo-lattice was identified. Concomitant with this a metal to insulator was found at roughly $x = 2.25$ with decreasing Ru content. The combination of detailed XANES and thermogravimetric investigations revealed a constant Ru^{4+} valence while the Cu valence decreases linearly from +2 for the titanates to +1.6 for the ruthenates. In addition, ESR measurements and DFT calculations were performed allowing to conclude that the Cu $3d$ electrons become itinerant and interact Kondo-like with the localized Ru $4d$ electrons, resulting in the heavy-fermion state.

Bibliography

[Abr78] F. Abraham, J. Trehoux, D. Thomas, Mater. Res. Bull. **13**, 805 (1978)

[Abr80] F. Abraham, J. Trehoux, D. Thomas, J. Solid State Chem. **32**, 151 (1980)

[Agu08] R. Aguiar, *Synthesis, properties and applications of AB(O,N)$_3$ oxynitride perovskites*, Dissertation, Universität Augsburg (2008)

[Agu09] M. H. Aguirre, D. Logvinovich, L. Bocher, R. Robert, S. G. Ebbinghaus, A. Weidenkaff, Acta Materialia **57**, 108 (2009)

[Ali97] F. Ali, A. V. Chadwick, M. E. Smith, J. Mater. Chem. **7**(2), 285 (1997)

[All03] R. Allmann, *Röntgenpulverdiffraktometrie: Rechnergestützte Auswertung, Phasenanalyse und Strukturbestimmung*, Springer, Berlin, Heidelberg - New York (2003)

[And59] P. W. Anderson, Phys. Rev. **115**, 2 (1959)

[Ank98] A. L. Ankudinov, B. Ravel, J. J. Rehr, S. D. Conradson, Phys. Rev. B **39**, 125 (1998)

[Arc07] I. Arcon, A. Bencan, A. Kodre, M. Kosec, X-Ray Spec. **36**, 301 (2007)

[Auc97] O. Auciello, Integrated Ferroelectrics **15**, 211 (1997)

[Bea67] J. A. Bearden, A. F. Burr, Rev. Mod. Phys. **58**, 7565 (1967)

[Ben05] A. Benčan, M. Hrovat, J. Holc, G. Dražič, M. Kosec, J. Eur. Ceram. Soc. **25**, 943 (2005)

[Ben90] W. Bensch, H. W. Schmalle, A. Reller, Solid State Ionics **43**, 171 (1990)

[Bha00] A. S. Bhalla, R. Guo, R. Roy, Mater. Res. Innovat. **4**, 3 (2000)

[Bij11] S. Bijani, M. Gabas, G. Subias, J. Garcia, L. Sanchez, J. Morales, L. Martinez, J. R. Ramos-Barrado, J. Mater. Chem. **21**, 5368 (2011)

[Bin86] K. Binder, A. P. Young, Rev. Mod. Phys. **58**, 801 (1986)

[Bla09] B. Blau, K. N. Clausen, S. Gvasaliya, M. Janoschek, S. Janssen, L. Keller, B. Roessli, J. Schefer, P. Tregenna-Piggott, W. Wagner, O. Zaharko, Neutron News **20**, 5 (2009)

[Blu08] S. J. Blundell, T. Lancaster, P. J. Baker, W. Hayes, F. L. Pratt, T. Atake, D. S. Rana, S. K. Malik, Phys. Rev. B **77**, 094424 (2008)

[Boc74] B. Bochu, J. Chenavas, J. C. Joubert, M. Marezio, J. Solid State Chem. **11**, 88 (1974)

[Boc79] B. Bochu, M. N. Deschizeaux, J. C. Joubert, A. Collomb, J. Chenavas, M. Marezio, J. Solid State Chem. **29**, 29 (1979)

[Bor02] W. Borchardt-Ott, *Kristallographie*, Springer, Berlin - Heidelberg - New York (2002)

[Bor27] M. Born, R. Oppenheimer, Ann. d. Physik **84**, 30 (1927)

[Bou72] R. J. Bouchard, J. F. Weiher, J. Solid State Chem. **4**, 80 (1972)

[Bou03] P. Boullay, D. Mercurio, A. Bencan, A. Meden, G. Drazic, M. Kosec, J. Solid State Chem. **170**, 294 (2003)

[Bri01] F. Bridges, C. H. Booth, M. Anderson, G. H. Kwei, J. J. Neumeier, J. Snyder, J. Mitchell, J. S. Gardner, E. Brosha, Phys. Rev. B **63**, 214405 (2001)

[Bri45] G. W. Brindley, Phil. Mag. **36**, 347 (1945)

[Bri90] C. J. Brinker, G. W. Scherer, *Sol-Gel Science - The Physics and Chemistry of Sol-Gel Processing*, Academic Press, San Diego - London (1990)

[Bri83] L. H. Brixner, E. P. Moore, Acta Cryst. Sect. C **39**, 1316 (1983)

[Bro85] I. D. Brown, D. Altermatt, Acta Cryst. Sect. B **41**, 244 (1985)

[Bue10] N. Büttgen, H.-A. Krug von Nidda, W. Krätschmer, A. Günther, S. Widmann, S. Riegg, A. Krimmel, A. Loidl, J. Low Temp. Phys. **161**, 148 (2010)

[Bul78] L. N. Bulaevskii, A. I. Buzdin, D. I. Khomskii, Solid State Commun. **27**, 5 (1978)

[Cal11] C. de la Calle, J. Sánchez-Benítez, F. Barbanson, N. Nemes, M. T. Fernández-Díaz, J. A. Alonso, J. Appl. Phys. **109**, 123914 (2011)

[Cao01] G. Cao, S. McCall, Z. X. Zhou, C. S. Alexander, J. E. Crow, R.P. Guertin, C. H. Mielke, Phys. Rev. B **63**, 144427 (2001)

[Cao05] G. Cao, S. Chikara, X. N. Lin, E. Elhami, V. Durairaj, P. Schlottmann, Phys. Rev. B **71**, 035104 (2005)

[Car93] J. Rodriguez-Carvajal, Physica B **192**, 55 (1993)

[Cav81] R. J. Cava, R. S. Roth, J. Solid State Chem. **36**, 139 (1981)

[Cav04] R. J. Cava, Dalton Transact. **2004**, 2979 (2004)

[Cha08] E. Chalmin, F. Farges, G. E. Brown Jr, Contrib. Mineral Petrol **157**, 111 (2008)

[Cho94] J.-H. Choy, D.-K. Kim, S.-H. Hwang, G. Demazeau, Phys. Rev. B **50**, 16631 (1994)

[Cla11] J. H. Clark, M. S. Dyer, R. G. Palgrave, C. P. Ireland, J. R. Darwent, J. B. Claridge, M. J. Rosseinsky, J. Am. Chem. Soc. **133**, 1016 (2011)

[Cot78] A. Cotton, C. E. Rice, J. Solid State Chem. **25**, 137 (1978)

[Dag96] E. Dagotto, T. M. Rice, Science **271**, 618 (1996)

[Dag01] E. Dagotto, T. Hotta, A. Moreo, Physics Reports **344**, 1 (2001)

[Dag05] E. Dagotto, Science **309**, 257 (2005)

[Dam05] D. Damjanovic, J. Am. Ceram. Soc. **88**, 2663 (2005)

[Deg03] F. Deganello, A. Longo, A. Martorana, J. Solid State Chem. **175**, 289 (2003)

[DeJ90] L. J. de Jongh, *Magnetic Properties of Layered Transition Metal Compounds* edited by L. J. de Jongh, Kluwer Academic Publishers, Dordrecht, Boston, London (1990), pp. 1 - 51

[Des67] A. Deschanvres, B.Raveau, F. Tollemer, Bull. Soc. Chim. Fr., 4077 (1967)

[Dit11] A. Dittl, S. Krohns, J. Sebald, F. Schrettle, M Hemmida, H.-A. Krug von Nidda, S. Riegg, A. Reller, S. G. Ebbinghaus, A. Loidl, Eur. Phys. J. B **79**, 391 (2011)

[Dix80] S. Dixon, J. Marr, E. E. Lachowski, J. A. Gard, F. P. Glasser, Mater. Res. Bull. **15**, 1811 (1980)

[Don65] P. J. Donohue, L. Katz, R. Ward, Inorg. Chem. **4**, 306 (1965)

[Dou89] A. Douy, P. Odier, Mater. Res. Bull. **24**, 1119 (1989)

[Ebb97] S. Ebbinghaus, M. Fröba, A. Reller, J. Phys. Chem. B **101**, 9909 (1997)

[Ebb98] S. G. Ebbinghaus, *Struktur und physikalische Eigenschaften perowskit-verwandter Metalloxide vom Typ $La_{2-x}Sr_xCu_{1-y}Ru_yO_{4-\delta}$*, Dissertation, Universität Hamburg (1998)

[Ebb01] S. G. Ebbinghaus, Z. Hu, A. Reller, J. Solid State Chem. **156**, 194 (2001)

[Ebb02] S. G. Ebbinghaus, A. Weidenkaff, R. J. Cava, J. Solid State Chem. **167**, 289 (2002)

[Ebb04] S. G. Ebbinghaus, J. Solid State Chem. **177**, 817 (2004)

[Ebb05] S. G. Ebbinghaus, Acta Cryst. Sect. C **61**, i96 (2005)

[Ebb06] S. G. Ebbinghaus, *On the Structural and Phenomenological Diversity of Perovskites Containing 4d and 5d transition Metals*, Habilitationsschrift, Universität Augsburg (2006)

[Ebb07] S. G. Ebbinghaus, E.-W. Scheidt, T. Götzfried, Phys. Rev. B **75**, 144414 (2007)

[Ebb07a] S. G. Ebbinghaus, Prog. Solid State Chem. **35**, 421 (2007)

[Ebb09] S. G. Ebbinghaus, H.-P. Abicht, R. Dronskowski, T. Müller, A. Reller, A. Weidenkaff, Prog. Solid State Chem. **37**, 173 (2009)

[Ebb10] S. G. Ebbinghaus, S. Riegg, T. Götzfried, A. Reller, Eur. Phys. J. Special Topics **180**, 91 (2010)

[Ere76] M. V. Eremin, Fizika Tverdogo Tela (Physics of the Solid State) **18**, 2088 (1976)

[Eri90] O. Eriksson, M. S. S. Brooks, B. Johansson, Phys. Rev. B **41**, 7311 (1990)

[Esc03] H. Eschrig, *The Fundamentals of Density Functional Theory*, Edition am Gutenbergplatz, Leipzig (2003)

[Esc03a] H. Eschrig, K. Koepernick, I. Chaplygin, J. Solid State Chem. **176**, 482 (2003)

[Eye00] V. Eyert, U. Eckern, Physik in unserer Zeit **31**, 276 (2000)

[Eye06] V. Eyert, S. G. Ebbinghaus, T. Kopp, Phys. Rev. Lett. **96**, 256401 (2006)

[Eye07] V. Eyert, S. G. Ebbinghaus, Prog. Solid State Chem. **35**, 433 (2007)

[Fag05] S. B. Fagan, A. G. Souza Filho, A. P. Ayala, J. Mendes Filho, Phys. Rev. B **72**, 014106 (2005)

[Far05] F. Farges, Phys. Rev. B **71**, 155109 (2005)

[Fis97] W. E. Fischer, Physica B **234 - 236**, 1202 (1997)

[Fis00] P. Fischer, G. Frey, M. Koch, M. Könnecke, V. Pomjakushin, J. Schefer, R. Thut, N. Schlumpf, R. Bürge, U. Greuter, S. Bondt, E. Berruyer, Physica B **276 - 278**, 146 (2000)

[Fi97] Z. Fisk, J. L. Sarrao, Annu. Rev. Mater. Sci. **27**, 35 (1997)

[Gal02] D. J. Gallon, P. D. Battle, S. J. Blundell, J. C. Burley, A. I. Coldea, E. J. Cussen, M. J. Rosseinsky, C. Steer, Chem. Mater. **14**, 3976 (2002)

[Gar10] J. Garcia, G. Subias, V. Cuartero, J. Herrero-Martin, J. Synch. Rad. **17**, 386 (2010)

[Gla72] A. M. Glazer, Acta Cryst. Sect. B **28**, 3384 (1972)

[Goe05] T. Götzfried, A. Reller, S. G. Ebbinghaus, Inorg. Chem. **44**, 6550 (2005)

[Goe06] T. Götzfried, *Strukturelle, elektronische und magnetische Eigenschaften hexagonaler Perowskite der Platinmetalle*, Dissertation, Universität Augsburg (2006)

[Gol26] V. M. Goldschmidt, Skr. Nor. Vidensk. Akad. Mat. Naturvidensk. Kl. **2**, 1 (1926)

[Goo63] J. B. Goodenough, *Magnetism and the Chemical Bond*, John Wiley & Sons, New York - London (1963)

[Goo01] J. B. Goodenough (Editor), *Structure and Bonding, Localized to Itinerant Electronic Transition in Perovskite Oxides, General Considerations* pp. 1-16, Springer, Berlin - Heidelberg (2001)

[Gui66] M. Guillen, E. F. Bertaut, Bull. Soc. Fr. Ceram. **72**, 57 (1966)

[Guo90] D. Guo, T. Kennedy, S. Mazumdar, Phys. Rev. B **41**, 9592 (1990)

[Hah05] T. Hahn, *International Tables for Crystallography, Volume A, Space-Group Symmetry, 5th edition*, John Wiley & Sons, New York (2005)

[Hal83] F. D. M. Haldane, Phys. Lett. **93A**, 464 (1983)

[Has93] M. Hase, I. Terasaki, K. Uchinokura, Phys. Rev. Lett. **70**, 3651 (1993)

[HAS12] HASYLAB homepage, *http://hasylab.desy.de/facilities/doris_iii/beamlines /x1_roemo_ii/beamline/index_eng.html* (2012)

[Hay11] W. M. Haynes, *CRC Handbook of Chemistry and Physics: 92nd Edition* edited by W. M. Haynes, CRC Press, Boca Raton (2011)

[He02] L. He, J. B. Neaton, M. H. Cohen, D. Vanderbilt, C. C. Homes, Phys. Rev. B **65**, 214112 (2002)

[He03] L. He, J. B. Neaton, D. Vanderbilt, M. H. Cohen, Phys. Rev. B **67**, 012103 (2003)

[Hea07] R. Heary, D. Coffey, M. De Marco, P. Khalifah, S. Toorongian, M. Haka, Physica B **393**, 78 (2007)

[Hei01] M. Heinrich, H.-A. Krug von Nidda, V. Fritsch, A. Loidl, Phys. Rev. B **63**, 193103 (2001)

[Hei04] M. Heinrich, *Dynamische Suszeptibilität niedrigdimensionaler Übergangsmetalloxide*, Dissertation, Universität Augsburg (2004)

[Hel03] O. Hellwig, T. L. Kirk, J. B. Kortright, A. Berger, E. E. Fullerton, Nature Materials **2**, 112 (2003)

[Hem89] W. F. Hemminger, H. K. Camenga, *Methoden der thermischen Analyse*, Springer, Berlin (1989)

[Her97] W. Herrendorf, H. Bärnighausen, *HABITUS: Program for the optimization of the shape of single crystals for numerical absorption correction in the suite X-SHAPE*, Universität Karlsruhe (1997)

[Hil87]   R. J. Hill, H. D. J. Flack, J. Appl. Crystallogr. **20**, 356 (1987)

[Hof87]   R. Hoffmann, Angew. Chem. Int. Ed. Engl. **26**, 846 (1987)

[Hof88]   R. Hoffmann, *Solids and Surfaces: A Chemist's View on Bonding in Extended Structures*, VCH, New York (1988)

[Hoh64]   P. Hohenberg, W. Kohn, Phys. Rev. **136**, B864 (1964)

[Hom01]   C. C. Homes, T. Vogt, S. M. Shapiro, S. Wakimoto, A. P. Ramirez, Science **293**, 673 (2001)

[Hom03]   C. C. Homes, T. Vogt, S. M. Shapiro, S. Wakimoto, M. A. Subramanian, A. P. Ramirez, Phys. Rev. B **67**, 092106 (2003)

[Hon97]   S.-T. Hong, A. W. Sleight, J. Solid State Chem. **128**, 251 (1997)

[Hot02]   T. Hotta, E. Dagotto, Phys. Rev. Lett. **88**, 017201 (2001)

[Hsu03]   Y. Y. Hsu, B. N. Lin, J. F. Lee, L. Y. Jang, H. C. Ku, J. Low Temp. Phys. **131**, 343 (2003)

[Hub77]   G. Huber, K. Syassen, W. B. Holzapfel, Phys. Rev. B **15**, 5123 (1977)

[Ima98]   M. Imada, A. Fujimori, Y. Tokura, Rev. Mod. Phys. **70**, 1039 (1998)

[Iso96]   M. Isobe, Y. Ueda, J. Phys. Soc. Jpn. **65**, 1178 (1996)

[Iwa96]   H. Iwase, M. Isobe, Y. Ueda, H. Yasuoka, J. Phys. Soc. Jpn. **65**, 2397 (1996)

[Jah37]   H. A. Jahn, E. Teller, Proceedings of the Royal Society of London: Series A Mathematical and Physical Sciences **161**, 220 (1937)

[Kan59]   J. Kanamori, J. Phys. Chem. Solids **10**, 87 (1959)

[Kan10]   Ch. Kant, J. Deisenhofer, A. Günther, F. Schrettle, A. Loidl, M. Rotter, D. Johrendt, Phys. Rev. B **81**, 014529 (2010)

[Ken96]   B. J. Kennedy, T. Vogt, J. Solid State Chem. **126**, 261 (1996)

[Kha00]   P. Khalifah, Q. Huang, J. W. Lynn, R. W. Erwin, R. J. Cava, Mater. Res. Bull. **35**, 1 (2000)

[Kha02]   P. Khalifah, R. Osborn, Q. Huang, H. W. Zandbergen, R. Jin, Y. Liu, D. Mandrus, R. J. Cava, Science **297**, 2237 (2002)

[Kho05]   D. I. Khomskii, T. Mizokawa, Phys. Rev. Lett. **94**, 156402 (2005)

[Kik99]   J. Kikuchi, K. Motoya, T. Yamauchi, Y. Ueda, Phys. Rev. B **60**, 6731 (1999)

[Kim02] Y. J. Kim, S. Wakimoto, S. M. Shapiro, P. M. Gehring, A. P. Ramirez, Solid State Commun. **121**, 625 (2002)

[Kit91] C. Kittel, *Einführung in die Festkörperphysik, 9. Auflage*, Oldenbourg, München - Wien (1991)

[Kle01] K. V. Klementiev, J. Phys. D: Appl. Phys. **34**, 209 (2001)

[Kna04a] M. Knapp, C. Baehtz, H. Ehrenberg, H. Fuess, J. Synchrotron Rad. **11**, 328 (2004)

[Kna04b] M. Knapp, V. Joco, C. Baehtz, H. H. Brecht, A. Berghaeuser, H. Ehrenberg, H. von Seggern, H. Fuess, Nucl. Instr. and Meth. A **521**, 565 (2004)

[Kob04] W. Kobayashi, I. Terasaki, J. Takeya, I. Tsukada, Y. Ando, J. Phys. Soc. Japan **73**, 2373 (2004)

[Koc82] L. L. Kochergina, O. I. Kondratov, Yu. S. Shorikov, V. V. Fomichev, K. I. Petrov, Russ. J. of Inor. Chem. **27**, 1137 (1982)

[Koe97] K. Koepernick, B. Velicky, R. Hayn, H. Eschrig, Phys. Rev. B **55**, 5717 (1997)

[Koe99] K. Koepernick, H. Eschrig, Phys. Rev. B **59**, 1743 (1999)

[Koh65] W. Kohn, L. J. Sham, Phys. Rev. **140**, A1133 (1965)

[Kon88] D. C. Koningsberger, R. Prins, *X-Ray Absorption*, John Wiley and Sons, New York (1988)

[Kor50] J. Korringa, Physica **16**, 601 (1950)

[Kos89] N. Kosugi, H. Kondoh, H. Tajima, H. Kuroda, Chem. Phys. **135**, 149 (1989)

[Kri08] A. Krimmel, A. Günther, W. Kraetschmer, H. Dekinger, N. Büttgen, A. Loidl, S. G. Ebbinghaus, E.-W. Scheidt, W. Scherer, Phys. Rev. B **78**, 165126 (2008)

[Kri09] A. Krimmel, A. Günther, W. Kraetschmer, H. Dekinger, N. Büttgen, V. Eyert, A. Loidl, D. V. Sheptyakov, E.-W. Scheidt, W. Scherer, Phys. Rev. B **80**, 121101(R) (2009)

[Kro07] S. Krohns, P. Lunkenheimer, S. G. Ebbinghaus, A. Loidl, Appl. Phys. Lett. **91**, 022910 (2007)

[Kro09] S. Krohns, P. Lunkenheimer, C. Kant, A. V. Pronin, H. B. Brom, A. A. Nugroho, M. Diatoro, A. Loidl, Appl. Phys. Lett. **94**, 122903 (2009)

[Kro10] S. Krohns, *Grenzflächenpolarisationen in Übergangsmetalloxiden: Von der Grundlagenforschung zur Anwendung*, Dissertation, Universität Augsburg (2010)

[Kro84] A. Krolzig, G. Materlik, M. Swars, J. Zegenhagen, Nucl. Instr. and Meth. **219**, 430 (1984)

[Kub31] P. Kubelka, F. Munk, Z. techn. Phys. **12**, 531 (1931)

[Kug82] K. I. Kugel, D. I. Khomskii, Sov. Phys. Usp. **25**, 231 (1982)

[Kun10] C. A. Kuntscher, M. Klemm, S. Horn, M. Sing, R. Claessen, Eur. Phys. J. Special Topics **180**, 29 (2010)

[Lab80] M. Labeau, B. Bochu, J. C. Joubert, J. Chenavas, J. Solid State Chem. **33**, 257 (1980)

[Lan64] H. H. Landolt, R. Börnstein, *Zahlenwerte und Funktionen aus Physik, Chemie, Astronomie, Geophysik und Technik: Band IV, Technik, Teil 2b*, Springer, Berlin - Heidelberg (1964)

[Las03] J. C. Lashley, M. F. Hundley, A. Migliori, J. L. Sarrao, P. G. Paglusio, T. W. Darling, M. Jaime, J. C. Cooley, W. L. Hults, L. Morales, D. J. Thoma, J. L. Smith, J. Boerio-Goates, B. F. Woodfield, G. R. Stewart, R. A. Fisher, N. E. Phillips, Cryogenics **43**, 369 (2003)

[Lay09] S. Layek, V. K. Anand, Z. Hossain, J. Magnetism and Magn. Mat. **321**, 3447 (2009)

[Lee75] P. A. Lee, J. B. Pendry, Phys. Rev. B **11**, 4146 (1975)

[Lei01] C. Leighton, M. R. Fitzsimmons, P. Yashar, A. Hoffmann, J. Nogues, J. Dura, C. F. Majkrzak, I. K. Schuller, Phys. Rev. Lett. **86**, 4394 (2001)

[Li05] G.-L. Li, Z. Yin, M.-S. Zhang, Phys. Lett. A **344**, 238 (2005)

[Lic01] F. Lichtenberg, A. Herrnberger, K. Wiedenmann, J. Mannhart, Prog. Solid State Chem. **29**, 1 (2001)

[Loc07] S. Locmelis, C. Brüning, M. Binnewies, A. Börger, K. D. Becker, T. Homann, T. Bredow, J. Mater. Sci. **42**, 1965 (2007)

[Lon09] Y. W. Long, N. Hayashi, T. Saito, M. Azuma, S. Muranaka, Y. Shimakawa, Nature **458**, 160 (2009)

[Lue99] H. Lueken, *Magnetochemie*, Teubner, Stuttgart - Leipzig (1999)

[Lun99] P. Lunkenheimer, *Dielectric spectroscopy of glassy dynamics*, Habilitationsschrift, Universität Augsburg (1999)

[Lun10] P. Lunkenheimer, S. Krohns, S. Riegg, S. G. Ebbinghaus, A. Reller, A. Loidl, Eur. Phys. J. Special Topics **180**, 61 (2010)

[Mae94] Y. Maeno, H. Hashimoto, K. Yoshida, S. Nishizaki, T. Fujita, J. G. Bednorz, F. Lichtenberg, Nature **372**, 532 (1994)

[Mal94] P. Malet, M. J. Capitan, M. A. Centeno, J. A. Odriozola, I. Carrizosa, J. Chem. Soc. Faraday Trans. **90**(18), 2783 (1994)

[Mal79] H. Maletta, W. Felsch, Phys. Rev. B **20**, 1245 (1979)

[Mal05] S. K. Malik, D. C. Kundaliya, R. D. Kale, Solid State Commun. **135**, 166 (2005)

[Man98] S. S. Manoharan, H. L. Ju, K. M. Krishnan, J. Appl. Phys. **83**, 7183 (1998)

[Mas07] W. Massa, *Kristallstrukturbestimmung*, Teubner, Wiesbaden (2007)

[Mat06] M. Matos, L. Walmsley, J. Phys.: Condens. Matter **18**, 1793 (2006)

[Mat96] M. Matsuda, K. Katsumata, H. Eisaki, N. Motoyama, S. Uchida, S. M. Shapiro, G. Shirane, Phys. Rev. B **54**, 12199 (1996)

[Men06] C. Mennerich, H.-H. Klauss, M. Broekelmann, F. J. Litterst, C. Golze, R. Klingeler, V. Kataev, B. Büchner, S.-N. Grossjohann, W. Brenig, M. Goiran, H. Rakoto, J.-M. Broto, O. Kataeva, D. J. Price, Phys. Rev. B **73**, 174415 (2006)

[Moc03] C. Mocuta, A. Barbier, S. Lafaye, P. Bayle-Guillemaud, M. Panabiere, Phys. Rev. B **68**, 014416 (2003)

[Moo08] S. J. Moon, W. S. Choi, S. J. Kim, Y. S. Lee, P. G. Khalifah, D. Mandrus, T. W. Noh, Phys. Rev. Lett. **100**, 116404 (2008)

[Mor96] Y. Moritomo, A. Asamitsu, H. Kuwahara, Y. Tokura, Nature **380**, 141 (1996)

[Mot70] K. Motida, S. Miyahara, J. Phys. Soc. Jpn. **28**, 1188 (1970)

[Mot49] N. F. Mott, Proc. Phys. Soc. London Sect. A **62**, 416 (1949)

[Mul86] J. Muller, A. Haouzi, C. Laviron, M. Labeau, J. C. Joubert, Mater. Res. Bull. **21**, 1131 (1986)

[Mum68] W. G. Mumme, A. D. Wadsley, Acta Cryst. Sect. B **24**, 1327 (1968)

[Myd93] J. A. Mydosh, *Spin Glasses: An Experimental Introduction*, Taylor & Francis, London, Washington D.C. (1993)

[Nin08] T. Ning, C. Chen, Y. Zhou, H. Lu, D. Zhang, H. Ming, G. Yang, Appl. Phys. A: Mater. Sci. and Proc. **94**, 567 (2008)

[Och13] M. Ochi, I. Yamada, K. Ohgushi, Y. Kusano, M. Mizumaki, R. Takahashi, S. Yagi, N. Nishiyama, T. Inoue, T. Irifune, Inorg. Chem. **52**, 3985 (2013)

[Odo06] B. Odom, D. Hanneke, B. D'Urso, G. Gabrielse, Phys. Rev. Lett. **97**, 030801 (2006)

[Ohn10] T. Ohnishi, M. Naito, S. Mizusaki, Y. Nagata, Y. Noro, J. Electronic Materials **40**, 915 (2010)

[Ono96] M. Onoda, N. Nishiguchi, J. Solid State Chem. **127**, 359 (1996)

[Opa99] I. Opahle, K. Koepernick, H. Eschrig, Phys. Rev. B **60**, 14035 (1999)

[Osw85] H. R. Oswald, A. Reller, Thermochim. Acta **95**, 311 (1985)

[Osw88] H. R. Oswald, A. Reller, J. Therm. Analysis **33**, 67 (1988)

[Osw93] H. R. Oswald, S. Felder-Casagrande, A. Reller, Solid State Ionics **63 - 65**, 565 (1993)

[Pan91] S. K. Pandey, A. R. Chetal, P. R. Sarode, Physica B **172**, 324 (1991)

[Pec67] M. P. Pechini, US Patent 3,330,697 (1967)

[Pen32] W. G. Penney, R. Schlapp, Phys. Rev. **41**, 194 (1932)

[Per05] J. P. Perdew, A. Ruzsinszki, J. Tao, V. N. Staroverov, G. E. Scuseria, G. I. Csonka, J. Chem. Phys. **123**, 062201 (2005)

[Pet03] M. A. Petrova, A. S. Novikova, R. G. Grebenshchikov, Inorg. Mat. **39**, 509 (2003)

[Pic97] W. E. Pickett, Phys. Rev. Lett. **79**, 1746 (1997)

[Pom13] V. Pomjakushin, D Sheptyakov, *HRPT - High resolution powder diffractometer for thermal neutrons, Source: http://sinq.web.psi.ch/sinq/instr/hrpt/index.html*, PSI-Villigen (2013)

[Puc02] K. Pucher, J. Hemberger, F. Mayr, V. Fritsch, A. Loidl, E.-W. Scheidt, S. Klimm, R. Horny, S. Horn, S. G. Ebbinghaus, A. Reller, R. J. Cava, Phys. Rev. B **65**, 104523 (2002)

[Pyt74] E. Pytte, Phys. Rev. B **10**, 4637 (1974)

[Ram94] A. P. Ramirez, Ann. Rev. Mater. Sci. **24**, 453 (1994)

[Ram04] A. P. Ramirez, G. Lawes, D. Li, M. A. Subramanian, Solid State Commun. **131**, 251 (2004)

[Reh00] J. J. Rehr, R. C. Albers, Rev. Mod. Phys. **72**, 621 (2000)

[Res97] T. Ressler, J. Phys. IV (France) **7**, C2-269 (1997)

[Res98] T. Ressler, J. Synch. Rad. **5**, 118 (1998)

[Rie11] S. Riegg, U. Sazama, M. Fröba, A. Reller, S. G. Ebbinghaus, Phys. Rev. B **84**, 014403 (2011)

[Rie12a] S. Riegg, A. Reller, S. G. Ebbinghaus, J. Solid State Chem. **188**, 17 (2012)

[Rie12b] S. Riegg, A. Günther, H.-A. Krug von Nidda, A. Loidl, M. V. Eremin, A. Reller, S. G. Ebbinghaus, Phys. Rev. B **86**, 115125 (2012)

[Rie12c] S. Riegg, A. Günther, H.-A. Krug von Nidda, M. V. Eremin, A. Reller, A. Loidl, S. G. Ebbinghaus, Eur. Phys. J. B **85**, 413 (2012)

[Rie12d] S. Riegg, T. Müller, S. G. Ebbinghaus, Solid State Sci. **20**, 97 (2013)

[Rie13a] S. Riegg, S. Widmann, A. Günther, H.-A. Krug von Nidda, A. Reller, A. Loidl, S. G. Ebbinghaus, J. Phys.: Condens. Matter **25**, 126002 (2013)

[Rie13b] S. Riegg, A. Loidl, A. Reller, S. G. Ebbinghaus, Mater. Res. Bull. **48**, 4583 (2013)

[Rie13c] S. Riegg, A. Loidl, F. J. Garcia Garcia, A. Reller, S. G. Ebbinghaus, Phys. Rev. B, submitted (2013)

[Rie13d] S. Riegg, A. Wintermeier, H.-A. Krug von Nidda, S. Widmann, A. Günther, A. Reller, S. G. Ebbinghaus, A. Loidl, Phys. Rev. B, submitted (2013)

[Rie67] H. M. Rietveld, Acta Cryst. **22**, 151 (1967)

[Rie69] H. M. Rietveld, J. Appl. Crystallogr. **2**, 65 (1969)

[Rij99] J. T. Rijssenbeek, R. Jin, Yu. Zadorozhny, Y. Liu, B. Batlogg, R. J. Cava, Phys. Rev. B **59**, 4561 (1999)

[Riv11] B. Rivas-Murias, H. D. Zhou, J. Rivas, F. Rivadulla, Phys. Rev. B **83**, 165131 (2011)

[Rud57] S. N. Ruddlesden, P. Popper, Acta Cryst. **10**, 538 (1957)

[Rud58] S. N. Ruddlesden, P. Popper, Acta Cryst. **11**, 54 (1958)

[Rus58] G. S. Rushbrooke, P. J. Wood, Mol. Phys. **1**, 257 (1958)

[Sam10] E. C. Samulon, *Magnetic Phases of the Frustrated Spin Dimer Compound $Ba_3Mn_2O_8$*, Dissertation, Stanford University (2010)

[Sam11] E. C. Samulon, M. C. Shapiro, I. R. Fisher, Phys. Rev. B **84**, 054417 (2011)

[Sch12] B. Schmidt, *Metall-Isolator Übergang in $LaCu_3Ru_xTi_{4-x}O_{12}$ - Probenpräparation und paramagnetische Resonanz*, Bachelor-thesis, Universität Augsburg (2011)

[Sch04] B. Schüpp, K. Dörr, K. Ruck, K. Nenkov, K.-H. Müller, G. Krabbes, Solid State Sci. **7**, 17 (2004)

[Sch90] F. Schwabl, *Quantenmechanik*, Springer, Berlin - New York (1990)

[Sea92] V. F. Sears, Neutron News **3**, 29 (1992)

[Seb10] J. Sebald, S. Krohns, P. Lunkenheimer, S. G. Ebbinghaus, S. Riegg, A. Reller, A. Loidl, Solid State Commun. **150**, 857 (2010)

[Sha76] R. D. Shannon, Acta Cryst. Sect. A **32**, 751 (1976)

[Sha07] S. F. Shao, J. L. Zhang, P. Zheng, C. L. Wang, J. C. Li, M. L. Zhao, Appl. Phys. Lett. **91**, 042905 (2007)

[She97a] G. M. Sheldrick, *XPREP, Program for single crystal intensity data treatment and analysis*, Universität Göttingen (1997)

[She97b] G. M. Sheldrick, *SHELXS-97 and SHELXL-97, Program suite for the solution and refinement of crystal structures*, Universität Göttingen (1997)

[She08] G. M. Sheldrick, Acta Cryst. Sect. A **64**, 112 (2008)

[Shi07] H. Shiraki, T. Saito, T. Yamada, M. Tsujimoto, M. Azuma, H. Kurata, S. Isoda, M. Takano, Y. Shimakawa, Phys. Rev. B **76**, 140403(R) (2007)

[Sin08] R. P. Singh, C. V. Tomy, J. Phys.: Condens. Matter **20**, 235209 (2008)

[Soa12] I. B. P. Soares, L. B. Carvalho, J. A. H. Coaquira, G. A. Cabrera-Pasca, A. W. Carbonari, S. K. Malik, J. Appl. Phys. **112**, 063915 (2012)

[Spe09] A. L. Spek, Acta Cryst. Sect. D **65**, 148 (2009)

[Spi05] L. Spiess, R. Schwarzer, H. Behnken, G. Teichert, *Moderne Röntgenbeugung: Röntgendiffraktometrie für Materialwissenschaftler, Physiker und Chemiker*, Teubner, Wiesbaden (2005)

[Sub00] M. A. Subramanian, D. Li, N. Duan, B. A. Reisner, A. W. Sleight, J. Solid State Chem. **151**, 323 (2000)

[Sub02] M. A. Subramanian, A. W. Sleight, Solid State Sci. **4**, 374 (2002)

[Tad02] M. Tada, K. Tomita, V. Petrykin, M. Kakihana, Solid State Ionics **151**, 293 (2002)

[Tam95] N. Tamari, T. Tanaka, K. Tanaka, I. Kondoh, M. Kawahara, M. Tokita, J. Ceramic Soc. Japan **103**, 740 (1995)

[Tar03] A. Tari, *The specific heat of matter at low temperatures*, Imperial College Press, London (2003)

[Tem09] W. M. Temmermann, L. Petit, A. Svane, Z. Szotek, M. Lüders, P. Strange, J. B. Staunton, I. D. Hughes, B. L. Gyorffy, *Handbook on the Physics and Chemistry of Rare Earths, Volume 39: The Dual, Localized or Band-Like Character of the 4f-States*, Elsevier, North-Holland (2009)

[Teo81] Boon-Keng Teo, J. Am. Chem. Soc. **103**, 3990 (1981)

[Ter10] I. Terasaki, M. Iwakawa, T. Nakano, A. Tsukuda, W. Kobayashi, Dalton Trans. **39**, 1005 (2010)

[Tho80] J. L. Tholence, Solid State Commun. **35**, 113 (1980)

[Tho87] P. Thompson, D. E. Cox, J. B. Hastings, J. Appl. Cryst. **20**, 79 (1987)

[Tra06] T. T. Tran, K. Takubo, T. Mikozawa, W. Kobayashi, I. Terasaki, Phys. Rev. B **73**, 193105 (2006)

[Tro88] I. O. Troyanchuk, L. A. Bashkirov, A. N. Pirogov, L. V. Balyko, Yu. G. Zonov, Inorg. Mater. **24**, 704 (1988)

[Tsu09] I. Tsukuda, R. Kammuri, T. Kida, S. Yoshii, T. Takeuchi, M. Hagiwara, M. Iwakawa, W. Kobayashi, I. Terasaki, Phys. Rev. B **79**, 054403 (2009)

[Uch02] M. Uchida, H. Tanaka, H. Mitamura, F. Ishikawa, T. Goto, Phys. Rev. B **66**, 054429 (2002)

[Uch99] Y. Uchiyama, Y. Sasago, I. Tsukada, K. Uchinokura, A. Zheludev, T. Hayashi, N. Miura, P. Boni, Phys. Rev. Lett. **83**, 632 (1999)

[Uru95] A. Urushibara, Y. Moritomo, T. Arima, A. Asamitsu, G. Kido, Y. Tokura, Phys. Rev. B **51**, 14103 (1995)

[Vas04] A. N. Vasiliev, O. L. Ignatchik, M. Isobe, Y. Ueda, Phys. Rev. B **70**, 132415 (2004)

[Vas05] A. N. Vasil'ev, M. M. Markina, E. A. Popova, Low Temp. Phys. **31**, 203 (2005)

[Vas07] A. N. Vasil'ev, O. S. Volkova, Low Temp. Phys. **33**, 895 (2007)

[Veg21] L. Vegard, Z. Phys. **5**, 17 (1921)

[Vic48] J. A. Victoreen, J. Appl. Phys. **19**, 855 (1948)

[Wan05] X. Wang, J. A. Rodriguez, J. C. Hanson, D. Gamarra, A. Martinez-Arias, M. Fernandez-Garcia, J. Phys. Chem. B **109**, 19595 (2005)

[Wat07] E. B. Watson, E. F. Baxter, Earth and Planetary Science Letters **253**, 307 (2007)

[Weh01] R. Weht, W. E. Pickett, Phys. Rev. B **65**, 014415 (2001)

[Wei02] F. Weigand, S. Gold, A. Schmid, J. Geissler, E. Goering, K. Dörr, G. Krabbes, K. Ruck, Appl. Phys. Lett. **81**, 2035 (2002)

[Wes99] A. R. West, *Basic Solid State Chemistry (Second Edition)*, John Wiley & Sons, Chichester (1999)

[Wha81] M.-H.Whangbo, J. Chem. Phys. **75**, 4983 (1981)

[Wid12] S. Widmann, *Metall-Isolator Übergang in Titan-dotiertem LaCu$_3$Ru$_4$O$_{12}$*, Diplomarbeit, Universität Augsburg (2012)

[Wil88] K.-Th. Wilke, J. Bohm, *Kristallzüchtung*, Verlag Harri Deutsch, Thun - Frankfurt/Main (1988)

[Woo97a] P. M. Woodward, Acta Cryst. Sect. B **53**, 32 (1997)

[Woo97b] P. M. Woodward, Acta Cryst. Sect. B **53**, 44 (1997)

[Wu96] Z. Wu, M. Benfatto, C. R. Natoli, Phys. Rev. B **54**, 13409 (1996)

[Wu06] H. Wu, Z. Hu, T. Burnus, J. D. Denlinger, P. G. Khalifah, D. G. Mandrus, L.-Y. Jang, H. H. Hsieh, A. Tanaka, K. S. Liang, J. W. Allen, R. J. Cava, D. I. Khomskii, L. H. Tjeng, Phys. Rev. Lett. **96**, 256402 (2006)

[Wu08] D. Wu, P. G. Khalifah, D. G. Mandrus, N. L. Wang, J. Phys.: Condens. Matter **20**, 325204 (2008)

[Wur96] K. Wurr, A. Reller, J. Therm. Analysis **47**, 339 (1996)

[Yam94] T. Yamamoto, R. Kanno, Y. Takeda, O. Yamamoto, Y. Kawamoto, M. Takano, J. Solid State Chem. **109**, 372 (1994)

[Yam05] T. Yamamoto, T. Mizoguchi, I. Takana, Phys. Rev. B **71**, 245113 (2005)

[Yam08] I. Yamada, K. Takata, N. Hayashi, S. Shinohara, M. Azuma, S. Mori, S. Muranaka, Y. Shimakawa, M. Takano, Angew. Chem. Int. Ed. **47**, 7032 (2008)

[Yok95] T. Yokoo, T. Sakaguchi, K. Kakurai, J. Akimitsu, J. Phys. Soc. Jpn. **64**, 3651 (1995)

[Zak08] D. Zakharov, H.-A. Krug von Nidda, M. Eremin, J. Deisenhofer, R. Eremina, A. Loidl, *NATO Science for Peace and Security Series B: Physics and Biophysics, Quantum-Magnetism* edited by B. Barbara *et al.*, pp. 193 (2008)

[Zha07] X.-Y. Zhang, Y. Chen, Z.-Y. Li, C. Vittoria, V. G. Harris, J. Phys.: Condens. Matter **19**, 266211 (2007)

[Zha08] X.-Y. Zhang, Y. Chen, Z.-Y. Li, J. Appl. Phys. **103**, 07B303 (2008)

[Zhe10] J.-C. Zheng, A. I. Frenkel, L. Wu, J. Hanson, W. Ku, E. S. Božin, S. J. L. Billinge, Y. Zhu, Phys. Rev. B **81**, 144203 (2010)

A. Appendix

A.1. List of Used Chemicals

Table A.1.: Used chemicals for the sample synthesis.

Sum formula	Producer	Purity
Ruthenium		
Ru (metal powder)	Merck	$\geq$99.9%
RuO_2	Chempur	99.9%
$RuCl_3 \cdot n\,H_2O$	Merck	Ru-content 35%-40%
Ru-acetyleacetonate (Ru-AcAc)	Chempur	Ru-content 22.4% - 22.9%
Ru-nitrosyleacetate (Ru-NOAc)	Aldrich	99.9%
Other		
Ti (metal powder)	Aldrich	99.7%
TiO_2	Aldrich	$\geq$99%
CuO	Helm AG	99.5%
$Mn(NO_3).4\,H_2O$	Merck	99.98%
$CaCO_3$	Aldrich	$\geq$99%
$SrCO_3$	Aldrich	99.9+%
$BaCl_2 \cdot 2\,H_2O$	Aldrich	99+%

Table A.2.: Used chemicals for the sample synthesis.

Sum formula	Producer	Purity
Rare earths		
Y_2O_3	Aldrich	99.99%
La_2O_3	Chempur	99.9%
$La(NO_3)_3 \cdot 6H_2O$	Fluka	99.9%
$La(NO_3)_3 \cdot 6H_2O$	Chempur	99.9%
CeO_2	Chempur	99.9%
Pr_2O_3	MaTecK	99.9%
$Pr(NO_3)_3 \cdot 5.7H_2O$	Chempur	99.9%
Nd_2O_3	Aldrich	99.9%
$Nd(NO_3)_3 \cdot 5.8H_2O$	Aldrich	99.9%
Sm_2O_3	Aldrich	99.99%
$Sm(NO_3)_3 \cdot 5.4H_2O$	Merck	p.a.
Eu_2O_3	MaTecK	99.9%
Gd_2O_3	Aldrich	99.9%
$Gd(NO_3)_3 \cdot 6H_2O$	Aldrich	99.9%
Tb_2O_3	MaTecK	99.9%
Dy_2O_3	Fluka	99.9%
$Dy(NO_3)_3 \cdot 5.34H_2O$	Alfa Aesar	99.9%
Ho_2O_3	Merck	LAB
Er_2O_3	Aldrich	99.9%
Tm_2O_3	Aldrich	99.9%
Yb_2O_3	Aldrich	99.9%

A.2. La$_2$RuO$_5$ Single-Crystal Data

Table A.3.: La$_2$RuO$_5$ single-crystal refinement parameters.

Sum formula	La$_2$RuO$_5$
Molar mass (g/mol)	458.885
Crystal system	monoclinic
Space group	P2$_1$/c (No. 14)
Diffractometer	STOE IPDS 2T
Radiation:	Mo-K$_\alpha$: λ = 0.71073 Å
a (Å)	9.1881(12)
b (Å)	5.8311(7)
c (Å)	7.9658(9)
β (deg)	100.793(10)
Volume (Å^3)	419.23
Formula units per cell	4
Temperature (K)	293(2)
Calculated density (g/cm^3)	7.27
Crystal size (mm^3)	0.05 $\times$ 0.05 $\times$ 0.02
Absorption coefficient (mm^{-1})	23.47
F(000)	792.0
2θ range ($^\circ$)	8.72 $\leq$ 2θ $\leq$ 79.98
Range in *hkl*	$\pm 16, \pm 9, \pm 11$
Total no. of reflections	3888
No. of rejected reflections	159
Independent reflections	1428 (R_{int} = 0.0566)
Reflections with $I > 4\sigma(I)$	903 (R_σ = 0.0601)
Data/parameters	1428/74
Absorption correction	Numerical
Goodness-of-fit (F^2)	0.939
Final R indices ($I > 4\sigma(I)$)	R_1 = 0.0386, wR_2 = 0.0883
R indices (all data)	R_1 = 0.0730
Largest differ. peak/deepest hole ($e\cdot$ Å^3)	2.11/-2.31

Table A.4.: Atomic coordinates and isotropic equivalent displacement parameters U_{eq} in Å^2 for the La$_2$RuO$_5$ single crystal. U_{eq} is defined as one third of the trace of the orthogonalized U_{ij} tensor.

Atom	x	y	z	U_{eq}
La1	0.1689(1)	0.2504(1)	0.0387(1)	0.0077(1)
La2	0.5519(1)	0.2628(1)	0.3794(1)	0.0072(1)
Ru	0.8504(1)	0.2540(1)	0.2114(1)	0.0051(1)
O1	0.8544(9)	0.3325(12)	0.4623(6)	0.0090(11)
O2	0.6880(9)	0.4607(12)	0.1300(7)	0.0101(12)
O3	0.7231(10)	-0.0111(12)	0.2213(8)	0.0127(15)
O4	1.0211(11)	0.0441(14)	0.2933(8)	0.0155(15)
O5	0.4237(9)	0.3328(12)	0.6030(7)	0.0093(11)

Table A.5.: Anisotropic displacement factors U_{ij} in Å^2 for the La$_2$RuO$_5$ single crystal .

Atom	U_{11}	U_{22}	U_{33}
La1	0.0081(2)	0.0066(2)	0.0083(2)
La2	0.0098(2)	0.0062(2)	0.0059(2)
Ru	0.0059(3)	0.0045(2)	0.0052(2)
O1	0.0110(37)	0.0095(29)	0.0073(25)
O2	0.0094(38)	0.0098(31)	0.0102(27)
O3	0.0215(51)	0.0098(32)	0.0086(30)
O4	0.0189(44)	0.0134(37)	0.0123(30)
O5	0.0116(35)	0.0122(30)	0.0041(25)
Atom	U_{23}	U_{13}	U_{12}
La1	0.0005(1)	0.0011(1)	0.0002(2)
La2	-0.0014(2)	0.0023(1)	-0.0003(2)
Ru	0.0004(2)	0.0015(1)	-0.0002(3)
O1	-0.0004(17)	0.0035(17)	0.0046(24)
O2	-0.0031(17)	-0.0008(18)	-0.0046(24)
O3	-0.0014(18)	0.0070(23)	0.0003(28)
O4	-0.0021(20)	-0.0004(21)	0.0089(31)
O5	0.0025(16)	0.0013(17)	0.0025(24)

Table A.6.: Selected bond lengths and interatomic distances for the La$_2$RuO$_5$ single crystal.

Bond	d(Å)	Bond	d(Å)
Ru–O1	2.044(5)	La1–La1 (x2)	3.9829(6)
Ru–O1	2.055(5)	La1–La1	4.2149(6)
Ru–O2	1.933(8)	La1–La1	4.2219(6)
Ru–O3	1.949(8)	La1–La2	3.8030(6)
Ru–O4	2.001(8)	La1–La2	3.9123(6)
Ru–O4	2.067(8)	La1–La2	3.9596(6)
		La1–La2	4.0224(6)
Ru–La1	3.4588(8)	La2–La1	3.8030(6)
Ru–La1	3.4957(9)	La2–La1	3.9123(6)
Ru–La1	3.5359(9)	La2–La1	3.9596(6)
Ru–La1	3.5361(9)	La2–La1	4.0224(6)
Ru–La1	3.5388(9)	La2–La2 (x2)	3.5950(6)
Ru–La1	3.5703(9)	La2–La2	3.5973(6)
Ru–La2	3.2690(8)	La2–La2	3.8321(6)
Ru–La2	3.4364(8)	La2–La2 (x2)	3.9857(6)

A.3. La$_{2/3}$Cu$_3$Ti$_4$O$_{12}$ and SrCu$_3$Ru$_4$O$_{12}$ Single-Crystal Data

Table A.7.: La$_{2/3}$Cu$_3$Ti$_4$O$_{12}$ single-crystal refinement parameters.

Sum formula	La$_{2/3}$Cu$_3$Ti$_4$O$_{12}$
Molar mass (g/mol)	667.29
Crystal system	cubic
Space group	Im$\bar{3}$ (No. 204)
Diffractometer	Syntex P2$_1$
Radiation:	Mo-K$_\alpha$: $\lambda = 0.71073$ Å
a (Å)	7.4361(13)
Volume (Å^3)	411.18
Formula units per cell	2
Temperature (K)	293(2)
Calculated density (g/cm^3)	5.390
Crystal size (mm^3) pyramidal	0.25(top : 0.19) $\times$ 0.2(top : 0.125) $\times$ 0.09
Absorption coefficient (mm^{-1})	7.38
F(000)	309.2
2θ range ($^\circ$)	$5 \leq 2\theta \leq 89.76$
Range in hkl	$\pm 14, \pm 14, \pm 14$
Total no. of reflections	4048
No. of rejected reflections	0
Independent reflections	332 ($R_{int} = 0.0605$)
Reflections with $I > 4\sigma(I)$	320 ($R_\sigma = 0.0187$)
Data/parameters	332/16
Absorption correction	Crystal shape and PLATON
Goodness-of-fit (F^2)	1.287
Final R indices ($I > 4\sigma(I)$)	$R_1 = 0.0235$, $wR_2 = 0.0618$
R indices (all data)	$R_1 = 0.0243$
Largest differ. peak/deepest hole ($e\cdot$ Å^3)	1.65/-0.94

Table A.8.: SrCu$_3$Ru$_4$O$_{12}$ single-crystal refinement parameters.

Sum formula	SrCu$_3$Ru$_4$O$_{12}$
Molar mass (g/mol)	874.52
Crystal system	cubic
Space group	Im$\bar{3}$ (No. 204)
Diffractometer	STOE IPDS 2T
Radiation:	Mo-K$_\alpha$: λ = 0.71073 Å
a (Å)	7.4418(9)
Volume (Å^3)	412.13
Formula units per cell	2
Temperature (K)	293(2)
Calculated density (g/cm^3)	7.047
Crystal size (mm^3)	$0.08 \times 0.08 \times 0.08$
Absorption coefficient (mm^{-1})	21.20
F(000)	794.0
2θ range ($^\circ$)	$8.72 \leq 2\theta \leq 99.11$
Range in *hkl*	$-14 < h < 6, -4 < k < 15, -2 < l < 15$
Total no. of reflections	1452
No. of rejected reflections	238
Independent reflections	399 ($R_{int} = 0.0267$)
Reflections with $I > 4\sigma(I)$	309 ($R_\sigma = 0.0174$)
Data/parameters	399/13
Absorption correction	Numerical
Goodness-of-fit (F^2)	1.225
Final R indices ($I > 4\sigma(I)$)	$R_1 = 0.0535, wR_2 = 0.1215$
R indices (all data)	$R_1 = 0.0682$
Largest differ. peak/deepest hole ($e\cdot$ Å^3)	2.60/-6.95

Table A.9.: Atomic coordinates and isotropic equivalent displacement parameters U_{eq} in Å^2 for the $La_{2/3}Cu_3Ti_4O_{12}$ and $SrCu_3Ru_4O_{12}$ single crystals. U_{eq} is defined as one third of the trace of the orthogonalized U_{ij} tensor.

$La_{2/3}Cu_3Ti_4O_{12}$				
Atom	x	y	z	U_{eq}
La	0	0	0	0.0033(1)
Cu	0.5	0	0	0.0043(1)
Ti	0.25	0.25	0.25	0.0058(1)
O	0.1807(1)	0.3036(1)	0	0.0048(1)
$SrCu_3Ru_4O_{12}$				
Atom	x	y	z	U_{eq}
Sr	0	0	0	0.0030(2)
Cu	0.5	0	0	0.0046(2)
Ru	0.25	0.25	0.25	0.0022(2)
O	0.1755(1)	0.3088(1)	0	0.0044(4)

Table A.10.: Anisotropic displacement factors U_{ij} in Å^2 for the $La_{2/3}Cu_3Ti_4O_{12}$ and $SrCu_3Ru_4O_{12}$ single crystals.

$La_{2/3}Cu_3Ti_4O_{12}$						
Atom	U_{11}	U_{22}	U_{33}	U_{23}	U_{13}	U_{12}
La	0.0033(1)	0.0033(1)	0.0033(1)	0	0	0
Cu	0.0029(2)	0.0069(2)	0.0029(2)	0	0	0
Ti	0.0058(1)	0.0058(1)	0.0058(1)	0.0017(1)	0.0017(1)	0.0017(1)
O	0.0047(3)	0.0064(3)	0.0032(3)	0	0	0.0011(2)
$SrCu_3Ru_4O_{12}$						
Atom	U_{11}	U_{22}	U_{33}	U_{23}	U_{13}	U_{12}
Sr	0.0030(2)	0.0030(2)	0.0030(2)	0	0	0
Cu	0.0064(4)	0.0037(3)	0.0036(3)	0	0	0
Ru	0.0022(2)	0.0022(2)	0.0022(2)	-0.0001(1)	-0.0001(1)	-0.0001(1)
O	0.0024(8)	0.0054(9)	0.0056(1)	-0.0008(8)	0	0.0011(1)

B. List of Publications

B.1. List of Publications in Scientific Journals

1) C. G. F. Blum, C. A. Jenkins, J. Barth, C. Felser, S. Wurmehl, G. Friemel, C. Hess, G. Behr, B. Buchner, A. Reller, **S. Riegg**, S. G. Ebbinghaus, T. Ellis, P. J. Jacobs, J. T. Kohlhepp, H. J. M. Swagten,
Highly ordered, half-metallic Co_2FeSi single crystals
Applied Physics Letters **95**, 161903 (1 - 3), 2009

2) S. G. Ebbinghaus, **S. Riegg**, T. Götzfried, A. Reller,
Co-operative and frustration effects in novel perovskite-related phases
European Physical Journal Special Topics **180**, 91 - 116, 2010

3) P. Lunkenheimer, S. Krohns, **S. Riegg**, S. G. Ebbinghaus, A. Reller, A. Loidl
Colossal dielectric constants in transition-metal oxides
European Physical Journal Special Topics **180**, 61 - 89, 2010

4) J. Sebald, S. Krohns, P. Lunkenheimer, S. G. Ebbinghaus, **S. Riegg**, A. Reller, A. Loidl
Colossal dielectric constants: A common phenomenon in $CaCu_3Ti_4O_{12}$ related materials
Solid State Communications **150**, 857 - 860, 2010

5) N. Büttgen, H.-A. Krug von Nidda, W. Krätschmer, A. Günther, S. Widmann, **S. Riegg**, A. Krimmel, A. Loidl
Quantum Criticality in Transition-Metal Oxides
Journal of Low Temperature Physics **161**, 148 - 166, 2010

6) A. Dittl, S. Krohns, J. Sebald, F. Schrettle, M. Hemmidda, H.-A, Krug von Nidda, **S. Riegg**, A. Reller, S. G. Ebbinghaus, A. Loidl
On the magnetism of $Ln_{2/3}Cu_3Ti_4O_{12}$ (Ln = lanthanide)
European Physical Journal B **79**, 391 - 400, 2011

7) **S. Riegg**, U. Sazama, M. Fröba, A. Reller, S. G. Ebbinghaus
Synthesis, structure, and magnetic characterization of $La_{2-x}R_xRuO_5$ (R = Pr, Nd, Sm, Gd, Dy)
Physical Review B **84**, 014403 (1-12), 2011

8) **S. Riegg**, A. Reller, S. G. Ebbinghaus
Single crystalline and rare earth substituted La_2RuO_5 investigated by x-ray diffraction and

EXAFS spectroscopy
Journal of Solid State Chemistry **188**, 17 - 25, 2012

9) P. Sippel, S. Krohns, E. Thoms, E. Ruff, **S. Riegg**, H. Kirchhain, F. Schrettle, A. Reller, P. Lunkenheimer, A. Loidl
Dielectric signature of charge order in lanthanum nickelates
European Physical Journal B **85**, 235 - 242, 2012

10) **S. Riegg**, A. Günther, H.-A. Krug von Nidda, A. Loidl, M. V. Eremin, A. Reller, S. G. Ebbinghaus
Spin-singlet dimerization in La_2RuO_5 investigated using magnetic susceptibility and specific heat measurements
Physical Review B **86**, 115125 (1 - 8), 2012

11) **S. Riegg**, A. Günther, H.-A. Krug von Nidda, M. V. Eremin, A. Reller, A. Loidl, S. G. Ebbinghaus
Spin-dimerization in rare-earth substituted La_2RuO_5
European Physical Journal B **85**, 413 (1 - 10), 2012
(The cover artwork of the december issue 2012 was taken from this article.)

12) S. Yoon, E. H. Otal, A. E. Maegli, L. Karvonen, S. K. Matam, **S. Riegg**, S. G. Ebbinghaus, J. C. Fallas, H. Hagemann, B. Walfort, S. Pokrant, A. Weidenkaff
Improved photoluminescence and afterglow of $CaTiO_3:Pr^{3+}$ by ammonia treatment
Optical Materials Express **3**, 248 - 259, 2013

13) **S. Riegg**, S. Widmann, A. Günther, H.-A. Krug von Nidda, A. Reller, A. Loidl, S. G. Ebbinghaus
Suppression of the Ru (S = 1) dimerization in La_2RuO_5 by Ti substitution
Journal of Physics: Condensed Matter **25**, 126002 (1 - 12), 2013
(The cover artwork of issue 12, 2013 was taken from this article.)

14) **S. Riegg**, T. Müller, S. G. Ebbinghaus
Problems with the thermogravimetric determination of oxygen stoichiometries in pure and rare-earth substituted La_2RuO_5
Solid State Sciences **20**, 97 - 102, 2013

15) **S. Riegg**, A. Loidl, A. Reller, S. G. Ebbinghaus
Crystal structure and magnetic properties of Pr- and Ti-substituted La_2RuO_5
Materials Research Bulletin **48**, 4583 - 4589, 2013

16) S. Yoon, A. E. Maegli, L. Karvonen, S. K. Matam, A. Shkabko, **S. Riegg**, T. Großmann, S. G. Ebbinghaus, S. Pokrant, A. Weidenkaff
Bandgap tuning in $SrTi(N,O,F)_3$ by anionic-lattice variation
Journal of Solid State Chemistry **206**, 226 - 232, 2013

17) **S. Riegg**, A. Loidl, F. J. Garcia Garcia, A. Reller, S. G. Ebbinghaus
Mn Substituted Spin-Dimer System La$_2$RuO$_5$: I. Synthesis, Crystal Structure, and Valences
Physical Review B, submitted, 2013

18) **S. Riegg**, A. Wintermeier, H.-A. Krug von Nidda, S. Widmann, A. Günther, A. Reller, S. G. Ebbinghaus, A. Loidl
Mn Substituted Spin-Dimer System La$_2$RuO$_5$: II. Magnetic and Thermodynamic Properties
Physical Review B, submitted, 2013

B.2. List of Short Reports and Abstracts

1) S. G. Ebbinghaus, **S. Riegg**
   Strukturelle, magnetische und elektrische Aspekte rutheniumhaltiger Perowskite
   Z. Allg. Anorg. Chem. **634**, 2036, 2008

2) S. G. Ebbinghaus, **S. Riegg**
   Location of Rare Earth - substitutions in perovskite related La_2RuO_5
   HASYLAB Annual Report, HASYLAB, 2008

3) S. G. Ebbinghaus, M. Zenkner, **S. Riegg**
   Sn-L_{III} XANES on tin-substituted $BaTiO_3$
   HASYLAB Annual Report, HASYLAB, 2008

4) **S. Riegg**, S. G. Ebbinghaus, M. Zenkner, C. Ehrhardt
   Investigation and Comparison of the Ru-Valence in $LnCu_3Ti_{4-x}Ru_xO_{12}$ (Ln = La, Pr, Nd; $0.5 \leq x \leq 4$) at the L_{III}- and K-Absorption Edge studied with XANES
   HASYLAB Annual Report, HASYLAB, 2009

5) S. G. Ebbinghaus, R. Aguiar, **S. Riegg**, A. Weidenkaff
   EXAFS investigation of the local coordination geometry in oxynitrides $AB(N,O)_3$
   HASYLAB Annual Report, HASYLAB, 2009

6) S. G. Ebbinghaus, **S. Riegg**, R. Aguiar, D. Logvinovich, A. Weidenkaff
   XANES investigations on the chemical and valence shift in perovskite oxynitrides
   HASYLAB Annual Report, HASYLAB, 2009

7) **S. Riegg**, M. Zenkner, C. Ehrhardt, S. G. Ebbinghaus
   EXAFS Studies of the Rare Earth K-Edges in $La_{2-x}Ln_xRuO_5$ (Ln = Pr, Nd)
   HASYLAB Annual Report, HASYLAB, 2010

8) **S. Riegg**, S. G. Ebbinghaus
   Distribution of Pr on two crystallographic sites in $La_{2-x}Pr_xRuO_5$
   PSI Annual Report, Paul Scherrer Institut - SINQ, 2010

9) **S. Riegg**, H. Krause, S. Yoon, A. Weidenkaff, S. G. Ebbinghaus
   Investigation of the Mn- and Ru Valence in $La_2Ru_{1-x}Mn_xO_5$ ($0 \leq x \leq 0.25$) using XANES
   HASYLAB Annual Report, HASYLAB, 2011

10) **S. Riegg**, H. Krause, L. Karvonen, A. Weidenkaff, S. G. Ebbinghaus
    Studies on the Cu oxidation states of $LnCu_3Ru_xTi_{4-x}O_{12}$ (Ln = La,Pr,Nd) by Cu-K edge XANES
    HASYLAB Annual Report, HASYLAB, 2011

11) **S. Riegg**, H. Krause, S. Yoon, A. Weidenkaff, S. G. Ebbinghaus
    Ru-K edge EXAFS investigations of $La_{2-x}Ln_xRuO_5$ (Ln = Pr, Nd) after thermogravimetric

reduction
HASYLAB Annual Report, HASYLAB, 2011

12) S. Yoon, A. E. Maegli, L. Karvonen, **S. Riegg**, H. Krause, S. G. Ebbinghaus, A. Weidenkaff
Ti K-edge XANES study of SrTi(N,O,F)$_3$
HASYLAB Annual Report, HASYLAB, 2011

13) S. G. Ebbinghaus, **S. Riegg**, H. Krause, V. Pomjakushin
Structural Investigations of La$_4$Ru$_2$O$_9$ Using Powder Neutron Diffraction
PSI Annual Report, Paul Scherrer Institut - SINQ, 2012

14) **S. Riegg**, T. Walther, S. Yoon, A. E. Maegli, A. Weidenkaff, S. G. Ebbinghaus
Suppression of the structural transition in Ti-substituted La$_2$RuO$_5$
HASYLAB Annual Report, HASYLAB, 2012

15) **S. Riegg**, T. Walther, S. Yoon, A. E. Maegli, A. Weidenkaff, S. G. Ebbinghaus
Temperature dependence of the crystal structure of Mn-substituted La$_2$RuO$_5$
HASYLAB Annual Report, HASYLAB, 2012

16) T. Walther, S. Yoon, A. E. Maegli, **S. Riegg**, A. Weidenkaff, S. G. Ebbinghaus
Fe-K EXAFS and XANES studies of ferrite spinels MFe$_2$O$_4$ (M = Co, Ni, Mg, Mn, Zn)
HASYLAB Annual Report, HASYLAB, 2012

C. Danksagung

286

D. Lebenslauf

Name:	Stefan Riegg
Geburtstag:	27. April 1980
Geburtsort:	Landsberg am Lech
Familienstand:	ledig

Schulbildung:

1986 - 1990:	Grundschule Kaufering
1990 - 1999:	Dominikus-Zimmermann-Gymnasium Landsberg am Lech
	Abschluss: Abitur zur allgemeinen Hochschulreife

Wehrdienst:

1999 - 2000:	Technischer Zug der Flugbetriebsstaffel des JaboG 32 Lagerlechfeld

Studium:

10/2000 - 01/2007	Physikstudium an der Universität Augsburg
10/2002	Vordiplom Physik
01/2007	Abschluss des Physikstudiums als Diplom Physiker
	Thema der Diplomarbeit:
	"Erste Messungen von Plasmaparametern mit optischer Emissions- spektroskopie in Quellen für negative Ionen (H^-, D^-)"

Promotion:

02/2007 - 01/2014	Promotion am Lehrstuhl für Festkörperchemie und Lehrstuhl für Experimentalphysik V an der Universität Augsburg
02/2007 - 12/2009	Wissenschaftlicher Mitarbeiter im SFB 484
01/2010 - 06/2010	Wissenschaftlicher Mitarbeiter des Lehrstuhls für Festkörperchemie
07/2010 - 01/2014	Wissenschaftlicher Mitarbeiter des Lehrstuhls EP V (und TRR 80)
seit 07/2012	Mitglied der Graduiertenschule "Resource strategy concepts for sustainable energy systems" des Instituts für Materials Resource Management